Republic of Iraq
Ministry of Higher Education and Scientific Research
University of Babylon
College of Materials Engineering
Department of Metallurgical Engineering

Surface Modification of Ti-6Al-7Nb Biomedical Alloy using Bioceramics Coatings by Micro-Arc Oxidation (MAO) Process

A thesis

Submitted to the Council of the College of Materials Engineering/ University of Babylon in Partial Fulfillment of the Requirements for the Degree of Doctor of Philosophy in Materials Engineering/Metallurgical Engineering

Qabas Khalid Naji Salah

(B.Sc. in Metallurgical Engineering, 2013)
(M.Sc. in Metallurgical Engineering, 2016)

Supervised by

Prof. Jassim Mohammed Salman (Ph.D.)
Prof. Nawel Mohamed Dawood (Ph.D.)

2022 A.D 1443 A.H

وَلَقَد اتَيْنَا دَاوُودَ وَسُلَيْمَانَ عِلْمًا وَقَالَا الْحَمْدُ للهِ الَّذِي فَضَّلَنَا عَلَى كَثِيرٍ مِنْ عِبَادِهِ الْمُؤْمِنِينَ

صدق اللهُ العلِي العظيمُ

سورة النمل (أية 15)

Dedication

It is dedicated to:

My merciful God

Imam AL-Mahdi (Alloh hastens his reappearance)

To the light of my eyes, the light of my path, and the joy of my life.

My mother, then my mother, then my mother….

Whose prayers and words were the companion of brilliance and excellence.

Qabas 2022

(Examining Committee Approval Sheet)

We certify that we have read this thesis entitled ***"Surface Modification of Ti-6Al-7Nb Biomedical Alloy using Bioceramics Coatings by Micro-Arc Oxidation (MAO) Process"*** and as an examining committee, we have examined the student ***(Qabas Khalid Naji)*** in contents and that is related to it. And that in our opinion it meets the standard of a thesis for the Degree of Philosophy-Doctorate in Materials Engineering.

Signature
Prof. Dr. Sami A. Ajeel
Committee Chair
Date: / / 2022

Signature
Prof. Dr. Hayder H. J. Jamal Al- Deen
Committee Member
Date: / / 2022

Signature
Prof. Dr. Samir Hamid Awad
Committee Member
Date: / / 2022

Signature
Prof. Dr. Ayad M. Takhakh
Committee Member
Date: / / 2022

Signature
Prof. Dr. Ekbal M.S. Salih
Committee Member
Date: / / 2022

Signature
Prof. Dr. Jassim M. Salman Al-Murshdy
Supervisor Member
Date: / / 2022

Signature
Prof. Dr. Nawal Mohamed Dawood
Supervisor Member
Date: / / 2022

Approval of the Department of
Metallurgical Engineering
Head of Department.

Approval of the College
of Materials Engineering
Dean of college.

Signature
Prof. Dr. Saad Hameed Al-Shafaie
Date: / / 2022

Signature
Prof. Dr. Imad Ali Disher
Date: / / 2022

Supervisors' Certificate

we certify that this thesis entitled **"Surface Modification of Ti-6Al-7Nb Biomedical Alloys using Bioceramics Coating by Micro-Arc Oxidation (MAO) Process"** was Prepared by **(Qabas Khalid Naji)** under my supervision at the Department of Metallurgical Engineering/ College of materials Engineering/ University of Babylon in partial fulfillment of the requirements for the degree of Philosophy-Doctorate in Materials Engineering/Metallurgical

Signature:

Prof. Dr.	Prof. Dr.
Jassim Mohammed Salman	Nawal Mohammed Dawood
/ / 2022	/ / 2022

Acknowledgements

All Praise is for ***Allah***, The Almighty for granting me the bless of finishing this thesis.

First, I would like to express my thanks, respect and deepest appreciation to my supervisor ***Prof. Dr. Jassim Mohammed Salman*** for his incessant advice, unlimited encouragement and endless help throughout the whole work.

Secondly, I would like to thank my ***Prof. Dr. Nawal Mohammed Dawood*** (University of Babylon) for her effortless helps and scientific tips that helped to facilitate doing the project in the right path to success.

I would also like to thank ***Prof. Dr. Samir Hamid Awad*** (department of ceramics) for his scientific tips that helped to facilitate doing the coating and ***Ms. Farqad Saleem Murad*** (in material engineering department of ceramics) for her help to tutorial on coating device.

Lastly, I am so grateful to my family especially my lovely ***"mother"*** is deeply appreciated. Their love has been for me a powerful source of inspiration and energy. I am enormously grateful and thankful to all persons who believed in me and provided me with the love, support and encouragement that have made all this possible.

Qabas Khalid Naji

Abstract:

The current study aims to use Ti-6Al-7Nb alloy in medical applications include (orthopedic and dental implant) but it has poor wear resistance and hardness. So, Micro-Arc Oxidation (MAO) technique is adopted by applying breakdown voltage to an aqueous solution containing modifying components. It is an innovative chemical/electrochemical way of producing thick and durable ceramic coatings on titanium alloys.

In MAO electrolyte, nano additives like as hydroxyapatite (HA) and zirconia (ZrO_2) are used. The process was carried with different voltages (300, 350, and 400) V, current of (1-5) A, and deposition times (7, 15, 30, and 60) min by a home-made coating system. The coating characteristics are identified by using field emission scanning electron microscopy (FESEM), (EDX), atomic force microscopy (AFM) and the resulted phases are identified by X-Ray diffraction (XRD), mechanical test (microhardness, wear, and adhesion test). The electrochemical test in the Ringer's and Saliva's solution using a potentiodynamic and cyclic polarization tests and ion release. Moreover, the antibacterial behavior with bacterial strains of *E.coli* is investigated for the coating layer.

The results of the tests showed the possibility of deposition of ceramics coatings on the surface of Ti-6Al-7Nb alloy by using additives and different voltages and deposition times. The ceramics layer of titanium oxide (TiO_2) which is formed during coating porous and homogenous distribution in group A and high hardness (311.5HV) at (350V & 30min) and wear resistance which leads to weight loss and decreases wear rate (9.46×10^{-6}) and corrosion rate

equals to (C_R= 0.1114 mpy) in Ringer's solution with increased voltage and time increased thickness layer (56µm) and increased porosity and roughness and increase wettability. A composite nano ceramic layer was obtained from hydroxyapatite (HA) with TiO_2 in group B, nano ZrO_2 with TiO_2 in group C, and HA, ZrO_2 with TiO_2 in group D were observed with increased voltage and time increased thickness layer and concentration of HA and ZrO_2 and decreased porosity compared TiO_2 layer thus, the best results were obtained in terms of hardness (368.1 HV at HA/TiO_2 layer for 400V&30min), (466.7 HV at ZrO_2/TiO_2 layer for 400V&30min), and (584.9 HV at HA/ZrO_2/TiO_2 for 400V&15min). The wear resistance equal to (4.33×10^{-7} at HA/TiO_2 layer for 400V&30min), (1.06×10^{-7} at ZrO_2/TiO_2 layer for 400V&30min), and (9.84×10^{-8} at HA/ZrO_2/TiO_2 for 400V&15min).

Improvement corrosion resistance in two solutions by using a potentiodynamic and cyclic polarization equals (87.4% and 87.83% for sample B_{11} in Ringer's and Saliva's solutions respectively), (94% and 88.13% for sample C_{11} in two solutions), and (88% and 91.12% at HA/ZrO_2/TiO_2 for 400V and 30min in two solution) and increased wettability by decreased contact angle.

The amount of ions released are less than that of the base alloy in two solutions equal to (0.0183, and 0.0191) ppm in Ringer's and Saliva's solution for TiO_2 coating and (0.0074, and 0.0077) ppm, HA/TiO_2, and ZrO_2/TiO_2 reshod to (0.0066, and 0.0048) ppm, for nano composite coating HA/ZrO_2/TiO_2 (0.0017, and 0.0011) pp. The ZrO_2/TiO_2 and HA/ZrO_2/TiO_2 coating has a strong antibacterial effect that could prevent the bacteria growth.

List of Contents

Lest of Abbreviations

Abbreviations	Description	Units
AC	Alternating Current	
AFM	Atomic Force Microscopy	
AEO	Anodizing Electrolytic Oxidation	
APTT	Activated Partial Thromboplastin Time	
BCC	Body Centered Cubic	
BM	Base Metals	
BG	Bio glass	
BFGF	Basic Fibroblast Growth Factor	
CA	Contact Angle	degree
CVD	Chemical Vaper Deposition	
DC	Direct Current	
EDS	Energy Dispersive Spectrometer	
EPD	Electrophoretic Deposition	
EW	Equivalent Weight	
FCC	Face Center Cubic	
FESEM	Field Emission Scanning Electron Microscopy	
HA	Hydroxyapatite	
HBSS	Hanks' Balanced Salt Solution	
HV	Hardness Vickers	Kg/cm^3
HCP	Hexagonal Crystal Structure	
LOM	Light Optical Microscope	

MAO	Micro-Arc Oxidation	
MAH	Alkali Heat Treatment	
MFR	Mixed Fretting Regime	
OCP	Open Circuit Potential	mV
PBS	Phosphate Buffered Saline Solution	
PD	Plasma Discharging	
PEO	Plasma Electrolytic Oxidation	
PETP	Poly Ethylene Terephthalate	
PT	Prothrombin Time	
PP	PolyPropylene	
PPM	Part Per Million	Mg/l
PVD	Physical Vaper Deposition	
SAOS-2	Human Osteoblastic Cell Line	
SBF	Simulated Bodily Fluid	
SEM	Scanning Electron Microscopy	
SCE	Saturated Calomel Electrode	
SR	Slip Regime	
TF-XRD	Thin Film X-ray Diffraction	
THR	Total Hip Replacement	
TKR	Total Knee Replacement	
XRD	X-ray Diffraction	
XPS	X-Ray Photoelectron Spectroscopy	

Lest of symbols

Abbreviations	Description	Units
A	Anatase	
Ca, EDTA	Calcium, Ethylene Diamine Tetra Acetate	
C_R^o	Corrosion Rate of Master Sample (Before Coating)	mpy
C_R	Corrosion Rate of Master Sample (After Coating)	mpy
D	Displacement Amplitudes	mm
$E_{corr.}$	Corrosion Potential	mV
HA	Hydroxyapatite	
$i_{corr.}$	Corrosion Current Density	$\mu A/cm^2$
mpy	Mils Per Year	
R	Rutile	
TiO_2	Titania or Titanium Dioxide	
Y_2O_3	Yttrium	
ZrO_2	Zirconia	
α	Alpha	
β	Beta	
T_β	Transformation Temperature of β phase	
T_α	Transformation Temperature of α phase	
F_n	Normal load	N

List of Figures

List of Tables

Chapter One
Introduction

CHAPTER ONE
INTRODUCTION

1.1 General Review

Biomaterials are now widely used in medicine to help patients recover function and heal after an accident or sickness. As a result, biomaterials aid in enhancing human quality of life and longevity, and the area of biomaterials has experienced fast expansion in response to the demands of an aging population [1].

The usage of biomaterials may be traced back to antiquity, when ancient Egyptians utilized animal sinew sutures. Biomaterials is a modern field that combines medicine, biology, physics, and chemistry, as well as tissue engineering and materials science [2]. Implants (sutures, bone plates, and joint replacements) and clinical devices (pacemakers, synthetic hearts, and blood tubes) are commonly employed to update and/or restore the features of damaged or deteriorating tissues or organs, resulting in improved patient satisfaction [3].

Since the development of biomaterials in the preceding decade, tissue engineering, regenerative medicine, and various metals, ceramics, polymer, and even living cells and tissue have all been discovered to be beneficial. For usage in biomedical goods and equipment, they can be molded or machined into components, coatings, fibers, films, foams, and fabrics [4].

The acceptance of the biomaterial by the human body is the first and most important criterion for its selection. A biomaterial used for an implant should have certain characteristics in order to be utilized in the body for a long time without causing rejection [5].

Metals, polymers, ceramics, and composites are the most prevalent types of biomedical materials [6]. The classes are employed alone and in combination to

create most today's implantation devices in Table (1.1). Depending on the implant's requirements, composites of the same material or composites of various materials were utilized to create the implant [3, 7].

The biomaterial must not contain any of the following: [7]

1. Activated unfavorable responses by altering plasma proteins (including enzymes).
2. Induced thrombus development, an inflammatory reaction, or malignancy (cancer).
3. damage or sensitize the blood's cellular components
4. Elicit poisonous or allergic reactions
5. Electrolyted depletion.
6. Sterilization may have an impact.

Because of their high heat conductivity and mechanical characteristics, metals are employed (used) as biomaterials. Stainless steel 316L, cobalt chromium alloys (CoCrMo), Ti-alloys, and a range of other materials are commonly employed in load-bearing applications and must have adequate fatigue energy to resist the rigors of daily life (including tantalum, gold, dental amalgams, and other "specialty" metals) are increasingly often used for biomedical application [8].

Titanium alloys are rapidly gaining popularity as a technological material. as a result of their excellent properties, an interest in their usage in mechanical and tribological additives within the biomedical area (field) is rapidly growing [9].

Table (1.1): Advantages, disadvantages and application of metals, ceramics and polymers [3,7].

Biomaterial	Example	Advantage	Disadvantage	Application
Metallic	Stainless steel	High strength, tough, high ductility, biocompatible	May corrode, dense, difficult to make.	Joint replacements, bone plates, screws, dental root implants, Artificial heart valves, pacemaker cases and vascular stents.
	Co-Cr alloys			
	Ti and its Alloys			
	Gold or platinum			Dental fillngs, electrodes for cohlear implants.
	Ag-Sn-Cu alloys			Dental amalgams.
Ceramic	Alumina	Very biocompatible, inert, strong in Compression.	Brittle, not resilient, difficult to make, low tensile and shear strength under fatigue loading.	Dental, femoral head of hip replacement, coating of dental and orthopedic implants, acetabular and femoral components, vertebrae spacers and extensors.
	Zirconia			
	Calcium phosphates			
	Bio glass-ceramic			
Polymers	Polyethylene,	Resilient, Easy to fabricate.	Not strong, Deforms with time, may degrade.	Sutures, blood vessels, hip socket, ear, nose, lenses, heart valves, and other soft tissues.
	Polypropylene,			
	Collagen			
	PVC			

Titanium alloys are rapidly becoming the material of choice for nearly all applications, owing to their high strength, light weight, excellent corrosion resistance, complete inertness to the frame environment, better interoperability, low Elastic modulus, and real potential to sign up with bone or other tissues [10]. Describes various Titanium alloys' biological uses in Figure (1.1) [11-14].

Because of their thermal stability, chemical inertia, and limited solubility in bodily fluids, titanium alloys spontaneously develop a passive oxide layer (primarily TiO_2) that can shield (protect) these alloys from corrosion to some extent [15].

Low wear, abrasion resistance and hardness, are problems that are solved by surface modification to enhance the abrasive wear corrosion resistance [16]. Therefore, a modification is required to overcome these limitations by coating of the metallic substrate with bioactive or bioceramic materials. Using the bioactive coatings on the implants is requisite for achieving the sufficient bioactivity of the implant [17].

The coating layer promotes the osseointegration and decreases the corrosion rate by acting as a barrier to prevent or reduce the undesired release of toxic metallic ions to the surrounding tissue. The bioceramic coatings are applicable in dentistry, joint replacement, tissue engineering and surgical transplant of bone [18].

To enhance the surface characteristics of Ti implants, a variety of methods have been devised. Electrophoretic deposition EPD, ion implantation, sol gel, chemical vapor deposition, plasma spray deposition micro-Arc oxidation (MAO), and other methods are among them [19].

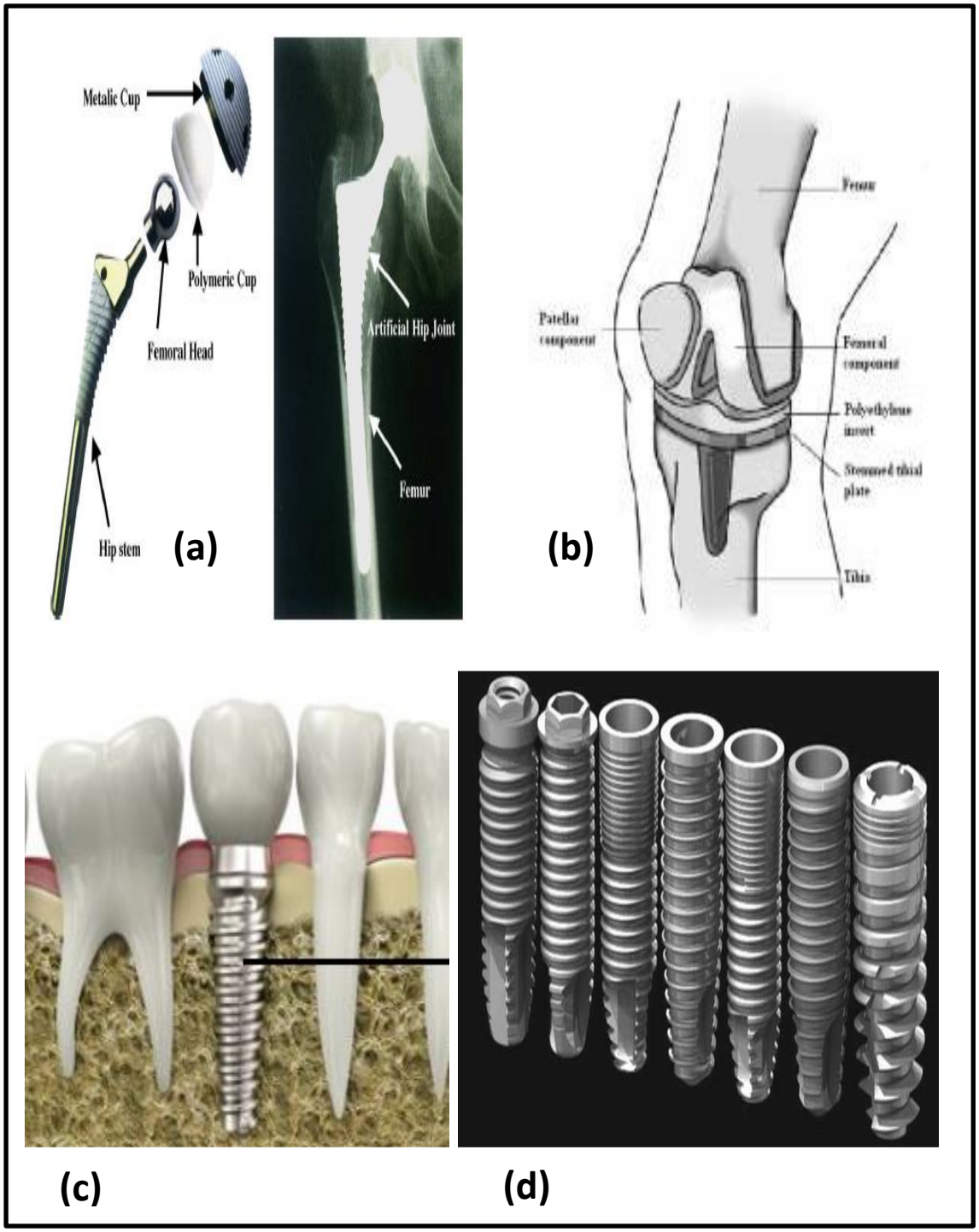

Figure (1.1): some of Ti alloys biological applications (a) An implant for total knee replacement [11], (b) An implant for total hip replacement [12], (c) the development of root form designs of titanium implant [13], and (d) a photograph of commercial dental implant designs [14].

Hydroxyapatite (HAp) coatings or its variations can be applied to otherwise bioinactive implants to make their surface bioactive, thus achieving fast healing and recovery. HAp [Ca_{10} $(PO_4)6(OH)_2$] has a bone-like structure and is not only biocompatible but is also bioactive [20]. The HAp coating on metal implants are bonded to the surrounding tissue and exhibited good fixation to the host bones and also supported the substrate from corrosion attack in contact to the body fluids, while the underlying metal substrate afford the load [21]. Despite the biocompatibility and bioactivity of the HAp coating, the major limitation of the HAp is its weak mechanical integrity, brittle material and not adequate bone growth, which limit its application to the non-load bearing regions only in the human body [22].

To enhance the mechanical properties of the HAp and to produce coatings that are more bioactive with better mechanical properties, another type of bioceramics materials is combined with the HAp like Zirconia (ZrO_2) which appears bioinert ceramics materials [23].

Because of its great mechanical strength and fracture toughness, ZrO_2 is a biomaterial with a promising future. ZrO_2 ceramics have several advantages over other ceramic materials due to the transformation toughening mechanisms operating in their microstructure that can be manifested in components made out of them. Although, investigations for various therapeutic devices are ongoing, the usage of zirconia ceramics as biomaterials began over 20 years ago and is presently used in total hip replacement (THR) but developments are in progress for application in other medical devices [24].

1.2 Aim of the work

The aim of the current work using the MAO technique to deposit a suitable layer of nanocomposite coating of HA/TiO_2, ZrO_2/TiO_2 and HA/ZrO_2/TiO_2 on the Ti-6Al-7Nb substrate and investigate of the most essential variables (voltage and deposition time) to obtain the best properties of coating layer in order to improves biocompatibility, and bioactivity in dental and orthopedic implants. The study includes:

1. Enhancing of corrosion performance.
2. lowering the amount of metallic ions released from the implant by exhibiting an efficacious chemical barrier against the metal ions release from the metallic implant.
3. Increasing hardness and wear resistance.
4. Improving an antibacterial coating layer.

Chapter Two
Theoretical Part & Literature Review

CHAPTER TWO
THEORETICAL PART AND LITERATURE REVIEW

2.1 Introduction

This chapter is divided into two sections; the first one presents the definition of biomaterials, properties, classification of Ti-alloys, properties of Ti-6Al-7Nb alloy, and surface modification. In addition, it explains the Micro arc oxidation (MAO) process, the methods used to deposit Tianna layer, process parameters, advantages and disadvantages of Micro Arc Oxidation, and method's applications have been mentioned. Also, titanium oxide, Hydroxyapatite, and zirconia oxide were explained. The second section includes the related literature survey.

2.1 Introduction to Biomaterial

Biomaterials are artificial or natural materials that are designed to operate properly in biological environments where they are utilized to direct complement or substitute the function of the human body's living tissues [25]. Biomaterials are commonly utilized for repairing or replacing musculoskeletal system components such as bones, joints, and teeth. These materials utilized as implants or as prostheses [26].

An implant material's design should seek to give the necessary durability, functionality, and biological response. Functionality and durability depend on the material's bulk characteristics, while biological reaction depends on the material’s surface characteristics such as topography, roughness, chemistry, wettability and charge of the material surface. Biocompatible implant materials must be non-toxic, non-carcinogenic, with small or no response of the host body as well as have chemical stabilization and resistant to corrosion [27].

Biocompatibility classifies implants based on the sort of biological reaction they generate in long-term interactions with the host tissue

Implant biocompatibility may be divided into three categories [28]:

- Biodegradable / bioresorbable: gradually resorbed implant and substituted significantly by fresh bone growth.
- Bioinert: no important biological bond between implants and bone.
- Bioactive: bone and implant connect to each other immediately after implantation leads to the formation of chemical bonds along the interface.

Different material classes such as metals, ceramics, polymers and composites are now commonly used in the manufacture of bio-implants. Bio implants are widely used in orthopedic, cardiovascular, dental, experimental and veterinary medicine as shown in Figure (2.1) [3].

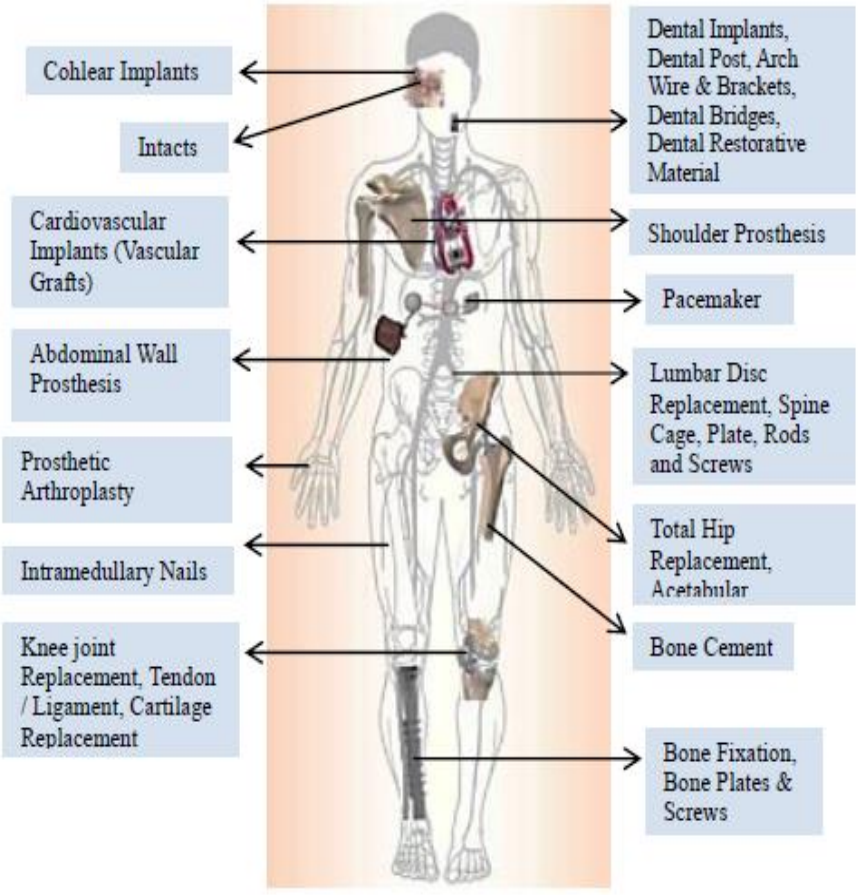

Figure (2.1): Biomaterials for human application [3].

2.3 Requirements Properties for bimetallic implant

The most important indications of the appropriateness of metallic implants in hostile settings are corrosion resistance and biocompatibility [29]. These biomaterials are superior metallic materials due to of their ability to carry significant stress and go through the plastic deformation prior unit to the fail, as this shown their specific UTS and fracture toughness [30].

Biomaterial design and selection are influenced by the medical use. New biomaterial development is a multidisciplinary endeavor that frequently necessitates collaboration among biomedical engineers, pathologists, and clinicians are all examples of material scientists and engineers. An implant should have the following characteristics to serve for a prolonged amount of time without rejection [31].

2.3.1 Mechanical characteristics

The mechanical characteristics of a material determine the type of material that will be used for a specific application. Hardness, tensile strength, modulus, and elongation are some of the most important characteristics [32]. The fatigue strength of a material defines its reaction to repeated cycle loads or stresses, and this characteristic has an impact on the long-term success of a cyclic-loading implant [33], as illustrated in Table (2.1) [34].

Biomechanical incompatibility occurs when an implant break owing to insufficient strength or a mechanical mismatch between the bone and the implant. The material that will be used to substitute bone is predicted to have the same modulus as bone. The magnitude of the bone modulus varies from (10 to 40) Gpa depending on the type of bone and the direction of measuring [34].

Table (2.1): The mechanical properties of various biomaterials [34].

Material	Density (g/cc)	Compressive strength (MPa)	Elastic Modulus (GPa)	Toughness (MPa $m^{1/2}$)	Tensile strength (MPa)
Human Bone: Cancellous Bone Cortical Bone	 1.8-2.1	 4-12 130-180	 0.02-0.5 10-40	 3-6	 10-20 82-114
Metals: Ti and Alloys Co-Cr-Mo al-loys Stainless Steel Magnesium	 4.4-4.5 8.3-9.2 7.9-8.1 3.1	 590-1117 450-1896 170-310 65-100	 55-117 200-253 189-205 41-45	 55-115 100 50-200 15-40	 900-1172 400-1030 515-620
Polymers: HDPE UHMWPE PTFE PMMA	 0.94-0.96 0.41-0.49 2.1-2.2 1.12-1.2	 25 28 30-60 45-107	 1-2 1 0.3-0.7 0.8-1.3	 - 20 1.8-3.3	 27 38-48 15-40 38-80
Ceramics: Zirconia Alumina Bio glass HAP AW glass Ce-ramic	 6.1 3.98 2.7 3.1 -	 2000 4000-5000 1000 600 1080	 220 380-420 75 73-117 118	 9 3-5 - 0.7 1.9-2	 800-1500 282-551 38-48
Composites: CF/PMMA CF/Polysulfon e CF/Epoxy Stycast CF/Epoxy Hy-sol			 55 76 30 24		 772 938 535 207

2.3.2 Biocompatibility

The materials utilized as implants should be extremely safe and should not induce any inflammatory or allergic reactions in humans. The bio-

materials' success is mostly determined by the human body's reaction to the implant, which determines a material's biocompatibility [36].

The host reaction generated by the material and the material's deterioration in the bodily environment are the two primary variables that impact a material's biocompatibility. When implants come into contact with human tissues and fluids, various responses occur between the host and the implant material, and these reactions determine whether or not the materials are acceptable to our system. Thrombosis, which includes blood coagulation and platelet adherence to biomaterial surfaces, and fibrous tissue encapsulation of biomaterials implanted in soft tissues are two biocompatibility concerns [37]. Implant biocompatibility is influenced by a number of variables, including size, form, material composition, surface wettability, surface roughness, and charge are all factors to be considered [38], as illustrated in Figure (2.2) [34].

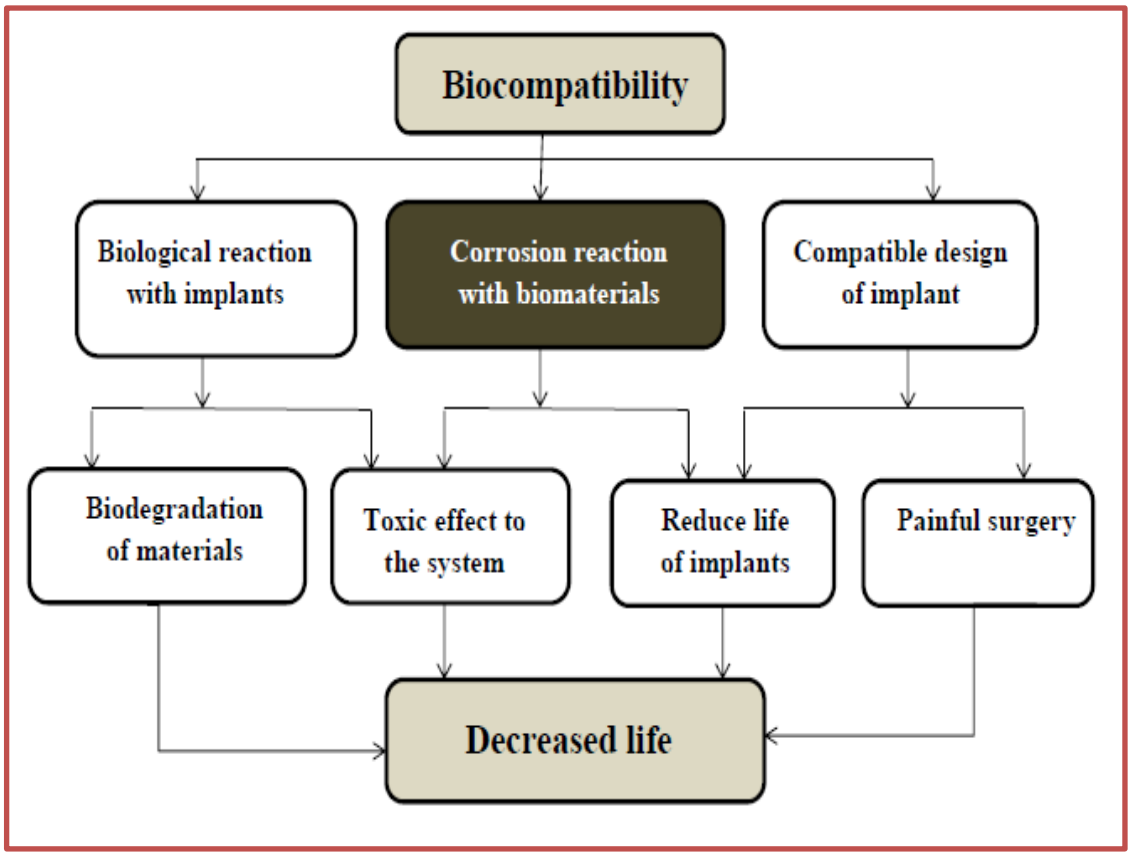

Figure (2.2): Factors affecting biocompatibility [34].

2.3.3 Resistance of corrosion and wear

The corrosion resistance and wear of the implants in body fluid are limited because leak non-compatible metal ions into the body, as shown in Figure (2.3) [39]. Allergic and toxic responses have been seen in response to the discharged ions [40]. Low wear resistance leads to implant loosening, and wear debris has been shown to trigger a variety of responses in the tissue where it is deposited [31].

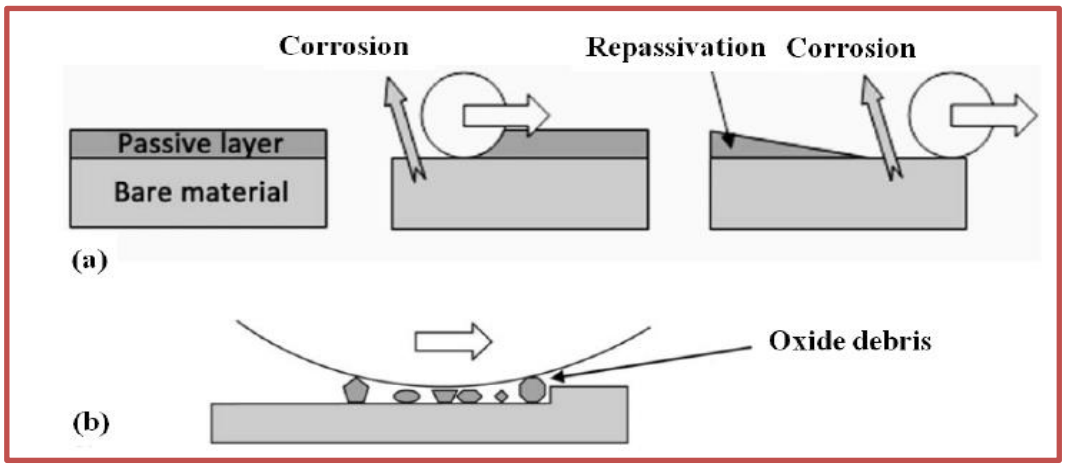

Figure (2.3): Synergistic effect of corrosion on wear and vice versa: (a) Corrosion accelerated by friction; (b) Abrasion accelerated by corrosion products [39].

2.3.4 Osseointegration

Osseointegration is defined as direct contact between viable remodeling bone and an implant with no intervening soft tissue [41]. Implant loosening is caused by the failure of an implant surface to integrate with the surrounding bone and other tissues owing to micromotions [15]. If the implant is not adequately integrated with the bone, a fibrous tissue forms between the bone and the implant [38]. As a result, materials with the right surface are critical for the implant to integrate effectively with the surrounding bone. Surface chemistry, surface roughness, and surface topography all have a role in osseointegration development [31].

2.3.5 Non-toxic

The material should not be genotoxic (causes harm to individual cells) or cytotoxic (alters the DNA of the genome) [40].

2.3.6 Host Response

The host response is the reaction of the host organism to the implanted substance or device (both local and systemic) [3].

2.3.7 Bio-functionality

In physical and mechanical terms, bio-functionality serves a specific purpose. In service, the material must meet its design requirements[3]:

- Stress distribution and load transmission (e.g. bone replacement).
- Movement is made possible through articulation (e.g. joint replacement for the knee).
- Blood and fluid flow regulation (e.g. artificial heart).
- Filling the empty space (e.g. cosmetic surgery).
- Stimuli electrical (e.g. pacemaker).
- Sound transmission (e.g. implanted lenses).
- Light transmission (e.g. implanted lenses and cochlear implant).

2.3.8 Tissue Pathobiology and Functional Structure

Biomaterials containing medical devices are implanted into tissues and organs. As a result, field workers must understand essential concepts determining the structure of normal and pathological cells, tissues, and organs, as well as the methods for researching the structure and function of normal and abnormal tissues, and the underlying mechanisms of disease processes [3].

2.3.9 Appropriate Design and Manufacturability

Machineable, moldable, and extrudable biomaterials are ideal. Finite element analysis is a powerful analytical tool that may be used in the design of any implant. In order to provide the quality required in orthopaedic devices, sophisticated production techniques are now required [3].

2.3.10 Adequate Strength

The strength of the materials used to make the implants has an impact on the artificial organ's fracture. The implant might be fractured if the strength is insufficient. When the bone implant interface begins to deteriorate, under stress, the creation of soft fibrous tissue at the implant-bone interface can allow for higher relative movement between the implant and the bone [42]. This causes the patient agony, and over time, the pain becomes unbearable, prompting a revision surgery to replace the implant [3].

2.2.10 Modulus equivalent to that of bone

Yield strength is essentially connected with the necessity of a lower modulus near that of human bones for important applications such as total joint replacement [43]. Large differences in Young's modulus between implant material and surrounding bone can contribute to the generation of severe stress concentrations, such as load shielding from natural bone, which can weaken the bone and deteriorate the implant/bone interface, causing implant loosening and failure [44]. The juvenile moduli of biomaterials are compared in Figure (2.4) [45]. The modulus of any biomaterial is a key consideration [43, 44].

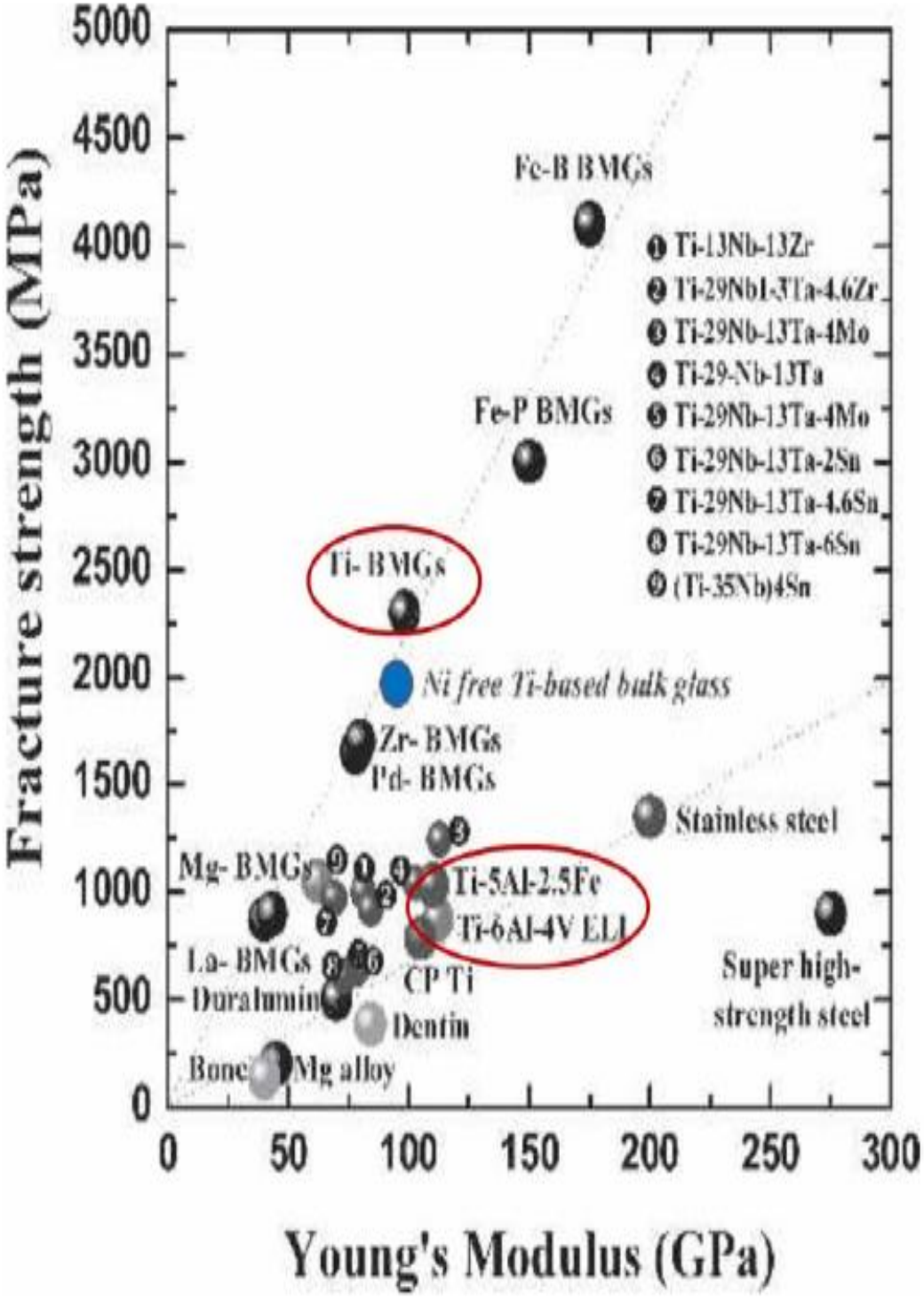

Figure (2.4): Relationship between tensile strength and Young's modulus for some typical biomaterials [45].

2.4 Failures of implant devices

Metallic orthopedic implants are often used as components of reconstructive devices (e.g. hip or knee joint replacement) or fracture fixation products in the skeletal system of a person (e.g. plates, screws and nails). The design of these implants is governed and limited by the architecture and physiology of the human body's skeletal structure [46]. The mechanical and chemical stability of implant materials, as well as their biocompatibility in the milieu of tissues and bodily fluids, are critical for the effective treatment of bone fractures and replacements [30].

Corrosion is the major problem affecting the service life of orthopaedic implants. Adding inhibitors, changing the pH of the electrolyte and its composition, lowering temperature, adding protective coatings, providing electrical current, and other methods are used in industry to regulate this phenomenon. Unfortunately, most of these techniques are ineffective for orthopaedic implants since the bodily environment is set and cannot be changed without causing biological effects [46]. Figure (2.5) [30] graphically depicts the different reasons for revision surgery as well as the primary remedies.

Tissue reactions to biomaterials can be divided into four categories [40]:

- The material is toxic, and the surrounding tissue dies.
- The material is nontoxic and biologically inactive.
- The material is nontoxic and active, and the tissue bonds with it.
- The material is nontoxic and dissolves, and the surrounding tissue replaces.

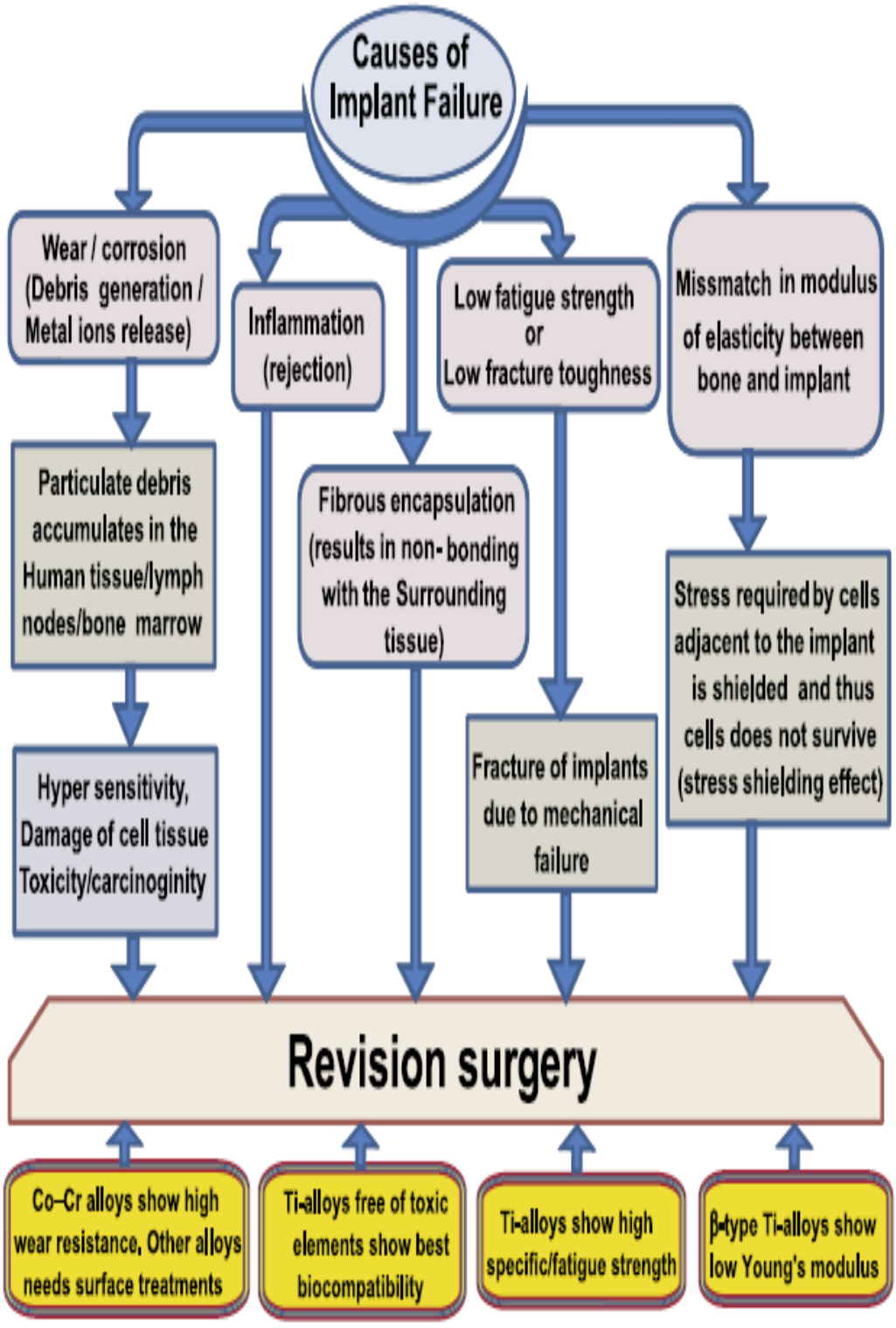

Figure (2.5): Various causes for failure of implants that leads to revision surgery, footed with a proposed system for better performance [30].

2.5 Corrosion of Orthopedic Implants

Orthopedic implants include both temporary implants such as plates and screws and permanent implants that are used to replace hip, knee, spinal, shoulder, toe, finger etc. The corrosion mechanisms that occur in temporary implants are crevice corrosion at shielded sites in screw/plate interface and beneath the heads of fixing screws and pitting corrosion of the implants made of SS [47]. Types of corrosion in biomaterial implants made of conventional materials as shown in Table (2.2) [9].

Wear is the main cause of orthopedic implant failure, which in turn is found to accelerate the corrosion. As a result, high wear resistant materials like ceramics and Co-Cr are frequently used to make orthopedic implants. Only Ti-based alloys are utilized in hip implants for the femoral component, whereas the ball is constructed of Co-Cr or other strong ceramics [48]. The type and distribution of corrosion products produced into the body by these orthopaedic implants, on the other hand, continues to be a major concern [39]. As a result, metallic biomaterials' corrosion resistance is critical. Titanium and its alloys, unlike many other materials, corrode either rapidly or slowly, depending on the environment [49]. Titanium and titanium-based alloys are utilized extensively in biomedical and dental applications, as previously stated. This is due in part to the native titanium dioxide layer that shields the metal from further oxidation [50], which provides stability and corrosion resistance.

The major consideration when designing and selecting metals and alloys for in vivo use is corrosion. During corrosion processes, allergenic, toxic / cytotoxic, or carcinogenic species (e.g., Ni, Co, Cr, V, Al) may be released into the body [51].

Table (2.2): Types of Corrosion in the Conventional Materials Used for Biomaterial Implants [9].

Type of Corrosion	Material	Implant Location	Shape of the Implant
Pitting	304 SS, Cobalt based alloy	Orthopedic/ Dental alloy	
Crevice	316 L stainless steel	Bone plates and screws	
Stress Corrosion cracking	C0CrMo, 316 LSS	Only in *in vitro*	
Corrosion fatigue	316 SS, CoCrNiFe	Bone cement	
Fretting	Ti6Al4V, CoCrSS	Ball Joints	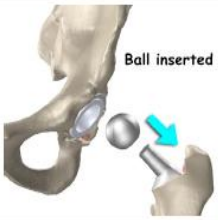
Galvanic	304SS/316SS, CoCr+Ti6Al4V, 316SS/Ti6Al4V Or CoCrMo	Oral Implants Skrews and nuts	
Selective Leaching	Mercury from gold	Oral implants	

2.6 Wear resistance

The damage to a solid surface, generally involving progressive loss of material, due to relative motion between that surface and a contacting substance or substances is wear [52]. The type of materials utilized, lubricant, contact pressures, surface hardness and roughness , fretting / sliding / rolling velocity, number of application cycles, and environment are all said to affect wear mechanisms in biomedical implants.

The abrasion and wear resistance of a metallic biomaterial determines its service life. Incompatible metal ions are released into the body when the implant's wear resistance is lowered, loosening the implant as depicted in Figure (2.6). Furthermore, the buildup of wear particles in tissue can cause a range of reactions. As a result, producing biomaterials with high wear resistance is critical for extending the life of the biomaterial [32].

wear mechanisms for titanium alloys are roughly grouped into abrasive wear and adhesion wear dependent on the kind of alloy and its microstructures. However, the wear resistance is altered according to the testing conditions. Based on friction wear tests at various loads [53].

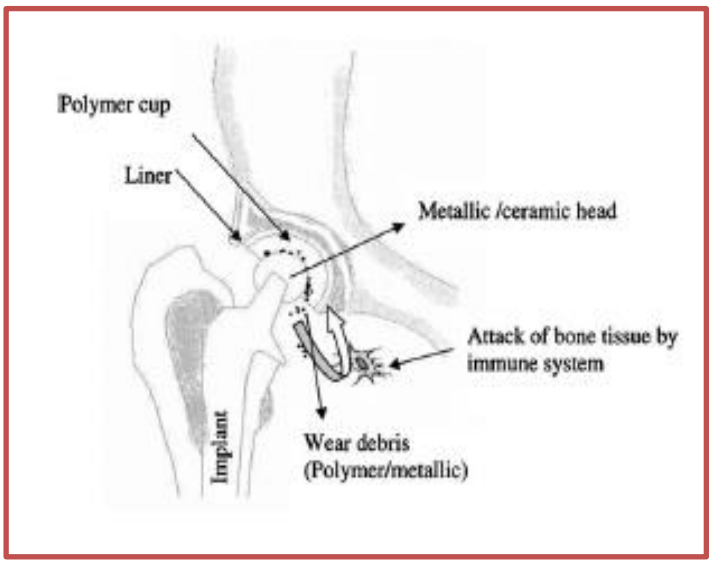

Figure (2.6): Wear of implant [31].

2.6.1 Classification of wear mechanisms

Wear can occur in biomedical applications such as implants through five major mechanisms, as shown in Figure (2.7) [41]:

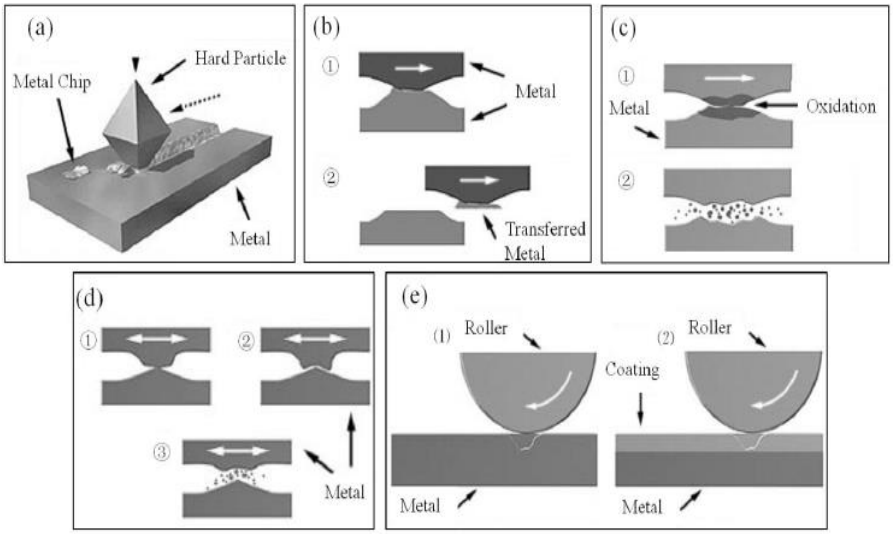

Figure (2.7): Schematic representations of wear mechanisms in biomedical implants: (a) abrasive wear; (b) adhesive wear; (c) oxidative wear; (d) fretting wear; (e) fatigue wear in metal-on-metal mode (1) and metal-on-coating mode (2), respectively [41].

1. Abrasive wear: happens when a hard, rough surface slides across a softer surface, causing material loss mostly on the latter. The two most common abrasive wear modes are two-body and three-body abrasive wears [54].
2. Adhesive wear: occurs when two solid surfaces in close proximity move against one another under pressure [32]. It refers to the undesired displacement and attachment of wear debris and material compounds from one surface to another between surfaces during frictional contact [39]. Adhesion is influenced by a variety of factors, including counterpart material, relative velocity, contact pressure, and actual contact area are all important factors to consider. The counterpart material, relative velocity, contact pressure, and actual contact area are all important factors to consider all have a role in adhesion. A high adhesion results in the transfer of

polymer to the metal surface due to the strong affinity between metals and carbon or hydrogen [39].

3. Oxidative (Corrosive) wear: When chemical processes cause an oxide layer to develop on a surface, corrosion occurs. This is then eliminated as a result of normal wear. The implant metals are vulnerable to the releasing particles and metal ions once the oxide layer has dissolved [39]. In oxidative wear, the oxide particles combine with the metal and create a debris layer [32]. This form of wear is highly influenced by the environment, which influences the rate of development of surface oxide coatings [39].
4. Fretting wear: is the repeated cyclical rubbing of two surfaces over a period of time that removes material from one or both of the surfaces in contact [39, 55]. Fretting wear is the damage caused by repetitive relative surface motion [55]. In orthopedic applications such as hip joint prosthesis, fatigue wear has been recognized as one of the primary issues related with implant failure as shown in Figure (2.8) [55].

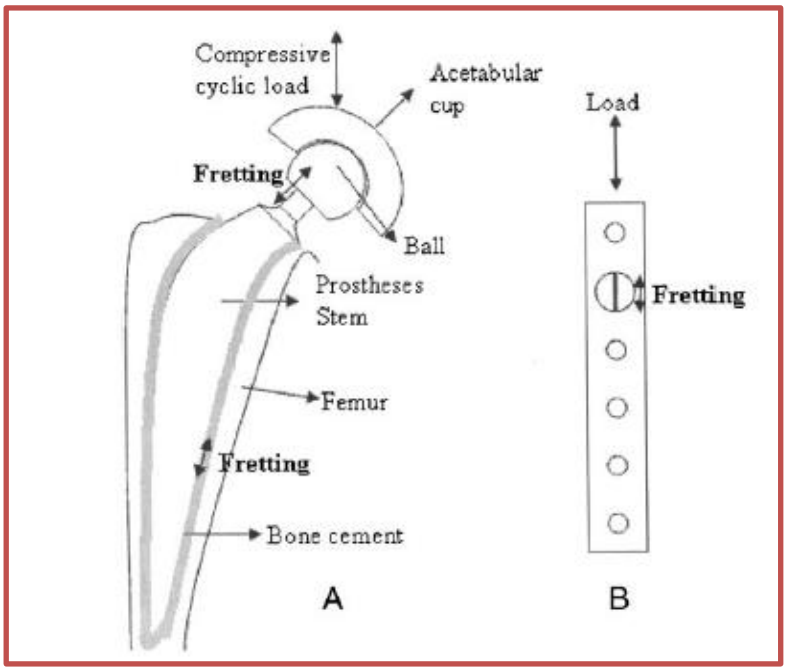

Figure (2.8): Fretting fatigue of (A) hip implant and (B) bone plate [55].

5. Fatigue wear: cyclic loading degrades the surface of a material, causing surface cyclic shear stresses or strains to exceed the material's fatigue limit [39]. It is produced when the wear particles are detached by cyclic crack growth of micro cracks (either superficial cracks or subsurface cracks) [39].

2.7 Metallic Biomaterials

Metallic materials can be considered as the most significant engineering materials; they are utilized as biomaterials owing to their high heat conductivity and mechanical characteristics [56]. The fundamental feature required of a metal as biomaterial is that it does not elicit an unfavorable reaction when placed into services, that means to be a biocompatible material [57].

For load-bearing implants and inner fixing systems, metallic materials are the most frequently used. The primary functions of orthopedic implants systems are to restore the load-bearing joints function that undergo to elevate levels of mechanical stress, wear, and fatigue during ordinary activity [37]. Important orthopedic implants are prostheses for ankle, knee, hip, shoulder, elbow joints and also need equipment like cables, screws, plates, pins, etc. that used in the fixation of fracture [58].

Metals are powerful, and most of them are capable to be formed into complicated forms. During or after final formation, the required mechanical characteristics of metals can be accomplished by heat and mechanical processing. In addition, the correct treatment of components produced from chosen metal compositions can achieve a degree of corrosion and wear resistance. The high tensile strength, high yield strength, fatigue resistance and corrosion resistance are some of the features of metallic materials [48].

2.7.1 Titanium alloys

After aluminum, iron, and magnesium, titanium has been known as a chemical element for about 220 years, and its abundance in the earth's crust ranks fourth among metals. It is described as a black, refractory metal (melting temperature: 1668 °C) in most references [59]. Titanium comes in two different allotropic forms. It possesses a closed packed hexagonal crystal structure (HCP) at low temperatures in α phase, and a body centered cubic structure (BCC) at 883ºC in β phase [60].

Titanium and its alloys have distinct benefits over steels in medicine, including low weight, strong corrosion resistance to a variety of hostile environments, low density, low thermal conductivity, non-magnetism, processing workability, and other properties that make it a highly appealing material [61]. Table (2.3) shows mechanical properties of Ti-alloys [7].

Table (2.3) : Comparison of mechanical properties of Ti and its alloys [7].

Alloy Designation	Microstructure	Young's Modulus (GPa)	Yield Strength (MPa)	Ultimate Tensile Strength (MPa)
Cp-Ti	α	105	692	785
Ti-6A1-4V	α/β	110	850-900	960-970
Ti-6Al-7Nb	α/β	105	921	1024
Ti-5Al-2.5Fe	α/β	110	914	1033
Ti-5Al-5Fe	Metastable β	74-85	1000-1060	1060-1100
Ti-15Mo-5Zr-3Al	Metastable β	75	870-968	882-975
	Aged β+α	88-113	1087-1284	1099-1312
Ti-15Mo-2.8Nb-3Al	Metastable β	82	771	812
	Aged β+α	100	1215	1310
Ti-13Nb-13Zr	α/β	79	900	1030
Ti-15Mo-3Nb-0.3O (21SRx)	Metastable β+silicide	82	1020	1020
Ti-35Nb-7Zr-5Ta	Metastable β	55	530	590
Ti-35Nb-7Zr-5Ta-0.4O	Metastable β	66	976	1010

The modulus of elasticity of titanium and its alloys is closer to that of bone than the moduli of stainless steels and cobalt-based alloys, thus the concern over stress shielding is reduced [35]. Comparison of modulus of elasticity of biomedical Ti-alloy as shown in Figure (2.9) [35]. Because of a TiO_2 solid oxide layer, the principal features of Ti alloys have resulted in them being one of the most popular options in biomedical applications. On the other hand, have poor tribological characteristics due to their low resistance to plastic shearing, low work hardening, and lack of surface oxide protection [57]. This titanium surface oxide layer, which is generally a few nanometres thick, has high passivity and resistance to chemical attack [62]. Titanium and its alloys have a high price, as well as a high vulnerability to friction and wear, due to the coarse microstructure of cast alloys (as shown by a high coefficient of friction), poor shear strength, low fatigue strength, and limited elongation compared to wrought alloys. As a result, additional microstructural modification is frequently necessary to increase mechanical properties while preserving the shape of the product [63].

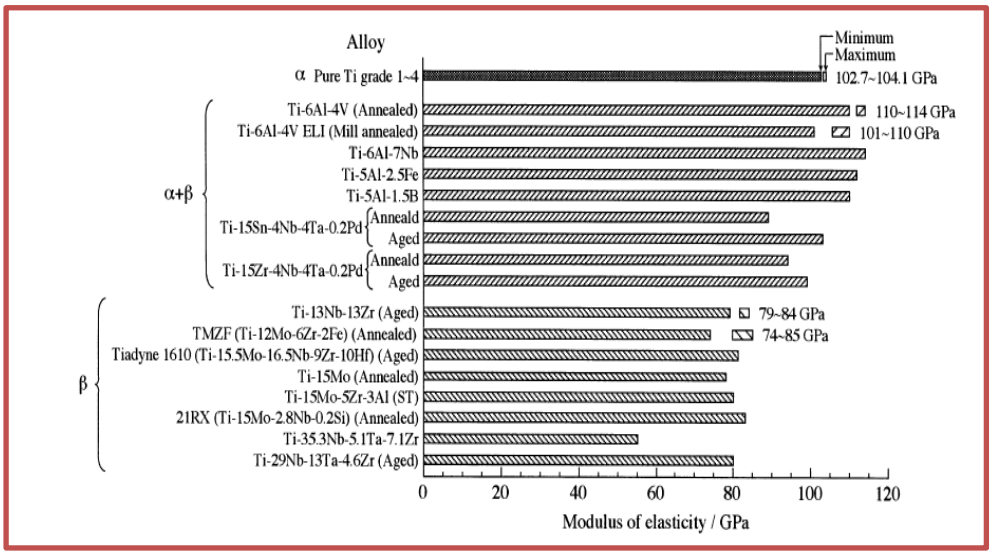

Figure (2.9): Comparison of modulus of elasticity of biomedical Ti-alloy [35].

2.7.1.1 Classification of Ti-alloys

There are many classifications for titanium alloys according to [64]:

- The method of obtaining - deformable and molded.
- Mechanical properties - alloys with low strength and high ductility, tensile alloys with medium and high strength alloys.
- The terms of application - cold resistant, refractory and corrosion.
- The ability to hardening with the use of thermal processing strengthened and non – strengthened.
- The microstructure in annealed condition alpha and alpha near alloys (the structure is fully alpha or 5% beta phase), alpha - beta and beta alloys (the structure is a stable beta phase).

Differences in mechanical properties of different brands technically pure titanium are mainly due to the different maximum levels of the elements forming interstitial solid solution - mainly oxygen and besides him and carbon, hydrogen, and nitrogen. The latter is the most effective element of a reinforcing titanium alloy, followed by oxygen [64].

Alloying elements can be generally classified as alpha (α) or beta (β) stabilizers. Depending on the nature of the alloying components, the to transition temperature of pure titanium rises or lowers [65]. Stabilizers are alloying elements such as (Al, O, N, etc.) that tend to stabilize the α phase, while elements that stabilize β phase are known as β stabilizers (V, Mo, Nb, Fe, Cr, etc.) and Hafnium and zirconium are unique in that they are isomorphous with both the α and β phases [60]. In Figure (2.10) Influence of impurities and alloying elements on α to β transformation temperature is shown [60].

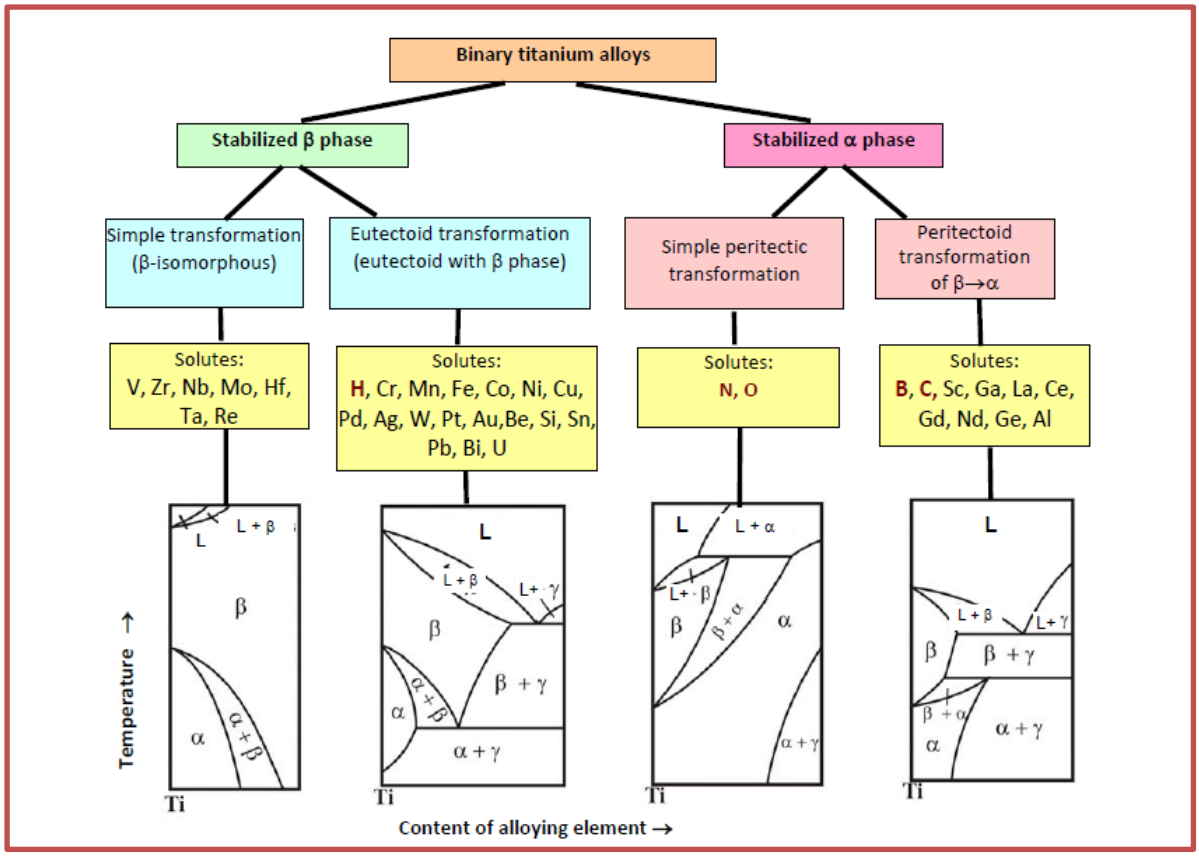

Figure (2.10): Influence of impurities and alloying elements on α to β transformation temperature (T_β) of titanium: a) and b) additives lower the T_β temperature; c) and d) additives increase the T_β temperature [60].

2.7.1.2 Ti-6Al-7Nb alloy

Ti-6Al-7Nb is one of the Ti-alloys composed of a hexagonal α phase (stabilized by aluminum) and a regular body-centered phase β (stabilized by niobium) [66]. The shape and fractional volume of the phases present in the alloy are largely determined by factors collected during the production process [67]. The Ti-6Al-7Nb alloys have fatigue and tensile strengths that are comparable to or better than those of Ti-6Al-4V, although their Young's modulus values are somewhat lower than Ti-6Al-4V [68]. Higher corrosion and wear resistance of Ti-6Al-7Nb compared to Ti6Al4V alloy is attributed to the formation of Nb_2O_5, which is chemically more stable, less soluble, and more biocompatible compared to V_2O_5 formed on Ti6Al4V alloy, The inclusion of Nb improves passivation by forming a Nb rich pentoxide

that is extremely stable in the body environment, resulting in increased resistance of corrosion [26]. Ti-6Al-7Nb oxides are saturated in the body and are not transferred in vivo or a bioburden. The alloy causes fewer large cell nuclei and has no deleterious tissue tolerance responses [69]. In addition, Ti-6Al-7Nb has a good compatibility with human ingrowth [68].

2.7.2 Biomedical application of Ti-alloys

Due to its high biocompatibility, little response to surrounding tissues, and good corrosion resistance, titanium alloys are frequently utilized as biomaterials. The various implant applications In both, medical and dental fields, that include in artificial hip and knee joint replacements and dental implant prosthesis [70].

2.7.2.1 Orthopedic application

Orthopedic implants include both temporary implants such as plates and screws and permanent implants that are used to replace hip, knee, spinal, shoulder, toe, finger etc. These are being used in different fields in orthopaedics: fracture repair, total hip and knee arthroplasty [9].

2.7.2.1.1 Hip replacement

Because the spherical head of the thighbone (femur) moves inside the cup-shaped hollow socket (acetabulum) of the pelvis, the hip joint is referred to as a ball-and-socket structure. A complete hip replacement generally includes three components to approximate this anatomy [13, 71]:

1. Stem that fits into the femur.
2. Ball that replaces the spherical head of the femur.
3. Cup that fits into the worn-out acetabulum.

hip implants are composed of high-performance metal alloys, Specifically, the stem is usually made of Ti-6Al-4V or Ti-6Al-7Nb alloys used only for making the femoral component [71], as shown in Figure (2.11) [72].

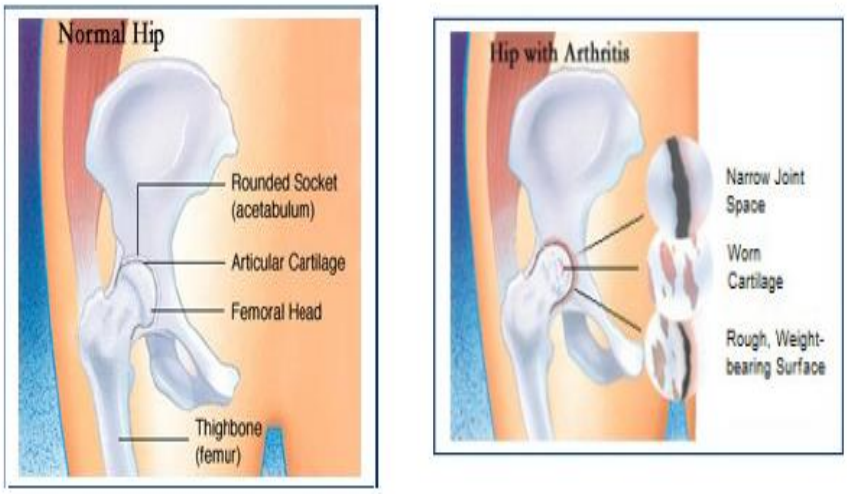

Figure (2.11): Normal hip vs. Arthritic hip [72].

2.6.2.1.2 Knee replacement

knee can be simply considered as a hinge joint. In reality, it includes more complicated motions like rolling and gliding (TKR) as shown in Figure (2.12) [58]. all of them are composed of three parts [13, 58]:

1. Curved femoral component to replace the lower end of the thighbone.
2. Flat tibial component to replace the top surface of the shinbone.
3. Dome-shaped patella component to replace the kneecap.

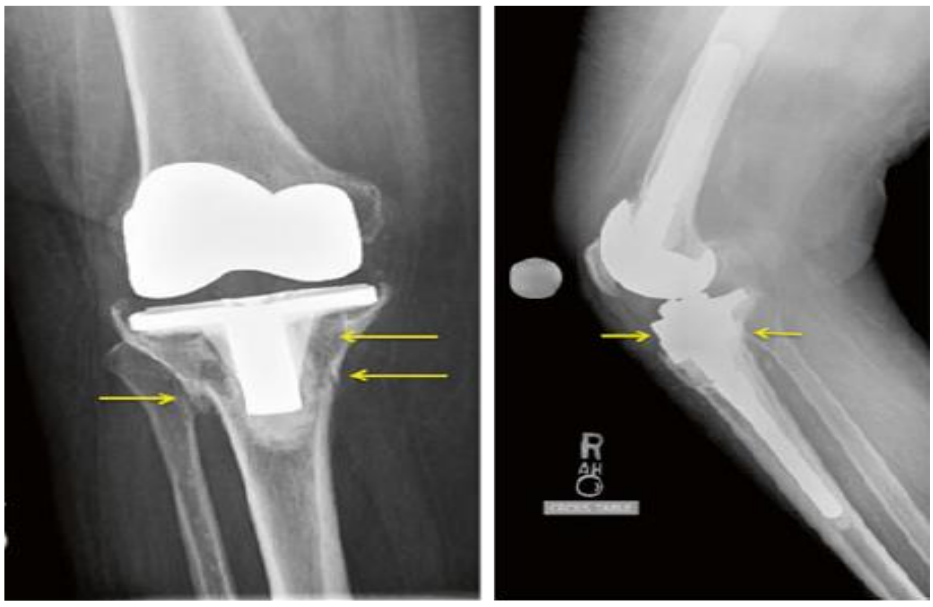

Figure (2.12): Total Knee Replacement [58].

2.6.2.2 Dentistry application

Titanium and its alloys are also used for dentistry devices such as implants, crowns, bridges, overdentures, and dental implant prosthesis components (screw and abutment) [70]. When bone forming cells attach themselves to the titanium implant, a structural and functional bridge forms between the body's bone and the newly implanted, foreign object. There are three types of dental implant [70, 73] as shown in Figure (2.13) [70]:

1. Osseointegrated: as a direct bone-to-implant contact and later on it is defined on a more functional basis as a direct bone-to-implant contact under load.
2. Mini-implant for orthodontic anchorage used generally to secure anchorage in contemporary orthodontic treatments
3. Zygomatic.

Each group requires unique mechanical characteristics and must be constructed from titanium alloy [74]. Ti-6Al-7Nb alloy is preferred for endosseous dental implant applications commercially [73].

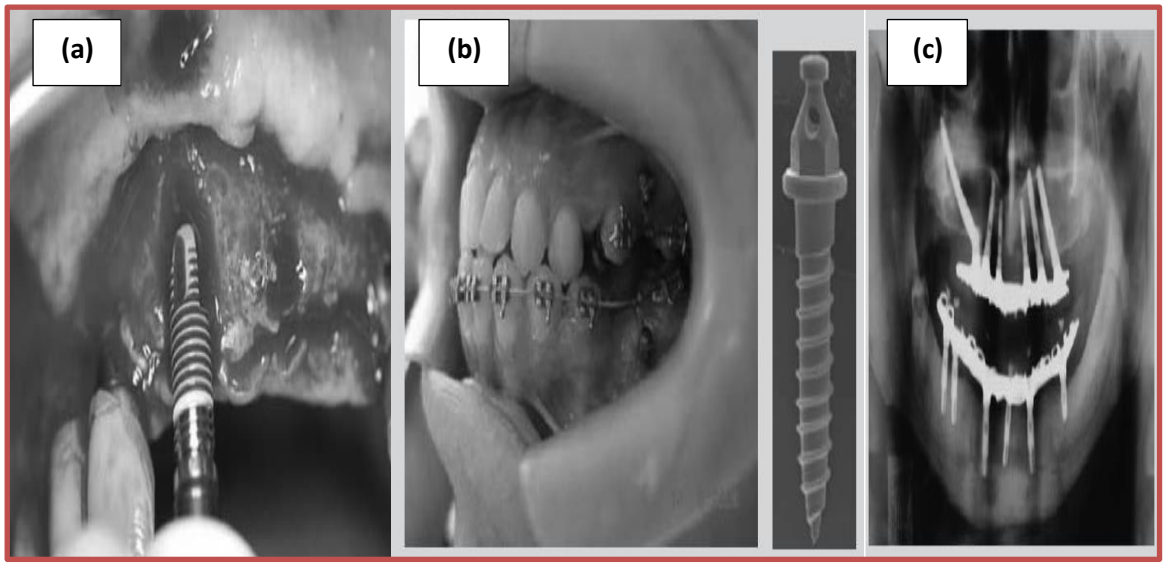

Figure (2.13): Types of dental implants : (a) Examples of Commercial Dental Implant Designs, (b) an Orthodontic mini-implant for Anchorage Application, and (c) A zigomatic Implant [70].

2.8 Surface Modification of Ti-alloys

Surface modifications of biomedical implants are common to improve corrosion resistance, wear resistance, surface texture, and biocompatibility [75]. All altered surfaces should be tested for corrosion behavior in addition to improving other desirable properties. A thorough understanding of the interactions that take place at the atomic level between the surface of the implant, the host, and the biological environment, including all types of micromotions of the implants kept inside the human system, should be studied in greater detail in order to obtain implants that can sustain for a longer period in the human system [76].

The material surface plays an extremely important role in the response of biological environment to the artificial medical devices [77]. Surface modification does more than simply change the appearance of the surface; it also enhances adhesion properties, micro cleaning, functionalization of amine, and biocompatibility [78]. Many types of surfaces may be created using the surface modification approach to control correct biological response in a specific cell/tissue scenario, with the goal of reducing healing time and limiting harmful reactions [79].

Because titanium and its alloys have poor tribological properties, such as low wear resistance, the implant's service life is shortened. Surface coatings can help to solve this problem to a considerable extent. Surface engineering can significantly improve the performance of titanium orthopedic devices, allowing them to outperform their inherent capabilities [80].

All possible surface changes can be generally categorized as follows [81, 82]. Some examples of surface modification processes: physical and chemical method, laser cladding, thermal oxidation, plasma spray, and ion implantation as shown in Table (2.4) [11].

Table (2.4): Overview of surface modification methods for Ti and its alloys [11].

Surface modification methods	Modified layer	Objective
Mechanical methods Machining Grinding Polishing Blasting	Rough or smooth surface formed by subtraction process	Produce specific surface topographies; clean and roughen surface; improve adhesion bonding
Chemical methods: Acidic treatment Alkaline treatment	<10 nm of surface oxide layer. ~1 μm of sodium titanate gel.	Remove oxide scales. Improving biocompatibility, bioactivity or bone conductivity
Hydrogen peroxide treatment	~5 nm of dense inner oxide and porous outer layer.	Improve biocompatibility, bioactivity or bone conductivity.
Sol–gel	~10 μm of thin film, such as calcium phosphate, TiO2.	improve biocompatibility, bioactivity or bone conductivity
Anodic oxidation	~10 nm to 40 μm of TiO2 layer.	Produce specific surface topographies, improved corrosion.
CVD	~1 μm of TiN, TiC, TiCN, diamond and diamond-like carbon thin film.	Improve wear resistance, corrosion resistance and blood compatibility.
Biochemical methods	Modification through silanized	Induce specific cell and

	titania, photochemistry, self-assembled monolayers, protein-resistance, etc.	tissue response by means of surface-immobilized peptides, proteins, or growth factors
Physical methods Thermal spray Flame spray Plasma spray HVOF and DGUN	~30 to 200 μm of coatings, such as titanium, HA, calcium silicate, Al2O3, ZrO2, TiO2.	Improve wear resistance, corrosion resistance and biological properties
PVD Evaporation Ion plating Sputtering	~1μm of TiN, TiC, TiCN, diamond and diamond-like carbon thin film	Improve wear resistance, corrosion resistance and blood compatibility
Ion implantation and deposition Beam-line ion implantation PIII	~10 nm of surface modified layer and/or ~μm of thin film	Modify surface composition; improve wear, corrosion resistance, and biocompatibility
Glow discharge plasma treatment	~1 nm to ~100 nm of surface modified layer	Clean, sterilize, oxide, nitride surface; remove native oxide layer

2.8.1 Hydroxyapatite (HA)

Hydroxyapatite (HA) is calcium phosphate ceramic material that has been used for manufacturing various forms of implants. The inorganic portions of the human bone and teeth have a morphology and composition that

is extremely like that of the inorganic sections of the human bone and teeth. HAp was commonly utilized in biomedical applications due to its excellent osteoconductivity, biocompatibility and bioactivity [83].

2.8.1.1 Crystal structure and phase of HA

Because the Ca:P ratio of calcium phosphate is 10:6, it can crystallize into salts like hydroxyapatite [$Ca_{10}(PO_4)_6(OH)_2$] and β-whitlockite shown in Figure (2.14) [26]. The atomic structure of hydroxyapatite is projected down the c-axis onto the basal plane. The hydroxyl ions are found on the corners of the projected basal plane at equidistant intervals (3.44A^o) along the columns perpendicular to the basal plane and parallel to the c-axis. Six of the ten calcium ions in the unit cell are associated with the hydroxyls in these columns, resulting in strong interactions among them [26].

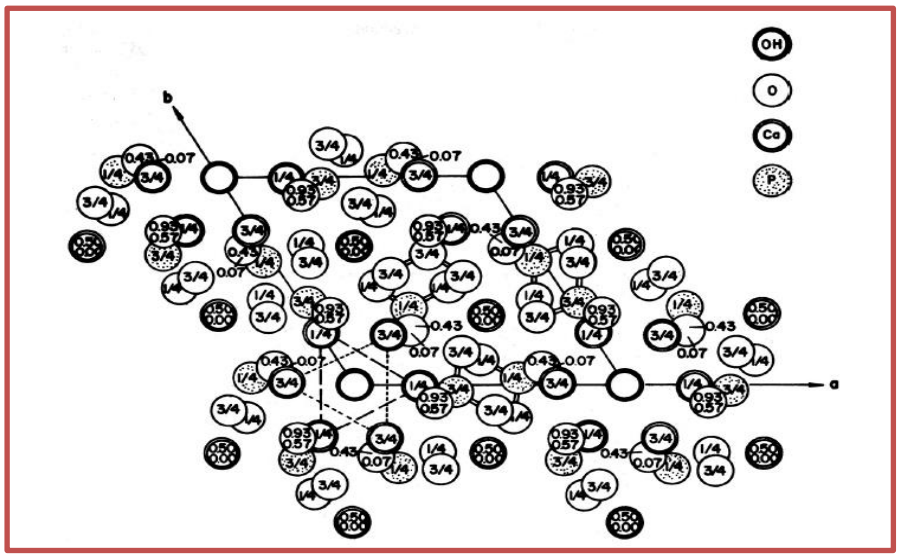

Figure (2.14): Hydroxyapatite structure projected down the *c*-axis onto the basal plane [26].

2.8.1.2 Properties of HA

HA has Attractive properties of HA such as lack of toxicity and high elastic modulus as shown in Table (2.5) [46]. During stress shielding, the pressure placed on the implant during movement is transferred through the

rigid implant rather than the bone, resulting in cortical bone atrophic loss [84]. HAp appears to forma direct chemical bond with hard tissues [46]. One of the main constraints of HAp is its low fracture toughness compared to compact cortical bone which means that HAp behaves as a relatively brittle material [85].

Table (2.5): Mechanical properties of bone VS. HAp [46].

Mechanical properties	Cortical bone	HAp
Compressive strength, MPa	100-230	120-900
Tensile strength, MPa	50-150	38-300
Fracture toughness, $MPa.m^{1/2}$	2-12	1
Young's/Elastic modulus, GPa	18-22	35-120
Density, g/cm^3	2.9-3.88	3.156

2.8.1.3 The HAp coating

This coating of HAp coating improves the bone/implant bonding characteristics and boosts the substrate's corrosion resistance. Because the components comprise the primary inorganic element of the bone composition, HA coatings have a close composition match with that of the bones. These coatings promote osseointegration by allowing for rapid and selective bone ingrowth. Biocompatibility and the development of a bone/implant contact are both enhanced by HA [86].

The bioactivity of the HAp makes it an outstanding material for the metallic implants coating since it has the ability to form and grow to the surrounding tissues of the bones [87]. An intimate contact between the surface of metallic implant and the adjacent bone tissue required for posterior bone growth. However, coating of the metallic implant with the HAp results in a fast bonding between them. Using of the HAp as coating on the metallic

implant combines the strength and toughness of the implant material with the bioactive properties of the HAp coating layer that can promote the surrounding bone tissue growths and future chemical bonding formations. Moreover, the existence of the HAp can enhance the corrosion resistance of the implant in the human body, thus reducing the release of metallic ions and promoting fixation through chemical bonding [88].

3.8.1.4 Advantages of HAp

The advantages of HAp coatings applied to implant surfaces are numerous. Such coatings appear to shorten the time, it takes for metallic implants to osseointegrate [22].

1. High biocompatibility.
2. High bioactivity.
3. There is no fibrils connective tissue forming around the implant, isolating it from the bone.
4. Osseointegration even in the presence of implant-bone micromotion.
5. The formation of a strong tensile connection between the implant and the bone.
6. Reduction of pain after operation.
7. Earlier implant loading after healing phase possible.
8. Variable metallic substrates possible.
9. Variable surface structures possible, including mesh, artificial spongiosa, porous coatings and roughened surfaces.
10. Thickness of HAp coating depending on application.
11. Rarely problems with delamination and spalling in vivo.
12. Reduced or even completely alleviated release on metallic ions to the surrounding tissue.
13. High dissolution/resorption resistance in contact with body fluid
14. Quality control and standard according to ASTM.

2.8.1.5 Applications of the HAp

The HAp has a broad range of applications in bone and tooth repairing as shown in Figure (2.15) [89]. Because of its resemblance to the human bone and teeth, HAp regards a perfect candidate for [26]:

a. Hard tissue repair, such as:

1. Powders or granules for bone and tooth defect filling.
2. Particles as the component for toothpastes and bone cements.
3. Small and unloaded implants, such as in the middle ear.

4. biocompatible and bioactive coatings on metal components.

5. Femoral plugs in total hip replacement.

b. Soft tissue repairs, such as:

1. Support the healing of skin wounds.

2. Therapy or prevention of nerve injury.

3. HAp bioceramics contact tightly and adhere strongly with skin tissue to prevent exit-site and tunnel bacterial infection.

Figure (2.15): Micro-textured and HAp-coated acetabulum cups and femoral stem of hip surgery implants [89].

2.8.2 Zirconia (ZrO_2)

Zirconia is an inert bioceramics materials. High density ZrO_2 shows excellent compatibility with autogenous bone and is completely nonreactive [90]. ZrO_2 shows excellent biocompatibility and good wear and friction

properties, making it suitable for application in biomedical materials [26]. Because of the transformation toughening mechanisms acting in their microstructure, ZrO_2 ceramics offer several advantages over other ceramic materials that may be exhibited in components constructed of them [90].

2.8.2.1 Crystal structure and phase of ZrO_2

ZrO_2 is an extremely capable ceramic exists in three polymorphic forms at ambient pressure: monoclinic at <1,170 ºC, tetragonal at 1,170–2,370 ºC temperature range; and cubic at >2,370 ºC, until it melts at 2,706 ºC [91]. Pure ZrO_2 can be obtained from chemical conversion of ($ZrSiO_4$), which is an abundant mineral deposit. a = 5.145 A^o, b = 0.521 A^o, c = 5.311 A^o, and $\beta = 99.14^o$.

2.8.2.2 Properties of ZrO_2

ZrO_2 posses a unique combination of physicochemical properties, such as [90].

1. biocompatibility and bioactivity: Zirconia is biocompatible and stimulates osteogenic cell proliferation and differentiation.
2. Osseointegration: numerous studies have shown that bone attachment to ZrO2 surfaces and the development of a direct contact between bone and zirconia is equivalent to or even better than titania implants.
3. radiopaqueness: this makes it visible in radiographs, allowing for monitoring of its function.
4. mechanical strength and toughness: that is ascribed to the transformation toughening mechanism of ZrO2 ceramics.

The properties of ZrO_2 are shown in Table (2.6) [22].

Table (2.6): Mechanical characteristics of commercially available zirconia [22].

Properties	Range
Density (Mg/m^3)	6.05-6.09
Vickers hardness (HV)	1200-1300
Young's Moduluos	150-210
Compressive strength (MPa)	>2000
Tensile strength (MPa)	>650
Flexural strength (MPa)	900-1300
Fracture toughness ($MN/m^{-3/2}$)	7-9

2.8.2.3 ZrO_2 coating

Various zirconia ceramics are now used in modern bone replacement and repair applications as orthopedic implants, thin films and coatings on other metallic implants, porous bone scaffolds and bone graft materials, and bone cements and spinal stabilization devices [89]. ZrO_2 are usually encapsulated with a thick fibrous tissue after their in vivo implantation, leading to possible aseptic loosening of the implants. It has been accepted that no foreign material placed within a living body is completely compatible [22].

2.8.2.4 Application of ZrO_2

ZrO_2 is one of the strongest ceramic materials suited for medical applications. Under typical laboratory hip simulation circumstances, ZrO_2 femoral balls articulated for hip prosthesis have been described [3]. Furthermore, as demonstrated in Figure (2.16) [90], zirconia is exceptionally hard and has good mechanical characteristics for hip replacements, knee replacements, teeth, tendons and ligaments, periodontal disease repair, and bone fillers following tumor surgery. ZrO_2 has a wide range of applications [90]:

1. In reconstruction of acetabular cavity.
2. as bone plates and screws.
3. As drug delivery devices.
4. As femoral heads.
5. As middle ear.
6. In the reconstruction of orbital rims.
7. As components of total and partial hips.
8. In the repair of the cardiovascular area.

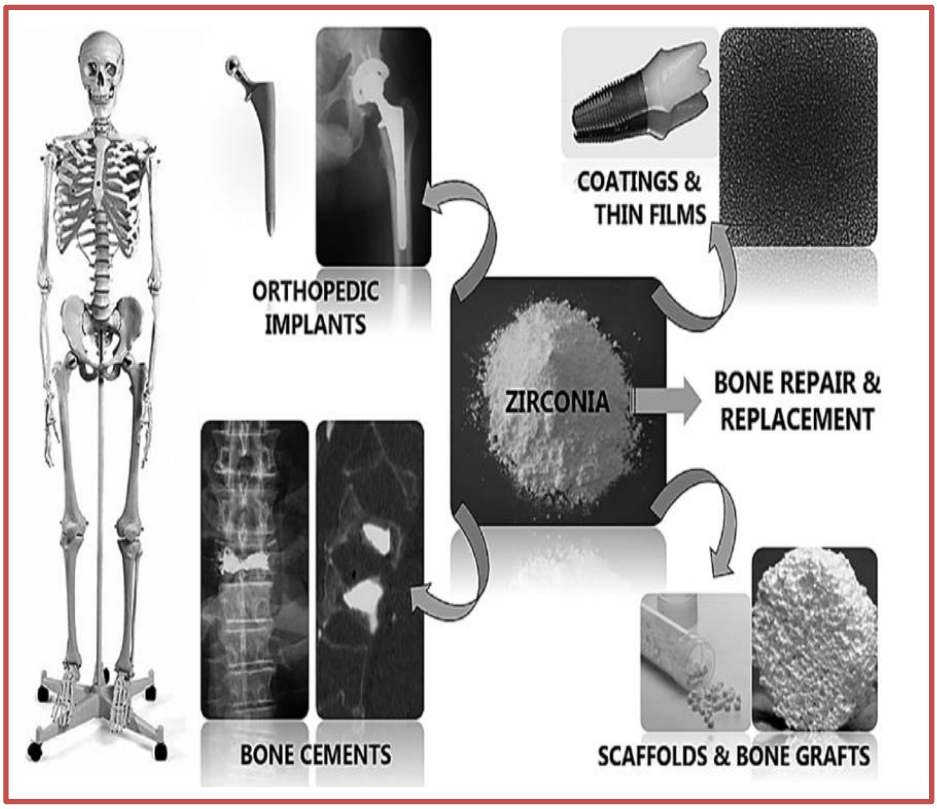

Figure (2.16): Biomedical uses of zirconia ceramics in modern bone replacement and repair applications [90].

2.9 Micro-Arc Oxidation (MAO) process

Micro-arc oxidation (MAO) is an electrochemical surface treatment process to produce oxide protective coatings on some metals [92]. MAO can be regarded as a developed method from anodic oxidation by discharging

sparks at a high voltage which is also named anodic spark oxidation or plasma electrolytic oxidation [93]. Many metals, including Ti, Al, Zr, Mg, and others, can be coated with ceramic coatings using this approach. The sample is employed as an anode and submerged in an aqueous solution with a reasonably high voltage during the MAO process, as illustrated in Figure (2.17) [92]. This voltage must be greater than the produced oxides break-down limit. As a result, sparking occurs often on the surface of treated samples, resulting in less homogeneous and porous oxide coatings [93].

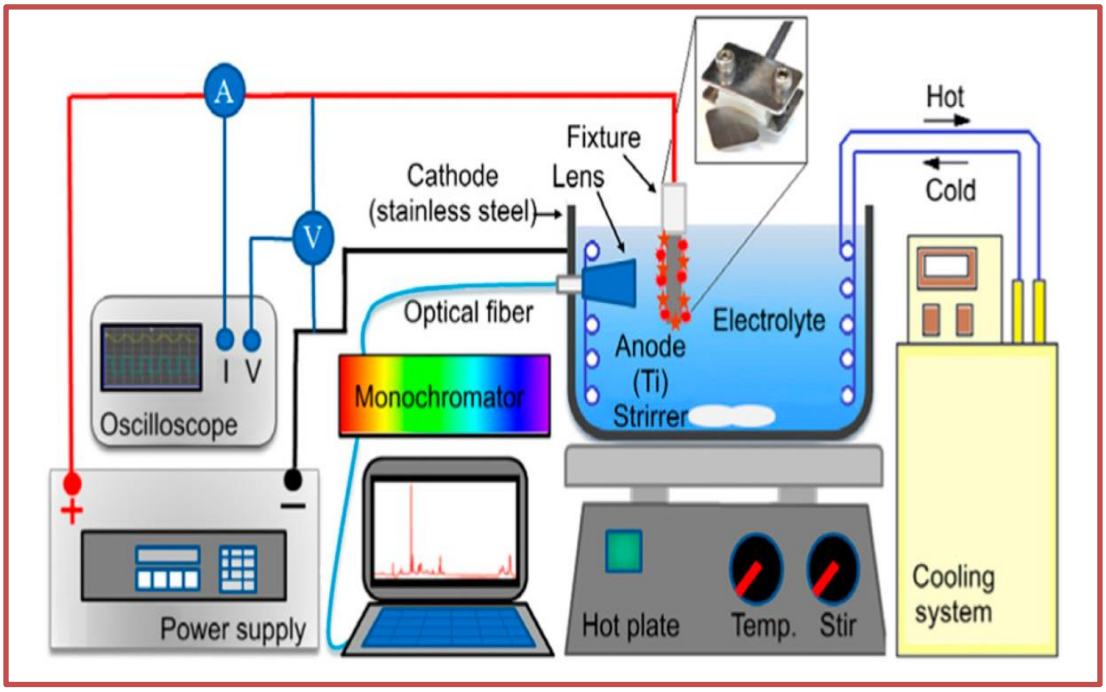

Figure (2.17): Schematic diagram of the micro-arc oxidation (MAO) process [92].

MAO is often performed in an aqueous electrolyte, which necessitates rapid bath cooling and results in the development of a coating containing contaminants from the electrolyte [93]. The comparison between MAO and hard anodizing methods is given in Table (2.7) [94]. Process factors such as applied voltage frequency, processing time, and electrolyte composition may all be adjusted to influence the creation and characteristics of coatings.

One of the coatings generated in several electrolytes has high mechanical characteristics as well as bioactivity [86]. The composition of the electrolyte and the electrical parameters of the MAO process done with a pulsed DC power supply have a significant influence on the structural characteristics of the produced coatings [95].

Table (2.7): Comparison of MAO with hard anodizing methods [94].

Process	MAO	Hard anodizing
Voltage and current density.	High voltage and current density.	Low current and voltage density.
Rate of deposition	Quick (1~2μm/min)	Low (~0.3μm/min)
Mechanism of Oxidation	Plasma chemical reactions and chemical / electrochemical reactions.	Chemical / electrochemical reactions.
Coating on selected alloys.	Practical for different types of Al, Mg, and Ti alloys.	Practical for different types of Al, Mg, and Ti alloys.
Microstructure	Crystalline phase / inner dense film, amorphous, and outer porous film.	Very thin barrier, amorphous/columnar porous film.
Relatively (corrosion resistance)	Excellent	Good
Hardness	High (~1600HV)	Low (600HV max)
Relatively (wear resistance) .	Stellar	Fair
Thermal protection	Excellent	Good
Dielectric strength	Stellar	Fair

2.9.1 Principle of MAO process

The detailed mechanism of MAO process has not yet been revealed; however, most investigators agree that during each alternating current (AC) period several principal stages occur [96]:

Stage I: The voltage approaches the breakdown voltage, it increases rapidly and linearly as shown in Figure 2.18 (a) [96] some small oxygen bubbles and an oxide layer on the sample surface, which corresponds to the conventional anodizing step.

Stage II: Dielectric breakdown occurs when the applied voltage surpasses a certain point, leading in the production of spark discharges. The current flow focuses exclusively in regions of breakdown at this step, resulting in localized oxide layer thickening. The newly created coating can restore current flow resistance, whereas other areas with lower resistance are more prone to collapse as shown in Figure 2.18 (b) [96]. It's showing a stage when a shrill sound is accompanied by a large number of tiny white sparks that are randomly dispersed and rapidly traveling across the whole anode surface.

Stage III: The cell potential fluctuates due to the continual production and breakdown of the oxide layer. The immediate production of ceramic oxide coating is enabled by gasification of both the valve metals and the electrolyte. The coating breaks down at a susceptible location in the developing oxide sheet. The discharge sparks become larger as the processing time increases, and their hue changes from white to orange or red. It shows how the micro-arcs convert into strong arcs in this location as shown in Figure 2.18 (c) [96].

Stage IV: The huge pores and thermal breaking of the film are caused by the strong sparking and gas release. The voltage drops fast together with the absence of sparks and gas bubbles, indicating the conclusion of the MAO

process. The MAO coating has a two-layered design, with a barrier inner layer and a porous outer layer with many fine and coarse cavities. The coating thickness ranges from 1 to 100 meters as shown in Figure 2.18 (d) [96].

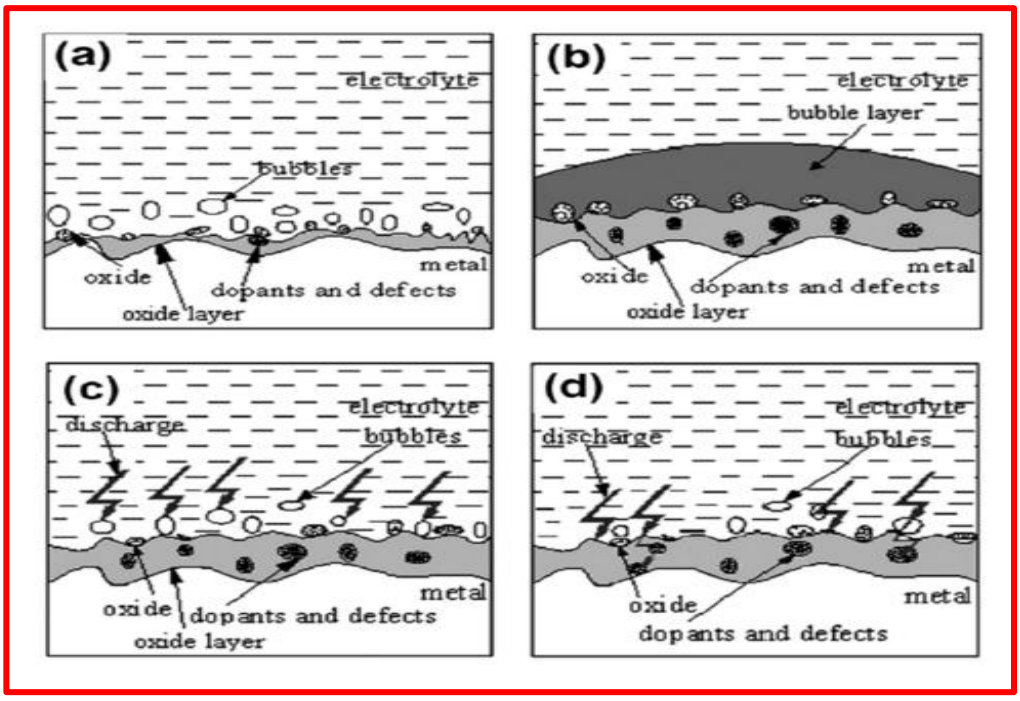

Figure (2.18): Schematic illustration of the plasma discharge during different stages of the MAO process. (a) Stage I, (b) stage II, (c) stage III, and (d) stage IV [96].

So far, the mechanism of MAO has remained a mystery, making it impossible to develop a precise theory to guide the functioning. The presence of an electrical breakdown throughout the operation is acknowledged, and the breakdown mechanism is based on the solid liquid contact. A thermal electron emission process was proposed as the cause of the discharge along the dielectric surface. believed that an electron current forms along the dielectric's surface as a result of the tunnel effect and impurity ionization [97].

2.9.2 Advantage of MAO process

1. The MAO has provided ceramic coatings that are extremely hard and resistant to multiple exposures over the last decade; such coatings

have excellent adhesion and hardness with the surface of treated metal due to an intermediate film between coatings and metal, depending on future and purpose operational conditions of parts [98].

2. Technique has great substrate bonding strength, controlled shape, and high composition quality [99].
3. Coatings with thicknesses varying from fractions to several micrometers may be created using this technique, obtaining a variety of characteristics; it's also possible to treat tough components because to the electrolyte's strong dissipation capacity, and to form numerous coatings on one material [98].
4. Improvement the bioactivity and biocompatibility of Ti-alloys by improving corrosion and wear resistance, inhibiting the release of harmful ions. As a result, the MAO technique is largely employed in biomedical applications and bone proliferation [92].
5. MAO films have high dielectric characteristics and photocatalytic performance, and MAO technology is used in the electronics and environmental protection industries [97].

2.9.3 Disadvantage of MAO process

1. Due to the expensive cost of MAO and low processing rate and high energy cost would limit its use in the industrial business [98].
2. The thickness of the MAO layer is not homogeneous due to the limitation of geometry [98].
3. MAO of metals is a complicated process that combines many fractional oxides layer generation methods (dissolution of preexisting layer, anodic gas evolution and dielectric collapse). The possibility of predominance for which of these fractional techniques was determined by the metal's complexion, the components and concentration of the electrolytic solution, as well as the current density [100].

2.9.4 Application of MAO process

Applications of MAO processes in specified descriptions could be subdivided to:

1. Chemical Applications: At mid-levels temperature, it resists strong acid and bases [101].
2. Mechanical Applications: Oxide layers deposited by MAO process have higher harness than 1300 kg/mm². This elevated hardness values is among aspects that increase abrasive, sliding, and erosive wear resistance. The friction coefficient's efficiency makes it useful in operations with minimal lubrication [101].
3. Thermal Applications: Thermal inductivities of oxide films are lower than those of other materials, which make them could be used for providing the same distribution of heat and so they could be used for increasing thermal shocks resistance [101].
4. Electronic and Electric Applications: It may be used as an insulator layer on electric and electronic components, making it ideal for inner-region hard coatings (for cavital cylindrically regions, or conical) [94].
5. Medical Application: MAO treatment improves biocompatibility, bioactivity, and antibacterial characteristics in dental and orthopedic implants [81].

2.9.5 Factors influence on MAO process

The chemical compositions, morphologies, and microstructures of MAO-produced coatings are influenced by MAO parameters such as alloy compositions, electrolyte, temperature, time, voltage, duty cycle, and current density [102].

1. Substrate's composition: The substrate composition has an impact on the components and features of MAO coatings. MAO stands for metal-oxide. It is based on anodic oxidation in electrolytic solution and the application of a voltage that is greater than the collapse voltage of the developing oxide layer on the surface, with different surfaces coated producing different properties and applications [103].
2. Choice of electrolyte: The concentration has a significant impact on the morphological features, porosity, thickness, corrosion resistance, and biocompatibility of MAO coatings [102,104]. Different types of electrolytic solutions can be used in MAO process as shown in Table (2.8) [104].

Table (2.8): Various types of electrolytic solution [104].

Process	Purpose
Carbonization such as (K_2CO_3, $C_3H_5(OH)_3$, Na_2CO_3)	Increase wear resistance, fatigue strength, and hardness of coating.
Nitriding such as ($NaNO_3$)	Increase wear and corrosion resistance, fatigue strength, and hardness of coating.
Nitriding + saturation with boron ($NaNO_2$, $Na_2B_4O_7$)	Increase corrosion resistance, and hardness of coating.
Carbonization + nitriding ($C_3H_5(OH)_3$, Na_2NO_2)	Increase wear resistance, and hardness of coating.
Binding such as (NaOH, KOH)	Increase the electrolyte conductivity, and wear resistance.
Carbonization + saturation with boron ($NaNO_2$,$Na_2B_4O_7$)	Increase wear resistance, and hardness of coating.

3. Voltage: one of the most important electrical parameters that impacts the characteristics of MAO coatings applied on Ti alloys [96]. Voltage has a significant impact on the microstructures and properties of MAO coatings. Constant voltage mode during MAO results in a freely declining current density, resulting in a very flat surface with negligible porosity [96, 102].
4. Duty cycle: The ratio of on time to total period (on time off time) is known as the duty cycle. The greater the duty cycle, the longer each cycle lasts, and the more energy is released every pulse. An increase in duty cycle corresponds to a longer period of current/voltage applied each cycle. On the properties of MAO coatings, the duty cycle has a comparable impact as the applied voltage [96,103].
5. Current density: In general, current density is another factor that influences the coating's microstructure and characteristics. However, when a constant current density is used, the strength of the spark discharge increases but the number of spark discharges decreases as the process time increases [96, 98].
6. MAO duration: The effect of treatment time on the characterization of MAO coatings placed on Ti/Ti alloys is also an essential parameter [100, 102].

2.10 Literature Review

2.10.1 TiO_2 coating by MAO of Ti-alloys

In 2010, LIN Xiu-zhou *et.al* [105] studied wear characteristics of the MAO coating and its Ti-6Al-4V alloy substrates using fretting wear without lubrication under a range of displacement amplitudes (D) from 3 to 40 m, a constant normal load (F_n) of 300N, and a frequency of $5H_z$. The findings revealed that the rutile and anatase of TiO_2 phases made up most of the

MAO coating, which had a rough and porous surface with a high hardness. The MAO coating might change the mixed fretting regime (MFR) and slip regime (SR) to a direction with lesser displacement amplitude as compared to the substrate. In the MFR, the friction coefficient of the coating was lower than that of the substrate as a result of the prevention of plastic deformation by the hard ceramic surface.

In 2010, Z.Q. Yao *et.al* [106] enhanced the Ti surfaces used in research implants have a high bioactivity. MAO was used to arrange Ca/P-containing porous titanium coatings over ultrafine-grained and coarse-grained Ti. Following that, the thermal equilibrium duration of MAO as well as the segment description, shape, morphology, and microstructure of ultrafine grained Ti coatings were examined.

In 2011, Xue Han *et.al* [107] investigated MAO and MAH to see whether they might improve the cytocompatibility of a newly developed Ti-24Nb-4Zr-8Sn alloy. Commercially pure titanium (CP-Ti) and Ti-24Nb-4Zr-8Sn were utilized in this investigation. A two-step treatment of micro-arc oxidation (MAO) and alkali heat treatment was used to modify the surface of Ti-24Nb-4Zr-8Sn. Scanning electron microscopy (SEM), thin film X-ray diffraction (TF-XRD), and X-ray photoelectron spectroscopy were used to characterize the surfaces (XPS). In comparison to the MAO layer, the MAH layer featured finer crystals and a higher degree of crystallization and stability. To explore the influence of the varied surfaces on the bone integration property in vitro, biocompatibility research was conducted on treated and untreated Ti-24Nb-4Zr-8Sn in comparison to CP-Ti.

In 2012, Su Cheng *et.al* [108] studying the effects of MAO coatings on microstructures and factor distribution on the inner coating surface were explored when pure Ti was used. The findings demonstrated that as the

MAO period lengthens, the coating floor, which comprises of Ti, O, Si, Ca, and Na, grows. The rate of growth of factors information material reduces when the MAO time approaches ten minutes. The rate of pore length expansion and pore quantity decrease slows down as the MAO time approaches five minutes.

In 2013, Laís T. Duarte *et.al* [109] studied the oxide layers were produced on the biocompatible Ti-13Nb-13Zr alloy, potentiodynamically up to 8V, or by (MAO) at 300V. In a phosphate buffered saline solution, their electrochemical characteristics were tested (PBS). The potentiodynamically produced oxide films were compact and behaved as a monolayer, but the MAO oxide was a bilayered film, according to EIS and SEM findings (compact inner and porous outer layers).

In 2014, Leonardo C. Campanelli *et.al* [110] studied the influence of (MAO) technique on the fatigue characteristics of Ti–6Al–7Nb and commercially available materials (CP-Ti). Both polished and anodized specimens of both materials were examined in axial fatigue to produce S–N curves, and the oxide layer was described to aid in the comparison of fatigue characteristics caused by different surface conditions. The MAO technique produced extremely porous oxides with a consistent distribution of pores; the oxide films were made of anatase TiO_2 and included no Al or other alloying elements. These shape, structure, and composition are desired on the surface coating for improving the bonding qualities between the implant and the bone, hence facilitating implantation.

In 2015, A.R. Ribeiro *et.al* [111] investigated the formation development of calcium and phosphorus-doped oxide coatings on titanium surfaces using MAO. As a result, a nanometric-thick calcium-rich amorphous layer forms on the top surface of the oxide film, This is required for rapid

osteoblast adhesion and spreading, as well as enhanced levels of IFN-cytokine production, rearrangement, and cell spreading. Inflammatory reactions and bone microarchitecture (preventing osteoporosis) are governed by this protein, in addition to cell spreading.

In 2016, Wang Ping *et.al* [112] studied deposition of TiO_2 on pure Ti using MAO in a solution of $NaAlO_2$ concentrations . Because the attention of $NaAlO_2$ will rise, the voltage must be raised to sell the increased charge of MAO on herbal titanium. According to X-ray diffraction (XRD) studies, MAO coatings include rutile, and anatase.

In 2017, Lin Xu *et.al* [113] investigation increase the blood compatibility and wettability of ultrafine-grained natural titanium, scientists used the MAO approach to synthesize TiO_2 on an ultrafine-grained pure titanium surface. Compared to the other coatings, the MAO coating exhibited a rougher surface, lower distilled water contact angles, and greater surface energy. Reduced hemolysis, longer dynamic coagulation time, prothrombin time (PT), and activated partial thromboplastin time (APTT), decreased platelet adhesion and deformation, and improved blood compatibility were all benefits of the MAO mutation. The sample with the greatest surface energy, the highest PT and APTT values, the lowest hemolysis rate, much less platelet adhesion, a lower degree of deformation, and better blood compatibility had the longest oxidation duration (9 minutes).

In 2018, C. Wang *et.al* [114] studied the characterization of pure Ti, Ti-6Al-4V, and Ti-35Nb-2Ta-3Zr alloys treated in an electrolyte of sodium silicate using MAO technique. The results show that a nested membrane with a porous structure developed on its cover has better film forming properties than a Ti-35Nb-2Ta-3Zr alloy. In comparison to pure Ti and Ti-6Al-4V, the relative concentration of anatase phase with biological activity is

significantly higher than that of the rutile phase, which may effectively increase apatite deposition capability. Furthermore, Ti-35Nb-2Ta-3Zr exhibits good corrosion resistance following (MAO) process because to its denser and thicker layers. As well as the formation of the passivation film owing to the existence of Nb_2O_5 phase on the surface.

In 2019, A. Sobolev *et.al* [115] investigated the micro arc oxidation (MAO) process has been applied to produce ceramic oxide coating on Ti-6Al-4V alloy. In an electrolyte comprising Na_2CO_3 and Na_2SiO_3, the MAO process was carried out using a symmetric bipolar square pulse. The impact of current frequency on surface shape, chemical and phase compositions, and corrosion resistance was investigated. Electron microscopy morphology and cross-sectional analysis revealed a more compacted and porous coating generated by increased current frequency (1000 Hz). In compared to the untreated alloy, this alloy had a strong corrosion resistance.

In 2020, A. Zakaria *et.al* [116] studied the influence of an electrolyte including trisodium orthophosphate, potassium hydroxide, and calcium fluoride, fluoridated hydroxyapatite was used as a biofunctional coating on Ti6Al4V. Using field emission scanning electron microscopy (FESEM) and an energy dispersive spectrometer, the coating surface and cross-section morphologies were studied, the species in the electrolyte solution were identified, and irregular micropore forms were discovered (EDS). A microscratch test was used to assess the phase composition of the TiO_2 coated surface (anatase and rutile) as well as the coating's adhesive strength. The bioactivity of the coating was tested using a simulated bodily fluid (SBF) immersion test. Result that the PEO technique has a good potential to develop bio-functional surface modifications that can affect the chemical composition and roughness of the coating surface.

In 2020, M. Dziaduszewska *et.al* [117] investigated of Titania-based formed by MAO process on selective laser melted Ti13Zr13Nb have been to evaluate the impact of MAO process parameters in calcium and phosphate (Ca+P) containing electrolyte on surface characteristics, early-stage bioactivity, mechanical properties, and adhesion between the oxide coatings and substrate at different process parameters (voltage, current, and processing time). All coatings were tested for surface topography, surface roughness, pore diameter, elemental content, crystal structure, surface wettability, and early-stage bioactivity in Hank's solution. Resulted in the predictable structure, high Ca/P ratio, high hydrophilicity, and higher critical load of adhesion and total delamination.

2.10.2 Composite and duplex coatings by MAO on Ti-alloys

In 2000, X. Nie *et.al* [118] studied efforts improvement implant combination treatment of (MAO) and electrophoretic deposition was used to improve biocompatibility and durability of (Ti-6Al-4V) alloy. The electrolyte for micro-arc oxidation and the solution for HA electrophoretic deposition, respectively, were a phosphate salt solution and a HA powder aqueous suspension. It is demonstrated that an anodic MAO of titanium can produce a relatively thick and hard TiO_2 coating that is effective as chemical barriers against the in-vivo release of metal ions from the implants, and that a HA coating incorporated on top of the TiO_2 layer can be formed simultaneously using a combination of plasma electrolysis and electrophoresis known as a double layer HA/TiO_2 coating on titanium alloys with HA as the top layer and a dense Ti.

In 2005, B. Sing Ng [119] studied the TiO_2 coating was applied on Ti6Al4V by electrochemical anodisation in two dissimilar electrolytes. After that, the secondary calcium phosphate (CaP) coating was applied by

immersing the substrates in a simulated bodily fluid (SBF) with a threefold concentration (SBF), simulating biomineralisation in biological bone. In SBF, electrochemical impedance spectroscopy and potentiodynamic polarisation measurements indicated that the anodic TiO_2 layer is compact, with in vitro corrosion resistance up to four times that of unanodised Ti6Al4V. These findings indicate that by anodizing Ti6Al4V and then immersing it in SBF, a duplex coating consisting of a compact TiO2 with improved in vitro corrosion resistance and a bone-like apatite coating can be applied.

In 2008, Yan Li *et.al* [120] studied improvement osseointegration, there have been many efforts to modify the surface composition and topography of dental implants. Recently, the anodic oxidation treatment of titanium (Ti) has attracted a great deal of attention. CaP, on the other hand, is frequently used as a coating material on metallic implants for rapid fixation and firm implant bone attachment due to its shown bioactive and osteoconductive characteristics. Anodized surfaces and CaP deposition by electron beam evaporation were coupled in this work. On the micro-arc oxidized Ti, a nanostructured calcium phosphate layer was deposited. When the coated film was incubated in DPBS solution at 37oC, a new apatite layer developed readily. The basic fibroblast growth factor (BFGF) may be immobilized in the newly created apatite layer by adding it to the DPBS solution.

In 2011, H. Cimenoglua *et.al* [121] studied the in-vitro biological reactions of two competing titanium alloys (Ti6Al4V and Ti6Al7Nb) after their surfaces modification by (MAO) technique in a $(CH_3COO)_2Ca.H_2O$ and Na_3PO_4 containing electrolyte under equal electrical conditions and exposure duration. The Ti6Al4V alloy's oxide layer was porous and had HA precipitates, whereas the Ti6Al7Nb alloy's oxide layer was grainy and contained calcium titanate precipitates. The biological performance of the alloys was compared using simulated bodily fluid (SBF) and cell culture ex-

periments. Despite the fact both oxidized alloys responded similarly in SBF tests, the number of SAOS-2 cells adhered to the oxide layer of the Ti6Al4V alloy was higher than the Ti6Al7Nb alloy.

In 2011, YU Sen *et.al* [122] studied a layer of porous film containing Ca and P was generated by MAO on Ti-3Zr-2Sn-3Mo-25Nb alloy, and then the NH2 active group was added to the films by activation treatment. XRD, SEM, EDS, and XPS were used to investigate the phase composition, surface micro-topography, and elemental characteristics of the micro-arc oxidation films, and the osteoinduction of the micro-arc oxidation films was tested using simulated body fluid immersion, in-vitro osteoblast cultivation, and an animal experiment. The results show that the oxide layer is a kind of porous ceramic intermixture and contains Ca and P. The films in the simulated body fluid can induce apatite formation, resulting in excellent bioactivity.

In 2011, Min-Ho Hong *et.al* [123] studied the coating of TiO_2 and HA using MAO, a relatively new surface modification technique where thick, hard, and anticorrosive oxide coatings can be easily and cost-effectively fabricated. The Ti alloy substrate was exposed to pulsed DC electricity and different voltages. Citric acid, ethylene diamine, and ammonium phosphate were also used as electrolytes, which were then mixed with HA nanoparticles. The bonding strength, bioactivity, cell adhesion, and cytotoxicity were all studied in relation to the composition and applied voltage. The TiO_2 and HA samples that were coated concurrently demonstrated enhanced bioactivity, cell adhesion, and viability while preserving the bonding strength between the coated film and substrate.

In 2017, In-Jo Hwang *et.al* [124] studied the HA coatings incorporating Zn and Si on Ti-6Al-4V alloy by PAO. The electrolyte concentration

determines pore size, and the particle size and number of pores increase as the surface and pore components become more complicated. The Zn/Si sample had a larger pore size than the Zn samples. The maximum size of pores reduced, whereas the minimum size shrank up to 10Zn/Si, and Zn and Si have an influence on the development of pore shape. The size of the particle tends to rise as the Zn ion concentration increases, while the number of particles on the surface portion decreases and the size and number of particles on the pore section increase. Zn is mostly found in the pores, while Si is mostly found on the surface. The crystallite size of anatase increased as the Zn ion concentration, whereas, in the case of Si ion added, crystallite size of anatase decreased.

In 2018, Huan-Ping Teng *et.al* [125] studied of HA (Sr-HAp) were directly generated on bulk Ti and TiN-coated substrates (PEO). PEO was carried out on bulk Ti in electrolytes containing (0.4M) $Ca(CH_3OOH)_2.H2O$ and (0.2M) $NaH_2PO_4.2H_2O$, as well as varying quantities of $Sr(OH)_2.8H_2O$ (0.01M). The relative integrated peak intensity, hydrophilicity, and cell survival of the resultant Sr-HAp coatings increased at initially, then fell when the Sr+2 concentration was increased. Sr-HAp coatings with a fine porous morphology were created. In addition, the average growth rate of the coatings over TiN/Si was substantially higher than that of raw Ti.

In 2018, Wei Yang *et.al* [126] studied the electrolytes containing K_2ZrF_6 or K_2TiF_6, the electrolyte composition absorbs into the produced (MAO) coatings on titanium and modifies the surface properties. The results revealed that the electrolyte composition might alter the arcing phenomena, and that it happened in the solution with K_2TiF_6 addition with a short arc beginning time and low arc starting voltage, resulting in a faster coating development rate, better hardness and corrosion resistance.

In 2018, D.R.N Correa *et.al* [127] studied the Ti-15Zr-xMo (x = 0, 5, 10, and 15) wt% alloys, the MAO process was utilized to manufacture porous oxide layers laden with bioactive ions (calcium and phosphorus) for use as Osseointegrative implants. Biocompatibility studies were conducted using the human osteoblastic cell line SAOS-2, which included metabolic activity, mineralization, and differentiation. A characteristic porous coating was generated in all samples, with identical morphologies and thicknesses, which was found to be dependent on the maximum applied voltage. The amorphous and nanocrystalline regions within the films, with a higher fraction of Ca atoms incorporated in the outer layer. Results the combined effect of textured surfaces and surface enrichment with Ca, P is a very promising approach to promote bone formation.

In 2020, C. Garcia-Cabezón [128] studied effect PEO treatment of Ti-6Al-4V alloy formed by powder metallurgy (PM) is an excellent candidate biomaterial for dental implant manufacturing, its intrinsic porosity causes it to have poorer corrosion behavior than alloys obtained by mixing two electrolytes with varying Ca and P contents. In these baths, a homogeneous and adherent layer containing anatasa and rutile phases has been found. In AS solution, electrochemical tests of coated and untreated PM Ti-6Al-4V alloys demonstrated that the PEO coatings not only improved passivation without indications of localized corrosion, but also had a better corrosion potential and reduced current density in the anodic branch of the polarization curve.

2.11 Summary of Literatures:

From the review of literatures, it is clear that many researchers have studied about MAO process coating on Ti-alloys, some researchers studied the effect of TiO_2 by MAO coating on hardness, wear, electrochemical properties and corrosion behavior, also others studied the effects of HA/TiO_2 on these

alloys. Table (2.9) shows comparison between some research and this study.

Table (2.9) comparison between some research and this study.

Reference	Alloy	Process Parameters	Test and character-izations
105	Ti-6Al-4V	maximum power: 60 kW	Vickers hardness test, (SEM), (EDX), (XRD), and Fretting wear
106	Pure Ti	Electrolyte solution: $((CH_3COO)_2Ca.H_2O)=0.1 mol^{-1}$,$(NaH_2PO_4.2H_2O) =0.06mol^{-1}$. Power: 2 kW Voltage: 550V Time: 2,5, 10, and 20 min.	Characterization of microstructure and composition of ox-ide layer (SEM), Nano indentation test (hardness and elastic modulus).
107	CP-Ti, Ti-24Nb-4Zr-8Sn	two-step treatment: (MAO) and alkali heat-ment (MAH) were ap-plied at 250 V.	Surface characteri-zations (SEM,(TF-XRD, XPS), cellular assays test.
108	Pure Ti	Electrolyte solution: con-taining Si, Ca and Na el-ements Time: 1, 3, 5,10, 15, and 30 min	(XRD), (SEM-EDX), micropores on the coating sur-face.
109	Ti-13Nb-	Three different oxides	electrochemical test

	13Zr	were formed in an aerated pH= 5 (0.252 mol/L Na_2HPO_4, 0.115 mol/L NaH_2PO_4): (a) a spontaneous oxide film (about 30min). (b) an oxide grown poten-tiodynamically at a sweep rate of 50 mV/s. (c) an oxide grown by (MAO) at 300 V for 60 s.	in (PBS), EIS and SEM test
110	Cp-Ti Ti-6Al-7Nb	Electrolyte solution: (0.252 mol/L Na_2HPO_4 and 0.115 mol/L NaH_2PO_4) of pH=5. 140 V for Ti-6Al-7Nb and 200 V for CP-Ti.	Raman test, (XPS), (SEM), (EIS), and Fatigue test
111	Cp- Ti	voltage: 300 V Time: 1 min	SEM, TEM, Raman test, and biological tests (Cytotoxicity assay).
112	Pure Ti	electrolyte solution: 5 g/L Na_2SiO_3, 0.1 g/ L NaOH, 3 ml/L $C_3H_8O_3$. The con-centration of $NaAlO_2$ in the base electrolyte varied in the range from 0 to 0.4 g/L. current density: 5	SEM, distribution of element determined by (EDS)

		A/cm^2 Time: 20 min.	
113	Cp- Ti	Electrolyte Solution: 10 g/L sodium silicate, 8 g/L sodium polyphosphate, and 20 g/L calcium acetate Current density :20 A/cm^2 oxidation times: 3, 6, 9, 12, and 15 min	(SEM), (EDS), Hemolysis test, Platelet, and (APTT) tests.
114	pure Ti, Ti-6Al-4V, and Ti-35Nb-2Ta-3Zr	Electrolyte Solution: $Na_2SiO_3{\cdot}_9H_2O$ (10 g L^{-1}), $(HOCH_2CH_2)3N$ (5 ml/L) and HCl (1 mol/L, be used to regulate the pH value to 11.5).	(SEM), (EDX), (XRD), Corrosion resistance tests, and Wetting angle test.
115	Ti-6Al-4V	Electrolyte solution: contained (Na_2CO_3 = 10 g/L and ($Na_2SiO_3.5H_2O$ = 2 g/L. Imax = 5 A, Umax = 1000 V.	Coating Characterization (SEM, EDX, and PIXE), and resistance test.
116	Ti-6Al-4V	Electrolyte Solution : 5 g of tri-sodium orthophosphate, 3 g of calcium fluoride , and 2 g of potassium hydroxide in 1000	FESEM, EDS, PDXL, XRD, Micro-Scratch Test, and In Vitro test.

		mL distilled water with a pH of 12.55. Voltage: 400V Maximum current applied: 1 A Treatment time: 10 min	
117	Ti13Zr13Nb	Electrolyte Solution: $C_3H_7CaO_6P$ (GP)= 0.1 $mol.L^{-1}$ and 0.15 $mol.L^{-1}$ $Ca(CH_3COO)_2$. Voltages: 200, 300, and 400 V. constant current: 32mA for 10 and 15 min, and a constant current of 50 mA for 10 min.	Coating Characterization (SEM, EDX, XRD), Nanomechanical (hardness, maximum indent depth, Young's modulus, Ecoating/Esubstrate) , and wettability test.
118	Ti-6Al-4V	Electrolyte Solution: A phosphate salt solution (8-10 g/l), 3 g/l of HA	(XRD), (SEM), (FTIR), corrosion test, Hardness test, and scratch adhesion tests.
119	Ti6Al4V	The electrolyte solution: (0.5 M) NaOH or 0.5 M H2SO4.	Corrosion resistance test,
120	Cp-Ti	……	(SEM), (TEM), and (XRD).
121	Ti6Al4V and	electrolyte solution: $(CH_3\text{-}COO)_2Ca{\cdot}H_2O$ and	(EDS), (SEM), (XRD) analysis,

	Ti6Al7Nb	Na_3PO_4. voltages: 500 and 83 V. Time: 5 min .	SBF Tests, and Cell Culture tests.
122	Ti-3Zr-2Sn-3Mo-25Nb	electrolytic solution: 0.08 mol/L ($C_3H_7Na_2O_6P·5H_2O$, β-GP) and 0.8 mol/L ($(CH_3COO)_2Ca·H_2O$). voltage: 250−500 V Time: 7 min.	Characterization of films (SEM and a quantative analysis of the chemical composition of the anodic layer), XPS analysis, Cell culture test, Osteoblast attachment and proliferation, Hard tissue reaction analysis, and Immersion tests.
123	Ti–6Al–4V	electrolytic solution: ($C_6H_8O_7$), [$C_2H_4(NH_2)2$], [$(NH_4)3PO_4$], and HA nanoparticles were dispersed into the prepared electrolyte to adjust the pH from 4 to 11. Voltage: 400, 480 V	Characterization of the TiO2 film (XRD, SEM, EDX), and Biological test.
124	Ti-6Al-4V	electrolytic solution: Ca/P, 5Zn, 10Zn , 20Zn 0.12 0.02 0.03 3 5Zn/5Si , 10Zn/5Si, and 20Zn/5SI	Surface characterization (XRD, FE-SEM, EDX).

		voltage: 280 V. Time: 3 min.	
125	bulk Ti	Electrolytes Solution: 0.4M $Ca(CH_3OOH)_2.H_2O$ and 0.2M $NaH_2PO_4.2H_2O$ mixed with various concentrations of $Sr(OH)_2.8H_2O$ ranging from 0- 0.1M Voltage: 350 V Time: 15 min .	(XRD, FE-SEM, EDX), contact angles test, MTT assay test.
126	pure Ti	Electrolytes Solution: (20 g/L) and silicate with the addition of K_2ZrF_6 (5g/L) or K_2TiF_6 (5g/L). maximum power: 30 kW. Time: 10 min. current density: 1 A/dm^2.	Coating characterization (XRD, SEM, EDX), Vickers hardness test, Tribological behavior, and Corrosion resistance.
127	Ti-15Zr-xMo (x = 0, 5, 10 and 15 wt%)	Electrolyte Solution: 0.15mol/L ($Ca(CH_3COO)2$) and 0.10 mol/L ($C_3H_7CaO_6P$), current density: 311 A/m2. Voltage: 300 V, 350 V and 400 V. Time: 10 min.	(SEM, XRD, EDX, and (TEM) , Bioactivity evaluation, Cell culture, Viability assay, Alkaline phosphatase staining, and Alizarin red staining.

128	Ti-6Al-4V obtained by powder metallurgy (PM)	Electrolytes Solution: (1) a commercial electrolyte provided from Keronite (Keronite Electrolyte 1003-01 for titanium) which is composed of 0.1–1% sodium fluoride (NaF) and other Ca- and P-based chemical compounds. (2) 0.35 M of calcium acetate hydrate and 0.02 M of glycerol phosphate disodium salt pentahydrate. current density: 25 A/cm^2. Time: 10 min.	Microstructural and Mechanical Characterization (optical metallography and (SEM/EDS), Corrosion Testing, Cytocompatibility tests.

2.12 Concluding Remarks

The previous workers in literature showed the effect of dispersant and the parameters of MAO like as applied potential, deposition time, suspension medium on the corrosion behavior and morphology of TiO_2, and HA/TiO_2 coated Ti-alloys substrates. The following remarks can be listed:

1. TiO_2 coatings by MAO process was suitable for deposition of high corrosion resistance in compassion to the uncoated sample.

2. Based on the substrates materials, selecting of MAO parameters depending on the optimum deposition voltage and time, could which result in less porous and good strength coating layer.
3. The addition of enough amount of HA to the deposited HA/TiO_2 composite coatings result in bond strength accretion to Ti substrate and cause a reduction of corrosion rate in solution. Moreover, the morphology of the composite coatings was uniform and less porous structure.

What distinguishes the current work is that the using of Ti-6Al-7Nb alloy exclusively as the substrate for the HA/TiO_2, ZrO_2/TiO_2, and HA/ZrO_2/TiO_2 nanocomposite deposition as utilized by the other researchers and investigations and thus it will give a high performance low cost biomaterial used in bone fixation for orthopedic applications.

Chapter Three
Experimental Work

Chapter Three
Experimental Work

3.1 Introduction

This chapter presents the materials that are utilized in the present work and preparation of these materials with the experimental procedure for MAO process as well as the testing and evaluation methods. The experimental part of this study involves the preparation of samples and suspension for coating by means of the MAO technique. In addition, the description of coating process, equipment and conditions are utilized in this chapter. The block diagram shown in Figure (3.1) clarifies the main activities of this work.

3.2 Materials

1. A rod of Ti-6Al-7Nb alloy made in (Shanxi Joint industry co., ltd), was used to prepare the substrates. The chemical composition of this alloy is shown in Table (3.1). This test was carried out in Science and Technology Ministry.

Table (3.1): Chemical composition analysis of the Ti-6Al-7Nb alloys.

Element	Al	Si	Fe	Ni	Nb	Ti
ASTM(Wt%)	5.5-6.5	≤ 0.31	≤ 0.25	≤ 0.31	6.5-7.5	Rem.
Wt%	6.12	0.11	0.21	0.29	7.26	Rem.

2. Hydroxyapatite nanopowder (Hualanchem, CAS No. 1306-06-5, China) with primary particles size of 40 nm and purity ≥ 96%.

3. Zirconia nanopowder (Skyspring, CAS No. 1317-70-0, USA) with primary particles size of (30±5) nm and purity >99.94%.

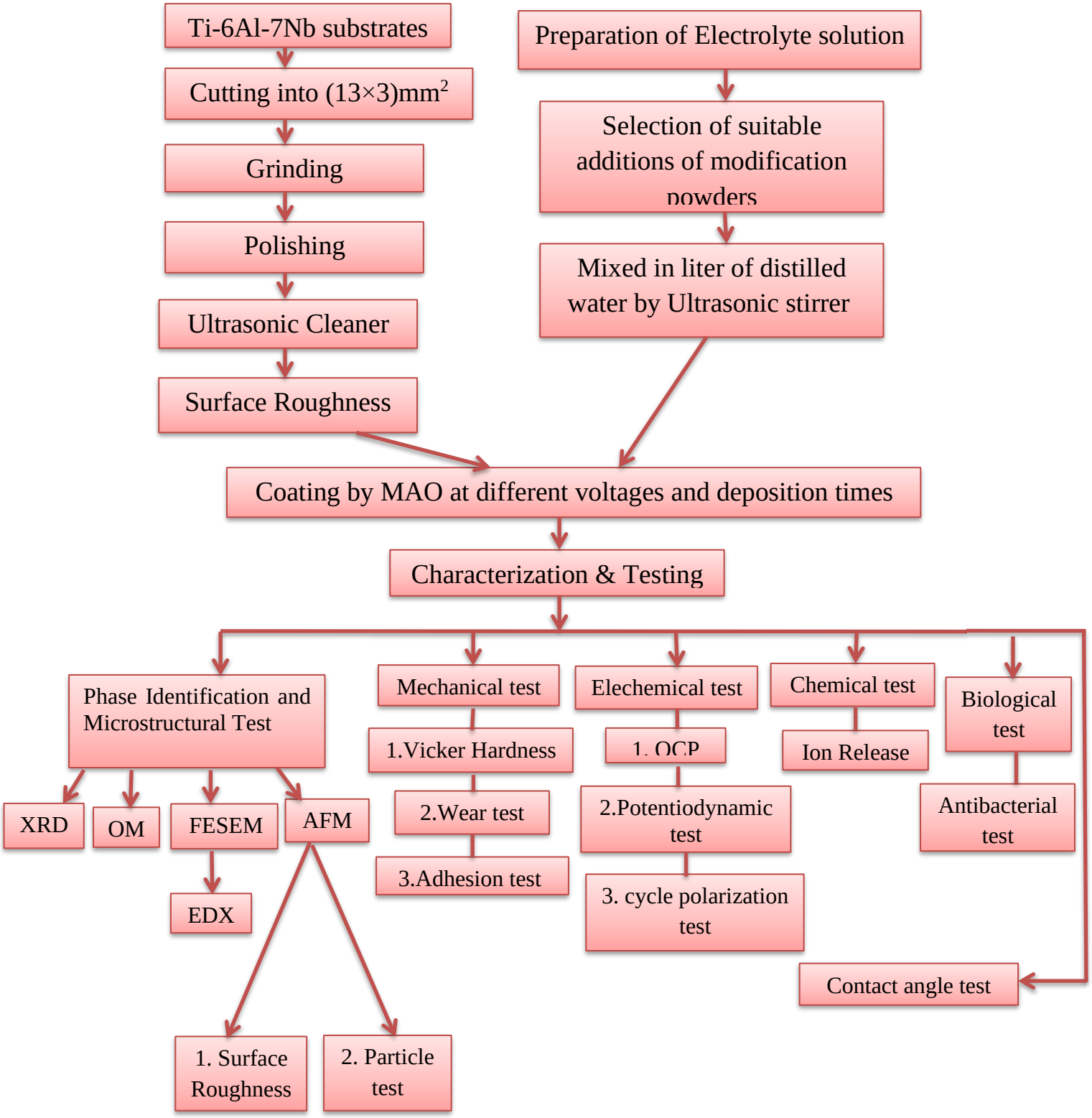

Figure (3.1): Block diagram of the experimental procedures.

3.3 Equipment and Instruments

The following equipment and devices were used in this work:

1. Wire cut machine (Germany origin).
2. Grinding and polishing device (UNI POL-820, MTI Corporation, made in Toky).
3. Ultrasonic cleaner.
4. Surface roughness tester (HSR210, made in china).
5. Light optical microscope, model (1280XEQ-MM300TUSB) (Metallurgical Department /materials engineering college/Babylon university).
6. XRD instrument type (XRD-6000) (Nanotechnology and Advanced Materials Research Center/ University of Technology.
7. Field-Emission Scanning electron microscopy (FE-SEM) (ΣIGMA, JSM-7610F, Carl Zeiss, made in Germany (Tehran University).
8. Laser particle size analyzer, better size 2000 (Ceramic Department / materials engineering college / Babylon university).
9. Ultrasonic Cell Crusher SJIA-1200W MTI Corporation (Polymer and Petrochemical Industries Department/materials engineering college/Babylon university)
10. pH meter (CAN/CSA STD C22.2 NO.61010-1, made in Germany).
11. Sensitive Balance Type (L220S– D) with (± 0.0001% accuracy), made in Germany.
12. A Dc-Ac homemade MAO deposition unit shown in Figures 3.3.
13. Vickers Hardness (HV-1000) model Reicherter, Ut l250.
14. Corrosion potentiostats, model Digi-lvy,112609 (Metallurgical Department /materials engineering college/Babylon university).
15. Contact angle test, model SL 200KS (Ceramic Department /materials engineering college/ Babylon university).

16. Atomic force microscopy (AFM) Type was PHYWE/Nano Compact, made in UK (Department of Science/University of Baghdad).
17. Wear test Type (Pin-on-Disc), MT 4003, TRIBOMETER model (MT/60/H), made in U.S.A.
18. Adhesion Test model (ATM), (POSITEST AT, AT09377, made in U.S.A. (Metallurgical Department/materials engineering college/Babylon university).

3.4 Sample Preparation

3.4.1 Sample Preparation for Metallographic Examination

The preparation of substrates was carried out by using a silicon carbide (SiC) emery papers (120, 220, 320, 400, 600, 800, 1000, 2000, 3000) μm grit size for grinding the surface of the sample, and then the substrate was rinsed with distilled water. After that, the substrates were polished by a diamond paste of 1.5μm to get a smooth mirror finish by using the grinding and polishing machine. Etching was made at room temperature using (10ml HF, 5ml HNO_3 and 85ml H_2O) solution according to ASTM [129]. After immersing the prepared samples in etching solution for 5-10 seconds, they washed with distilled water and dried, to be ready for microstructure analysis.

3.4.2 Sample Preparation for MAO

The Ti-6Al-7Nb alloy rod was cut by using a wire-cutting machine into $\phi 13 \times 3 mm^2$ dimension. In order to improve the mechanical bonding and adhesion between the coating and the substrate, prior to coating process, the average surface roughness (Ra) of (0.08μm) [130], degreased with acetone , then rinsed with distilled water , drilled for clamping to be used for MAO process.

3.5 MAO Process

The ceramic coatings were deposited using a DC-AC handmade MAO deposition device with a voltage of (0-500) V and a current of (0-5) A, as illustrated in Figures (3.2) and (3.3).

A three-litter container bath was utilized. The electrolyte was stirred and chilled in the plastic container using a mechanical stirrer and cooling system, respectively. A sample holder served as the anode, and a stainless steel 316L plate served as the cathode, in the plastic container. The cooling unit attached to the MAO unit keeps the temperature of the electrolyte solution below 30℃. It delivers chilled water to a large plastic container containing an electrolyte solution.

The electrolytic solutions were mixed after preparation before the MAO process. The current-voltages values in this study could prove the possibility of using the electrolytes in formation of titanium oxide layers and coatings Ti sample using moderate current and voltages shown in Table (3.2).

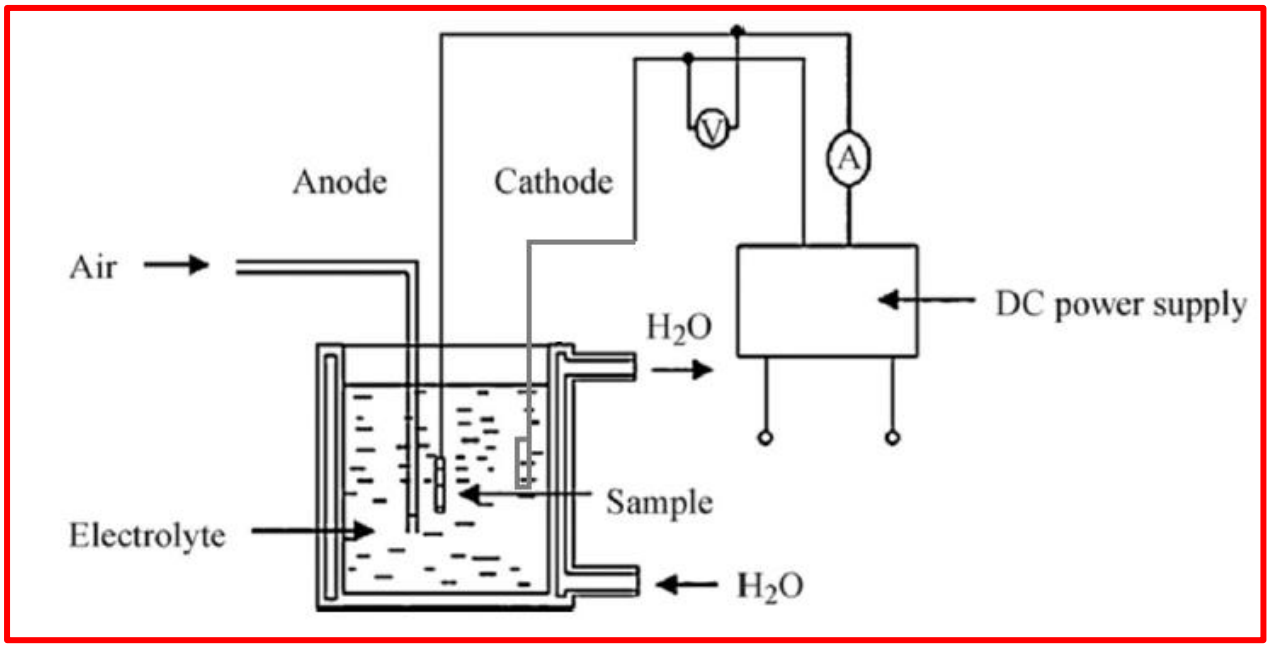

Figure (3.2): Schematic of equipment's for MAO coating.

Figure (3.3) : Photographs of MAO coating unit: (1) (cooling system), (2) Mixer, (3) coating container, (4) cooling container, and (5) power supply.

Table (3.2): Electrolyte solutions and Parameters of MAO process.

Group	Electrolyte solution types	PH	Voltage (V)	Times (min)
A	Na_2CO_3=10g/l Na_2SiO_3=2g/l	8	300,350, 400	7,15,30,60
B	HA=6g/l, EDTA=3g/l, NaOH=8g/l, KOH=1g/l	10.5	300,350, 400	7,15,30,60
C	ZrO_2=6g/l, Na_3PO_4=5g/l, KOH=1g/l	10	300,350, 400	7,15,30,60
D	HA=3g/l, ZrO_2=3g/l, Na_3PO_4=5g/l, CaF_2=2g/l, KOH=1g/l	11	300,350, 400	7,15,30,60

3.6 MAO Experimental Procedure

3.6.1 Preparing Electrolyte solution

Several attempts have been done to select the electrolytic solutions using different compositions of the MAO electrolytes containing nano powder of HA and ZrO_2 additives and other additives for property modification Na_3PO_4, EDTA, NaOH, Na_2CO_3, Na_2SiO_3 and KOH to increase conductivity [131], which was mixed in liter of distilled water by Ultrasonic stirrer before the deposition process. Table (3.3) show the main electrolytic solutions used in the MAO process.

Table (3.3): Composition of electrolytic solutions.

Group	Samples	Voltage (V)	Times (min)
A	A_1	300	7
	A_2		15
	A_3		30
	A_4		60
	A_5	350	7
	A_6		15
	A_7		30
	A_8		60

	A_9	400	7
	A_{10}		15
	A_{11}		30
	A_{12}		60
B	B_1	300	7
	B_2		15
	B_3		30
	B_4		60
	B_5	350	7
	B_6		15
	B_7		30
	B_8		60
	B_9	400	7
	B_{10}		15
	B_{11}		30
	B_{12}		60
C	C_1	300	7
	C_2		15
	C_3		30
	C_4		60
	C_5	350	7
	C_6		15
	C_7		30
	C_8		60
	C_9	400	7
	C_{10}		15
	C_{11}		30
	C_{12}		60
D	D_1	300	7
	D_2		15
	D_3		30
	D_4		60
	D_5	350	7
	D_6		15
	D_7		30
	D_8		60
	D_9	400	7
	D_{10}		15
	D_{11}		30
	D_{12}		60

3.6.2 MAO Coating Process:

This procedure was carried out according to the following steps:

1- Filling the electrolyte glass container with the specified electrolyte solution . see Figure (3.3).

2- Using a cooling device, chilling the solution to the starting temperature of 5°C.

3- Depositing ceramic coatings by the MAO unit. In this step, the DC current-Voltage values in steady state arcs during MAO process were recorded.

Different types of arcs could be observed during MAO process as shown in Figure (3.4), and different types of coated samples using those different electrolytes are shown in Figure (3.5).

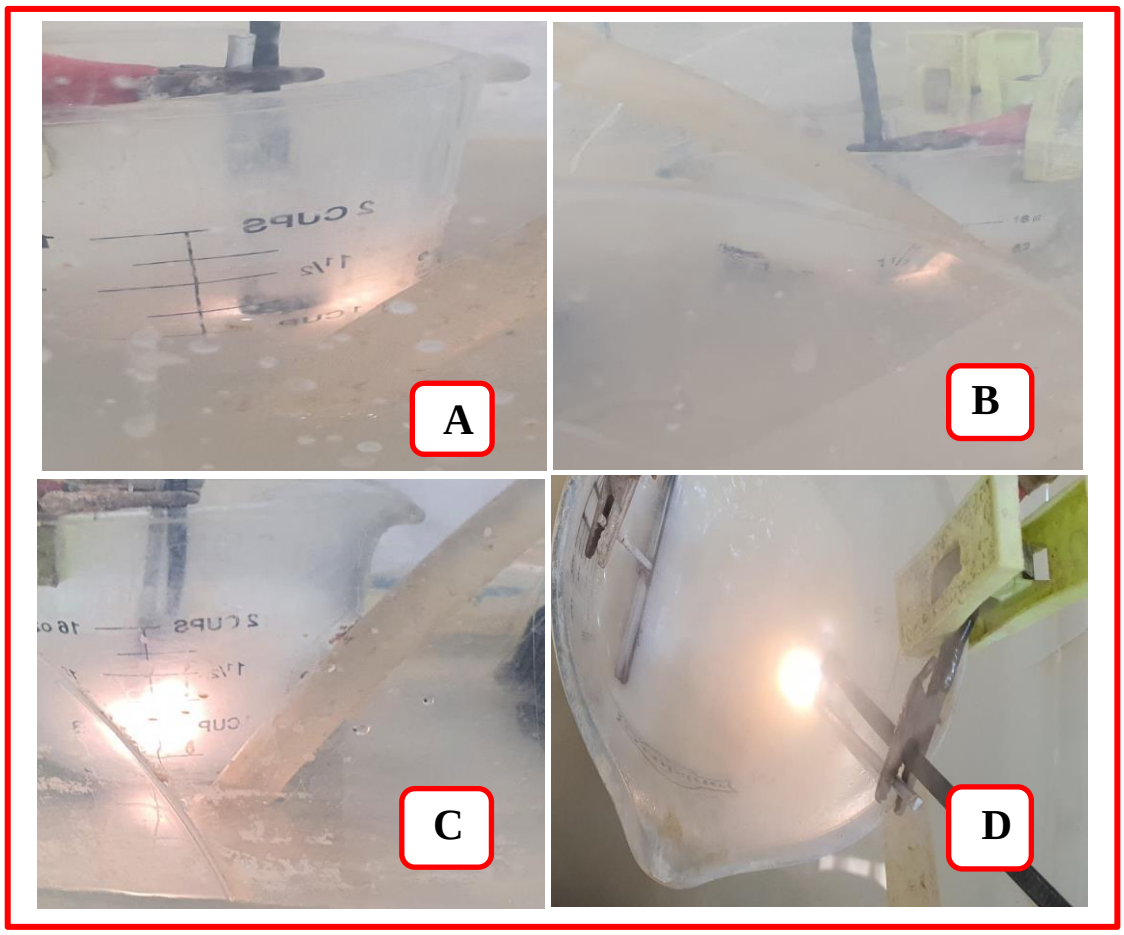

Figure (3.4): Micro sparks in different types of the electrolytes (Group A, B, C and D).

Figure (3.5): Coated samples using different electrolytes (A, B, C, and D).

3.7 Characterization of Powders and Coatings

3.7.1 Analysis of Partical size

The particle size analysis (PSA) of the (HA) powder and ZrO_2 was determined by (Type Better size 2000 laser particle size analyzer shown in Figure (3.6).

Figure (3.6): Particle size analyzer.

3.7.2 Phase Identification

The test of X-ray diffraction analysis (XRD- 6000) had been taken so as to characterize the nano powder (HA and ZrO_2) in the present work, also substrate Ti-6Al-7Nb alloy and coating samples, as shown in Figure (3.7) Cu Kα radiation (λ = 1.5405 Å) were used in the XRD, with a scanning speed of 3˚/min from (20º to 90º)of 2θ and a power of Kv/30 mA.

Figure (3.7): X-ray diffraction instrument.

3.7.3 Light Optical Microscope (LOM)

Involved identification and measurement of the phases, shape and grain size are some characteristics of grain boundaries could be evaluated by optical microscope, it was professional metallurgical microscope with polarizing dark field reflected light, as shown in Figure (3.8).

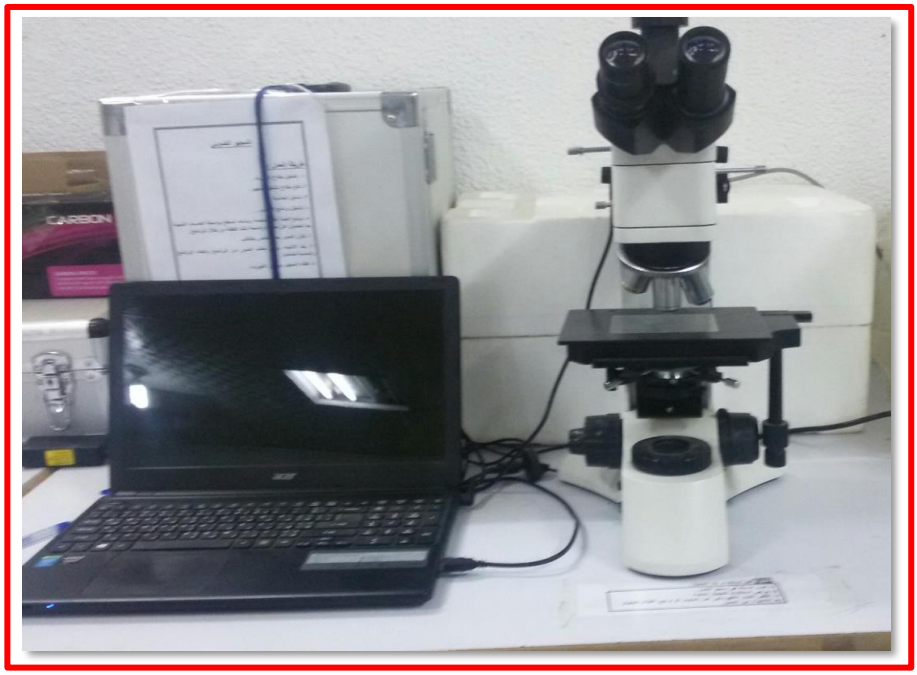

Figure (3.8): Shows Optical microscopy.

3.7.4 Field Emission Scanning Electron Microscopy (FE-SEM) and Electron Dispersive Spectroscopy (EDS)

SEM is one of the most widely used surface examination methods, allowing for the observation of a wide variety of scales and features. In the present work, SEM was used to reveal the microstructure of coated and uncoated substrates. It was used to characterize the morphology and microstructure of the coated surface in terms of uniformity as shown in Figure (3.9). Also, FESEM was used for the coated substrates because the high resolution to the topography of surface in nm.

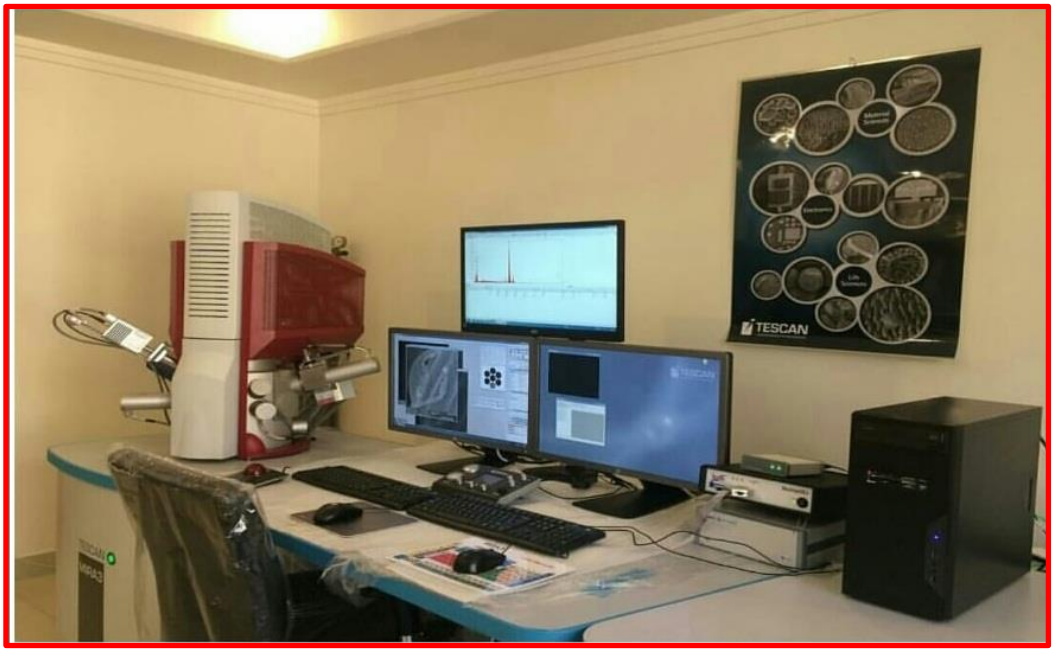

Figure (3.9): The Scanning Electron Microscope (SEM) Analyzer.

3.7.5 Atomic Force Microscope (AFM) Analysis

The depth morphology and surface roughness were investigated using atomic force microscope (AFM) for the coated and uncoated (Ti-6Al-7Nb) substrates as shown in Figure (3.10).

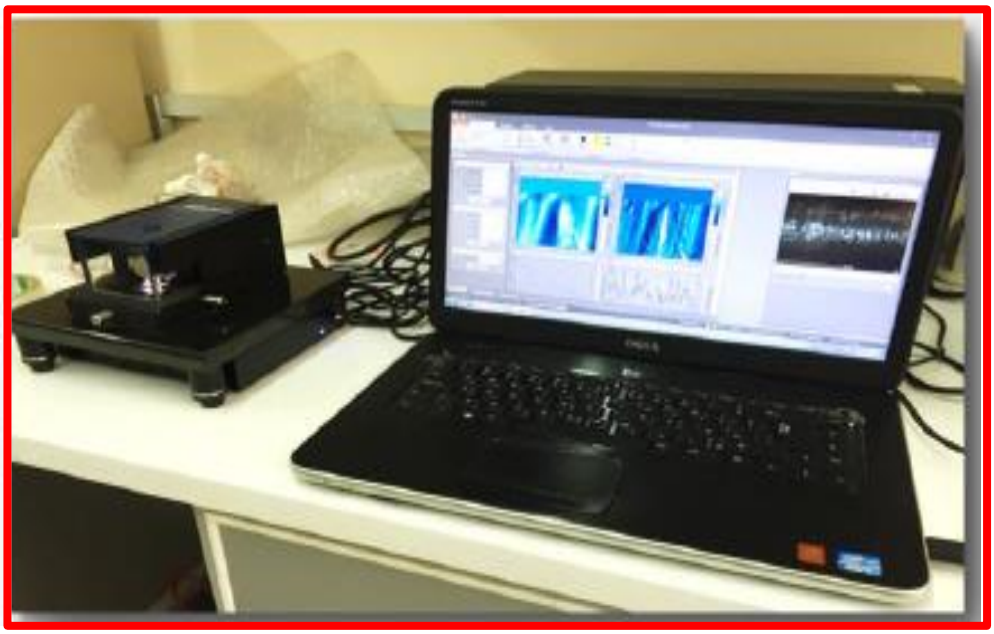

Figure (3.10): Atomic Force Microscope device.

3.8 Mechanical test

3.8.1 Hardness Test

Micro-hardness testing was used to measure the hardness values by (a Digital Micro hardness tested HV-1000) as shown in Figure (3.11). This test is used to measure the hardness of TiO_2 thin film, HA/TiO_2, ZrO_2/TiO_2 composite coating, uncoated sample, with different coating parameters (voltage and time) at load (0.49N) and holding time of 15 seconds.

Figure (3.11): Hardness test.

3.8.2 Wear Test

Tribology can be defined as the science and technology of two surfaces that interact in motion of subjects and practices relatively. Among the main causes of material wastage or decrease of mechanical performance is wear, therefore, reducing it might eventually result in considerable savings. Wear and dissipated energy are most often the result of friction [133]. Specific wear rate was measured by using the pin on disc devise type (PIN ON DISK TRIBOMETER model MT/60/H) shown in Figure (3.12).

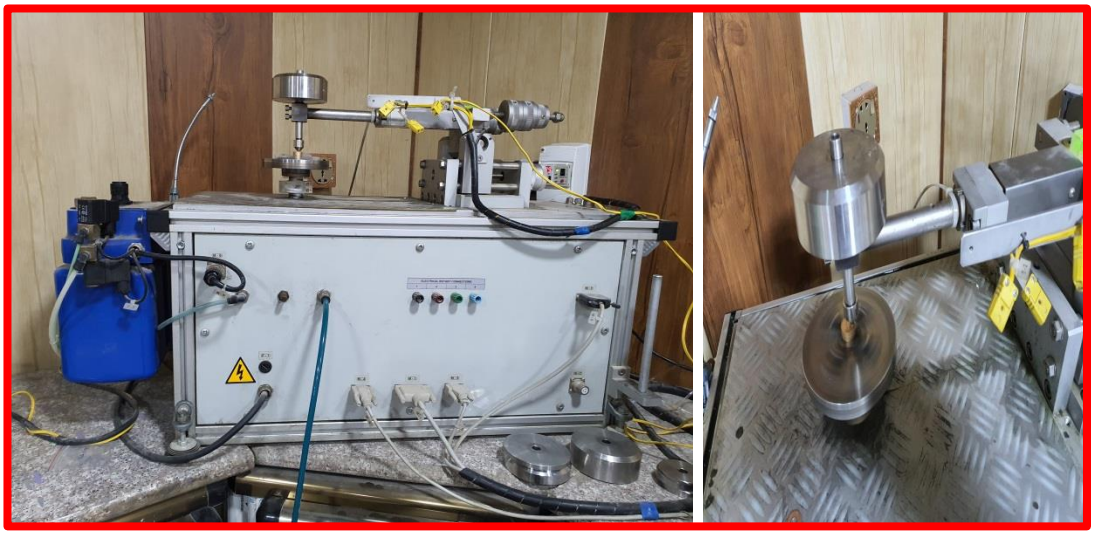

Figure (3.12): Wear test.

The weight of substrate was measured and considered as initial weight (w_o). It was inserted in the holder, making sure the end surface of specimen was parallel to the disc surface. Holder was adjusted to get the desirable wear track radius 6mm. The load was 10N with a rotation speed of 350rpm. The manner is repeated until reached to 30min. The wear rate was determined as in [134]:

$$\text{Specific wear rate} = \frac{\Delta W}{S}\left(\frac{g}{cm}\right) \ldots\ldots\ldots\ldots\ldots\ldots\ldots\ldots\ldots \text{equ. (3.1)}$$

Where:

$\Delta W = \text{Weight lost (g)}$

$S = \text{Sliding distance (263.76m)}$

$S = \text{Sliding Velocity (m/sec)} \times \text{time (sec)} \ldots\ldots\ldots\ldots \text{equ. (3.2)}$

$$\text{Sliding Velosity} = \frac{\pi DN}{30 \times 1000}$$

Where:

$D = \text{wear track diameter selected (10mm)}$

$N = \text{Speed of rotation disk (350rpm)}$

3.8.3 Adhesion testing:

The pull-off test is the most basic test technique in terms of idea. This test employs an adhesive-fixed stud that is peeled off the coating (ASTM D4541),

equipped with a force-recording mechanical testing equipment [135], as may be seen in Figure (3.13). The problem with this test is that the highest adhesive strength that can be measured is also the maximum adhesive strength that can be obtained. Tensile strength of high-performance adhesives is generally less than 100 MPa. In this test, the adhesive material utilized was (EPOXI-PATCH). Achieving this degree of stress in a practical test needs precise procedures to enhance adherence to the coating and keep the force direction perpendicular to the sample.

Figure (3.13): Conventional adhesion test method.

3.9 Contact Angle Test

Contact angle test was accomplished to evaluate the effect of additives on the wettability of pure materials by means of contact angle range (0^{o} to 180^{o}) as shown in Figure (3.14). This device makes calculation of contact angle and calculate their average values and giving a real-time data graph monitoring changes of contact angle with video recording.

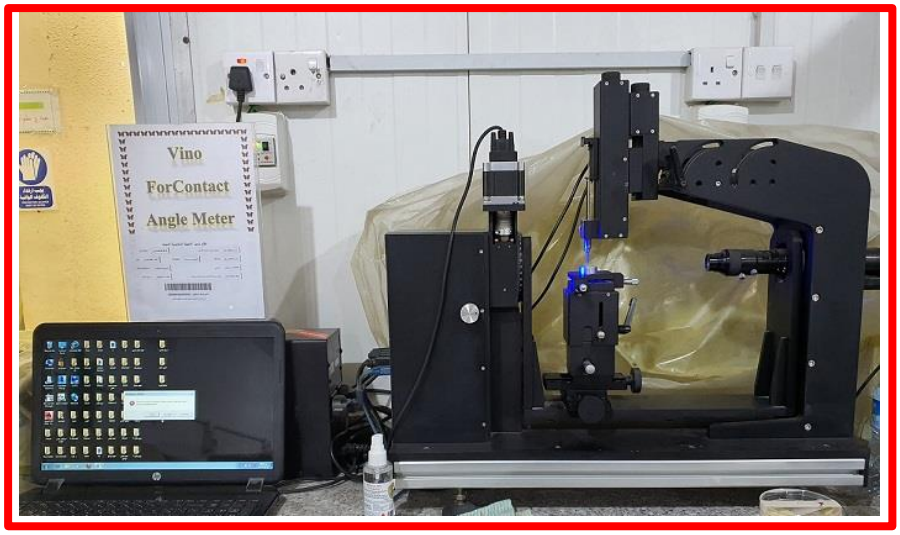

Figure (3.14): Contact Angle Device.

3.10 Electrochemical Test

Corrosion behavior of coated and uncoated substrates and coating was studied in two different solutions (Ringer and Saliva solution). The chemical compositions of Ringer and Saliva solution are illustrated in Tables (3.4) and (3.5) respectively. The pH of both solutions at 37C° were 7.3 and 7.4, respectively.

Table (3.4): Composition of Ringer solution [136].

NO.	Constituent	g/l
1	NaCl	9.00
2	KCl	0.43
3	CaCl2	0.24

Table (3.5): Composition of Artificial Saliva [137].

NO.	Constituent	g/l
1	NaCL	0.70
2	KCL	1.30
3	KSCN	0.33
4	NaHCO3	1.50
5	Na2HPO4	0.26
6	KH2PO4	0.20

3.10.1 Open circuit potential (OCP)

The goal of the OCP-time measurement is to better understand the corrosion behavior of coated and uncoated samples in Ringer and Saliva solution under equilibrated conditions. The OCP-time measurement is a crucial metric for determining the stability of the specimens' passive film. The samples were submerged in Ringer's and Saliva's solutions at 37°C, PH 7.3, and 7.4 correspondingly for the experiments. The working electrode's potential is monitored in relation to a Saturated Calomel electrode (SCE). Between the working electrode and the reference electrode is a voltmeter that is saturated. For each specimen 30 min open circuit potential measurement was performed, as shown in Figure (3.15). The first record was taken immediately after immersion then the voltage was monitored for the interred period of test at an interval of (5min).

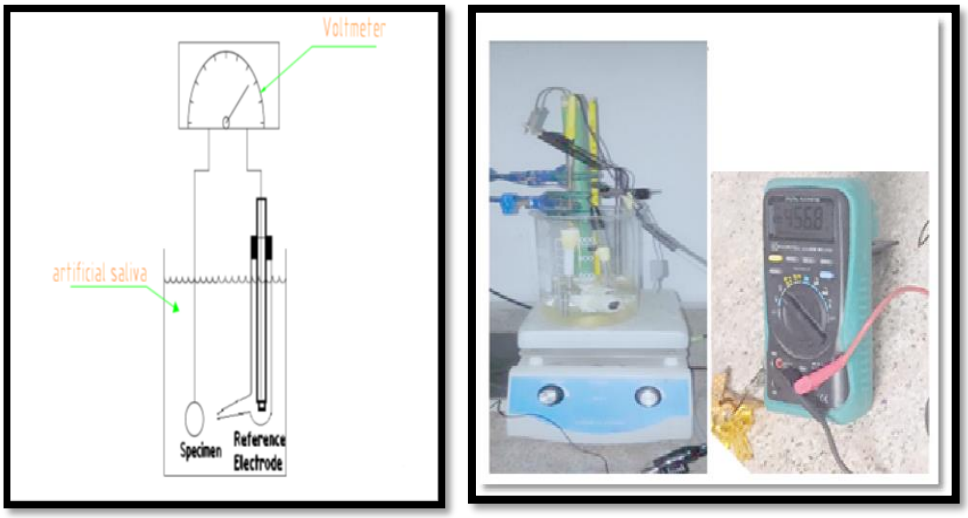

Figure (3.15): Schematic drawing of Open Circuit Potential Measurement.

3.10.2 Potentiodynamic and cycle polarization test

As an electrolyte potentiodynamic and cyclic polarization test, electrochemical tests were conducted in three electrode cells containing Ringer's solution and Saliva's solution. As indicated in Figure (3.16), the counter electrode was Pt, the reference electrode was SCE, and the working electrode was a specimen.

The corrosion cell consists of three electrodes:

1. The working electrode (Ti-6Al-7Nb sample).
2. The counter electrode (platinum rod).
3. The saturated calomel electrode (SCE).

Figure (3.16): Schematic Diagram of Potentiodynamic Polarization Cell.

The corrosion rate (CR) was calculated by Tafel plots by using anodic and cathodic branches. corrosion rate measurement is obtained by applying the following equation [138].

$$C_R = \frac{O.13\ \mathrm{I}_{corr.}(E.W)}{A.\rho} \ldots\ldots\ldots\ldots\ldots equ(3.3)$$

Where:

C_R = Corrosion rate
E. W. = equivalent weight (g/eq.)
A = area (cm^2)
ρ = density ($\mathrm{g/cm}^3$)
0.13 = metric and time conversion factor
$\mathrm{I}_{corr.}$ = The total current (μA)

$$\text{improvement percentage} = \frac{(C_R - C_{R^\circ})}{C_R} * 100\% \ldots\ldots\ldots equ(3.4)$$

Where:

CR° = the corrosion rate of master sample(without coated).

CR = the corrosion rate of coated sample (with coated).

3.11 Chemical Test

3.11.1 The ions release

This test was achieved by using atomic absorption spectroscopy device, shown in Figure (3.17). In order to determine the amount of Ti ions Al ions and Nb ions before and after coating into Ringer and Saliva solution. The dissolution test was used to measure the ions in both solutions from the samples immersed for 21 days at 37°C. A sample of each type, uncoated and coated TiO_2, HA/TiO_2 , ZrO_2/TiO_2, and HA/ZrO_2/TiO_2 composite coating samples are immersed in 50 ml of Ringer and Saliva solution in poly propylene (PPM) bottles. The (PPM) bottles were closed tightly and incubated in the thermostatic chambers at 37 °C for 21 days. All bottles were shaken gently for a few seconds every 3 days. After 21 days, the Ringer and Saliva solutions in the bottles were analyzed by atomic absorption spectroscopy to determine the amount of Ti, Al and Nb ions leached from each specimen.

Figure (3.17): Atomic absorption spectroscopy (AAS).

3.12 Biological Test

3.12.1 Antibacterial Test:

The danger of first microbial colonization and bacterial assault exists on the surface of biomaterial. The antibacterial activity of the TiO_2 and HA/TiO_2, ZrO_2/TiO_2, and $HA/ZrO_2/TiO_2$ nanocomposite by MAO process was investigated to evaluate whether the coated layer is antibacterial or not. The antibacterial activity was studied by using the inhibition zone method. An antibacterial kinetic test using Escherichia coli bacterial strains (*E.coli*, American type culture ATCC 25922, gram negative bacteria). The *E.coli* could spread hematogenous from a urinary tract infection and reach to the bone and cause osteomyelitis in an adult [139]. For the bacteria preparation, the *E.coli* was grown on a nutrient agar (N. agar) and placed in the incubator for 24 h at 37°C. Then the bacteria were spread on a petri dish where the suspensions were placed in four different regions on it then incubated at 37°C for 24 hours. After that the inhibition zones were observed.

Chapter Four
Results and Discussion

Chapter Four
Results and Discussion

4.1 Introduction

This chapter includes the explanation of the results and discussion of them. Results are analyzed to select the appropriate suspension for the MAO process and identify the best condition for the HA/TiO_2, ZrO_2/TiO_2, and HA/ZrO_2/TiO_2 nanocomposite ceramic coating on Ti-6Al-7Nb alloy. The results characterization and estimation are obtained by micro-hardness test, XRD, AFM, FESEM with EDS, wear test and adhesion test. In addition, the electrochemical corrosion behavior of the coating layer has been investigated in vitro by Ringer's and saliva solution at 37±1℃. Finally, the chemical test include ion release and antibacterial study test is also investigated.

4.2 Particle Size of Powders

Figure (4.1) shows the particle size distribution of HA nano powder. Particle's size of the HA nano particle distributes on the 1.033nm to 5.844nm with a mean size of 4.210nm.

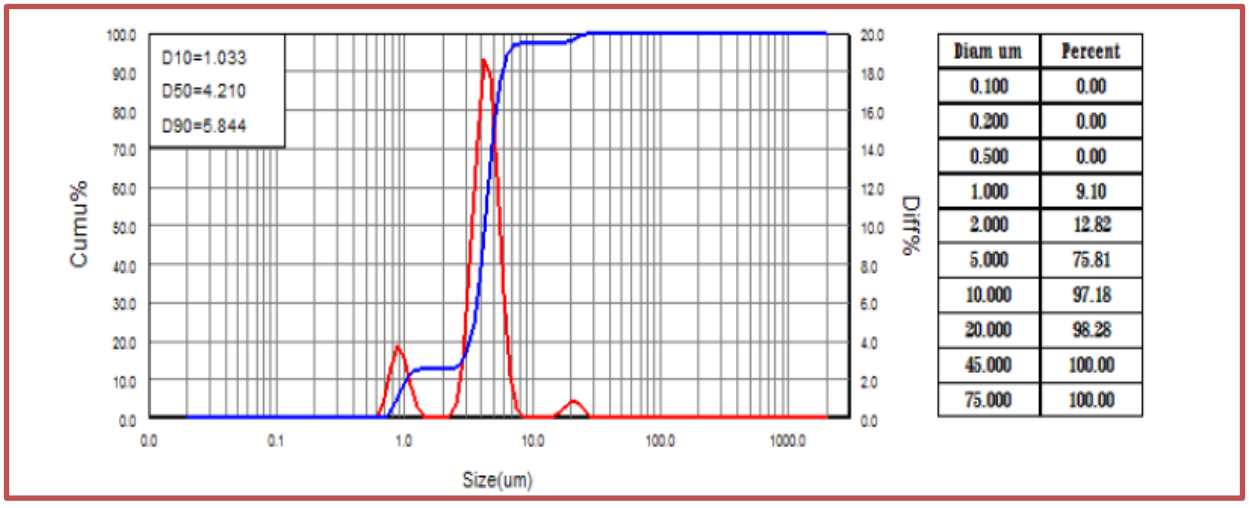

Diam um	Percent
0.100	0.00
0.200	0.00
0.500	0.00
1.000	9.10
2.000	12.82
5.000	75.81
10.000	97.18
20.000	98.28
45.000	100.00
75.000	100.00

Figure (4.1): Particle Size analysis of HA nano Powder used in this study.

Figure (4.2) shows the particle size distribution of ZrO_2 nano powder. It can be seen that particles size of the ZrO_2 particle distributed on the 0.226nm and 4.307nm with a mean size of 0.727nm.

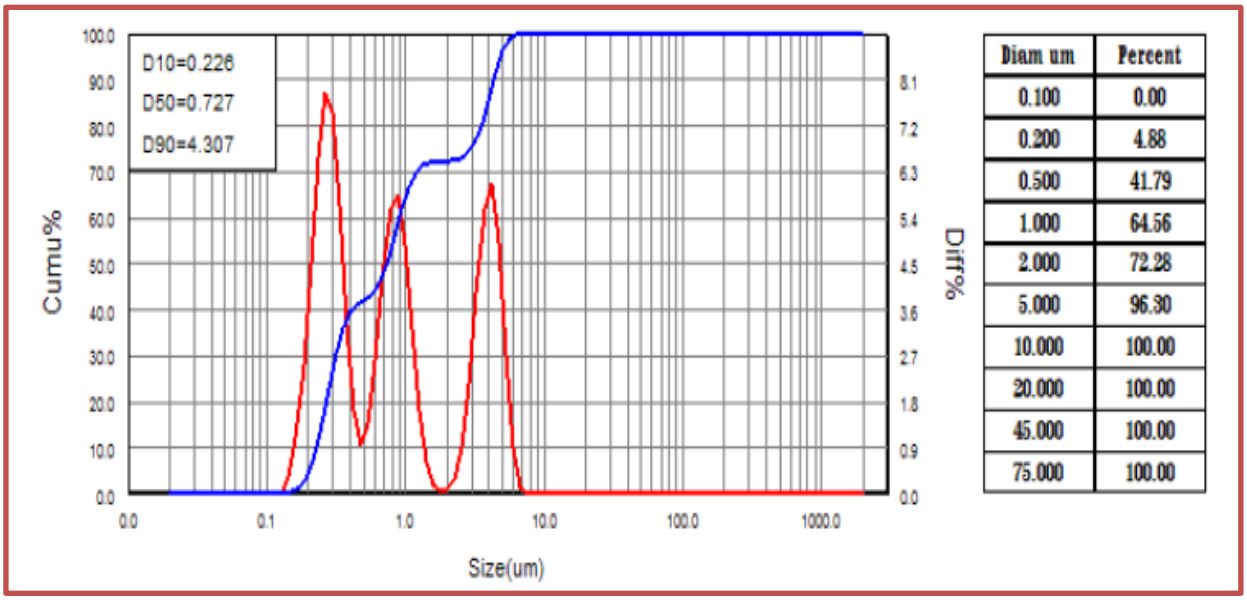

Diam um	Percent
0.100	0.00
0.200	4.88
0.500	41.79
1.000	64.56
2.000	72.28
5.000	96.30
10.000	100.00
20.000	100.00
45.000	100.00
75.000	100.00

Figure (4.2): Particle Size analysis of ZrO_2 nano Powder used in this study.

4.3 X-ray Diffraction

4.3.1 XRD of the powder

The X-ray diffraction of the nano powder HA and ZrO_2 was done is to ensure the type of powder as shown in Figure (4.3) shows the XRD patterns of HA nano powder at angle (2Θ) from 10° to 50°. The phases were identified by comparison with standard reference patterns for hydroxyapatite from powder file (JCPDS cards NO.09-0432). The XRD patterns of ZrO_2 nano powder from 10° to 70° are shown in Figure (4.4). The phases were identified by comparison with standard reference pattern from powder file (JCPDS cards NO.41-0017).

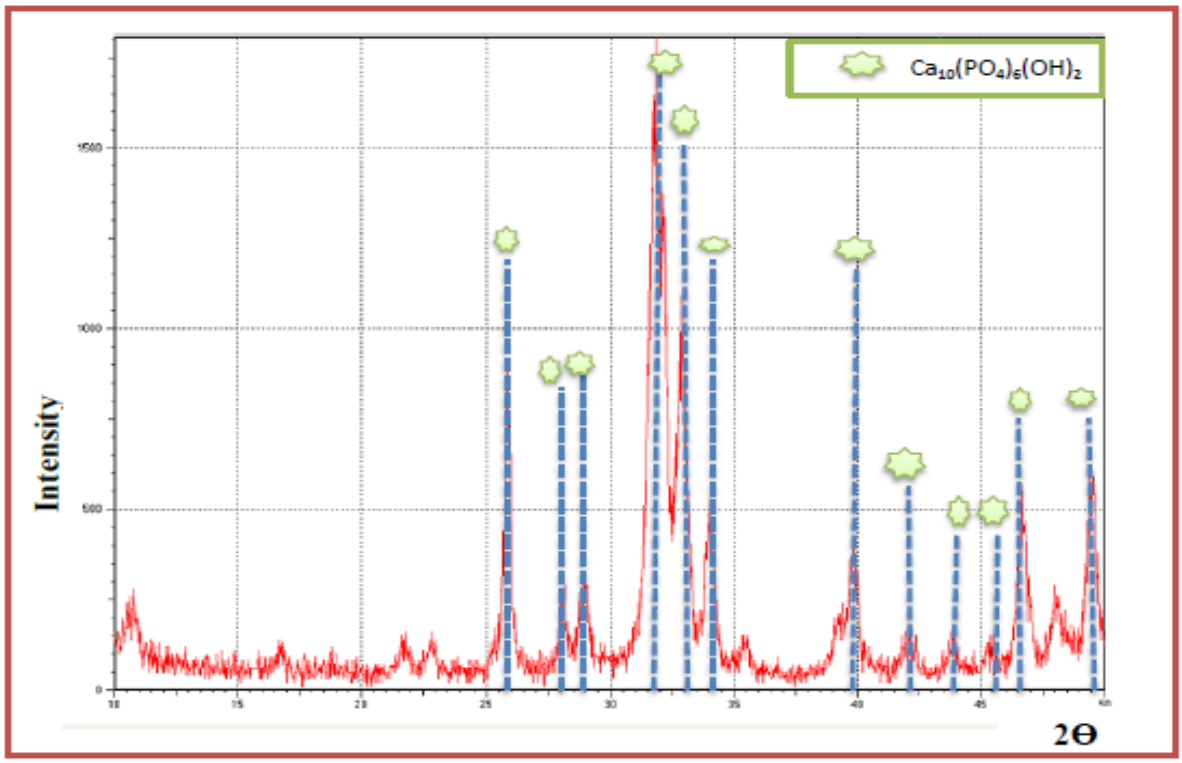

Figure (4.3) : XRD chart of HA nano powder.

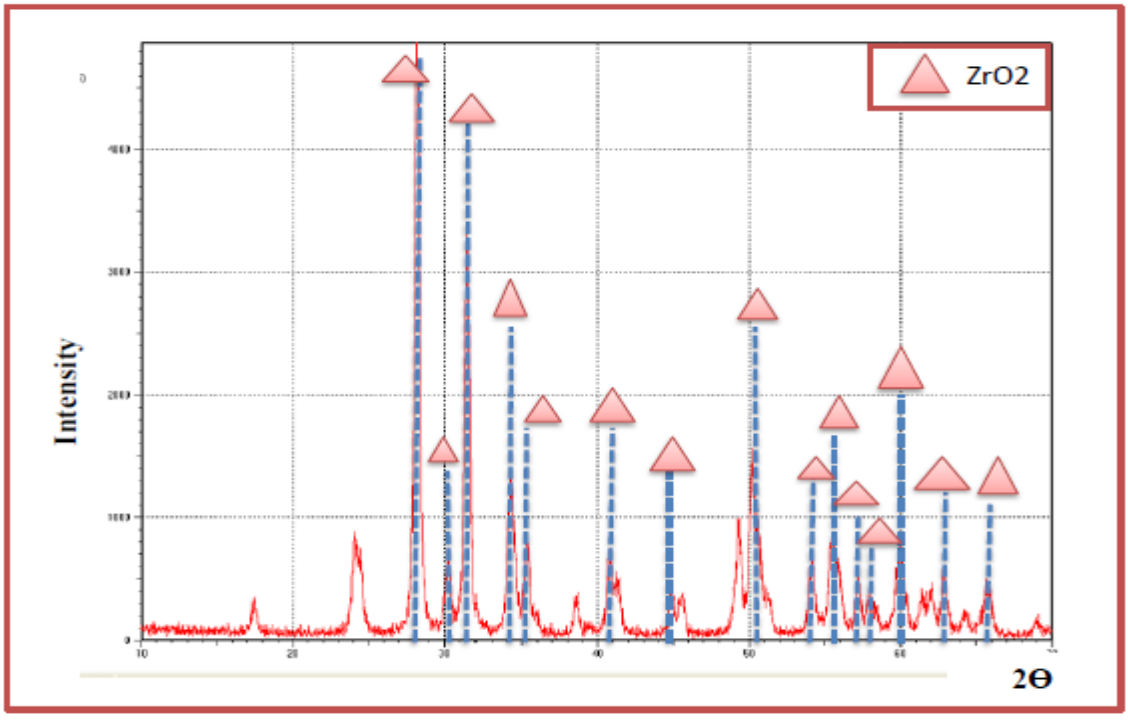

Figure (4.4) : XRD chart of ZrO_2 nano powder.

4.3.2 XRD of Ti-6Al-7Nb alloy substrate:

Identification of phases present in Ti-6Al-7Nb alloy substrate before coating as shown in Figure (4.5), where there are two main phases appeared, the alpha (α-HCP) and beta (β-BCC). These phases are identified with their crystalline planes according to the JCPDS card numbers where the diffraction pattern of the α phase match with the (JCPDS Card No.42-1136) peaks and the β phase match with the (JCPDS Card No.17- 0102).

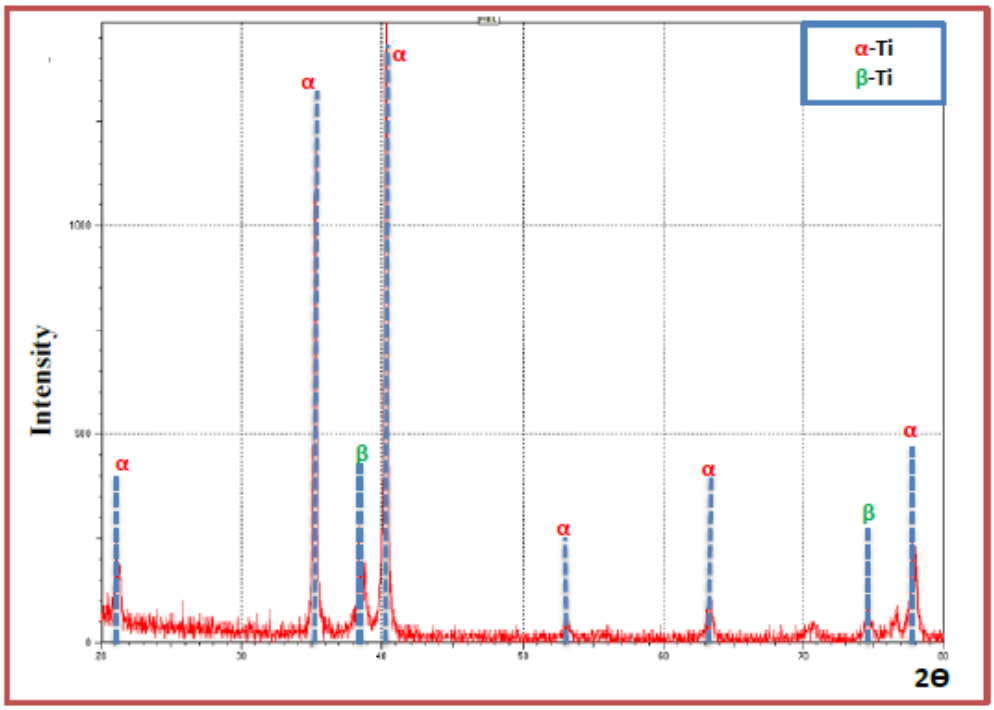

Figure (4.5): XRD chart of Ti-6Al-7Nb alloy substrate.

4.3.3 XRD Results of coatings:

Figures (4.6-4.17) display the XRD results for the coated specimen with different electrolytes. The XRD results proved the deposition of titanium oxide layer after MAO on the surface of the Ti-6Al-7Nb alloy substrate at (300V & 30min) in Figure (4.6). The formation of TiO_2 layer on the surface of specimen A_3 has crystalline phases:

rutile (tetragonal) and anatase (tetragonal) phases also the (α-HCP) and (β-BCC) return to the Ti-alloy. The peaks of rutile TiO_2 (200), (211), and (202) at 2Θ° (39.3, 54.2, and 76.0) and those of titania crystals structars (anatase) (101), (103), and (200) at 2Θ° (25.9, 37.9, and 48.3) are strongly increased compared to the untreated Ti sample while the intensity of the Ti-alloy peaks decreased after MAO process at 300V. The rutile phase is more important than other types of titania for medical application. This is due to the crystal structure of both types, the energy gaps for anatase are more than those of rutile, this makes the anatase more pores and its used in optical application while the rutile is with low energy gape and more stable at high temperatures and anatase to rutile conversion occurs as the duration and temperature of the plasma micro discharges for that its used for medical applications [140].

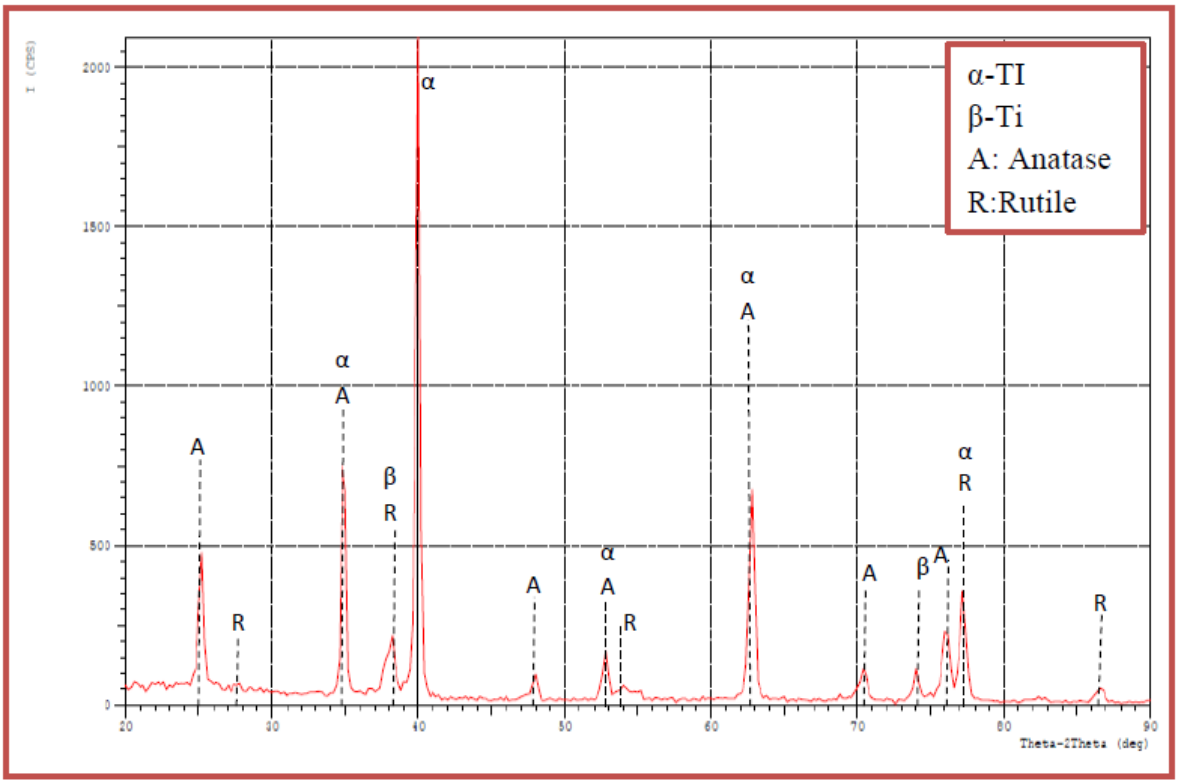

Figure (4.6): XRD patterns of specimen A_3 at (300V &30min).

The intensity of the peaks slightly increased with the increasing limiting voltage, which could be related to the oxide layer growth as shown in Figure (4.7) at 350V. For the highest applied (400V) in Figure (4.8) the oxidized surface layer became mainly a mixture of anatase and rutile. The presence of anatase suggests that a vigorous oxidation reaction has occurred on a titanium surface during the MAO process. It is therefore believed that the mixture of anatase and rutile crystal phases in the coated Ti-alloys specimen prepared in this work may positively influence the bioactivity of Ti-alloys by enhancing the osteogenic properties of Ti-alloys also indicates that mostly anatase is formed at lower forming voltages, while the combination of anatase and rutile phases appear at higher forming voltages since anatase as a metastable-phase gradually transforms into rutile at higher temperatures with the increasing dielectric breakdown phenomena [141].

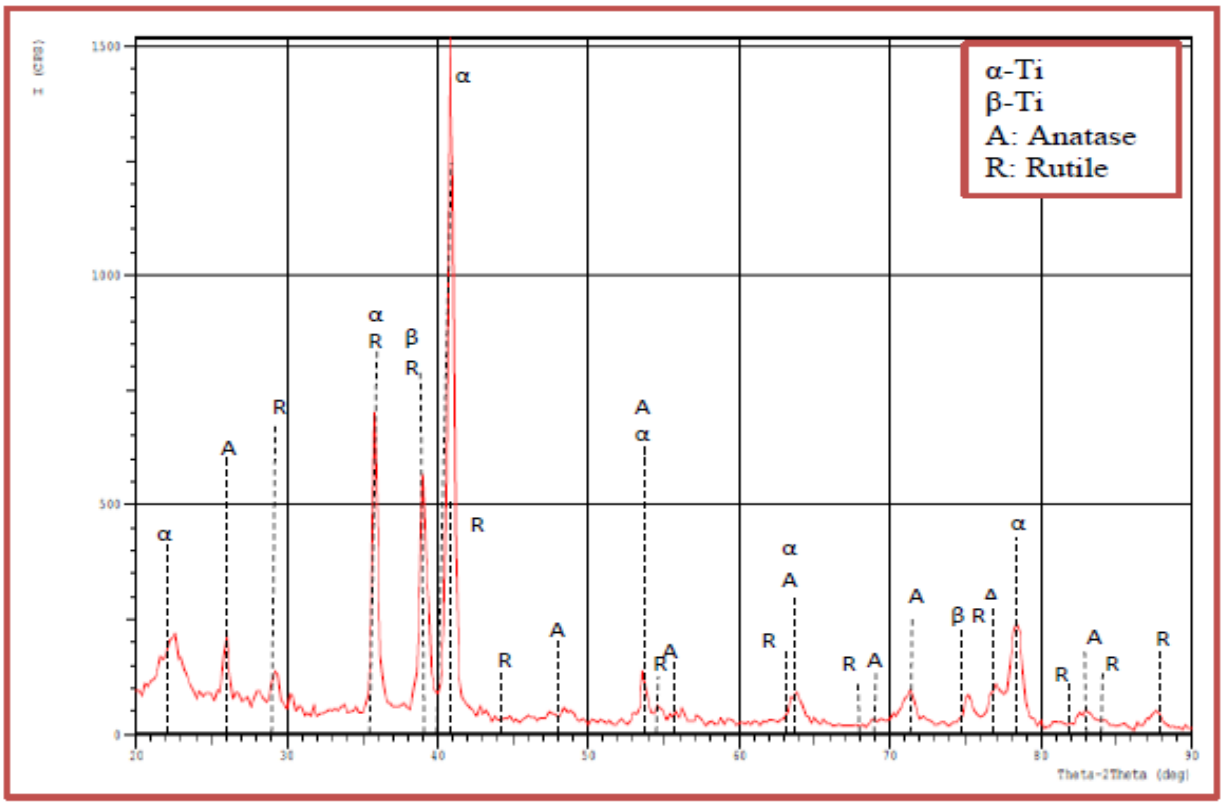

Figure (4.7): XRD patterns of specimen A_7 at (350V & 30min).

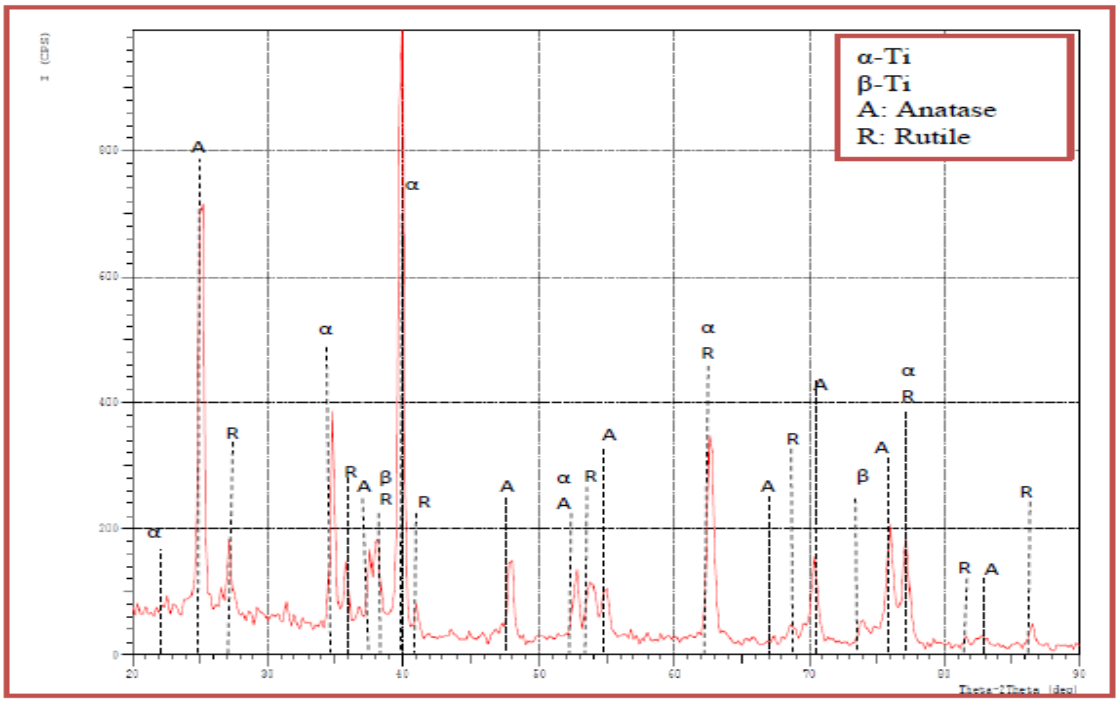

Figure (4.8): XRD patterns of specimen A_{11} at (400V &30min).

XRD analysis in Figures (4.9-4.11) reveals that the surfaces of the Ti-6Al-7Nb alloy are covered by HA/TiO_2 composite coating. HA peaks were also detected on XRD patterns of the oxidized Ti6Al7Nb alloys. In addition to the peaks of anatase, rutile, and HA, the appearance of Ti peaks on the XRD patterns, is most likely due to the penetration of the XRD beyond the oxide layers. The major phase that dominated is HA (310), (002), and (211) depending on thickness of coating layer at 2Θ° (39.8, 25.8, and 31.7). HA peaks are the highest intensities in all specimens coated at different thickness. Intensity increasing with increasing voltage, for the coatings deposited at 350V (specimen B_7) demonstrated the different halo in the angular range.

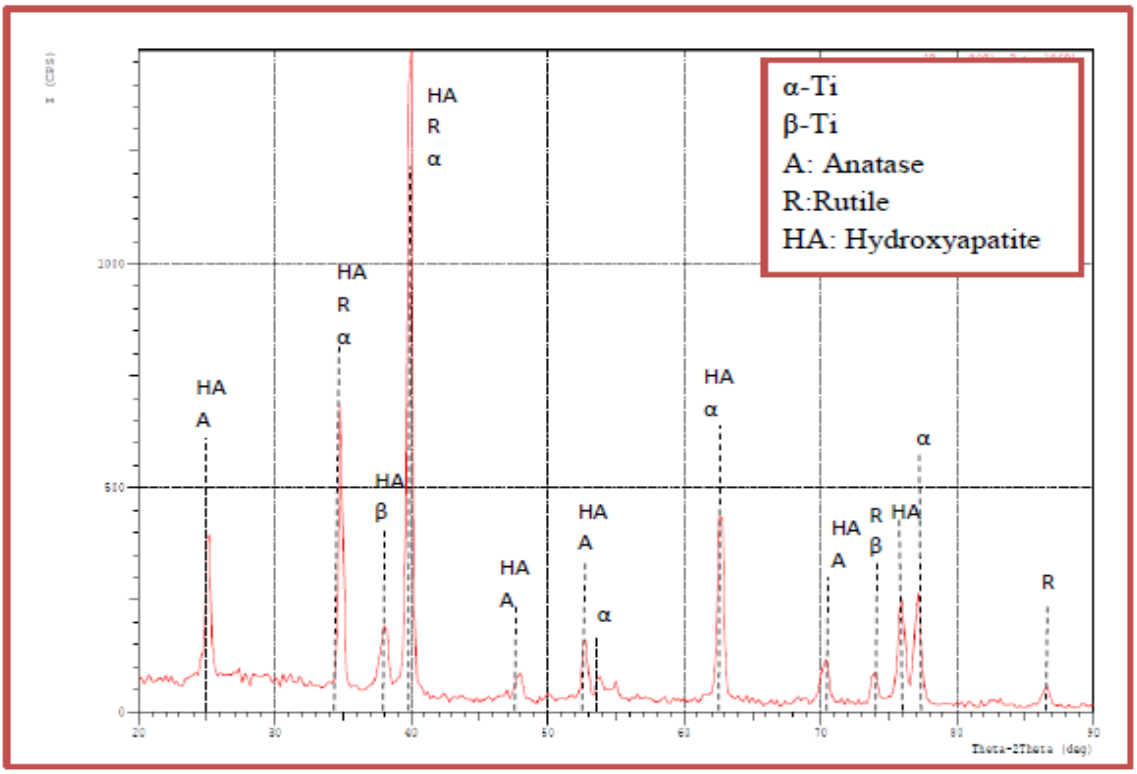

Figure (4.9): XRD patterns of specimen B_3 at (300V &30min).

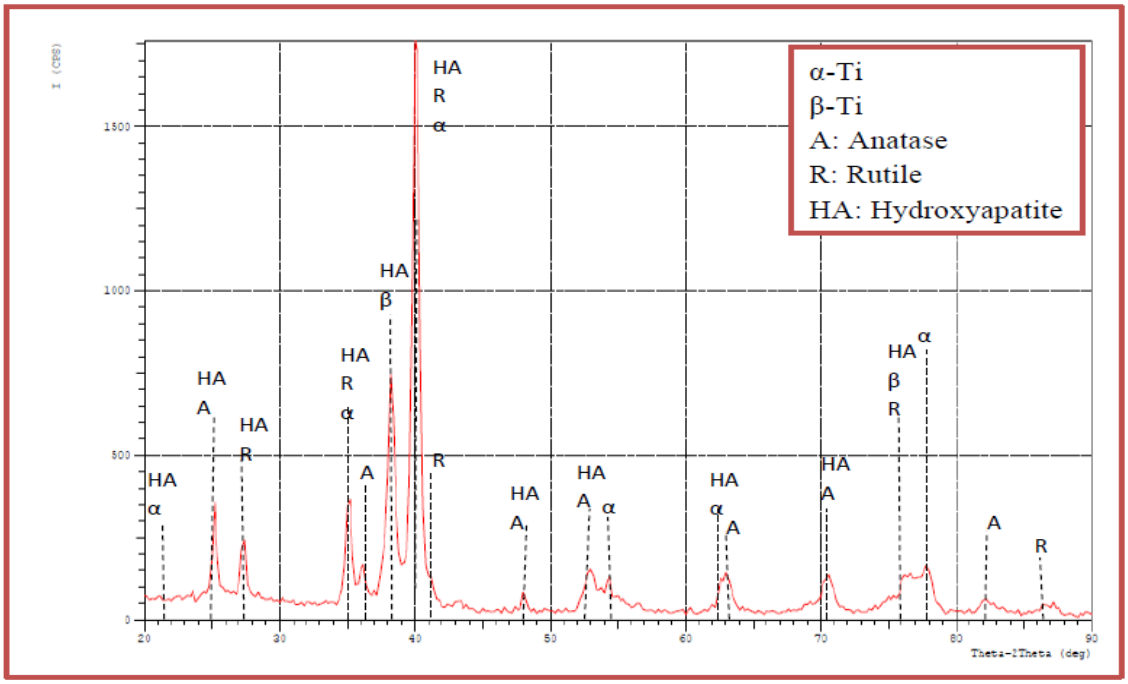

Figure (4.10): XRD patterns of specimen B_7 at (350V &30min).

When the voltage is increased at 400V in Figure (4.11), the intensities of reflexes of HA are increased at the specimen B_{11}. There was an improvement in the coating crystallization and the strong HA was at (310), (211), and (002) with a 100% intensity of HA at (310) which overlapped with (211). This preferred orientation suggested that high coating and chemical reaction between the different components were occurred. The (002) HA peak at $2\theta^{o}$ (25.8) was stronger compared to (310) and (211) HA peaks around $2\theta^{o}$ (31.7) specially for the HA/TiO_2 composite coating Ti-6Al-7Nb alloy.

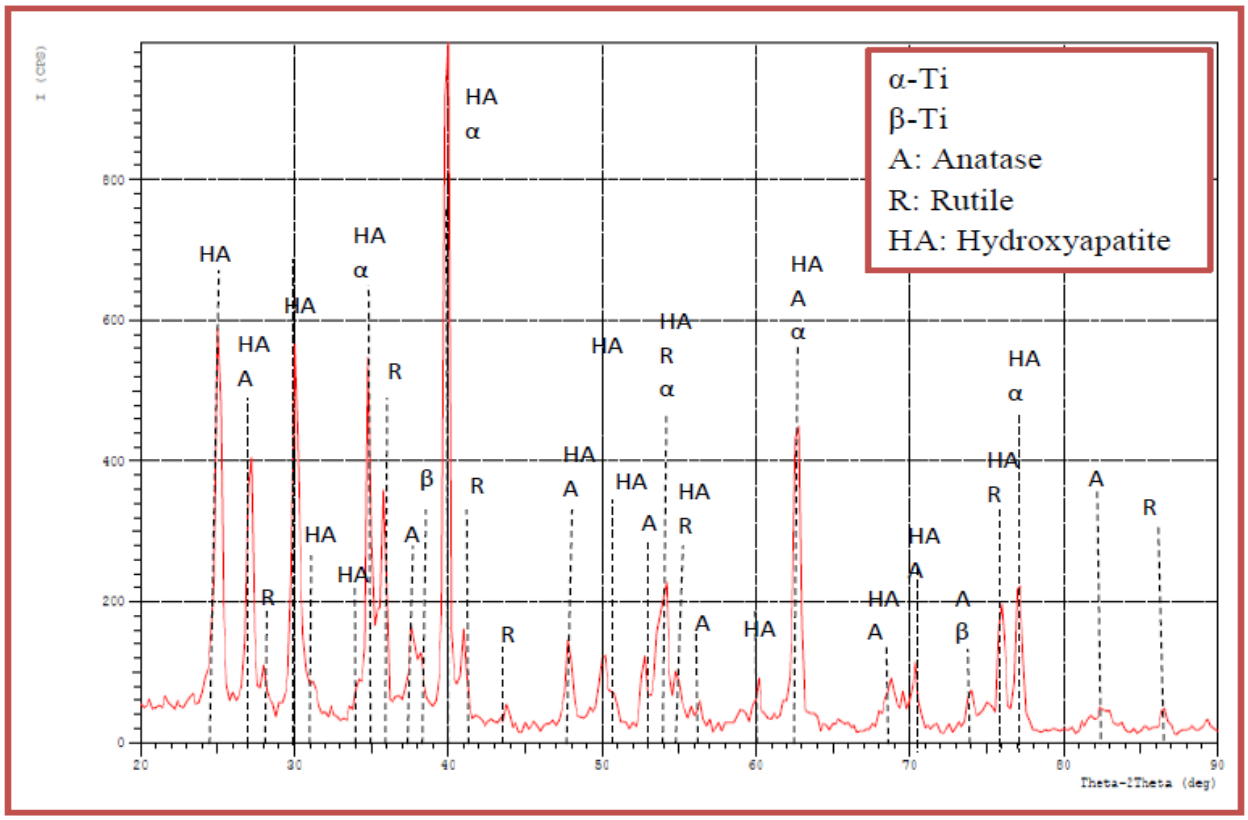

Figure (4.11): XRD patterns of specimen B_{11} at (400V &30min).

In Figures (4.12-4.14), the XRD patterns of ZrO_2/TiO_2 composites coating could be assigned to well-crystallized Zirconia (tetragonal) phase and (anatase, rutile) phases at TiO_2 at different voltages. The XRD patterns indicated that the peaks are composed of

ZrO_2 with anatase and rutile phases. At (300V& 30min) at specimen C_3 the phases of ZrO_2 showed low intensities. In fact, the discharge process can accelerate the hydrolysis which lead to an increasing number and ZrO_2 and TiO_2 in the channel under high temperature and high-pressure during MAO process at high voltage, the intensity zirconia peak increased gradually during increase voltage MAO process to the Ti-6Al-7Nb alloy substrates were exposed to the surface. We also could see that both the intensities rutile and anatase peaks increased gradually. At 400V voltage at specimen C_{11}, the intensity of those peaks 2Θ° (27.5 and 34.1) at (002) and (111) reached the maximum coating showed a strong ZrO_2 phase with a maximum thickness.

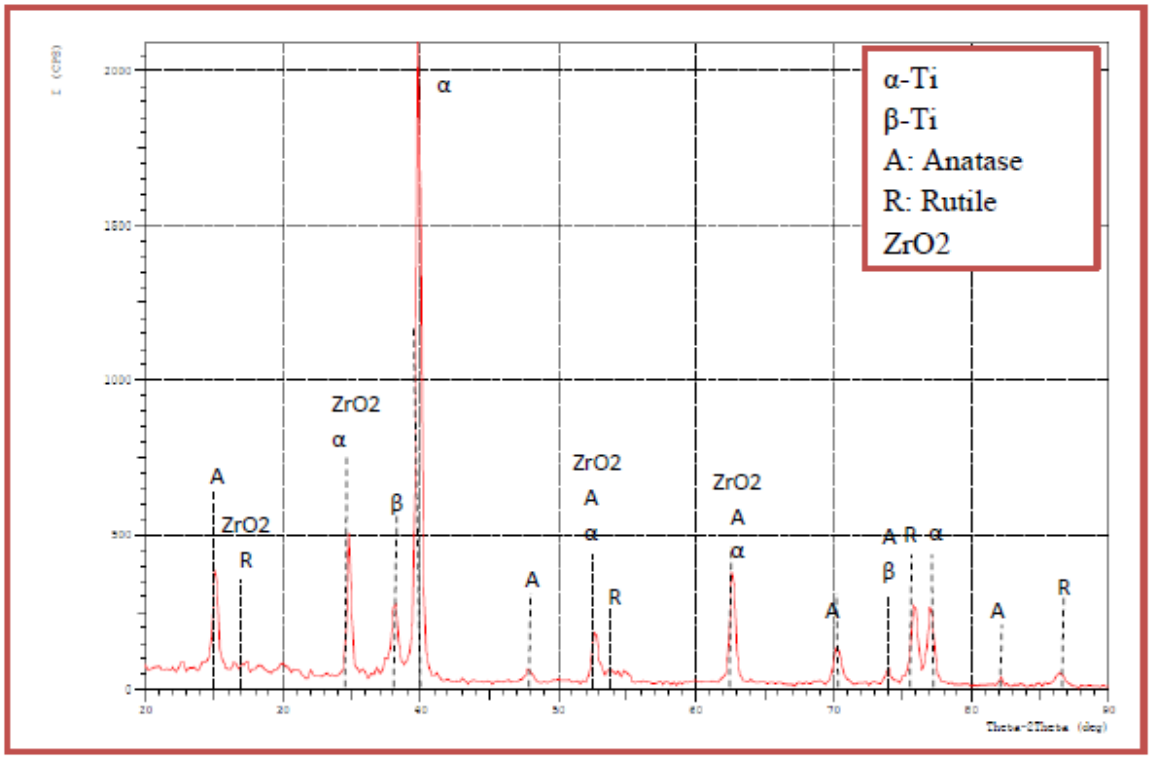

Figure (4.12): XRD patterns of specimen C_3 at (300V &30min).

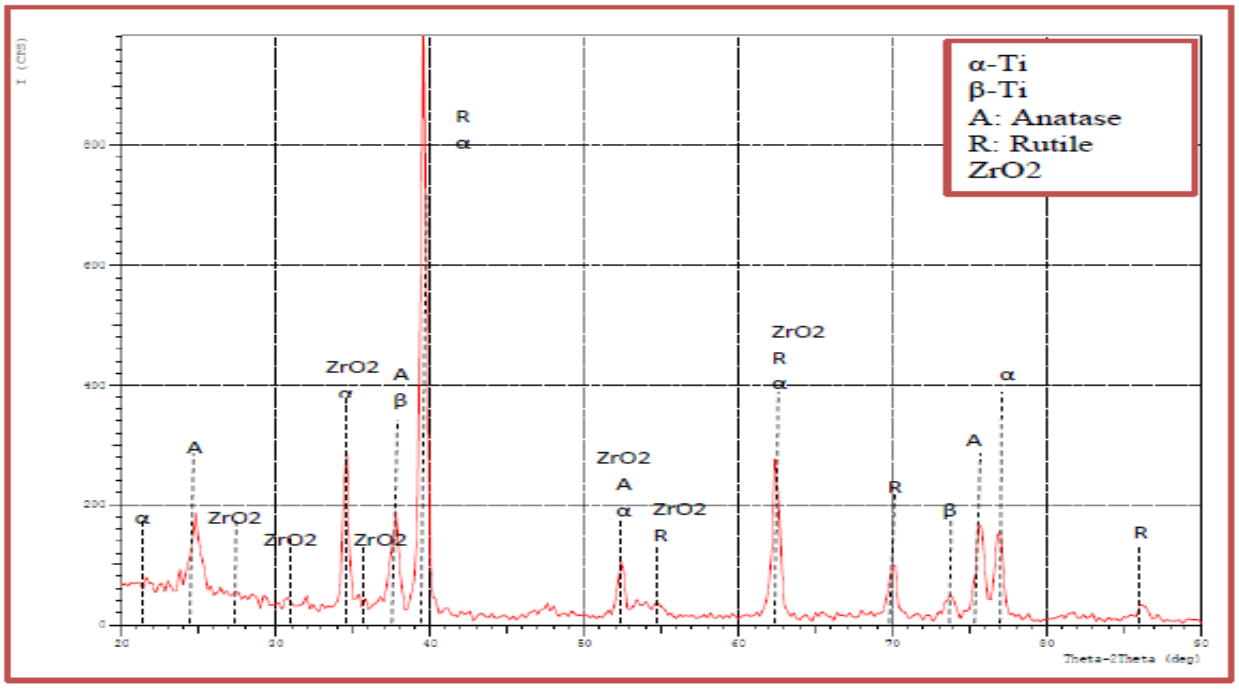

Figure (4.13) : XRD patterns of specimen C_7 at (350V &30min).

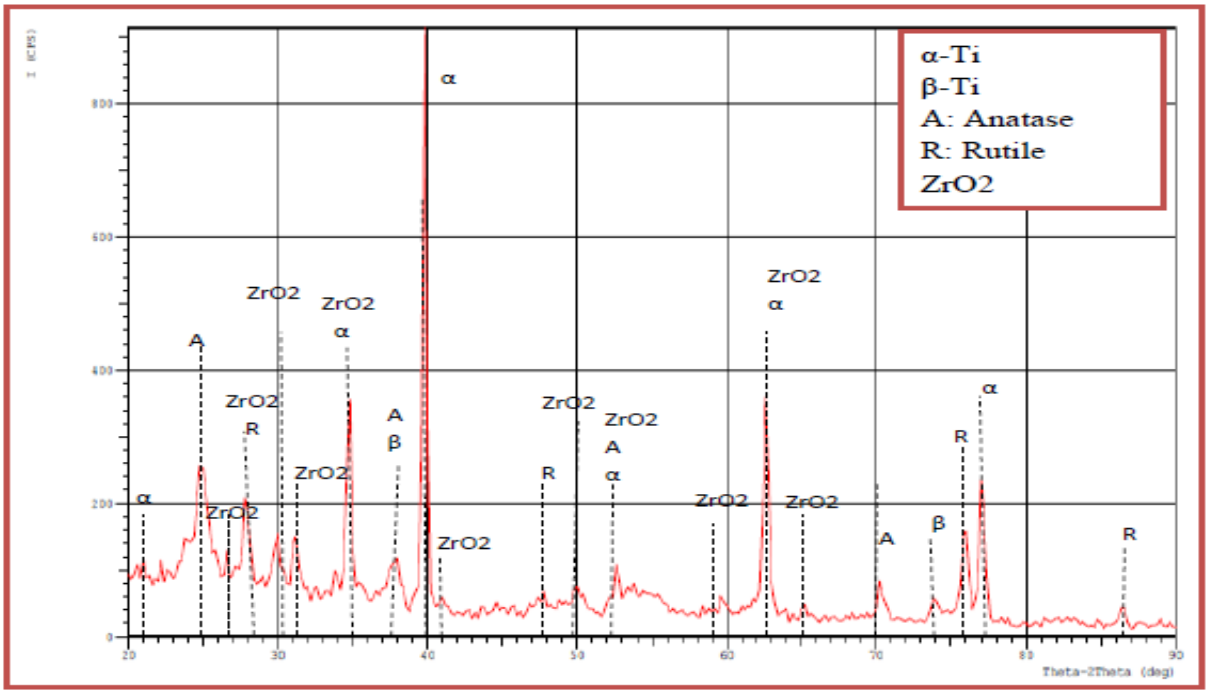

Figure (4.14): XRD patterns of specimen C_{11} at (400V &30min).

The nanocomposite layer coated specimens shows that the layer consisted of an alternating layer of HA and ZrO_2 add TiO_2 substrate coated on Ti-6Al-7Nb alloy by MAO process, followed by composite ceramic coating by MAO process. in Figure (4.15) results indicate that there are six types of diffraction peaks on the surface of the film, note that phase composition of the coating detected by XRD was continued HA major phase at 2Θ° (63.0 and 39.2) and ZrO_2 at 2Θ° (34.1). In the XRD patterns of specimens D_3 coated with HA and ZrO_2 at 300V show the formation of different ceramic compound including (502) and (212) at 2Θ° (63.0 and 39.2) for HA, and ZrO_2 (202) at 2Θ° (34.1). There are other peaks appeared dominated by TiO_2 for example (101), (103), and (213) at 2Θ° (25.2, 37.9, and 62.7) rutile phase and anatase phase (110), (200), and (202) at 2θ° (27.5, 39.3, and 76.0) respectively in addition to alloy phases.

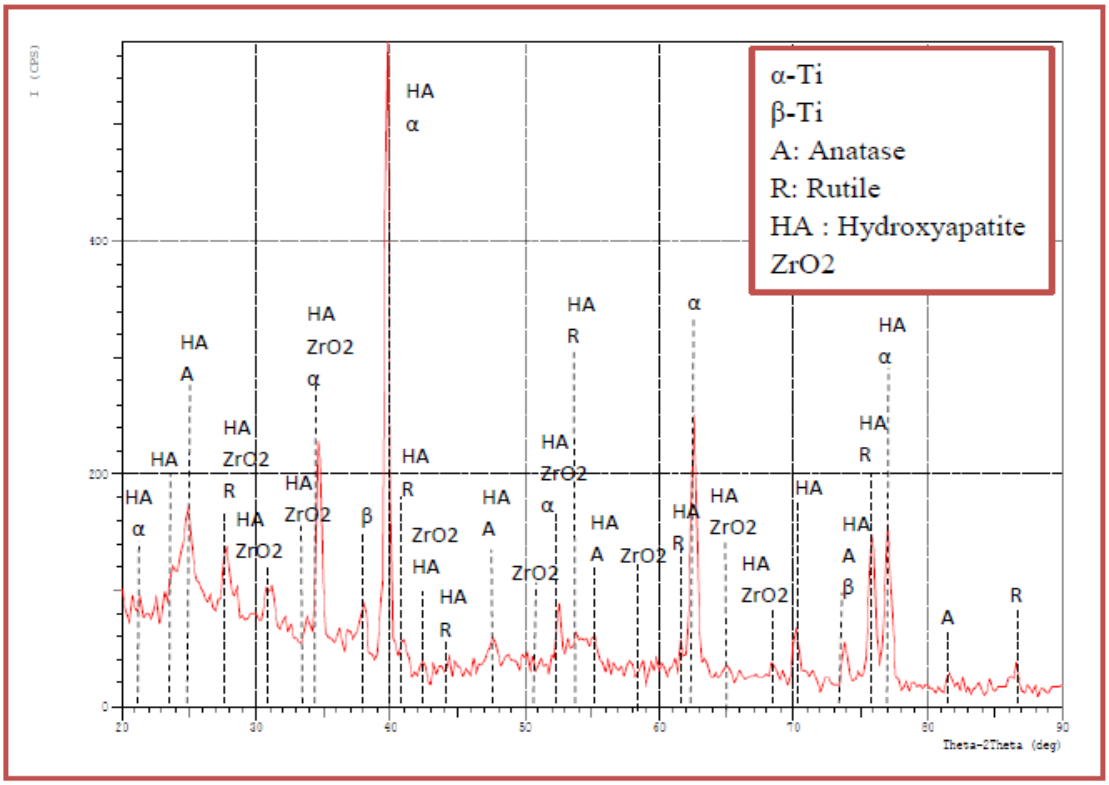

Figure (4.15): XRD patterns of specimen D_3 at (300V &30min).

In Figure (4.16) and (4.17), presence peaks of ZrO_2 and HA on Ti-6Al-7Nb alloy at (350-400) V. XRD phase at 2Θ° (39.2, 60.0, and 77.1) as result from natural oxide layer form (HA and ZrO_2) add TiO_2 Phase. The increase intensity at increasing voltage because increase thickness of coating layer means that the chemical reaction between HA, ZrO_2 and TiO_2 layers XRD showed improvement in coated. The depositions directory on the alloy surface are different with voltage which can give a pores layer. A strong structural interdependence appeared between the covering HA and the ZrO_2 composite layer with TiO_2 substrate. This means that the number of particles increase so that the intensity of the peak increased.

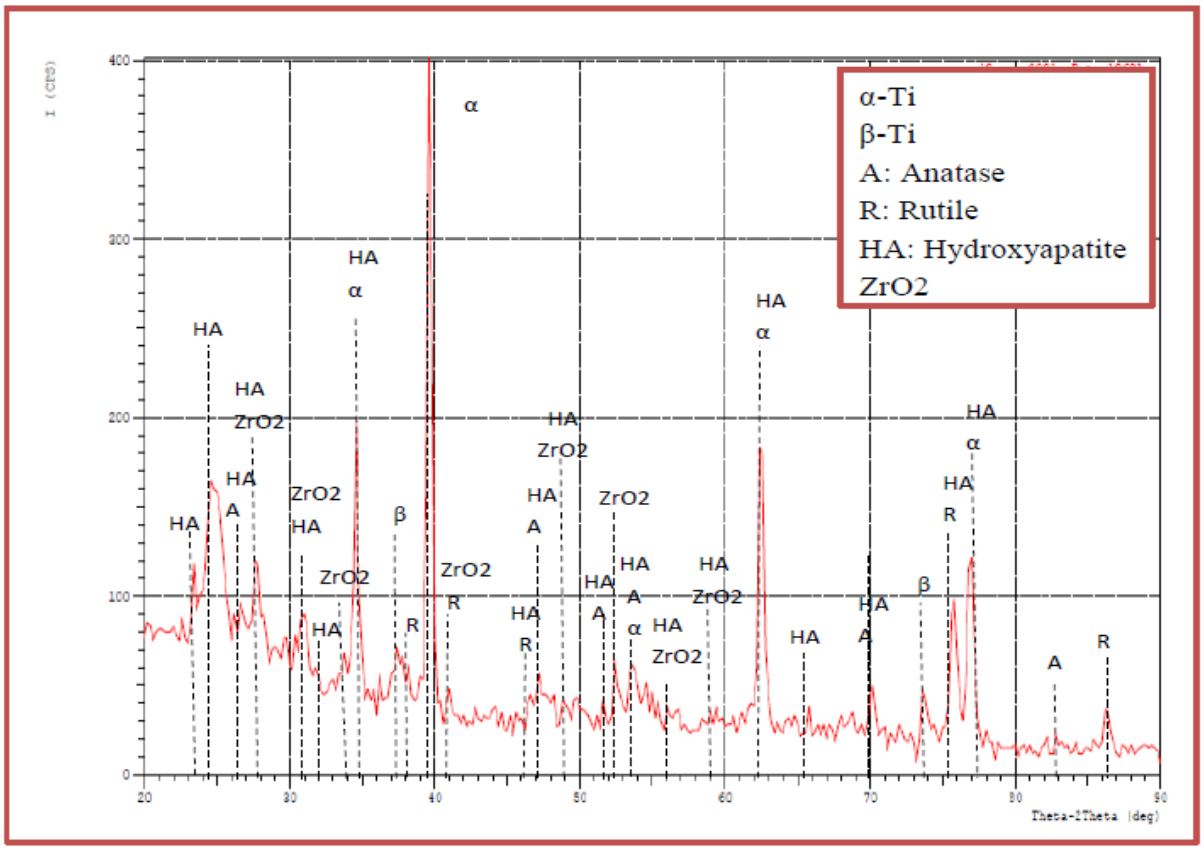

Figure (4.16): XRD patterns of specimen D_7 at (350V &30min).

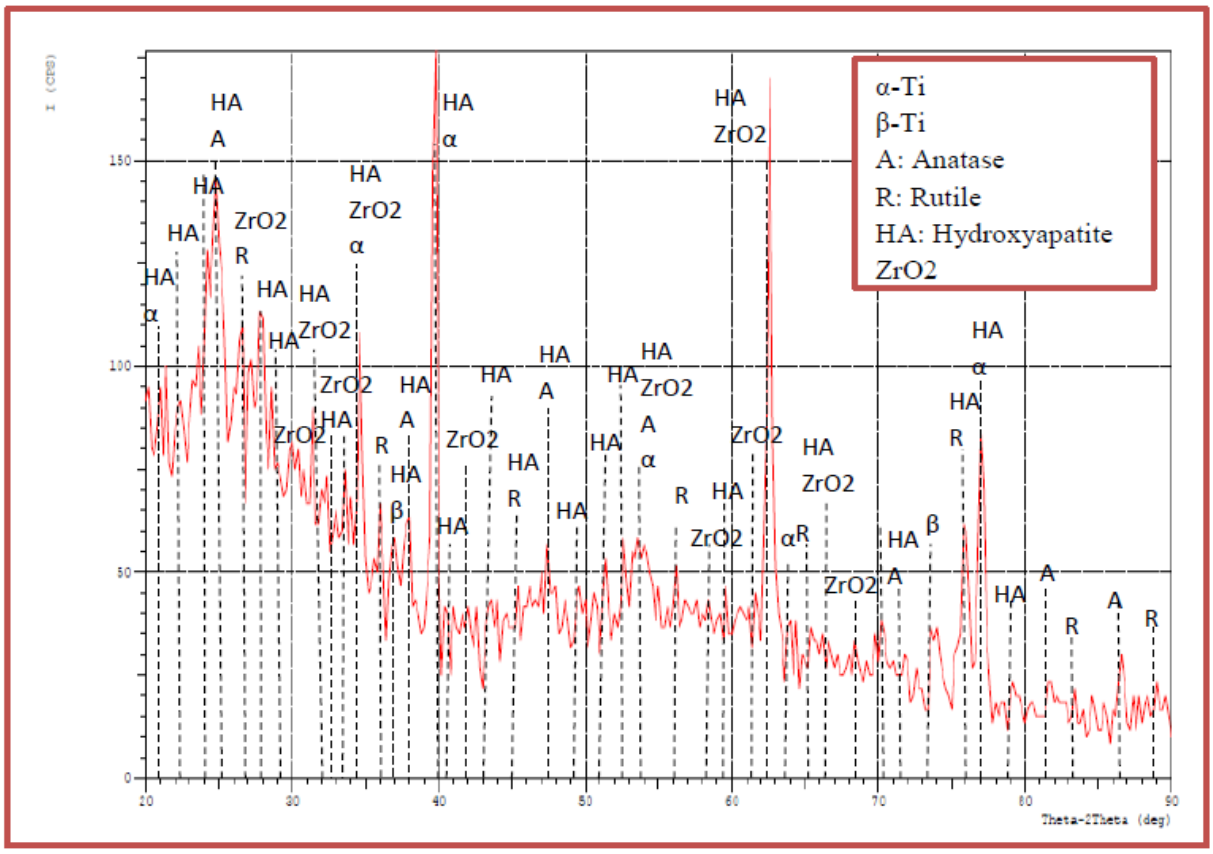

Figure (4.17): XRD patterns of specimen D_{11} at (400V &30min).

4.4 Microstructure Results

4.4.1 Optical Microstructure Observation

Figure (4.18) shows LOM micrographs of Ti-6Al-7Nb alloy substrates with two magnifications. The microstructure showed a duplex microstructure consisting of the near equiaxed alpha (α) (white phase) and transformed beta (β) (dark phase).

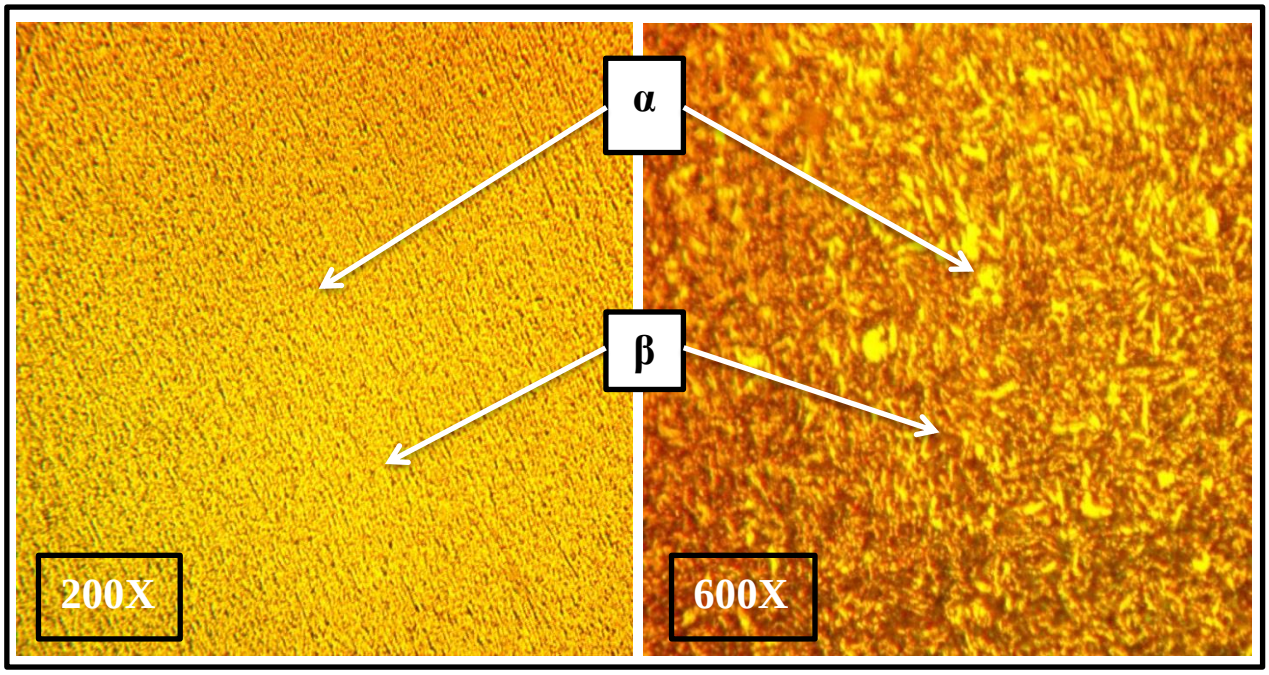

Figure (4.18) : Optical Micrographs of Ti6Al7Nb Alloy with two magnifications (200X &600X).

4.4.2 Field Emission Scanning Electron Microscopy (FESEM)

The FESEM results of microstructure coated specimen from Figures (4.19) which show that for surface morphology of the oxide layer TiO_2 to the Ti-6Al-7Nb alloys at different magnifications treated by MAO process relatively rougher and exhibited a grainy structure with limited amount of pores with different sizes by the spark discharges. The MAO coating showed two types of pores: micro-pores and submicro-pores. The micro-pores had a roughly circular or elliptical shape like volcanic vent [142].

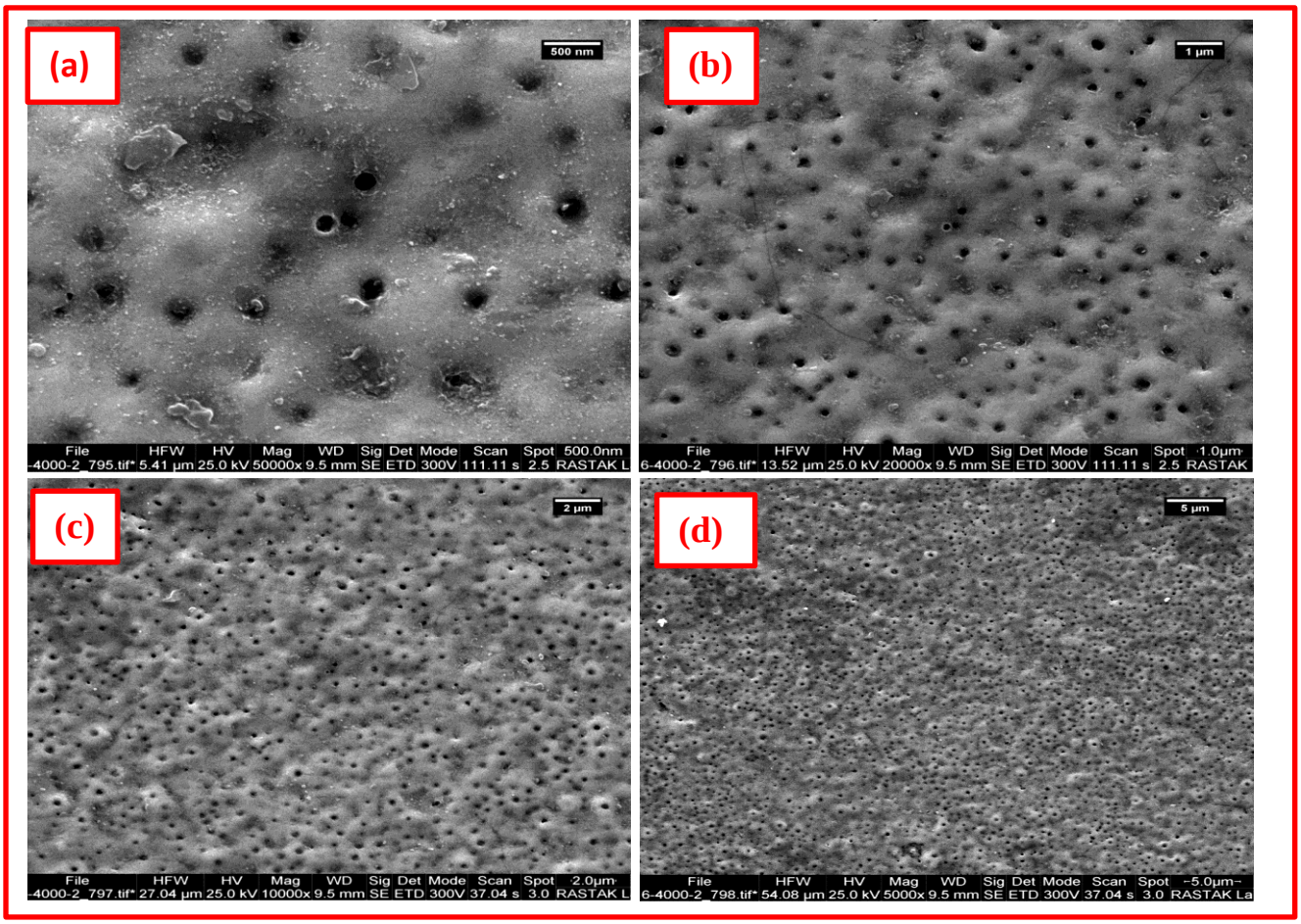

Figure (4.19) : FESEM micrographs of specimen A_3 (300V & 30min) at different magnifications.

A typical porous structure was also found in coating of sample A_7, whereby the pore size clearly was dependent on the limiting voltage as shown in Figure (4.20) 350V. Pores with maximum diameters and homogenous distribution can be observed on the surface of the Ti- alloy. As the voltage increased, it is clearly seen that the diameter of such pores and the surface roughness increased accordingly. As shown in Figure (4.21), after treatment for 400V, the pores sizes increased, and the coating surface gradually became rough. The oxide coating on both materials is formed by many micro-protrusions containing uniformly distributed pores with size varying from

sub-micron to few microns. The occurrence of this porosity favors the phenomenon of osseointegration when compared to the uncoated polished surface since the pores behave as sites that increase the contact area between the bone and the implant for bone tissue growth, consequently enhancing their anchorage, besides the benefits related to the capacity of retaining bioactive elements [110].

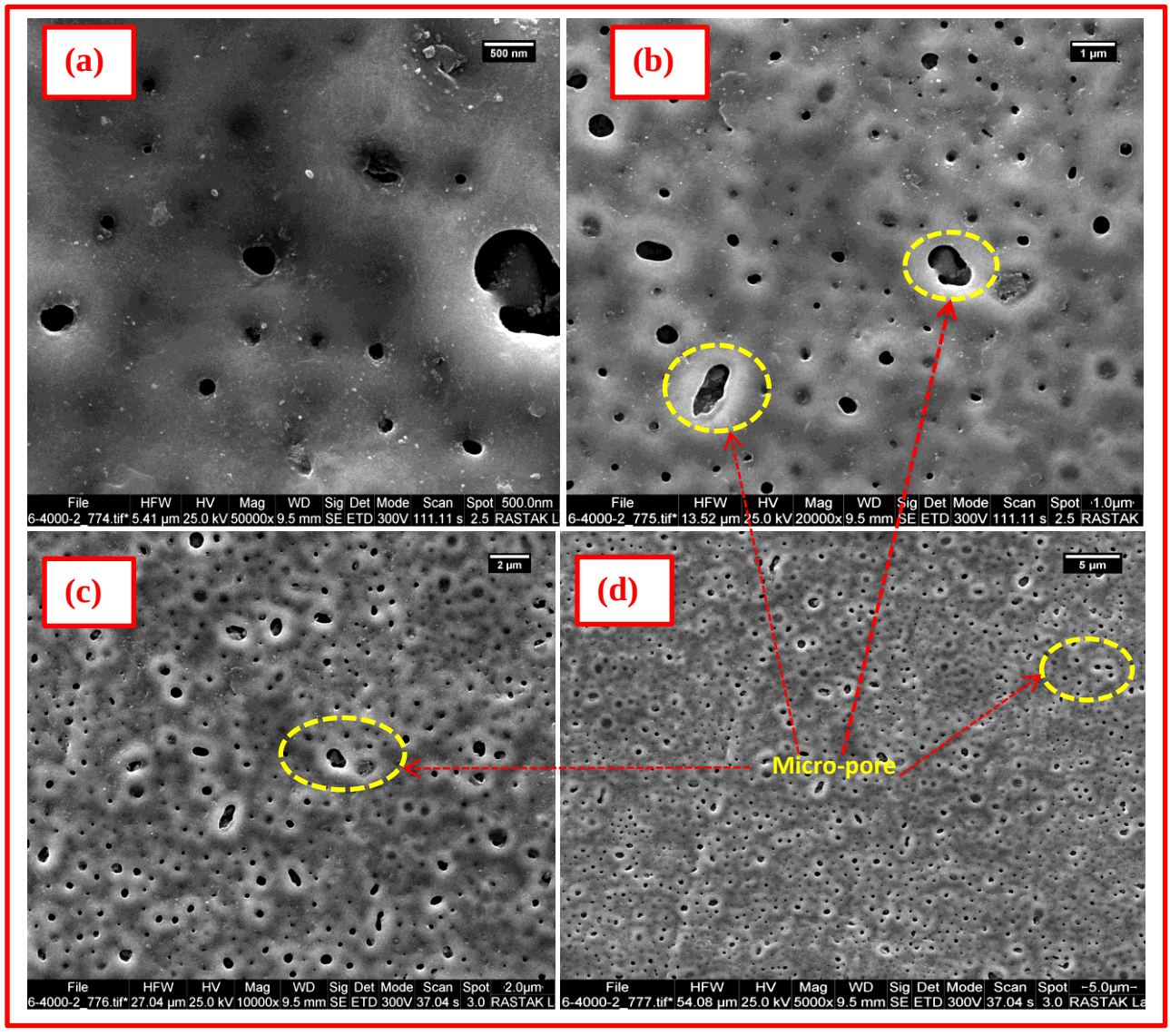

Figure (4.20) : FESEM micrographs of specimen A_7 (350V & 30min) at different magnifications.

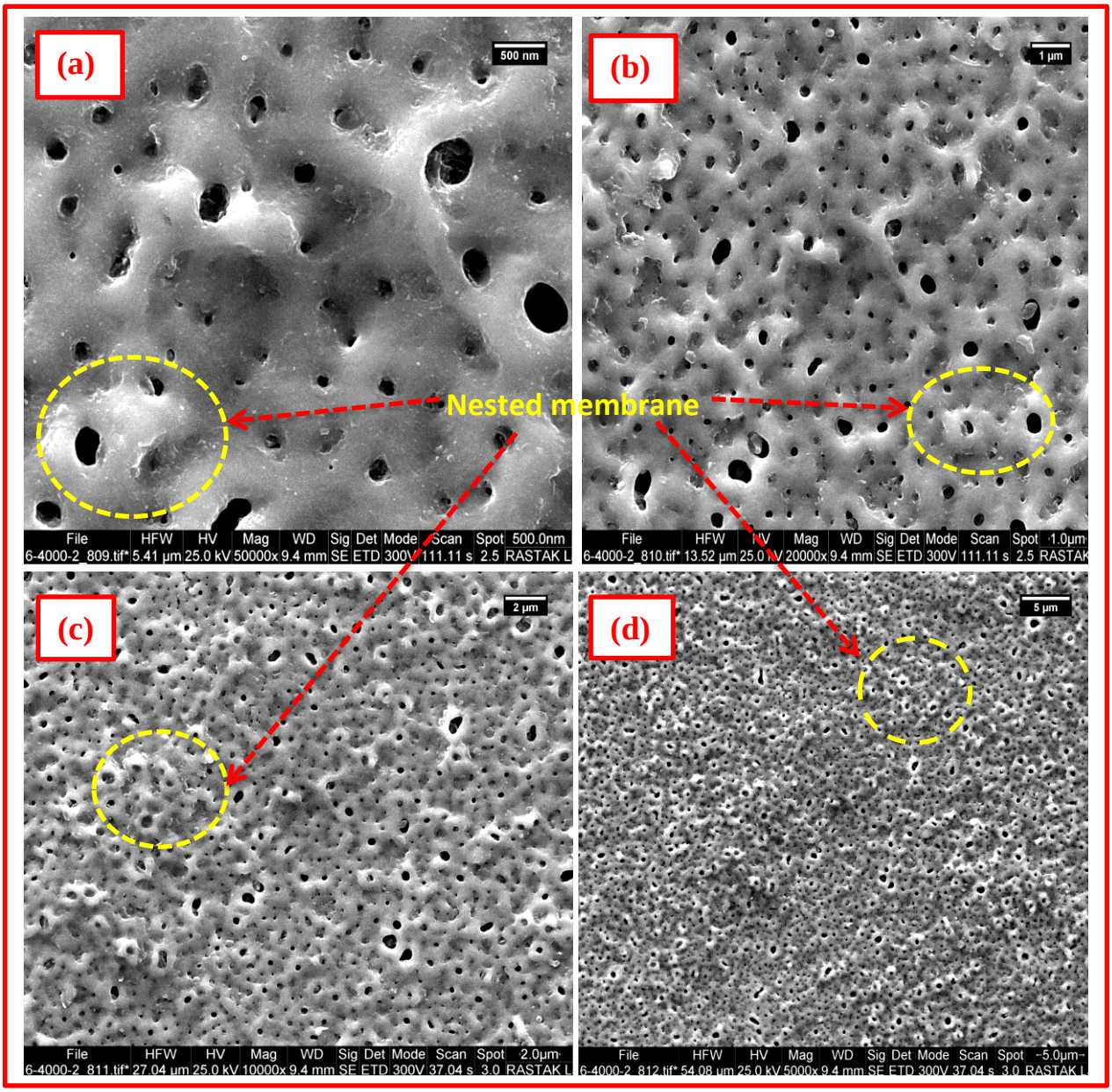

Figure (4.21) : FESEM micrographs of specimen A_{11} (400V & 30min) at different magnifications.

In Figure (4.22), for surface morphologies of HA/TiO_2 coatings, it can be observed that the porosity decreases with the addition of HA to the electrolyte, it may be

attributed to incorporation of components into the micro-pores ,which leads to reduce the amount of pores in the structure.

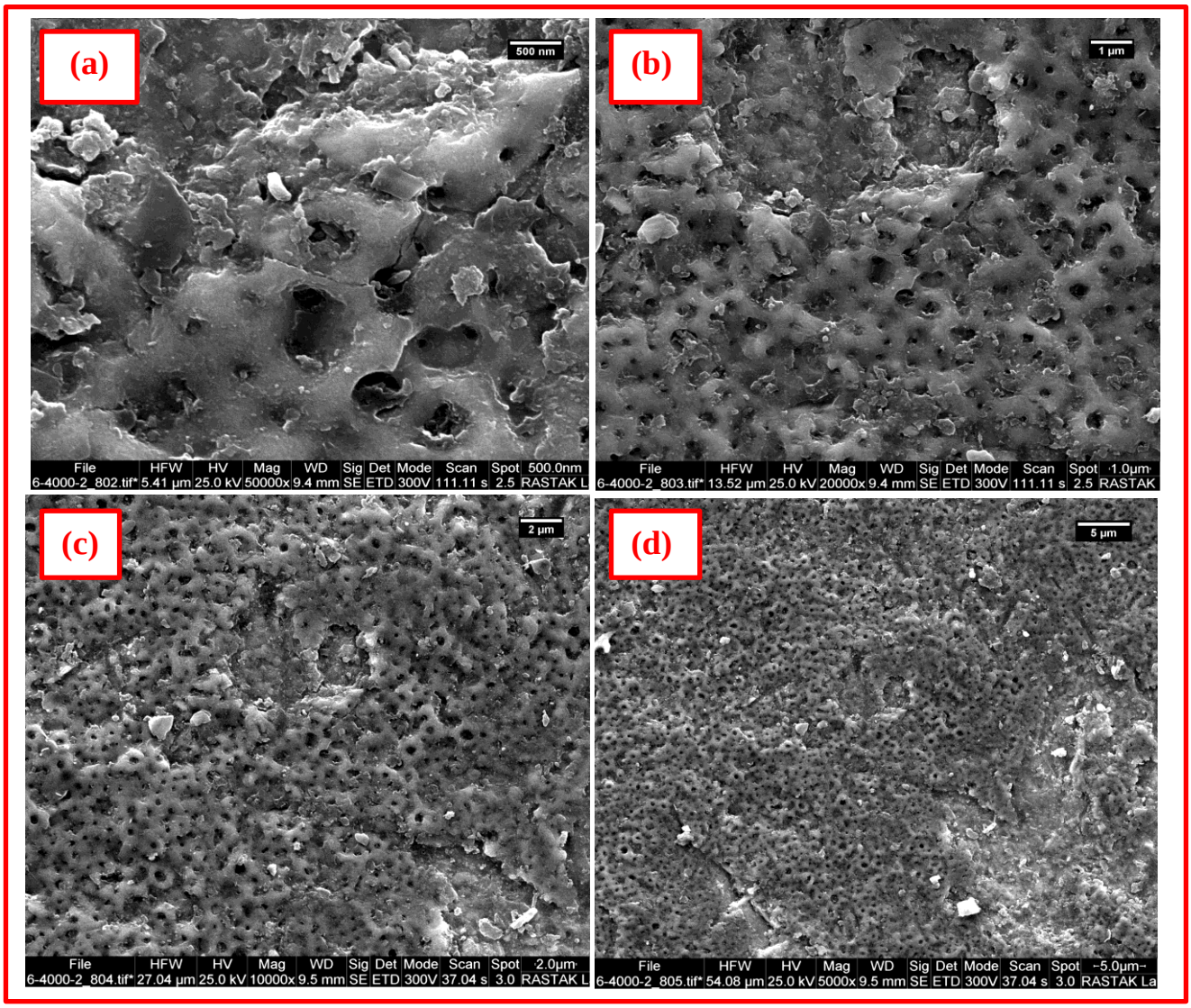

Figure (4.22) : FESEM micrographs of specimen B_3 (300V & 30min) at different magnifications.

With increasing voltage, numerous open pores were formed and thereby increasing precipitation of HA for specimen B_7, as shown in Figure (4.23). The homogenous

precipitate led to decrease pore ratio significantly. Surface are covered with a fine cellular-like oxide network, micro-pores [143].

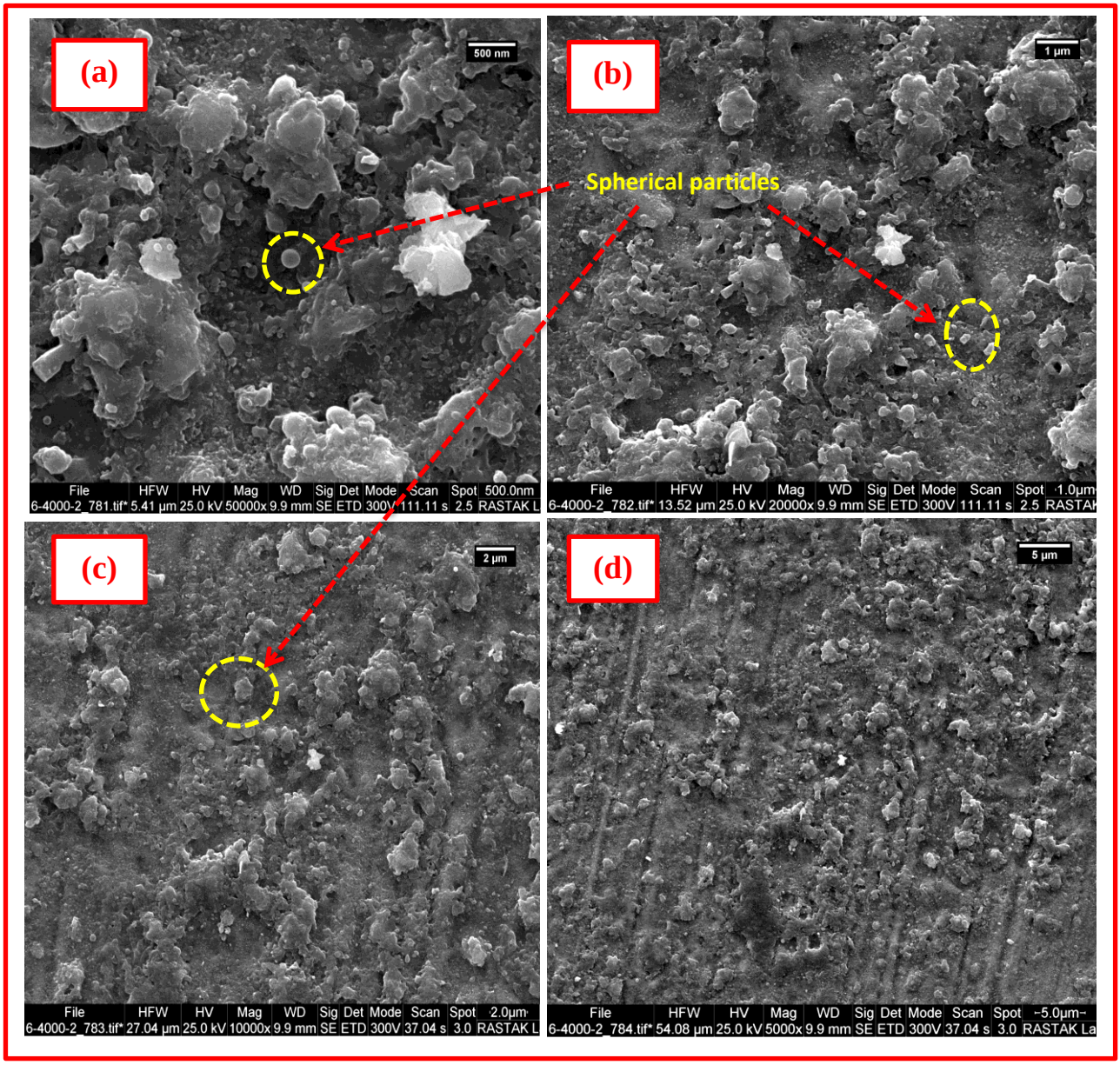

Figure (4.23) : FESEM micrographs of specimen B_7 (350V & 30min) at different magnifications.

In Figure (4.24), at 400V, the size of crater-like pores tends to be much bigger, and they connect together to make a rough surface. Showed that different size of pores distributed on the surface coating. it can be concluded that the increasing of voltage could increase the HA ratio increasing.

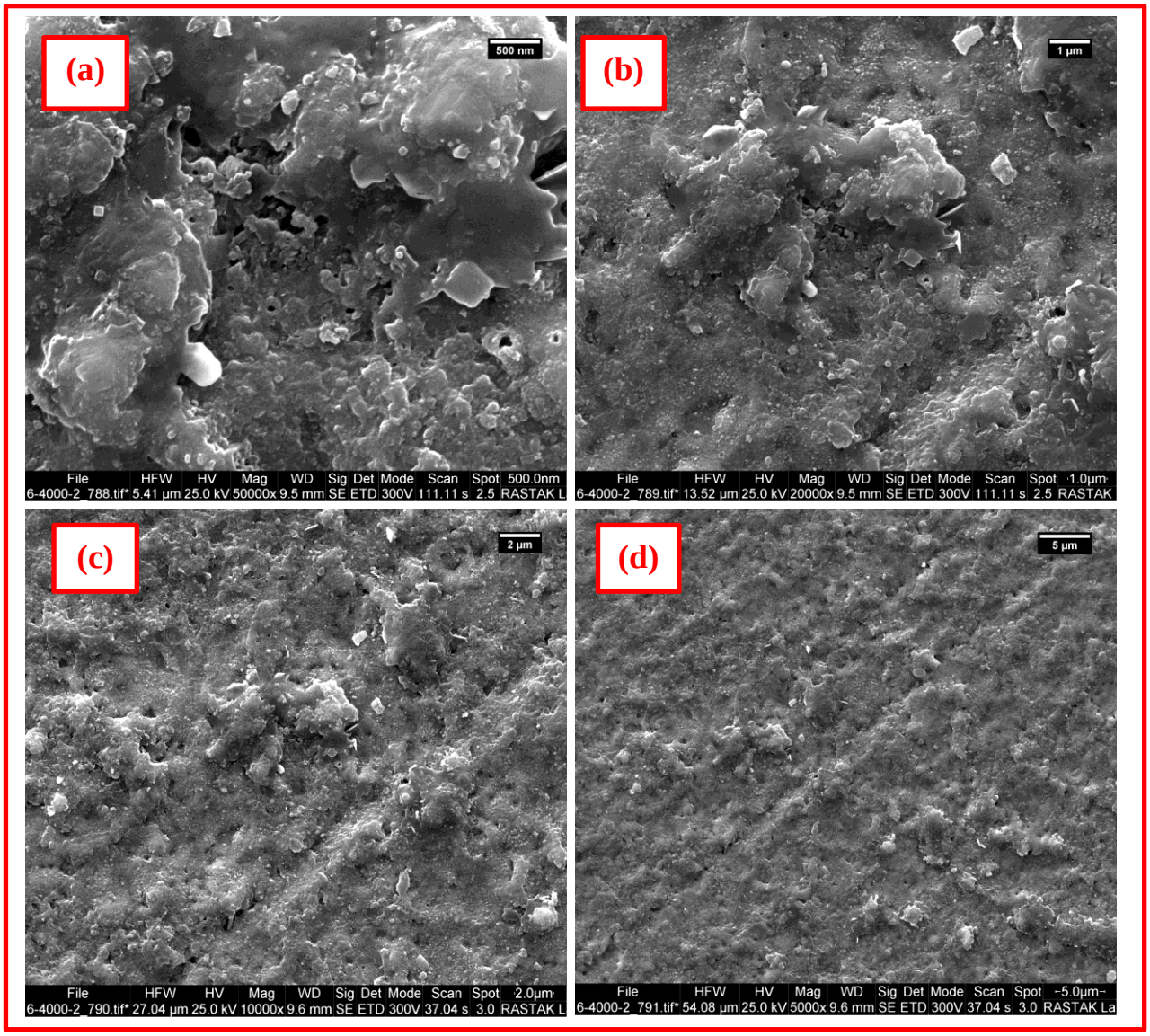

Figure (4.24) : FESEM micrographs of specimen B_{11} (400V & 30min) at different magnifications.

Figure (4.25) depicts the FESEM photographs of the surface microstructure of the samples coated in electrolytes containing of ZrO_2. It could be found that the surface of MAO film exhibited a low porous microstructure, and these scattered powders should come from the ZrO_2 added in the electrolyte. The porosity of the MAO film is limited and originated not only the reaction channels between electrolytes and substrates, but also the channels through which molten oxides ejected during the MAO process. The surface morphology seemed more homogenous. The ZrO_2 precipitation present as aggregate on the surface by small pores distribution on the surface, this leads to enhancement roughness of coatings

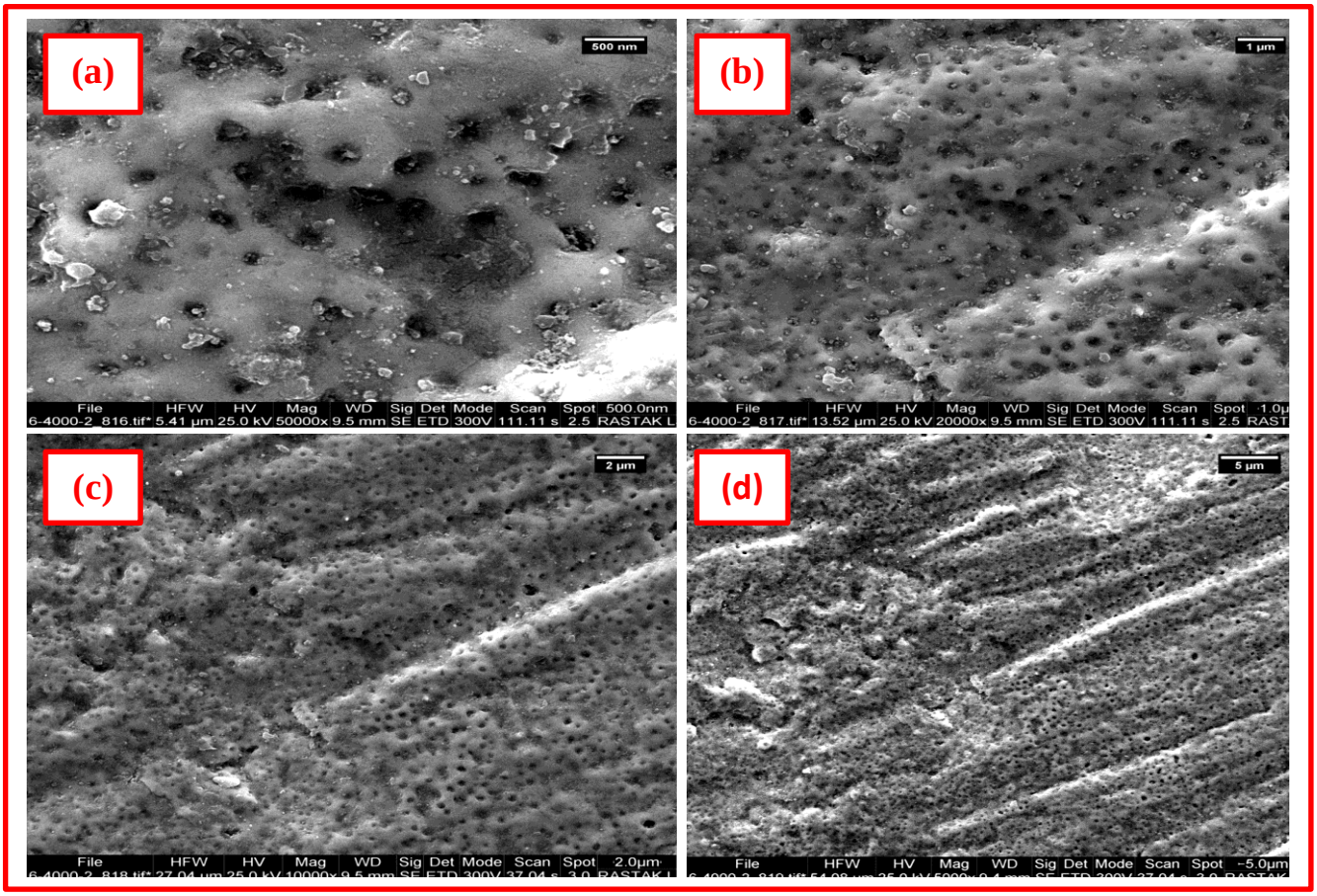

Figure (4.25) : FESEM micrographs of specimen C_3 (300V & 30min) at different magnifications.

In Figure (4.26) and (4.27) increasing the voltage lead to increasing concentrations of ZrO_2 coating structure, and increasing the size of pores and tunnels.

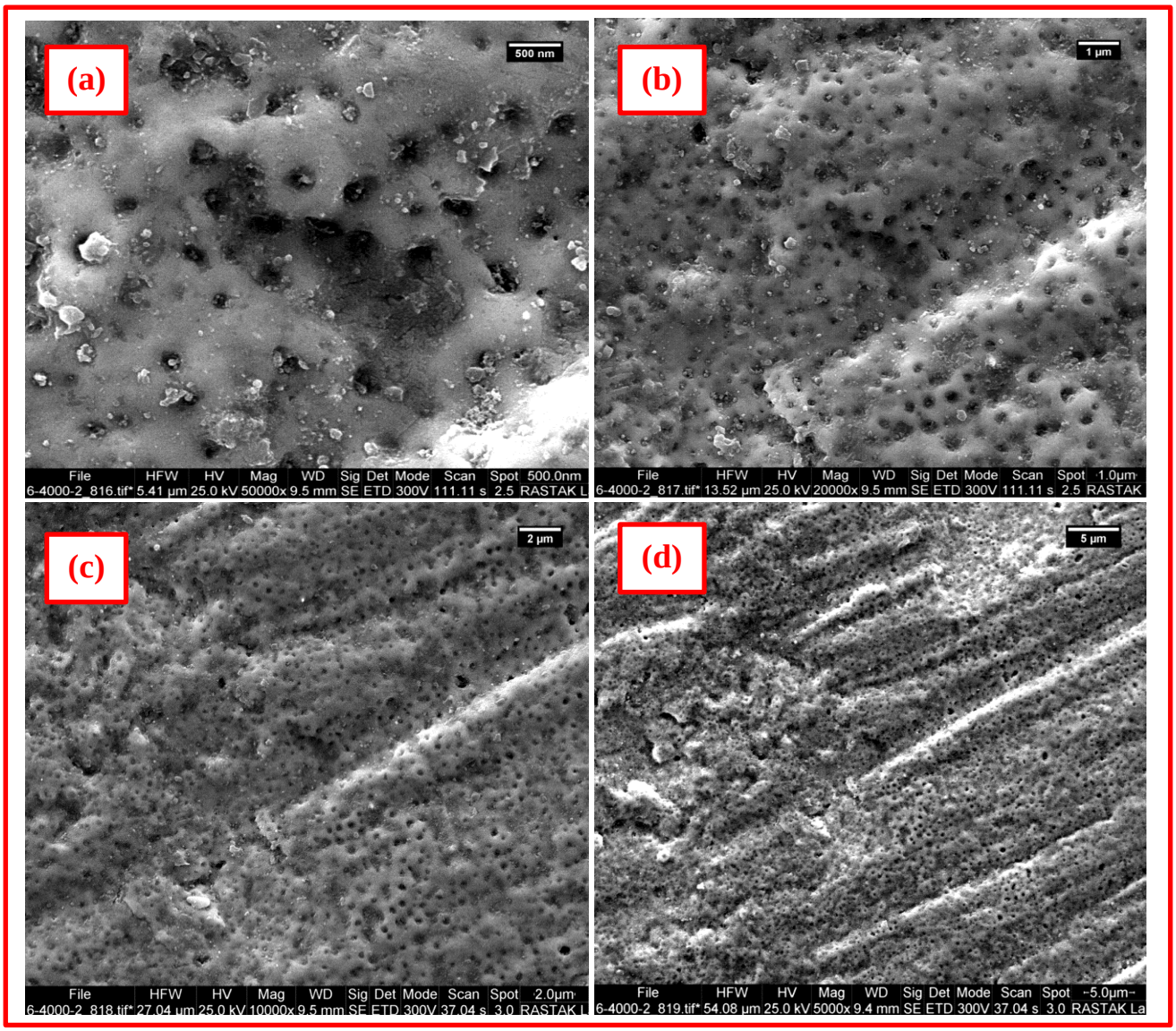

Figure (4.26) : FESEM micrographs of sample C_7 (350V & 30min) at different magnifications.

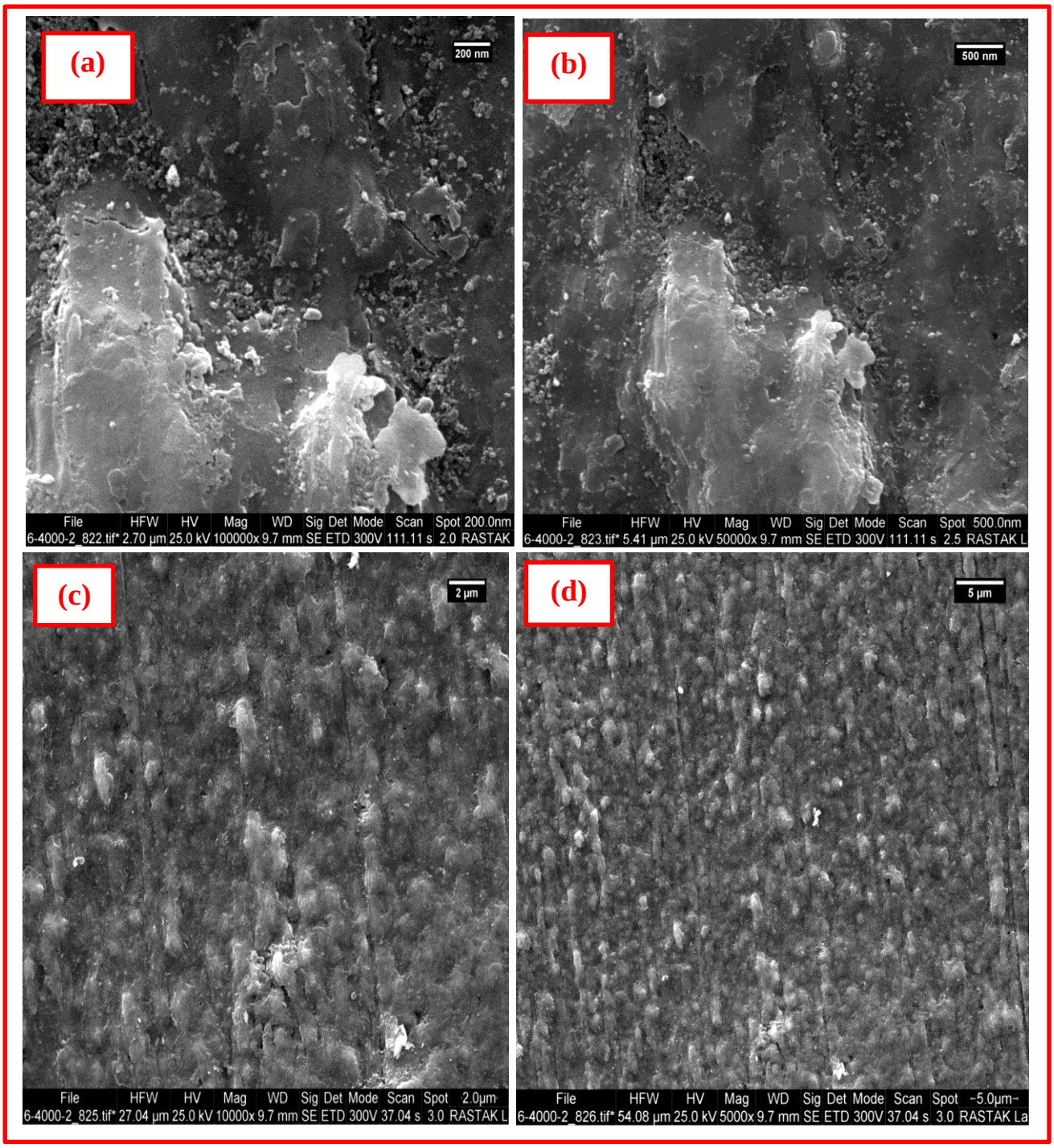

Figure (4.27) : FESEM micrographs of specimen C_{11} (400V & 30min) at different magnifications.

In Figures (4.28), the precipitation of nano particles HA and ZrO_2 can be seen as aggregates on the surface as the voltage increased, and the particle distributions seemed to be non-homogenous at HA/ZrO_2/TiO_2 composite ceramic coating. Also, it is interested to declare that despite the uniform distribution of pores for the specimen D_3.

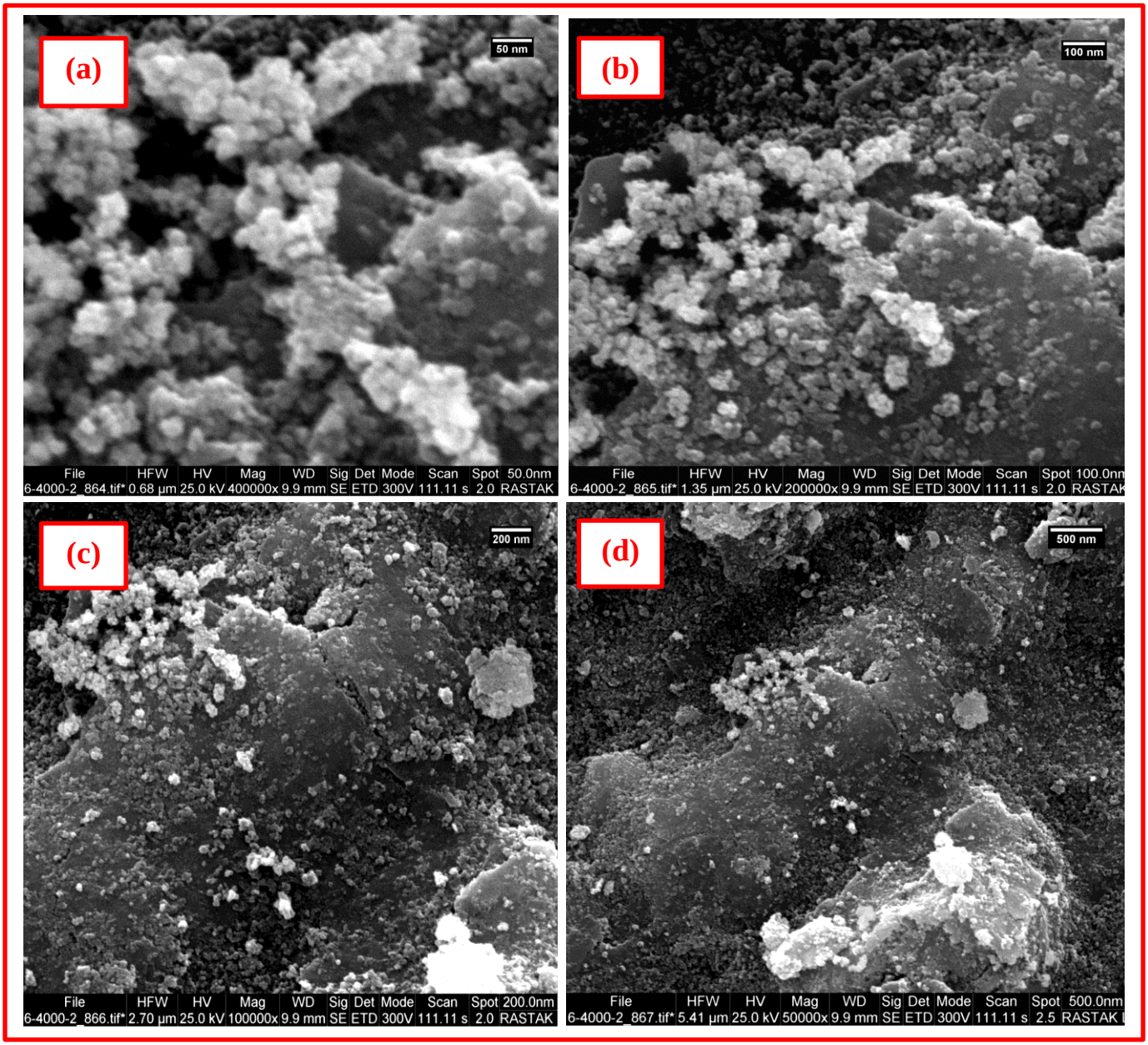

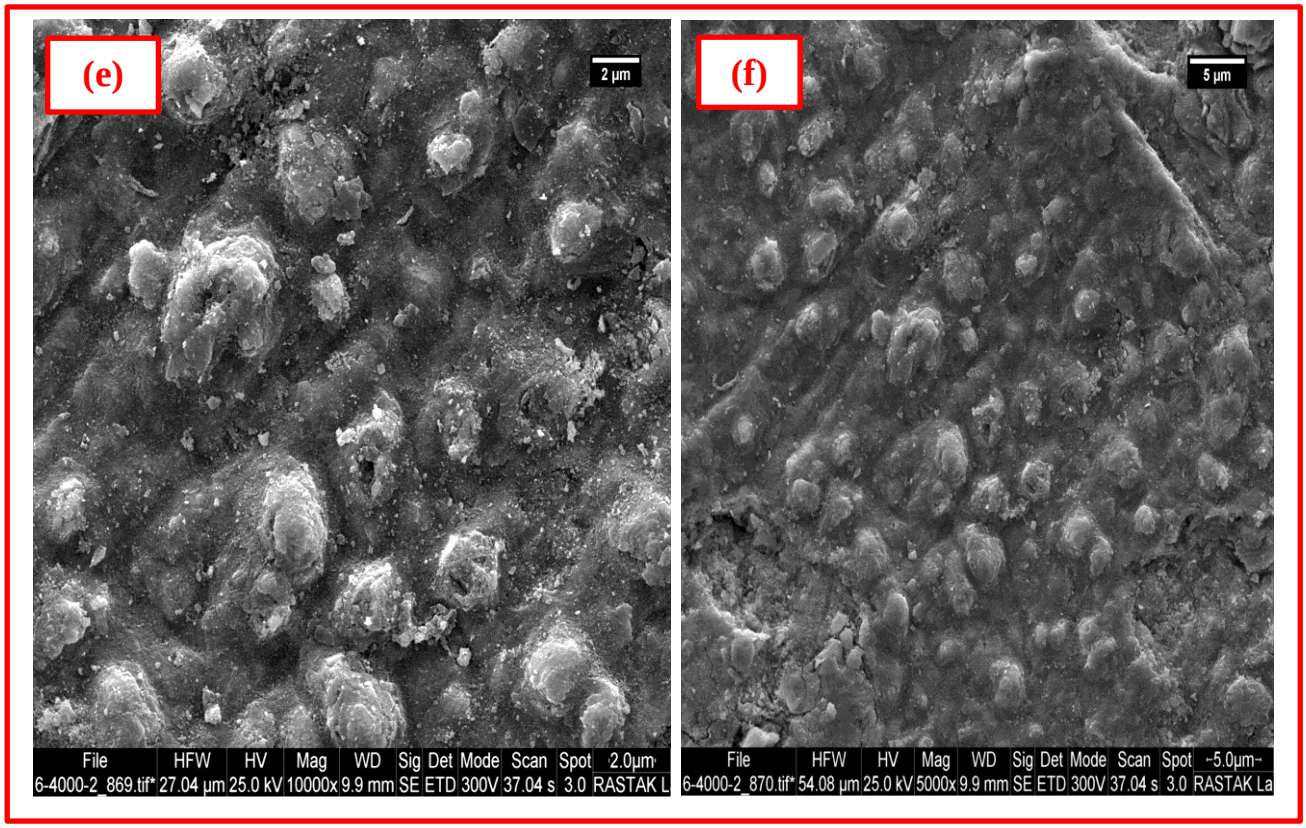

Figure (4.28) : FESEM micrographs of specimen D_3 (300V & 30min) at different magnifications.

It is clear from Figures (4.29) and (4.30) the less pores structure for samples D_7 and D_{11} at (350 and 400) V, also the uniform distribution of pores was observed. Micro-cracks observed at high concentrations of specimens D_3, D_7, and D_{11}.

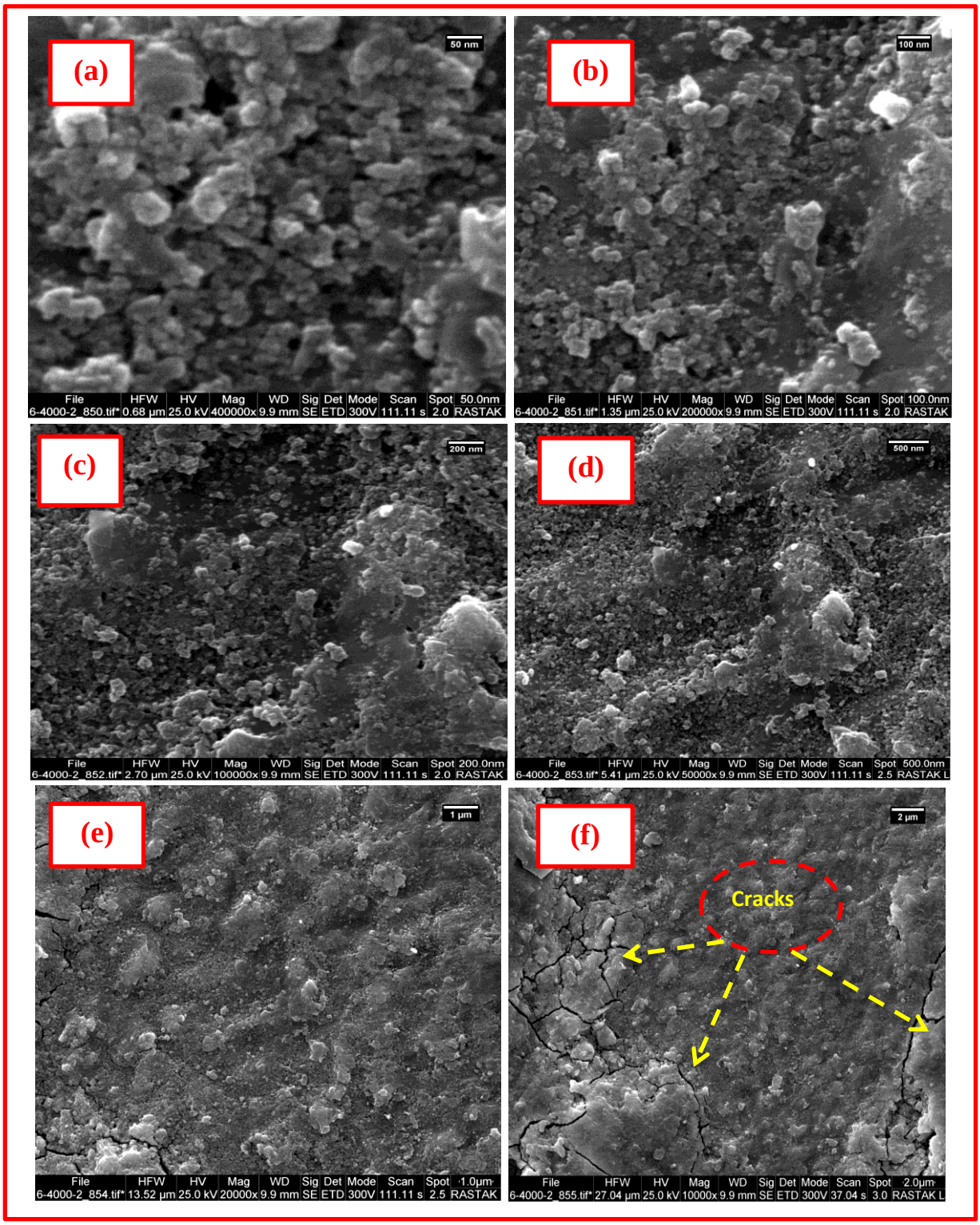

Figure (4.29) : FESEM micrographs of specimen D_7 (350V & 30min) at different magnifications.

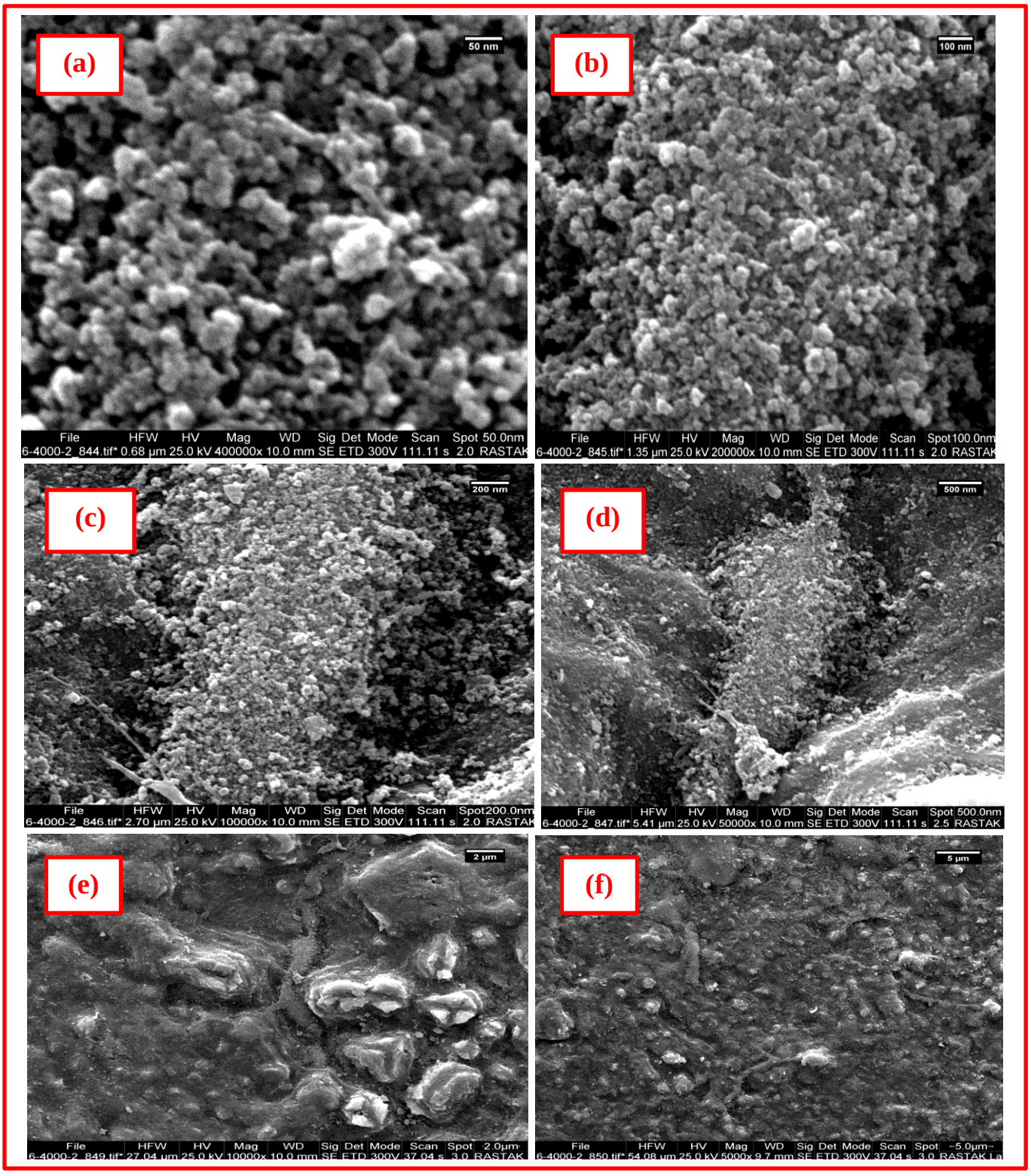

Figure (4.30) : FESEM micrographs of specimen D_{11} (400V & 30min) at different magnifications.

4.4.3 Thickness Coating Test

Figure 4.31 (a) illustrates the cross-sectional morphology by FESEM of TiO_2 coating on specimen A_3. The coated layer has a regular thin film structure in thickness with higher compact, homogeneity and complete adhesion between the coating and the underlying substrate. The coating layer of each sample consists of two parts: the compact diffusion layer in contact with the substrate and the external porous conversion region containing discharge channels. The average thickness of the diffusion layer remains constant during the processing. However, with the voltage increasing from (300 to 400) V, the average thickness of the external porous conversion layer increases as shown in Figure 4.31 (b and c). The formation of crossing pores and big pores distributed along the whole thickness.

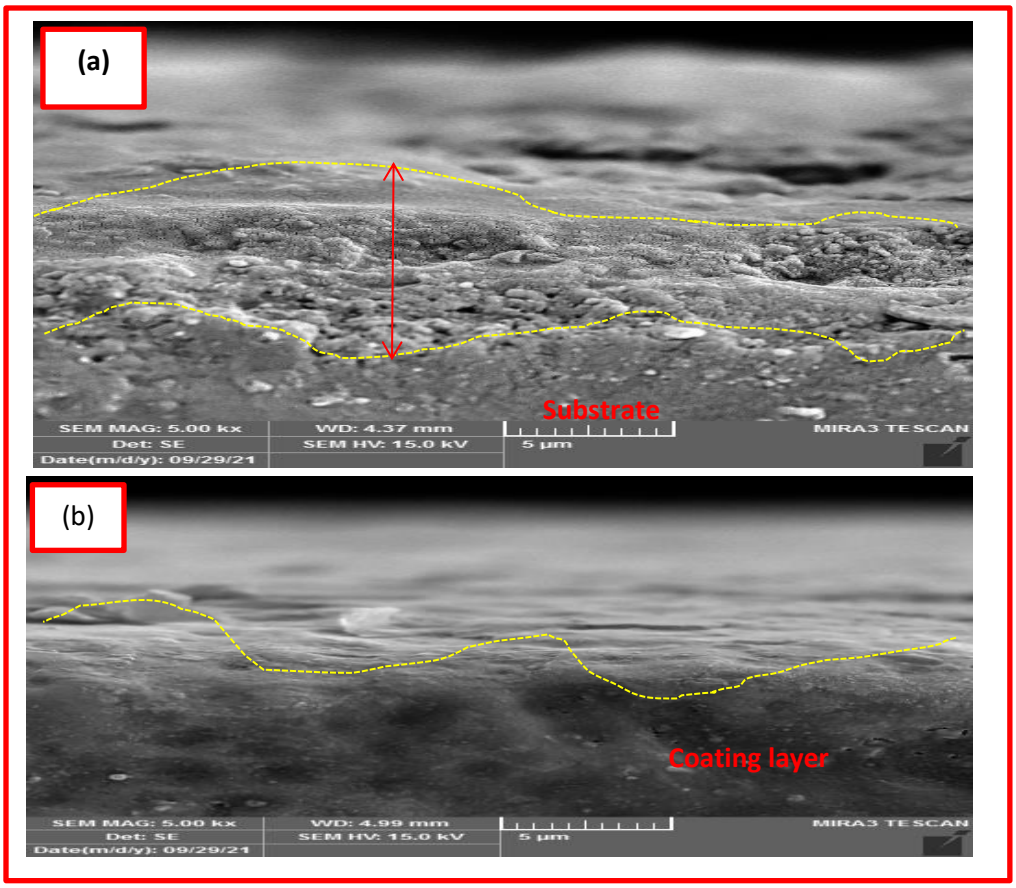

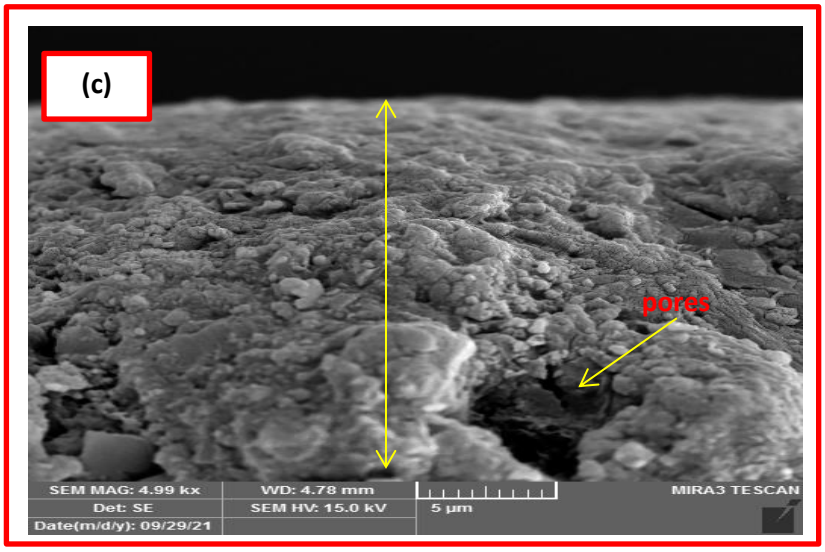

Figure (4.31): Cross section of MAO coatings: (a) A_3, (b) A_7, and (c) A_{11}.

In Figure 4.32, presents the cross-sectional morphologies of HA/TiO_2 nano composite coating with different voltages. The thickness of coating layer increased with voltage increasing and it was estimated to be (2.5µm) for specimen B_7. The interface between the film and the matrix is not obvious and, there is observable HA inside the pores.

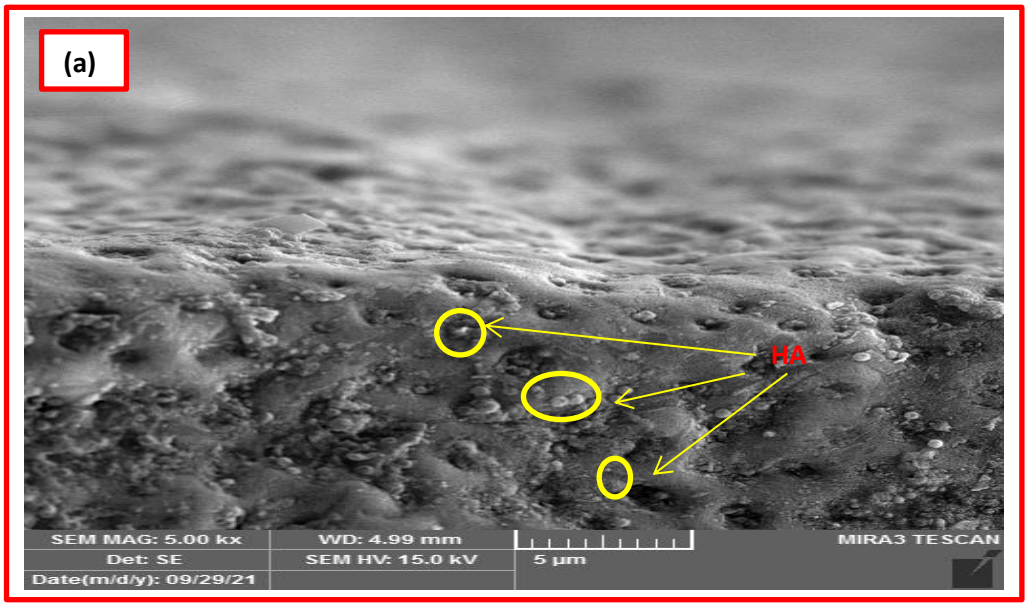

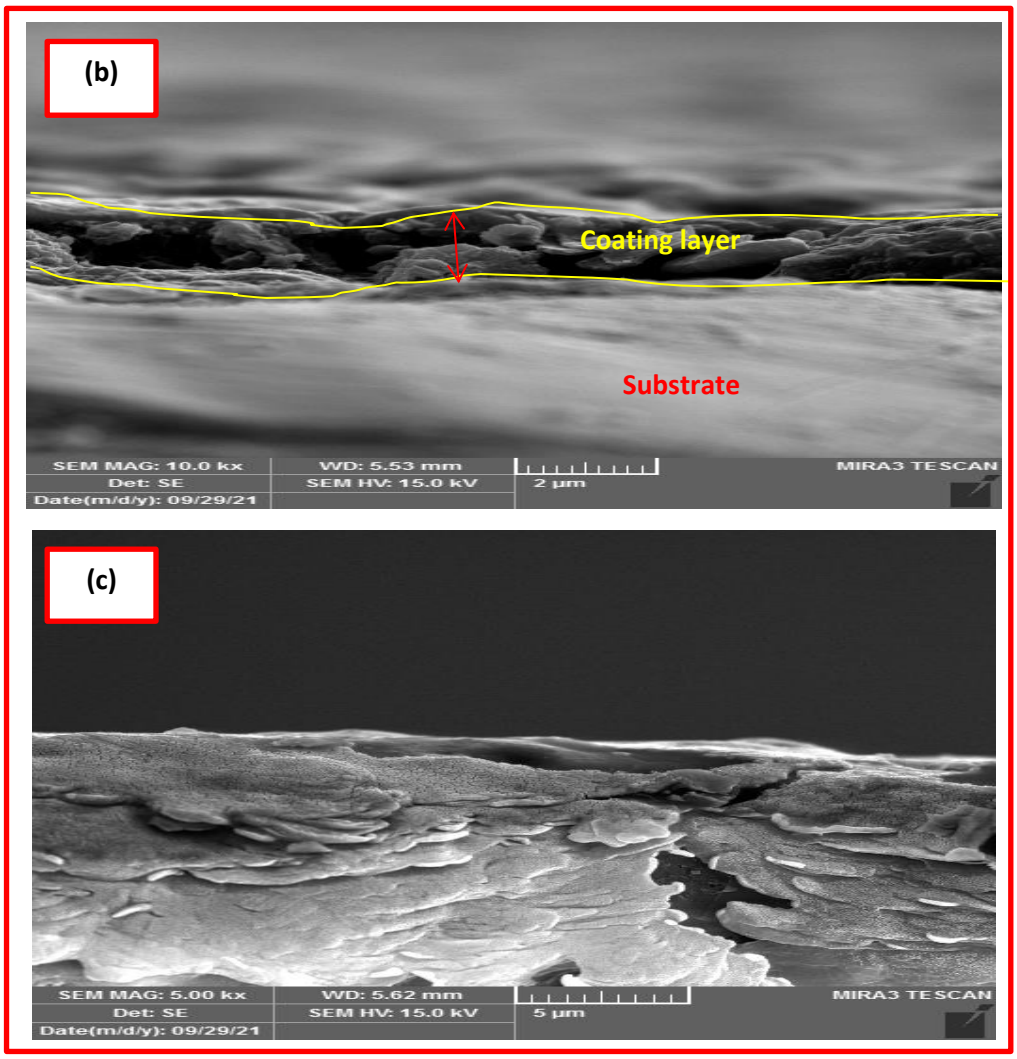

Figure (4.32): Cross section of MAO coating: (a) B_3, (b) B_7, and (c) B_{11}.

Cross-sectional images of the ZrO_2/TiO_2 coatings are displayed in Figure (4.33). Identical results were obtained for the other samples. The inner layer was found to be porous, while the outer region was dense, with only limited porosity. A typical porous structure was found, whereby the pore size clearly was dependent on the limiting voltage. Coating thickness increased with the limiting voltage increasing, and it equal to (1.944µm) for specimen C_{11}.

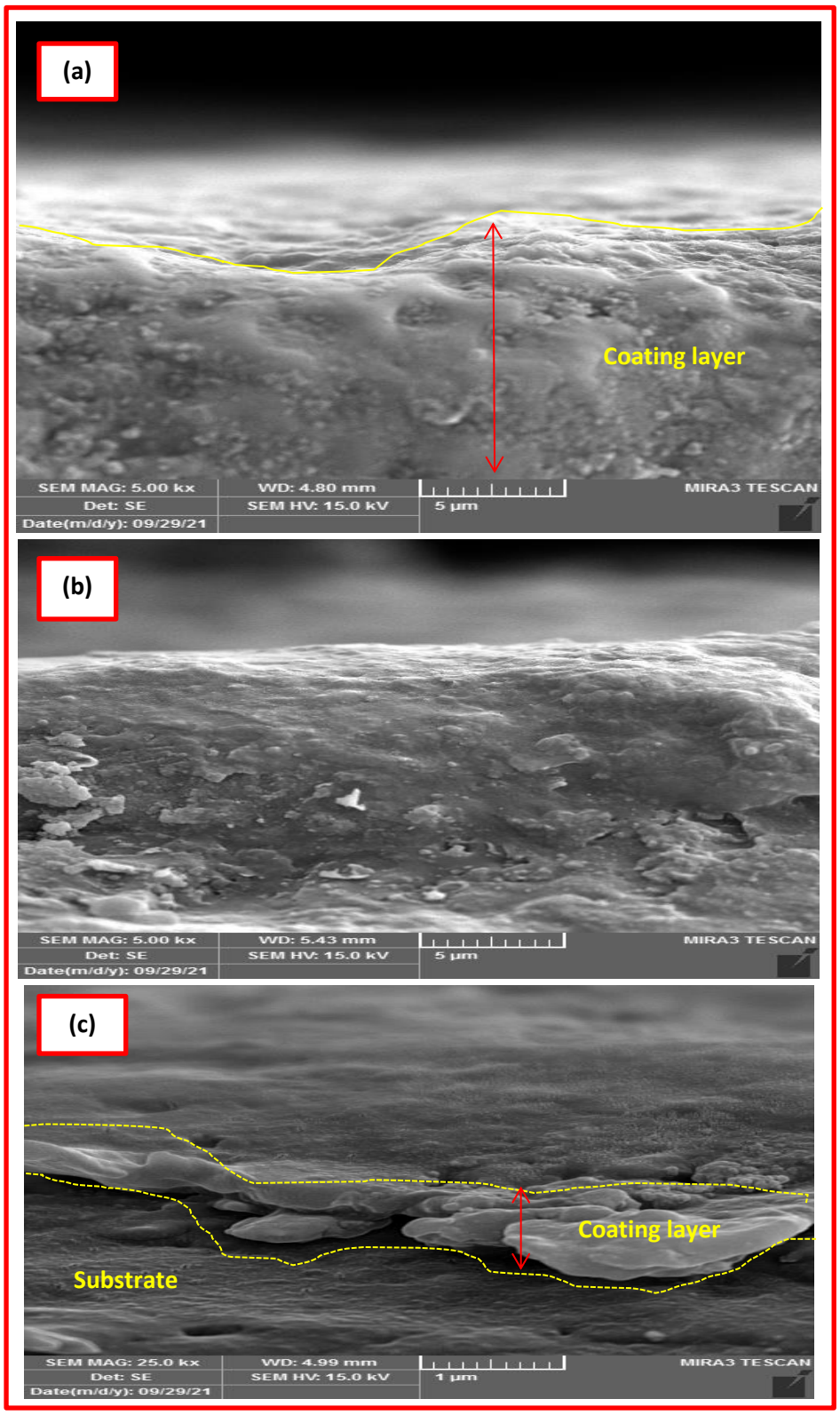

Figure (4.33): Cross section of MAO coating : (a) C_3, (b) C_7, and (c) C_{11}.

Figure 4.34 (a) shows the cross-section morphologies of HA/ZrO_2/TiO_2 coatings is about 2.54µm for sample D3. The internal oxide film is compact and close to the substrate, while the external film is messy and loose. The thickness of the HA/ZrO_2/TiO_2 film was uniform. It can be concluded that the applied voltage affected the concentration of HA and ZrO_2 in the TiO_2 film as well as with the thickness increased to 2.61µm for sample D_7 as shown in Figure 4.34 (b). Because of the absence of large volcano shaped pores, the coating layer is non-uniform, with large thickness variations. The micro-cracks could be observed on the surface of coating in specimen as in Figure 4.34 (c).

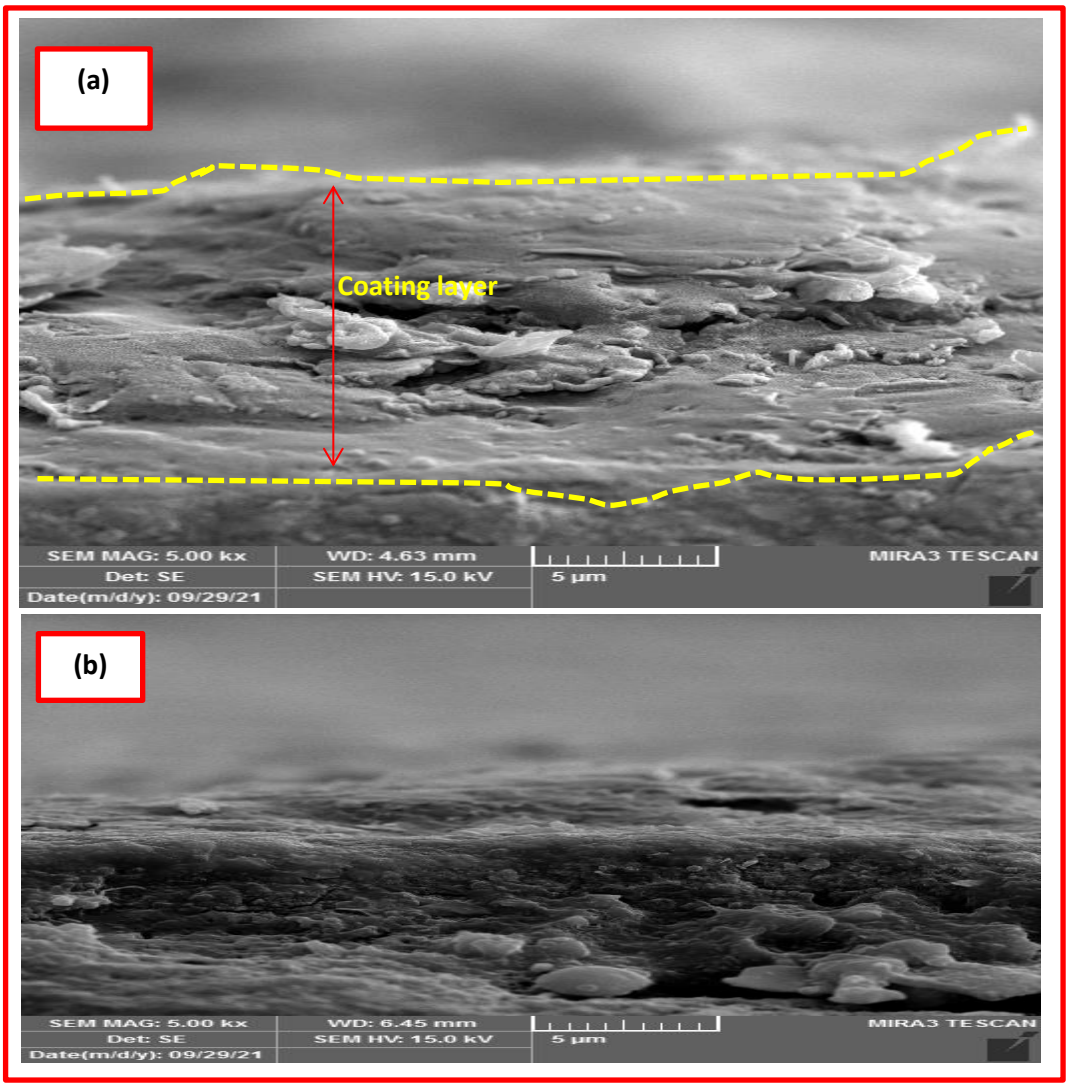

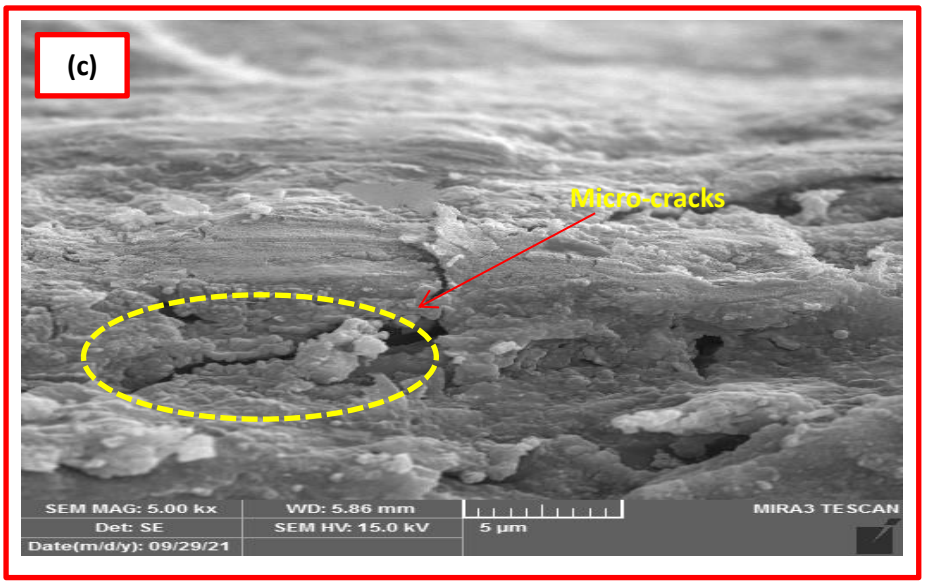

Figure (4.34): Cross section of coating by MAO process: (a) D_3, (b) D_7, and (c) D_{11}.

Generally, it can be seen that the coating thickness is increased with increasing voltage and deposition time because the voltage on the sample could not reach the sparking threshold, and a thin layer of oxide film quickly formed on the sample surface because of anodic oxidation. When the oxidation time was increased, the sparking voltage was reached and the energy rose; consequently, some discharge channels on the specimens became evident.

Oxide film formed on the inner and outer surfaces of the discharge channel as the reaction product erupted along the channel. With increases in the oxidation time, voltage and energy, repeated breakdown made the oxide film thicker. Moreover, the molten oxide overflowed through the discharge channel, cooled rapidly, and was deposited after reaching the surface. The process was repeated until the end of the oxidation reaction, causing incessant growth of the oxide film [144].

4.4.4 Electron Dispersive Spectroscopy (EDS)

Table (4.1) presents the schematic data of EDS results for MAO TiO2 coatings with different voltage on containing Ti, O, Al, and Nb ions. EDS analysis showed that increasing of voltage up to 400 V had it effects on the content of oxide layer as shown in Figure 4.35 for A_3, A_7, and A_{11} samples coated with different voltage. The existence of Ti and O_2 elements in the coatings, thereby, referred to the formation of TiO_2 layers with different weights of these modification elements.

Table (4.1): EDS results of TiO_2 layers at different voltages.

Samples	Element	Weight (%)	Atomic (%)	Net Int.
A_3	OK	28.84	55.46	213.29
	AlK	3.42	3.9	189.27
	NbL	9.25	3.06	406.15
	TiK	58.5	37.58	3585.76
A_7	OK	33.59	61.14	354.99
	AlK	0.96	1.03	72.41
	NbL	6.67	2.09	417.09
	TiK	58.78	35.73	5065.96
A_{11}	OK	35.73	63.12	471.18
	AlK	0.51	0.54	47.5
	NbL	4.51	1.37	348.62
	TiK	59.25	34.97	6323.64

(a)

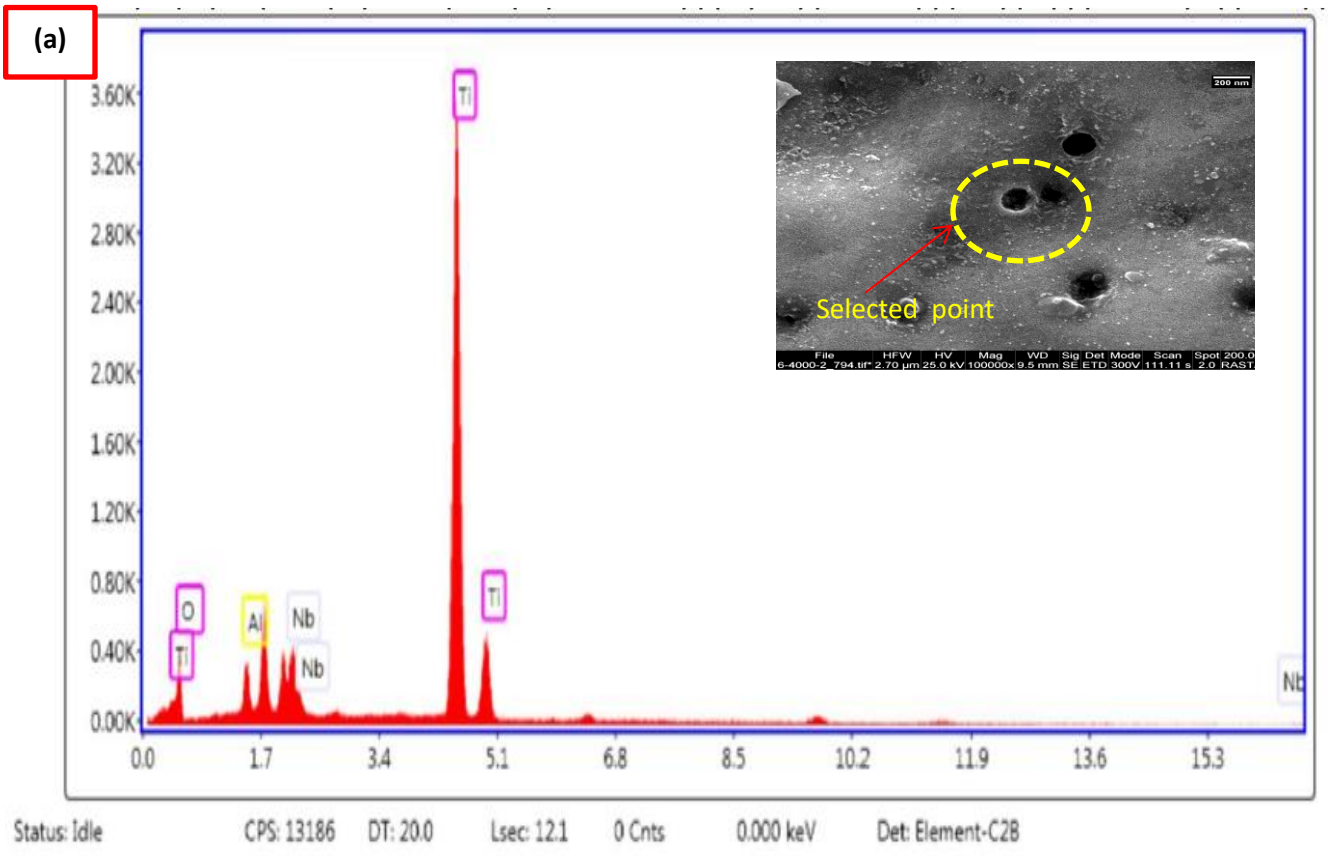
3.60K
3.20K
2.80K
2.40K
2.00K
1.60K
1.20K
0.80K
0.40K
0.00K
0.0
1.7
3.4
5.1
6.8
8.5
10.2
11.9
13.6
15.3
Ti
O
Al
Nb
Nb
Ti
Ti
Nb
Selected point
Status: Idle
CPS: 13186
DT: 20.0
Lsec: 12.1
0 Cnts
0.000 keV
Det: Element-C2B

(b)

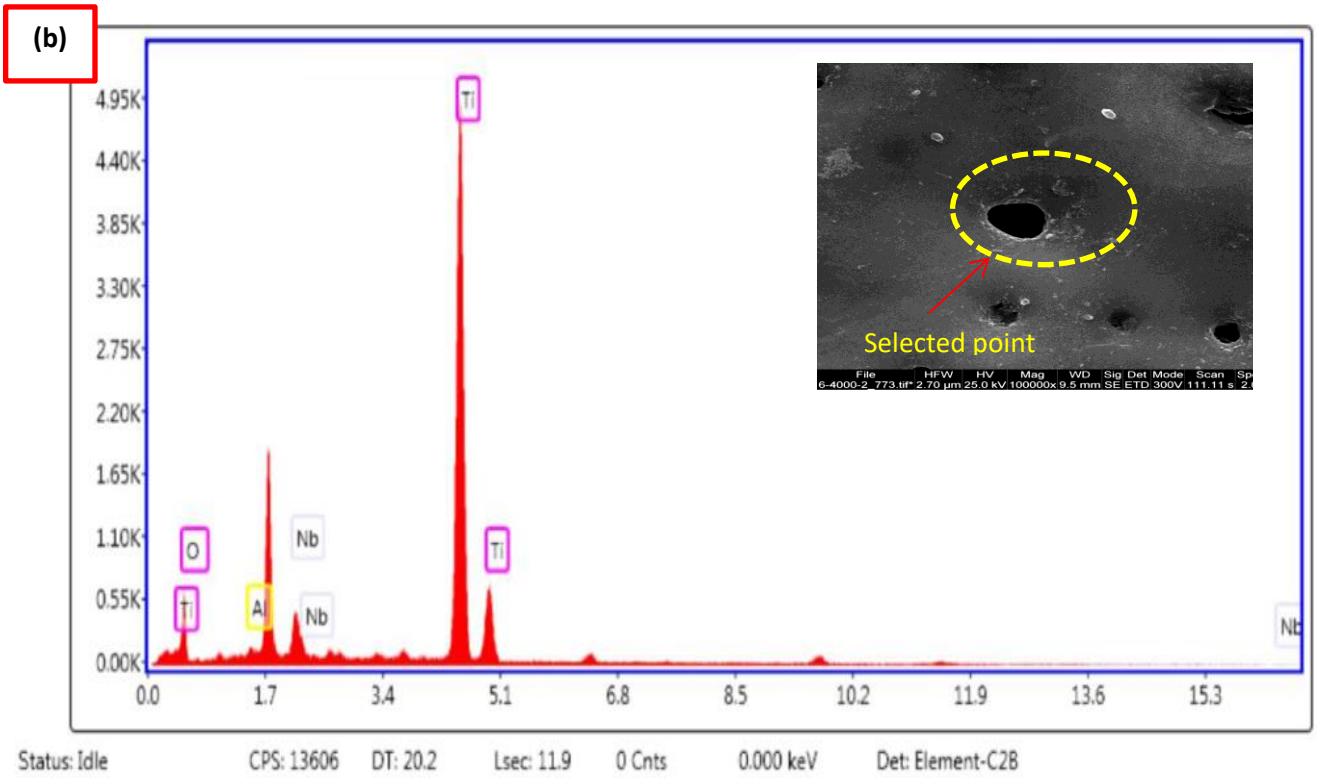
4.95K
4.40K
3.85K
3.30K
2.75K
2.20K
1.65K
1.10K
0.55K
0.00K
0.0
1.7
3.4
5.1
6.8
8.5
10.2
11.9
13.6
15.3
Ti
O
Nb
Ti
Ti
Al
Nb
Nb
Selected point
Status: Idle
CPS: 13606
DT: 20.2
Lsec: 11.9
0 Cnts
0.000 keV
Det: Element-C2B

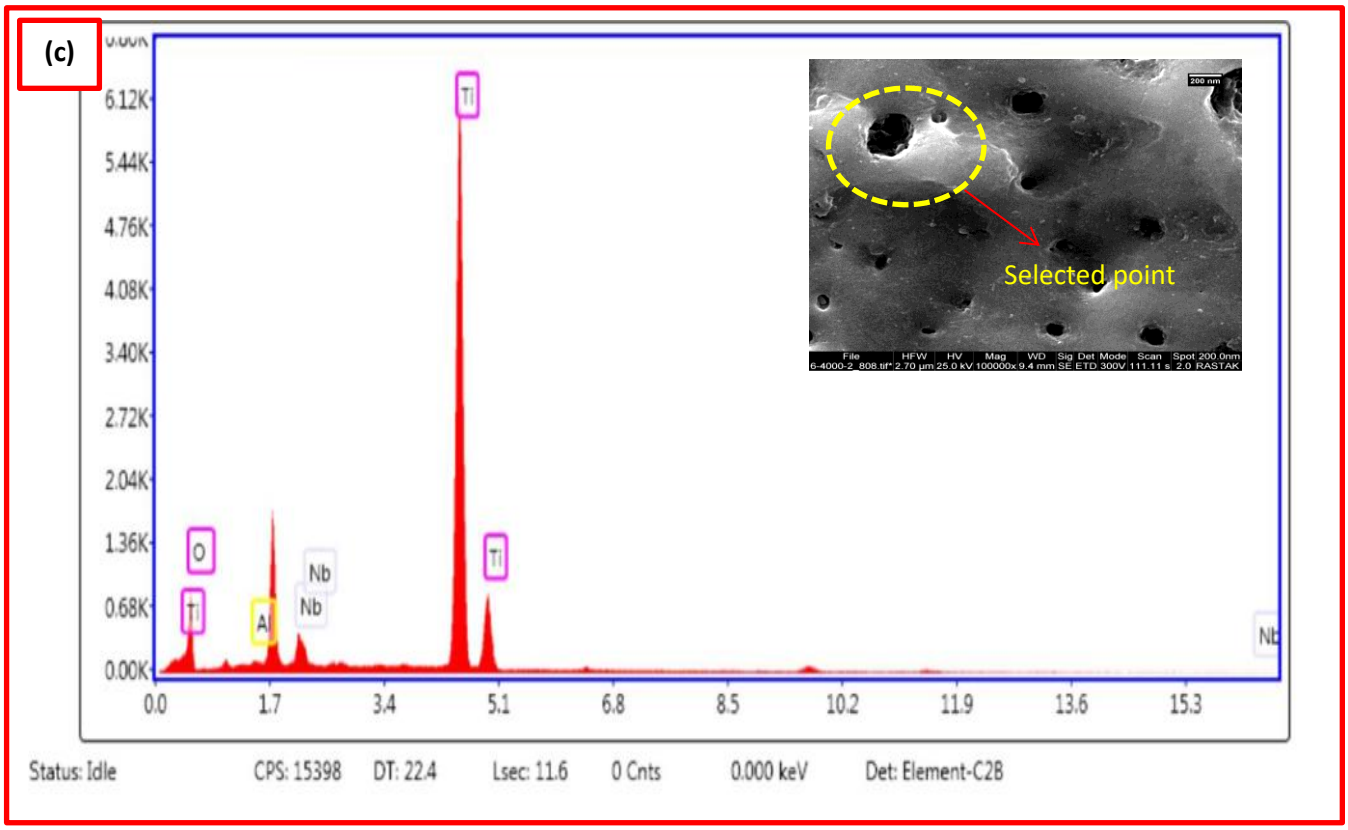

Figure (4.35): EDS result of (a) sample A_3, (b) samples A_7, and (c) samples A_{11}.

Ca and P atoms on the surface of the HA/TiO_2 film coated by MAO process could be observed in EDS results, as shown in Table (4.2). The calculated Ca/P ratios according to the EDS result differed with voltages differences, where the coating elements of Ca, P, O, Ti, Al, and Nb increased with voltages increasing in Figure (4.36). During the micro-arc discharge process under an applied voltage, intense plasma physical and chemical reactions occur in the discharge channel, accompanied by high pressure and high temperature conditions. Under these conditions, Ti near the surface of the titanium alloy substrate participates in the subsequent reactions and can be oxidized to form TiO_2. At the same time, Ca^{+2}, and $HPO4^{-2}$or $PO4^{-3}$ and OH^- from the ionization move to the anode easily in the electrolyte under the applied electric field respectively and are incorporated into the coatings. For biomedical

applications, Ca^{+2} and $PO3^{-4}$ Ions in the electrolyte enter the ceramic layer during the MAO process, so that the bioactivity of the Ti alloy increases [122].

Table (4.2): EDS results of HA/TiO_2 MAO coating at different voltages.

Samples	Element	Weight (%)	Atomic (%)	Net Int.
B_3	OK	25.7	49.58	222.01
	AlK	5.59	6.39	370.16
	PK	6.11	6.08	527.64
	NbL	7.9	2.62	364.28
	CaK	0.54	0.42	45.86
	Ti K	54.16	34.9	3726.8
B_7	OK	28.7	52.99	180.18
	AlK	6.46	7.08	299.15
	PK	5.99	5.71	355.74
	NbL	7.47	2.38	237.35
	CaK	1.3	0.96	74.9
	TiK	50.08	30.89	2371.73
B_{11}	OK	25.52	50.19	206.62
	AlK	0.14	0.16	8.92
	PK	3.41	3.47	318.58
	NbL	4.63	1.57	238.27
	CaK	8.22	6.45	747.51
	TiK	58.09	38.16	4082.46

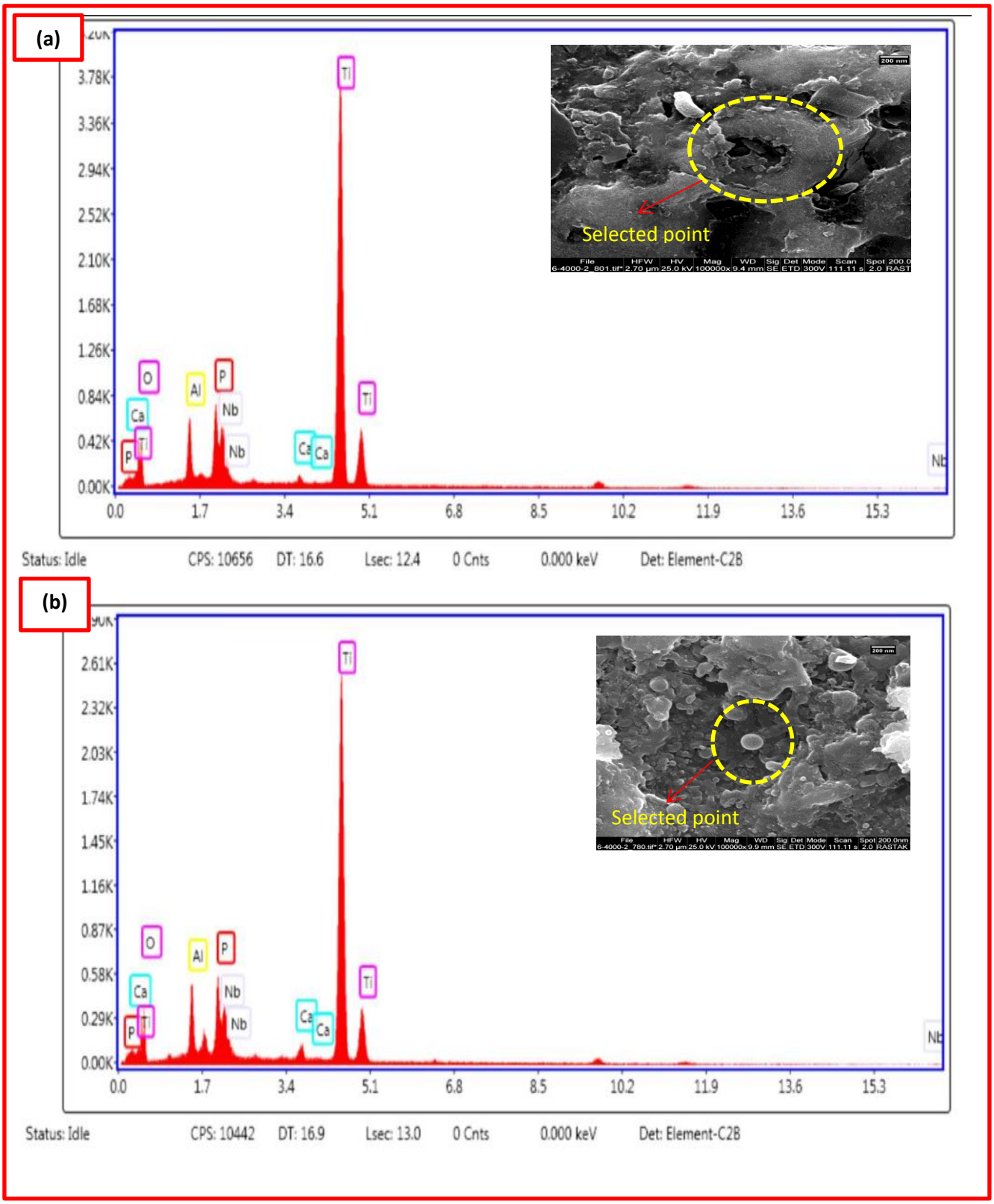
(a)
3.78K
3.36K
2.94K
2.52K
2.10K
1.68K
1.26K
0.84K
0.42K
0.00K
0.0
1.7
3.4
5.1
6.8
8.5
10.2
11.9
13.6
15.3
O
Al
P
Ca
Ti
Nb
Selected point
Status: Idle CPS: 10656 DT: 16.6 Lsec: 12.4 0 Cnts 0.000 keV Det: Element-C2B
(b)
2.61K
2.32K
2.03K
1.74K
1.45K
1.16K
0.87K
0.58K
0.29K
0.00K
Selected point
Status: Idle CPS: 10442 DT: 16.9 Lsec: 13.0 0 Cnts 0.000 keV Det: Element-C2B

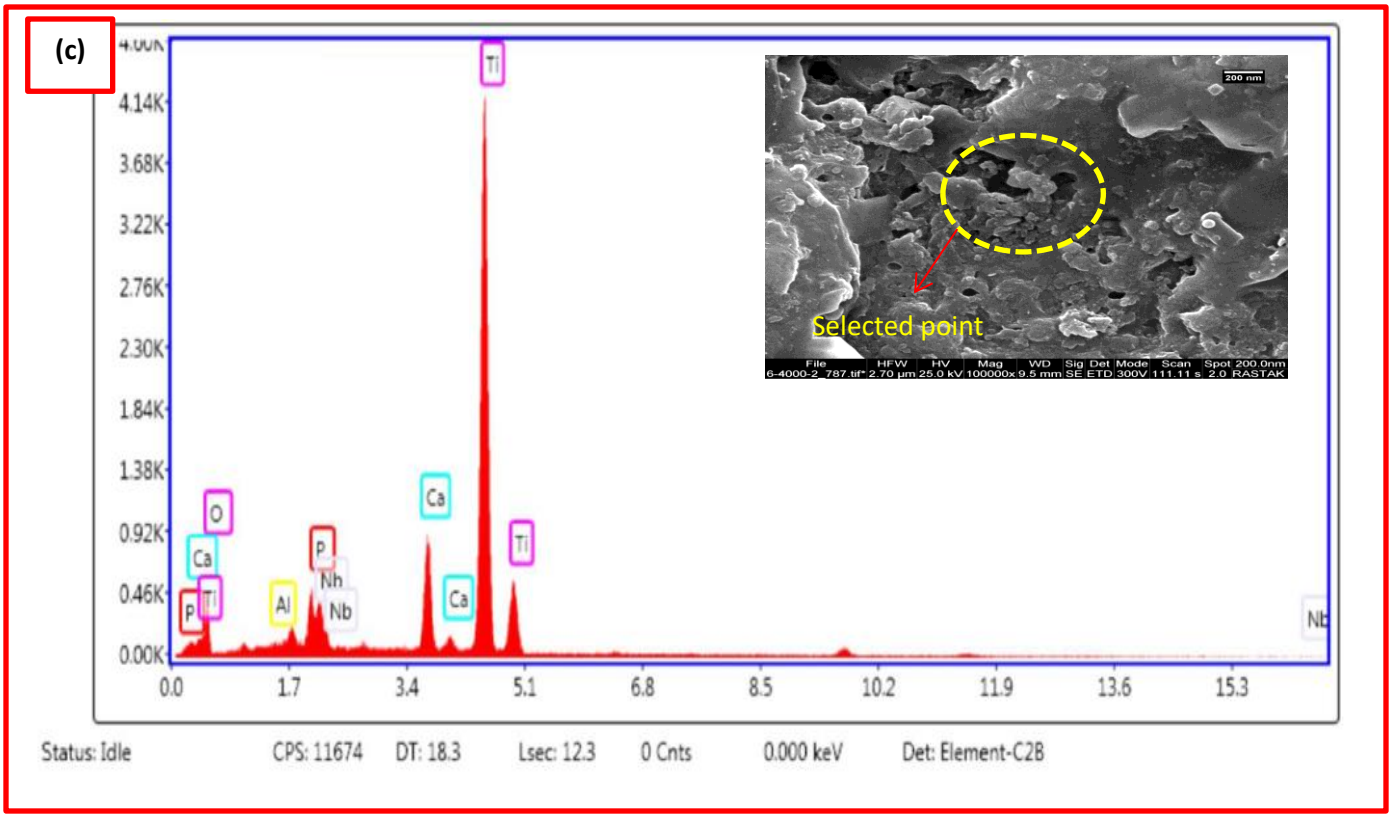

Figure (4.36): EDS result of (a) sample B_3, (b) samples B_7, and (c) samples B_{11}.

Incorporation of ZrO_2 nanoparticles precipitation by MAO coatings to the implant surfaces can affect the concentrations of elements (Zr, O, Al, Nb, and Ti) as shown in table (4.3) with different voltages. The ratio of Zr/O_2 was dependent on voltage, it was 1.09 for voltages (300V) and 12.78 for voltages (400V) as shown in Figure (4.37).

Table (4.3) : EDS results of ZrO_2/TiO_2 MAO coatings at different voltages.

Samples	Element	Weight (%)	Atomic (%)	Net Int.
C_3	OK	27.86	54.51	163.73
	AlK	0.14	0.16	6.4
	ZrL	1.09	0.37	39.87
	NbL	4.42	1.49	168.3
	TiK	66.49	43.46	3516.66
C_7	OK	31.37	58.52	188.48
	AlK	0.58	0.64	25.61
	ZrL	1.41	0.46	50.13
	NbK	3.75	1.2	138.47
	TiK	62.89	39.18	3233.1
C_{11}	OK	21.84	47.66	155.69
	AlK	3.43	4.44	193.55
	ZrL	12.78	4.89	535.21
	NbK	6.11	2.3	254.01
	TiK	55.84	40.71	3317.56

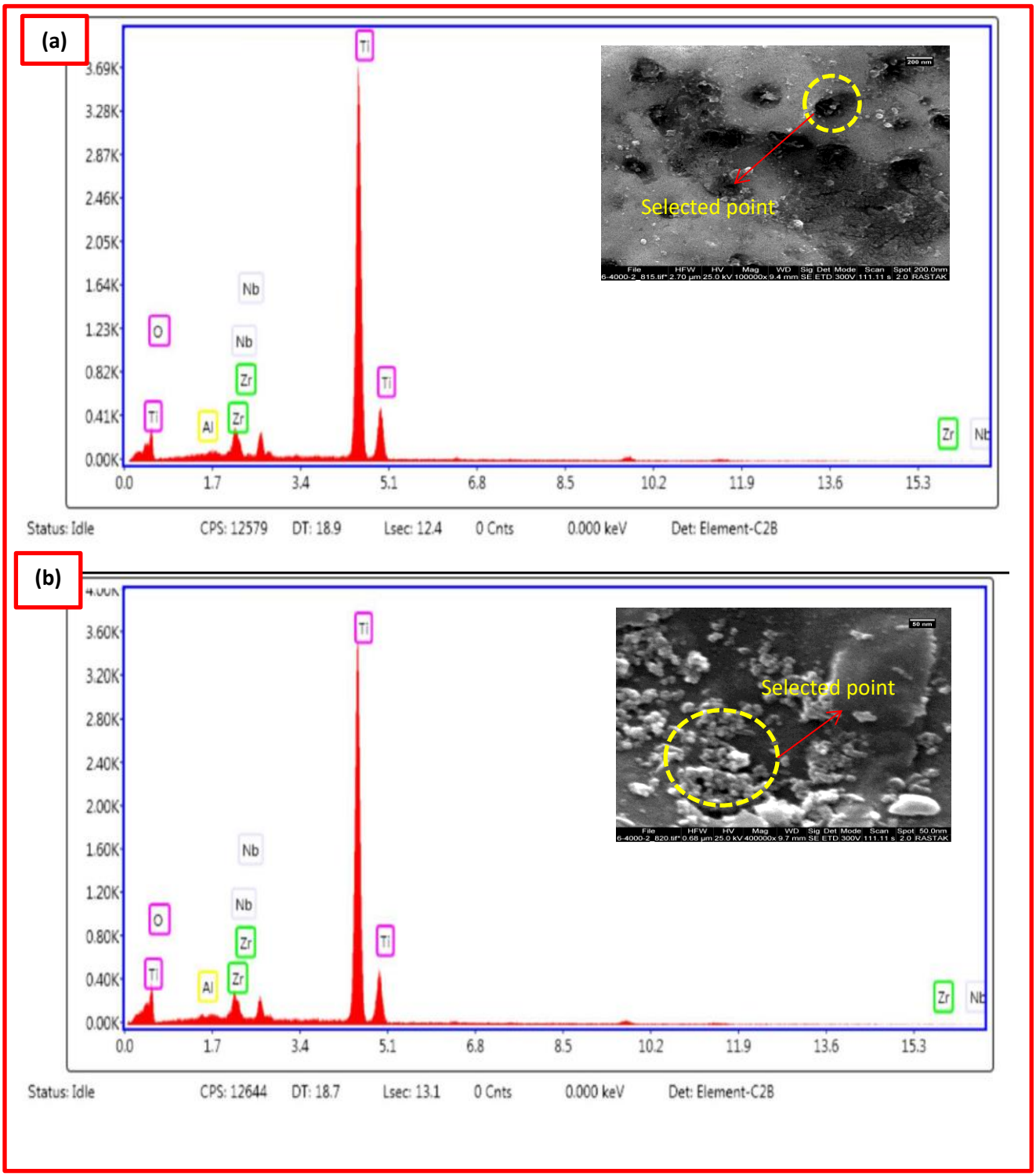
(a)
Selected point
Status: Idle CPS: 12579 DT: 18.9 Lsec: 12.4 0 Cnts 0.000 keV Det: Element-C2B
(b)
Selected point
Status: Idle CPS: 12644 DT: 18.7 Lsec: 13.1 0 Cnts 0.000 keV Det: Element-C2B

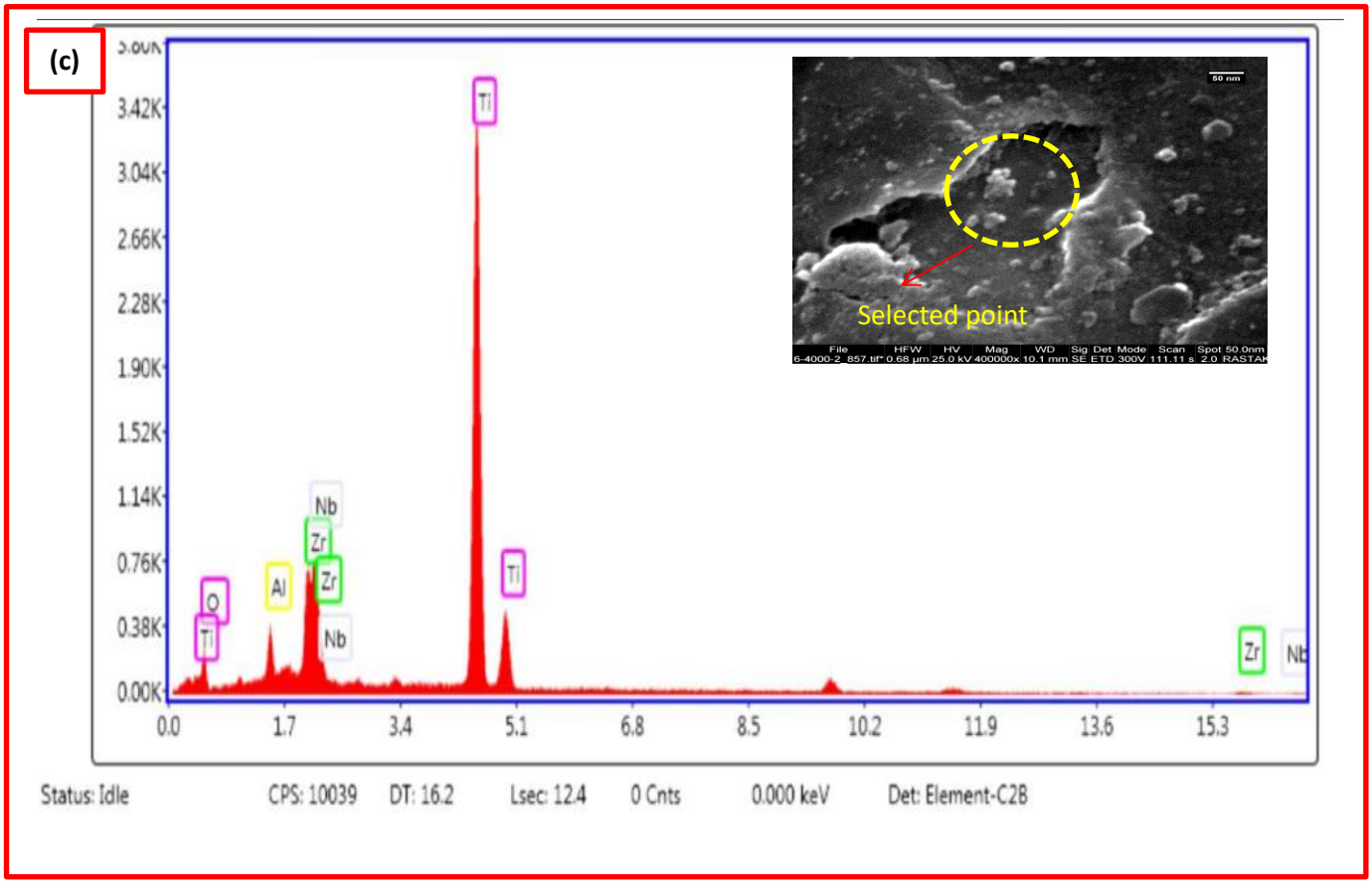

Figure (4.37): EDS result of (a) sample C_3, (b) samples C_7, and (c) samples C_{11}.

Table (4.4), shows the EDS results of HA and ZrO_2 precipitation in MAO process for samples D with different voltages. It can be observed that coating elements of Zr, O, Ca , and P increased with increased voltage. In Figure (4.38) atomic ratio of Ca/P increased from (1.6 to 1.84) % for samples D_3 to D_{11} respectively, similarly to the Zr/O atomic ratio increased from (1.72 to 2.5) % with increased voltage.

Table (4.4) : EDS results of HA/ZrO_2/TiO_2 MAO coatings at different voltages.

Samples	Element	Weight (%)	Atomic (%)	Net Int.
D_3	OK	28.59	55.99	170.82
	AlK	0.69	0.8	30.99
	PK	1.62	0.46	9.07
	ZrL	4.83	1.66	171.83
	NbL	5.01	1.69	182.46
	CaK	0.26	0.18	14.65
	TiK	58.97	39.64	3077.36
D_7	OK	27.5	53.9	147.8
	AlK	2.68	3.11	109.75
	PK	1.62	1.89	11.46
	Zr L	4.76	1.43	136.83
	NbK	7.47	2.38	237.35
	CaK	0.28	0.22	18.04
	TiK	55.69	39.3	2730.43
D_{11}	OK	39.74	68.15	269.35
	AlK	1.63	1.66	70.5
	PK	4.29	3.01	21.46
	ZrL	9.95	2.99	328.61
	NbK	4.63	1.57	238.27
	CaK	0.79	0.62	45.13
	TiK	41.54	26.25	2134.28

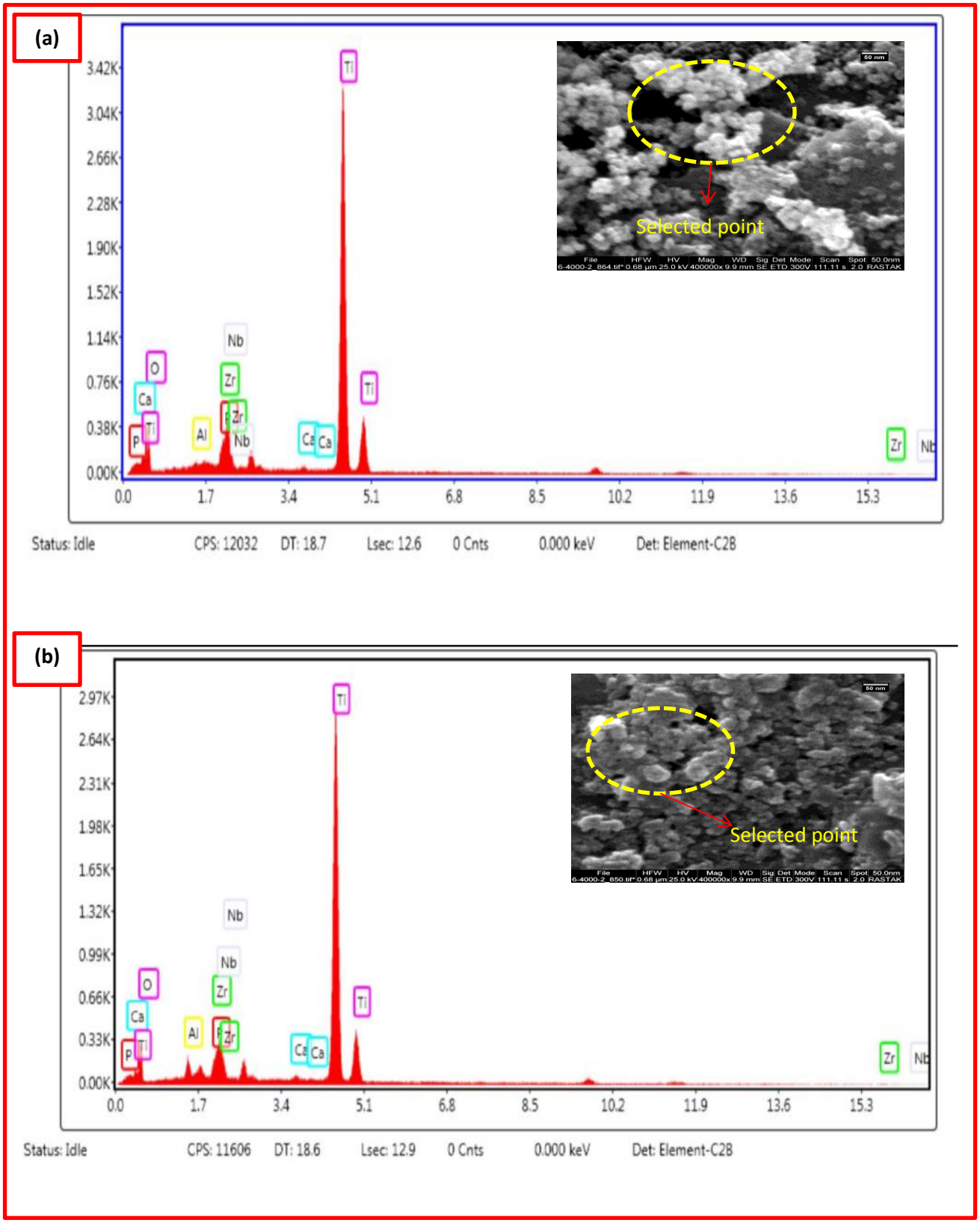
(a)
3.42K
3.04K
2.66K
2.28K
1.90K
1.52K
1.14K
0.76K
0.38K
0.00K
0.0
1.7
3.4
5.1
6.8
8.5
10.2
11.9
13.6
15.3
Ti
Nb
O
Zr
Ca
P
Al
Selected point
Status: Idle CPS: 12032 DT: 18.7 Lsec: 12.6 0 Cnts 0.000 keV Det: Element-C2B
(b)
2.97K
2.64K
2.31K
1.98K
1.65K
1.32K
0.99K
0.66K
0.33K
0.00K
Selected point
Status: Idle CPS: 11606 DT: 18.6 Lsec: 12.9 0 Cnts 0.000 keV Det: Element-C2B

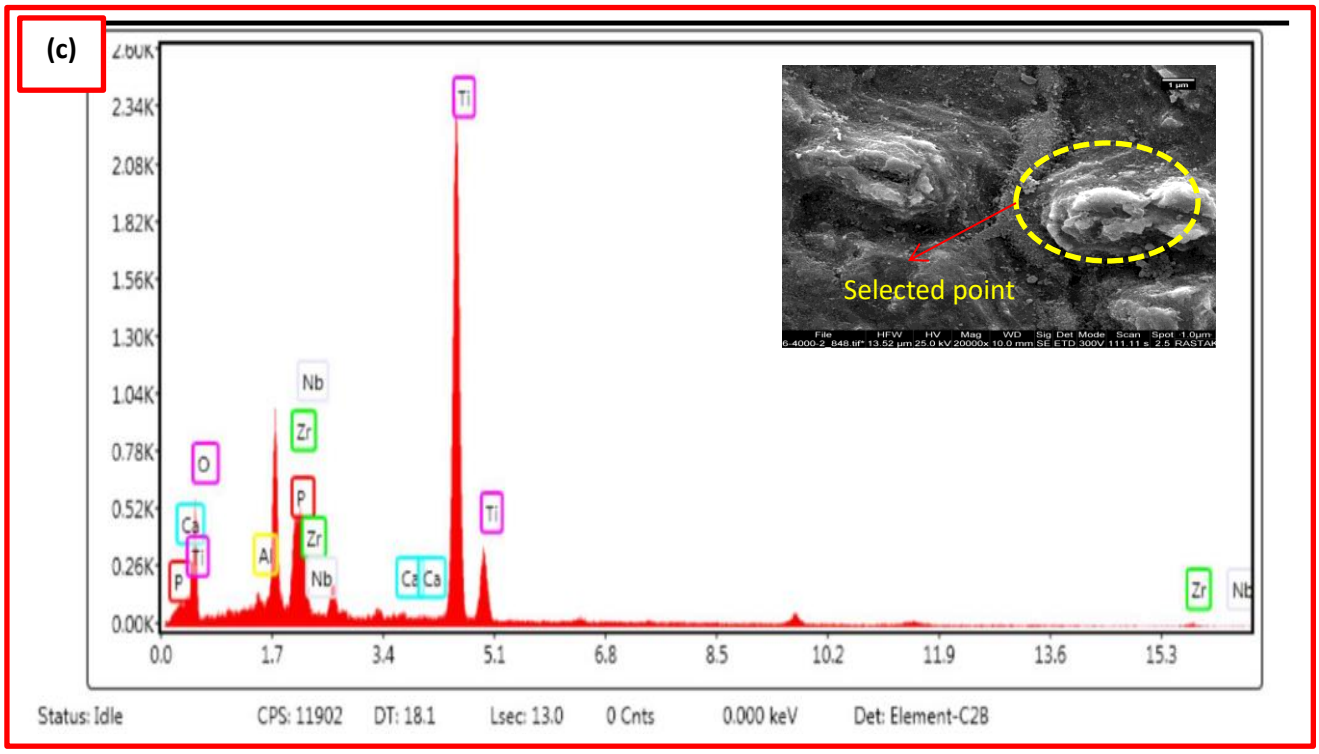

Figure (4.38): EDS results of (a) sample D_3, (b) samples D_7, and (c) samples D_{11}.

4.5 Atomic Force Microscope (AFM) Analysis

Results of AFM analysis are given in Figures (4.39) and Table (4.5), the differences in surface topography between the substrate and different coatings in 2D and 3D, where observed an increase in the roughness of the TiO_2 coatings because that the coatings grown on the surface have a rough surface depending on the phenomenon of micro-discharge resulting from the nature of MAO process [143]. The Ra of coatings were more than those of the substrates and increased with voltage increasing, it equal to (8.23nm) for sample A_3 to (25.3nm) for sample A_7 and deposition time roughness also increased from (7.19nm) for A_1 to (12.6nm) for samples A_4, (18.8nm) and (36.4nm) for A_9 to (45.6nm) for A_{12} with maximum surface roughness for samples A_{11} is (46.5nm) because increase oxidation time.

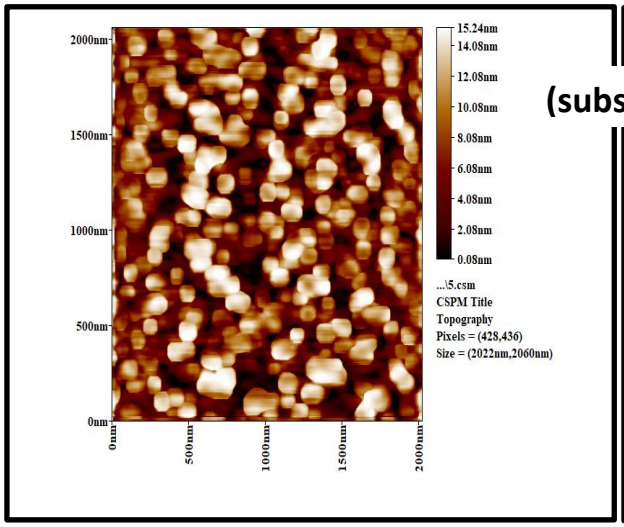

(substrate)

(a)

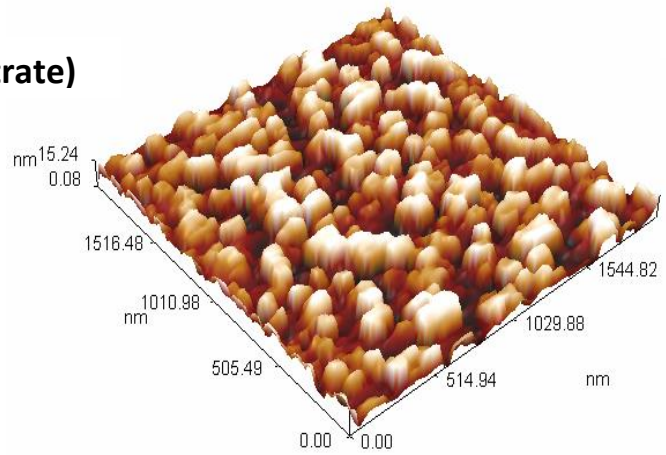

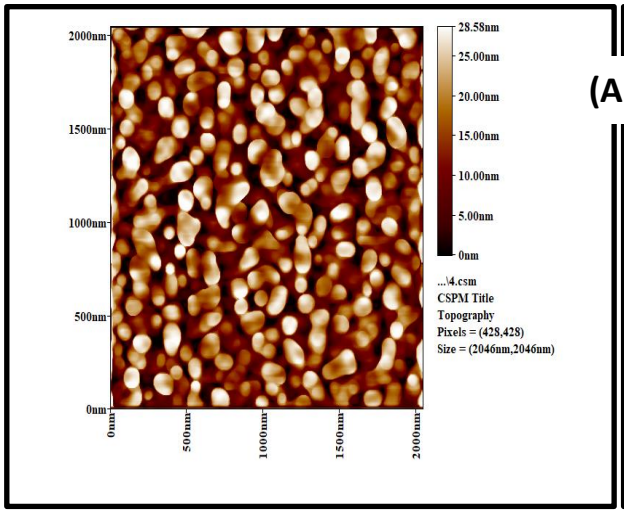

(A_1)

(b)

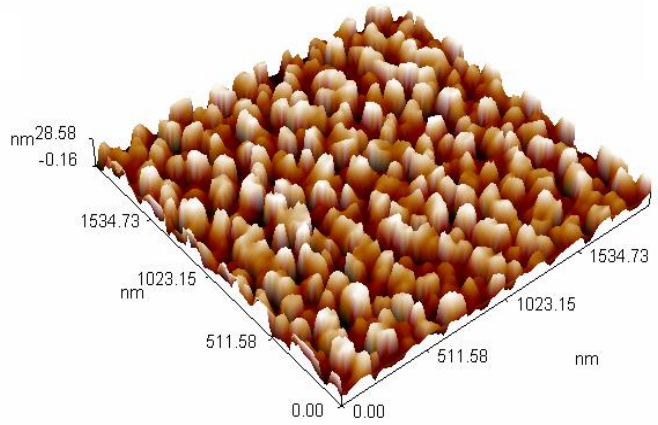

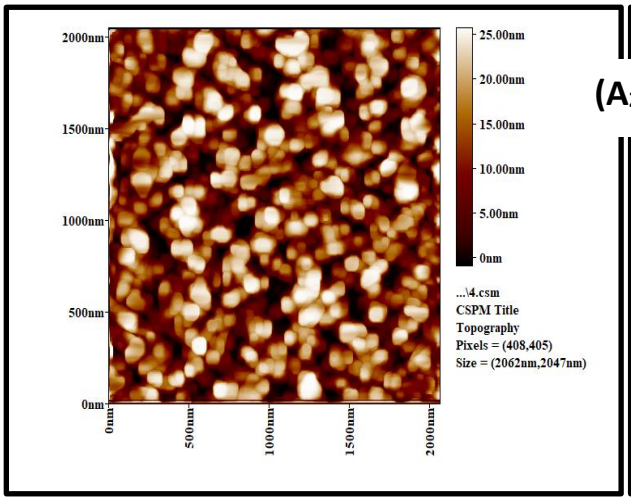

(A_2)

(c)

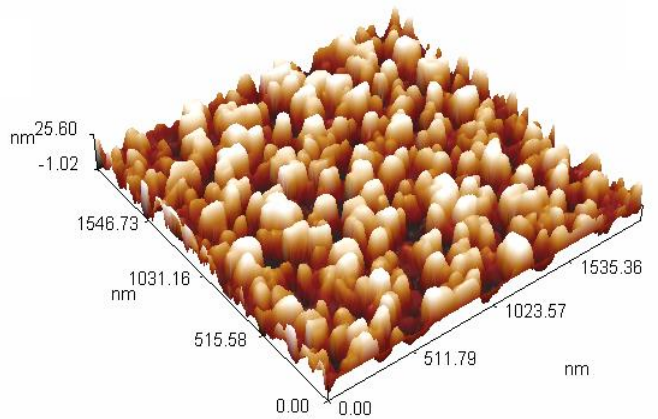

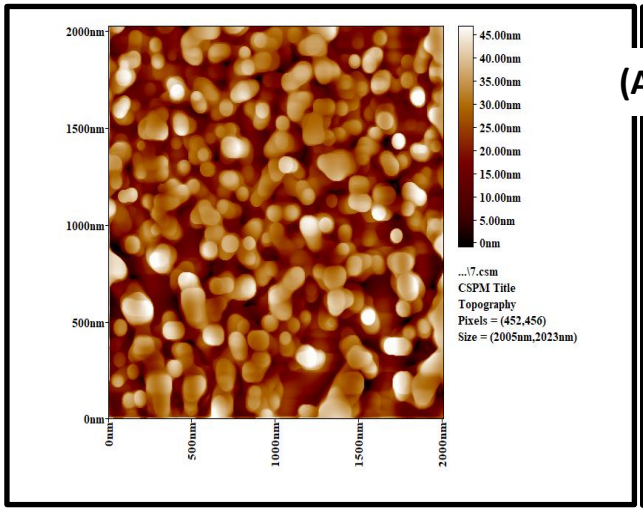
2000nm
1500nm
1000nm
500nm
0nm
0nm
500nm
1000nm
1500nm
2000nm
45.00nm
40.00nm
35.00nm
30.00nm
25.00nm
20.00nm
15.00nm
10.00nm
5.00nm
0nm
...\7.csm
CSPM Title
Topography
Pixels = (452,456)
Size = (2005nm,2023nm)

(A3)

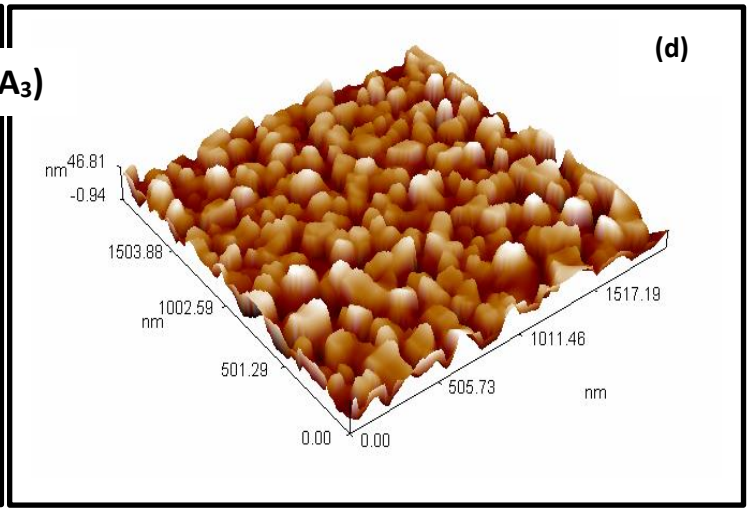
(d)
nm 46.81
-0.94
1503.88
1002.59
nm
501.29
0.00
0.00
505.73
1011.46
1517.19
nm

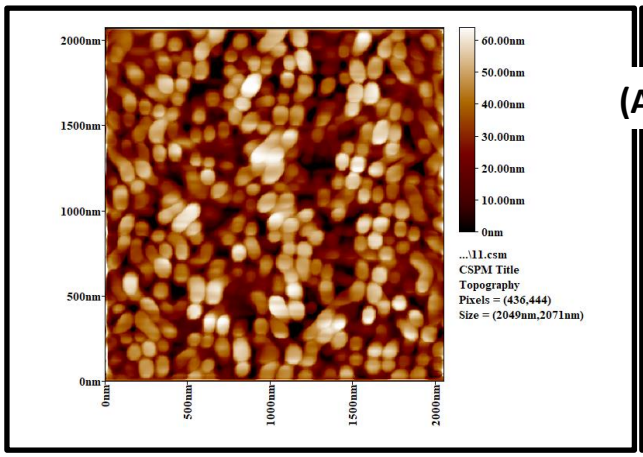
2000nm
1500nm
1000nm
500nm
0nm
0nm
500nm
1000nm
1500nm
2000nm
60.00nm
50.00nm
40.00nm
30.00nm
20.00nm
10.00nm
0nm
...\11.csm
CSPM Title
Topography
Pixels = (436,444)
Size = (2049nm,2071nm)

(A4)

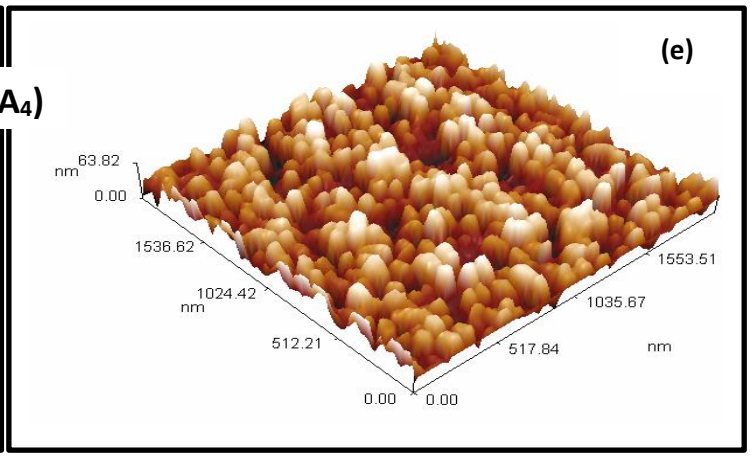
(e)
nm 63.82
0.00
1536.62
1024.42
nm
512.21
0.00
0.00
517.84
1035.67
1553.51
nm

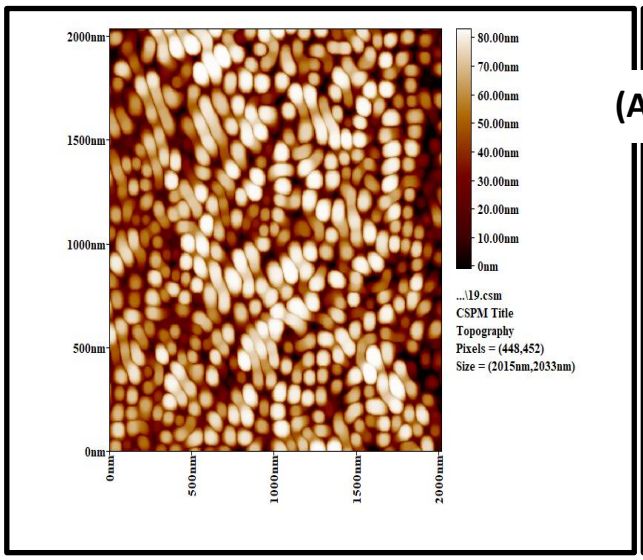
2000nm
1500nm
1000nm
500nm
0nm
0nm
500nm
1000nm
1500nm
2000nm
80.00nm
70.00nm
60.00nm
50.00nm
40.00nm
30.00nm
20.00nm
10.00nm
0nm
...\19.csm
CSPM Title
Topography
Pixels = (448,452)
Size = (2015nm,2033nm)

(A5)

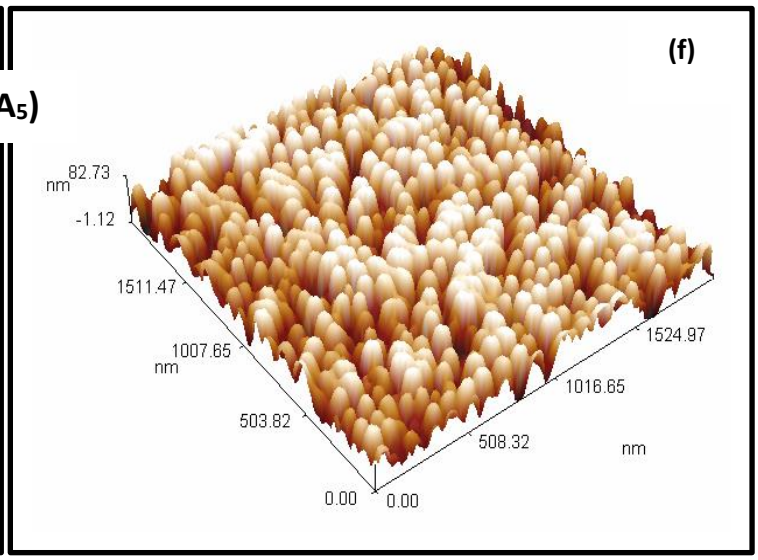
(f)
nm 82.73
-1.12
1511.47
1007.65
nm
503.82
0.00
0.00
508.32
1016.65
1524.97
nm

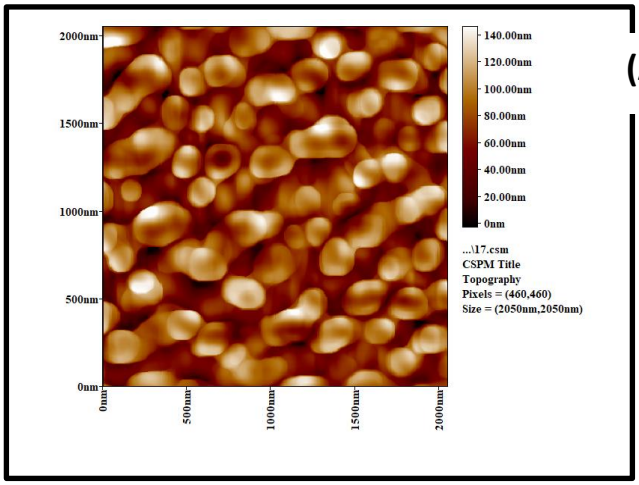
2000nm
1500nm
1000nm
500nm
0nm
0nm
500nm
1000nm
1500nm
2000nm
140.00nm
120.00nm
100.00nm
80.00nm
60.00nm
40.00nm
20.00nm
0nm
...\17.csm
CSPM Title
Topography
Pixels = (460,460)
Size = (2050nm,2050nm)

(A6)

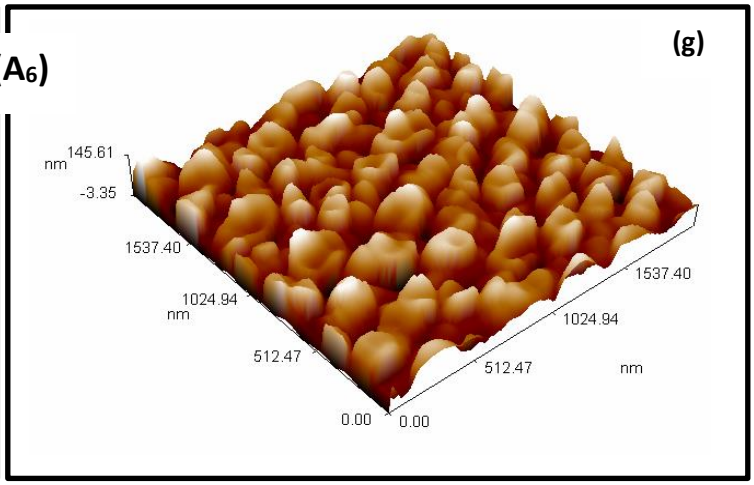
(g)
145.61
nm
-3.35
1537.40
1024.94
nm
512.47
0.00
0.00
512.47
nm
1024.94
1537.40

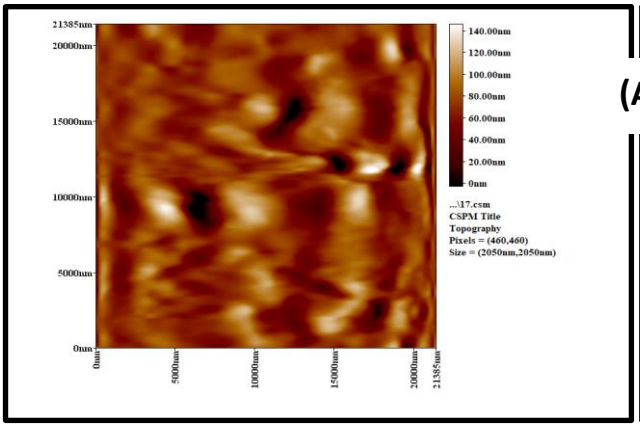
21385nm
20000nm
15000nm
10000nm
5000nm
0nm
0nm
5000nm
10000nm
15000nm
20000nm
21385nm
140.00nm
120.00nm
100.00nm
80.00nm
60.00nm
40.00nm
20.00nm
0nm
...\17.csm
CSPM Title
Topography
Pixels = (460,460)
Size = (2050nm,2050nm)

(A7)

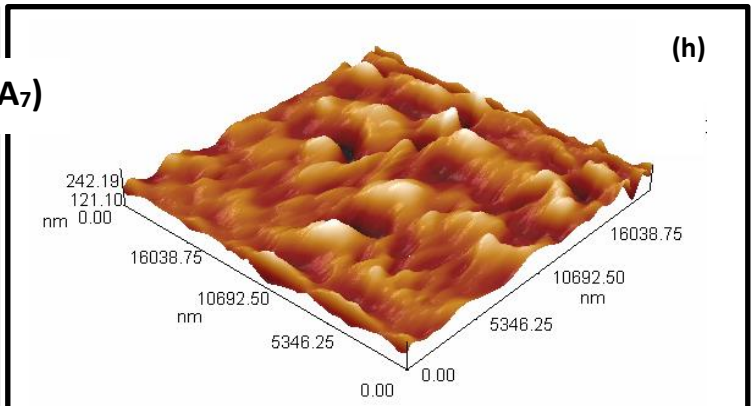
(h)
242.19
121.10
nm 0.00
16038.75
10692.50
nm
5346.25
0.00
0.00
5346.25
nm
10692.50
16038.75

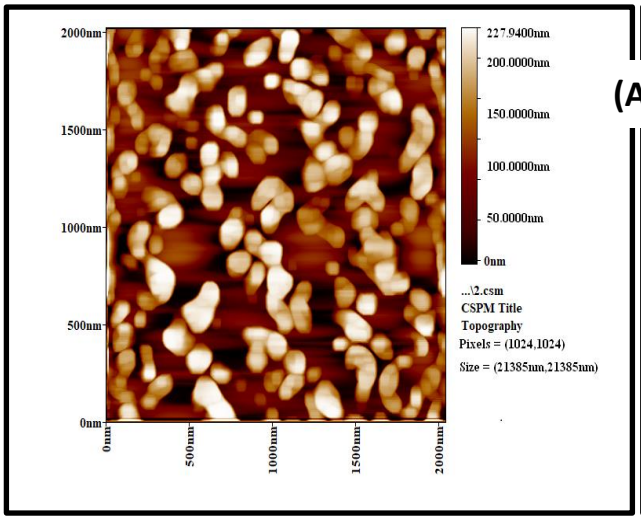
2000nm
1500nm
1000nm
500nm
0nm
0nm
500nm
1000nm
1500nm
2000nm
227.9400nm
200.0000nm
150.0000nm
100.0000nm
50.0000nm
0nm
...\2.csm
CSPM Title
Topography
Pixels = (1024,1024)
Size = (21385nm,21385nm)

(A8)

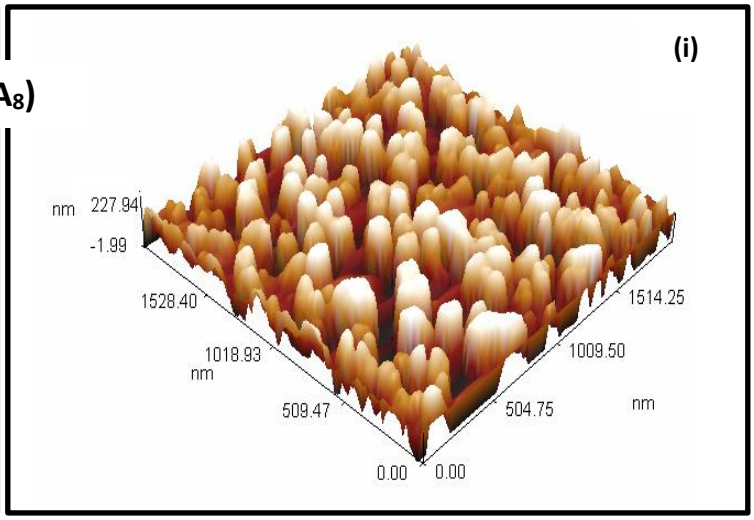
(i)
nm 227.94
-1.99
1528.40
1018.93
nm
509.47
0.00
0.00
504.75
nm
1009.50
1514.25

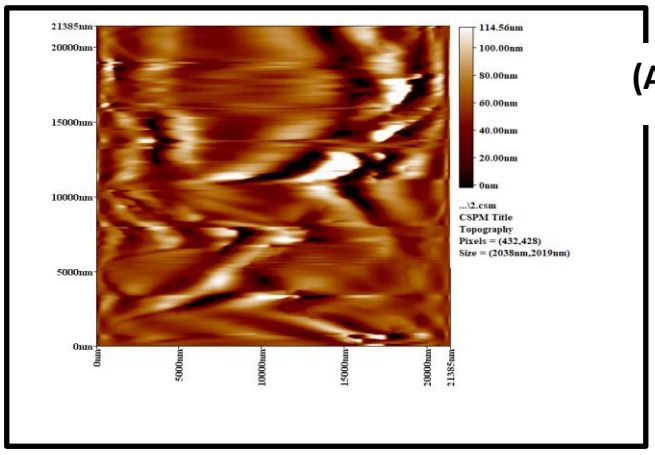
21385nm
20000nm
15000nm
10000nm
5000nm
0nm
0nm
500nm
1000nm
1500nm
2000nm
21385nm
114.56nm
100.00nm
80.00nm
60.00nm
40.00nm
20.00nm
0nm
...\2.csm
CSPM Title
Topography
Pixels = (432,428)
Size = (2038nm,2019nm)

(A9)

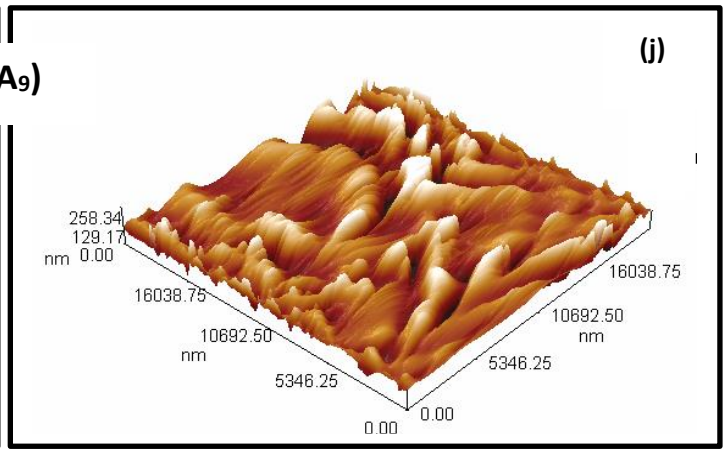
(j)
258.34
129.17
nm 0.00
16038.75
10692.50
nm
5346.25
0.00
0.00
16038.75
10692.50
nm
5346.25

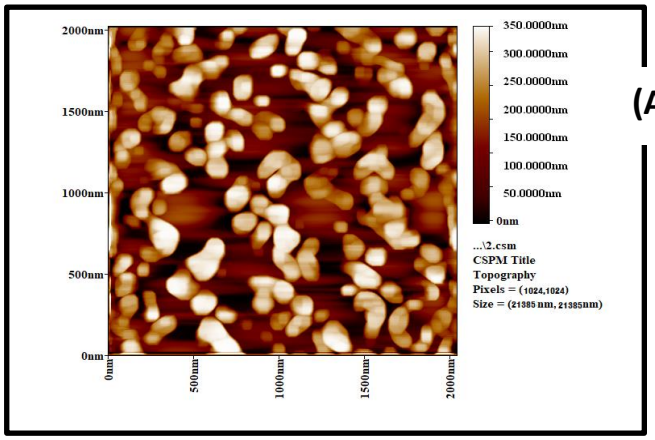
2000nm
1500nm
1000nm
500nm
0nm
0nm
500nm
1000nm
1500nm
2000nm
350.0000nm
300.0000nm
250.0000nm
200.0000nm
150.0000nm
100.0000nm
50.0000nm
0nm
...\2.csm
CSPM Title
Topography
Pixels = (1024,1024)
Size = (21385 nm, 21385nm)

(A10)

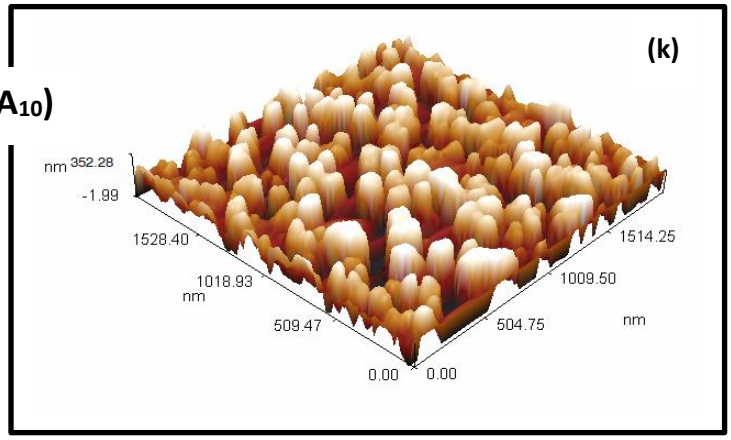
(k)
nm 352.28
-1.99
1528.40
1018.93
nm
509.47
0.00
0.00
1514.25
1009.50
504.75
nm

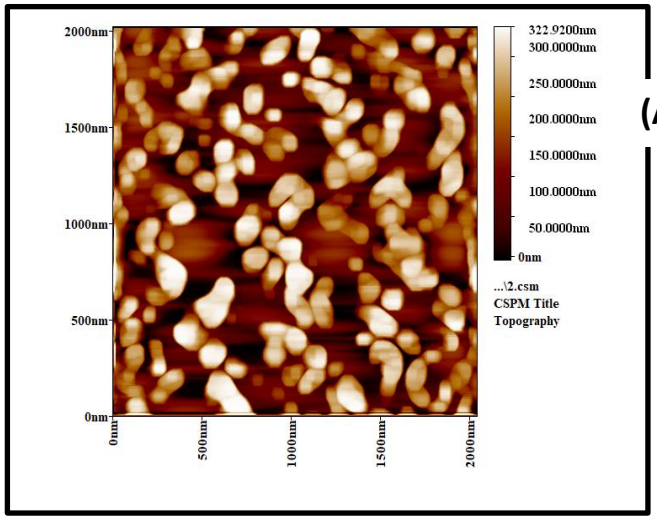
2000nm
1500nm
1000nm
500nm
0nm
0nm
500nm
1000nm
1500nm
2000nm
322.9200nm
300.0000nm
250.0000nm
200.0000nm
150.0000nm
100.0000nm
50.0000nm
0nm
...\2.csm
CSPM Title
Topography

(A11)

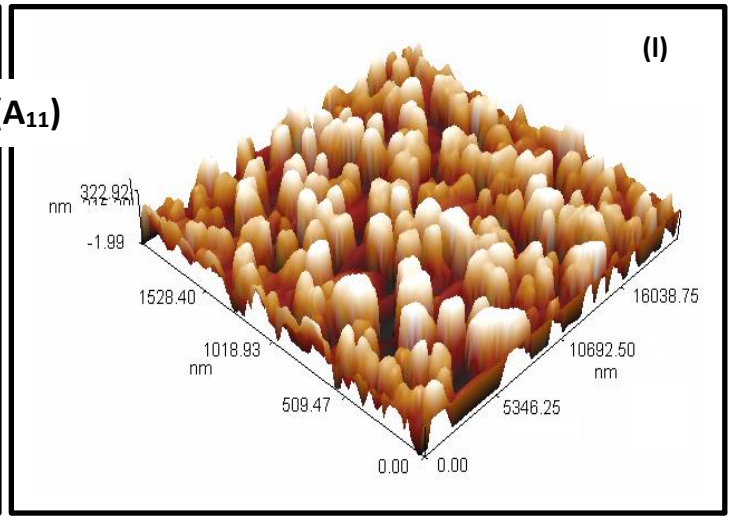
(l)
nm 322.92
-1.99
1528.40
1018.93
nm
509.47
0.00
0.00
16038.75
10692.50
nm
5346.25

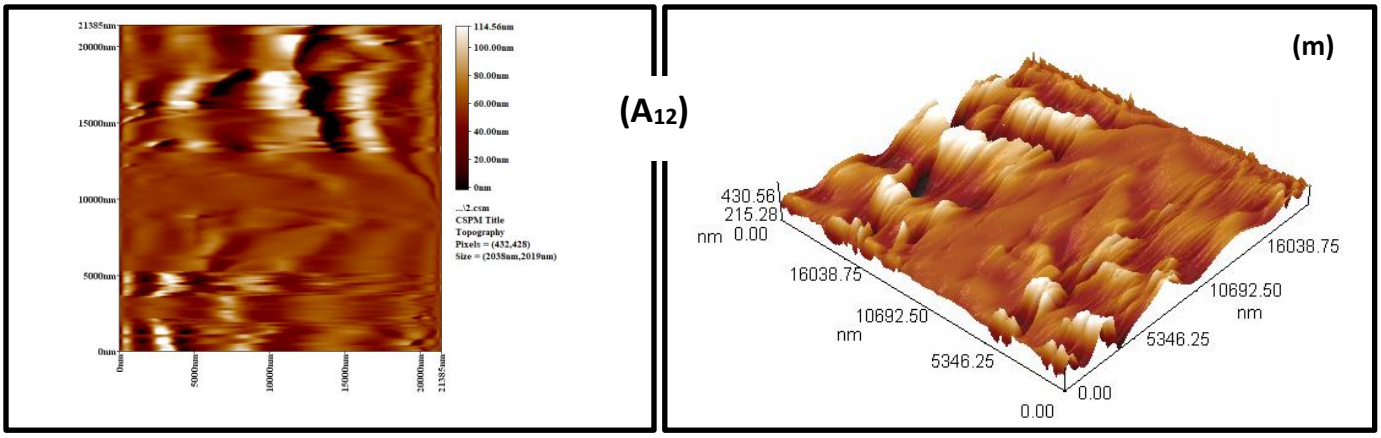

Figure (4.39): AFM results of samples (a) substrate, (b) A_1, (c) A_2, (d) A_3, (e) A_4, (f) A_5, (g) A_6, (h) A_7, (i) A_8, (j) A_9, (k) A_{10}, (l) A_{11}, and (m) A_{12}.

Figure 4.40 (a, b, c, d, e, f, g, h, i, j, k, and l), the increase of surface roughness as shown in samples (B) because the presence of HA precipitates closed the porous and prevent harmful ions to pass through it [123]. It can be observed that the surface roughness for samples A was higher than that for sample B, which indicated by the roughness average values (Ra) which were (29.1nm) for sample B_{12} compared roughness (Ra) equal (5.13nm) and (11.8) for samples B_4 and B_7 respectively, it means that the surface roughness increase with increase voltage and deposition time because increase oxidation time, due to increase coating thickness.

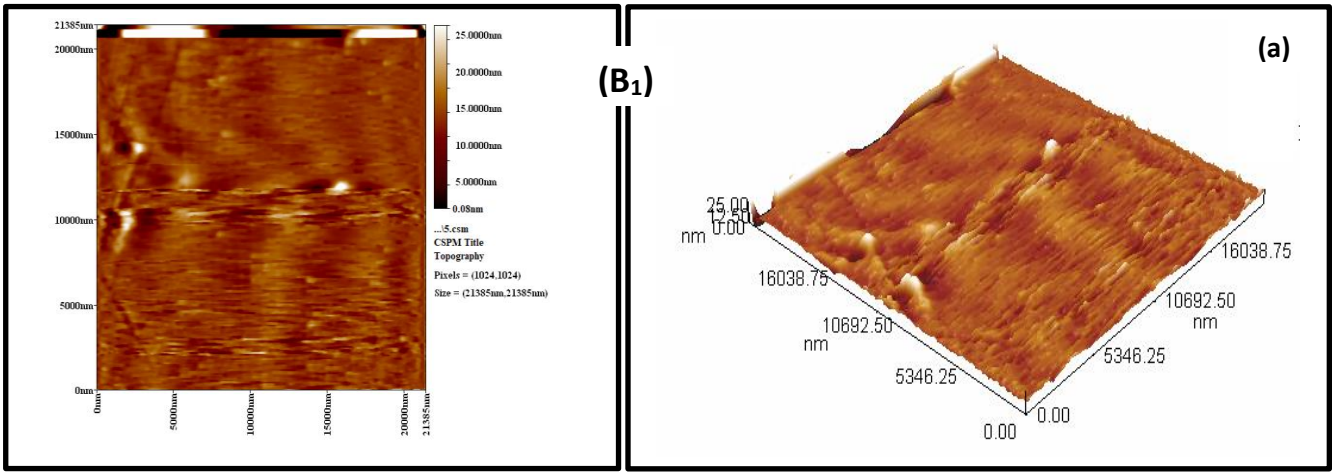

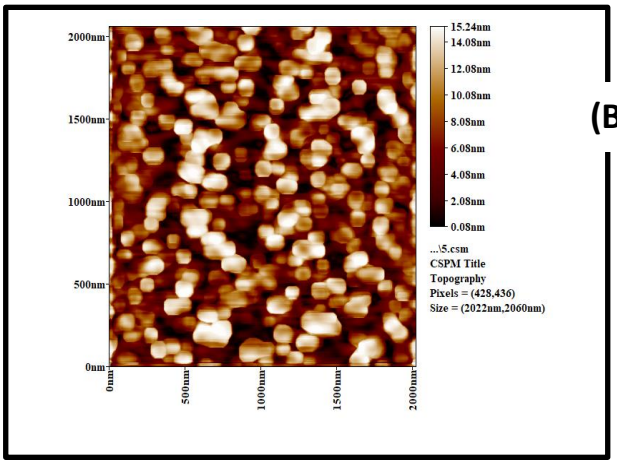
2000nm
1500nm
1000nm
500nm
0nm
0nm
500nm
1000nm
1500nm
2000nm
15.24nm
14.08nm
12.08nm
10.08nm
8.08nm
6.08nm
4.08nm
2.08nm
0.08nm
...\5.csm
CSPM Title
Topography
Pixels = (428,436)
Size = (2022nm,2060nm)

(B_2)

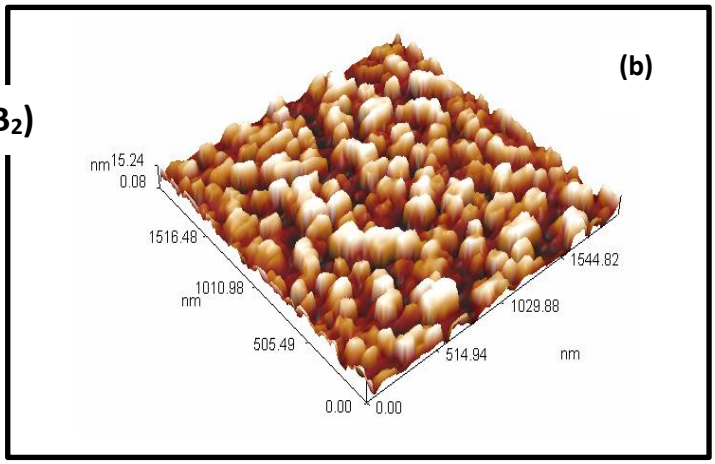
(b)
nm 15.24
0.08
1516.48
1010.98
nm
505.49
0.00
0.00
514.94
1029.88
1544.82
nm

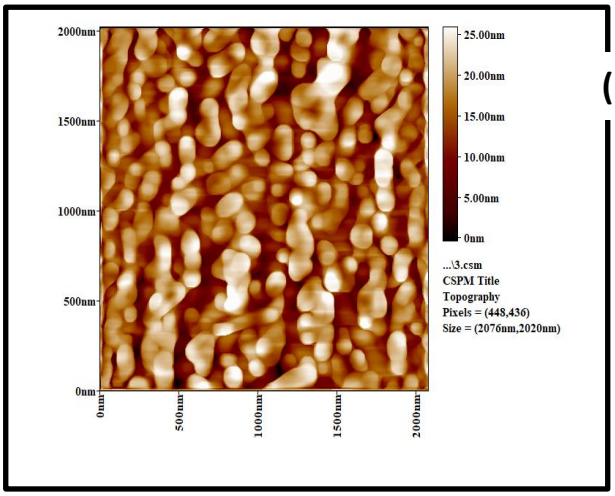
2000nm
1500nm
1000nm
500nm
0nm
0nm
500nm
1000nm
1500nm
2000nm
25.00nm
20.00nm
15.00nm
10.00nm
5.00nm
0nm
...\3.csm
CSPM Title
Topography
Pixels = (448,436)
Size = (2076nm,2020nm)

(B_3)

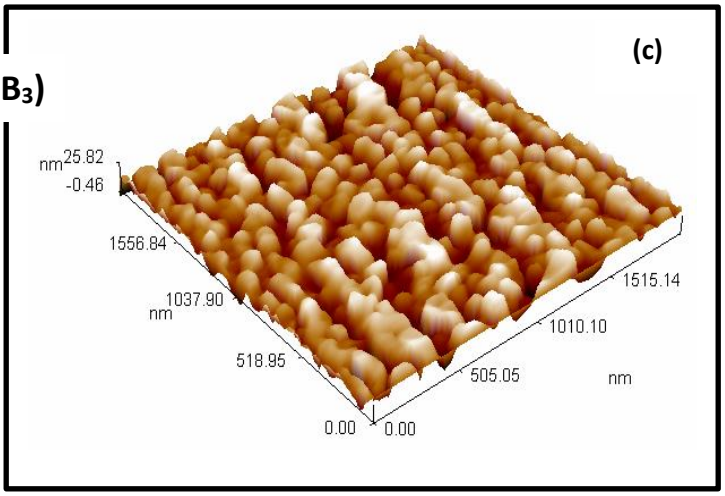
(c)
nm 25.82
-0.46
1556.84
1037.90
nm
518.95
0.00
0.00
505.05
1010.10
1515.14
nm

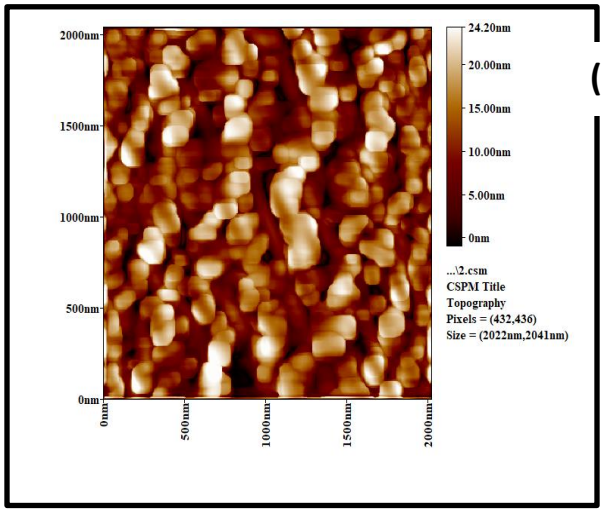
2000nm
1500nm
1000nm
500nm
0nm
0nm
500nm
1000nm
1500nm
2000nm
24.20nm
20.00nm
15.00nm
10.00nm
5.00nm
0nm
...\2.csm
CSPM Title
Topography
Pixels = (432,436)
Size = (2022nm,2041nm)

(B_4)

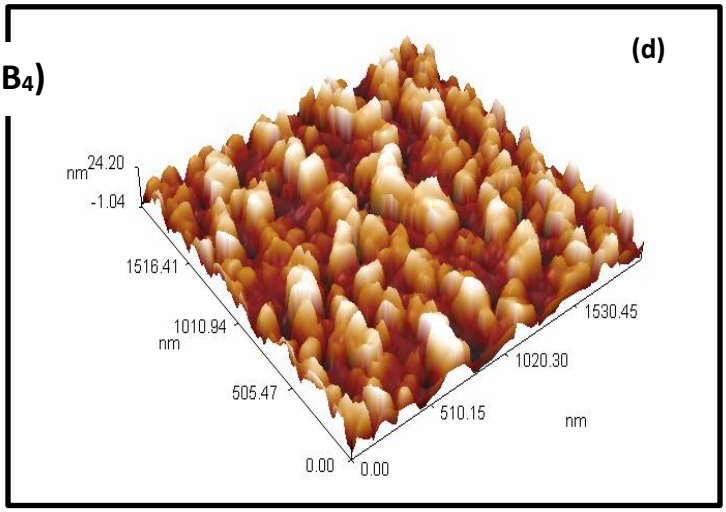
(d)
nm 24.20
-1.04
1516.41
1010.94
nm
505.47
0.00
0.00
510.15
1020.30
1530.45
nm

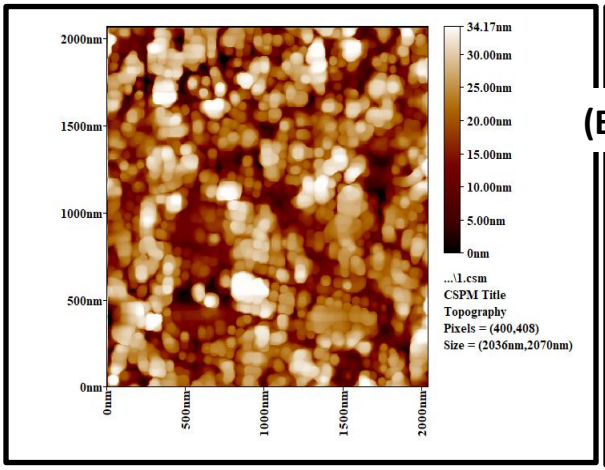
2000nm
1500nm
1000nm
500nm
0nm
0nm
500nm
1000nm
1500nm
2000nm
34.17nm
30.00nm
25.00nm
20.00nm
15.00nm
10.00nm
5.00nm
0nm
...\1.csm
CSPM Title
Topography
Pixels = (400,408)
Size = (2036nm,2070nm)

(B_5)

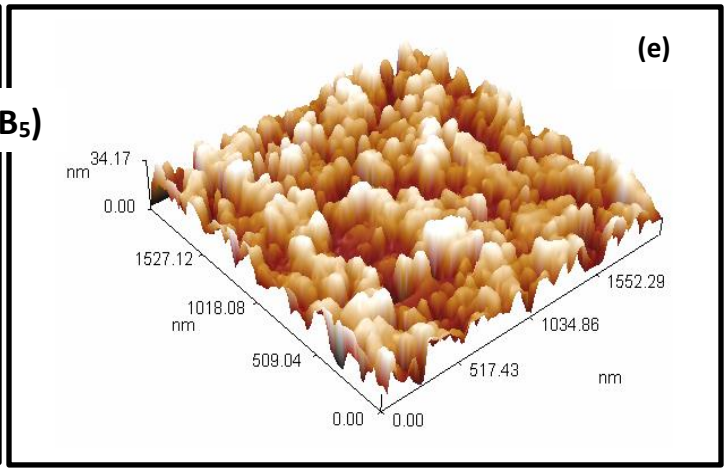
(e)
34.17
nm
0.00
1527.12
1018.08
nm
509.04
0.00
0.00
517.43
1034.86
1552.29
nm

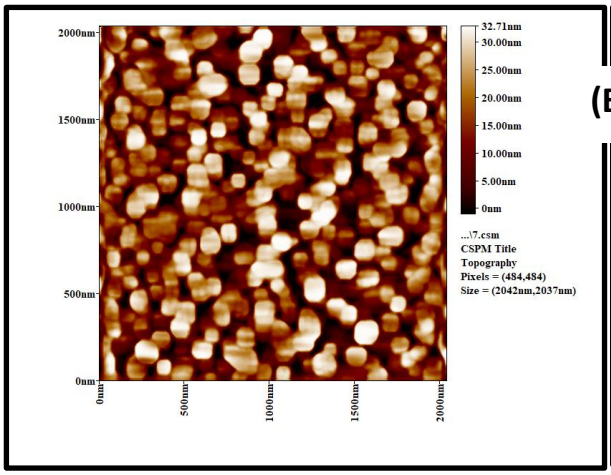
2000nm
1500nm
1000nm
500nm
0nm
0nm
500nm
1000nm
1500nm
2000nm
32.71nm
30.00nm
25.00nm
20.00nm
15.00nm
10.00nm
5.00nm
0nm
...\7.csm
CSPM Title
Topography
Pixels = (484,484)
Size = (2042nm,2037nm)

(B_6)

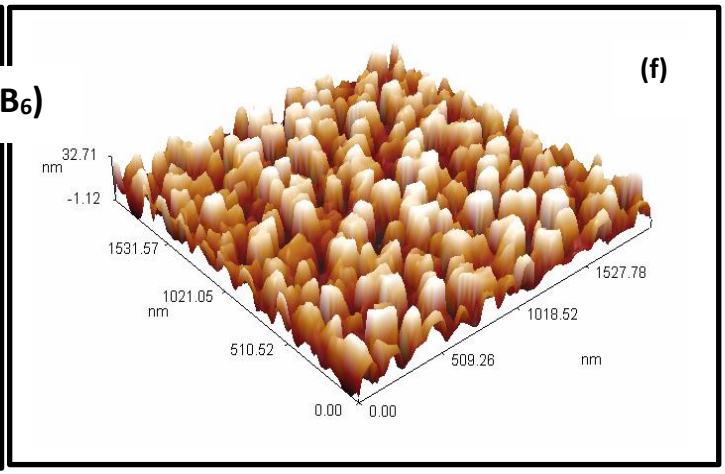
(f)
32.71
nm
-1.12
1531.57
1021.05
nm
510.52
0.00
0.00
509.26
1018.52
1527.78
nm

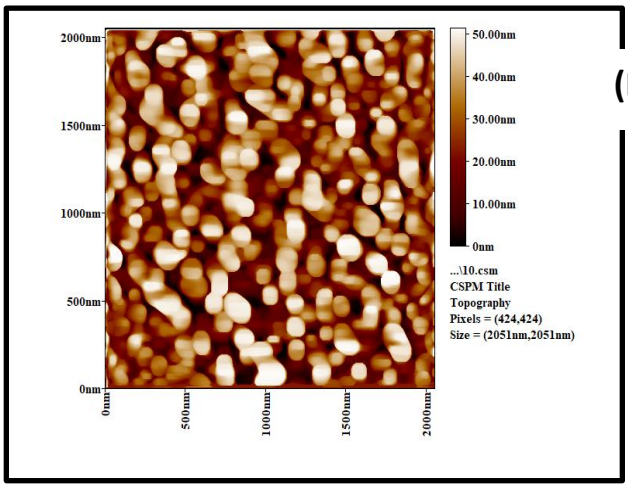
2000nm
1500nm
1000nm
500nm
0nm
0nm
500nm
1000nm
1500nm
2000nm
50.00nm
40.00nm
30.00nm
20.00nm
10.00nm
0nm
...\10.csm
CSPM Title
Topography
Pixels = (424,424)
Size = (2051nm,2051nm)

(B_7)

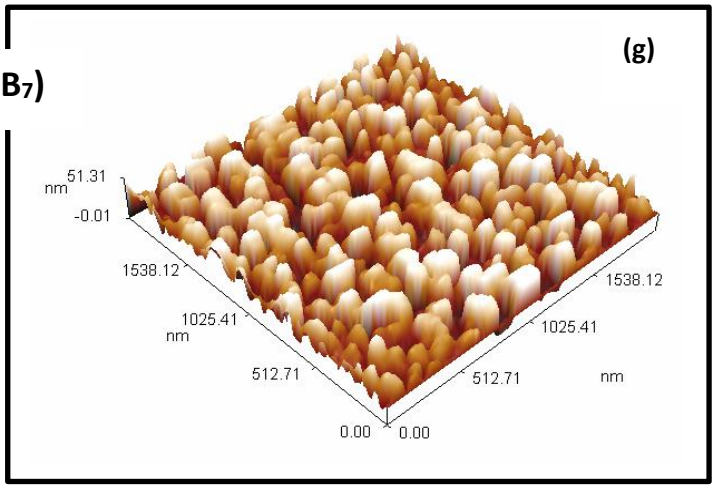
(g)
51.31
nm
-0.01
1538.12
1025.41
nm
512.71
0.00
0.00
512.71
1025.41
1538.12
nm

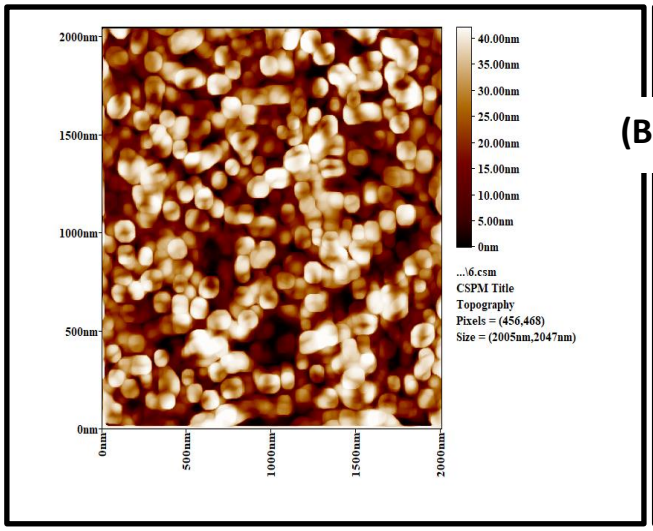
2000nm
1500nm
1000nm
500nm
0nm
0nm
500nm
1000nm
1500nm
2000nm
40.00nm
35.00nm
30.00nm
25.00nm
20.00nm
15.00nm
10.00nm
5.00nm
0nm
...\6.csm
CSPM Title
Topography
Pixels = (456,468)
Size = (2005nm,2047nm)

(B_8)

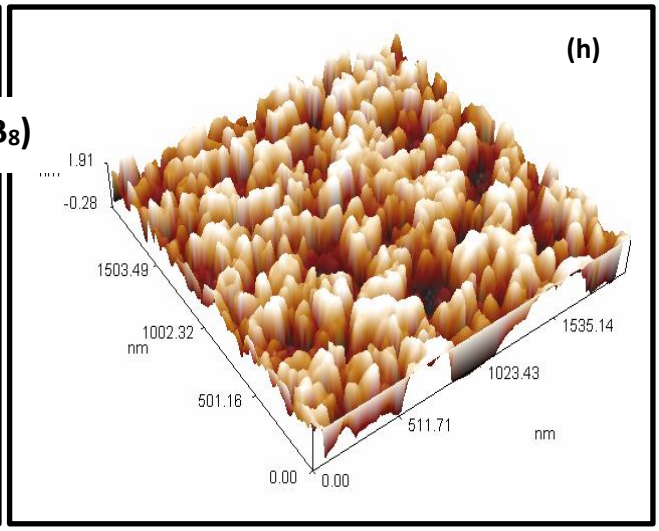
(h)
1.91
-0.28
1503.49
1002.32
nm
501.16
0.00
0.00
511.71
1023.43
1535.14
nm

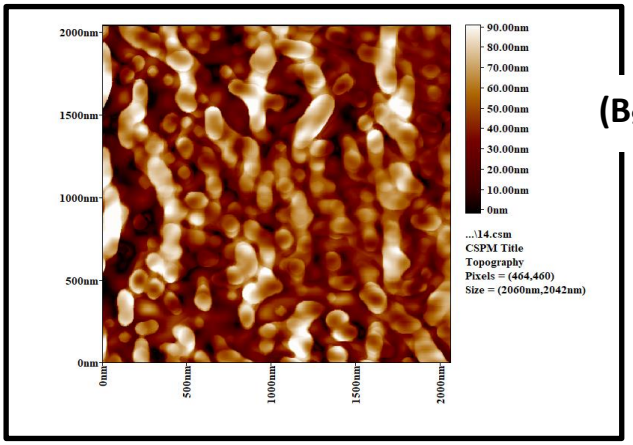
2000nm
1500nm
1000nm
500nm
0nm
0nm
500nm
1000nm
1500nm
2000nm
90.00nm
80.00nm
70.00nm
60.00nm
50.00nm
40.00nm
30.00nm
20.00nm
10.00nm
0nm
...\14.csm
CSPM Title
Topography
Pixels = (464,460)
Size = (2060nm,2042nm)

(B_9)

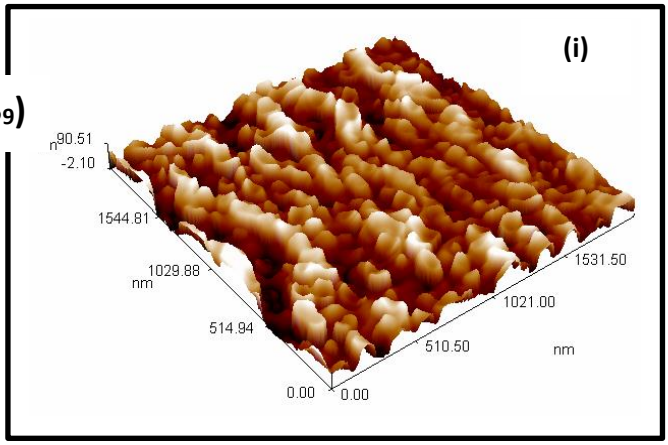
(i)
90.51
-2.10
1544.81
1029.88
nm
514.94
0.00
0.00
510.50
1021.00
1531.50
nm

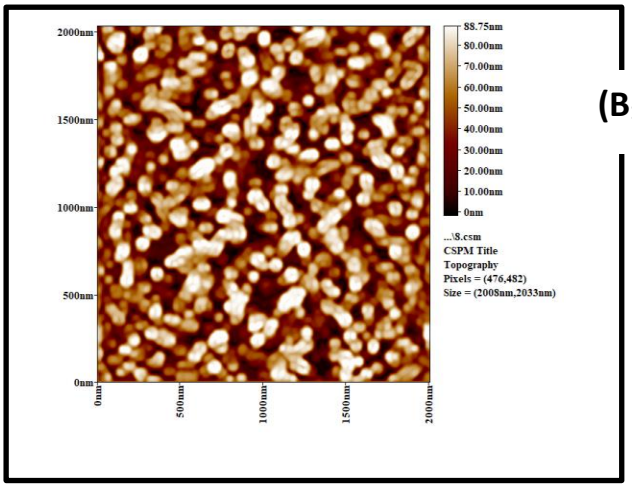
2000nm
1500nm
1000nm
500nm
0nm
0nm
500nm
1000nm
1500nm
2000nm
88.75nm
80.00nm
70.00nm
60.00nm
50.00nm
40.00nm
30.00nm
20.00nm
10.00nm
0nm
...\8.csm
CSPM Title
Topography
Pixels = (476,482)
Size = (2005nm,2033nm)

(B_{10})

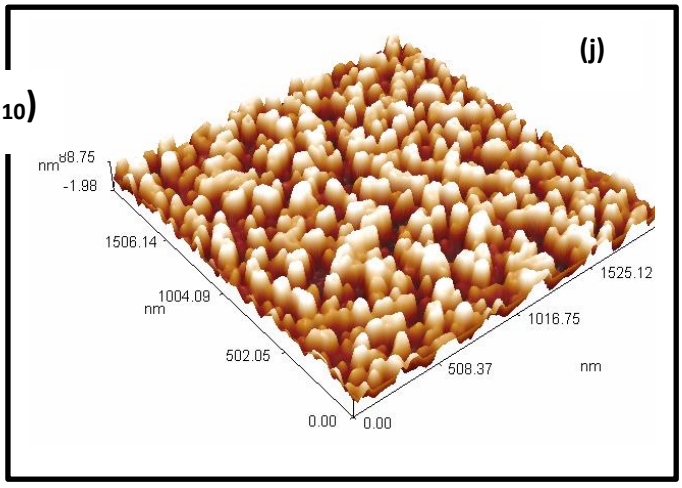
(j)
88.75
nm
-1.98
1506.14
1004.09
nm
502.05
0.00
0.00
508.37
1016.75
1525.12
nm

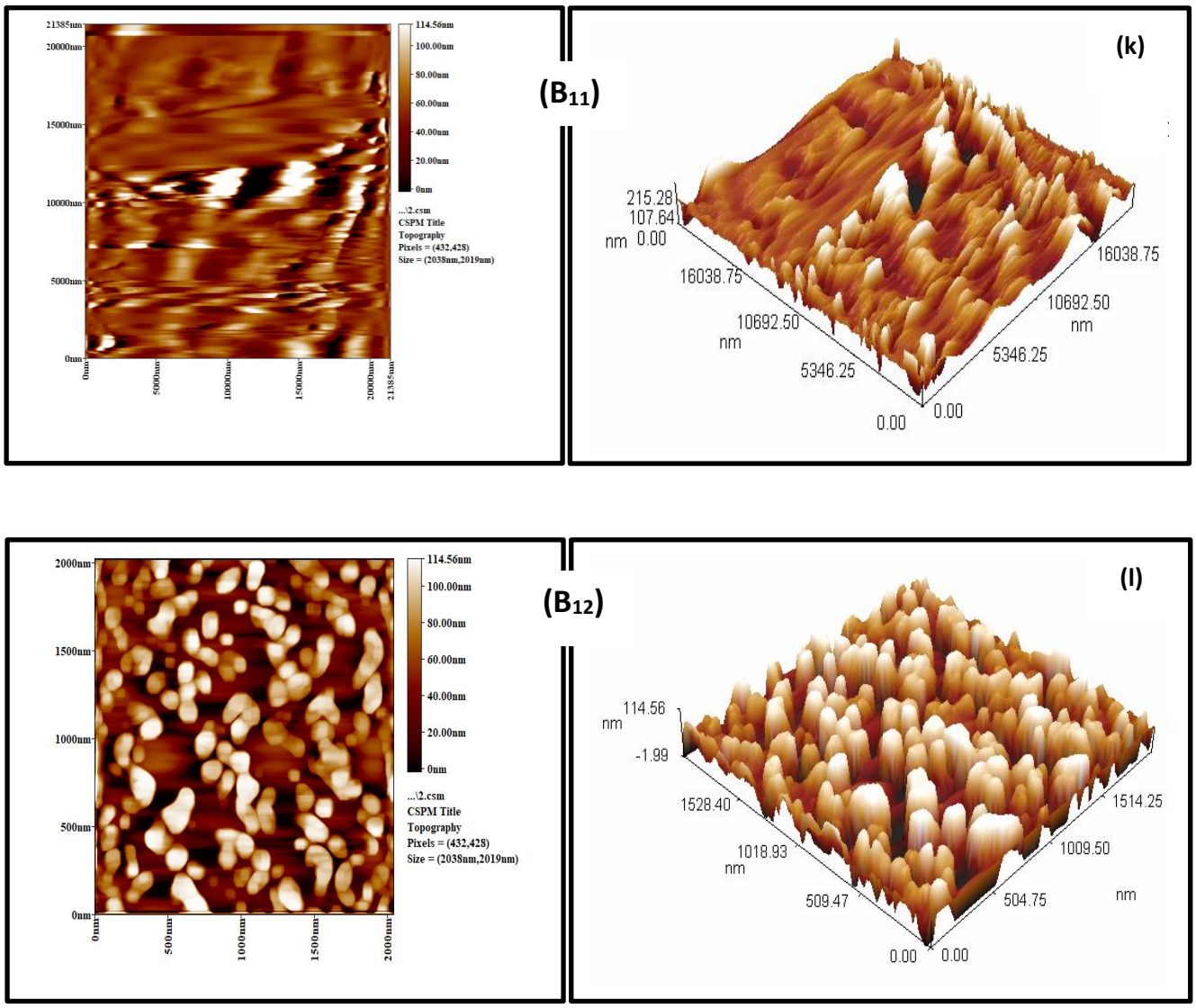

Figure (4.40): AFM result of (a) B_1, (b) B_2, (c) B_3, (d) B_4, (e) B_5, (f) B_6, (g) B_7, (h) B_8, (i) B_9, (j) B_{10}, (k) B_{11}, and (l) B_{12}.

In Figure (4.41), the morphology and coating surface topography of the samples ZrO_2/Tio_2 coatings by MAO process. An increased in Ra values can be observed, but remains less than those of samples A due to deposition of nano ZrO_2 in electrolytic solution that fill the pores formed in the MAO process reduces the roughness, but remain higher than those the substrate increased

gradually, voltage and deposition time, its initial from (4.21nm) at C_3 to (7.65nm) at C_7 finally reached (22.2nm) at C_{11} and (2.1nm) at C_1, reaching (4.19nm) at C_4, and (5.4nm) at C_5 to (9.01nm) at C_8 and finally (11nm) at C_9 to (27.9nm) C_{11} due to increased surface coating.

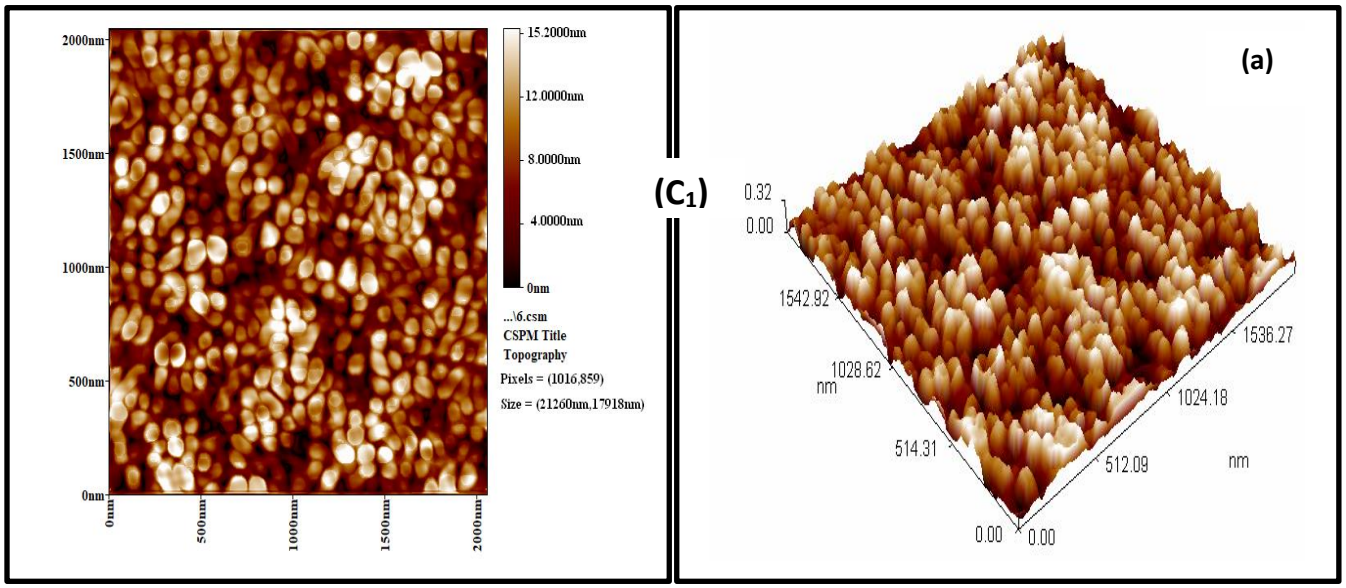

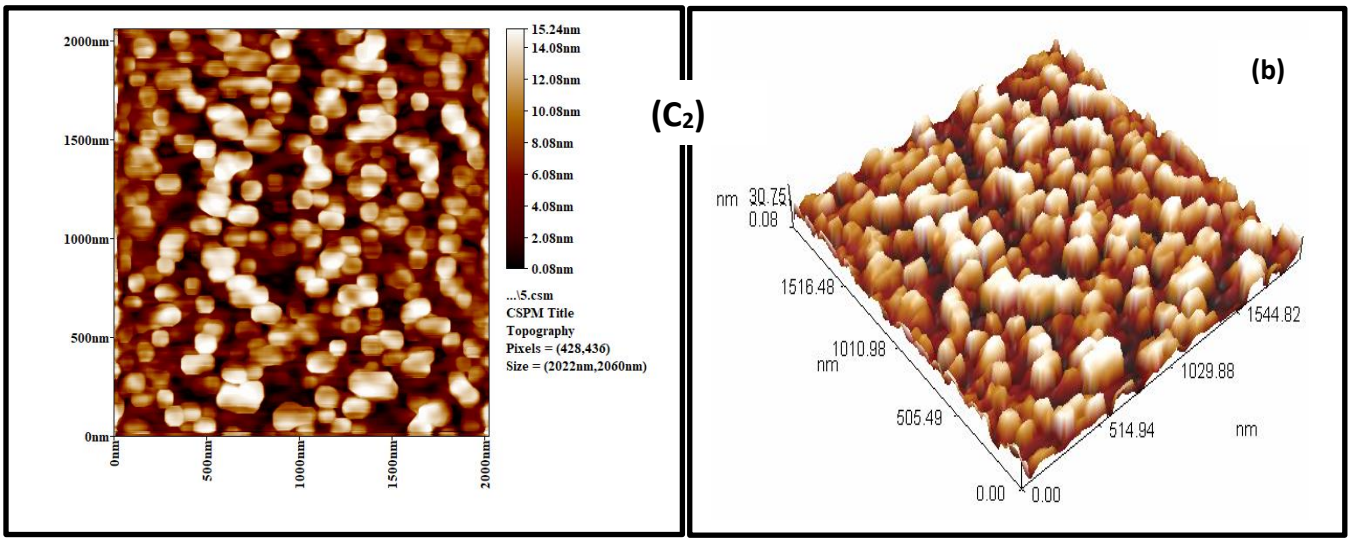

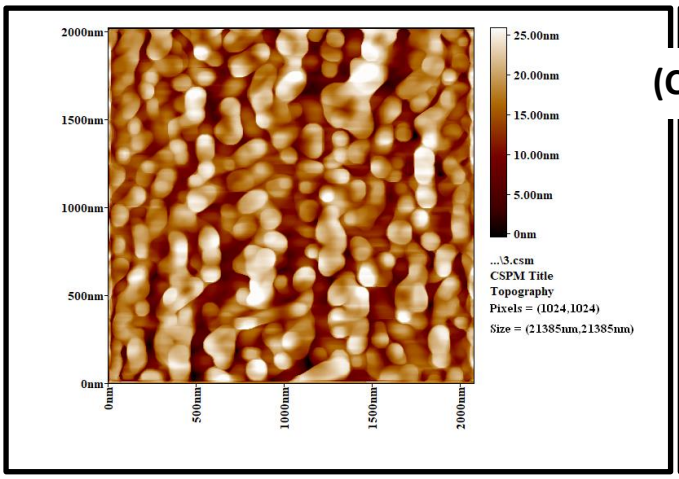
2000nm
1500nm
1000nm
500nm
0nm
0nm
500nm
1000nm
1500nm
2000nm
25.00nm
20.00nm
15.00nm
10.00nm
5.00nm
0nm
...\3.csm
CSPM Title
Topography
Pixels = (1024,1024)
Size = (21385nm,21385nm)

(C_3)

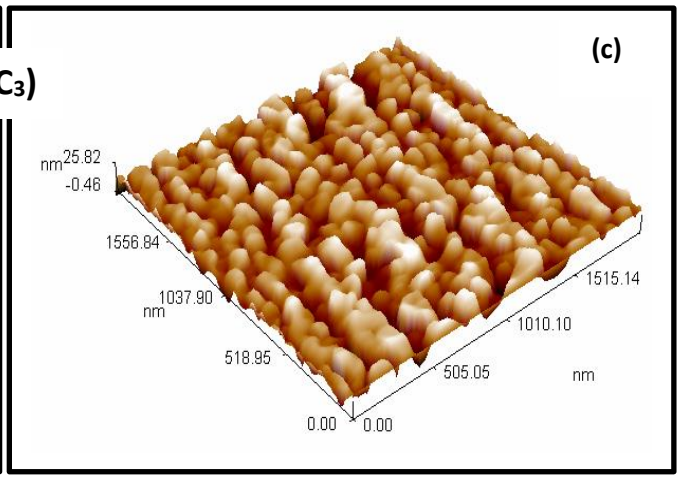
(c)
nm 25.82
-0.46
1556.84
1037.90
nm
518.95
0.00
0.00
505.05
1010.10
1515.14
nm

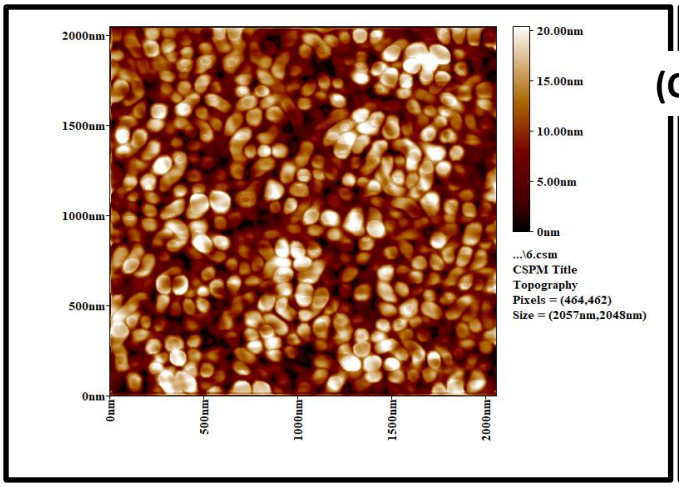
2000nm
1500nm
1000nm
500nm
0nm
0nm
500nm
1000nm
1500nm
2000nm
20.00nm
15.00nm
10.00nm
5.00nm
0nm
...\6.csm
CSPM Title
Topography
Pixels = (464,462)
Size = (2057nm,2048nm)

(C_4)

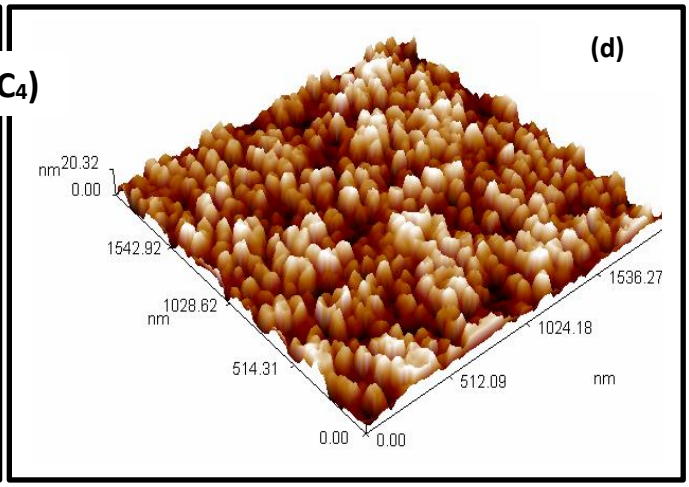
(d)
nm 20.32
0.00
1542.92
1028.62
nm
514.31
0.00
0.00
512.09
1024.18
1536.27
nm

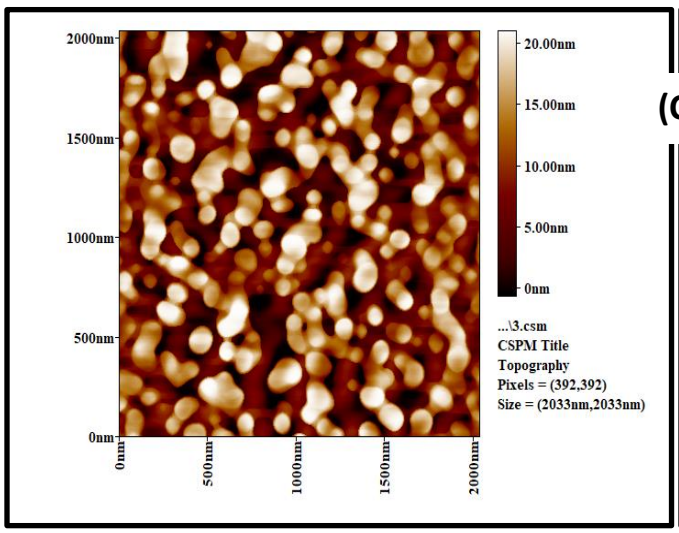
2000nm
1500nm
1000nm
500nm
0nm
0nm
500nm
1000nm
1500nm
2000nm
20.00nm
15.00nm
10.00nm
5.00nm
0nm
...\3.csm
CSPM Title
Topography
Pixels = (392,392)
Size = (2033nm,2033nm)

(C_5)

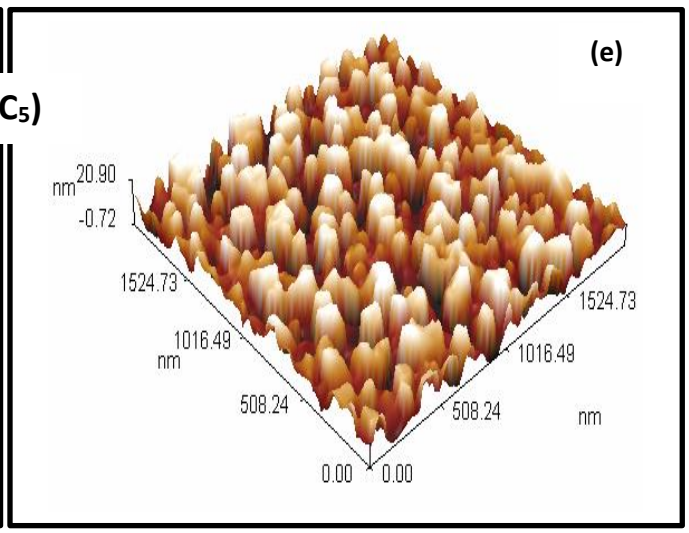
(e)
nm 20.90
-0.72
1524.73
1016.49
nm
508.24
0.00
0.00
508.24
1016.49
1524.73
nm

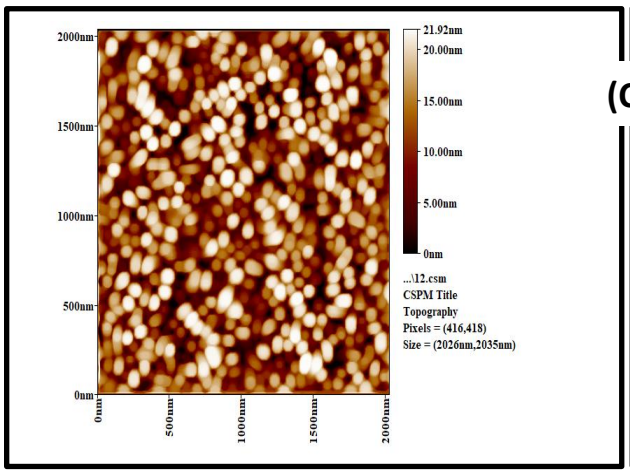
2000nm
1500nm
1000nm
500nm
0nm
0nm
500nm
1000nm
1500nm
2000nm
21.92nm
20.00nm
15.00nm
10.00nm
5.00nm
0nm
...\12.csm
CSPM Title
Topography
Pixels = (416,418)
Size = (2026nm,2035nm)

(C6)

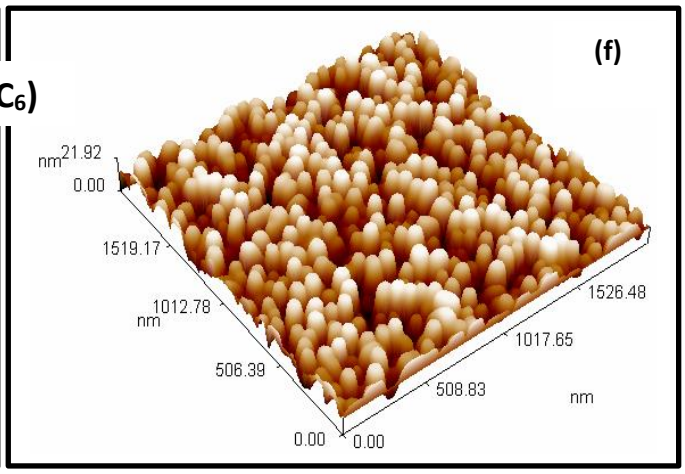
(f)
nm 21.92
0.00
1519.17
1012.78
nm
506.39
0.00
0.00
508.83
1017.65
1526.48
nm

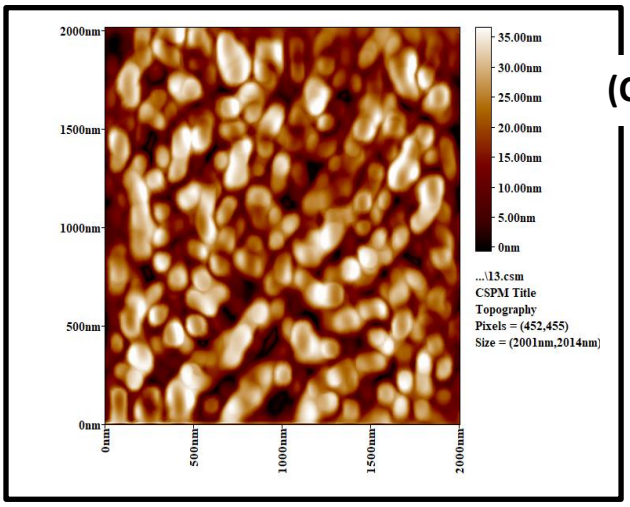
2000nm
1500nm
1000nm
500nm
0nm
0nm
500nm
1000nm
1500nm
2000nm
35.00nm
30.00nm
25.00nm
20.00nm
15.00nm
10.00nm
5.00nm
0nm
...\13.csm
CSPM Title
Topography
Pixels = (452,455)
Size = (2001nm,2014nm)

(C7)

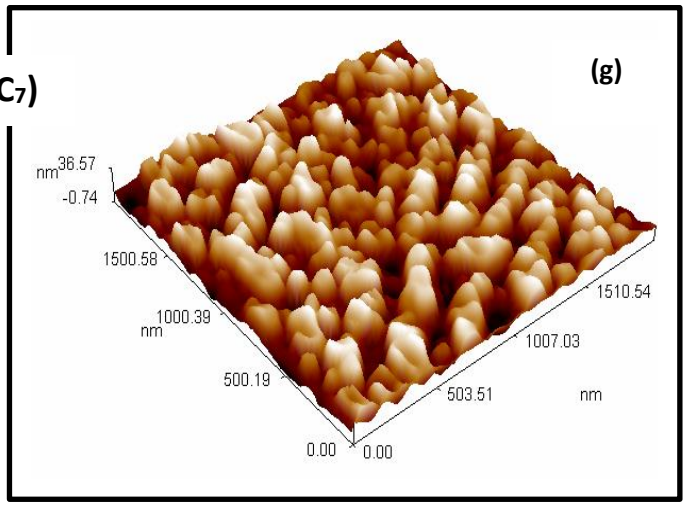
(g)
nm 36.57
-0.74
1500.58
1000.39
nm
500.19
0.00
0.00
503.51
1007.03
1510.54
nm

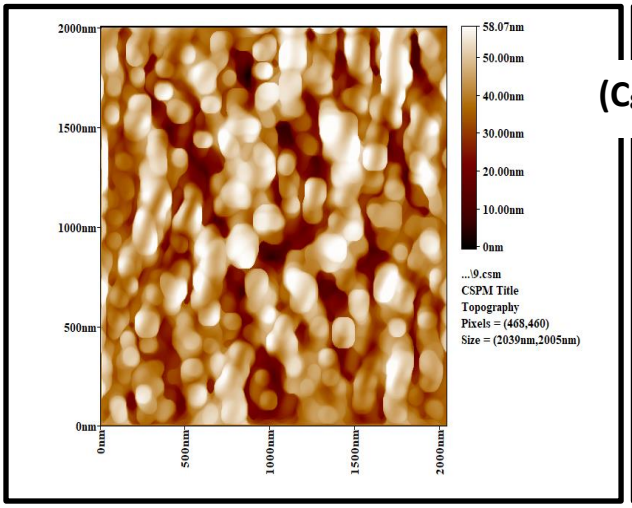
2000nm
1500nm
1000nm
500nm
0nm
0nm
500nm
1000nm
1500nm
2000nm
58.07nm
50.00nm
40.00nm
30.00nm
20.00nm
10.00nm
0nm
...\9.csm
CSPM Title
Topography
Pixels = (468,460)
Size = (2039nm,2005nm)

(C8)

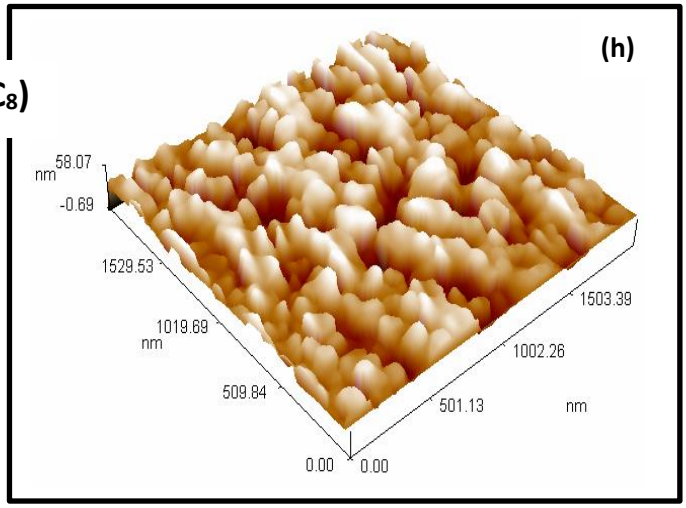
(h)
nm 58.07
-0.69
1529.53
1019.69
nm
509.84
0.00
0.00
501.13
1002.26
1503.39
nm

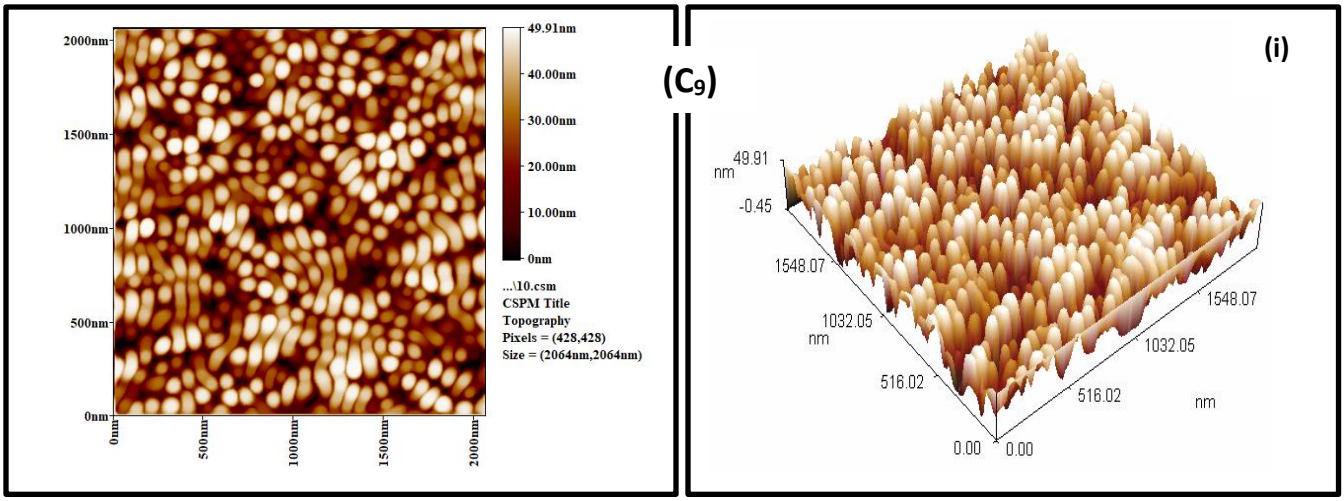
(C9)
(i)
2000nm
1500nm
1000nm
500nm
0nm
0nm
500nm
1000nm
1500nm
2000nm
49.91nm
40.00nm
30.00nm
20.00nm
10.00nm
0nm
...\10.csm
CSPM Title
Topography
Pixels = (428,428)
Size = (2064nm,2064nm)
49.91
nm
-0.45
1548.07
1032.05
nm
516.02
0.00
0.00
516.02
1032.05
1548.07
nm

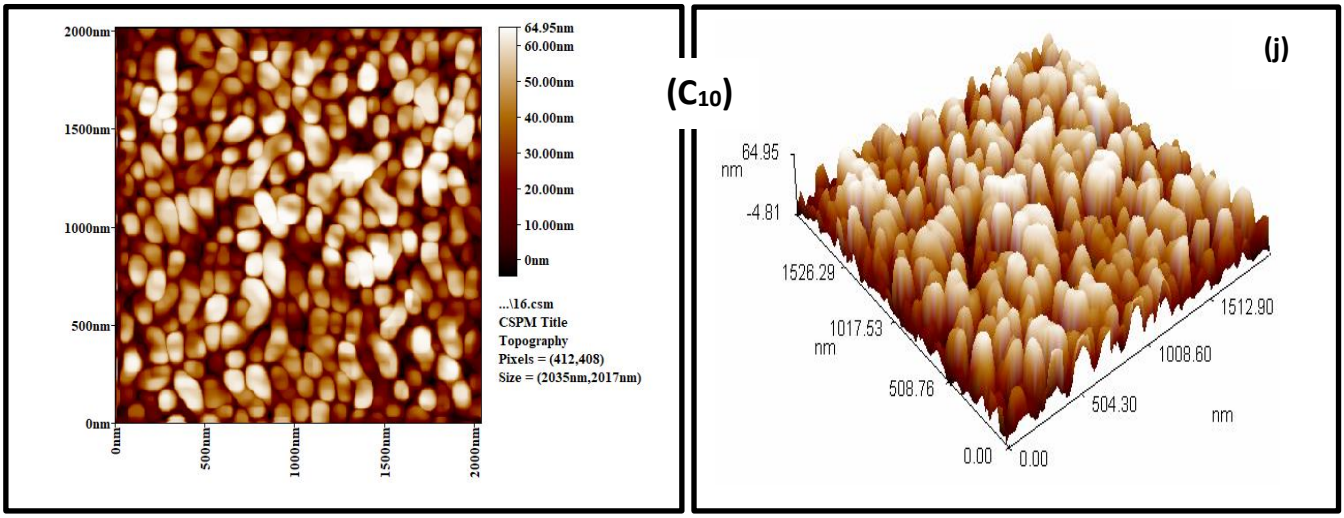
(C10)
(j)
2000nm
1500nm
1000nm
500nm
0nm
0nm
500nm
1000nm
1500nm
2000nm
64.95nm
60.00nm
50.00nm
40.00nm
30.00nm
20.00nm
10.00nm
0nm
...\16.csm
CSPM Title
Topography
Pixels = (412,408)
Size = (2035nm,2017nm)
64.95
nm
-4.81
1526.29
1017.53
nm
508.76
0.00
0.00
504.30
1008.60
1512.90
nm

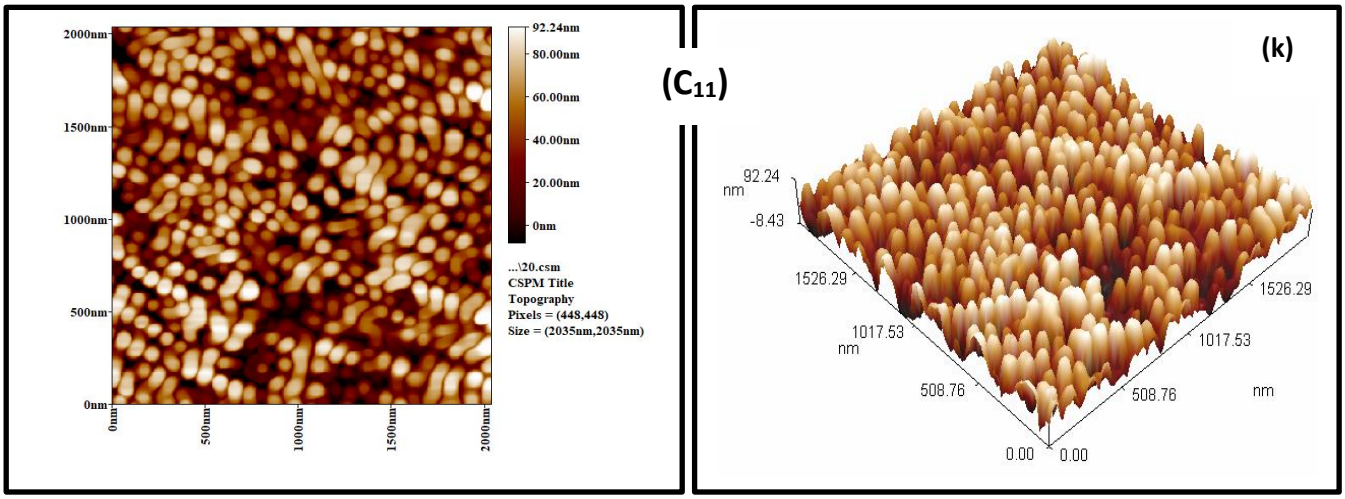
(C11)
(k)
2000nm
1500nm
1000nm
500nm
0nm
0nm
500nm
1000nm
1500nm
2000nm
92.24nm
80.00nm
60.00nm
40.00nm
20.00nm
0nm
...\20.csm
CSPM Title
Topography
Pixels = (448,448)
Size = (2035nm,2035nm)
92.24
nm
-8.43
1526.29
1017.53
nm
508.76
0.00
0.00
508.76
1017.53
1526.29
nm

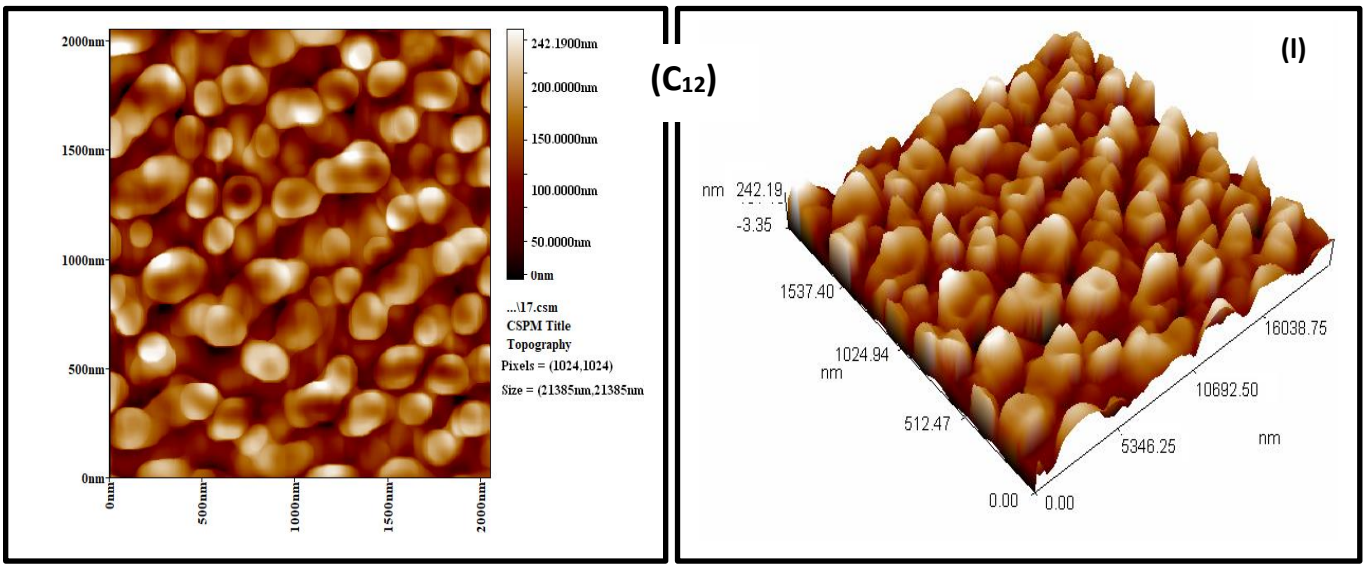

Figure (4.41): AFM result of samples (a) C_1, (b) C_2, (c) C_3, (d) C_4, (e) C_5, (f) C_6, (g) C_7, (h) C_8, (i) C_9, (j) C_{10}, (k) C_{11}, and (l) C_{12}.

Figures (4.42) show AFM results for $HA/ZrO_2/TiO_2$ samples D at different voltage and deposition time. It can be said that the surface roughness decreased with deposition of $HA/ZrO_2/TiO_2$ nanocomposite ceramic coatings by MAO process, which indicated by Ra values, (1.55 nm), (2.09 nm), and (11.3 nm) for D_1, D_5, and D_9 respectively. For sample D_{12} at (400V & 60min), the Ra increased to (18.2 nm), due to that increase in the coatings thickness. It most likely, increased voltage and deposition time exhibited roughness values higher those recorded in comparison with substrate due to the increase of pores in the coating which indicated by the increase of micro-hardness. Previous studies proved that implants with a rough surface are more suitable for the adhesion and proliferation of osteoblasts than those with a smooth surface [144].

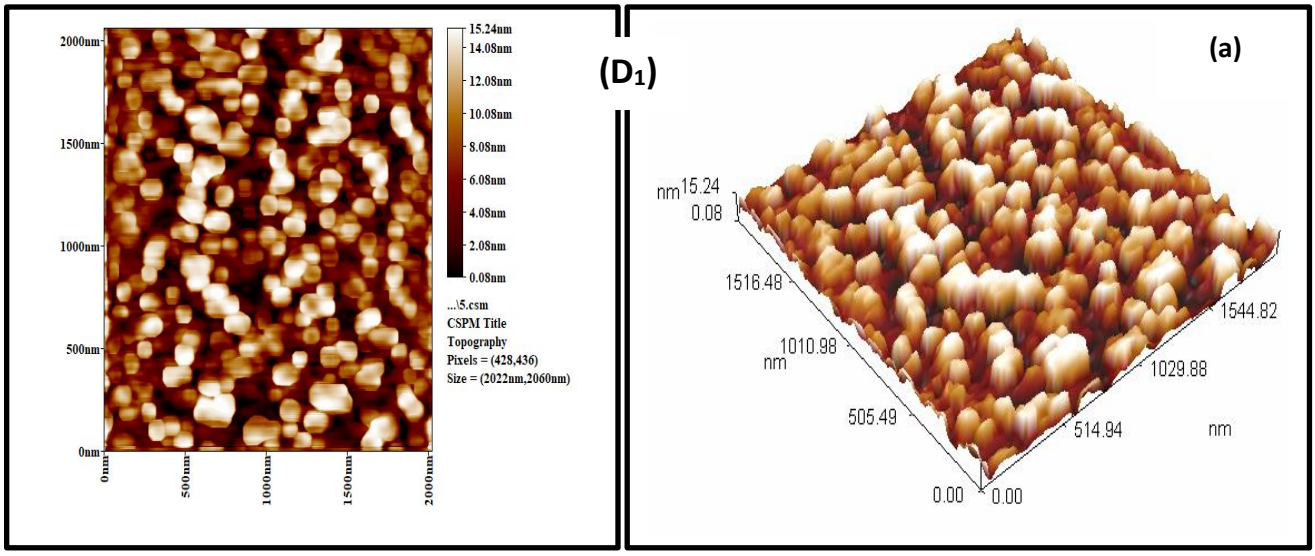
(D1)
(a)
2000nm
1500nm
1000nm
500nm
0nm
15.24nm
14.08nm
12.08nm
10.08nm
8.08nm
6.08nm
4.08nm
2.08nm
0.08nm
...\5.csm
CSPM Title
Topography
Pixels = (428,436)
Size = (2022nm,2060nm)
nm 15.24
0.08
1516.48
1010.98
nm
505.49
0.00
0.00
514.94
1029.88
1544.82
nm

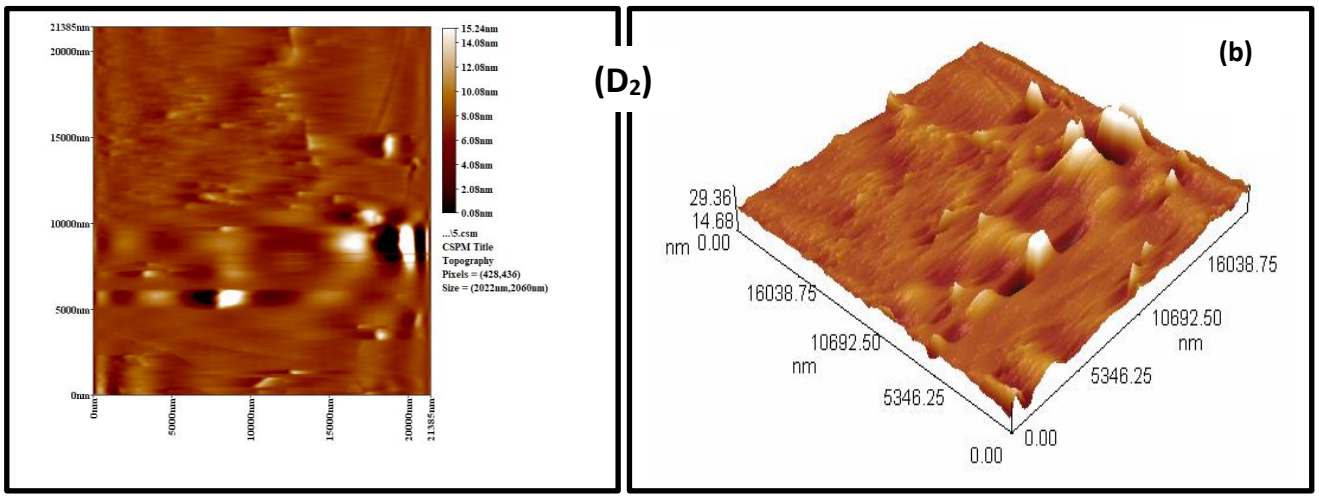
(D2)
(b)
21385nm
20000nm
15000nm
10000nm
5000nm
0nm
15.24nm
14.08nm
12.08nm
10.08nm
8.08nm
6.08nm
4.08nm
2.08nm
0.08nm
...\5.csm
CSPM Title
Topography
Pixels = (428,436)
Size = (2022nm,2060nm)
29.36
14.68
nm 0.00
16038.75
10692.50
nm
5346.25
0.00
0.00
16038.75
10692.50
nm
5346.25

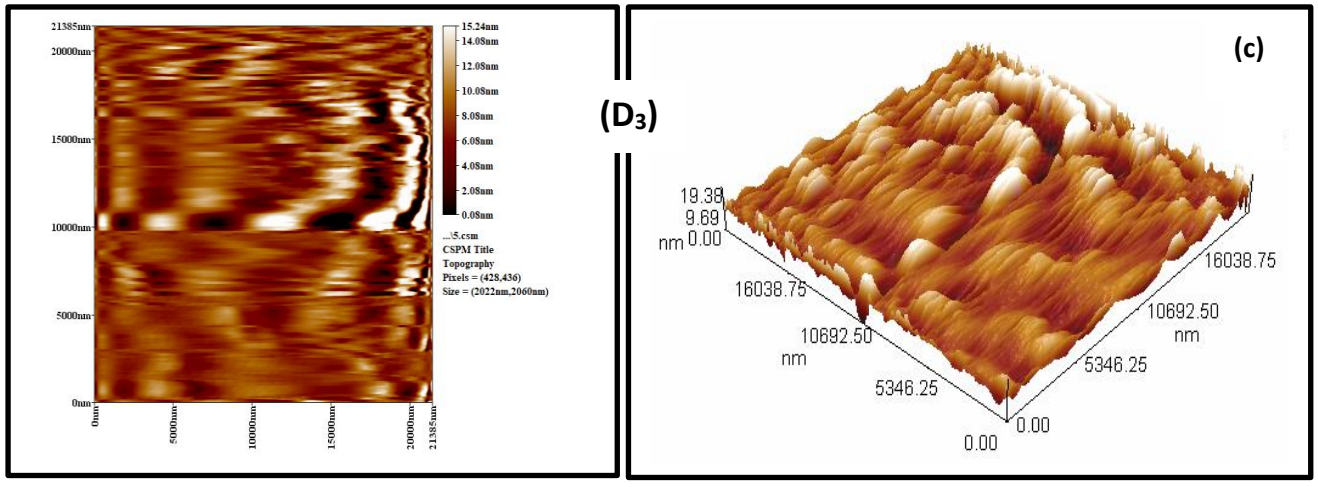
(D3)
(c)
21385nm
20000nm
15000nm
10000nm
5000nm
0nm
15.24nm
14.08nm
12.08nm
10.08nm
8.08nm
6.08nm
4.08nm
2.08nm
0.08nm
...\5.csm
CSPM Title
Topography
Pixels = (428,436)
Size = (2022nm,2060nm)
19.38
9.69
nm 0.00
16038.75
10692.50
nm
5346.25
0.00
0.00
16038.75
10692.50
nm
5346.25

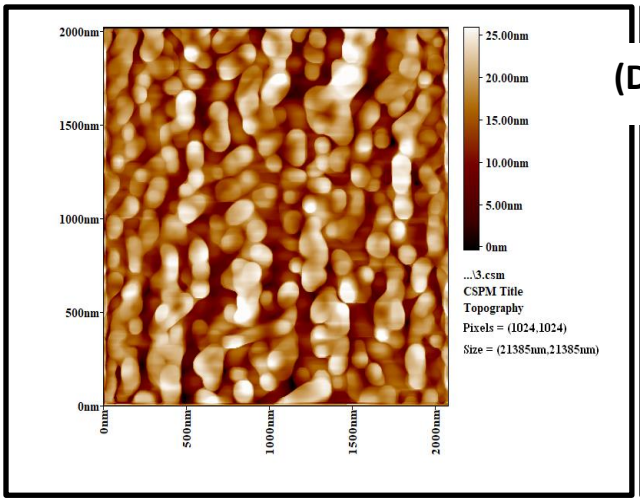
2000nm
1500nm
1000nm
500nm
0nm
0nm
500nm
1000nm
1500nm
2000nm
25.00nm
20.00nm
15.00nm
10.00nm
5.00nm
0nm
...\3.csm
CSPM Title
Topography
Pixels = (1024,1024)
Size = (21385nm,21385nm)

(D4)

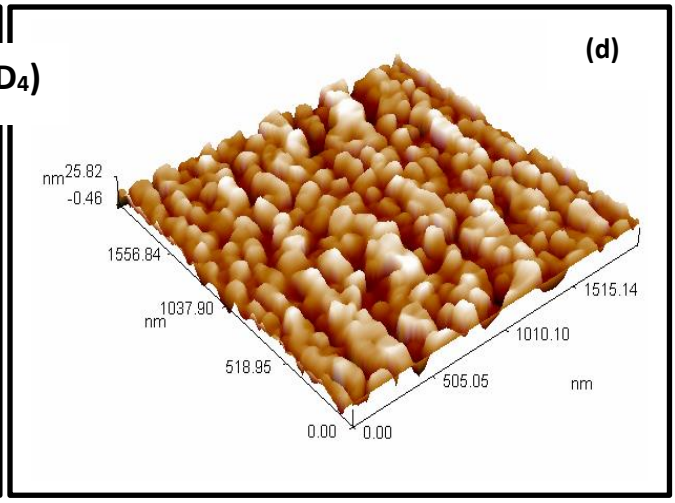
(d)
nm 25.82
-0.46
1556.84
1037.90
nm
518.95
0.00
0.00
505.05
1010.10
1515.14
nm

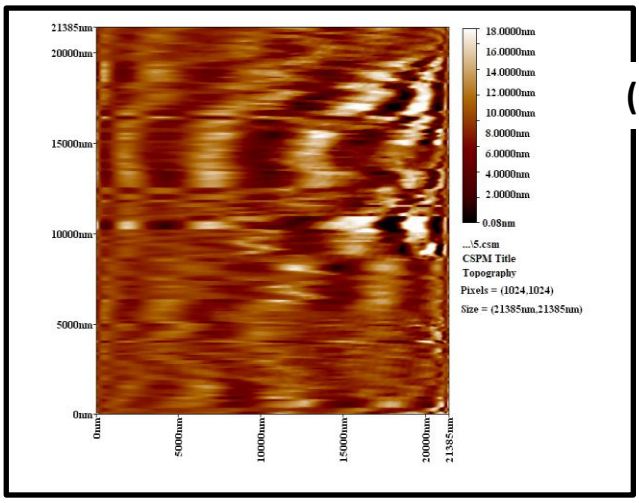
21385nm
20000nm
15000nm
10000nm
5000nm
0nm
0nm
5000nm
10000nm
15000nm
20000nm
21385nm
18.0000nm
16.0000nm
14.0000nm
12.0000nm
10.0000nm
8.0000nm
6.0000nm
4.0000nm
2.0000nm
0.08nm
...\5.csm
CSPM Title
Topography
Pixels = (1024,1024)
Size = (21385nm,21385nm)

(D5)

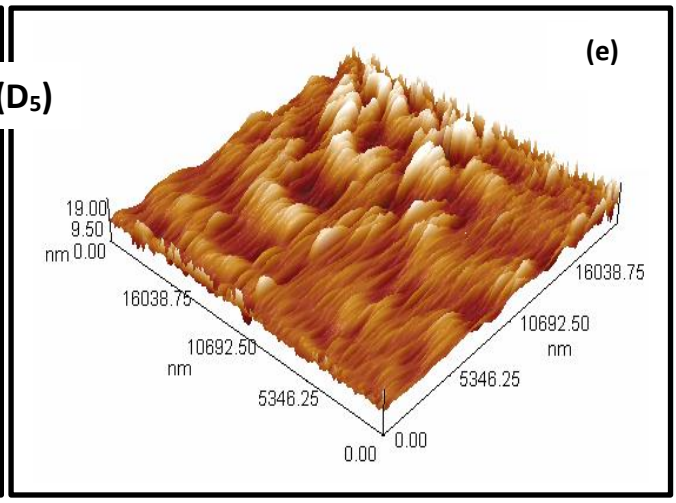
(e)
19.00
9.50
nm 0.00
16038.75
10692.50
nm
5346.25
0.00
0.00
5346.25
10692.50
nm
16038.75

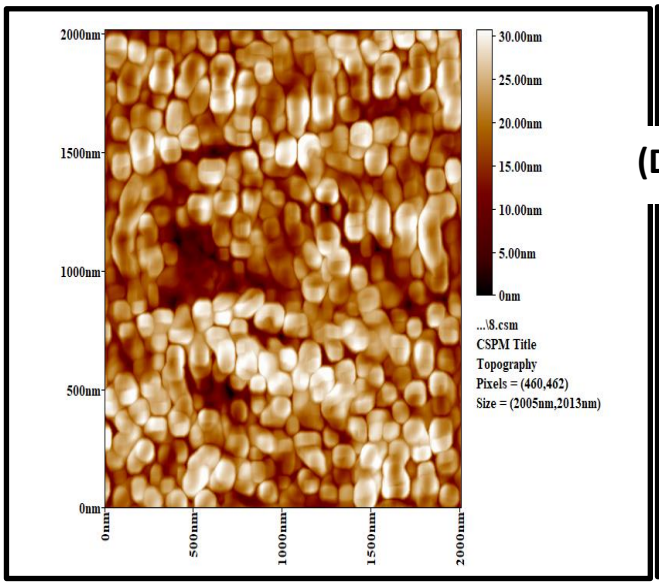
2000nm
1500nm
1000nm
500nm
0nm
0nm
500nm
1000nm
1500nm
2000nm
30.00nm
25.00nm
20.00nm
15.00nm
10.00nm
5.00nm
0nm
...\8.csm
CSPM Title
Topography
Pixels = (460,462)
Size = (2005nm,2013nm)

(D6)

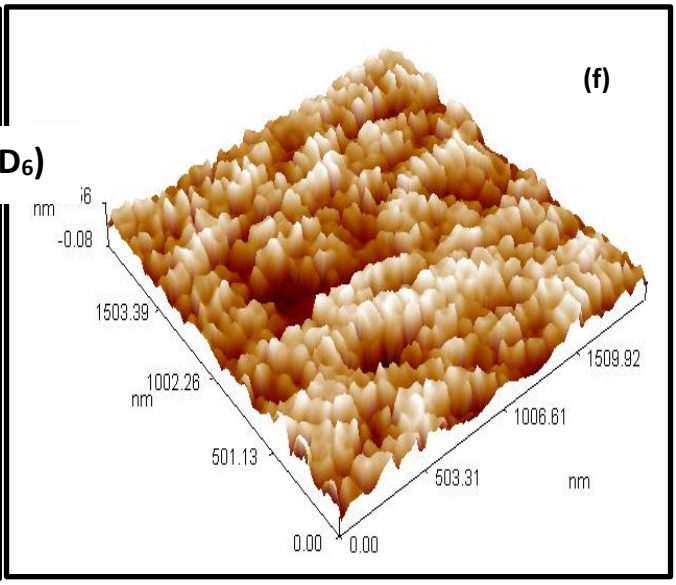
(f)
nm
-0.08
1503.39
1002.26
nm
501.13
0.00
0.00
503.31
1006.61
1509.92
nm

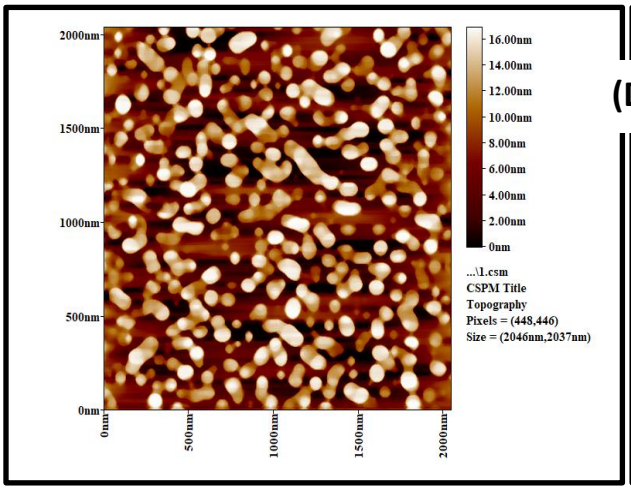
2000nm
1500nm
1000nm
500nm
0nm
0nm
500nm
1000nm
1500nm
2000nm
16.00nm
14.00nm
12.00nm
10.00nm
8.00nm
6.00nm
4.00nm
2.00nm
0nm
...\1.csm
CSPM Title
Topography
Pixels = (448,446)
Size = (2046nm,2037nm)

(D_7)

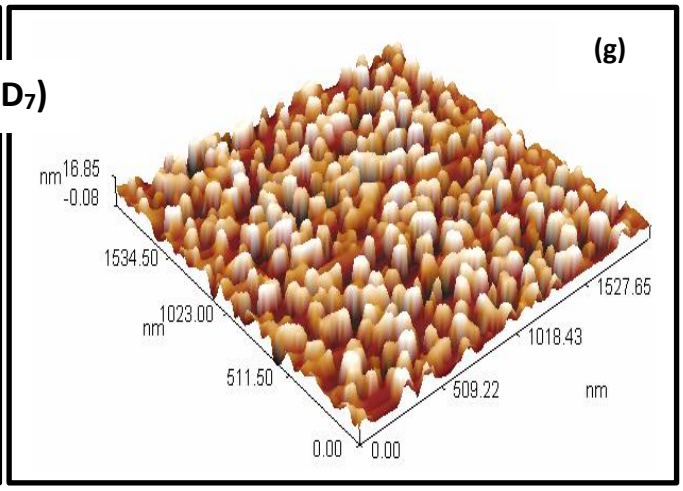
(g)
nm 16.85
-0.08
1534.50
1023.00
nm
511.50
0.00
0.00
509.22
1018.43
1527.65
nm

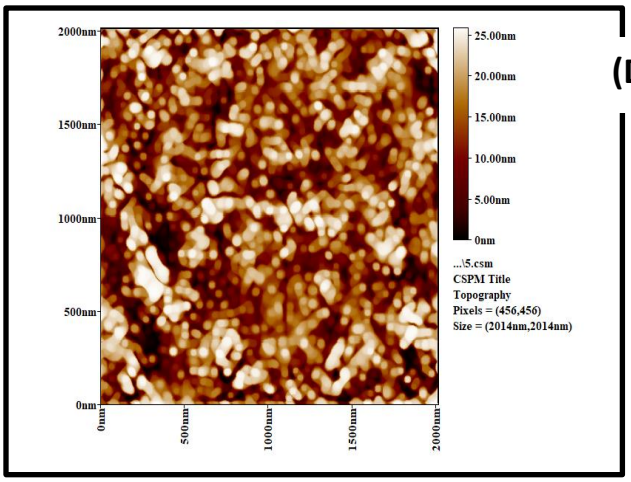
2000nm
1500nm
1000nm
500nm
0nm
0nm
500nm
1000nm
1500nm
2000nm
25.00nm
20.00nm
15.00nm
10.00nm
5.00nm
0nm
...\5.csm
CSPM Title
Topography
Pixels = (456,456)
Size = (2014nm,2014nm)

(D_8)

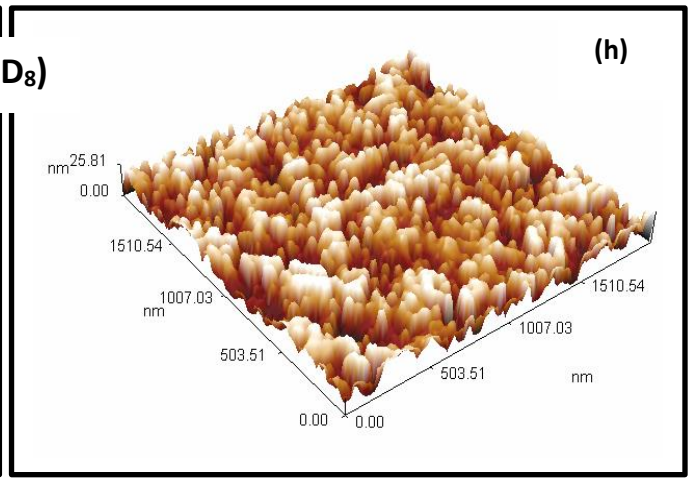
(h)
nm 25.81
0.00
1510.54
1007.03
nm
503.51
0.00
0.00
503.51
1007.03
1510.54
nm

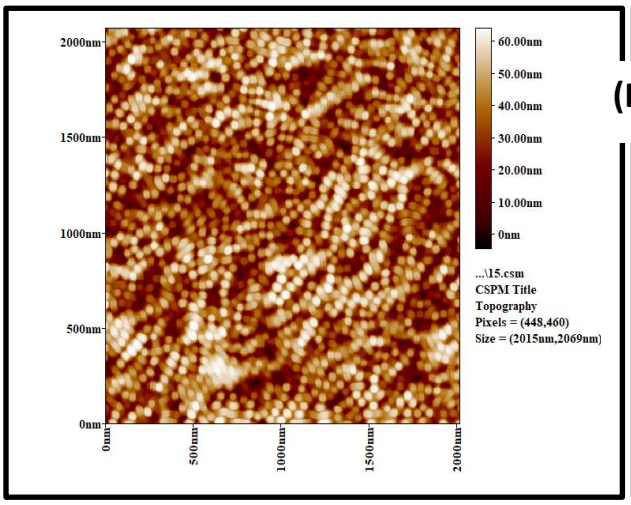
2000nm
1500nm
1000nm
500nm
0nm
0nm
500nm
1000nm
1500nm
2000nm
60.00nm
50.00nm
40.00nm
30.00nm
20.00nm
10.00nm
0nm
...\15.csm
CSPM Title
Topography
Pixels = (448,460)
Size = (2015nm,2069nm)

(D_9)

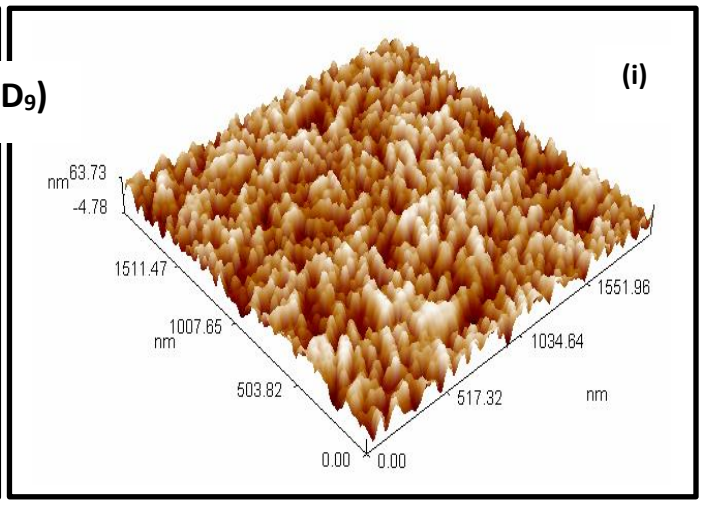
(i)
nm 63.73
-4.78
1511.47
1007.65
nm
503.82
0.00
0.00
517.32
1034.64
1551.96
nm

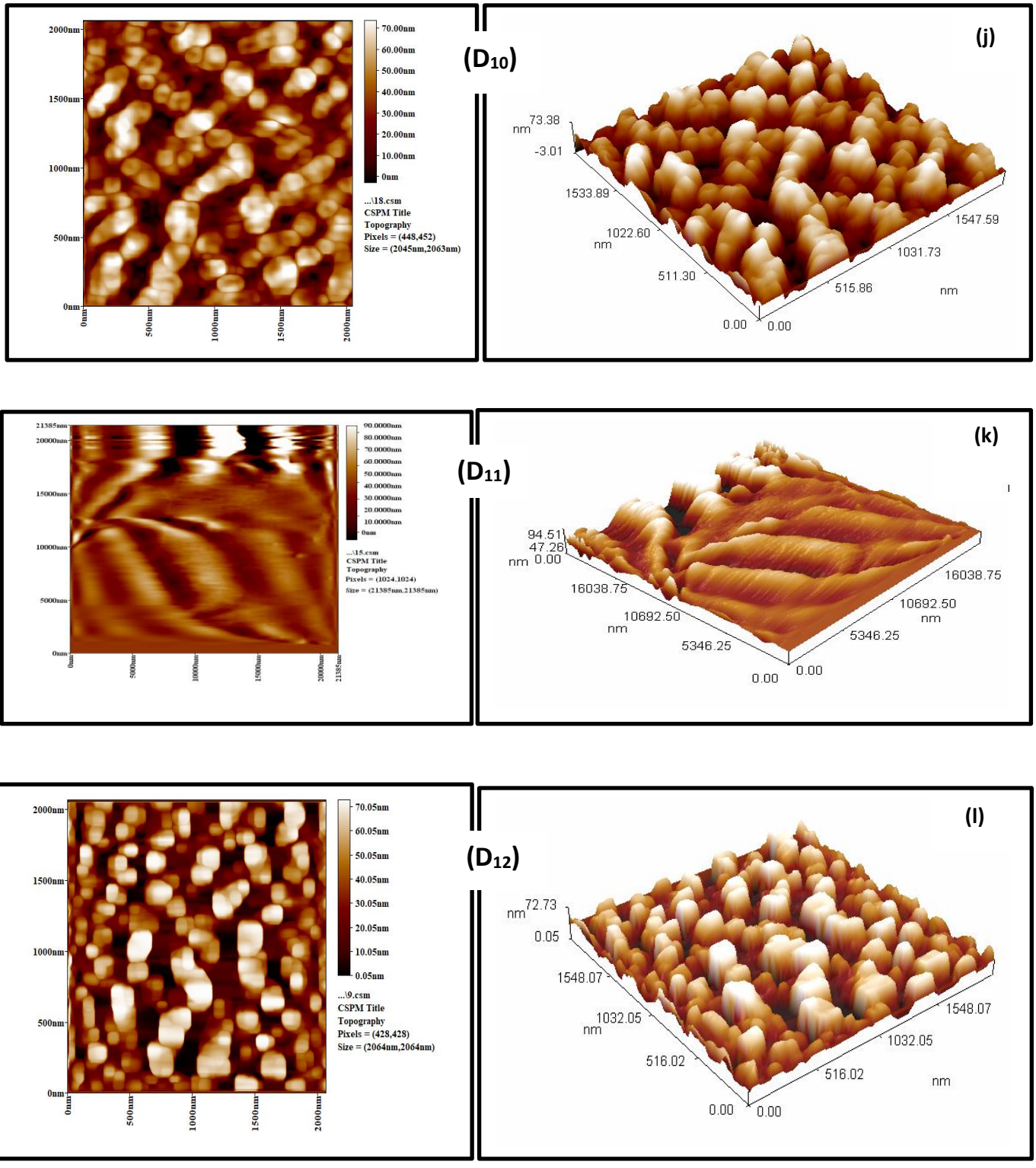

Figure (4.42): AFM results of samples (a) D_1, (b) D_2, (c) D_3, (d) D_4, (e) D_5, (f) D_6, (g) D_7, (h) D_8, (i) D_9, (j) D_{10}, (k) D_{11}, and (l) D_{12}.

Table (4.5): Surface roughness results.

Sample Code	Roughness	Sample Code	Roughness
Base	1.41	C_1	2.1
A_1	7.19	C_2	2.6
A_2	6.65	C_3	4.21
A_3	8.23	C_4	4.19
A_4	12.6	C_5	5.4
A_5	18.8	C_6	4.96
A_6	24.3	C_7	7.65
A_7	25.3	C_8	9.01
A_8	30.4	C_9	11
A_9	36.4	C_{10}	16.1
A_{10}	40	C_{11}	22.2
A_{11}	46.6	C_{12}	27.9
A_{12}	45.6	D_1	1.55
B_1	2.95	D_2	1.69
B_2	3.79	D_3	2.54
B_3	4.31	D_4	4.38
B_4	5.13	D_5	2.09
B_5	6.21	D_6	4.64
B_6	8.46	D_7	4.28
B_7	11.8	D_8	5.56
B_8	10.4	D_9	11.3
B_9	18.5	D_{10}	16.1
B_{10}	21.2	D_{11}	12.8
B_{11}	27.5	D_{12}	18.2
B_{12}	29.1		

4.6 Mechanical test

4.6.1 Hardness Test:

The results of micro-hardness at TiO_2 and nanocomposite ceramic coating HA/TiO_2, ZrO_2/TiO_2 and HA/ZrO_2/TiO_2 of the coated samples at a load of 50gm (0.49N) using a fixed loading duration of (15 sec.). In general, it can be observed that the hardness of coated samples is improved by MAO process. In Figure (4.43) Show that hardness value (268.55 HV at sample A_1) these values are significantly higher than that of Ti-6Al-7Nb alloy, and the increase hardness value with increase the voltage and deposition time to the (287.03HV for sample A_3) and (311.5 at sample A_7) because the formation of dense oxide layer which is attributed to formation of thermal micro arcs during MAO and increase thickness of ceramics coating [140]. The larger standard deviations on the MAO treated samples may also be attributed to their higher surface porosity lead to decrease hardness at (243.8HV for sample A_9) and (234.59HV for sample A_{12}).

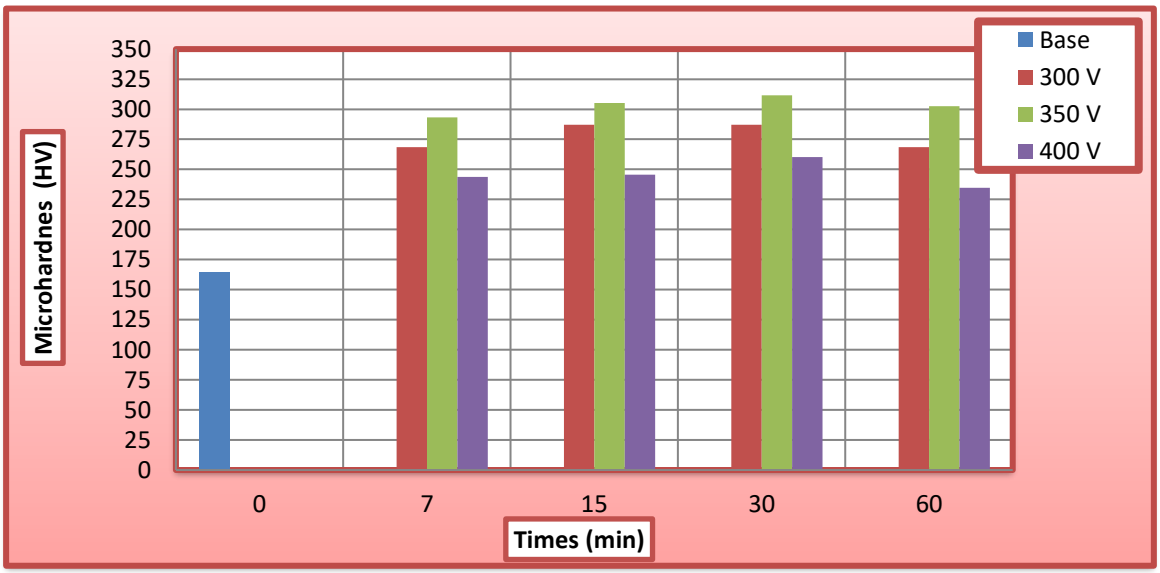

Figure (4.43): Relationship between the voltage, deposition time and the micro-hardness of coatings at TiO_2 by MAO process.

in Figure (4.44) the addition of nano-HA in electrolyte solution provides a higher hardness (310.22 HV for sample B_1). Show that with increased deposition time and voltage hardness increased due to the improvement in depth morphology, distribution and increasing in HA/ TiO_2 composite thickness which can be clearly observed in AFM results [143]. The thicker coating (B_{11}) has the higher value of hardness (368.1HV) among the other samples. In Figure (4.45) addition of nano-ZrO_2 recorded to the electrolyte provide excellent tribological behavior of hardness in comparison with samples A and B, with increasing the voltage and deposition time of ZrO_2/TiO_2 the hardness increased until (466.7HV for sample C_{11}) and (367.8HV for sample C_4), due to the decrease of pores which indicated by the SEM images.

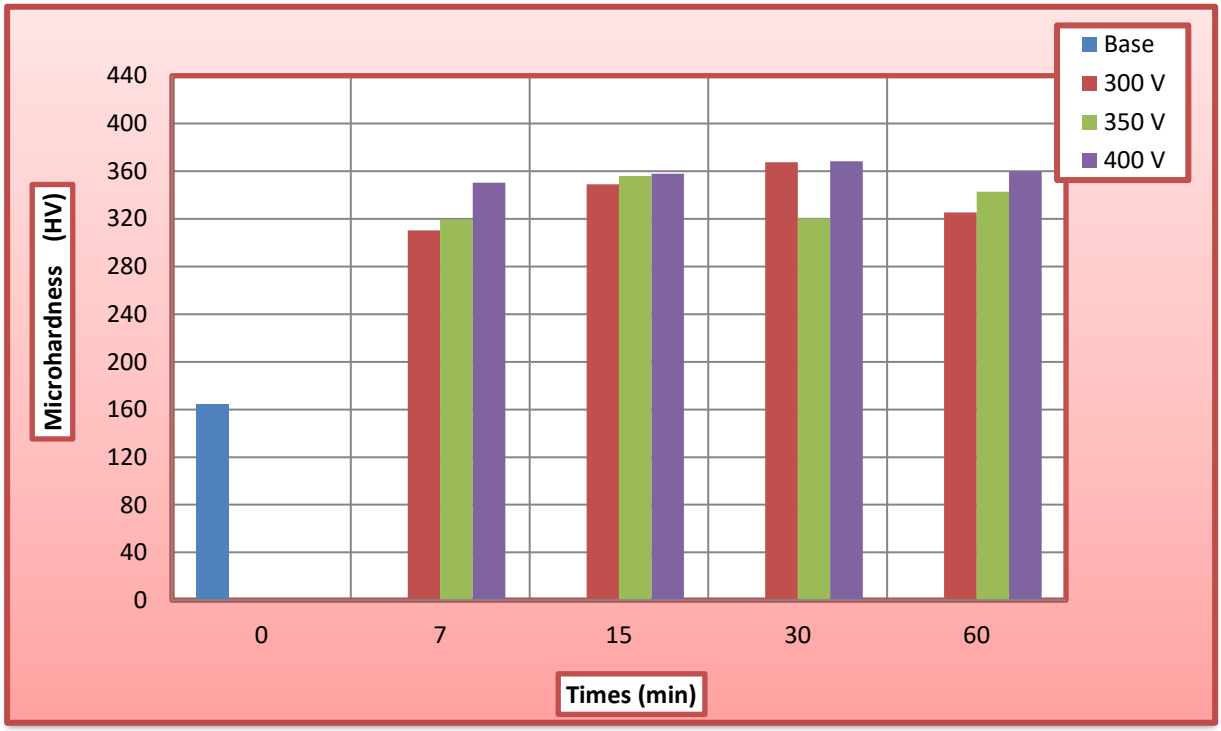

Figure (4.44): Relationship between the voltage, deposition time and the micro-hardness of coatings at HA/TiO_2 by MAO process.

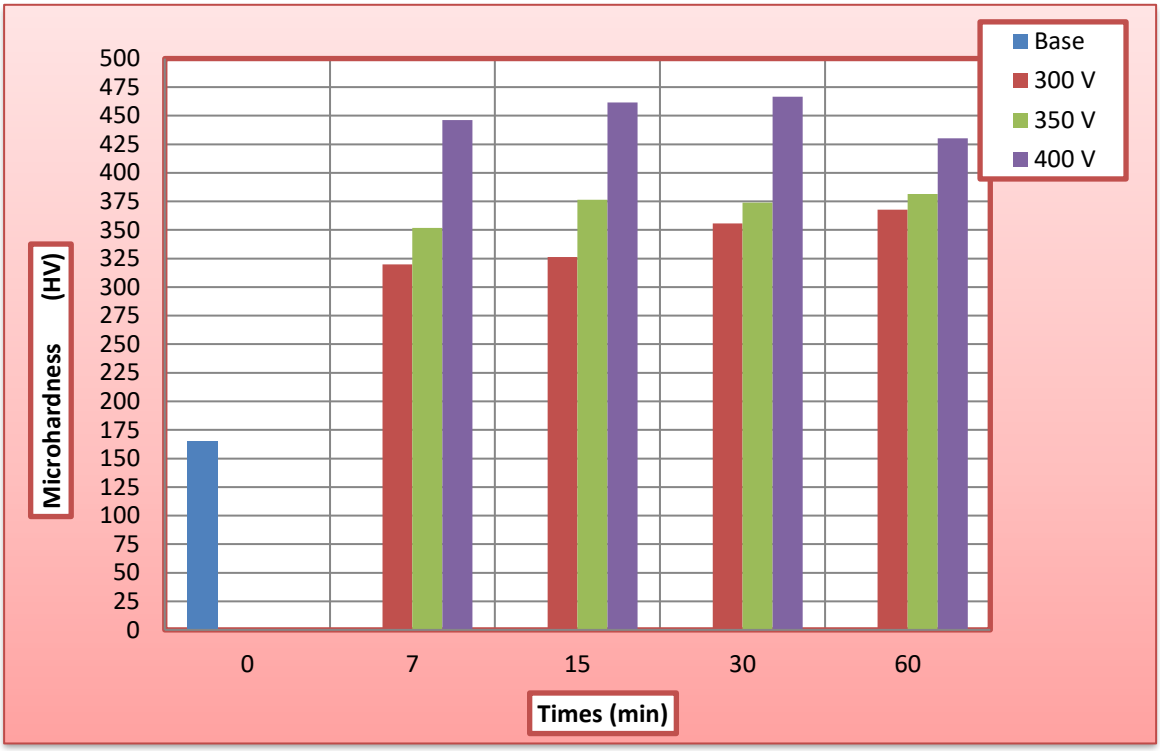

Figure (4.45): Relationship between the voltage, deposition time and the micro-hardness of coatings at ZrO_2/TiO_2 by MAO process.

The addition of nano-HA and ZrO_2 recorded a higher hardness than the D samples furthermore in Figure (4.46); the hardness value increased with increasing voltage and deposition time from (437.83HV for sample D_1). The decrease of micro-pores with increase HA and ZrO_2 and then the value increased deposition time (441.8HV for sample D_4) and voltage (480.1HV for sample D_9) and highest value at (584.9HV for sample D_{10}). For clinical applications, an increase in Ti surface micro-hardness could be beneficial, because it increases the resistance to wear of the material, thereby positively contributing to the longevity of a Ti implant [141].

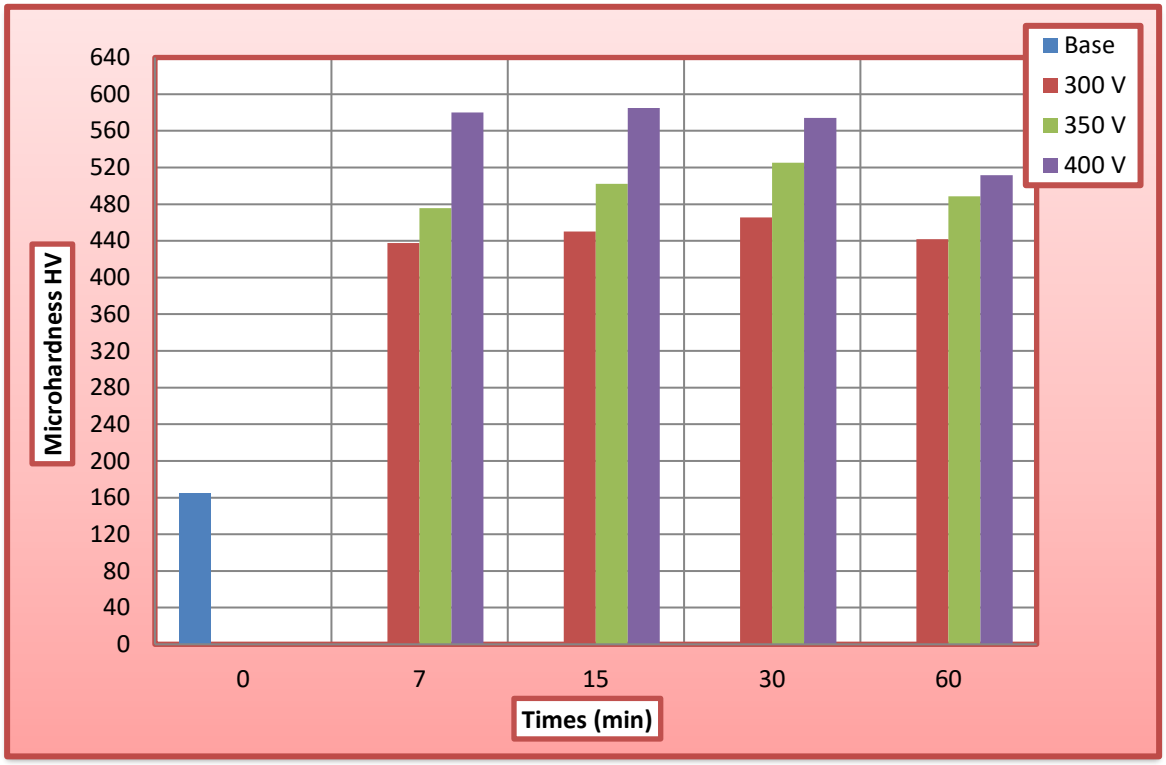

Figure (4.46): Relationship between the voltage, deposition time and the micro-hardness of coatings at HA/ZrO_2/TiO_2 by MAO process.

4.6.2 Wear test:

Wear resistant is the one of the most important implant mechanical properties that wear failure contributes from all implant's failure reasons. The wear rates produced by pin-on disc sliding wear test were determined by means of wear mass loss of test specimens under 10N load and several times (5, 10, 15, 20, 25, and 30) min. Generally, it can be observed that the weight loss increased with increasing of loading time. Figure (4.47) shows that high wear rate of Ti-6Al-7Nb alloy substrate comparison, with coating samples could prove the good wear resistance of the ceramic oxide layers which resulted in less wear rate.

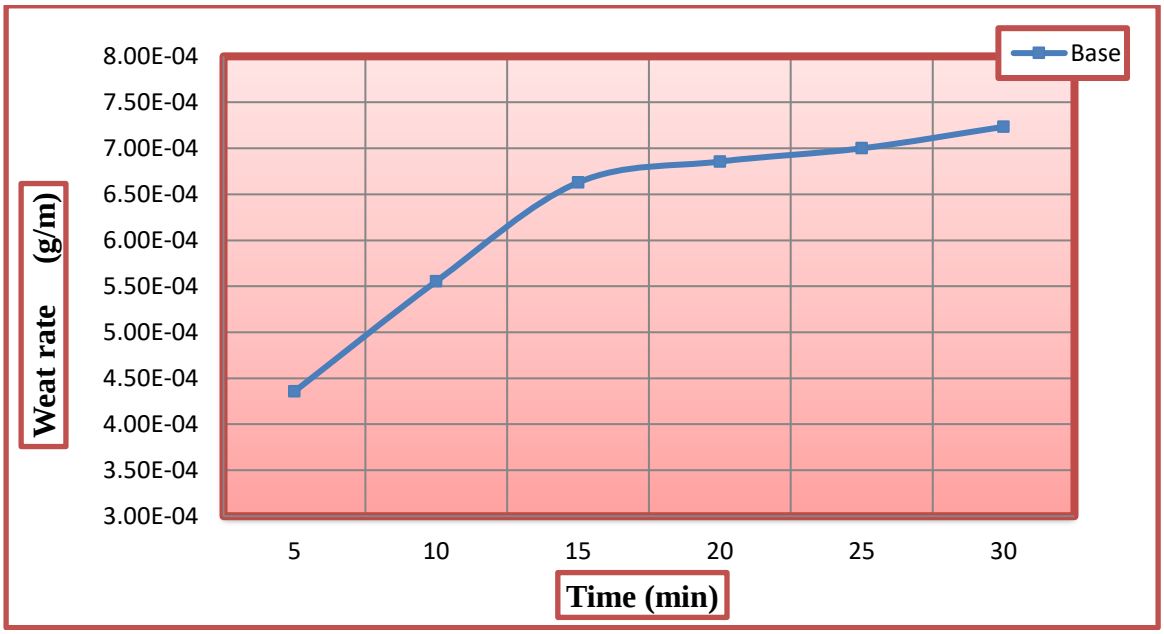

Figure (4.47): Relationship between wear rate and test time for Ti-6Al-7Nb alloy substrate.

In Figure (4.48), ceramic coatings deposited TiO_2 by MAO process, gave the best wear resistance and low wear rate (2.78×10^{-5}) for samples A_1 and (1.718×10^{-5}) for samples A_2. Due to improved hardness by presence of the alpha and beta titanium phases and presence of modified elements could be reduce the friction and increase wear resistance of coating by reduce wear rate. When the applied potential increases, the intensity of micro-discharges also increases (400V), making that the coating porosity increases, due to a decrease in the coating electric resistance. The coating porosity distribution influences both the mechanical and tribological behavior of the coatings [145]. This is confirmed by the present results, the coatings show higher wear rates for sample (A_5, A_6, A_7, and A_8) value of wear rate after pass 30min of wear test $(1.17 \times 10^{-5},\ 1.02 \times 10^{-5},\ 9.46 \times 10^{-6},$ and $1.25 \times 10^{-5})$ to $(5.45 \times 10^{-5},\ 2.35 \times 10^{-5},\ 2.95 \times 10^{-5},$ and $6.2 \times 10^{-5})$ for sample (A_9, A_{10}, A_{11}, and A_{12}) in Figure (4.49) and (4.50).

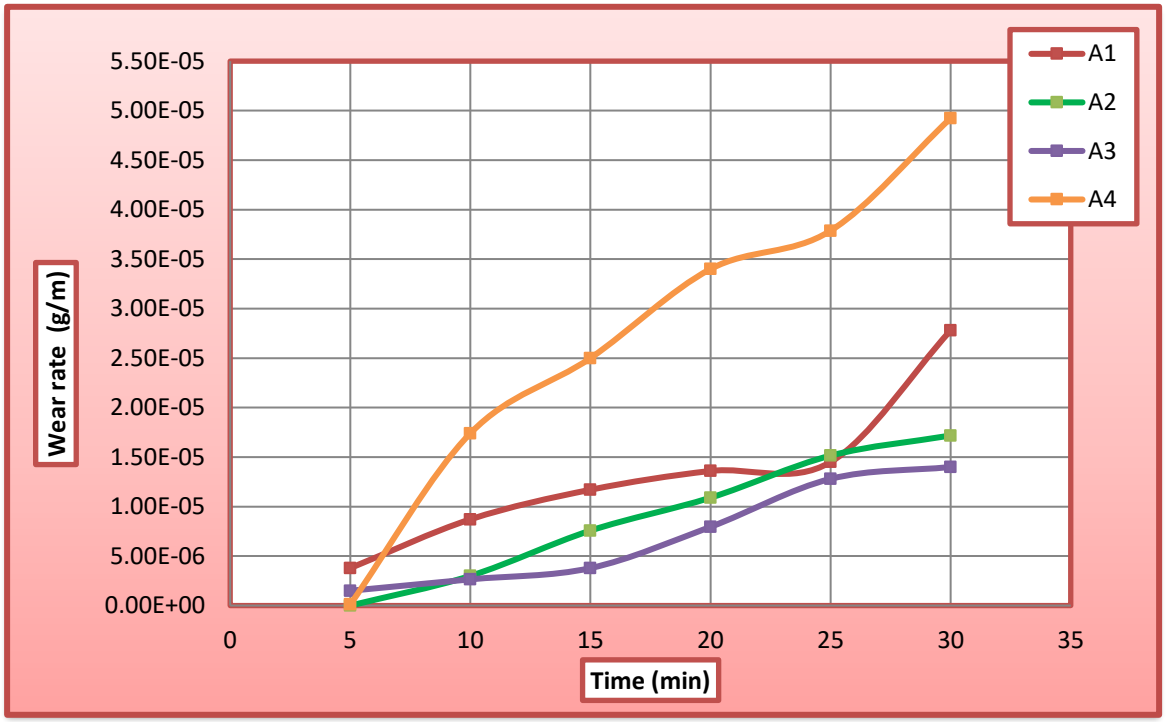

Figure (4.48): Relationship of TiO_2 coating by MAO process at (300V).

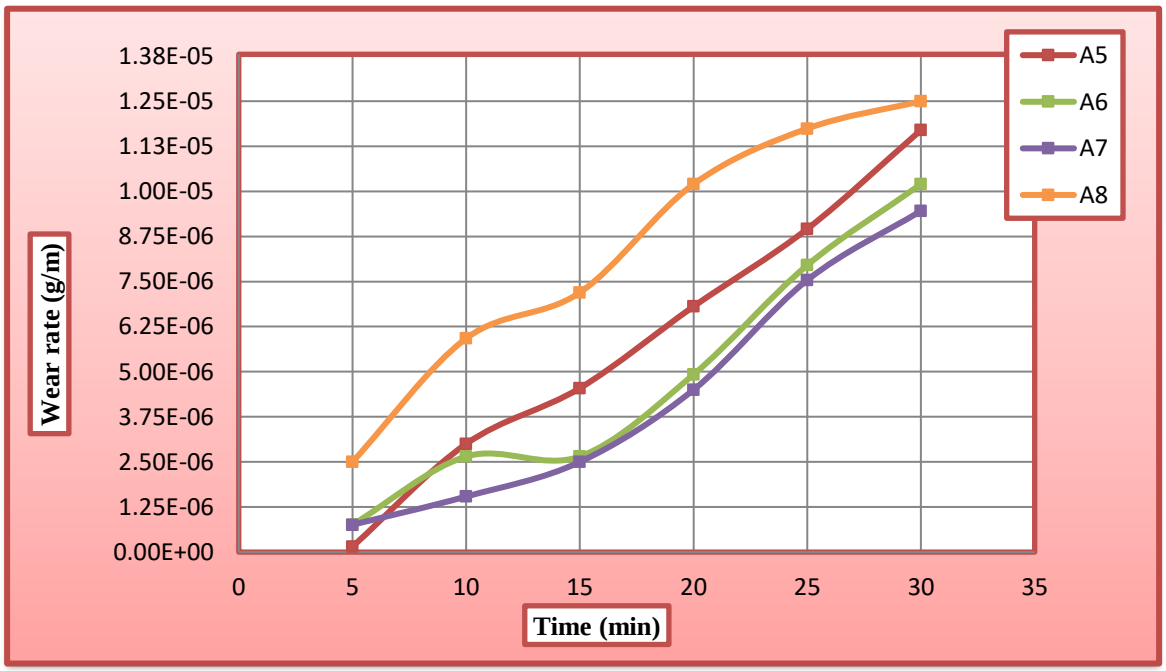

Figure (4.49): Relationship of TiO_2 coating by MAO process at 350V.

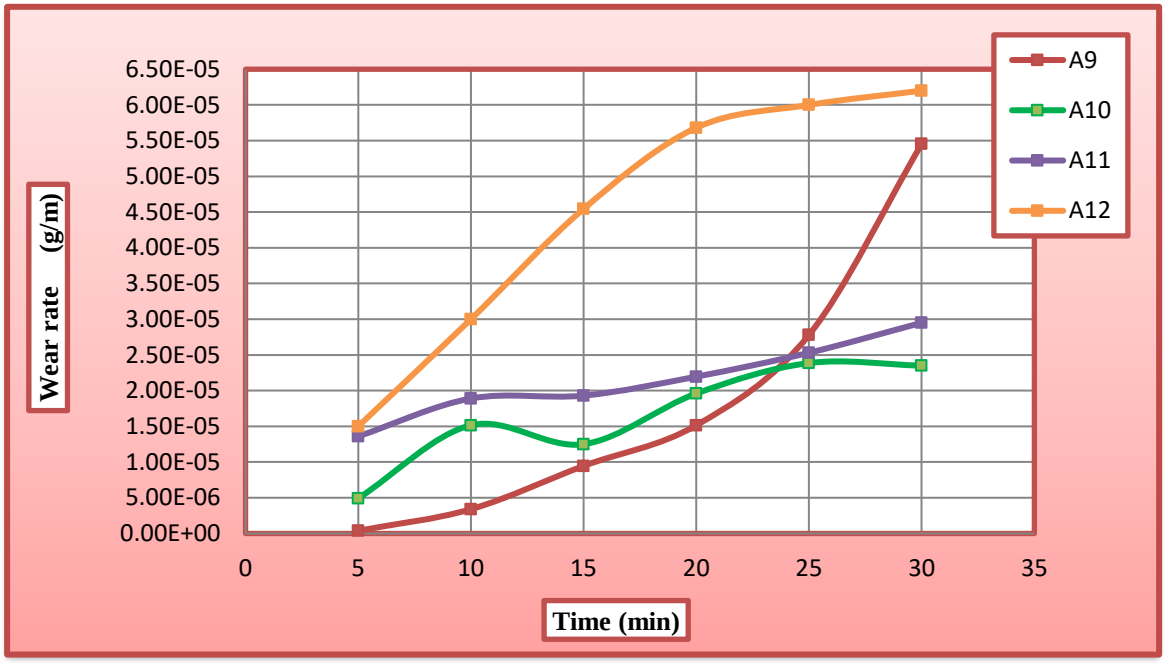

Figure (4.50): Relationship of TiO_2 coating by MAO process at 400V.

In Figure (4.51), lowest wear rate at nanocomposite ceramics coating by HA/TiO_2 with comparison to that for samples uncoated. It is also important to say that the wear resistance is higher because the hardness is higher, which leads to less mass loss. The wear resistance increased by decreased wear rate with increased voltage and deposition time for sample (B5, B6, B7, and B8) equal to ($2.4 \times 10^{-5}, 1.59 \times 10^{-5}, 1.43 \times 10^{-5}$, and 1.628×10^{-5}) respectively, to samples (B9, B10, B11, and B12) equal to ($1.28 \times 10^{-6}, 1.06 \times 10^{-6}, 4.33 \times 10^{-7}$, and 1.15×10^{-6}) in Figure (4.52) and (4.53).

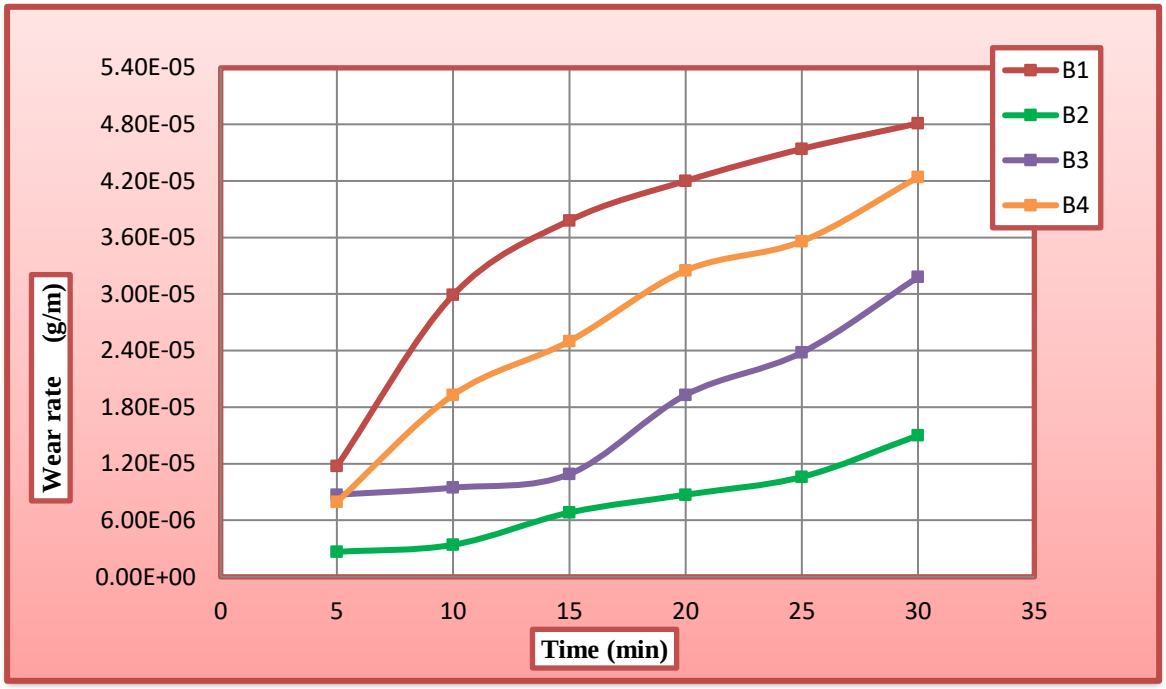

Figure (4.51): Relationship of HA/TiO_2 coating by MAO process at 300V.

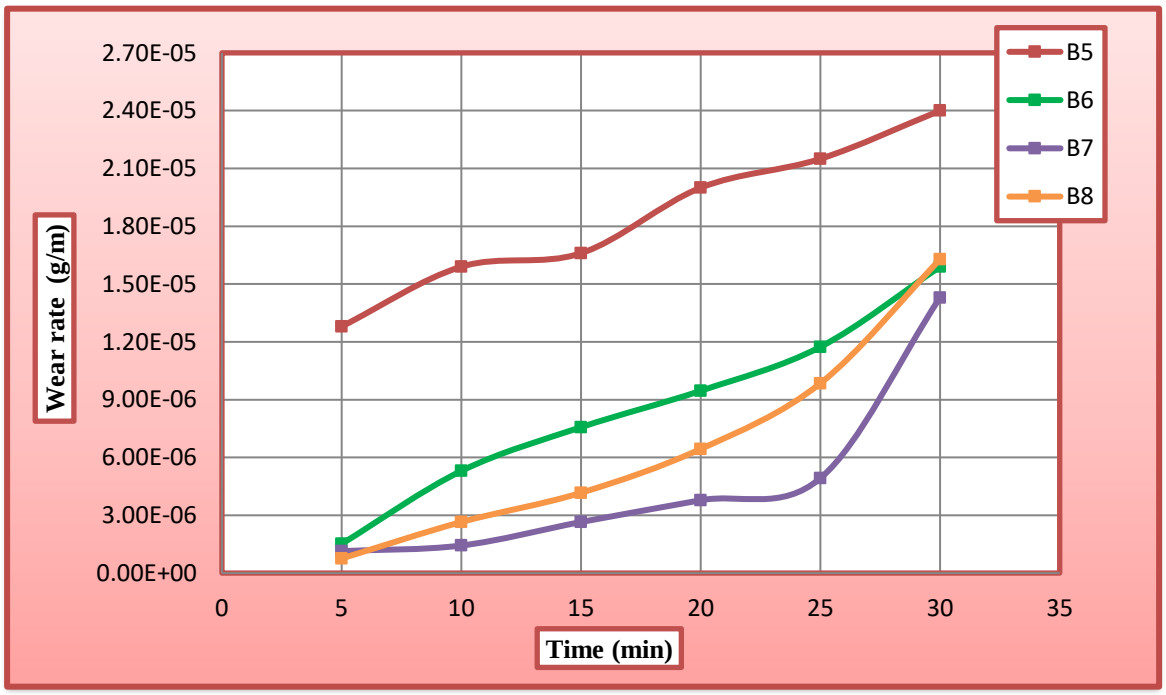

Figure (4.52): Relationship of HA/TiO_2 coating by MAO process at 350V.

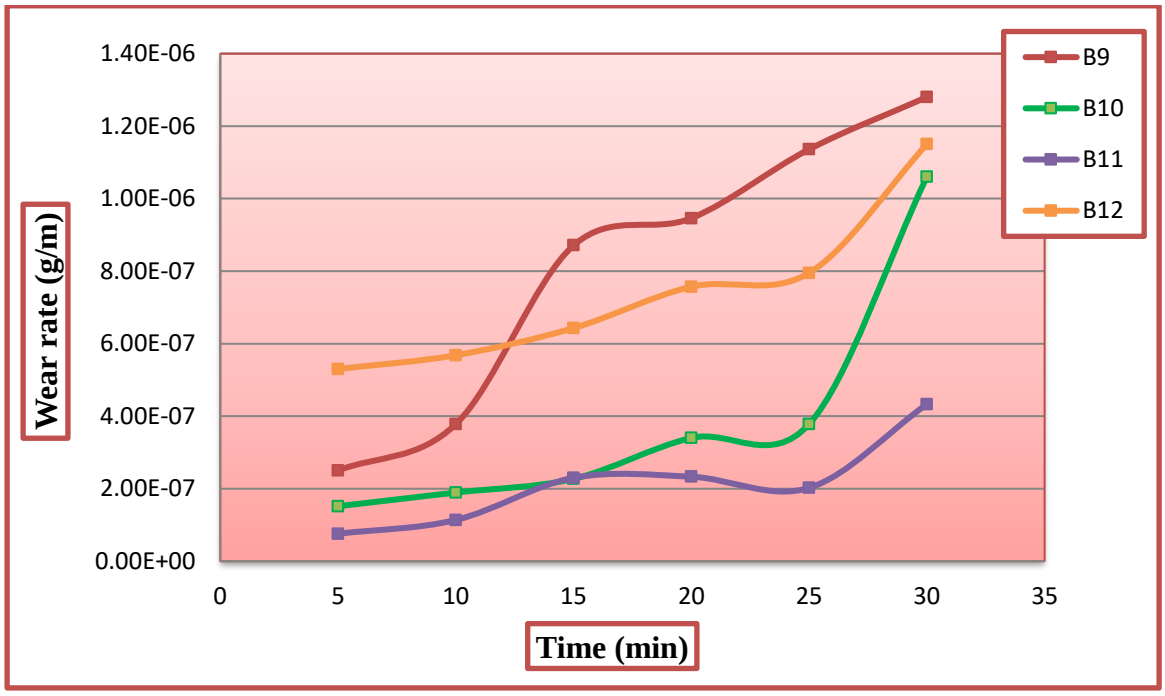

Figure (4.53): Relationship of HA/TiO_2 coating by MAO process at 400V.

The weight loss for samples is tested with deposited using the nano-ZrO_2 in the electrolytes gave the best wear resistance and low wear rate (2.15×10^{-5}) for samples at C_4 in Figures (4.54). It can be observed that the weight loss decreased due to the increasing of voltage and time in Figure (4.55) and (4.56) equal to value (1.06×10^{-7}). The nanoparticles addition leads to the formation of coatings with low porosity, which improves the mechanical and tribological performance, the control of the coating characteristics (porosity distribution, homogeneity in thickness) by the MAO parameters allows improving the mechanical and tribological properties [146].

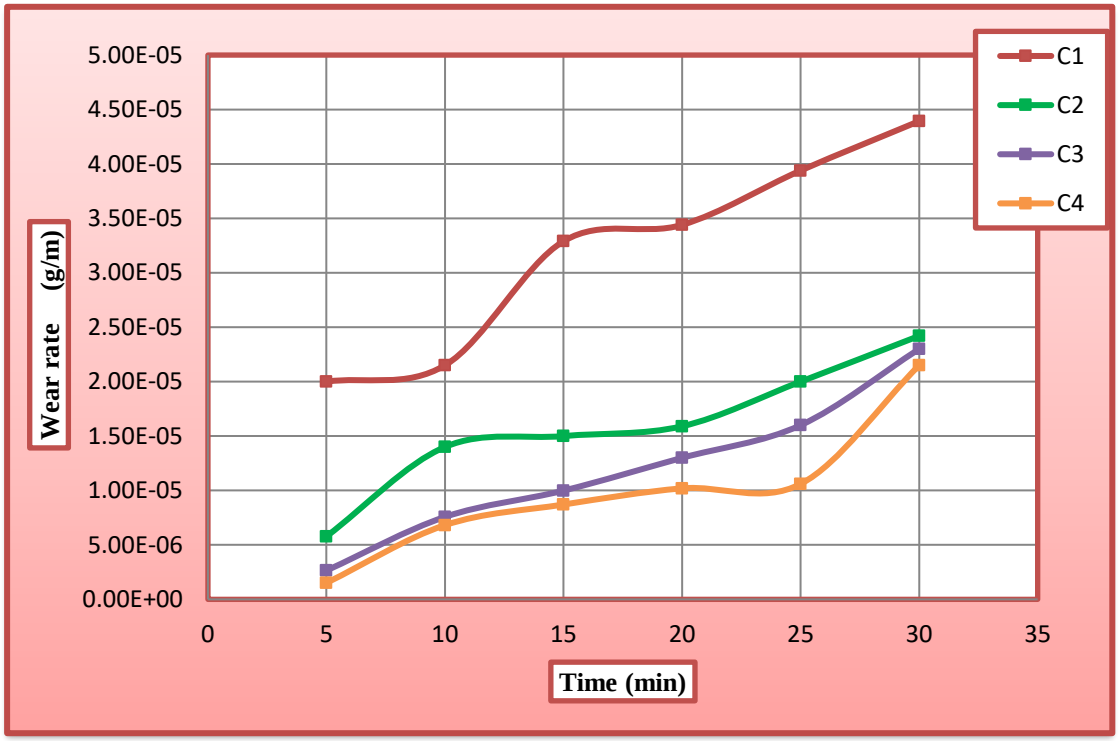

Figure (4.54): Relationship of ZrO_2/TiO_2 coating by MAO process at 300V.

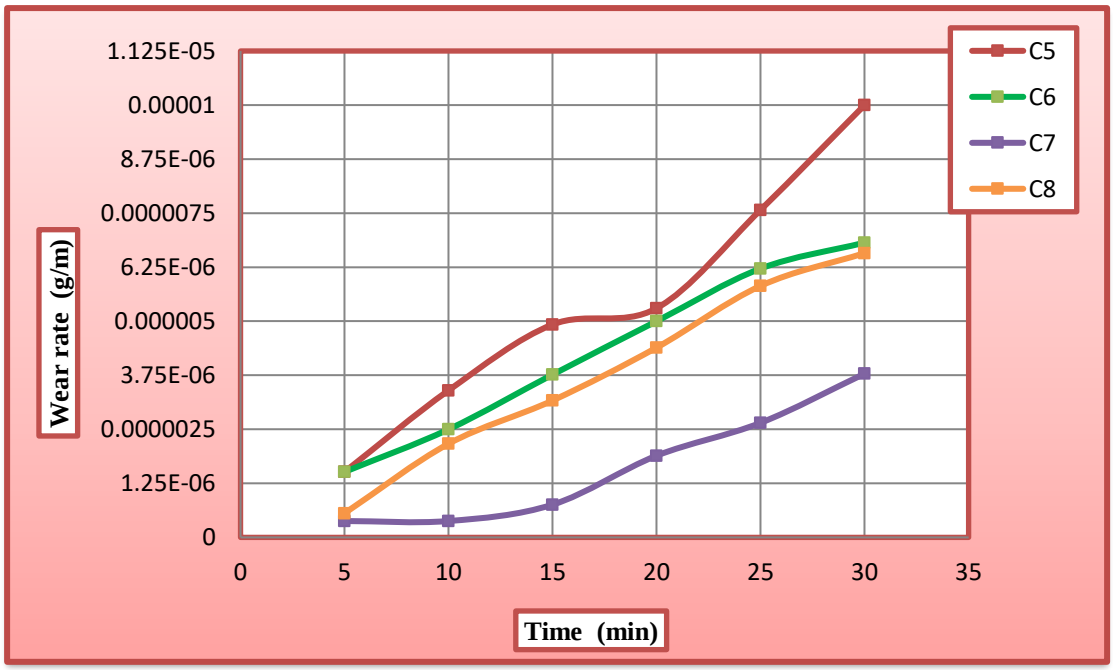

Figure (4.55): Relationship of ZrO_2/TiO_2 coating by MAO process at 350V.

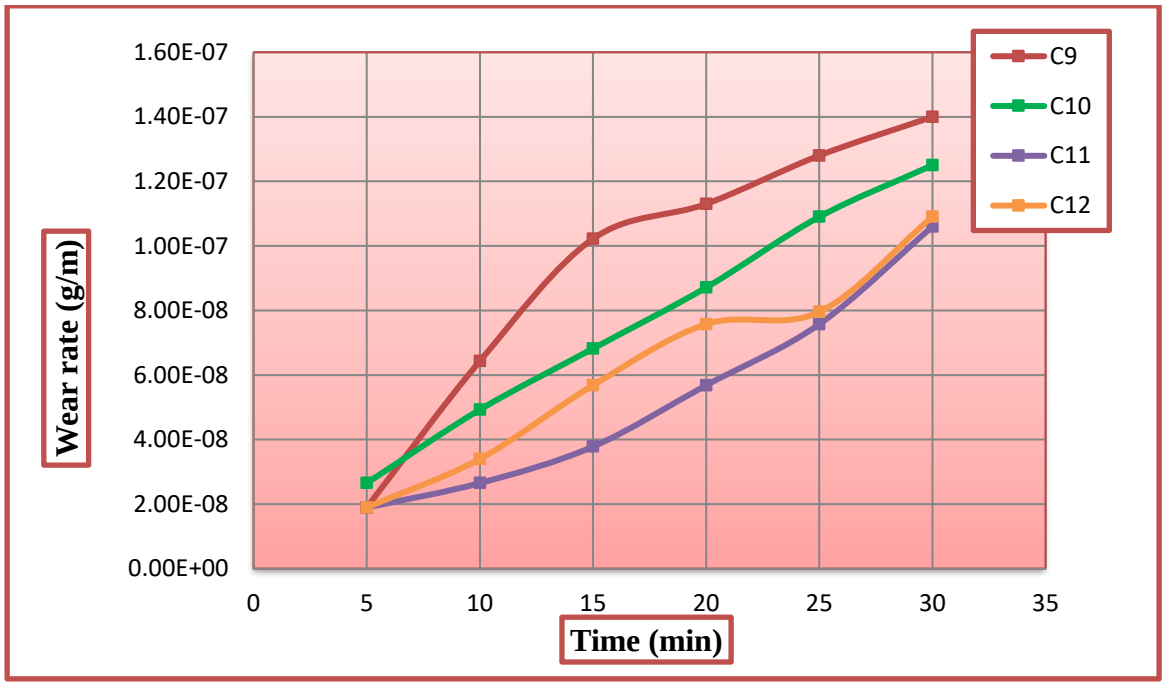

Figure (4.56): Relationship of ZrO_2/TiO_2 coating by MAO process at 400V.

Grain size, surface roughness and micro-hardness are important factors affecting the wear property. Figures (4.57-4.59) indicate the wear behavior of $HA/ZrO_2/TiO_2$ nanocomposite ceramic coating layer with different parameters (voltages and deposition times). Show that lower wear rate (2.19×10^{-5}) at sample D_2. Dependence between wear characteristics and hardness was reported earlier and it was observed that wear value decreased with hardness increase reached to (9.84×10^{-8}) for sample D_{10}. According to the Archard's law, the volumetric loss of the material is inversely proportional to the hardness value of the material [147]. One reason for reduced resistance of wear for researched alloys returns incapacity to produce defensive oxide film through wear. Ti-based alloys presented to oxidative quickly compose an oxide layer at surface because of their high reactivity, it's resulting eliminate through the sliding contact which the cause behind association between the tribologically interaction surface [148].

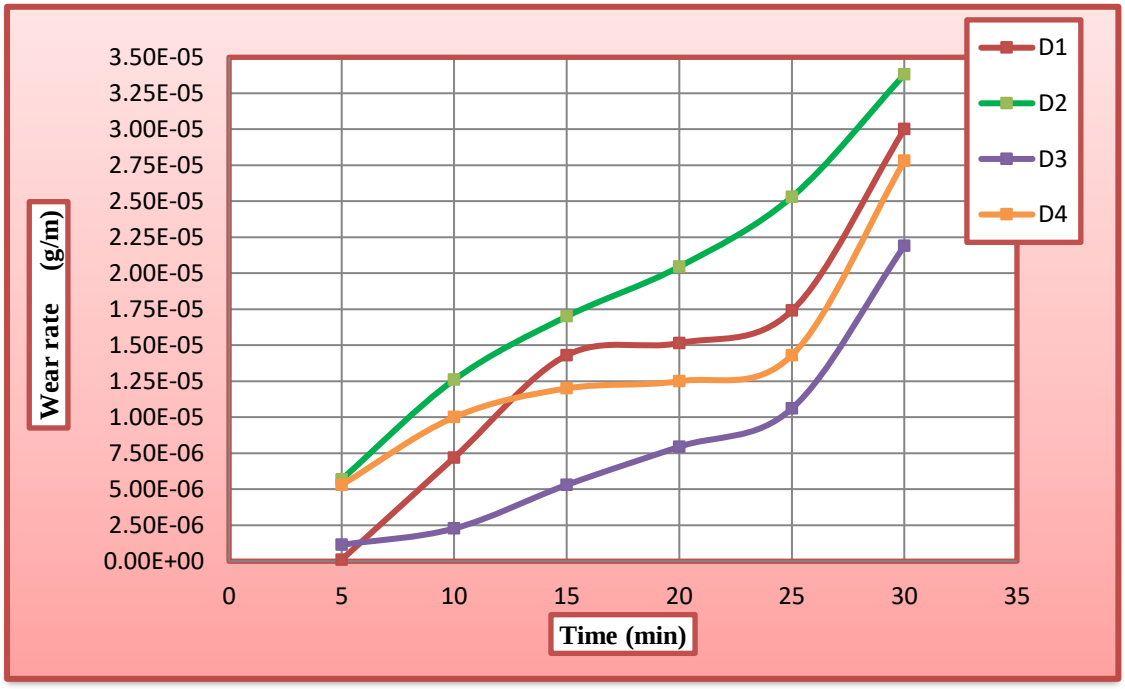

Figure (4.57): Relationship of $HA/ZrO_2/TiO_2$ coating by MAO process at 300V.

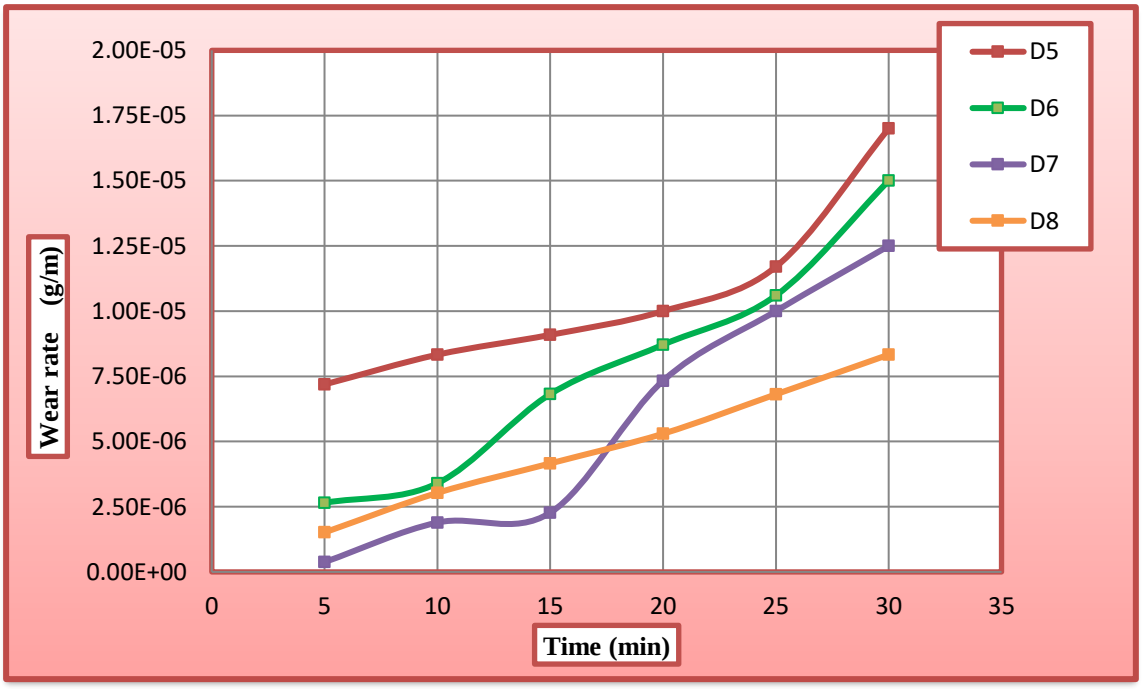

Figure (4.58): Relationship of $HA/ZrO_2/TiO_2$ coating by MAO process at 350V.

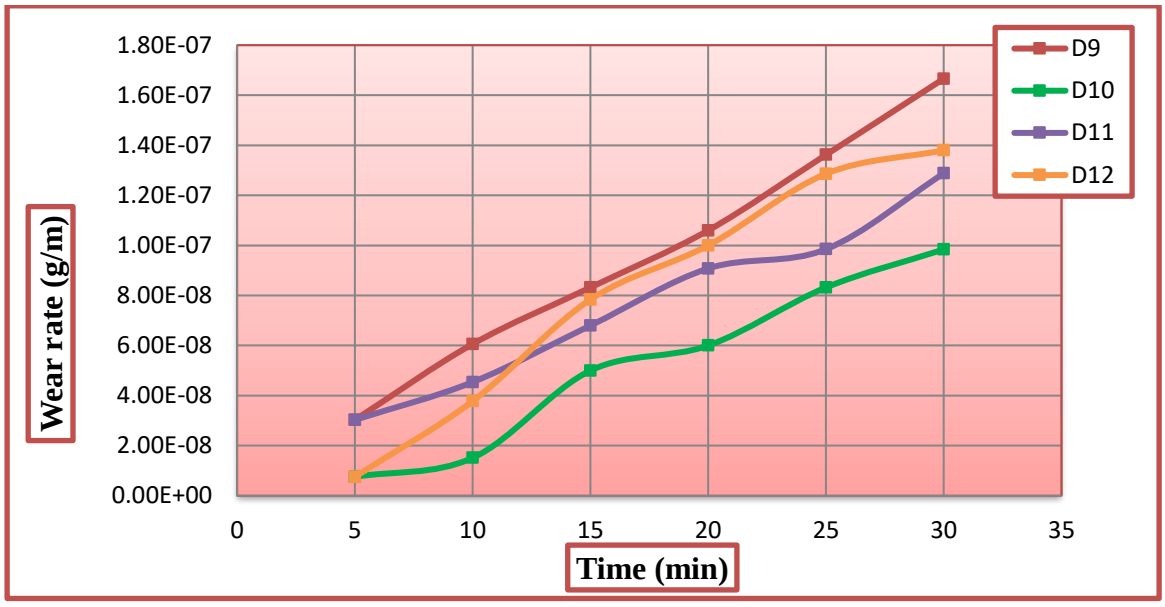

Figure (4.59): Relationship between wear rate and time of $HA/ZrO_2/TiO_2$ coating by MAO process at 400V.

4.6.3 Adhesion Test:

Adhesion has a strong influence on the wear and friction behavior of engineering materials. In Figure (4.60), adhesion strengths of TiO_2 coating by MAO process with different parameters (voltage and time) used for the pull-off strength test. The maximum adhesion strengths of (48.2MPa) for sample A_1 were obtained for the coatings deposited under (300 V & 7 min) on Ti-6Al-7Nb alloy. It is associated with the lowest thickness of such coatings increase of the oxidation voltage to 400V and time leads to the decrease of the coating adhesion strength to (23.13MPa) for sample A_{12}. In Figure (4.61) adhesion strength of composite coating HA/TiO_2 coating with different voltage and deposition time show that with increased thickness (64µm) at high voltage and time decrease adhesion strength at (14.8MPa) for sample B_{11}. HA is the most established bioactive material used in biomedical applications due to its excellent osteoconduction and chemical composition like that of the natural bone.

However, HA has poor mechanical properties. Particularly for artificial joints and dental implants, the adhesion strength between HA or other biomaterial coatings and metallic implants is important to ensure long-term fixation [149].

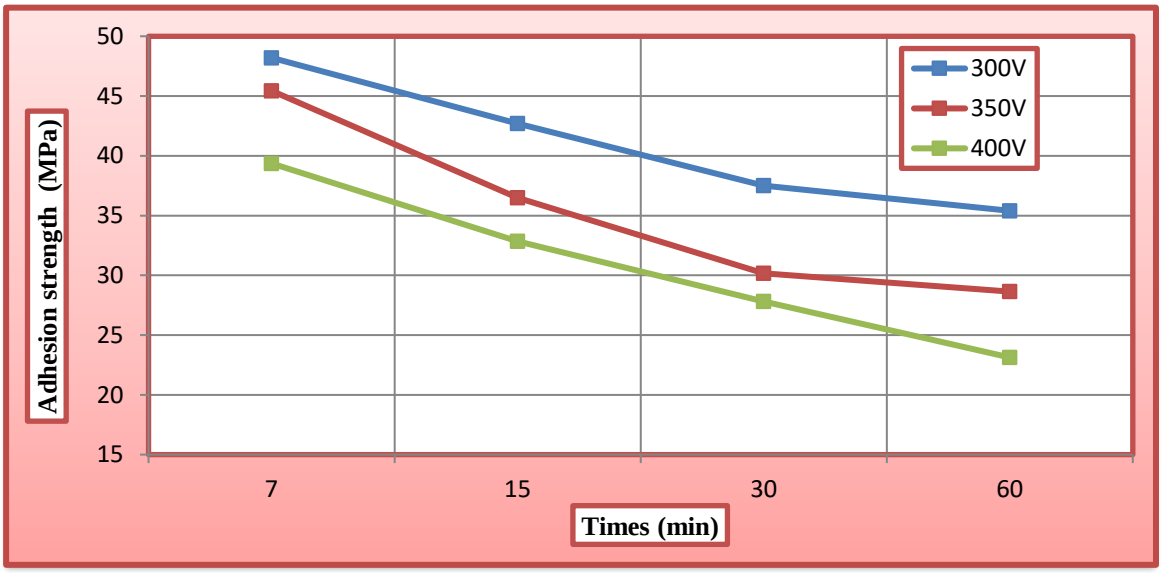

Figure (4.60): Relationship between adhesion strength and time of TiO_2 coating by MAO process with different parameters.

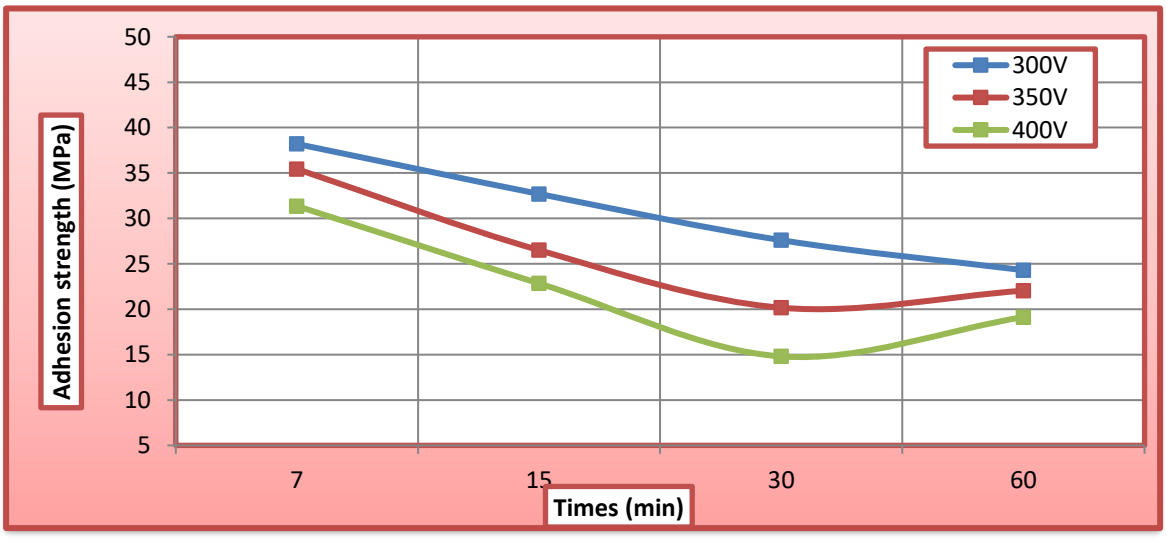

Figure (4.61): Relationship between adhesion strength and time of HA/TiO_2 coating by MAO process with different parameters.

In Figure (4.62), adhesion strength of ZrO_2/TiO_2 coating by MAO process show that decreased gradually, with increased voltage, time and thickness coating equal to (36.2MPa) for sample C_1 to (12.7MPa) for sample C_{12}. In Figure (4.63) show that lower adhesion strength of nanocomposite ceramic coating $HA/ZrO_2/TiO_2$ coating for sample D_1 equal to (28MPa) compared for other samples and decreased with thickness reached to (2.78 MPa) for sample D_{12}.

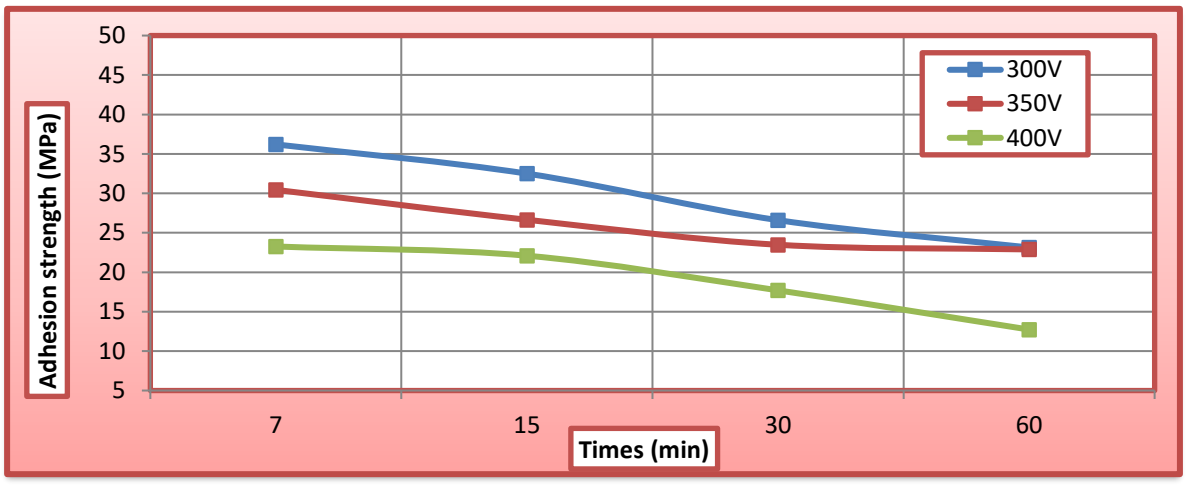

Figure (4.62): Relationship between adhesion strength and time of ZrO_2/TiO_2 coating by MAO process with different voltage.

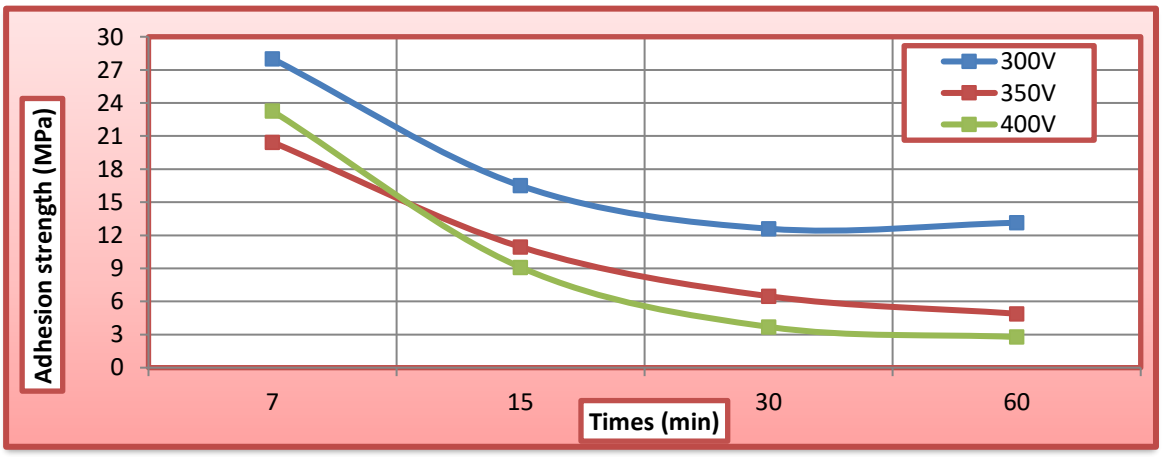

Figure (4.63): Relationship between adhesion strength and time of $HA/ZrO_2/TiO_2$ coating by MAO process with different parameters.

4.7 Contact Angle Test

Contact angle is an important measurement method to evaluate material surface wettability was also found to be another important aspect in improving the bioactivity of titanium surfaces.

Figures (4.64-4.66) show the contact angles tested of TiO_2 by MAO coatings prepared at various voltages and deposition times in Ringer's and Saliva's solution. The contact angle of the specimen decreases dramatically after MAO treatment with increase of surface roughness and porosity. The contact angle reached value to (56.74° for sample A_1 in ringer's solution and 54.7° in saliva's solution) and decreased with increase voltage and deposition time reached to (0° for sample A_{12} in ringer solution and 3.1° in saliva solution). The increase wettability of the MAO treated because a large amount of micro/nano-pores formed on the oxidation coating surface caused its specific surface area to increase, which benefited water retention, MAO processing resulted in an uneven coating surface, increased roughness, increased absorbability, and decreased contact angles, all of which together affected the surface energy; and the OH and O_2 oxygen-containing groups formed on the coating surface effectively introduced hydrophilic groups, changing the number of polar groups on the coating surface and causing surface polarity to increase, resulting in an increase in the surface energy [150].

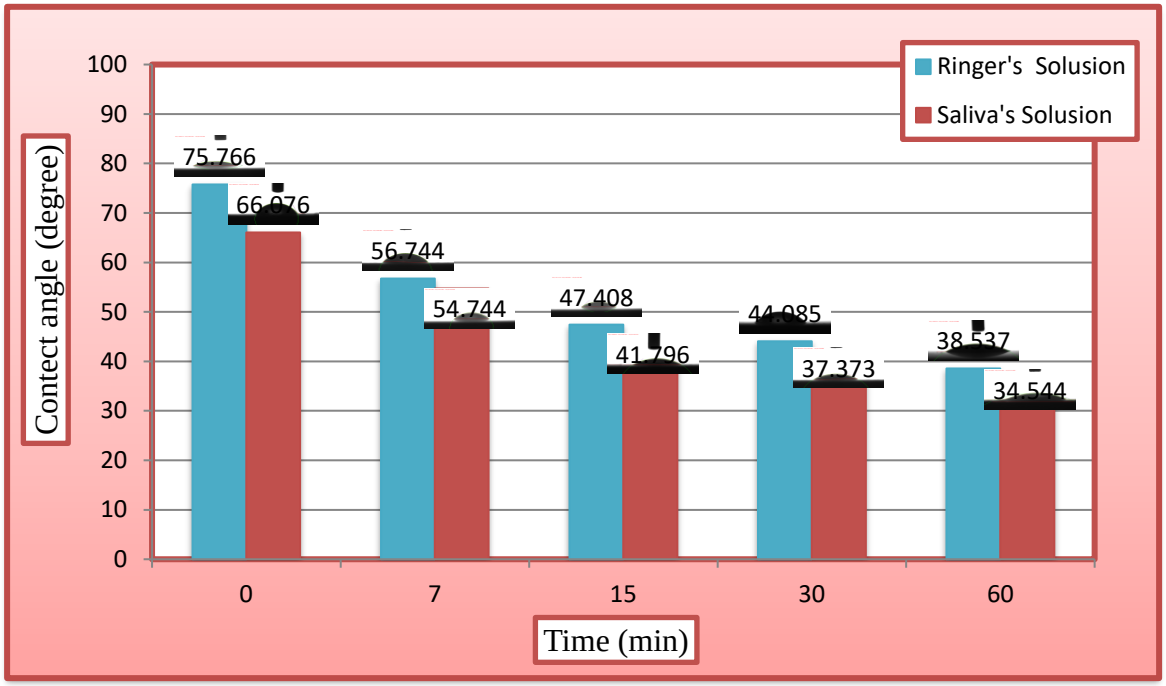

Figure (4.64): Results of contact angle in TiO_2 at 300V in Ringer's and Saliva's solutions.

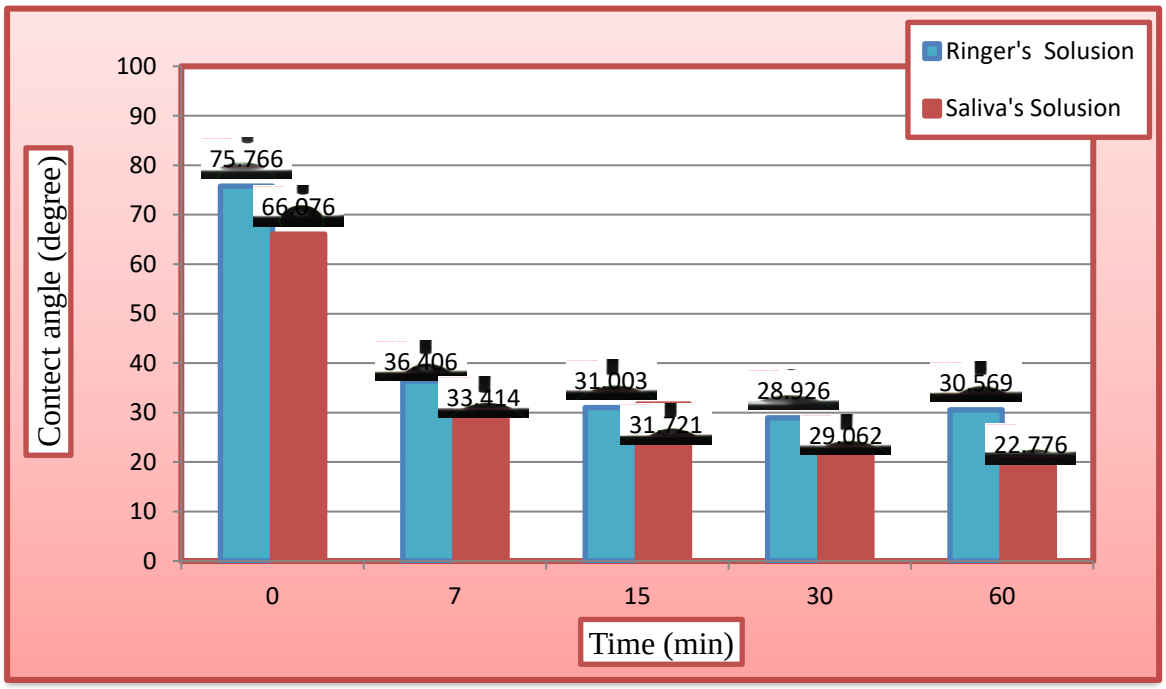

Figure (4.65): Results of contact angle in TiO_2 at 350V in Ringer's and Saliva's solution.

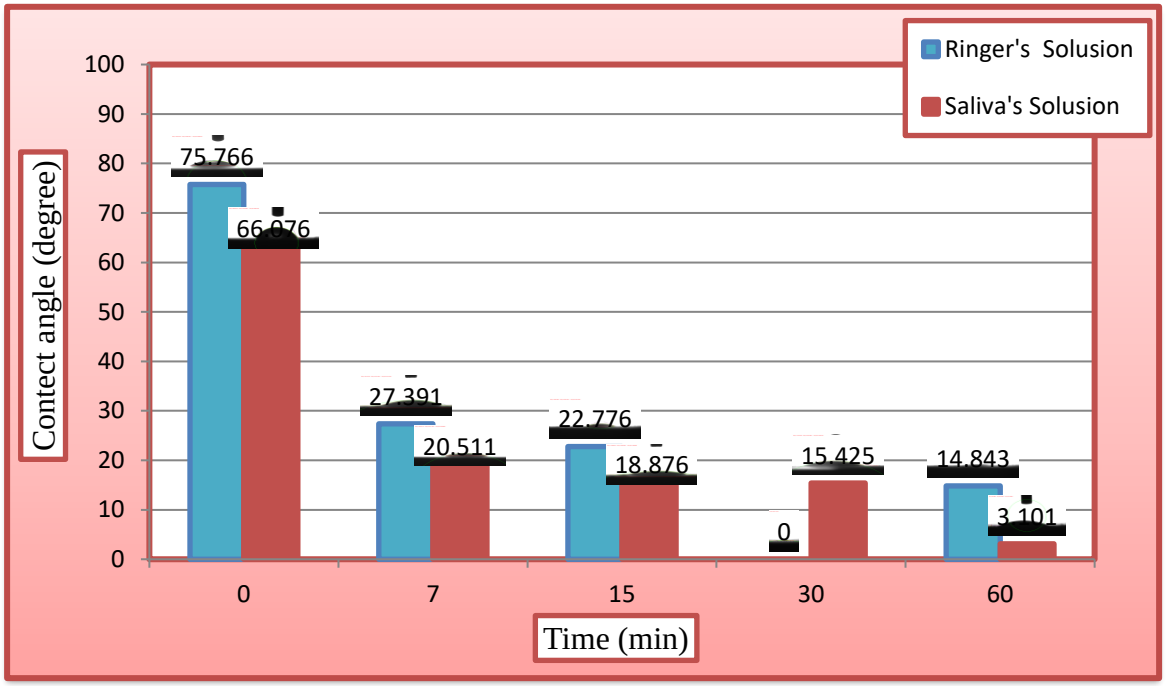

Figure (4.66): Results of contact angle in TiO_2 at 400V in Ringer's and Saliva's solution.

in Figures (4.67-4.69) the contact angle measurements of the nanocomposite ceramics coating HA/TiO_2 layered prepared by MAO are completely hydrophilic in this work, in (Ringer's & Saliva's) solution evaluate wetting properties of different parameters from about (6.726° and 5.912° for sample B_1) in Ringers and Saliva's solutions respectively, it can be seen the wetting angles of coatings are increased by increased voltage and time from (43.548° and 52.815° for sample B_{10}).

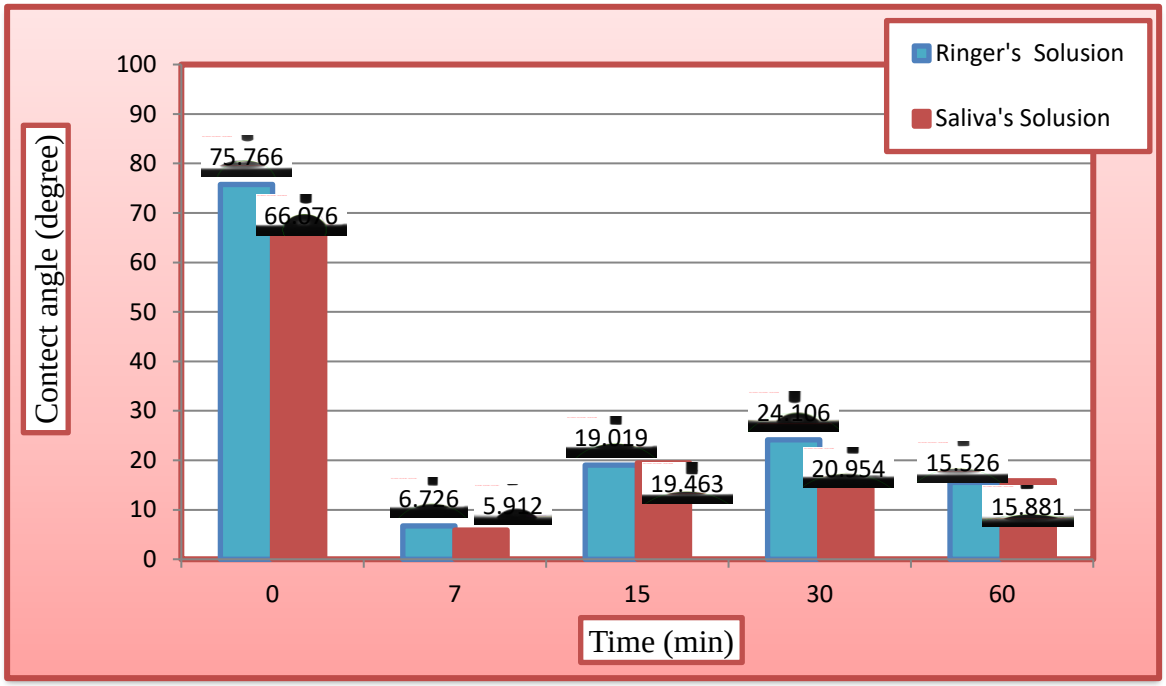

Figure (4.67): Results of contact angle in HA/TiO_2 at 300V in Ringer's and Saliva's solution.

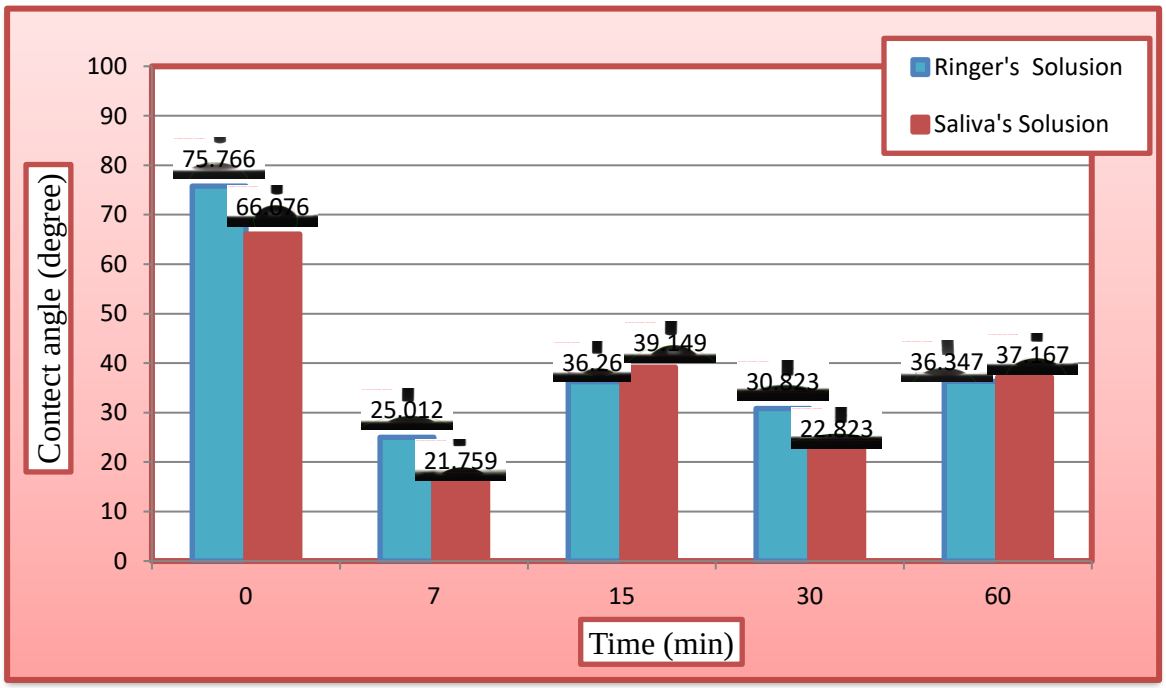

Figure (4.68): Results of contact angle in HA/TiO_2 at 350V in Ringer's and Saliva's solution.

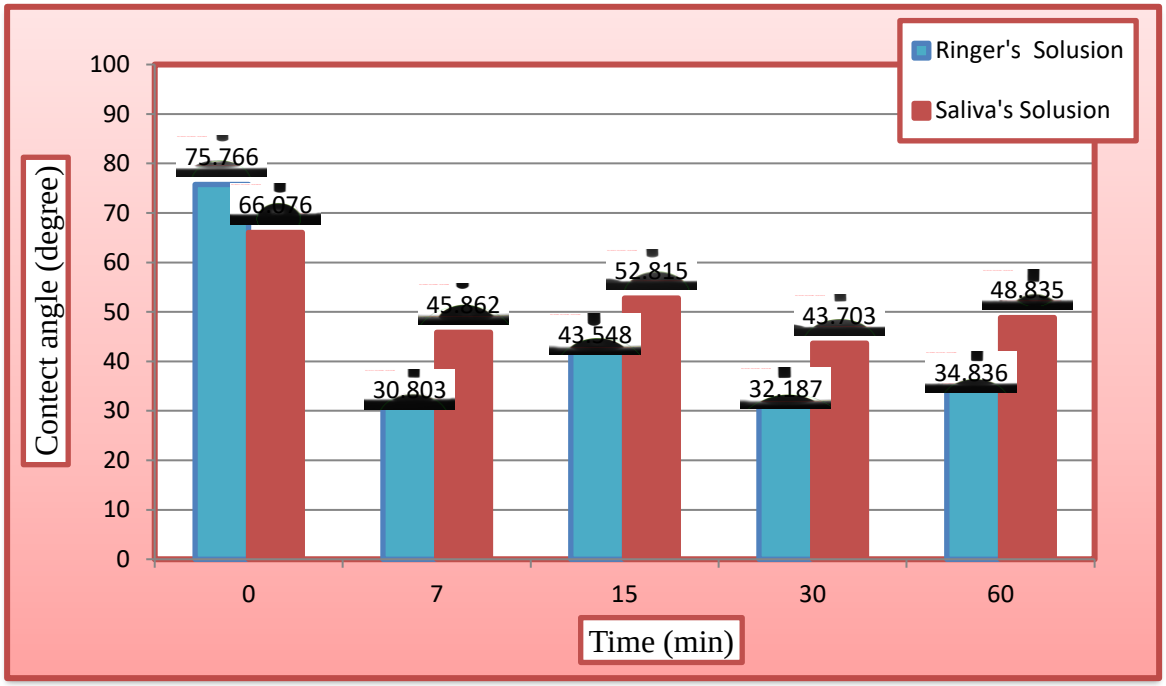

Figure (4.69): Results of contact angle in HA/TiO_2 at 400V in Ringer's and Saliva's solution.

Figure (4.70-4.72) contact angle on the surface of ZrO_2/TiO_2 prepared with different voltage and oxidation times equal to (11.667° in ringer's solution) and (0° in saliva's solution) for sample C_1 increase by increase voltage and time to (41.694° in ringer's solution) and (47.505° in saliva's solution) for sample C_{11} because the wettability is mainly determined by surface roughness and presence of nanoparticles of ZrO_2 in the electrolytic solution decreased the micro-pores. treated by MAO may be more helpful to shorten the bonding time between the implant and human cells [114].

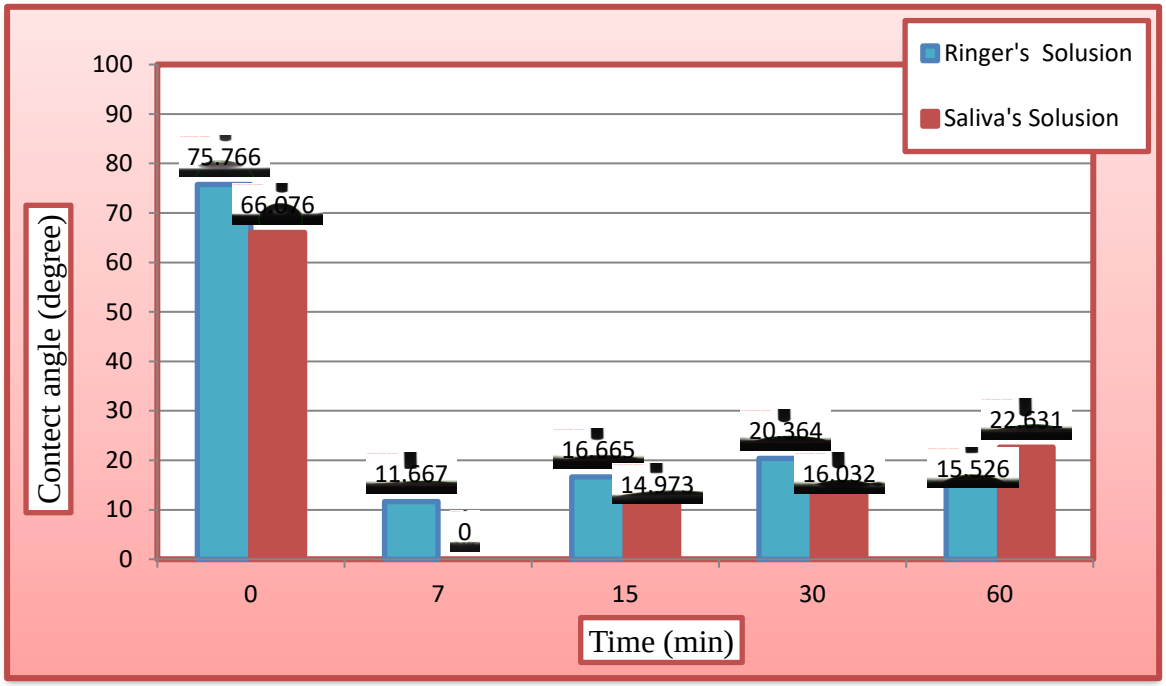

Figure (4.70): Results of contact angle in ZrO_2/TiO_2 at 300V in Ringer's and Saliva's solution.

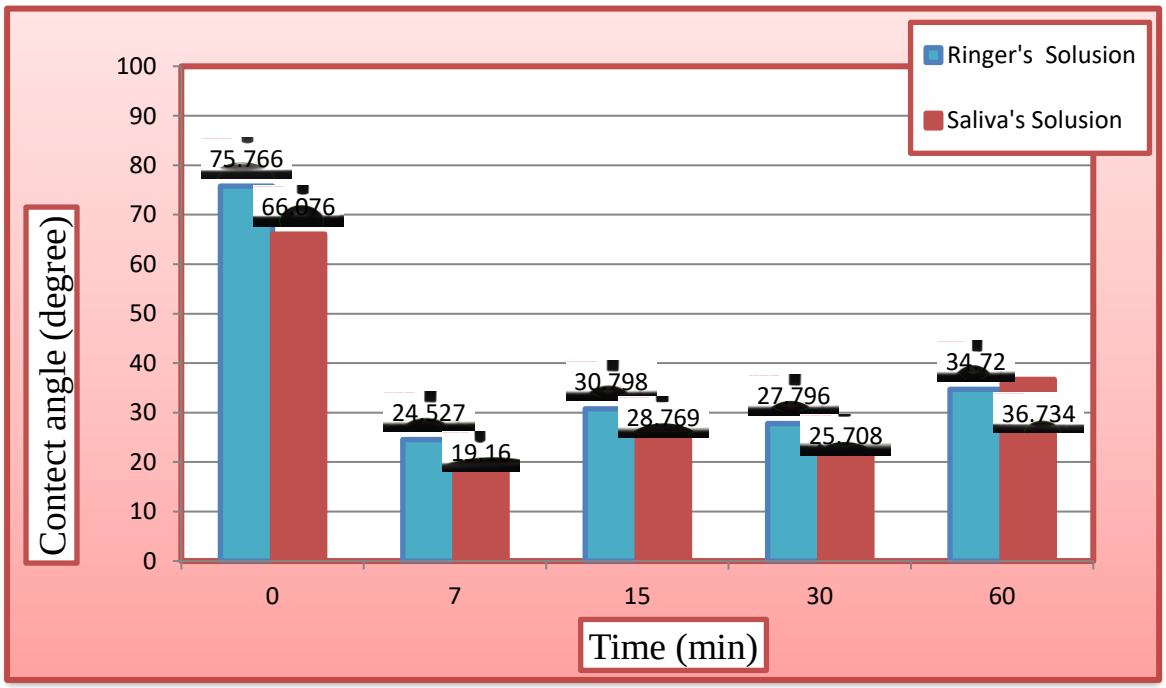

Figure (4.71): Results of contact angle in ZrO_2/TiO_2 at 350V in Ringer's and Saliva's solution.

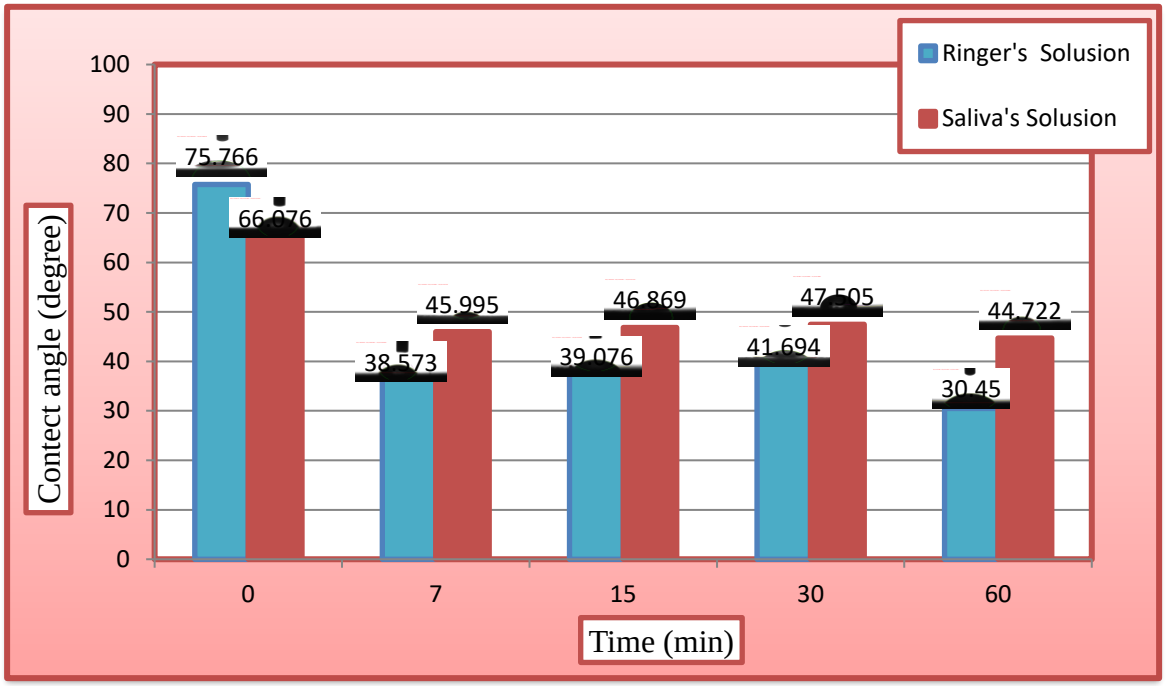

Figure (4.72): Results of contact angle in ZrO_2/TiO_2 at 400V in Ringer's and Saliva's solution.

Figure (4.73-4.75) increase the wettability and decrease contact angle by nanocomposite ceramics coating $HA/ZrO_2/TiO_2$ in both two solutions (Ringer's & Saliva's) equal to (15.414° and 13.536°) for sample D_1 compared uncoated alloys but increase voltage increased contact angle (24.451° and 23.818°) for sample D_3 and deposition time (39.838° and 41.128°) for sample D_{10} because decreased the porosity of the coating layer. High wettability may play a significant role in biocompatibility during implantation due to fast surface protein absorption after blood-implant contact. Antifouling properties of hydrophobic surface could induce additional antibacterial effects. On the other hand, it could decrease cell attachment to the surface. surface could induce additional antibacterial effects. On the other hand, it could decrease cell attachment to the surface [151, 152].

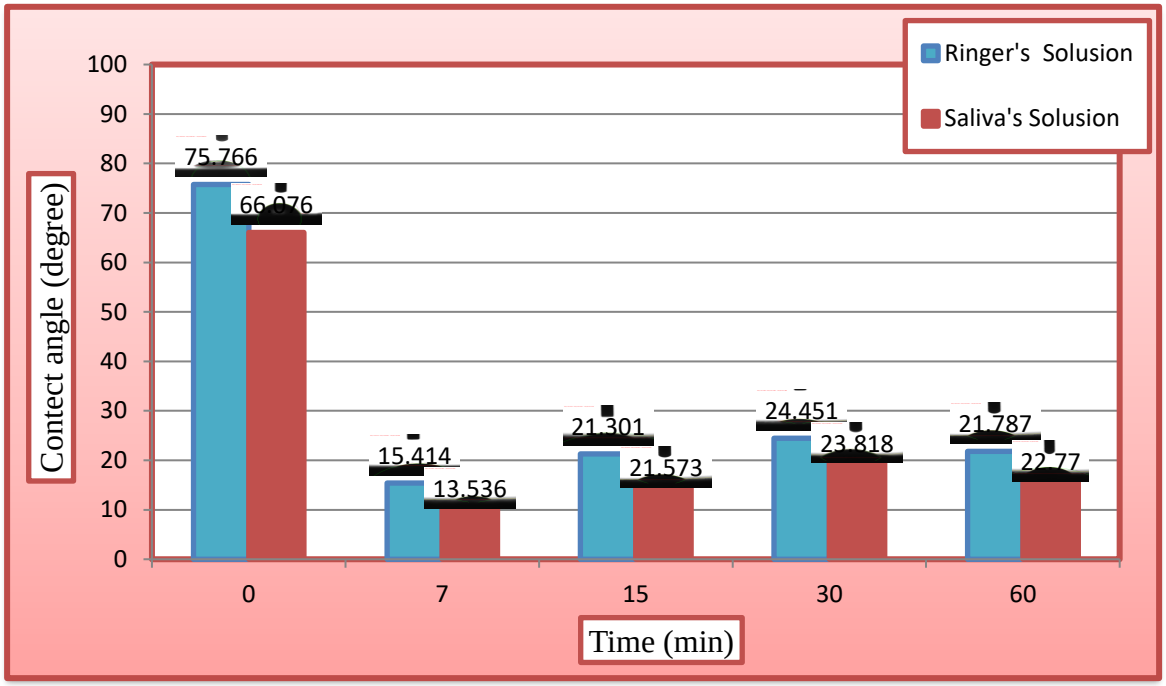

Figure (4.73): Results of contact angle at 300V in $HA/ZrO_2/TiO_2$ in Ringer's and Saliva's solution.

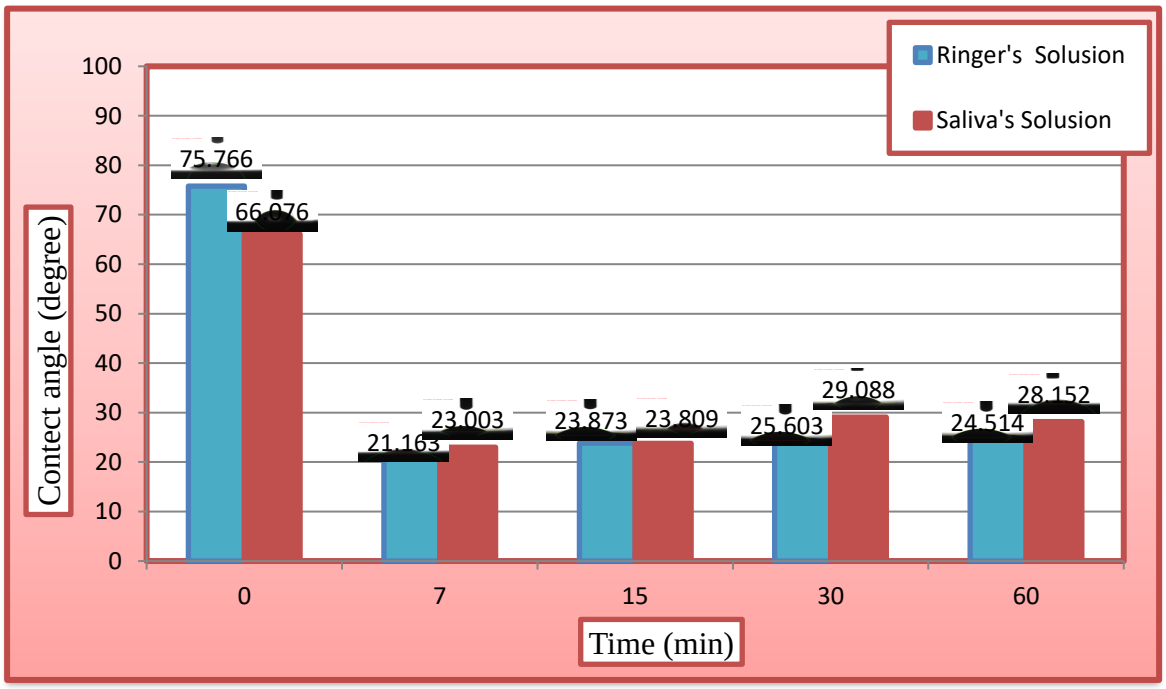

Figure (4.74): Results of contact angle at 350V in $HA/ZrO_2/TiO_2$ in Ringer's and Saliva's solution.

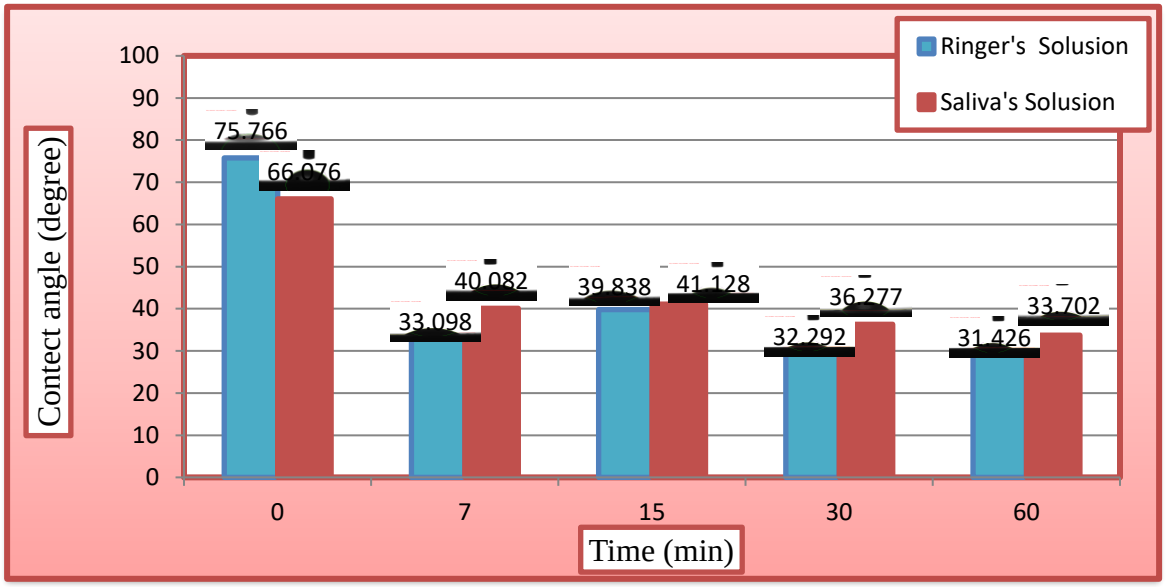

Figure (4.75): Results of contact angle at 400V in HA/ZrO_2/TiO_2 in Ringer's and Saliva's solution.

4.8 Corrosion Behavior Tests

Investigation of corrosion behavior of coating is obtained by potentiodynamic and cyclic polarization tests. At first, the sample is immersed in (Ringer's and Saliva's) solution and the open circuit potential (OCP) has been recorded after this period, where a steady state potential is attained. The corrosion behavior has been studied for both MAO parameters (voltage and time).

4.8.1 Open Circuit Potential (OCP)- Time Measurements

Open circuit potential (OCP) variations with time are related to the nature of reactions at the surface of the electrode when in contact with a specific medium (passivation, dissolution, or immunity) and therefore can be used as a criterion for corrosion behavior. Figure 4.76(a), and (b) shows the MAO variations with respect to voltage and time for the Ti6Al7Nb alloy and the corresponding comparison with uncoated alloy in (Ringer's & Saliva's) solution at 37±1C°. They indicate that this

change is related to the formation of an oxide film that passivates the metallic surface. On the other hand, OCP profiles for MAO treated samples exhibited very stable potentials during the test.

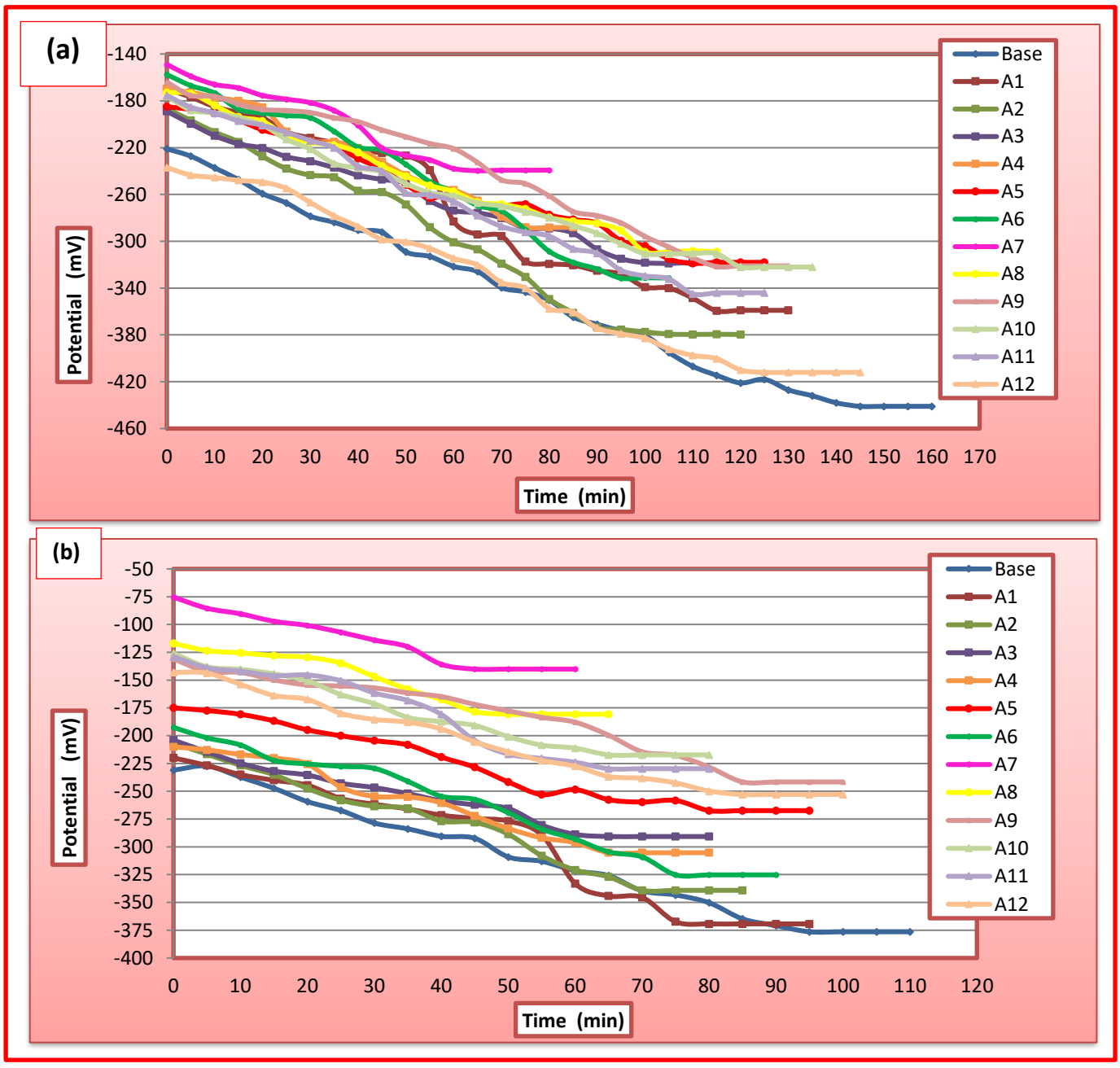

Figure (4.76): OCP-time of TiO_2 by MAO process: (a) in Ringer's solution, and (b) in Saliva's solution.

Figures 4.77(a), and (b) and 4.78 (a), and (b) show the OCP evolution for HA/TiO_2 and ZrO_2/TiO_2 nanocomposite ceramic coating by MAO process with different voltages and time in two solutions (Ringer's & Saliva's). They showed a stable scan with nobler potential values than non-coated sample while for the MAO sample, the OCP increased with the voltage and time until it stabilized at a stationary value more positive for sample B_{11}. A variety of parameters of the surface oxide films (composition, phases, and structural defects as porosity and cracking) could explain the different susceptibility to degradation of the modified surface. In Figure 4.79 (a), and (b), the OCP values are measured to $HA/ZrO_2/TiO_2$ nanocomposite ceramics coating by MAO process. The higher of the sedimentation time or the voltage value, the more inert.

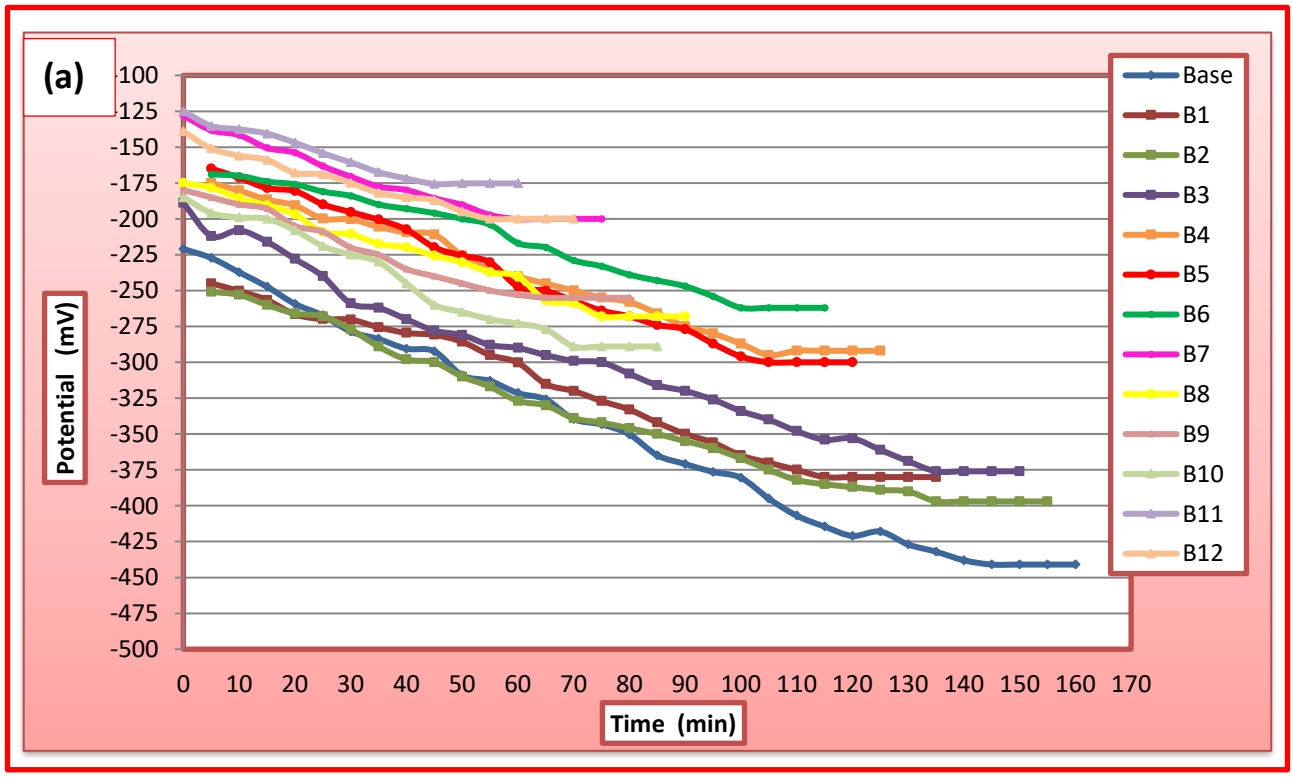

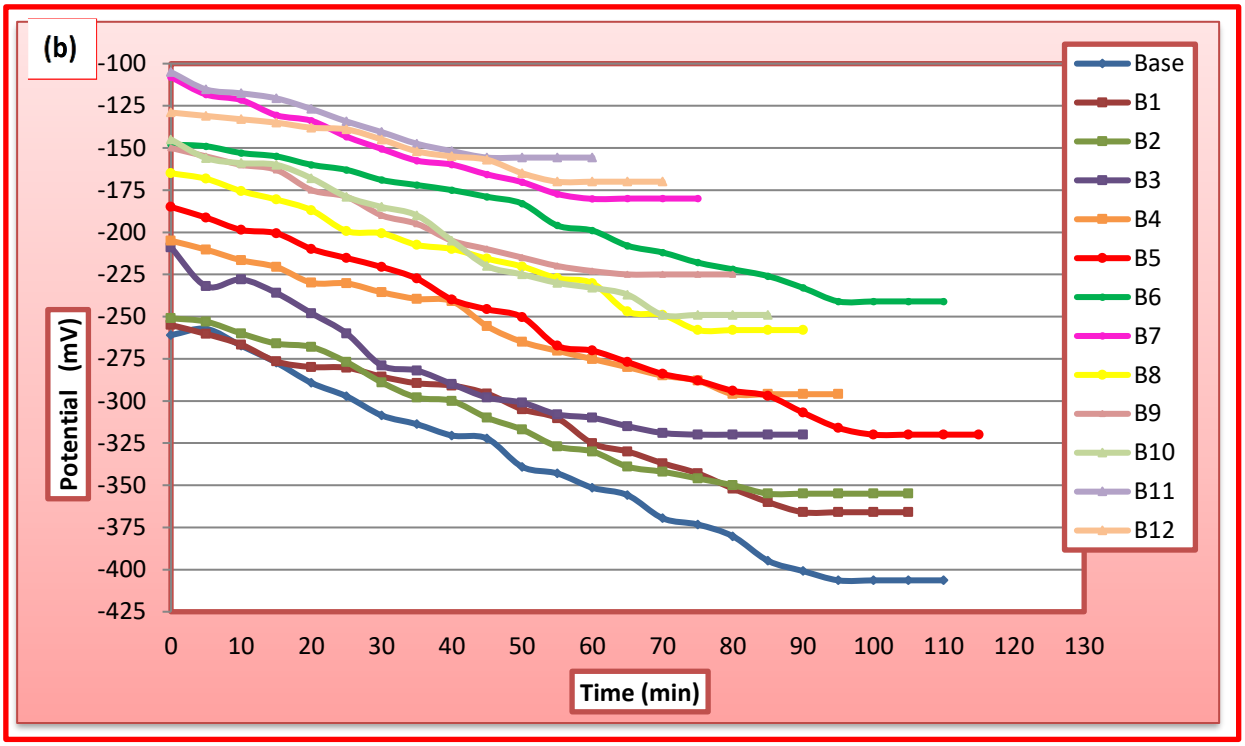

Figure (4.77): OCP-time of HA/TiO_2 by MAO process: (a) in Ringer's solution, and (b) in Saliva's solution.

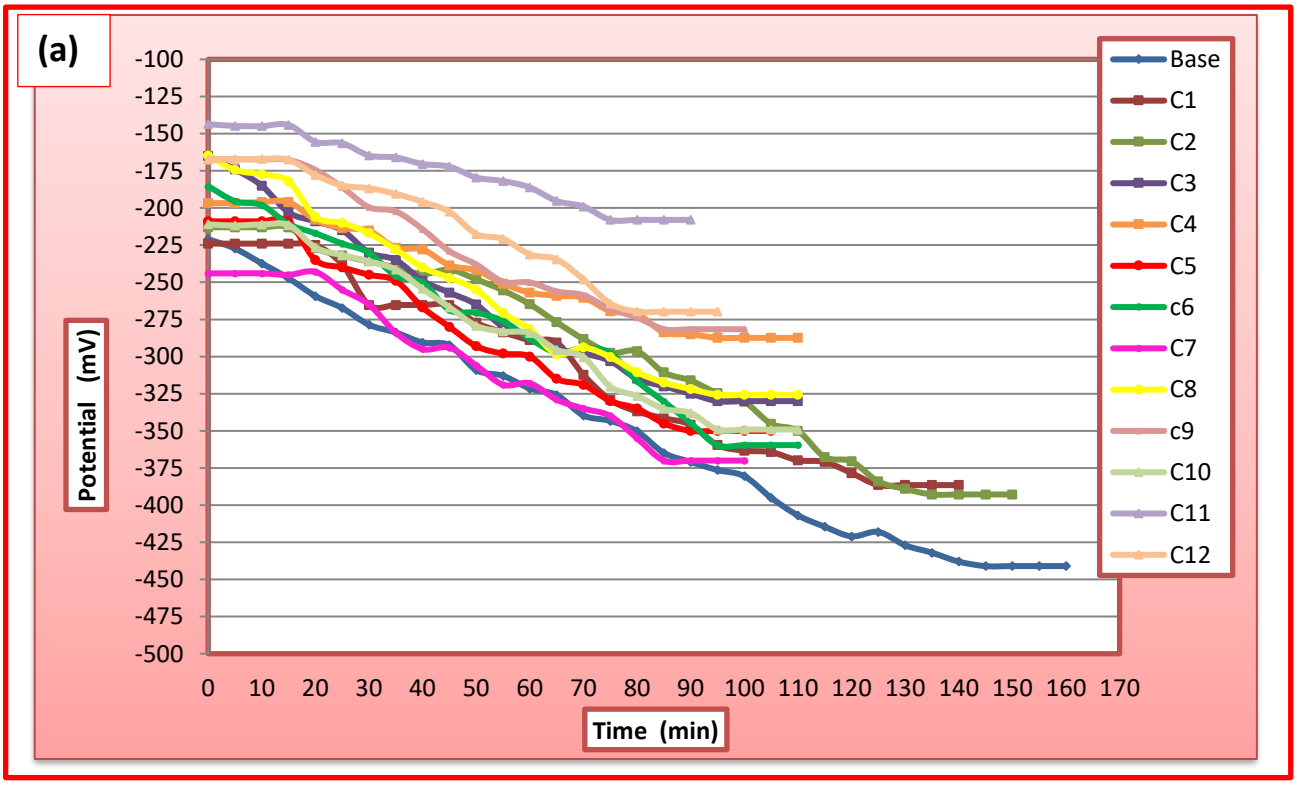

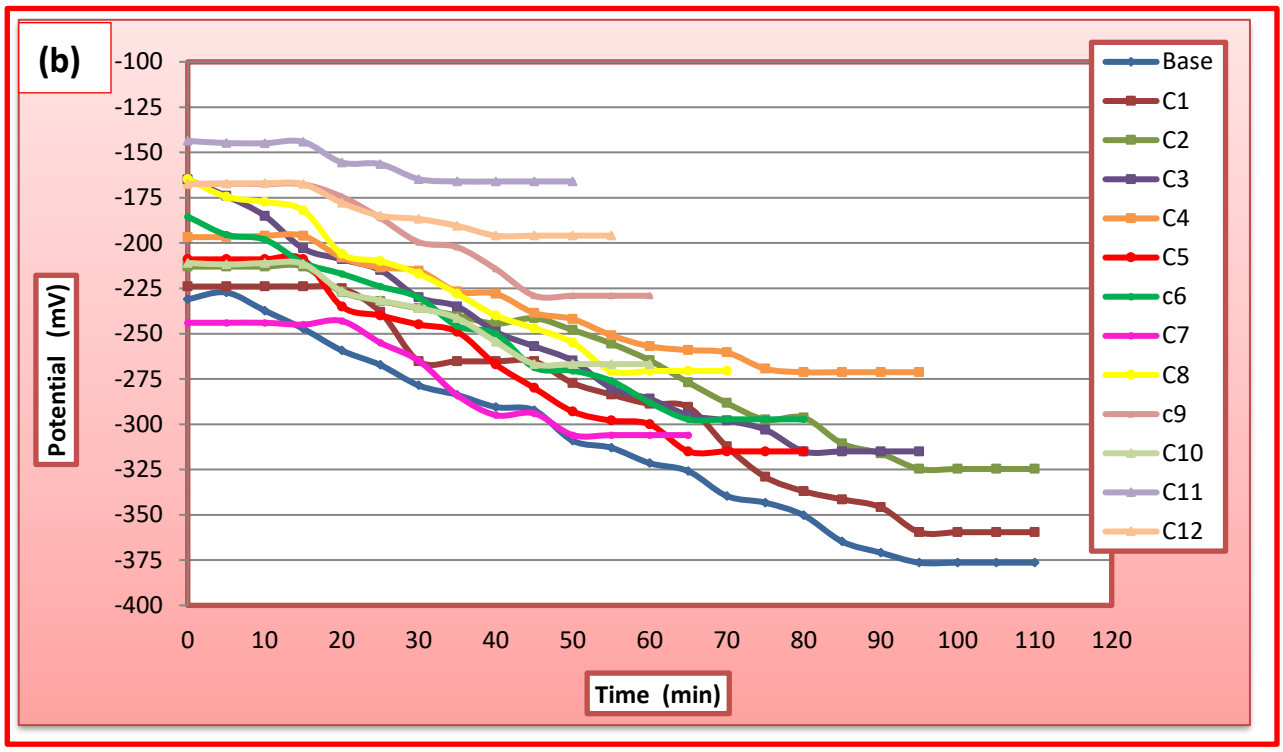

Figure (4.78): OCP-time of ZrO_2/TiO_2 by MAO process: (a) in Ringer's solution, and (b) in Saliva's solution.

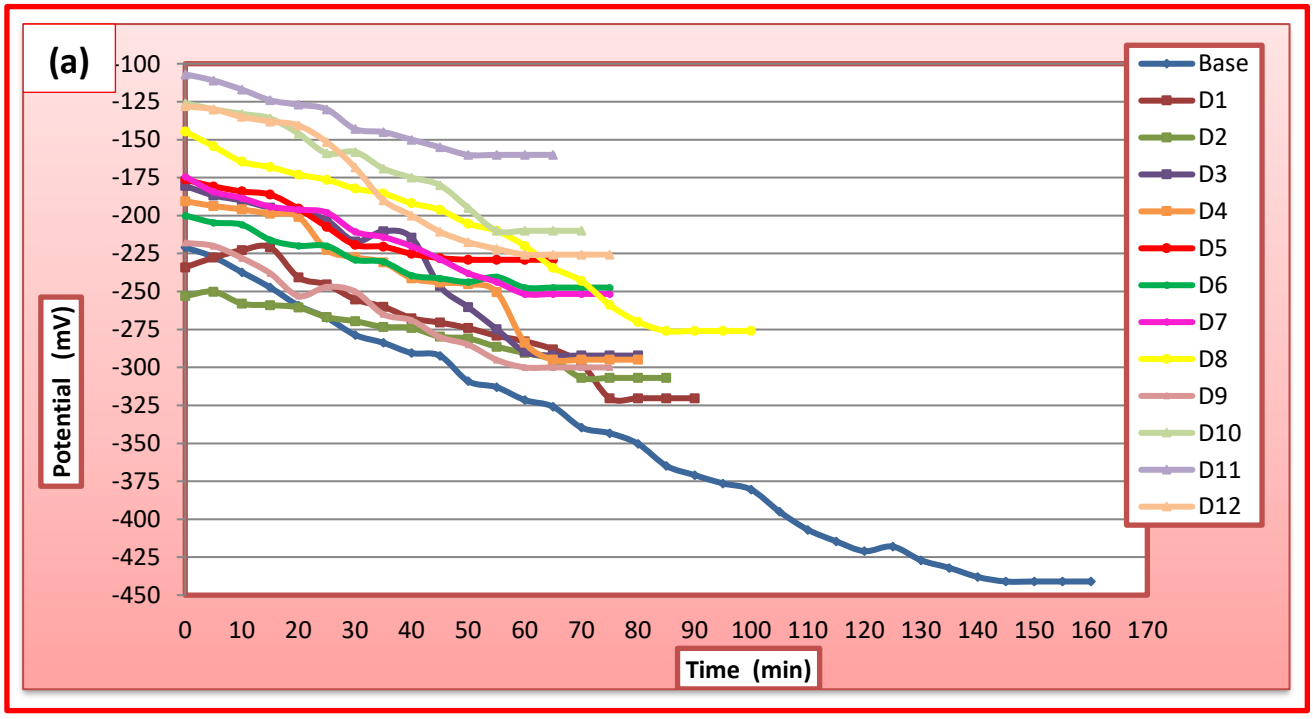

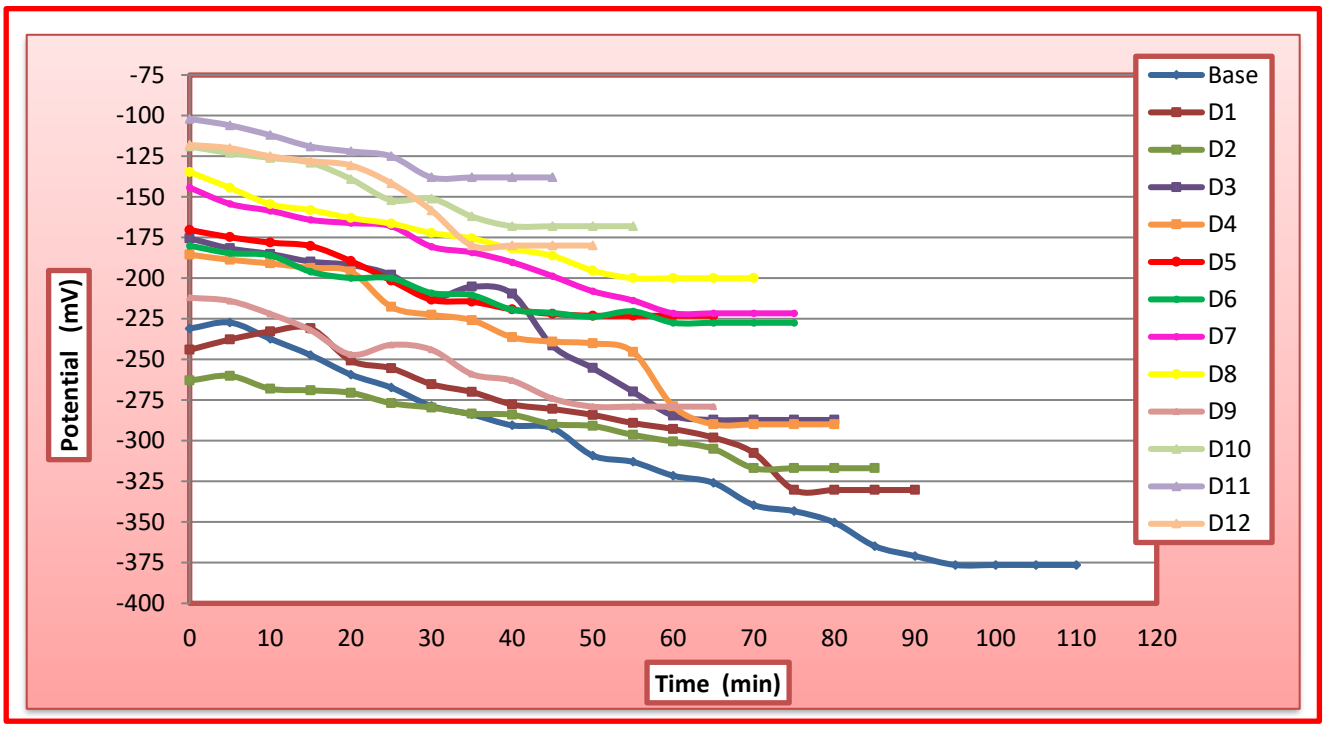

Figure (4.79): OCP-time of HA/ZrO_2/TiO_2 by MAO process: (a) in Ringer's solution, and (b) in Saliva's solution.

4.8.2 Potentiodynamic Polarization

Figures (4.80-4.82) shows the potentiodynamic polarization curves for the Ti-6Al-7Nb alloy substrate and TiO_2 coated by MAO process samples in the Ringer's solution at 37°C±1 for a different applied voltages and time. The corrosion current densities ($i_{corr.}$) and corrosion potentials ($E_{corr.}$) are derived from the potentiodynamic curves by employing Tafel extrapolation and it is listed in Table (4.6). In addition, the corrosion rates (C_R) were also included in this Table, and it calculated according to the equation (3.3).

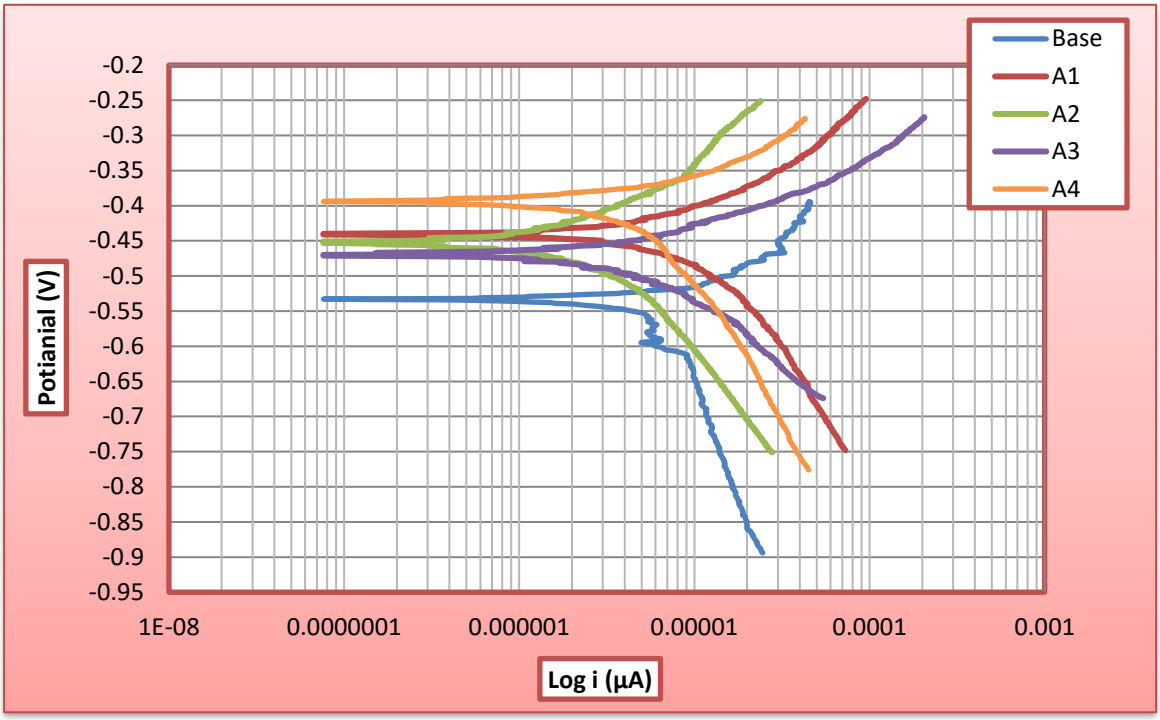

Figure (4.80): Potentiodynamic polarization curves of TiO_2 coated by MAO process and base at different time and applied voltages 300V in Ringer's solution.

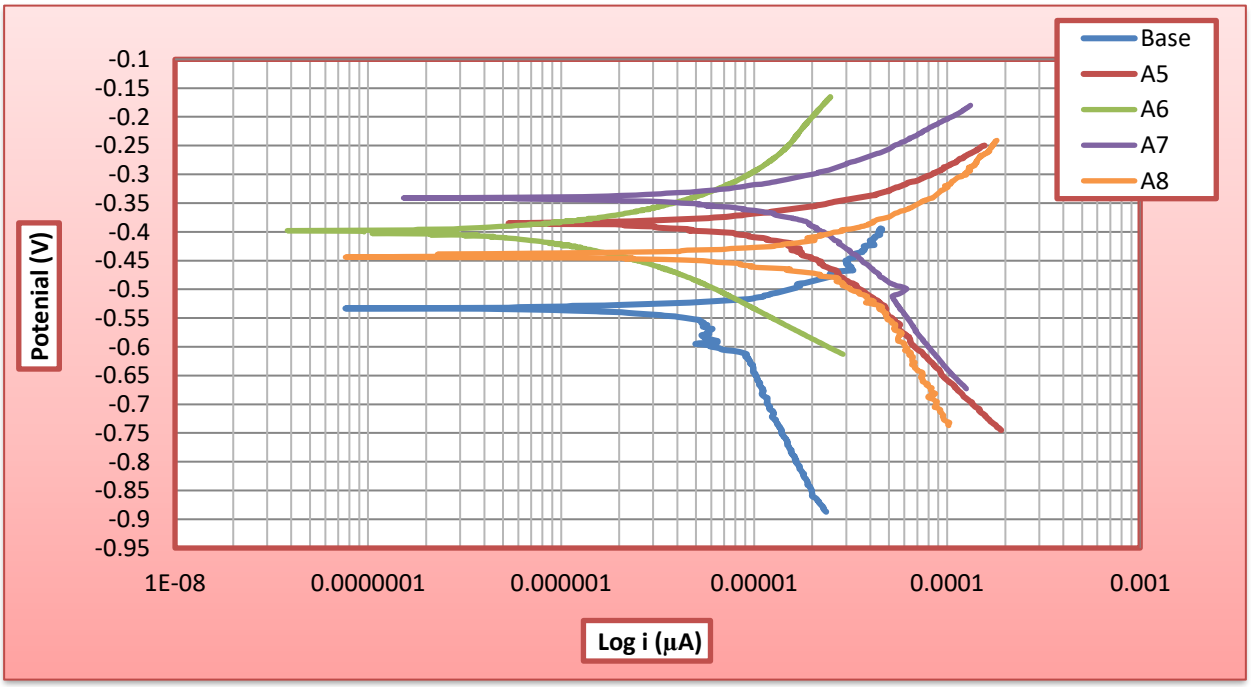

Figure (4.81): Potentiodynamic polarization curves of TiO_2 coated by MAO process and base at different time and applied voltages 350V in Ringer's solution.

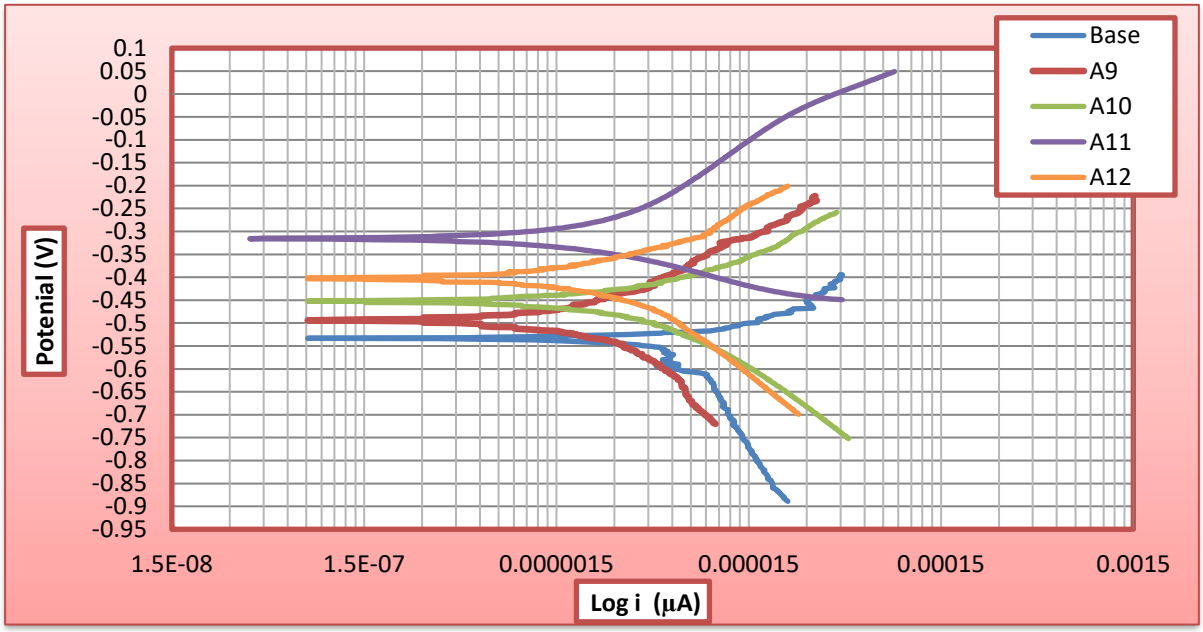

Figure (4.82): Potentiodynamic polarization curves of TiO_2 coated by MAO process and base at different time and applied voltages 400V in Ringer's solution.

Table (4.6): Electrochemical parameters of substrate and TiO_2 coated MAO at different applied voltages and time in Ringer's solution.

Sample Code	OCP (mV)	$I_{corr.}$ (µA)	$i_{corr.}$ (µA/cm^2)	$E_{corr.}$ (mV)	C_R*10^{-3} (mpy)	Improvement percentage(%)
Base	-441	9.059	6.8284	-533	8.437	/
A_1	-359	6.599	4.9741	-440	6.146	27
A_2	-379	5.574	4.2015	-450	5.191	38.5
A_3	-318	3.988	3.006	-490	3.714	56
A_4	-288	3.736	2.8161	-342	3.48	58.7
A_5	-318	1.439	1.0846	-385	1.34	84
A_6	-331	1.235	0.9309	-410	1.15	86
A_7	-239	0.1197	0.0902	-341	0.1114	98
A_8	-308	1.397	1.053	-438	1.3	85.6
A_9	-321	3.568	2.6894	-485	3.323	60.6
A_{10}	-310	2.709	2.0419	-452	2.523	70
A_{11}	-344	1.810	1.3643	-390	1.686	80
A_{12}	-397	1.811	1.3650	-405	1.68	79.8

It can be seen from the results obtained in Table (4.6), the uncoated substrate has higher corrosion current density (i_{corr}= 6.8284 µA/cm^2) and thus lowest corrosion resistance because of the occurrence of metal ions dissolution on the surface of the uncoated substrate. After coating by TiO_2, it can be observed that the corrosion current density of all coated samples by MAO decreases and corrosion rate, this mean that the TiO_2 coating provides a protective layer on the substrate surface that would reduce the corrosion rate. When coating at 300 V in Figure (4.80) and this Table (4.6), a lowest corrosion current ($i_{corr.}$= 4.9741, 4.2015, 3.006, and 2.8161 µA/cm^2) for samples (A_1, A_2, A_3, and A_4) and the increases corrosion potential of the specimens is obtained and this result has the lowers corrosion rate equal to (C_R= 3.48 ×10^{-3} mpy) for sample A_4 therefore, corrosion resistance is enhanced. In addition, the surface structure of the film also affects the corrosive properties of the material. Denser and thicker oxide layers can make materials generally exhibit better corrosion resistance as shown Figure (4.81) decreased corrosion current density and corrosion rate reached ($i_{corr.}$= 0.0902µA/cm^2), (C_R=0.1114×10^{-3} mpy) respectively, for sample A_7 at (350V & 30min). With increased voltage to (400V) in Figure (4.82) shows that porosity affected the corrosion behavior of highly porous with high voltage where decreased corrosion resistance because increased $i_{corr.}$ (2.6894, 2.0419, 1.3643, and 1.3650) µA/cm^2 and C_R (3.323, 2.523, 1.686, and 1.68) 10^{-3}mpy for samples (A_9, A_{10}, A_{11}, and A_{12}).

The corrosion behavior of porous metallic materials has in the present work, the oxygen/air entrapped in the most inner pores neither the difficulty of electrolyte penetration into these pores, which may lead to different passive states on the native oxide film. Nevertheless, the corrosion rate of highly porous structures is not just influenced by the surface area. Although Ti is known for its high resistance to localized corrosion, and the localized breakdown of its passive film occurs at relatively

higher potentials, stated that the increased corrosion density with the increased porosity level is due to the larger surface area in contact with the electrolyte, but crevices or restrictions to the flow of species into the interconnected pores can result in corrosion rates that are not proportional to the real contact surface area. Although these difficulties may result in increased corrosion kinetics, excellent passivation characteristics are still reported in the literature for porous Ti structures.

On the other hand, also reported decreased corrosion susceptibility (less negative values of $E_{corr.}$) with increasing amount of porosity, since the interconnected pores promoted the free flow of ionic species, whereas isolated pores trapped the electrolyte and exhausted the oxygen supply, resulting in a thinner oxide film. Apart from electrolyte penetration, entrapped air, and free flow of species [153].

The corrosion behavior in Saliva's solution of the alloy and coated samples (A) TiO_2 by MAO process in Figures (4.83-4.85) respectively, and Table (4.7), it is clear, that the specimen showed relatively similar behavior to that observed in saliva's solution such as MAO process for alloy improved corrosion resistance because of reduction in corrosion current [154].

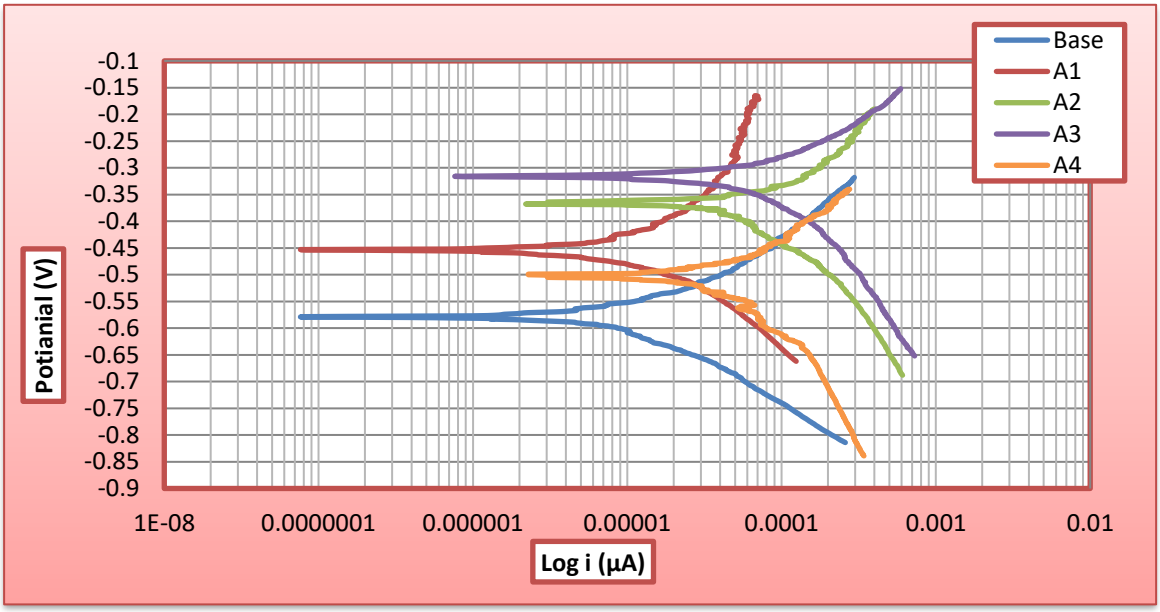

Figure (4.83): Potentiodynamic polarization curves of TiO_2 coated on Ti-6Al-7Nb alloy by MAO process and base at different time and applied voltages 300V in Saliva's solution.

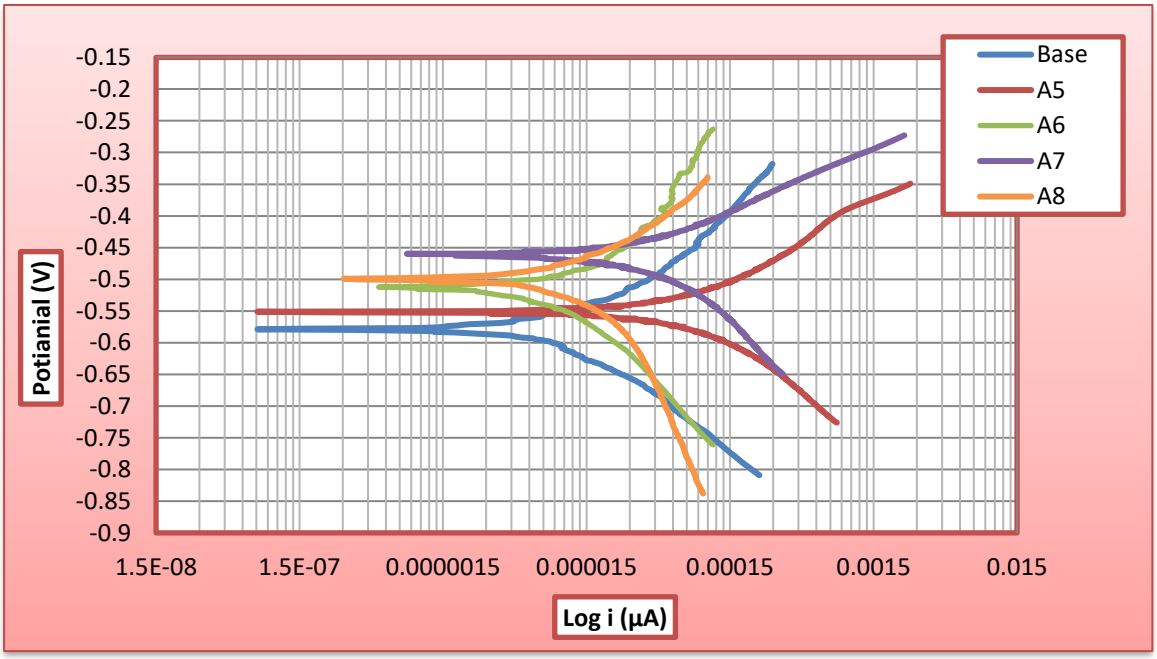

Figure (4.84): Potentiodynamic polarization curves of TiO_2 coated on Ti-6Al-7Nb alloy by MAO process and base at different time and applied voltages 350V in Saliva's solution.

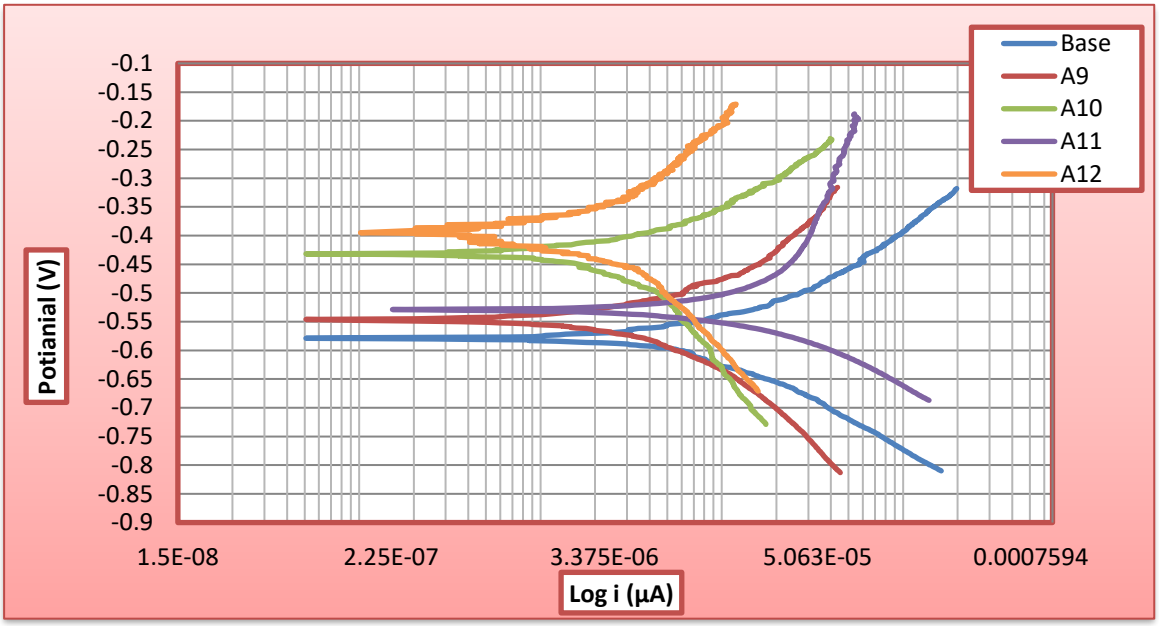

Figure (4.85): Potentiodynamic polarization curves of TiO_2 coated on Ti-6Al-7Nb alloy by MAO process and base at different time and applied voltages 400V in saliva's solution.

Table (4.7): Electrochemical parameters of substrate and TiO_2 coated at different MAO applied voltages and time in Saliva's solution.

Sample Code	OCP (mV)	$I_{corr.}$ (µA)	$i_{corr.}$ (µA/cm^2)	$E_{corr.}$ (mV)	C_R*10^{-3} (mpy)	Improvement percentage(%)
Base	-376	9.424	7.103	-579	8.777	/
A_1	-369	8.991	6.777	-453	8.37	4.63
A_2	-339	8.425	6.350	-362	7.8	11.13
A_3	-290	5.781	4.357	-365	5.4	38.47
A_4	-305	4.616	3.479	-491	4.3	51
A_5	-241	1.587	1.196	-548	1.47	83.25
A_6	-217	1.309	0.986	-518	1.22	86.1
A_7	-140	1.106	0.833	-472	1.03	88.26
A_8	-252	1.301	0.980	-499	1.21	86.21
A_9	-267	4.327	3.261	-547	4	54.4
A_{10}	-325	3.865	2.913	-432	3.6	59
A_{11}	-229	1.599	1.205	-529	1.48	83.13
A_{12}	300	1.957	1.475	-392	1.8	79.5

It is clear from Table (4.6) and Table (4.7), that the specimens in Saliva's solution showed relatively higher corrosion rate compared to specimens in Ringer's solution and this is ascribed to changing the type of biological solution. From the results of the potential for various parameters for coating specimens we observed the best corrosion resistance for specimen A_7 at (350V & 30min) has lower corrosion current density ($i_{corr.}$=0.833μA/cm^2) and thus lower corrosion rate (C_R= 1.03×10^{-3} mpy). These results indicate stability behavior of TiO_2 coating with increased thickness coating but at high voltage (400V) increased porosity led to increased corrosion current density and corrosion rate, in Figure (4.85) $i_{corr.}$ equal to (3.261, 2.913, 1.205, and 1.475) μA/cm^2 and C_R (4, 3.6, 1.48, and 1.8) ×10^{-3} mpy for samples (A_9, A_{10}, A_{11}, and A_{12}).

One of the two aims of surface modification of medical alloys is to protect the surface against corrosion which needs a porosity free surface to reduce the active ion attachment to the base metal and the second aim is to create a rough and porous surface to enhance the tissue-implant bonding [155].

The potentiodynamic polarisation curves of the nanocomposite ceramics HA/TiO_2 coating by MAO process with different parameters (voltage and time) in the Ringer's solution in Figures (4.86-4.88) respectively, and Table (4.8). the HA/TiO_2 coated Ti-6Al-7Nb alloy showed coating provides a protective layer on the substrate surface that would reduce the corrosion rate (C_R) and current density ($i_{corr.}$) and increased corrosion potential ($E_{corr.}$). These results indicate stability behavior of HA/TiO_2 composite coating layer, so with increase of concentration of coating material the corrosion resistance increase. Along with an improvement of corrosion resistance, this HA/TiO_2 coating can change the properties of the surface on the materials without affecting the properties of the bulk [123].

The corrosion current and calculated corrosion rate are relatively measured of corrosion and illustrated how much material is lost during the corrosion process.

Hence, the higher current density and calculated corrosion rate cause more materials lost. HA/ TiO_2 composite coating can reduce corrosion rate of the coating implant in human body, hence reduce the metallic ions release.

The improvement corrosion resistance of HA/TiO_2 nanocomposite coating with increased voltage and time ($i_{corr.}$) equal to (5.349, 4.510, 3.441, and 4.229) µA/cm^2 for samples B_1, B_2, B_3, and B_4 and (C_R) (6.61, 5.573, 4.25, and 5.226) $\times 10^{-3}$mpy to (2.894, 2.669, 1.732, and 2.082) µA/cm^2 and (3.5, 3.23, 2.14, and 2.573)$\times 10^{-3}$mpy for sample B_5, B_6, B_7, and B_8 in Ringer′s solution. The best improvement corrosion resistance and percentage for specimen B_{11} at (400V and 30min) is (87.4%).

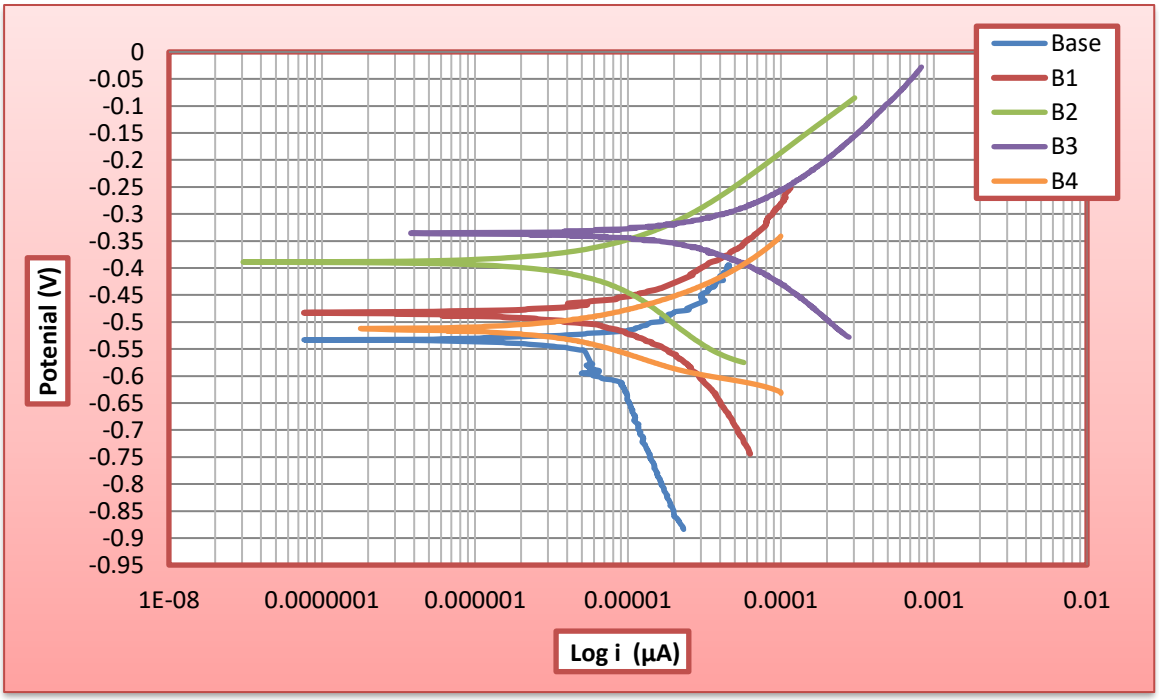

Figure (4.86): Potentiodynamic polarization curves of HA/TiO_2 coated on Ti-6Al-7Nb alloy by MAO process and base at different time and applied voltages 300V in Ringer's solution.

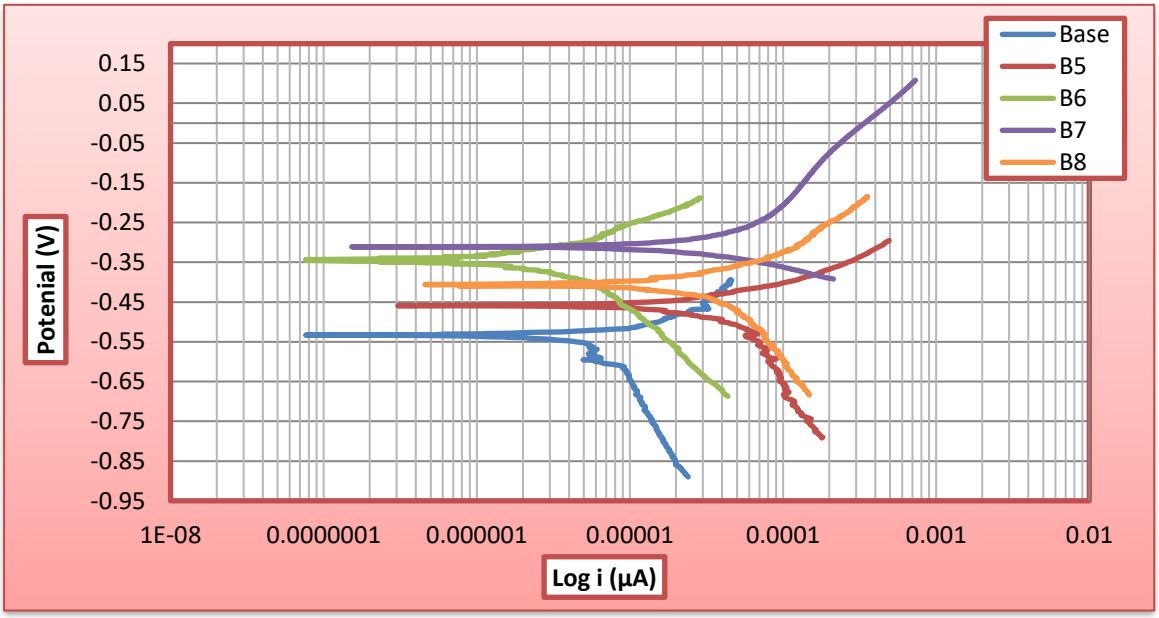

Figure (4.87): Potentiodynamic polarization curves of HA/TiO_2 coated on Ti-6Al-7Nb alloy by MAO process and base at different time and applied voltages 350V in Ringer's solution.

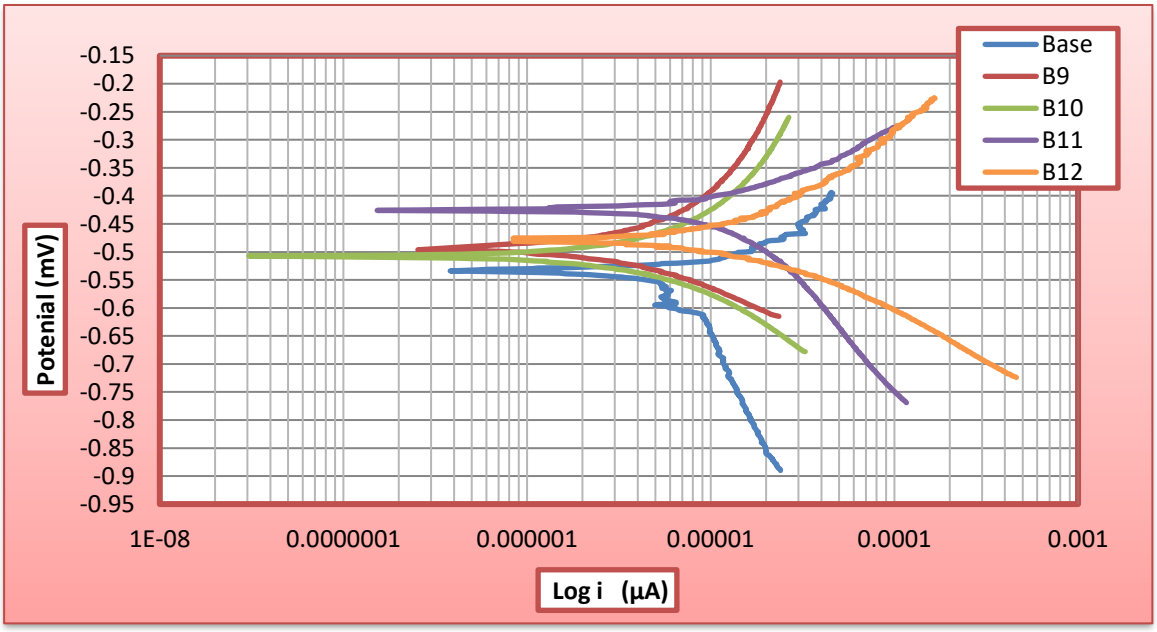

Figure (4.88): Potentiodynamic polarization curves of HA/TiO_2 coated on Ti-6Al-7Nb alloy by MAO process and base at different time and applied voltages 400V in Ringer's solution.

Table (4.8): Electrochemical parameters of substrate and HA/TiO_2 nanocomposite coated at different MAO applied voltages and time in Ringer's solution.

Sample Code	OCP (mV)	$I_{corr.}$ (µA)	$i_{corr.}$ (µA/cm^2)	$E_{corr.}$ (mV)	C_R*10^{-3} (mpy)	Improvement percentage (%)
Base	-441	9.059	6.828	-533	8.437	/
B_1	-497	7.097	5.349	-483	6.61	22
B_2	-397	5.984	4.510	-406	5.573	34
B_3	-376	4.566	3.441	-392	2.573	49.6
B_4	-292	5.611	4.229	-508	5.226	38
B_5	-300	3.840	2.894	-459	3.5	57.6
B_6	-262	3.542	2.669	-346	3.23	62
B_7	-200	2.298	1.732	-344	2.14	74.6
B_8	-268	2.763	2.082	-456	2.573	69.5
B_9	-255	1.854	1.397	-476	1.726	79.5
B_{10}	-289	1.632	1.230	-522	1.52	82
B_{11}	-175	1.136	0.856	-426	1.058	87.4
B_{12}	-200	1.196	0.901	-476	1.114	86.8

In Figures (4.89-4.91) respectively, the potentiodynamic polarisation carvers of HA/TiO_2 nanocomposite coating with different parameters of coating in Saliva's solution show that it is slimier behavior in two solutions. All samples excellent corrosion resistance. Showed the best improvement of corrosion resistance for sample B_{11} at (400V and 15min) is (87.83%). The specimens in saliva's solution showed relatively higher corrosion rate compared to specimens in ringer's solution and this is ascribed to changing the type of biological solution as shown in Tables (4.8) and (4.9). In cathodic polarization, the corrosion current decreases with increasing voltage until it reaches the lowest possible value. In anodic polarization, the corrosion current density increases with increasing voltage until it reaches voltage at which it decreases suddenly that due to the formation of passive film and with increasing voltage passive film broke and the current increases too.

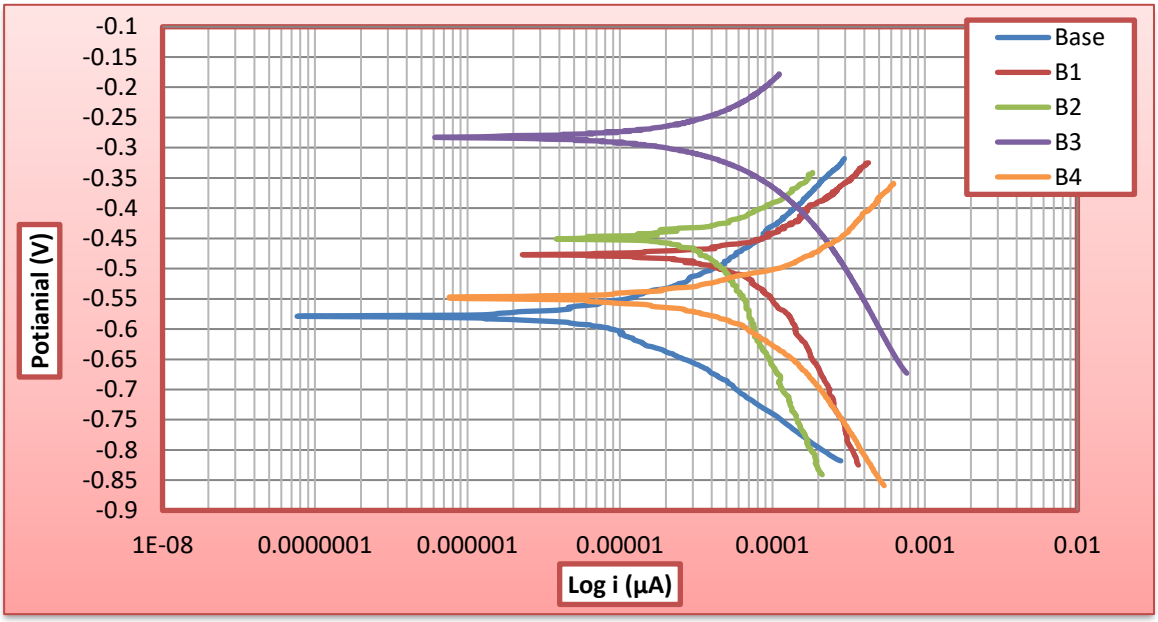

Figure (4.89): Potentiodynamic polarization curves of HA/TiO_2 coated on Ti-6Al-7Nb alloy by MAO process and base at different time and applied voltages 300V in Saliva's solution.

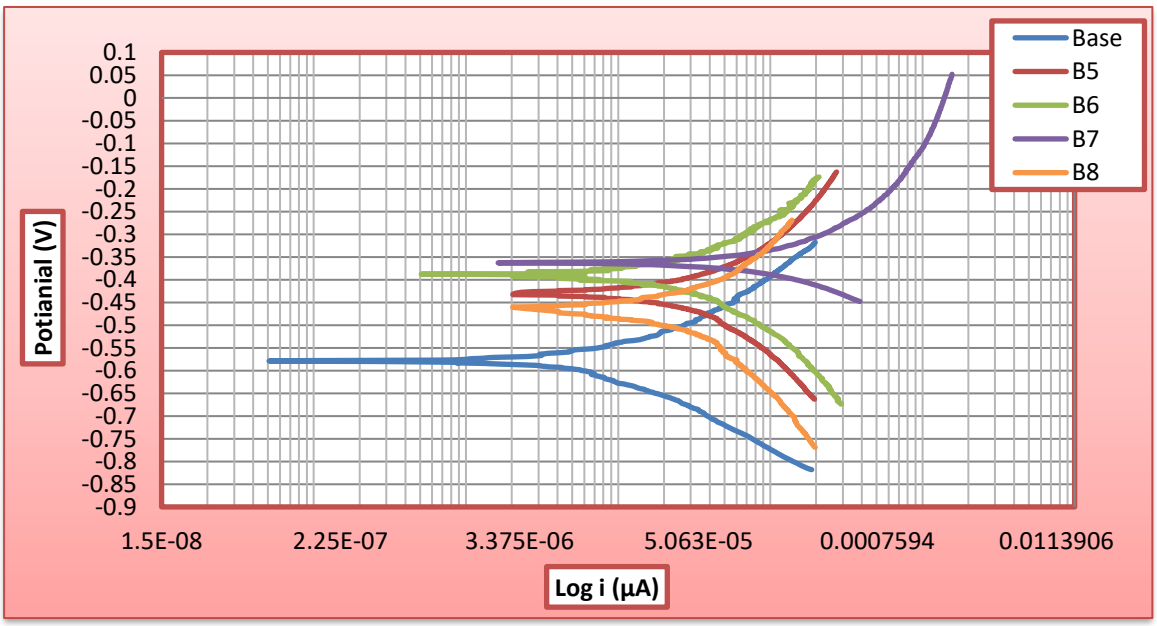

Figure (4.90): Potentiodynamic polarization curves of HA/TiO_2 coated on Ti-6Al-7Nb alloy by MAO process and base at different time and applied voltages 350V in Saliva's solution.

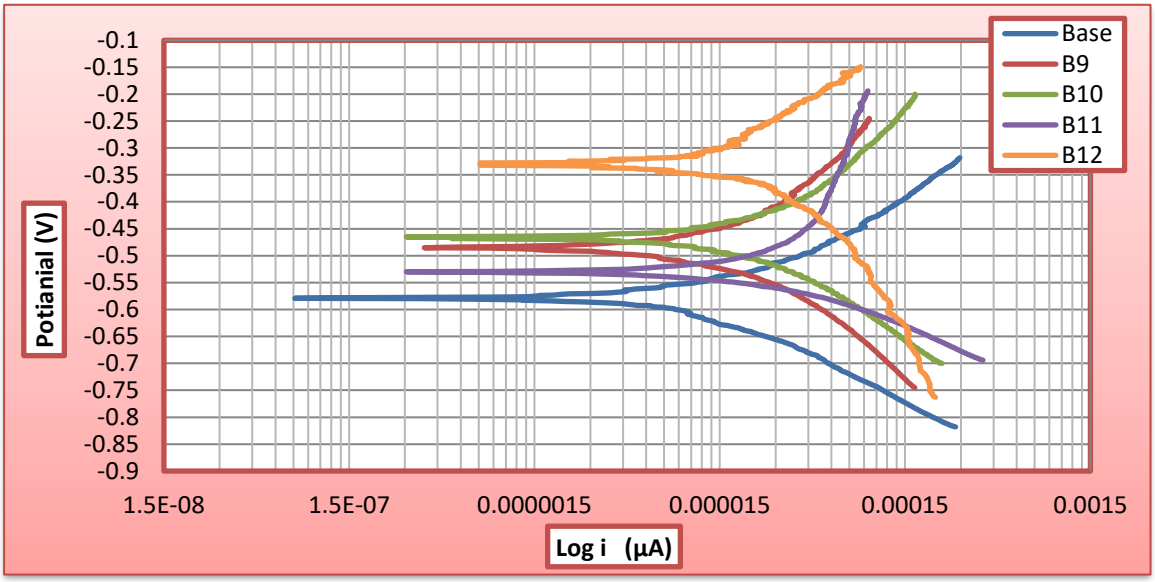

Figure (4.91): Potentiodynamic polarization curves of HA/TiO_2 coated on Ti-6Al-7Nb alloy by MAO process base at different time and applied voltages 400V in Saliva's solution.

Table (4.9): Electrochemical parameters of substrate and HA/TiO_2 nanocomposite coated at different MAO applied voltages and time in Saliva's solution.

Sample Code	OCP (mV)	$I_{corr.}$ (µA)	$i_{corr.}$ (µA/cm^2)	$E_{corr.}$ (mV)	C_R*10^{-3} (mpy)	Improvement percentage (%)
Base	-376	9.424	7.103	-579	8.777	/
B_1	-366	8.540	6.437	-477	7.95	9.42
B_2	-355	6.202	4.674	-419	5.776	31.19
B_3	-320	4.171	3.144	-316	4	54.44
B_4	-296	3.238	2.440	-548	3	65.8
B_5	-320	3.058	2.305	-427	2.85	67.5
B_6	-241	2.79	2.103	-390	2.56	70.8
B_7	-180	2.177	1.640	-377	2.02	74.6
B_8	-258	2.246	1.692	-463	2.1	76.9
B_9	-225	2.160	1.628	-480	2.01	77
B_{10}	-249	1.748	1.317	-515	1.628	81.45
B_{11}	-155	1.147	0.864	-485	1.068	87.83
B_{12}	-170	1.484	1.118	-330	1.38	84.2

Properties of HA gave a useful application in coating of porous metallic implants. After implantation of prostheses, a close surface contact between the metallic prosthesis and the surrounding bone tissue is needed for subsequent bone ingrowths. The presence of HA in the coating of the metallic implant leads to a rapid bonding between HA and surrounding bone tissue. Its application in coating implants combines the strength and toughness of the substrate with bioactive characteristics of HA which can induce the surrounding bone tissue ingrowths and future formation of chemical bonding.

The efficacy of the ZrO_2/TiO_2 nanocomposite ceramics coating by MAO process with different parameters (voltage and time) in the corrosion resistance, has been investigated in the Figures (4.92-4.94) respectively, in the Ringer's solution. When coating at (300V & 30min), a lowest corrosion current density ($i_{corr.}$= 3.377µA/cm^2) is obtained and this result highest corrosion resistance for sample C_3. Improvement in the corrosion resistance of the ZrO_2/TiO_2 coated strongly depends on the surface morphology and phases formed in composite film. Denser and thicker film with fine porosity is more useful for improving the corrosion resistance by inhibiting the attack from (Cl^-) ions in Ringer's solution [125]. It shows that in Table (4.10), with increased voltage and time increased corrosion resisters by decreased corrosion current density ($i_{corr.}$) from (1.673, 1.386, 1.231, and 1.257) µA/cm^2 and corrosion rate (C_R) equal (2.06, 1.712, 1.52, and 1.55) $\times 10^{-3}$ for sample C_5, C_6, C_7, and C_8 by increased concentration of ZrO_2 in the electrolytic. According to the surface and cross-sectional SEM micrographs of ZrO_2/TiO_2 composite coating with no obvious deep pores is formed on its surface. As a consequence, the film overlying on samples C_{11} ($i_{corr.}$=0.433µA/cm^2) shows highest protection efficiency against the corrosive ions present in physiological environment.

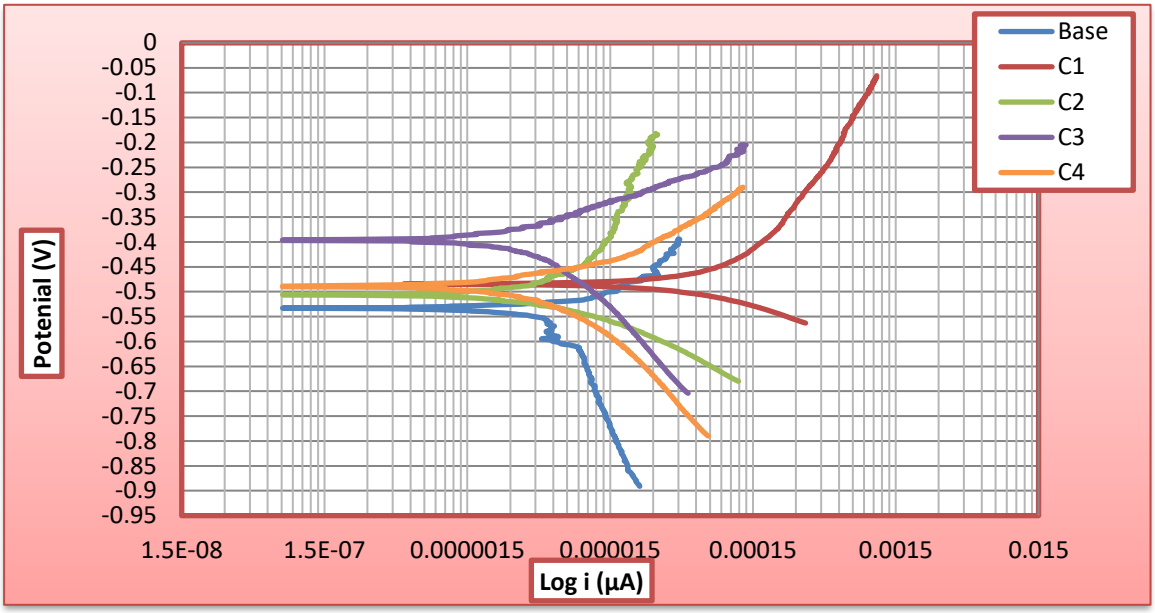

Figure (4.92): Potentiodynamic polarization curves of ZrO_2/TiO_2 coated on Ti-6Al-7Nb alloy by MAO process and base at different time and applied voltages 300V in Ringer's solution.

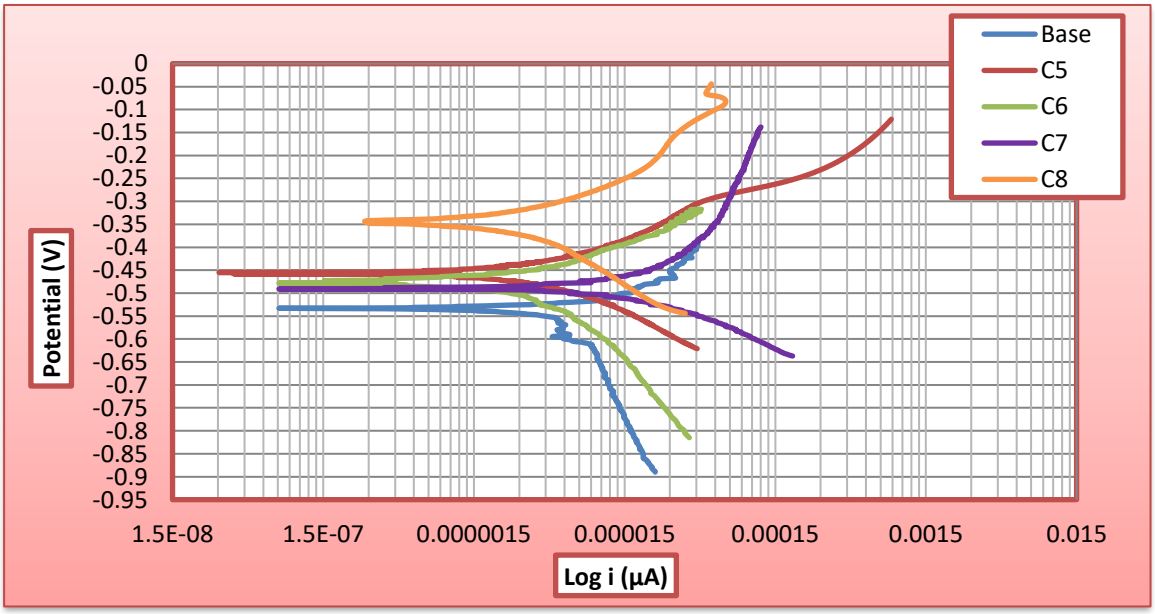

Figure (4.93): Potentiodynamic polarization curves of ZrO_2/TiO_2 coated on Ti-6Al-7Nb alloy by MAO process and base at different time and applied voltages 350V in Ringer's solution.

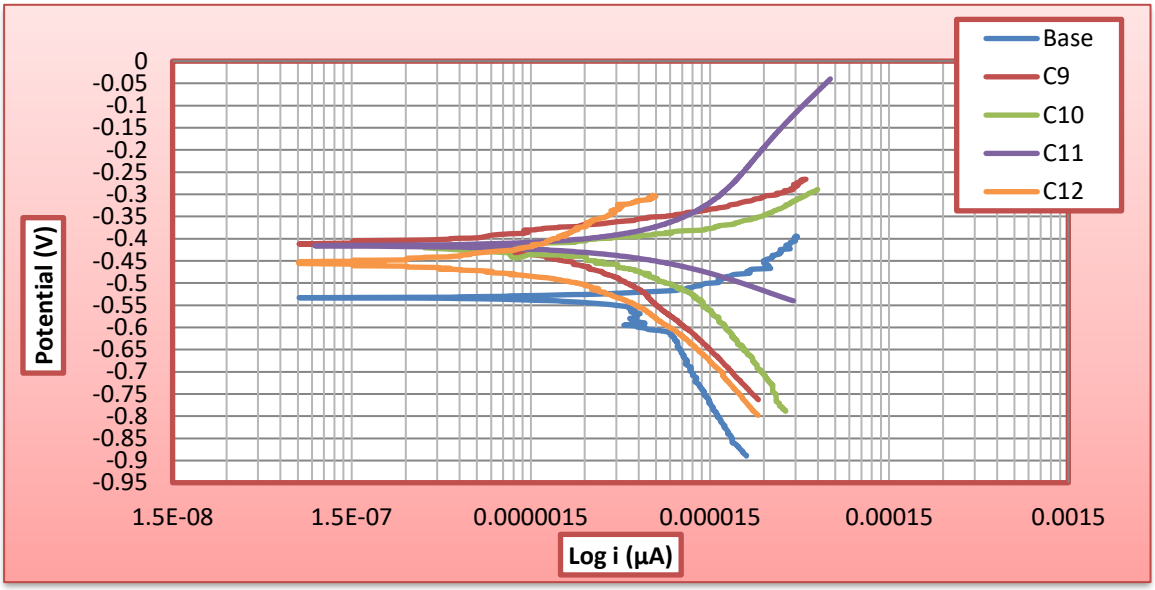

Figure (4.94): Potentiodynamic polarization curves of ZrO_2/TiO_2 coated on Ti-6Al-7Nb alloy by MAO process and base at different time and applied voltages 400V in Ringer's solution.

Table (4.10): Electrochemical parameters of substrate and ZrO_2/TiO_2 nanocomposite coated at different MAO applied voltages and time in Ringer's solution.

Sample Code	**OCP (mV)**	**$I_{corr.}$ (µA)**	**$i_{corr.}$ (µA/cm^2)**	**$E_{corr.}$ (mV)**	**C_R*10^{-3} (mpy)**	**Improvement percentage (%)**
Base	-441	9.059	6.828	-579	8.777	/
C_1	-386	7.311	5.510	-485	6.81	19.3
C_2	-392	6.128	4.619	-506	5.7	32.4
C_3	-330	4.481	3.377	-396	4.173	50.5
C_4	-287	4.522	3.408	-489	4.211	50
C_5	-350	2.220	1.673	-452	2.067	75.5
C_6	-359	1.839	1.386	-478	1.712	80
C_7	-370	1.634	1.231	-491	1.52	82
C_8	-325	1.668	1.257	-345	1.55	81.8
C_9	-281	1.437	1.083	-461	1.338	84
C_{10}	-349	1.158	0.872	-456	1.078	87.7
C_{11}	-208	0.5748	0.433	-422	0.5	94
C_{12}	-269	0.879	0.662	-430	0.8	90.5

Figures (4.95-4.97), corrosion behavior of the samples coated ZrO_2/TiO_2 at different voltage and time in Saliva's solution has a lower corrosion current density with corrosion rate is similar behavior in Ringer solution. This is due to thick and coarse ZrO_2/TiO_2 coated layer produced at higher deposition time and voltage during MAO process. On the other hand, the coating at 300 V has the lowest corrosion resistance ($i_{corr.}$= 2.240 µA/cm^2) for sample C_4 than the coating at (350 and 400)V, which equals (1.153 and 0.784) µA/cm^2 for sample C_7 and C_{11} respectively, in Table (4.11) as a result of the low layer thickness compared with the other samples. Moreover, the presence of porosity in the microstructure that allows the penetration of the corrosive fluid into the substrate and corrode it. The corrosion potential ($E_{corr.}$) for the coated samples raise toward values that are more positive when MAO voltage increase as it seen in Figure (4.97), rushed to ($E_{corr.}$= -168 mV) for sample C_{11}. This may be attributed to the increasing of coating thickness in balance with its porous structure.

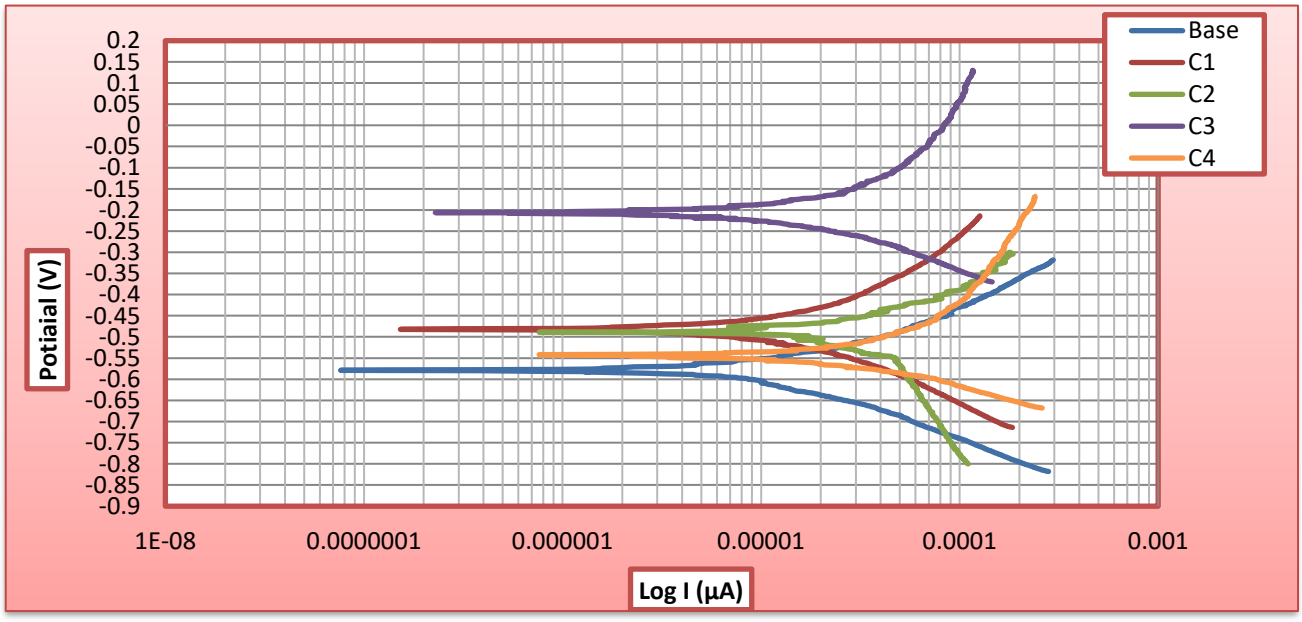

Figure (4.95): Potentiodynamic polarization curves of ZrO_2/TiO_2 coated on Ti-6Al-7Nb alloy by MAO process and base at different time and applied voltages 300V in Saliva's solution.

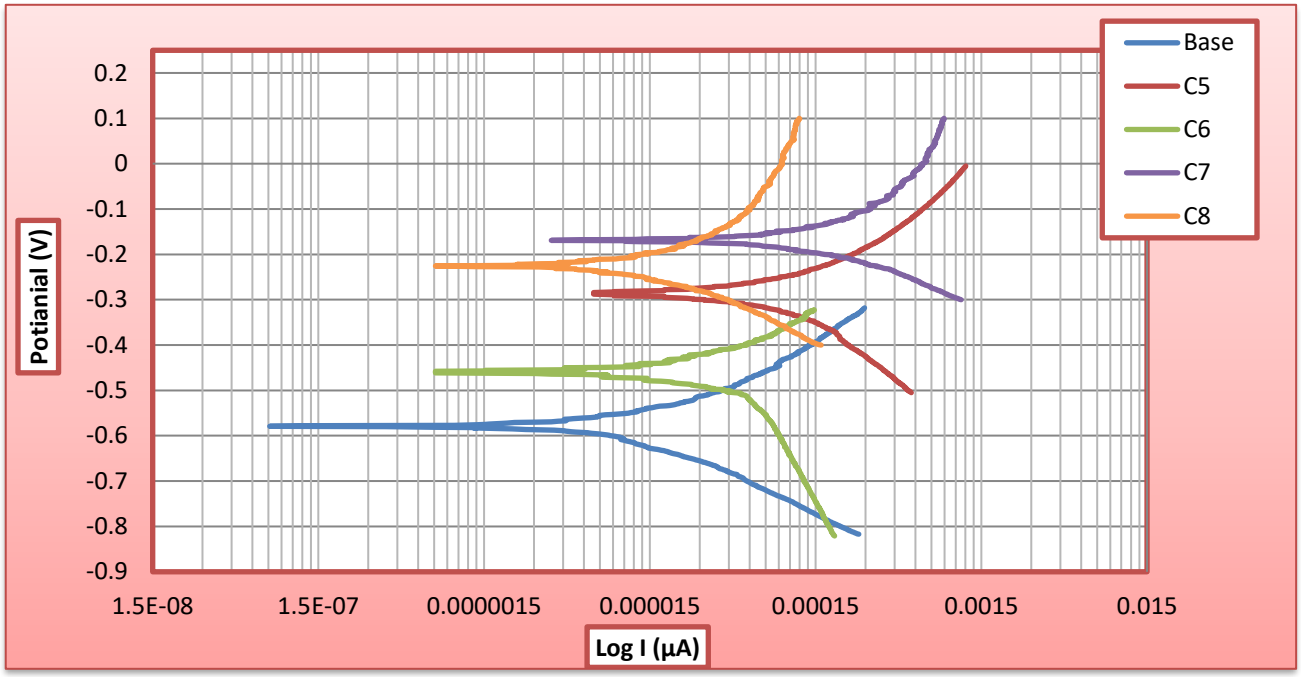

Figure (4.96): Potentiodynamic polarization curves of ZrO_2/TiO_2 coated on Ti-6Al-7Nb alloy by MAO process and base at different time and applied voltages 350V in Saliva's solution.

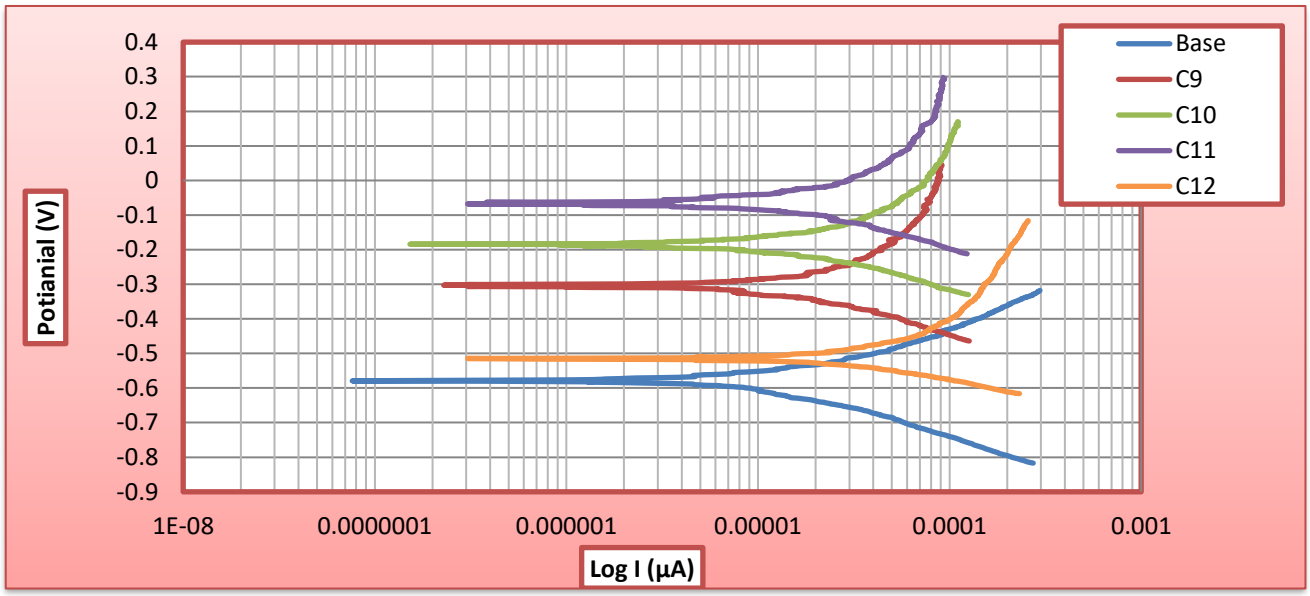

Figure (4.97): Potentiodynamic polarization curves of ZrO_2/TiO_2 coated on Ti-6Al-7Nb alloy by MAO process and base at different time and applied voltages 400V in Saliva's solution.

Table (4.11): Electrochemical parameters of substrate and ZrO_2/TiO_2 nanocomposite coated at different MAO applied voltages and time in Saliva's solution.

Sample Code	OCP (mV)	$I_{corr.}$ (µA)	$i_{corr.}$ (µA/cm^2)	$E_{corr.}$ (mV)	C_R*10^{-3} (mpy)	Improvement percentage (%)
Base	-376	9.424	7.103	-579	8.777	/
C_1	-359	8.998	6.782	-482	8.38	4.5
C_2	-324	4.052	3.054	-489	3.773	57
C_3	-315	3.580	2.698	-217	3.33	62
C_4	-271	2.973	2.240	-542	2.76	68.55
C_5	-315	2.898	2.184	-304	2.699	69.24
C_6	-297	2.195	1.654	-458	2.04	75
C_7	-306	1.530	1.153	-169	1.424	83.7
C_8	-270	1.786	1.346	-225	1.663	81
C_9	-229	1.310	0.987	-313	1.22	86.1
C_{10}	-266	1.128	0.850	-184	1.05	88
C_{11}	-166	1.041	0.784	-168	0.969	88.13
C_{12}	-195	1.242	0.936	-506	1.156	86.8

Figures (4.98-4.100) illustrate the potentiodynamic polarization curves for $HA/ZrO_2/TiO_2$ nanocomposite ceramics coating samples in Ringer's solution for a different deposition time and voltage. There are a clear improvement in the polarization behavior after coating in the values of $E_{corr.}$, $i_{corr.}$ and C_R. The value of $E_{corr.}$ after coating is shifted towards the positive noble direction of potential. With increases voltage (350V) and time of $HA/ZrO_2/TiO_2$ coated layer, the value of ($i_{corr.}$ = 1.554µA/cm^2) reduced and (C_R=1.920×10^{-3}mpy) are also reduced for sample D_7, which means increasing in the resistance of corrosion.

The appearance of cracks in the layer deposited shown in the micrograph SEM Figure 4.29(f), did not prevent the improvement in corrosion resistance of coated samples. From the data's in Table (4.12) show approximately the same positive corrosion behavior ($i_{corr.}$= 0.814µA/cm^2) for samples D_{11}.

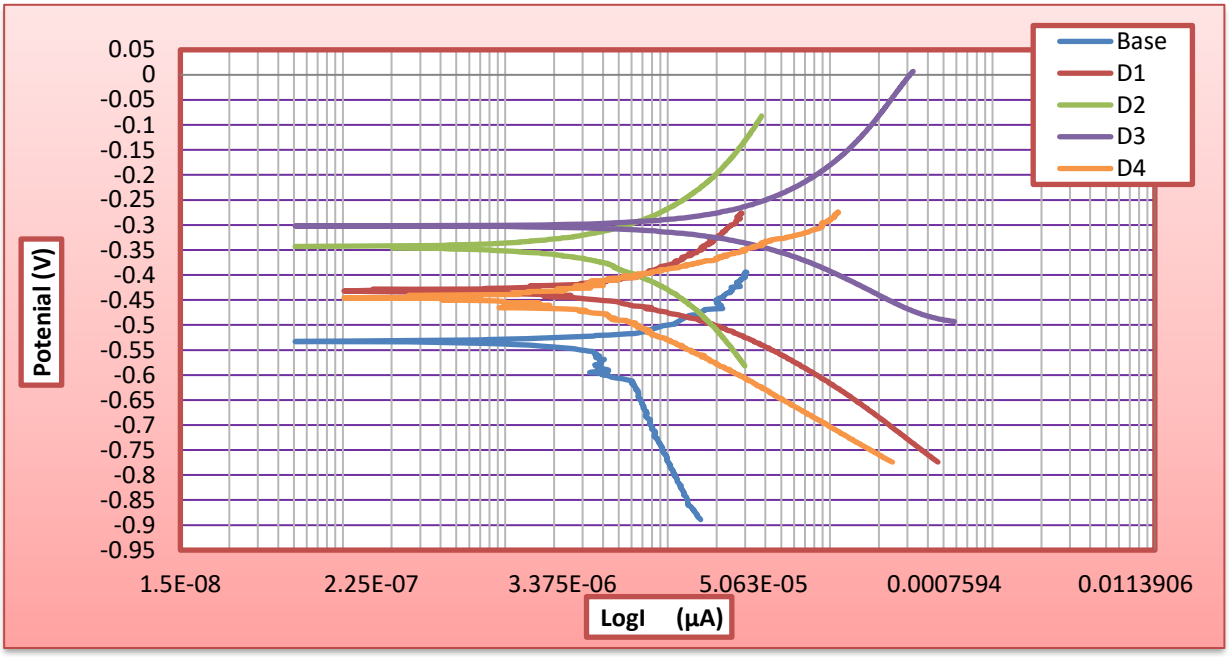

Figure (4.98): Potentiodynamic polarization curves of $HA/ZrO_2/TiO_2$ coated on Ti-6Al-7Nb alloy by MAO process and base at different time and applied voltages 300V in Ringer's solution.

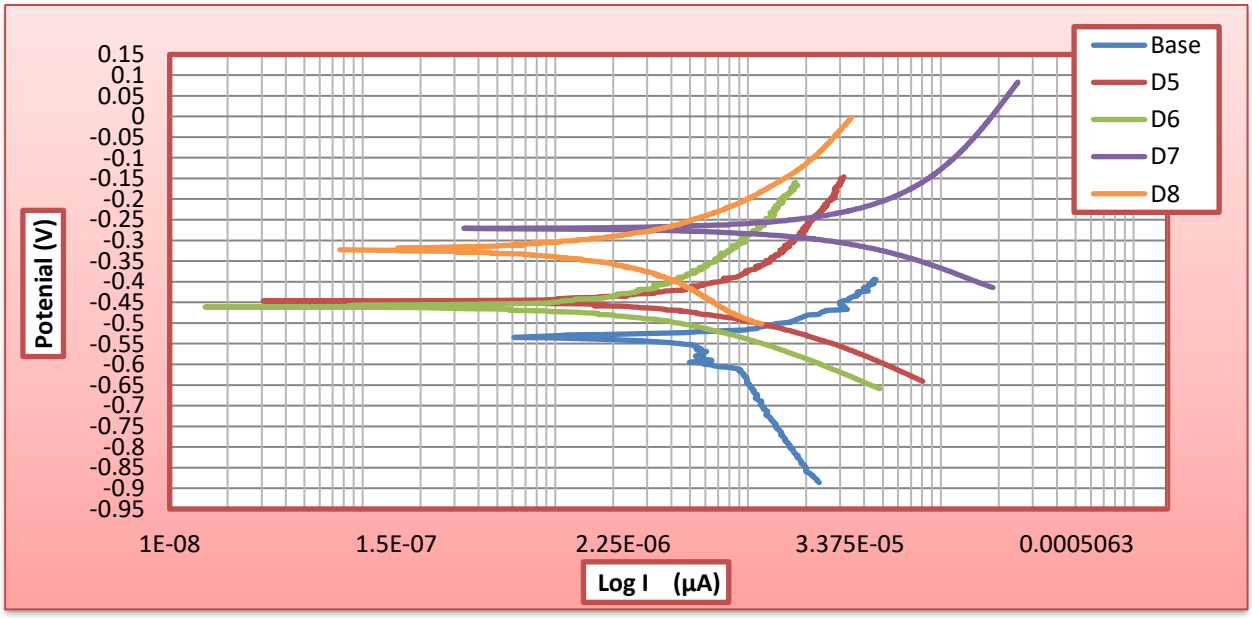

Figure (4.99): Potentiodynamic polarization curves of $HA/ZrO_2/TiO_2$ coated on Ti-6Al-7Nb alloy by MAO process and base at different time and applied voltages 350V in Ringer's solution.

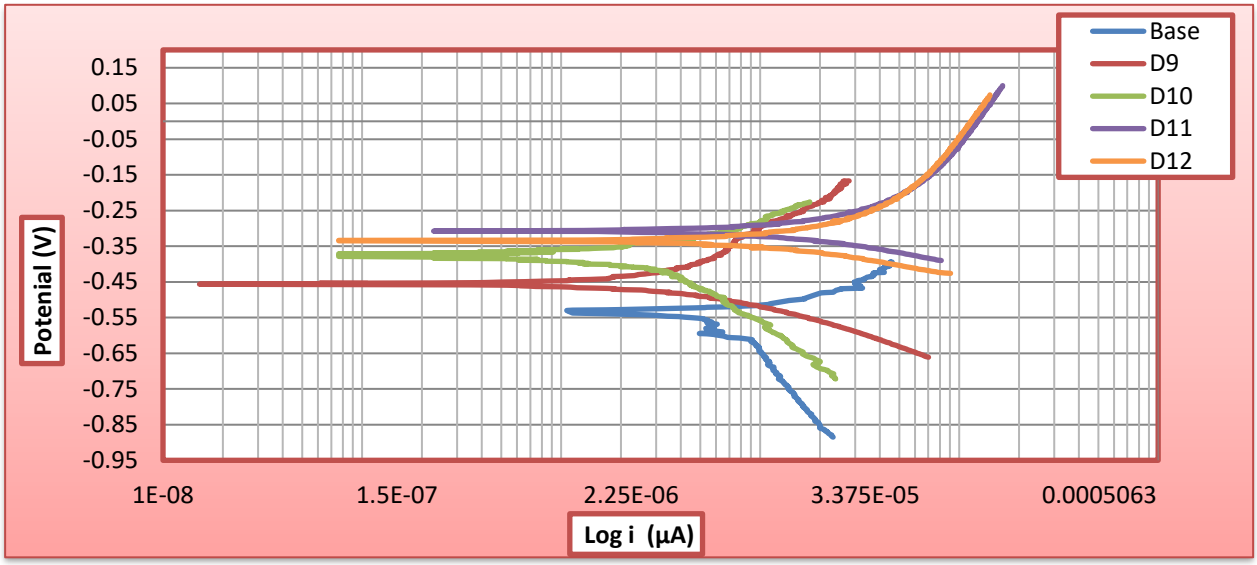

Figure (4.100): Potentiodynamic polarization curves of $HA/ZrO_2/TiO_2$ coated on Ti-6Al-7Nb alloy by MAO process and base at different time and applied voltages 400V in Ringer's solution.

Table (4.12): Electrochemical parameters of substrate and $HA/ZrO_2/TiO_2$ nanocomposite coated at different MAO applied voltages and time in Ringer's solution.

Sample Code	OCP (mV)	$I_{corr.}$ (µA)	$i_{corr.}$ (µA/cm^2)	$E_{corr.}$ (mV)	C_R*10^{-3} (mpy)	Improvement percentage (%)
Base	-441	9.059	6.828	-533	8.437	/
D_1	-320	7.593	5.723	-434	7.07	16.2
D_2	-306	4.954	3.734	-356	4.614	45.3
D_3	-292	3.018	2.274	-302	2.81	66.7
D_4	-294	4.812	3.627	-462	2.76	68.55
D_5	-229	2.388	1.8	-446	4.48	47
D_6	-247	2.053	1.547	-461	2.053	76.3
D_7	-251	2.062	1.554	-271	1.920	77.24
D_8	-276	2.158	1.626	-321	2	76.2
D_9	-300	1.449	1.09	-457	1.35	84
D_{10}	-210	1.431	1.078	-373	1.333	84.2
D_{11}	-160	1.08	0.814	-349	1.005	88
D_{12}	-225	1.201	0.905	-326	1.118	87

The corrosion behavior of HA/ZrO_2/TiO_2 coating in Saliva's solution in Figure (4.101-4.103), the $i_{corr.}$ value is much lower and for the increased voltage (400V). The shift $i_{corr.}$ towards the negative direction means improvement in the passivation layer after coating leads to reduce the $i_{corr.}$ value. Table (4.13), also shows that the passivation current density ($i_{corr.}$=3.388 µA/cm2) at (-313mV) for the HA/ZrO_2/TiO_2 nanocomposite coated are much less and the specimens were passive over long range of positive applied voltage as can be seen from samples D_3.

Corrosion characteristics of coatings are affected by (crystallinity, purity, brittle fractures, porosity and ion penetration the coating into substitution) there are brittle fractures possibility which can effect on the formation of passive region but this did not prevent the improvement in $I_{corr.}$ [8].

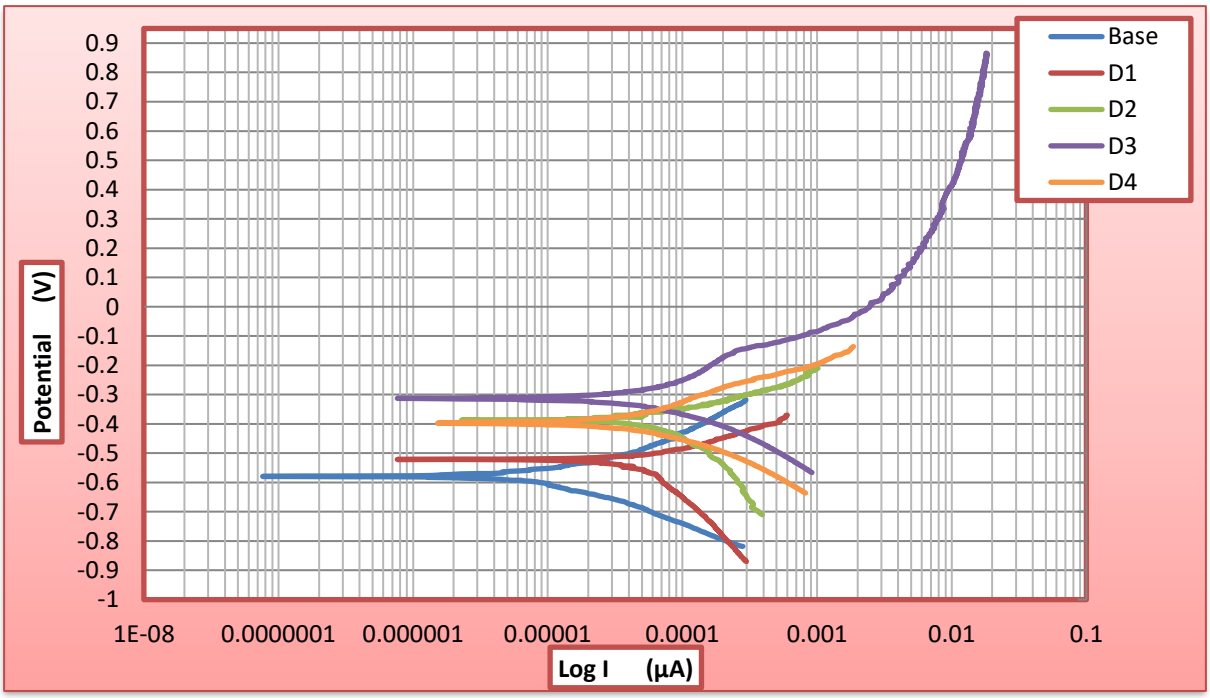

Figure (4.101): Potentiodynamic polarization curves of HA/ZrO_2/TiO_2 coated on Ti-6Al-7Nb alloy by MAO process and base at different time and applied voltages 300V in Saliva's solution.

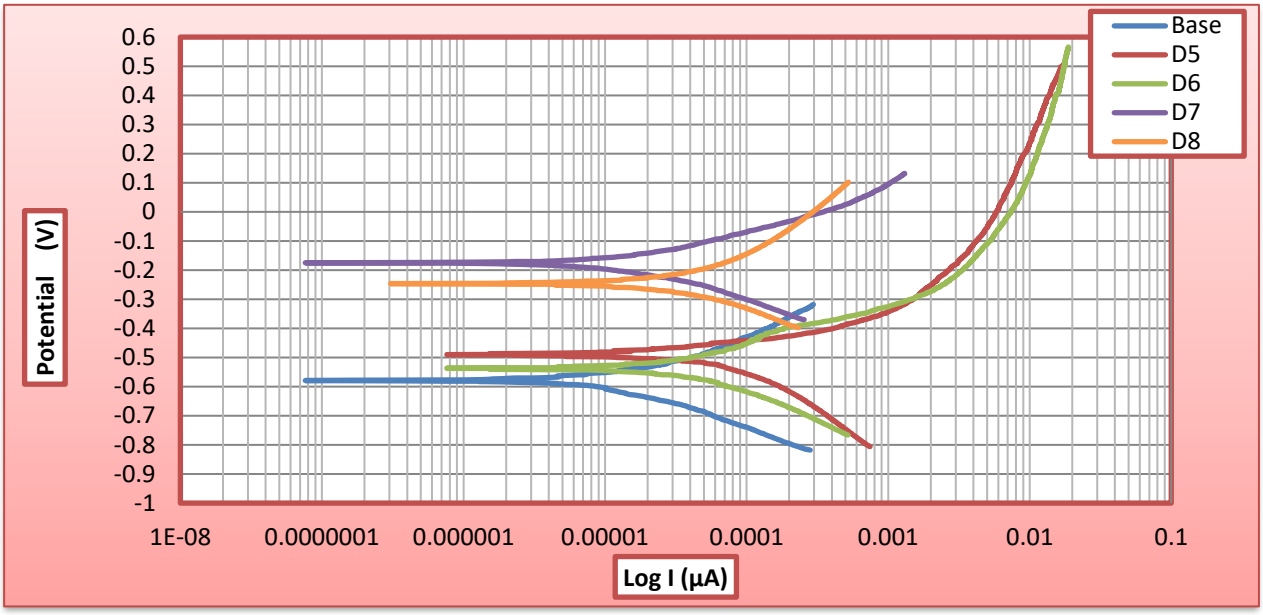

Figure (4.102): Potentiodynamic polarization curves of HA/ZrO_2/TiO_2 coated on Ti-6Al-7Nb alloy by MAO process and base at different time and applied voltages 350V in Saliva's solution.

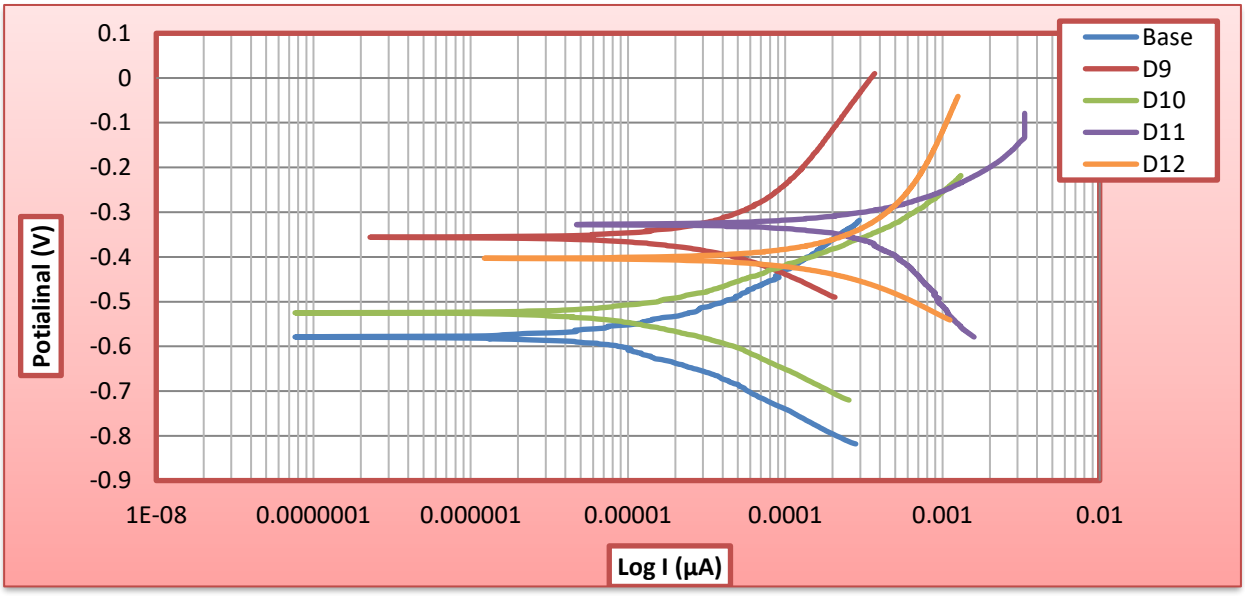

Figure (4.103): Potentiodynamic polarization curves of HA/ZrO_2/TiO_2 coated on Ti-6Al-7Nb alloy by MAO process and base at different time and applied voltages 400V in Saliva's solution.

Table (4.13): Electrochemical parameters of substrate and $HA/ZrO_2/TiO_2$ nanocomposite coated at different MAO applied voltages and time in Saliva's solution.

Sample Code	OCP (mV)	$I_{corr.}$ (µA)	$i_{corr.}$ (µA/cm^2)	$E_{corr.}$ (mV)	CR*10^{-3} (mpy)	Improvement percentage (%)
Base	-376	9.424	7.103	-579	8.777	/
D_1	-330	7.857	5.922	-521	7.317	16.63
D_2	-316	6.466	4.873	-387	6.022	31.38
D_3	-287	4.495	3.388	-313	4.186	52.3
D_4	-289	4.296	3.238	-497	4	54.42
D_5	-223	2.976	2.243	-490	2.77	68.4
D_6	-227	2.923	2.20	-540	2.72	69
D_7	-221	1.999	1.50	-236	1.86	78.8
D_8	-200	2.544	1.163	-246	2.37	73
D_9	-279	2.532	1.908	-356	2.358	73.1
D_{10}	-168	1.447	1.09	-525	1.347	84.65
D_{11}	-138	0.837	0.630	-352	0.779	91.12
D_{12}	-179	1.307	0.985	-313	1.217	86.1

Finally, nanocomposite ceramic coating $HA/ZrO_2/TiO_2$ prepared by MAO processes are to increasing the biocompatibility whereas, TiO_2, HA/TiO_2, and ZrO_2/TiO_2 are to enhance the corrosion behavior of the base metal. The corrosion progressed in the passive regain for the specimen coated with single layer more than uncoated one while the specimen coated with composite layers was quite effective against further corrosion due to the formation of stable oxide layer. It should be noted that in the medical applications, the presence of small amount of porosity is necessary for ingrowth the bone tissue toward the coating to produce efficient implant fixation. In the other word, the presence of porosity is advantageous as it enhances the osseointegration as a result of its bonding capability is improved to the metallic implants. However, the high porosity level will consider as a source for penetrating large amount of body fluid to the human body and become harmful. Increasing the

porosity level also has a negative influence on the mechanical properties, especially on bond strength, which will in turn lead to an easy fracture. Therefore, it proposes that the porosity level of the coatings must be well balanced to achieve the optimum mechanical and biological performance [155].

4.8.3 Cycle Polarization Test

The increased ion release rate due to different forms of localized corrosion, may lead to a series of undesirable biological responses and eventually, implant loosening. Susceptibility to these forms of corrosion is evaluated by cyclic polarization. The parameters obtained from the current-voltage curve can be associated with the localized corrosion mechanism. Typically, the reading starts at the open circuit potential and scans upwards until breakdown is attained. Then the direction of scan is inverted after specific amount of localized corrosion is established and the passive film is damaged [156]. The potential at which stable pit formed is called breakdown potential (E_b) or pitting potential (E_p). Consequently, the E_p implies the potential over which the pits initiated and developed. If the E_p is high, the material has high resistance to the pitting corrosion. The difference (ΔE) between E_p and E_{prot} will give an indication to the corrosion resistance of the sample, where the smaller ΔE value mean the highest corrosion resistance.

Figures (4.104-4.106) show the polarization curves obtained for uncoated Ti6Al7Nb and coating by MAO process with different parameters (voltage and time) in Ringer's solution. Significant differences were observed between the curves obtained for each sample. For the Ti-6Al-7Nb alloy, has the lowest E_p and E_{prot} value compared to the susceptibility to pitting corrosion of the TiO_2 specimens treated by MAO process. The cyclic polarization curves obtained for TiO_2 at different voltage and

time. As noted in the Table (4.14), the extent of the hysteresis loop is highly reduced and therefore, the corrosion mechanism operating on the substrate surface is less active when the TiO_2 coating. However, changed as MAO process parameters changed to (E_P= -310mV) for sample A_3. The values obtained are quite consistent and the variations in the values are small keeping in mind the random nature of the MAO process itself, porosity of the oxide coatings and local inhomogeneity of the samples.

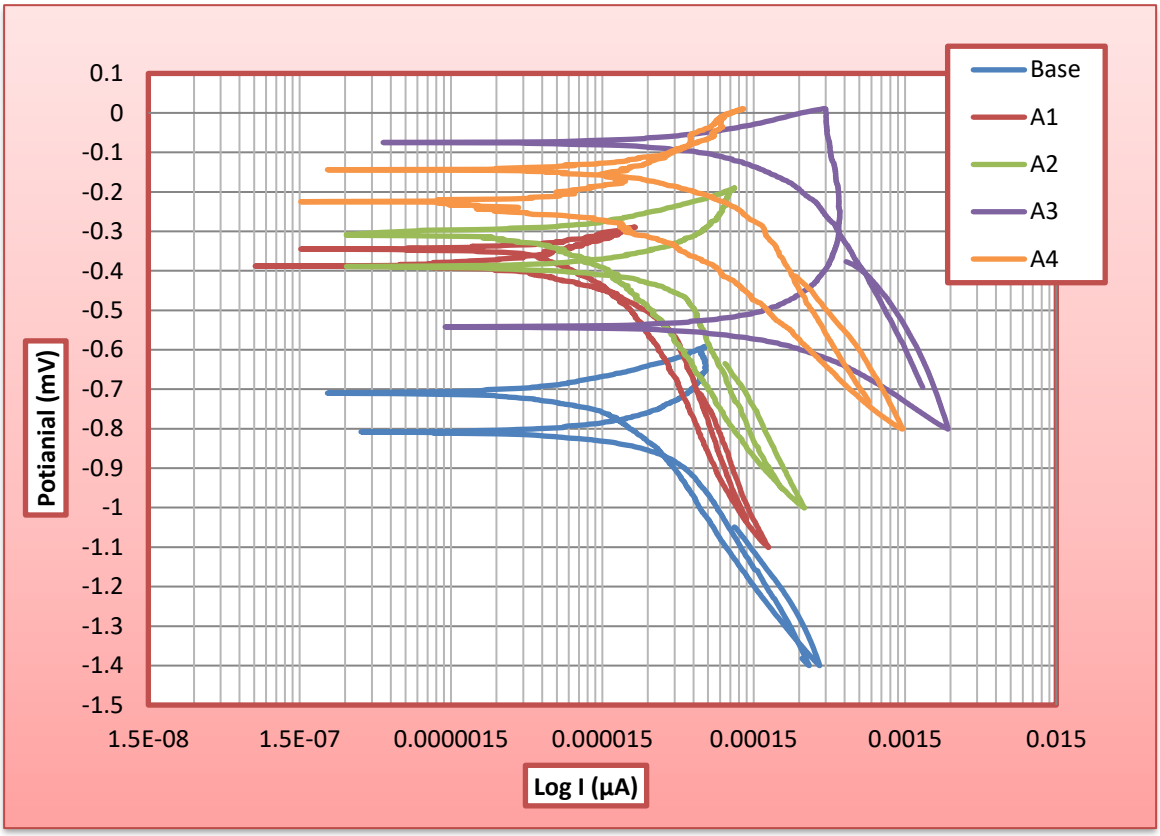

Figure (4.104): Cycle polarization curves of the base and TiO_2 coated on Ti-6Al-7Nb alloy by MAO process at different time at applied voltages 300V in Ringer's solution.

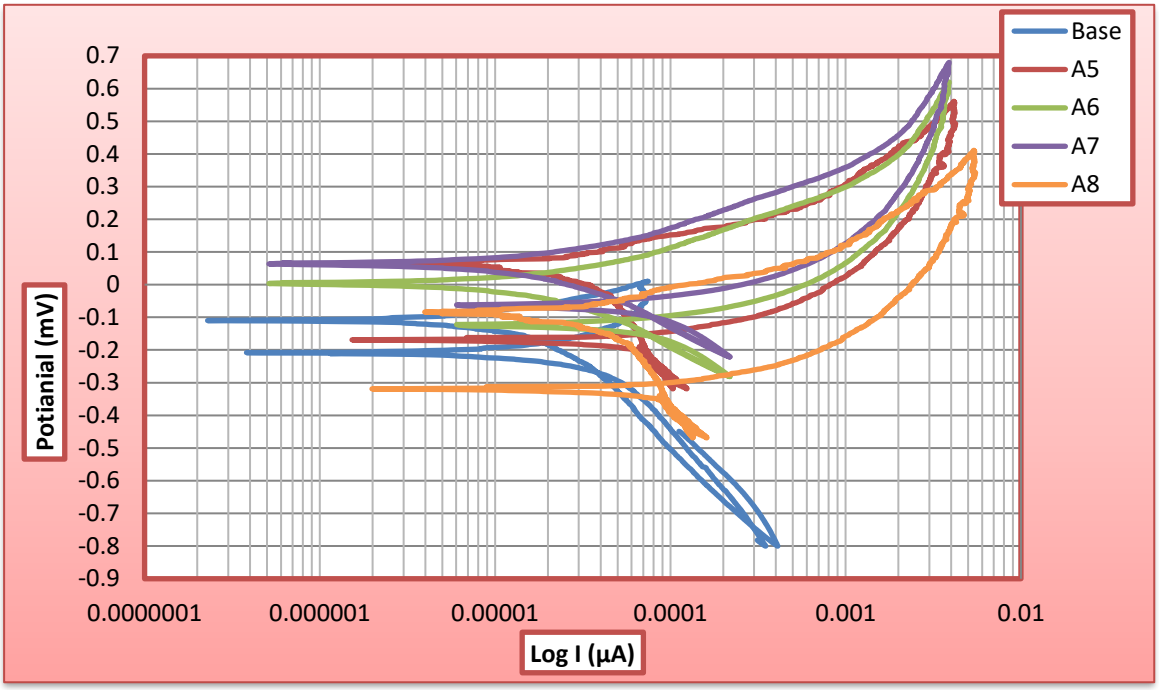

Figure (4.105): Cycle polarization curves of TiO_2 coated on Ti-6Al-7Nb alloy by MAO process at different time and applied voltages 350V in Ringer's solution.

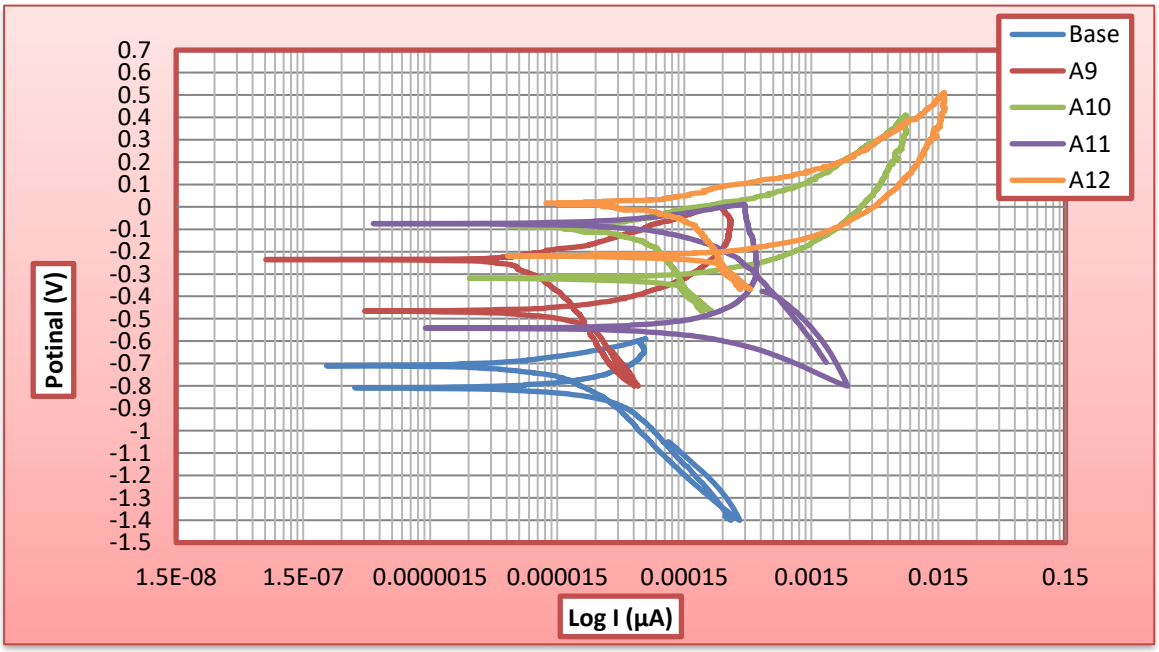

Figure (4.106): Cycle polarization curves of TiO_2 coated on Ti-6Al-7Nb alloy by MAO process at different time and applied voltages 400V in Ringer's solution.

Table (4.14): Values of electrochemical parameters of substrate and TiO_2 coated at different MAO applied voltages and time in Ringer's solution from cyclic polarization.

Sample Code	$I_{corr.}$ (μA)	$i_{corr.}$ (μA/cm^2)	$E_{p.}$ (mV)	E_{prot} (mV)	$\Delta E = (E_p - E_{prot})$ (mV)	$C_R * 10^{-3}$ (mpy)	Improvement percentage (%)
Base	9.505	7.164	-780	-630	-150	8.852	/
A_1	7.132	5.375	-330	-300	-30	6.64	25
A_2	6.908	5.207	-350	-300	-50	6.433	27.3
A_3	4.739	3.572	-310	-60	-250	4.413	50
A_4	5.418	4.083	-162	-40	-122	5.046	43
A_5	2.659	2.004	-270	450	-740	2.476	72
A_6	2.151	1.621	-280	80	-360	2	77.4
A_7	2.463	1.856	-100	160	-260	2.293	74
A_8	2.537	1.912	-310	-55	-256	2.363	73.3
A_9	1.969	1.484	-204	-30	-274	1.833	79.3
A_{10}	1.694	1.276	-313	-40	-273	1.577	82
A_{11}	1.118	0.84	-316	-100	-216	1.04	88.25
A_{12}	1.636	1.233	-120	50	-170	1.523	82.7

Figures (4.107-4.109) values of Ep and $i_{corr.}$ obtained for the TiO_2 treated alloys by MAO indicated lower corrosion rate and **Δ**E values for the specimen A_8 in Saliva's solution (-190 mV) compared of uncoated alloy. Although these results agree with the behavior of the samples during the values are different from tests, probably due to the change in the nature of the passive film (film thickness increases) during the cyclic polarization scan. A significant effect in enhancing the corrosion resistance of the alloy was noticeable because of the MAO process rushed to (-128mV) for sample A_{11}.

In general, the corrosion current density values obtained for TiO_2 treated by MAO process on Ti-6Al-7Nb alloy were lower values in two solution.

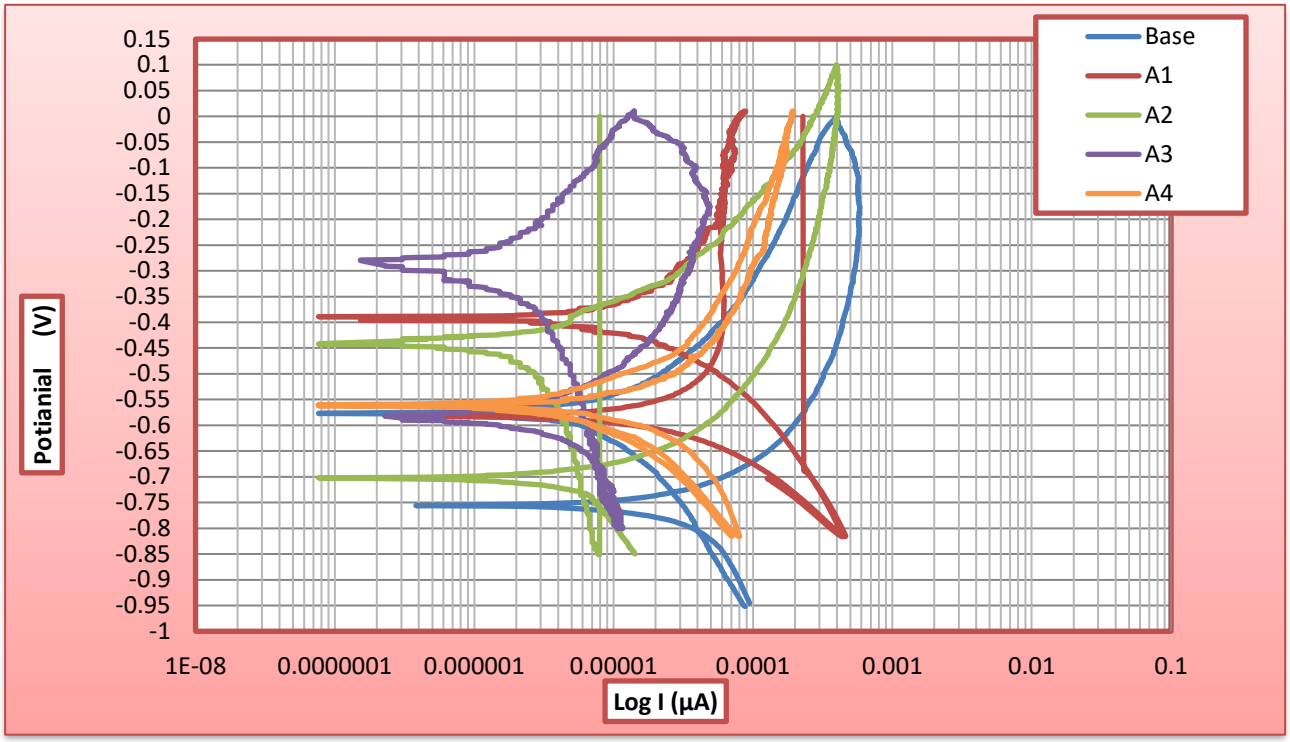

Figure (4.107): Cycle polarization curves of TiO_2 coated on Ti-6Al-7Nb alloy by MAO process at different time and applied voltages 300V in Saliva's solution.

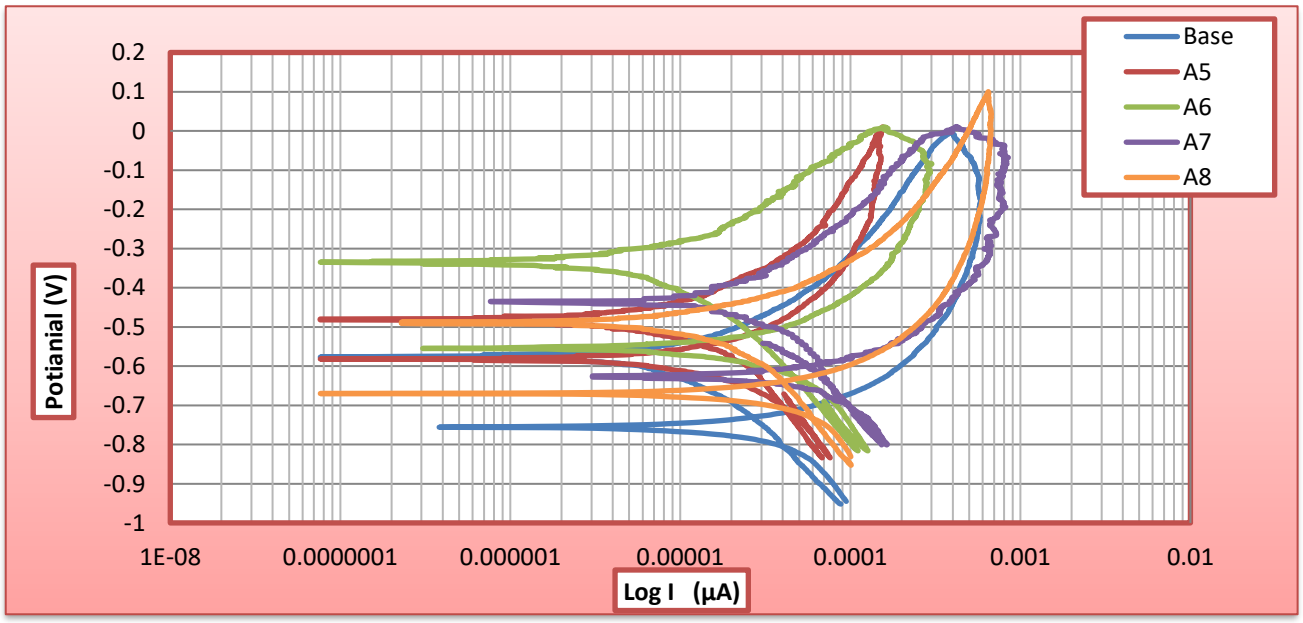

Figure (4.108): Cycle polarization curves of TiO_2 coated on Ti-6Al-7Nb alloy by MAO process at different time and applied voltages 350V in Saliva's solution.

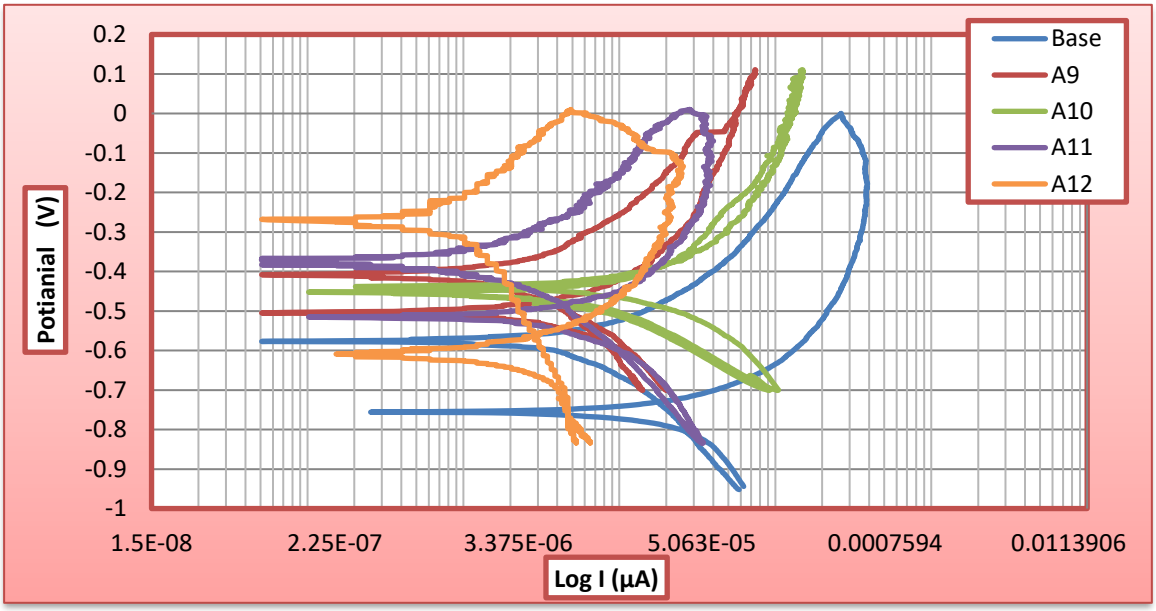

Figure (4.109): Potentiodynamic polarization curves of TiO_2 coated on Ti-6Al-7Nb alloy by MAO process at different time and applied voltages 400V in Saliva's solution.

Table (4.15): Values of electrochemical parameters of substrate and TiO_2 coated at different MAO applied voltages and time in Saliva's solution from cyclic polarization.

Sample Code	$I_{corr.}$ (µA)	$i_{corr.}$ (µA/cm^2)	$E_{p.}$(mV)	$E_{prop.}$ (Mv)	$\Delta E = (E_p - E_{prot})$ (mV)	$C_R * 10^{-3}$ (mpy)	Improvement percentage (%)
Base	9.750	7.34	-750	-515	-235	9.08	/
A_1	8.543	6.439	-570	-390	-180	8	11.89
A_2	6.566	4.949	-700	-465	-225	6.115	32.6
A_3	6.397	4.821	-580	-289	-181	5.95	34.5
A_4	4.587	3.457	-561	-500	-61	4.27	53
A_5	1.841	1.387	-590	-481	-109	1.714	81.12
A_6	1.451	1.093	-476	-336	-140	1.351	85
A_7	0.680	0.512	-612	-520	-92	0.634	93
A_8	0.977	0.736	-680	-490	-190	0.91	90
A_9	4.330	3.263	-509	-410	-99	4.03	55.6
A_{10}	3.797	2.862	-437	-409	-28	3.5	61.4
A_{11}	2.629	1.981	-508	-380	-128	2.25	75.2
A_{12}	3.164	2.384	-410	-273	-137	2.94	67.6

Figures (4.110-4.112) corrosion potential ($E_{corr.}$) or pitting potential (E_p) and the corrosion current density ($i_{corr.}$) were determined from the cyclic polarization tests in the HA/TiO_2 nanocomposite coating in Ringer's solution. It is reported that HA coated titanium alloys showed increased metal dissolution in the system through the passive film. values HA/TiO_2 coated samples are arranged in ascending manner according to their Ep values in Table (4.16): (E_p=-346 mV) for sample B_1 rushed (E_p= -207mV) for sample B_{11}. From these results, the value of Ep is increased with increasing voltage and time because increasing the coating layer porosity and thickness when using high voltage and time in the MAO process which is agree with the results conducted from the potentiodynamic results [156]. As stated previously, the resistance of pitting corrosion increased with increasing of E_p value. Therefore, based on this role, the deposition at 400V for sample B_{11} has the higher resistance to pitting corrosion due to it is high E_p value as compared with the other coated samples.

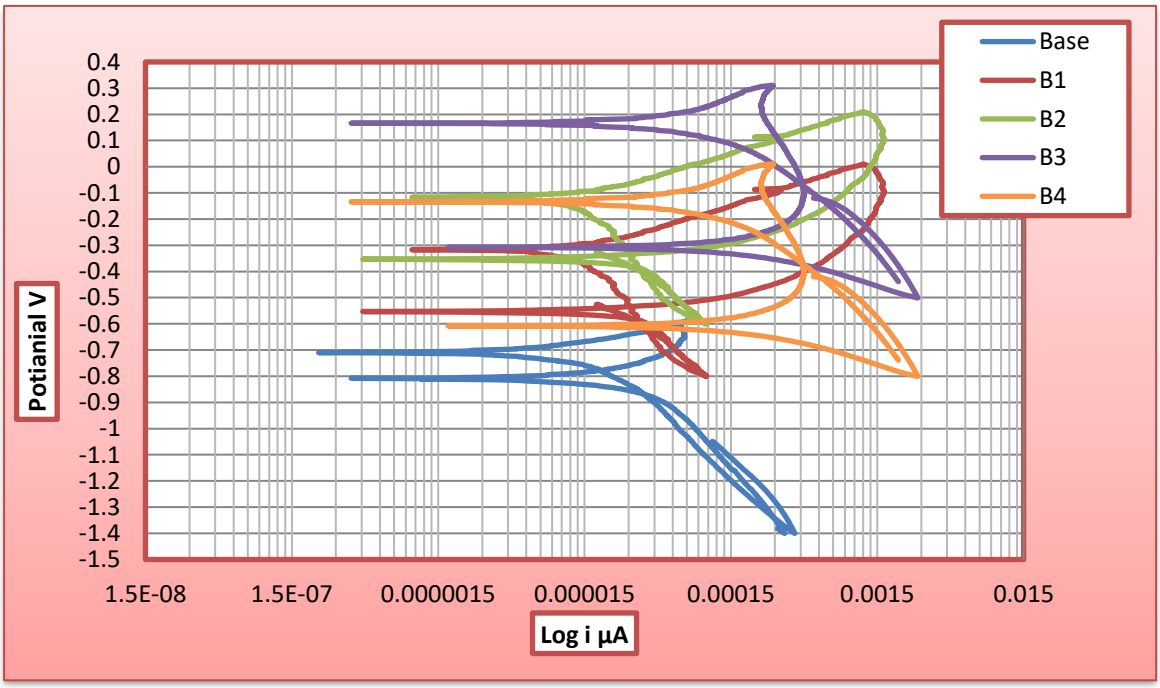

Figure (4.110): Cycle polarization curves of HA/TiO_2 coated on Ti-6Al-7Nb alloy by MAO process at different time and applied voltages 300V in Ringer's solution.

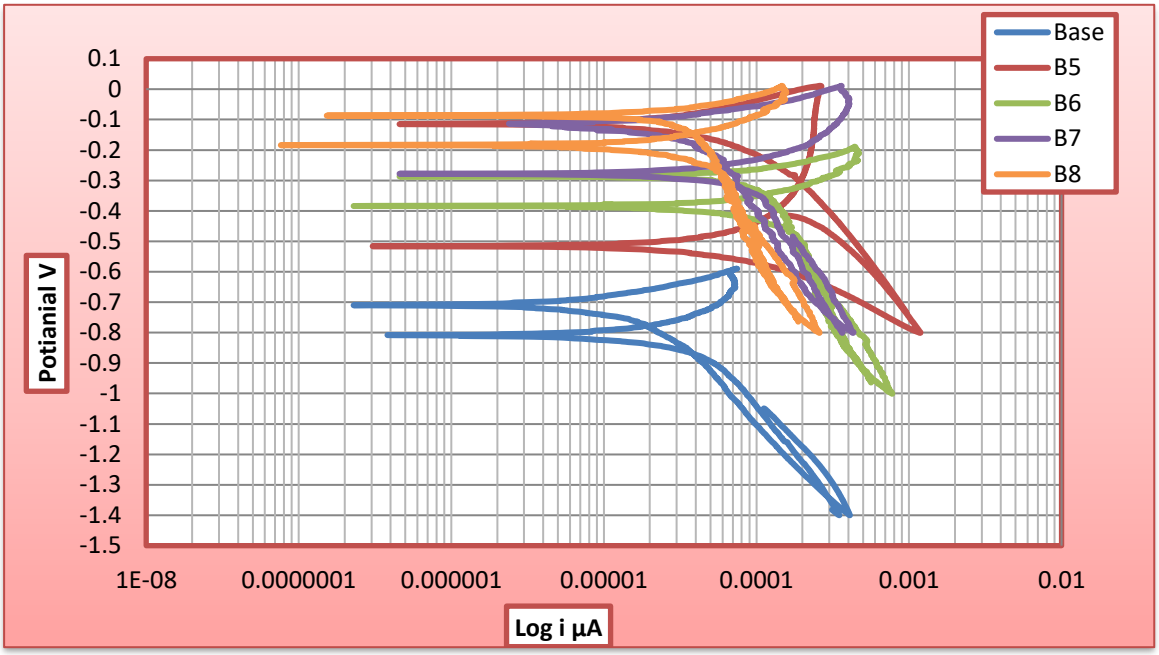

Figure (4.111): Cycle polarization curves of HA/TiO_2 coated on Ti-6Al-7Nb alloy by MAO process at different time and applied voltages 350V in Ringer's solution.

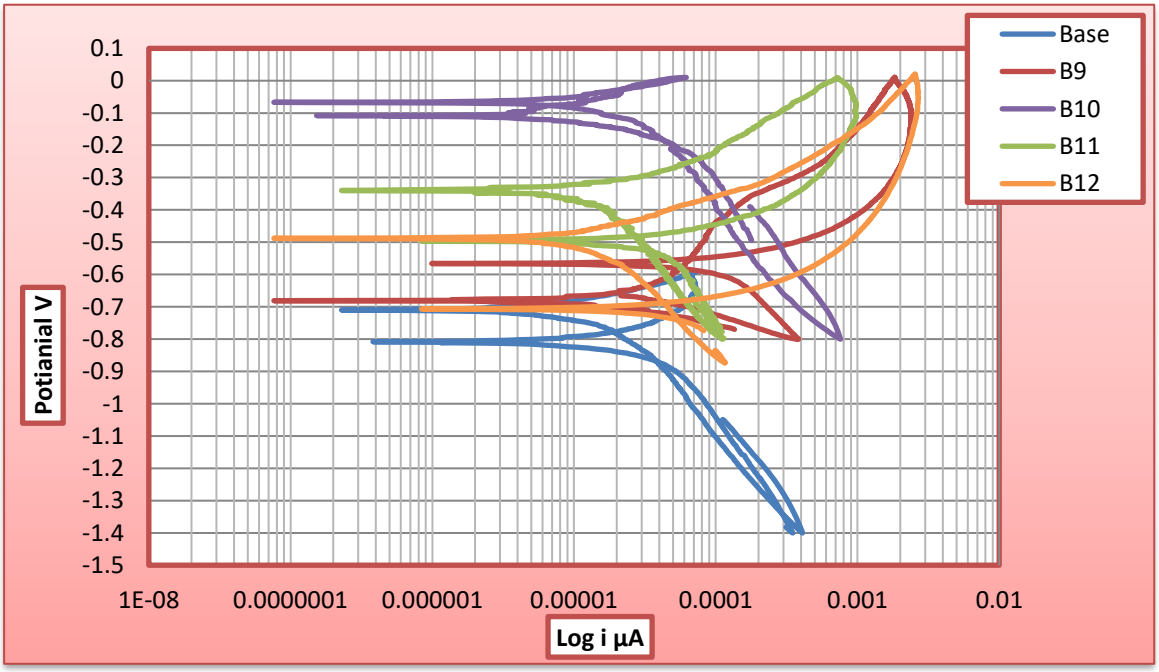

Figure (4.112)**:** Cycle polarization curves of HA/TiO_2 coated on Ti-6Al-7Nb alloy by MAO process at different time and applied voltages 400V in Ringer's solution.

Table (4.16): Values of electrochemical parameters of substrate and HA/TiO_2 coated at different MAO applied voltages and time in Ringer's solution from cyclic polarization.

Sample Code	$I_{corr.}$ (μA)	$i_{corr.}$ (μA/cm^2)	E_P (mV)	E_{prot} (mV)	$\Delta E = (E_p - E_{prot})$ (mV)	$C_R * 10^{-3}$ (mpy)	Improvement percentage (%)
Base	9.505	7.164	-780	-630	-150	8.852	/
B_1	9.067	6.834	-546	-300	-246	8.44	4.65
B_2	6.224	4.691	-320	15	-335	5.79	34.5
B_3	4.370	3.294	-124	200	-324	4.07	54
B_4	4.551	3.430	-400	-100	-300	4.23	52.2
B_5	3.989	3	-300	-100	-200	3.715	58
B_6	3.571	2.69	-184	-32	-152	3.32	62.5
B_7	2.151	1.621	-286	180	-466	2	77.4
B_8	2.454	1.849	-284	90	-374	2.285	74
B_9	2.011	1.515	-181	-20	-161	1.87	78.8
B_{10}	1.704	1.284	-97	-43	-54	1.58	82
B_{11}	1.118	0.842	-207	-23	-184	1.04	88.25
B_{12}	1.377	1.037	-260	-27	-233	1.282	85.5

The cyclic polarization of the HA/TiO_2 coated at different voltage and deposition time has been investigated also in the Saliva's solution as illustrated in Figures (4.113-4.115). Show that the HA/TiO_2 is the same behavior in Ringer's solution. The lowest value of ΔE and current density for the specimen coated with increased voltage and time and increased Ep show that improvement percentage is 95.7% for sample B_{11}. Therefore, based on the results from the cyclic polarization curves, it is suppose that coating layer at MAO process a strong ability to act as barrier to prevent the localized corrosion attack of many aggressive ions appeared in Ringer's and Saliva solution during the corrosion test.

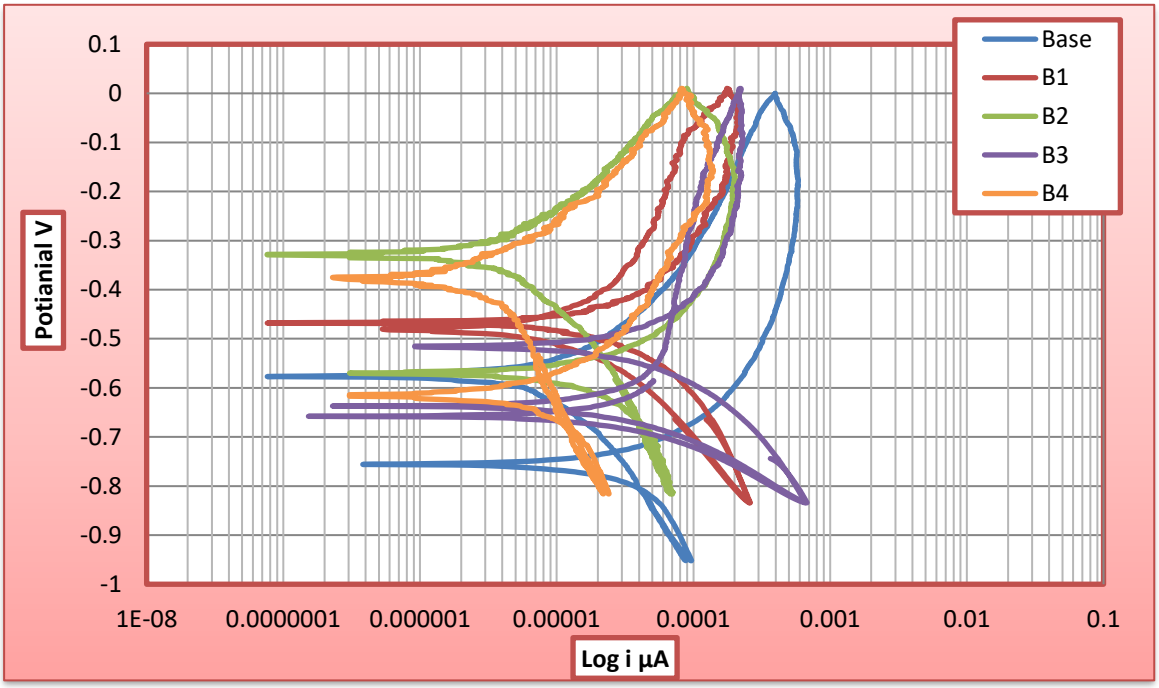

Figure (4.113): Cycle polarization curves of HA/TiO_2 coated on Ti-6Al-7Nb alloy by MAO process at different time and applied voltages 300V in Saliva's solution.

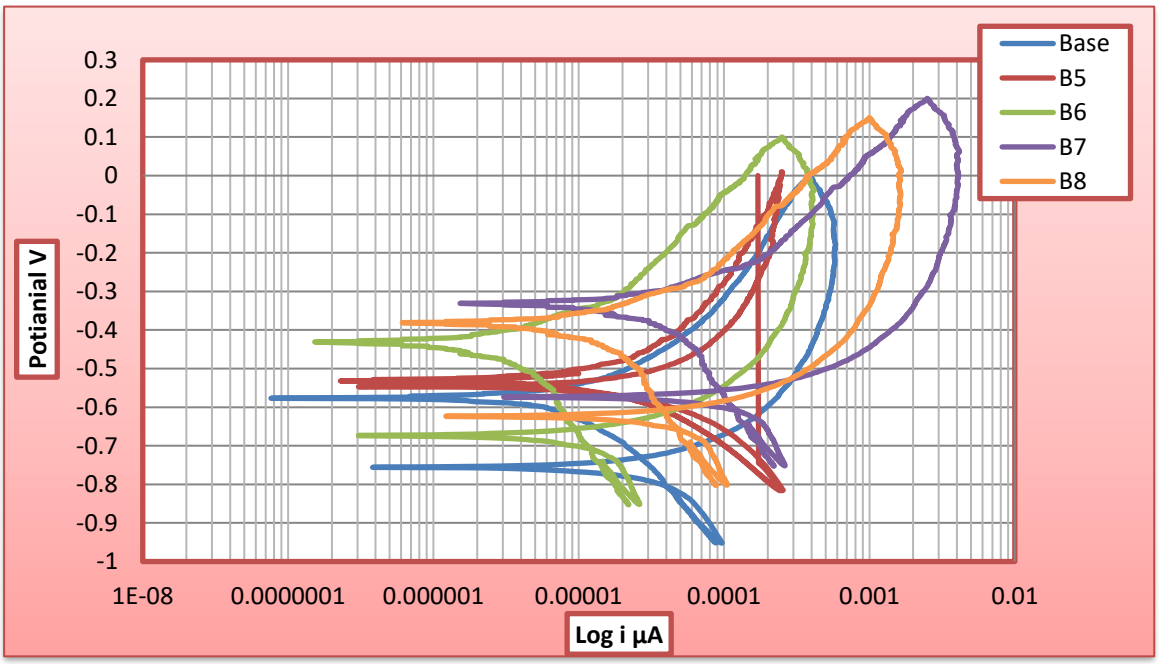

Figure (4.114): Cycle polarization curves of HA/TiO_2 coated on Ti-6Al-7Nb alloy by MAO process at different time and applied voltages 350V in Saliva's solution.

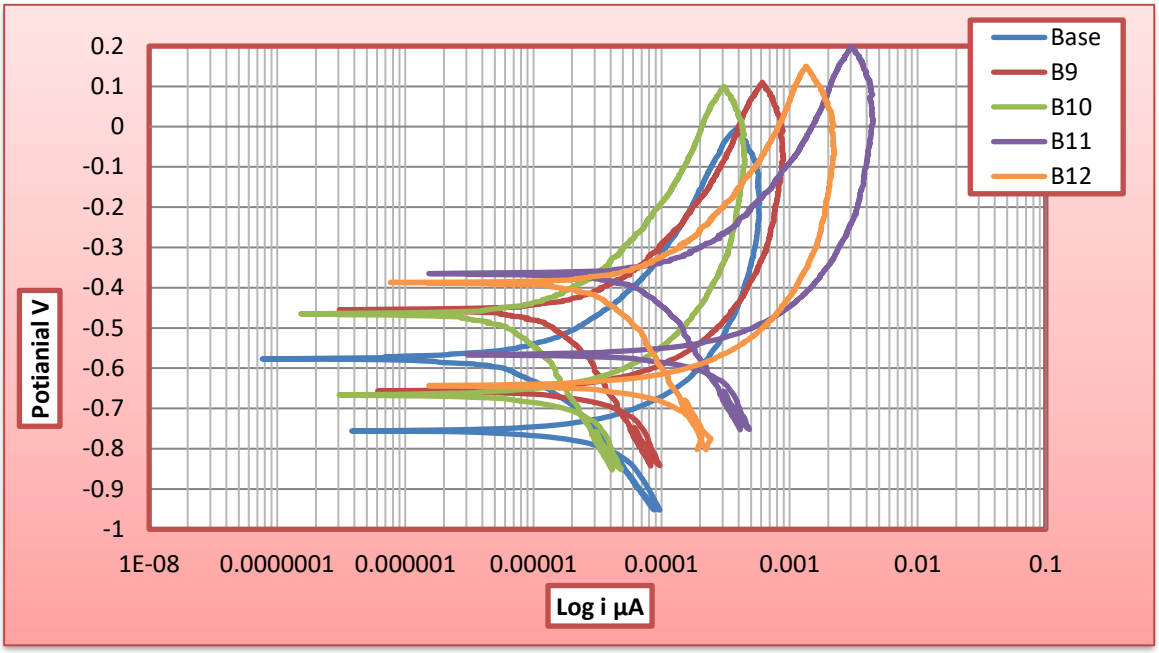

Figure (4.115): Cycle polarization curves of HA/TiO_2 coated on Ti-6Al-7Nb alloy by MAO process at different time and applied voltages 400V in Saliva solution.

Table (4.17): Values of electrochemical parameters of substrate and HA/TiO_2 coated at different MAO applied voltages and time in Saliva's solution from cyclic polarization.

Sample Code	$I_{corr.}$ (µA)	$i_{corr.}$ (µA/cm^2)	$E_{p.}$ (mV)	E_{prot} (mV)	$\Delta E = (E_p - E_{prot})$ (mV)	C_R* 10^{-3} (mpy)	Improvement percentage (%)
Base	9.750	7.34	-750	-515	-235	9.08	/
B_1	3.549	2.675	-550	-520	-30	3.3	63.6
B_2	3.229	2.433	-589	-310	-279	3	67
B_3	3.004	2.347	-672	-620	-52	2.76	69.3
B_4	2.451	1.847	-610	-378	-242	2.28	74.8
B_5	2.394	1.804	-567	-512	-55	2.22	75.5
B_6	2.236	1.685	-687	-433	-254	2.08	77
B_7	1.667	1.256	-550	-311	-239	1.5	83.5
B_8	2.046	1.542	-618	-428	-190	1.9	79
B_9	1.377	1.037	-680	-447	-233	1.28	86
B_{10}	1.028	0.774	-684	-465	-219	0.98	89.2
B_{11}	0.415	0.312	-540	-393	-147	0.387	95.7
B_{12}	0.586	0.441	-644	-350	-294	0.546	94

In Figures (4.116-4.118) respectively, and Table (4.18), the coated sample ZrO_2/TiO_2 nanocomposite coating in solution Ringer's has highest pitting and protection potential (E_p=-110mV) for sample C_3 with an open hysteresis loop where this polarization behavior tends to be resistance to the localized corrosion. In addition, the lowest value of (ΔE =-685 mV) for sample C_{11} is obtained and consequently this sample would have the more resistance to pitting corrosion and increased with voltage and time. This mean that this sample has appropriately hinder the pit initiation and propagation.

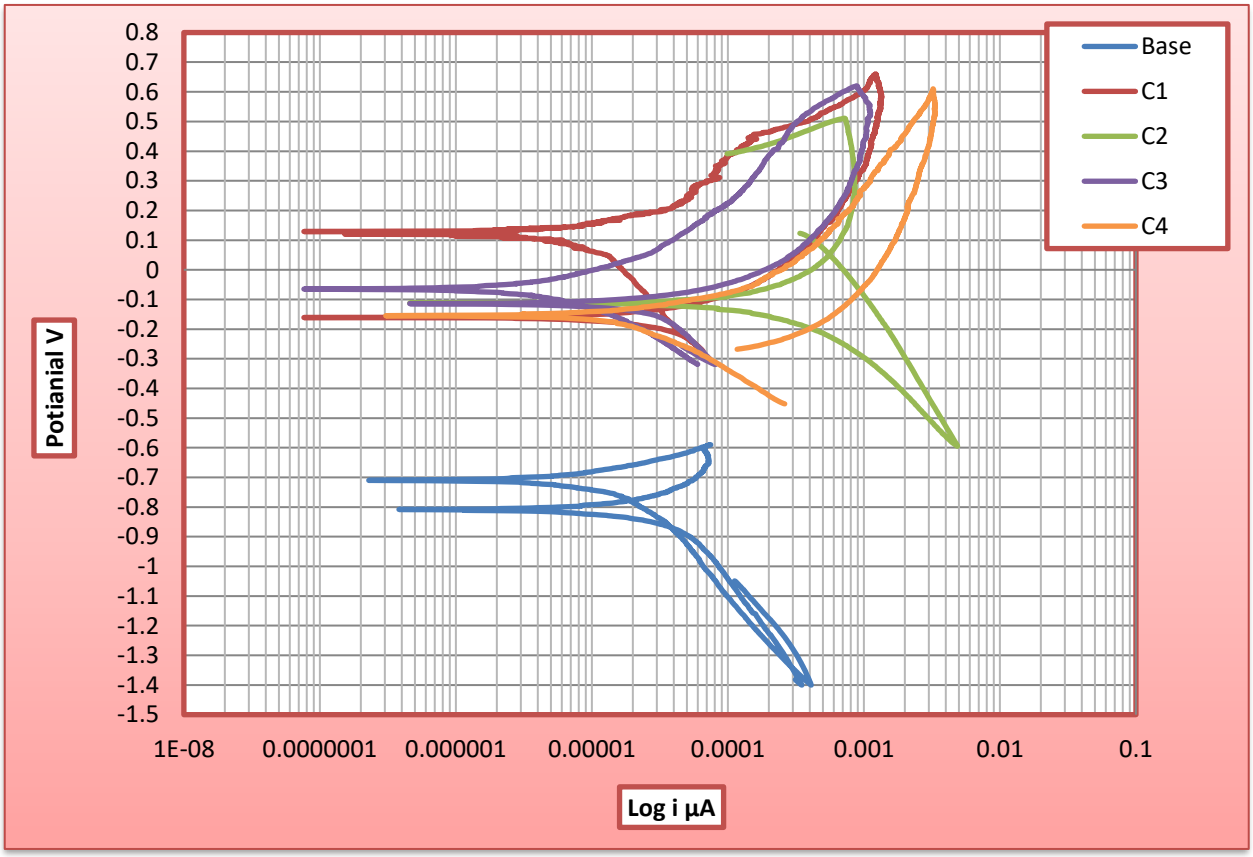

Figure (4.116): Cycle polarization curves of ZrO_2/TiO_2 coated on Ti-6Al-7Nb alloy by MAO process at different time and applied voltages 300V in Ringer's solution.

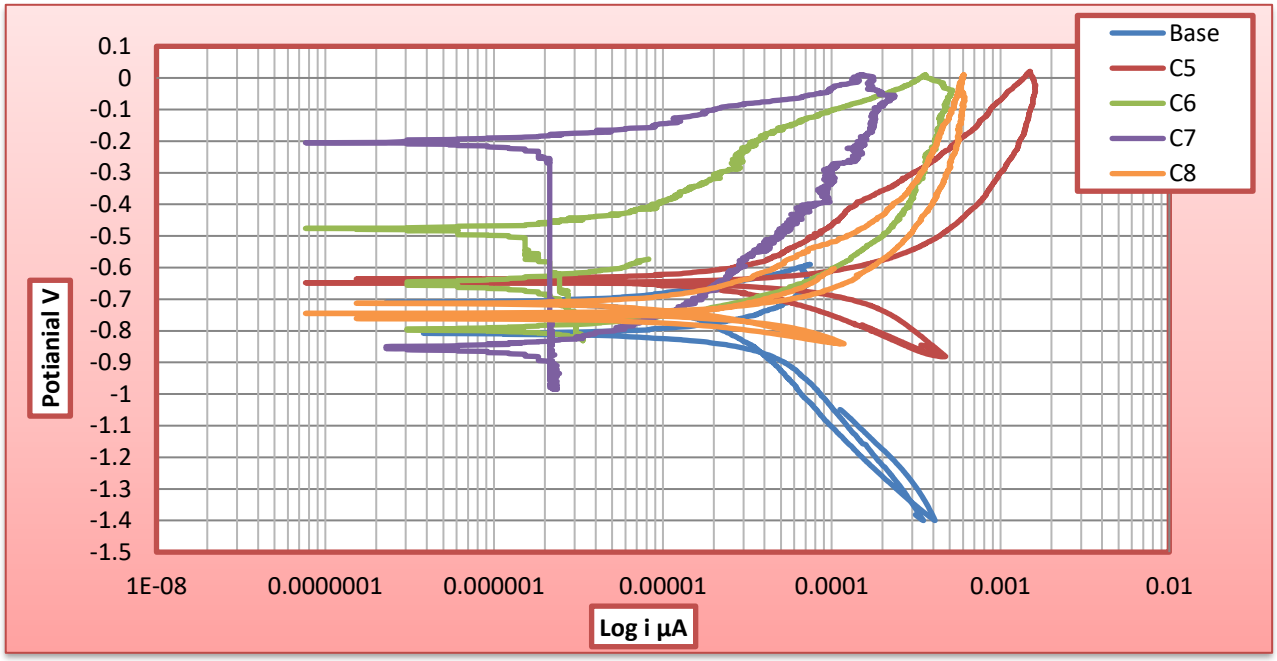

Figure (4.117): Cycle polarization curves of ZrO_2/TiO_2 coated on Ti-6Al-7Nb alloy by MAO process at different time and applied voltages 350V in Ringer's solution.

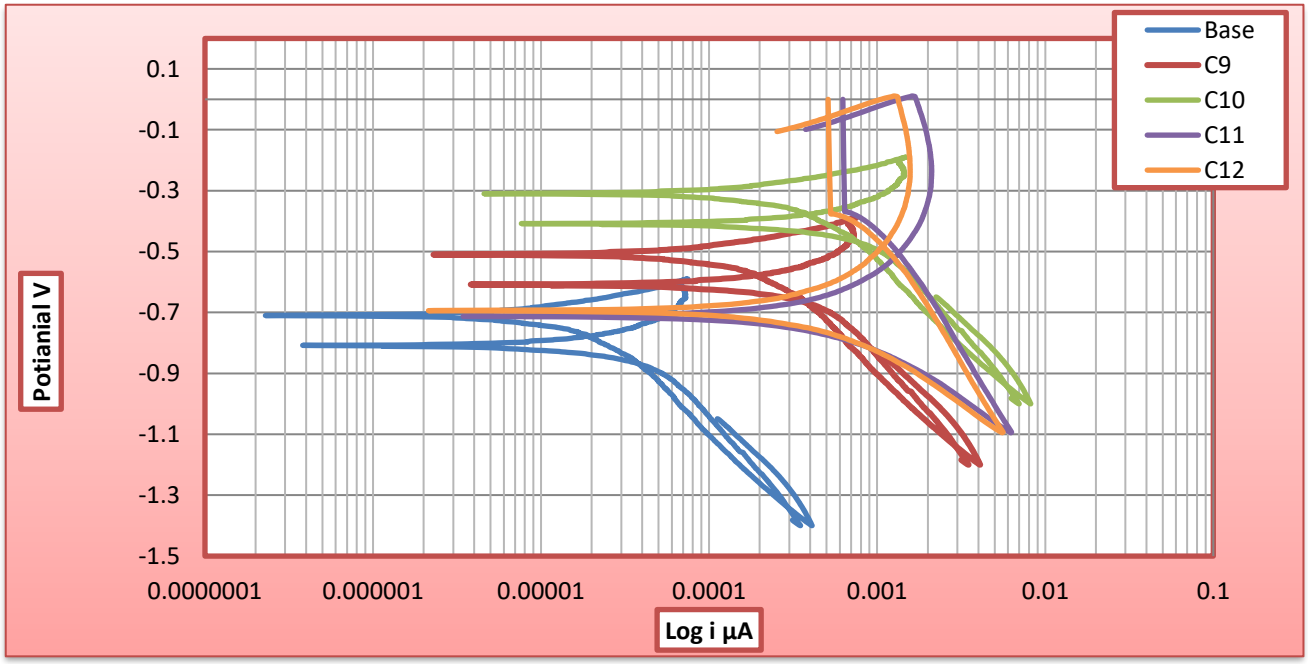

Figure (4.118): Cycle polarization curves of ZrO_2/TiO_2 coated on Ti-6Al-7Nb alloy by MAO process at different time and applied voltages 400V in Ringer's solution.

Table (4.18): Values of electrochemical parameters of substrate and ZrO_2/TiO_2 coated at different MAO applied voltages and time in Ringer's solution from cyclic polarization.

Sample Code	$I_{corr.}$ (µA)	$i_{corr.}$ (µA/cm^2)	$E_{P.}$ (mV)	E_{prot} (mV)	$\Delta E = (E_p - E_{prot})$ (mV)	$C_R * 10^{-3}$ (mpy)	Improvement percentage (%)
Base	9.505	7.164	-780	-630	-150	8.852	/
C_1	6.348	4.784	-180	220	-400	5.912	33.2
C_2	6.223	4.690	-46	400	-446	5.79	34.5
C_3	5.250	3.957	-110	-90	-30	4.88	44.8
C_4	2.574	1.940	-280	-108	-172	2.39	73
C_5	2.001	1.508	-659	-650	-9	1.86	79
C_6	1.981	1.493	-805	-610	-295	2	77.4
C_7	1.531	1.154	-848	-200	-648	1.845	79.15
C_8	1.744	1.314	-764	-750	-16	1.624	81.6
C_9	1.608	1.212	-610	-505	-105	1.49	83
C_{10}	1.432	1.079	-380	-300	-80	1.333	85
C_{11}	1.058	0.797	-785	-100	-685	1.01	88.5
C_{12}	1.227	0.924	-708	-110	-598	1.142	87

The cycle polarization in the ZrO_2/TiO_2 coating of the Saliva's solution show high corrosion in pitting same behavior in ringer's solution as shown in Figures (4.119 - 4.121). Have maximum value (Ep =30mV) for sample C_{11}. Corrosion resistance (affected by film features) is expected to increase for longer deposition time or increased current density during the MAO process.

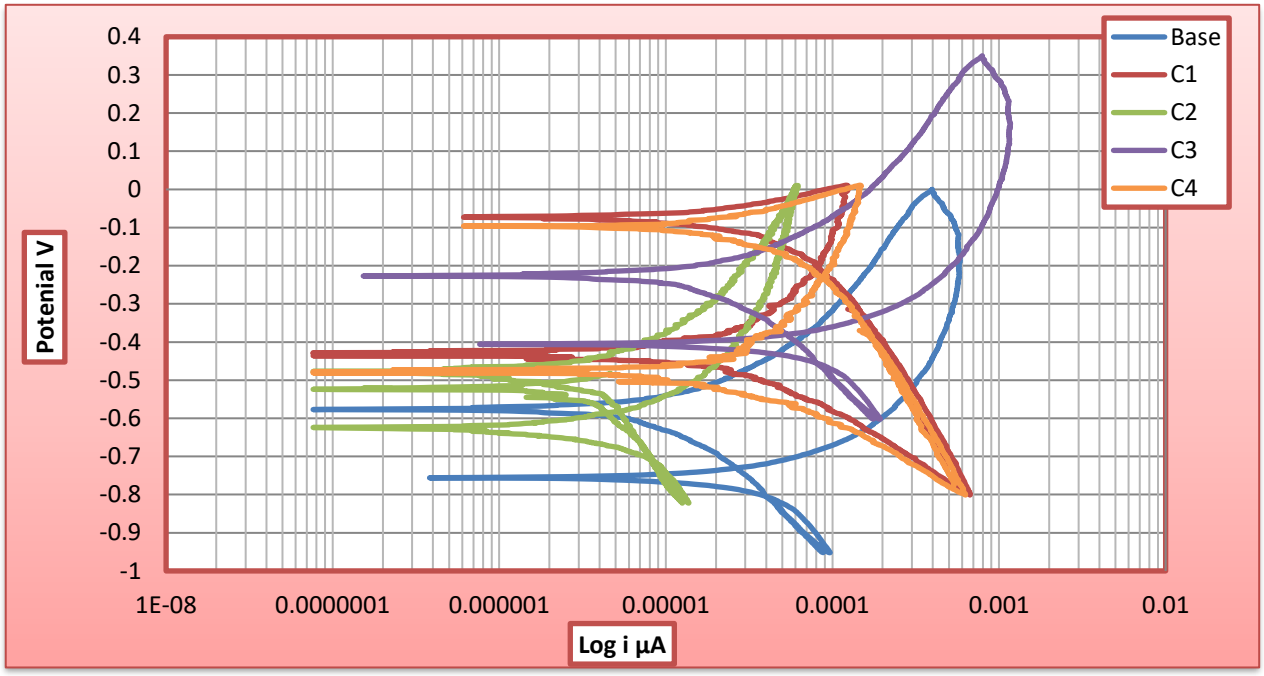

Figure (4.119): Cycle polarization curves of ZrO_2/TiO_2 coated on Ti-6Al-7Nb alloy by MAO process at different time and applied voltages 300V in Saliva's solution.

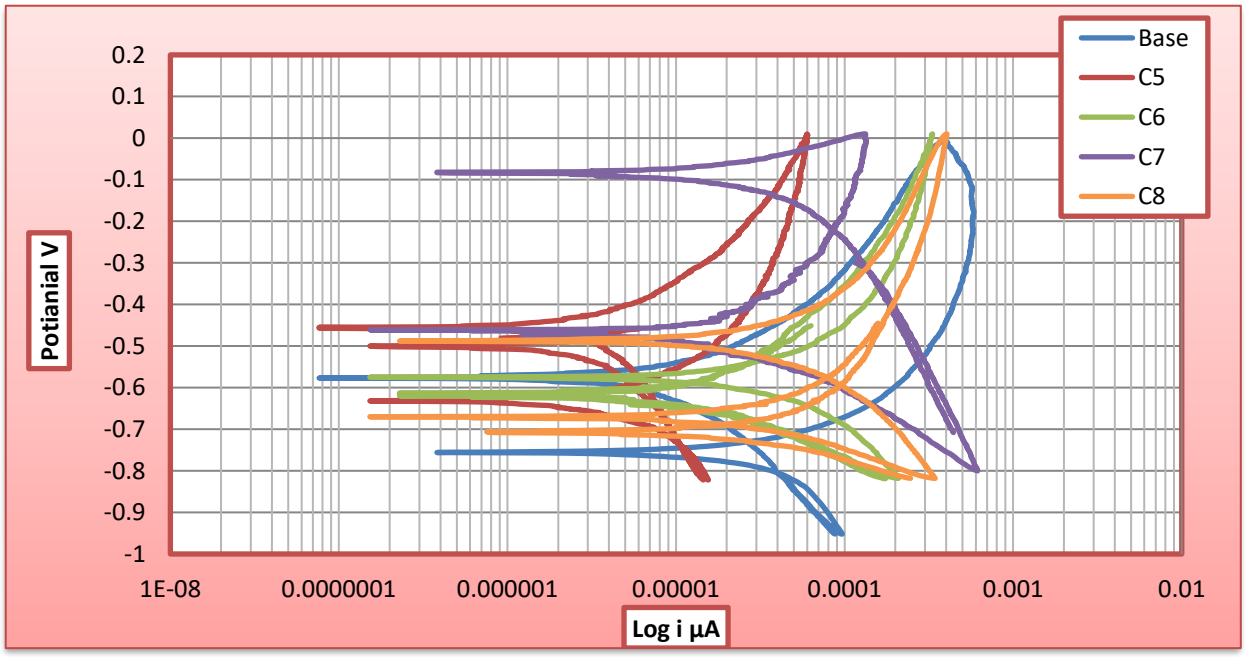

Figure (4.120): Cycle polarization curves of ZrO_2/TiO_2 coated on Ti-6Al-7Nb alloy by MAO process at different time and applied voltages 350V in Saliva's solution.

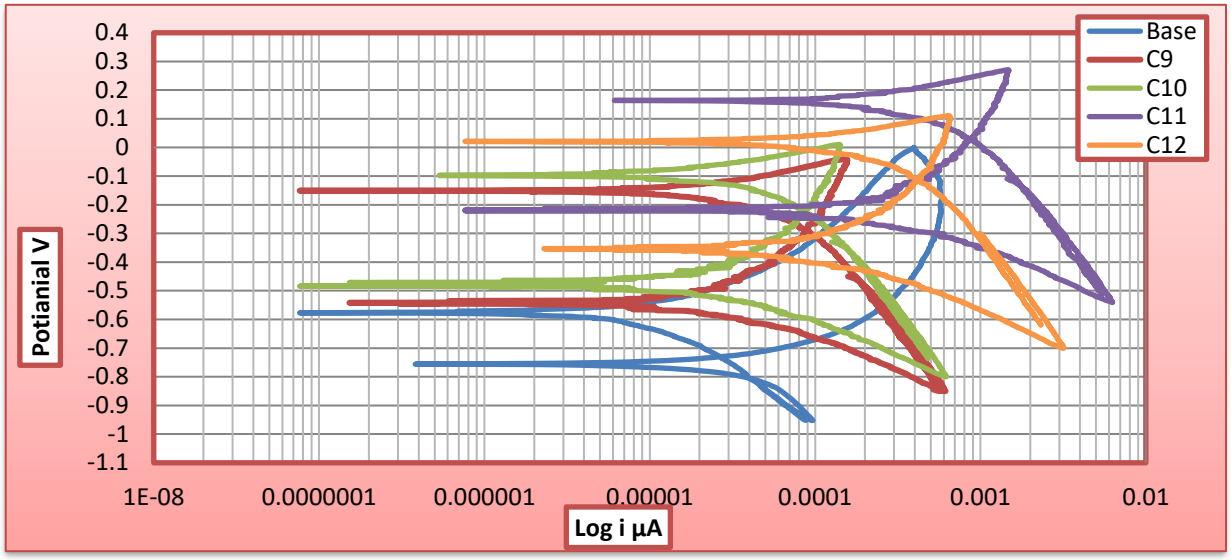

Figure (4.121): Cycle polarization curves of ZrO_2/TiO_2 coated on Ti-6Al-7Nb alloy by MAO process at different time and applied voltages 400V in Saliva's solution.

Table (4.19): Values of electrochemical parameters of substrate and ZrO_2/TiO_2 coated at different MAO applied voltages and time in Saliva's solution from cyclic polarization.

Sample Code	**$I_{corr.}$ (µA)**	**$i_{corr.}$ (µA/cm^2)**	**$E_{p.}$ (mV)**	**E_{prot} (mV)**	**$\Delta E = (E_p - E_{prot})$ (mV)**	**$C_R * 10^{-3}$ (mpy)**	**Improvement percentage (%)**
Base	9.750	7.34	-750	-515	-235	9.08	/
C_1	5.850	4.409	-436	-150	-286	5.448	40
C_2	5.113	3.854	-488	-197	-291	4.76	47.5
C_3	3.877	2.922	-400	-220	-180	3.61	60.24
C_4	2.965	2.234	-250	-120	-130	2.76	69.6
C_5	2.597	1.957	-549	-500	-49	2.118	73.3
C_6	2.536	1.911	-566	-612	36	2.362	74
C_7	2.263	1.705	-220	-86	-134	2.107	76.8
C_8	2.414	1.819	-490	-674	184	2.248	75.2
C_9	1.853	1.396	-280	-157	-123	1.726	81
C_{10}	1.567	1.181	-220	-100	-120	1.46	84
C_{11}	1.064	0.802	30	100	-70	0.99	89
C_{12}	1.309	0.986	-110	30	-140	1.219	86.5

Figures (4.122-4.127) show the corrosion behavior of HA/ZrO_2/TiO_2 nanocomposite coating with different parameters in two solutions (Ringer's and Saliva's). They show high resistance for pitting corrosion with increased voltage and time. This is attributed to the dependence of the film features on subtle changes in MAO process parameters and the uneven surfaces attained in some of the conditions due to successive breakdown of the film.

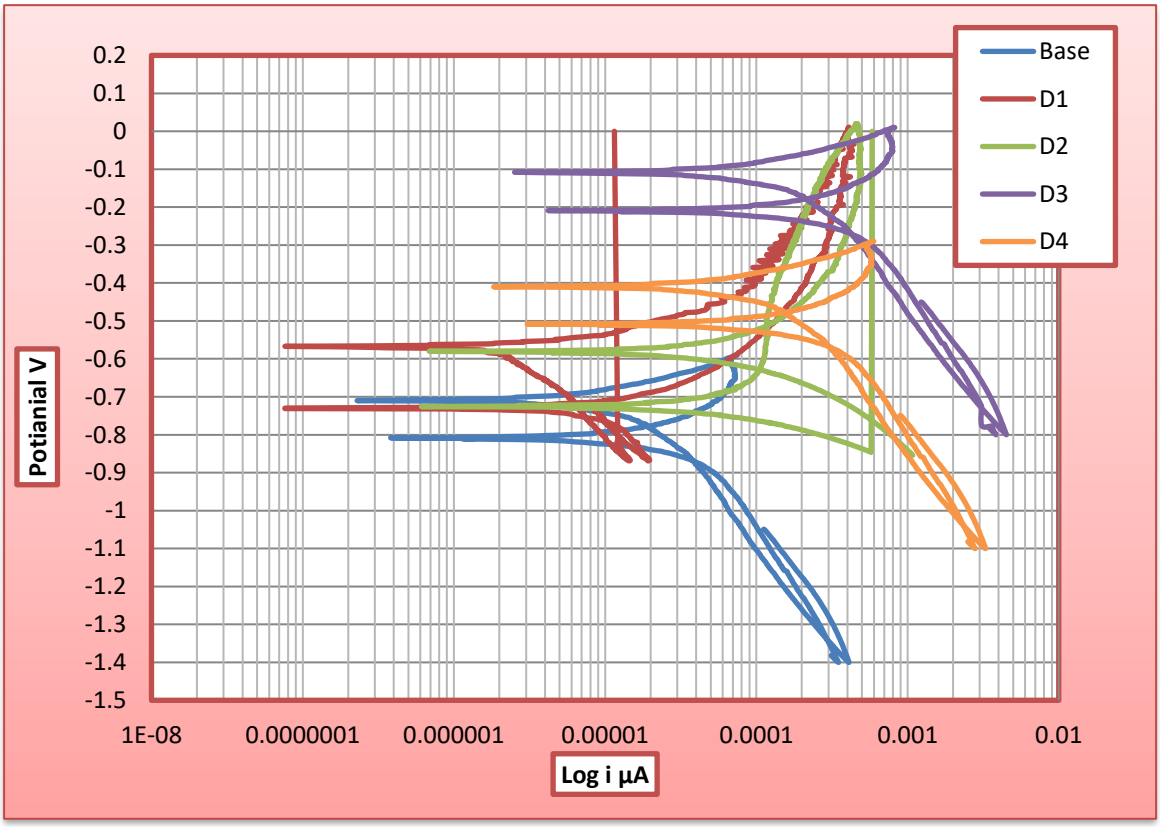

Figure (4.122): Cycle polarization curves of HA/ZrO_2/TiO_2 coated on Ti-6Al-7Nb alloy by MAO process at different time and applied voltages 300V in Ringer's solution.

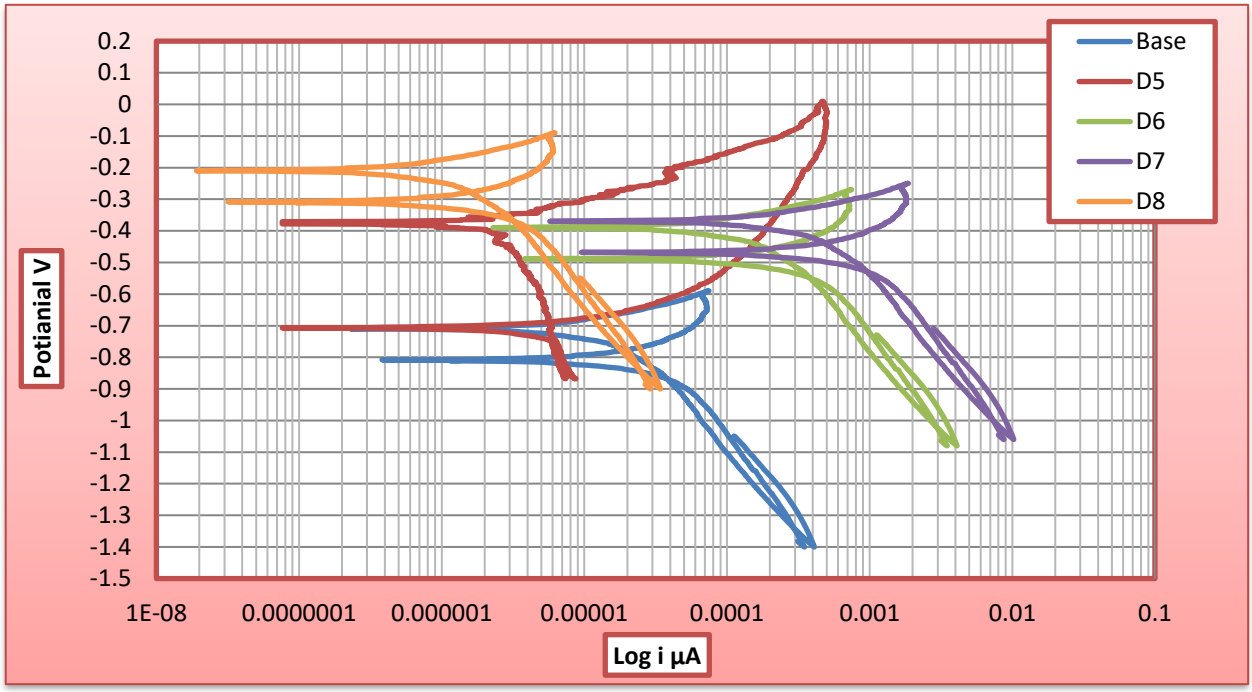

Figure (4.123): Cycle polarization curves of $HA/ZrO_2/TiO_2$ coated on Ti-6Al-7Nb alloy by MAO process at different time and applied voltages 350V in Ringer's solution.

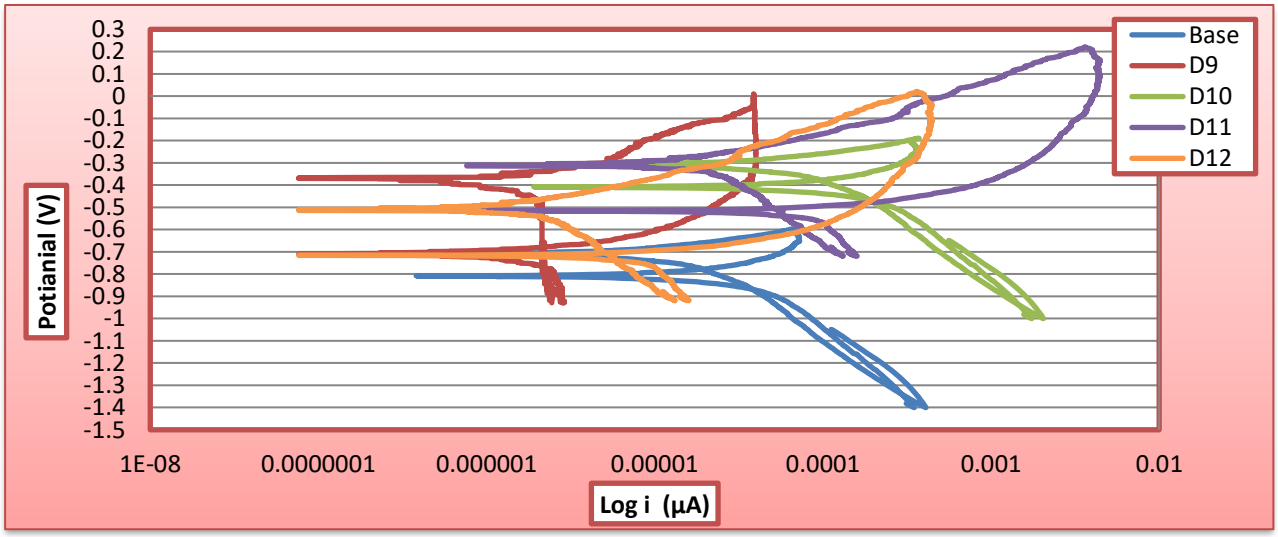

Figure (4.124): Cycle polarization curves of $HA/ZrO_2/TiO_2$ coated on Ti-6Al-7Nb alloy by MAO process at different time and applied voltages 400V in Ringer's solution.

Table (4.20): Values of electrochemical parameters of substrate and $HA/ZrO_2/TiO_2$ coated at different MAO applied voltages and time in Ringer's solution from cycle polarization.

Sample Code	$I_{corr.}$ (μA)	$i_{corr.}$ (μA/cm²)	$E_{p.}$ (mV)	E_{prot} (mV)	$\Delta E = (E_p - E_{prot})$ (mV)	$C_R * 10^{-3}$ (mpy)	Improvement percentage (%)
Base	9.505	7.164	-780	-630	-150	8.852	/
D_1	6.565	4.948	-720	-616	-104	6.114	31
D_2	5.748	4.332	-717	-675	-42	5.353	39.5
D_3	4.701	3.543	-190	-100	-90	4.378	50.5
D_4	4.507	3.397	-405	-400	-5	4.197	52.5
D_5	2.703	2.037	-700	-360	-340	2.517	71.5
D_6	2.084	1.570	-480	-372	-108	1.94	78
D_7	1.907	1.437	-483	-370	-113	1.776	79.15
D_8	1.878	1.415	-312	-213	-99	1.749	80
D_9	1.807	1.362	-692	-370	-322	1.75	80.23
D_{10}	1.669	1.258	-400	-318	-82	1.554	82.44
D_{11}	1.207	0.909	-513	-305	-208	1.124	87
D_{12}	1.807	1.362	-700	-500	-200	1.683	81

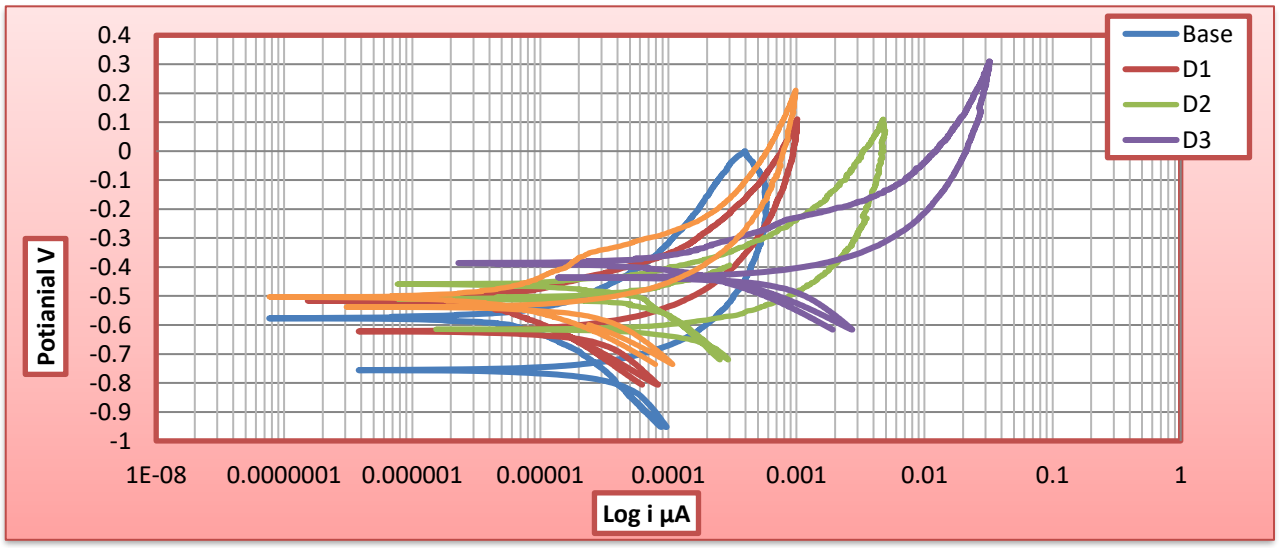

Figure (4.125): Cycle polarization curves of $HA/ZrO_2/TiO_2$ coated on Ti-6Al-7Nb alloy by MAO process at different time and applied voltages 300V in Saliva's solution.

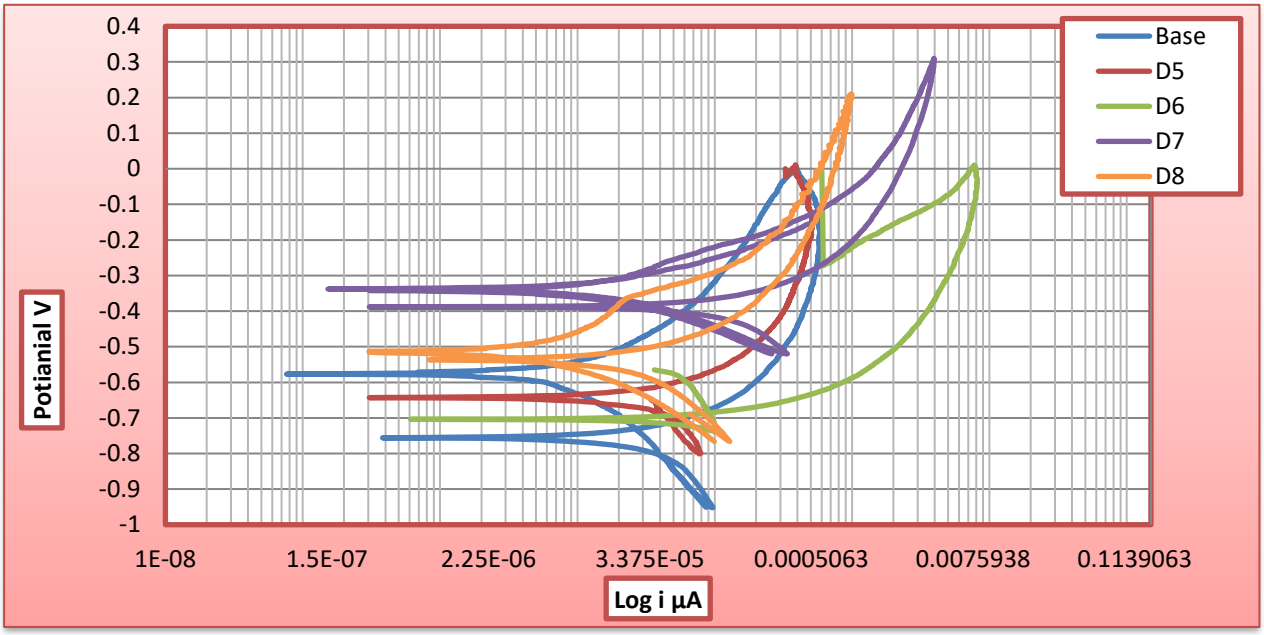

Figure (4.126): Cycle polarization curves of $HA/ZrO_2/TiO_2$ coated on Ti-6Al-7Nb alloy by MAO process at different time and applied voltages 350V in Saliva's solution.

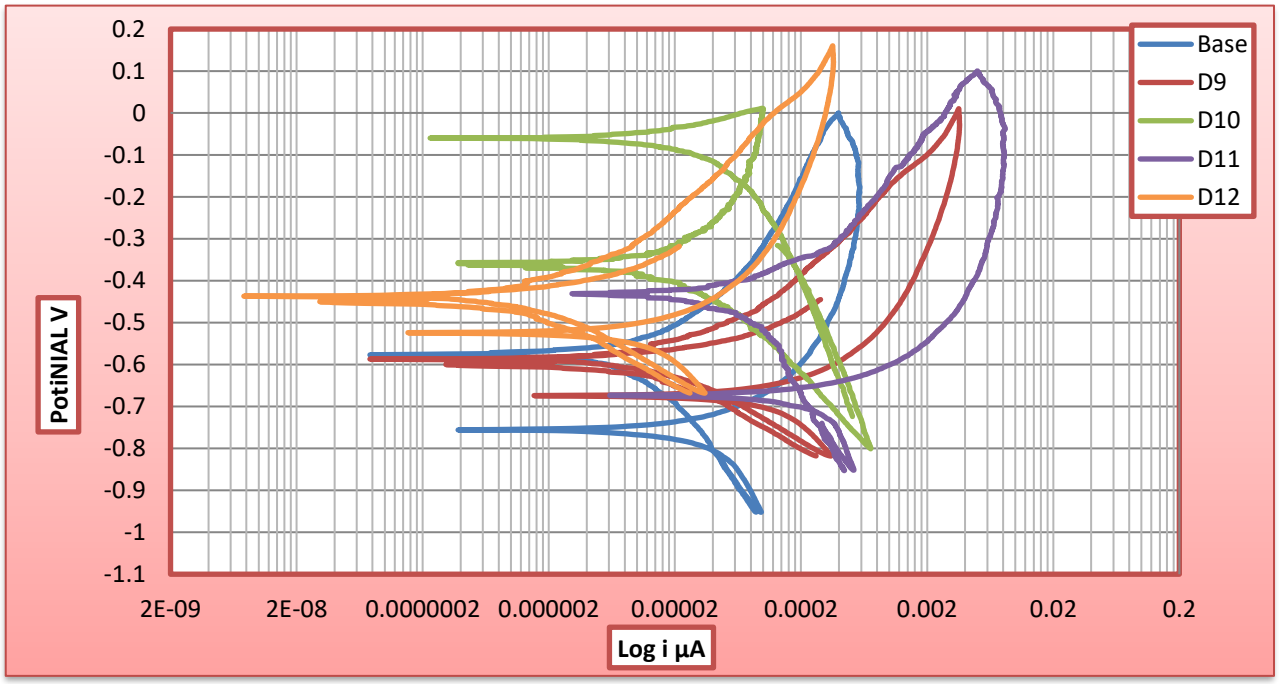

Figure (4.127): Cycle polarization curves of $HA/ZrO_2/TiO_2$ coated on Ti-6Al-7Nb alloy by MAO process at different time and applied voltages 400V in Saliva's solution.

Table (4.21): Values of electrochemical parameters of substrate and $HA/ZrO_2/TiO_2$ coated at different MAO applied voltages and time in Saliva's solution from cyclic polarization.

Sample Code	$I_{corr.}$ (µA)	$i_{corr.}$ (µA/cm^2)	$E_{corr.}$ (mV)	E_{prot} (mV)	$\Delta E = (E_p - E_{prot})$ (mV)	$C_R * 10^{-3}$ (mpy)	Improvement percentage (%)
Base	9.750	7.349	-750	-515	-235	9.08	/
D_1	7.430	5.6	-612	-506	-106	7	23
D_2	6.899	5.2	-620	-450	-170	6.425	29
D_3	5.019	3.783	-440	-402	-38	4.67	48.5
D_4	4.360	3.286	-543	-520	-23	4.06	55.3
D_5	4.298	3.239	-800	-626	-176	4	56
D_6	3.1	2.336	-788	-700	-88	2.88	68.3
D_7	1.524	1.148	-394	-322	-72	1.88	79.3
D_8	2.021	1.523	-547	-513	-34	1.728	81
D_9	1.856	1.399	-680	-593	-87	1.728	81
D_{10}	1.462	1.102	-678	-75	-603	1.36	85
D_{11}	0.645	0.486	-680	-471	-209	0.6	93.4
D_{12}	1.309	0.986	-523	-470	-53	1.219	86.5

The cyclic nature of the MAO process where the anodic oxide first created is broken down and later reformed albeit at a fixed current density during the process time results in a composite layer coating growth which in turn results in an inconsistency in the measured corrosion parameters. However, the corrosion properties of samples treated under the same MAO process conditions and times are quite similar highlighted by the small standard deviation in the data.

Consequently, the deposition of HA/TiO_2, ZrO_2/TiO_2, and $HA/ZrO_2/TiO_2$ nanocomposite coating on Ti-6Al-7Nb alloy have an excellent chemical stability, bioactivity, and mechanical integrity. Thus, the osseointegration properties could be improved and used as a biofilm for hard tissue implant applications.

4.9 Ion Release Test

Element of Ti-6Al-7Nb alloy was measured for coated and uncoated samples by using atomic absorption spectrometry in Ringer's solution at 37°C, PH 7.4 for 21 day and Saliva's solution at 37 Cº, PH 7.3 for 21 days.

Titanium ion release concentration in Ringer's solution shows in Figure (4.128) of the uncoated sample is (0.0301ppm). The lowest corresponding numbers of coated TiO_2 (0.0183ppm) and at HA/TiO_2 coated equal (0.0074ppm) and (0.0066ppm) for ZrO_2/TiO_2 coating and finally nanocomposite coating HA/ZrO_2/TiO_2 reduced to (0.0017ppm). This means that an improvement (39.2%, 75.4%, 78%, and 94.35%).

Titanium ion release concentration in Saliva's solution is shown in Figure (4.128) of the uncoated sample is (0.0274 ppm), the lowest corresponding numbers of sample TiO_2, HA/TiO_2, ZrO_2/TiO_2 and HA/ZrO_2/TiO_2 are (0.0191, 0.0077, 0.0048, and 0.0011) (ppm) respectively. This means that an improvement (30%, 71.89%, 82.48% and 95.98%) respectively. This enhancement in reducing titanium release is more likely due to HA/ZrO_2/TiO_2 layer provides an adherent and very protective layer which suppresses the Ti ion releasing because it isolates the surface completely from its surrounding.

Aluminum and Niobium ions release concentration in Ringer's solution is show in Figures (4.129) and (4.130) of the uncoated sample is (0.0172 and 0.0155) (ppm). The lowest corresponding numbers of coated TiO_2 (0.0043 and 0.0030) (ppm) and for HA/TiO_2 equal (0.0023 and 0.0024) (ppm) and (0.0019 and 0.0012) (ppm) for ZrO_2/TiO_2, and finally for HA/ZrO_2/TiO_2 equal to (0.0007 and 0.0004) (ppm) concentration of Al and Nb ion respectively. This means that improvements of Al ion were (75%, 86.6%, 88.95% and 96%) and Nb ion (80.6%, 84.5%, 93%, and 98.125%).

In Saliva's solution concentration of Al ion (0.016 ppm) and Nb ion (0.0147 ppm) as shown in Table (4.22), decreased concentration for TiO_2 coating (0.0026 and 0.0020) (ppm) for HA/TiO_2 (0.0013 and 0.0012) (ppm), (0.009 and 0.007) (ppm) for ZrO_2/TiO_2 and (0.0003 and 0.00025) for sample HA/ZrO_2/TiO_2. The improvement percentage equals to (83.75%, 91.8%, 94.37%, and 98.12%) for Al ions and (86.4%, 91.8%, 95.2%, and 98.3%) for Nb ions.

Table (4.22): The Amount of Ti, Al, and Nb ions Concentration in Ringer's solution at 37°C.

Sample Code	Ti		Al		Nb	
	Ringer's Solution	Saliva's Solution	Ringer's Solution	Saliva's Solution	Ringer's Solution	Saliva's Solution
Uncoated	0.0301	0.0274	0.0172	0.0160	0.0155	0.0147
TiO_2	0.0183	0.0191	0.0043	0.0026	0.0030	0.0020
HA/TiO_2	0.0074	0.0077	0.0023	0.0013	0.0024	0.0012
ZrO_2/TiO_2	0.0066	0.0048	0.0019	0.0009	0.0012	0.0007
HA/ZrO_2/TiO_2	0.0017	0.0011	0.0007	0.0003	0.0004	0.00025

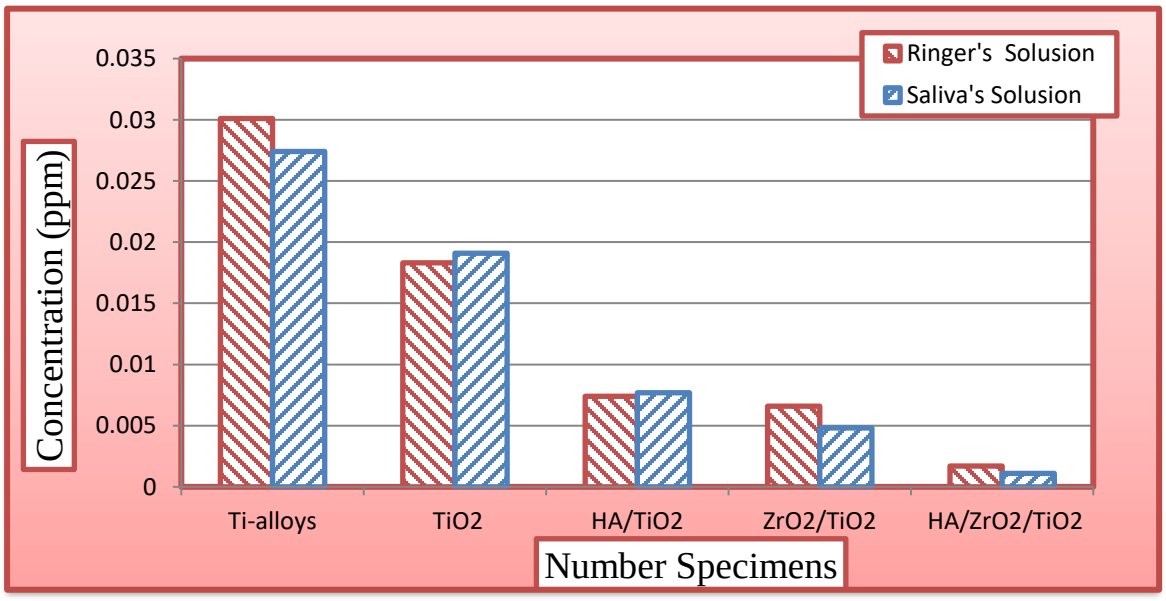

Figure (4.128): shows the amount of Ti ions concentration after immersion in Ringer's and Saliva's solution for 21 days.

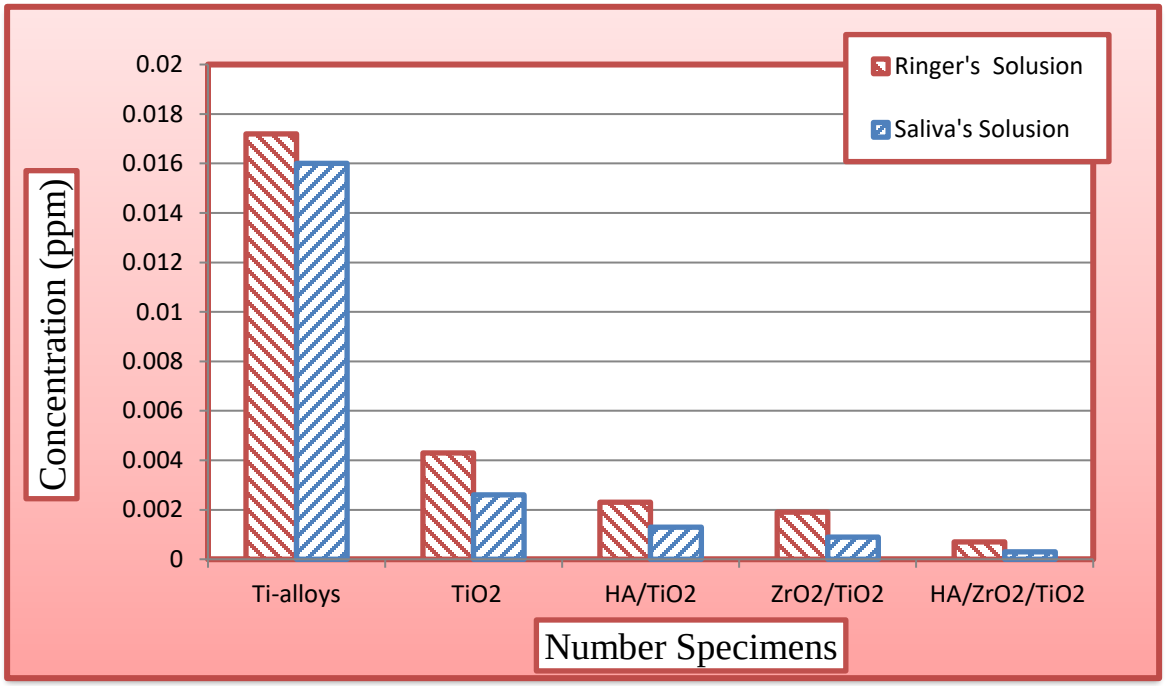

Figure (4.129): shows the amount of Al ions concentration after immersion in Ringer's and Saliva's solution for 21 days.

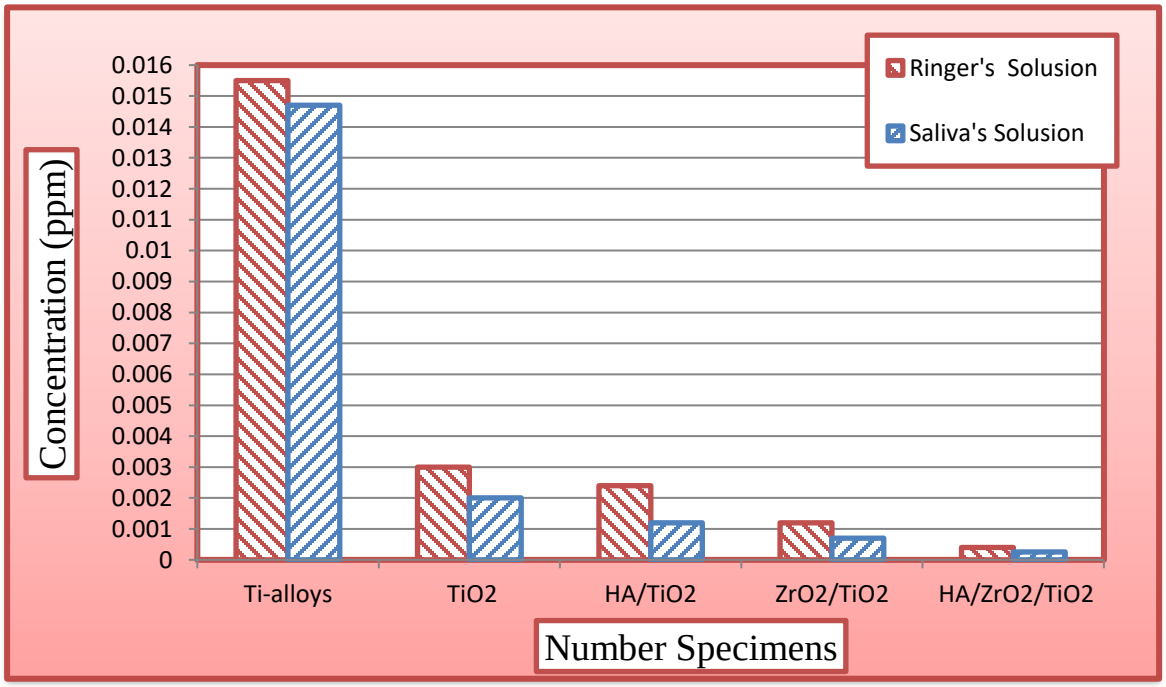

Figure (4.130): shows the amount of Nb ions concentration after immersion in Ringer's and Saliva's solution for 21 days.

4.10 Antibacterial Study

The antibacterial effect of the uncoated Ti-6Al-7Nb alloy and coating TiO_2 and nanocomposite ceramics coating layer HA/TiO_2, ZrO_2/TiO_2, and HA/ZrO_2/TiO_2 by MAO process. Suspensions were investigated against *E.coli* culture as shown in Figure (4.131). The formation of clear region around the disc refer to the bacterial inhibition zone. It can be observed that the coating samples cases exhibited good antibacterial effect towards *E.coli* after 24h of incubation period, but the uncoated alloy sample has a small inhibition zone as compared with the other coating samples. This is because of that the anatase TiO_2 itself is antibacterial [157] and therefore a strong antibacterial effect of the composite particles is obtained. Therefore, the presence of TiO_2 with nano particles in the HA and ZrO_2 coatings were effective in preventing of bacterial adhesion on the surface and in turn, preventing bacteria growth that would improve the antibacterial activity as shown in Figures (4.132- 4.135).

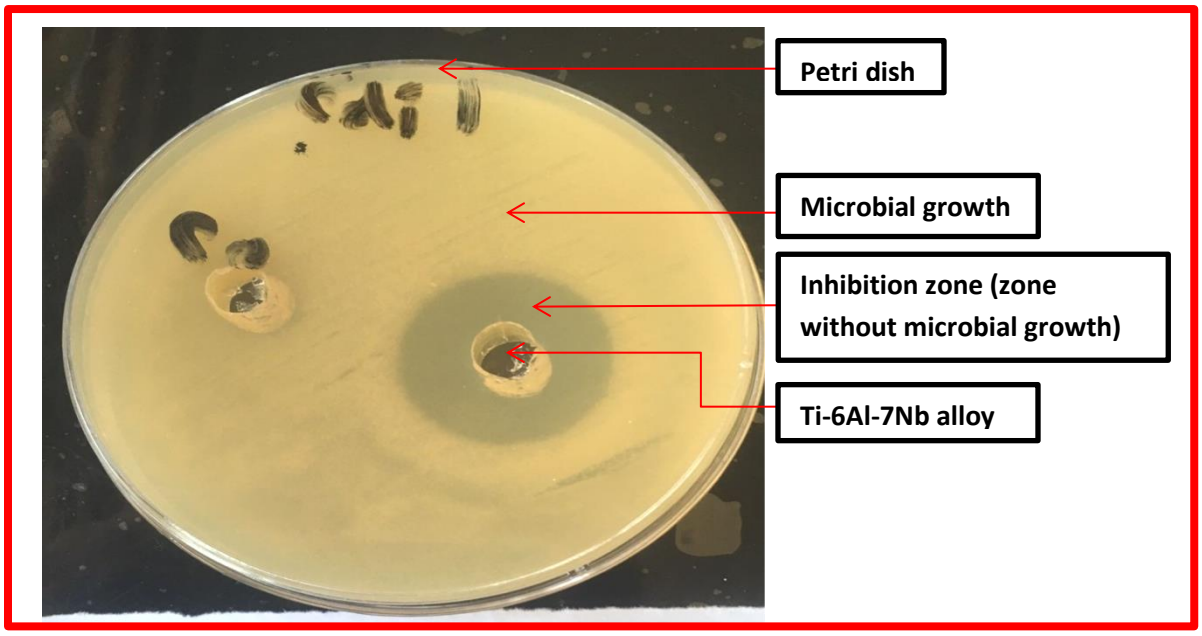

Figure (4.131): Visual photographs of antibacterial activity of E.coli performed for uncoated Ti-6Al-7Nb alloy.

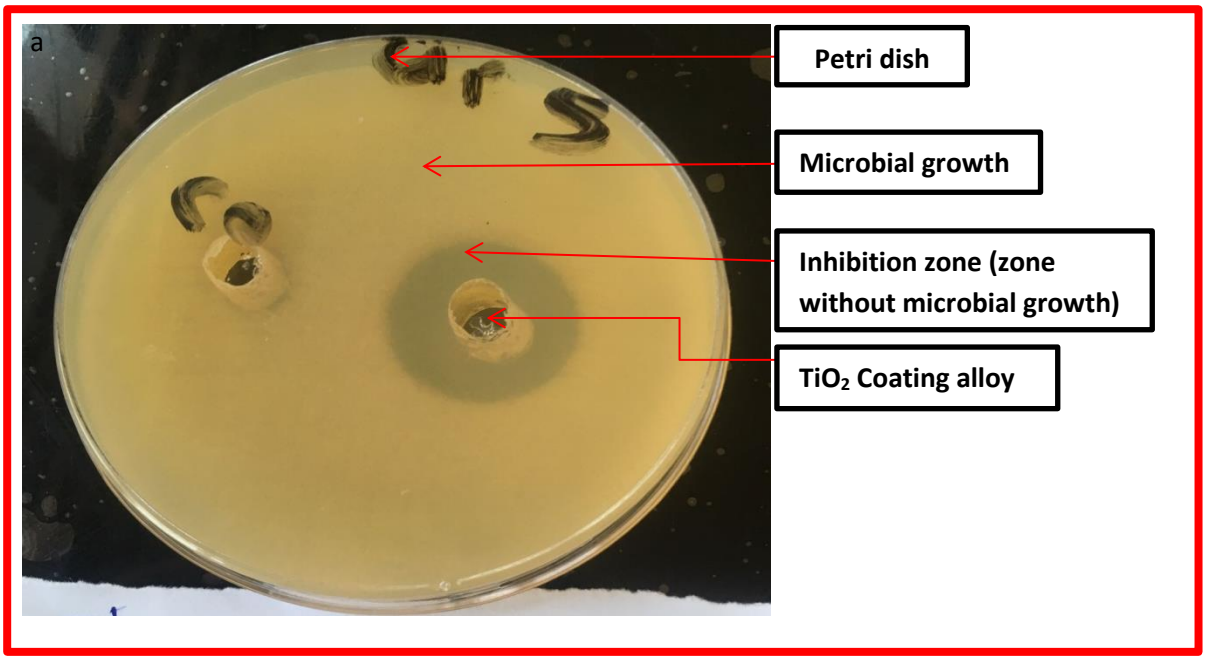

Figure (4.132): Visual photographs of antibacterial activity of E.coli performed for TiO_2 coated Ti-6Al-7Nb alloy.

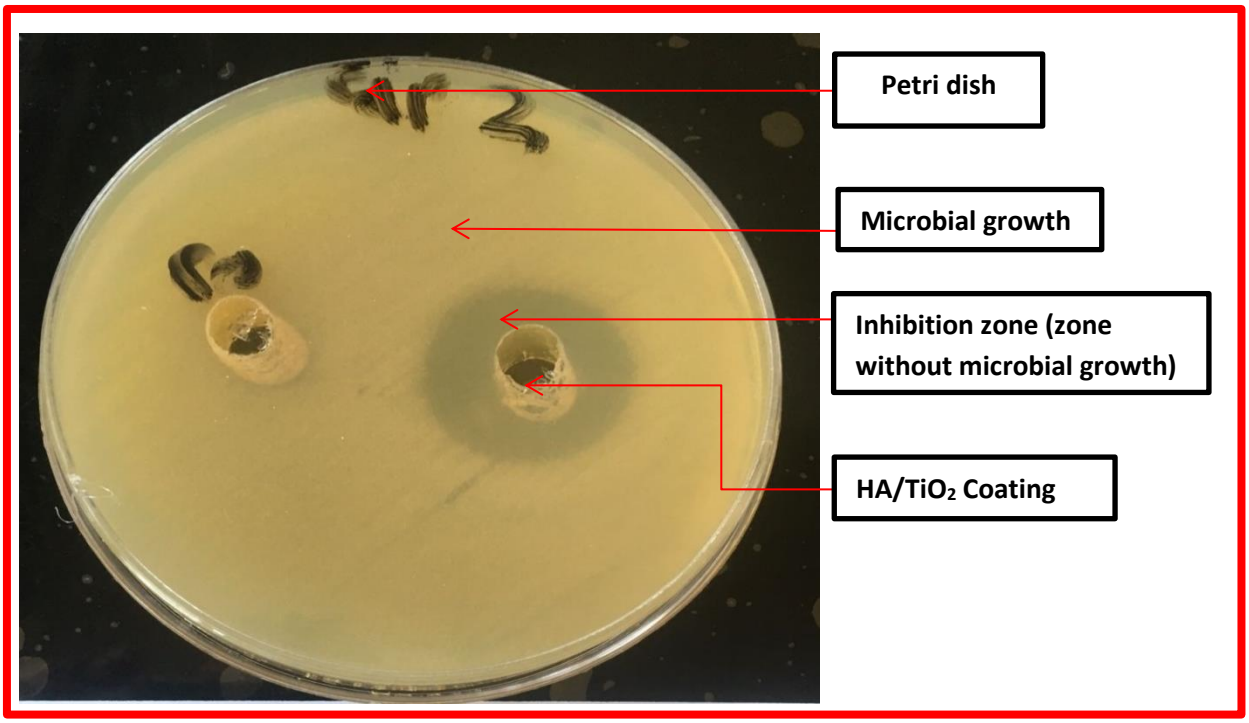

Figure (4.133): Visual photographs of antibacterial activity of E.coli performed for HA/TiO_2 coated Ti-6Al-7Nb alloy.

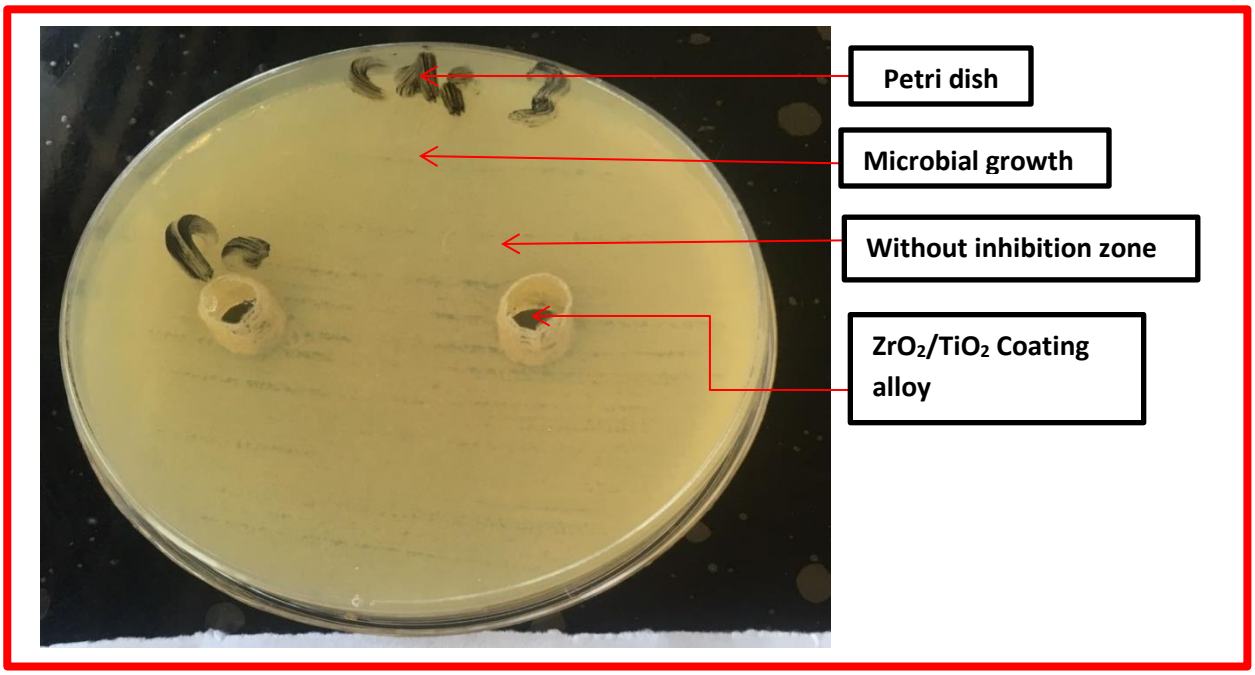

Figure (4.134): Visual photographs of antibacterial activity of E.coli performed for $ZrO_2//TiO_2$ coated Ti-6Al-7Nb alloy.

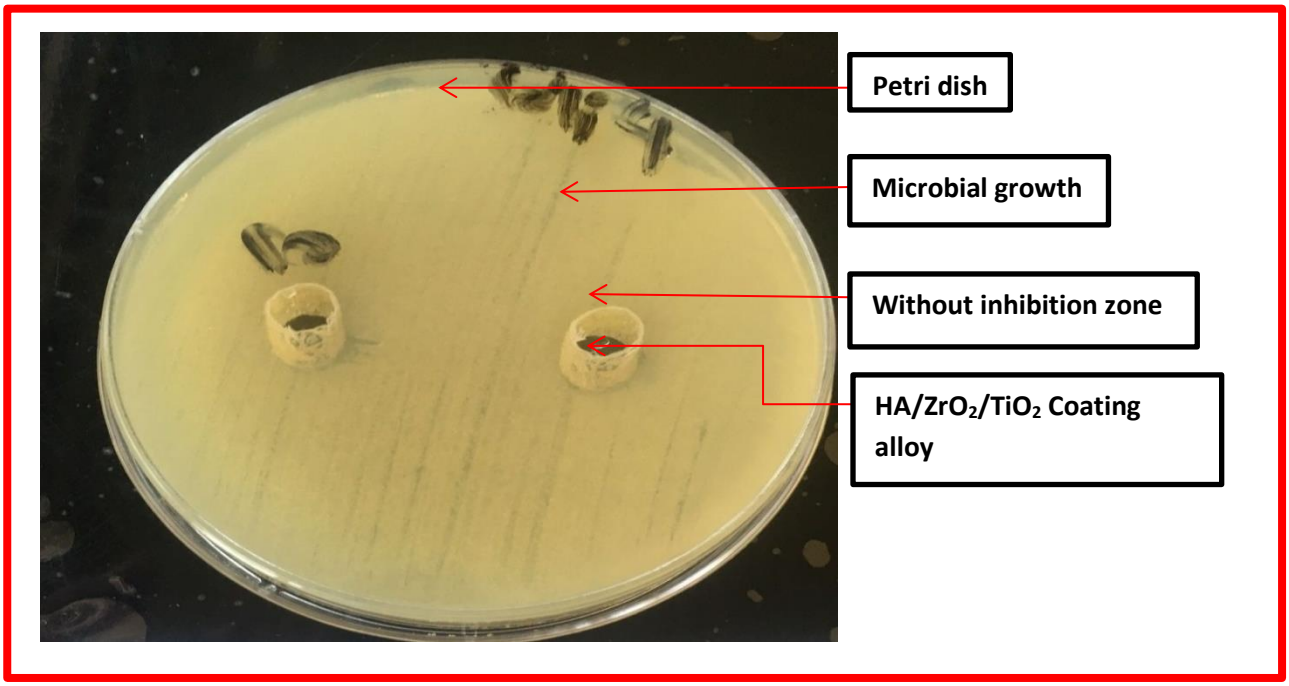

Figure (4.135): Visual photographs of antibacterial activity of *E.coli* performed for $HA/ZrO_2//TiO_2$ coated Ti-6Al-7Nb alloy.

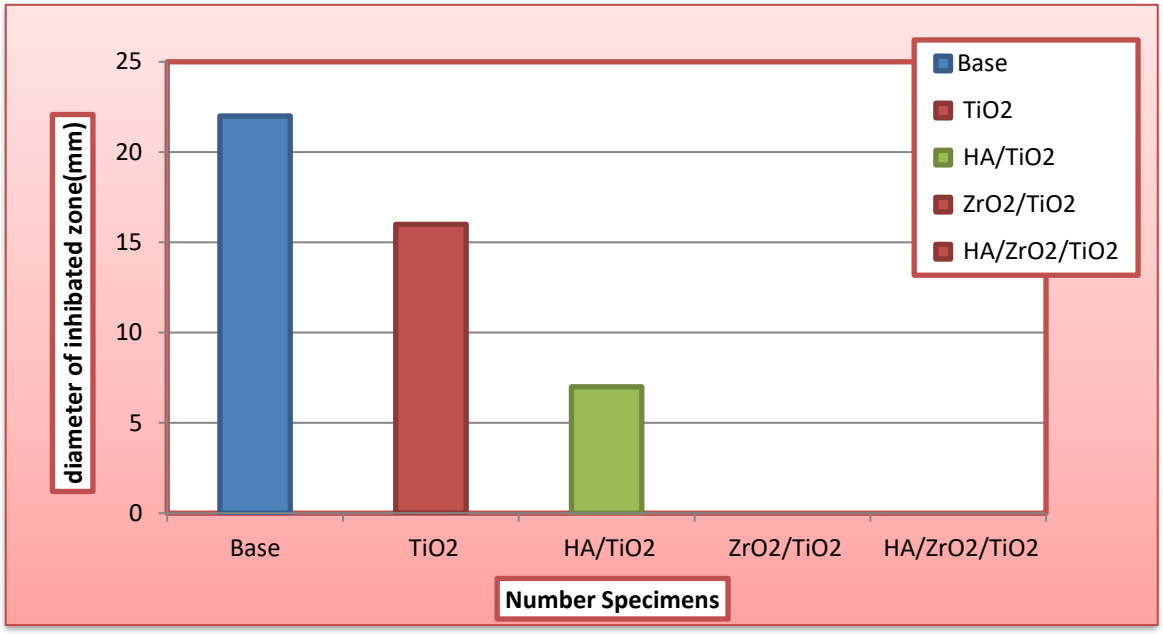

Figure (4.136): measurement diameter of inhibition zone of alloy and coating sample.

Chapter Five
Conclusion and Recommendations

Conclusions and Recommendations

5.1 Conclusions:

In the current study, the TiO_2 and nanocomposite coating HA/TiO_2, ZrO_2/TiO_2 and $HA/ZrO_2/TiO_2$ has been deposited on the surface of Ti-6Al-7Nb alloy successfully by using micro-arc oxidation process for biomedical applications. In view of the test results, the following conclusions can be presented:

1- It is observed that the TiO_2 layer grown on Ti-6Al-7Nb alloy base material with MAO method in specified parameters has circular micro pores in rough and volcanic structures because of continuous micro discharges occurring during the process. Rutile TiO_2 and anatase TiO_2 phases are determined on the material surface following the XRD analysis.

2- The average micro-hardness of the HA/TiO_2, ZrO_2/TiO_2, and $HA/ZrO_2/TiO_2$ nanocompasite coating is higher than the hardness of the TiO2 alone since that the presence of HA nano particles and ZrO_2 in the TiO_2 coating layer would improve the hardness and wear resistance of this layer.

3- The surface roughness of the substrate has an important role to improve the adhesion between coating and substrate. AFM topography shows homogenous and dense for the sample A_7 at (350V-30 min).

4- The morphology of composite coatings was homogenous and crack-free when coating with the best condition for sample D_7 at (350V- 30min).

5- The porosity analysis showed that the coating porosity increases with increasing voltage and deposition time.

6- EDS results showed that the ratio of Ca/P increased with voltage at coating HA/TiO_2 as well as, ZrO_2/TiO_2 coating.

7- The apparent contact angle decreases slightly after treated at different parameters (voltage and time). The significant change in the apparent contact angle of MAO coatings may result from surface morphology and content of the MAO coatings. The wettability of the MAO coating prepared at lower roughness may be under-estimated due to smaller pores. However, the wettability of the MAO coating prepared at higher roughness may be over-estimated due to no gas captured and coarser liquid/solid interface.

8- The potentiodynamic polarization results that Ti-6Al-7Nb base material , TiO_2, and HA/TiO_2, ZrO_2/TiO_2, and $HA/ZrO_2/TiO_2$ nanocomposite coating on Ti-6Al-7Nb alloys at different parameters in Ringer's solution and Saliva's solution; the best result for sample A_7 at TiO_2 coating equal ($i_{corr.}$=0.0902µA/cm^2) in Ringer's solution and ($i_{corr.}$= 0.833µA/cm^2) in Saliva's solution compared to the uncoated sample. The nanocomposite coating HA/TiO_2, ZrO_2/TiO_2, and $HA/ZrO_2/TiO_2$ has the lowest corrosion current density value (0.856, 0.864)µA/cm^2 in two solution and highest corrosion resistance for sample B_{11}, (0.433, 0.784)µA/cm^2 for sample C_{11}, and (0.814, 0.630)µA/cm^2 for sample D_{11} in two solution . In addition, the cyclic polarization results state improvement in the pitting corrosion resistance when immersed in the Ringer's solution and saliva's solution.

9- The ions release concentration (Ti, Al, and Nb) in Ringer's and saliva's solution significantly decreased for the coated samples compared with uncoated sample, as the concentration of ions is lower after being placed for 21 days in the Ringer's solution, which is for TiO_2 coating value (0.0183, 0.0043, and 0.003) ppm respectively, and in saliva solution (0.0191, 0.0026, and 0.002) ppm. This enhancement in reducing titanium, aluminum, and Niobium ions release is more likely due to $HA/ZrO_2/TiO_2$ layer provide an adherent and very protective layer.

10-The results of antibacterial analysis have confirmed that the ZrO_2/TiO_2 and $HA/ZrO_2/TiO_2$ nanocomposite coatings reveal a good antibacterial activity against gram negative *E.coli* which makes this coating safe and can be used for bone implant applications.

5.2 Recommendations:

1- Study the effect of using alternating current AC instead of direct current DC in the MAO coating with different alloys.
2- Studying MAO process for other titanium alloys.
3- Investigating effect of different concentrations of the electrolytic solution other material deposited by MAO process.
4- Studying other surface modification such as, laser surface treatment on the morphology and corrosion resistance of the $HA/ZrO_2/TiO_2$ nanocomposite coating should be scrutinized.
5- Studying the tribo-corrosion behavior of Ti-alloys modified by MAO process.
6- Studying MAO of titanium alloys in vivo.

Reference

References:

[1] A. Prof and A. Prof, “Surface modification of titanium and titanium alloys: technologies, developments and future interests” vol.10, pp.12-58, 2019.

[2] S. Dorozhkin, “Medical Application of Calcium Orthophosphate Bioceramics” Bio, vol. 1, no. 1, pp. 1–51, 2011.

[3] N. Patel and P. Gohil, “A review on biomaterials: scope, applications & human anatomy significance” Int. J. Emerg. Technol. Adv. Eng., vol. 2, no. 4, pp. 91–101, 2012.

[4] A. Nouri, P. D., and C. We, “Biomimetic Porous Titanium Scaffolds for Orthopedic and Dental Applications” Biomimetics Learn. from Nat., pp. 415–450, 2010.

[5] H. Chouirfa, H. Bouloussa, V. Migonney, and C. Falentin-Daudré, “Review of titanium surface modification techniques and coatings for antibacterial applications” Acta Biomater., vol. 83, pp. 37–54, 2019.

[6] S. Nag and R. Banerjee, “Materials for medical devices, fundamentals of medical implant materials” ASM Handbook, vol. 23, pp. 6–16, 2012.

[7] A.Cristea, " In Vitro Bioactivities of Anodised Titanium in Mixture of β-Glycerophosphate and Calcium Acetate for Biomedical Application" vol.9, no.2, p.10, 2016.

[8] N. Eliaz, “Corrosion of metallic biomaterials: A review” Materials (Basel)., vol. 12, no. 3, 2019.

[9] G. Manivasagam, D. Dhinasekaran, and A. Rajamanickam, “Biomedical Implants: Corrosion and its Prevention-A Review” Recent Patents Corros. Sci., vol. 2, no. 1, pp. 40–54, 2010.

[10] Y. Sasikumar, K. Indira, and N. Rajendran, “Surface Modification

References:

Methods for Titanium and Its Alloys and Their Corrosion Behavior in Biological Environment: A Review" J. Bio- Tribo-Corrosion, vol. 5, no. 2, p. 0, 2019.

[11] X. Liu, P.Chu, C.Ding "Surface Modification of Titanium, Titanium alloys, and related materials for biomedical applications" vol.47, no. 3-4, pp. 49-121, 2004.

[12] M. Nasab, M.Hassan, and B.Sahari "Metallic biomaterials of knee and hip - A review" vol.24, no.2, pp. 69-82, 2010.

[13] C. Yao, J. Lu, and T. J. Webster, "Titanium and cobalt-chromium alloys for hips and knees" Biomater. Artif. Organs, pp. 34–55, 2010.

[14] C.Prakash,S. Singh, and R. Singh, "Current Trends in Biomaterials and Bio-manufacturing" pp.1-271, 2019.

[15] P. Afzali, R. Ghomashchi, and R. H. Oskouei, "On the corrosion Behaviour of low modulus titanium alloys for medical implant applications: A review" Metals (Basel), vol. 9, no. 8, pp. 1–18, 2019.

[16] V. Vijay, K. Arjun, H. A. Kumar, A. V. Kumar, P. Chandrasekar, and V. Balusamy, "Review of various surface treatment techniques on titanium alloys and their protective effects against corrosion" J. Surf. Sci. Technol., vol. 23, no. 1–2, pp. 49–58, 2007.

[17] A. Kurella and N. B. Dahotre, "Review paper: Surface modification for bioimplants: The role of laser surface engineering", vol. 20, no. 1. 2005.

[18] M. Mozetič, "Surface Modification to Improve Properties of Materials" Materials (Basel)., vol. 12, no. 3, p. 441, 2019.

[19] A. Dehghanghadikolaei and B. Fotovvati, "Coating techniques for functional enhancement of metal implants for bone replacement: A

References:

review” Materials (Basel)., vol. 12, no. 11, 2019.

[20] W. Liu, S. Liu, and L. Wang, “Surface Modification of Biomedical Titanium Alloy: Micromorphology, Microstructure Evolution and Biomedical Applications” Coatings, vol. 9, no. 4, p. 249, 2019.

[21] M. R. Mucalo, "Animal-bone derived hydroxyapatite in biomedical applications". Elsevier Ltd., pp.307-342, 2015.

[22] T. M. Sridhar, “Nanobioceramic Coatings for Biomedical Applications” Mater. Technol., vol. 25, no. 3–4, pp. 184–195, 2010.

[23] Khaled R. Mohamed “Medical Bioceramic Materials Contents” 2017.

[24] A. Kumar, V. Kumar, M. Goel, R. Mehta, G. Bhayana, and S. Wadhwa, “Implant Surface Modification and Osseointegration-Past, Present and Future” J. Oral Heal. Community Dent., vol. 8, no. 2, pp. 113–118, 2014.

[25] A. Anvari, “Characterization of Implantation’s Biomaterials Based on the Patient and Doctor Expectations” Res. Med. Eng. Sci., vol. 4, no. 2, pp. 315–316, 2018.

[26] J. B. Park and J. D. Bronzino "Biomaterials Principles and applications" The Biomedical Engineering Handbook,2002 .

[27] A. Barfeie, J. Wilson, and J. Rees, “Implant surface characteristics and their effect on osseointegration” Br. Dent. J., vol. 218, no. 5, pp. 1–9, 2015.

[28] A. Radtke et al., “Optimization of the silver nanoparticles PEALD process on the surface of 1-D Titania coatings” Nanomaterials, vol. 7, no. 7, 2017.

[29] R. Article, “To The Point Review of Implant Materials Corrosion” vol. 2, pp. 1025–1029, 2016.

References:

[30] M. Abdel-Hady Gepreel and M. Niinomi, “Biocompatibility of Ti-alloys for long-term implantation” J. Mech. Behav. Biomed. Mater., vol. 20, pp. 407–415, 2013.

[31] M.Geetha, A.Singh, and R. Asokamani "Ti based biomaterials, the ultimate choice for orthopaedic implants- Areview" vol.54, no. 3, pp. 397-425.

[32] M. Niinomi, “Mechanical biocompatibilities of titanium alloys for biomedical applications” J. Mech. Behav. Biomed. Mater., vol. 1, no. 1, pp. 30–42, 2008.

[33] M. Kaur and K. Singh, “Review on titanium and titanium based alloys as biomaterials for orthopaedic applications” Mater. Sci. Eng. C, vol. 102, no. April, pp. 844–862, 2019.

[34] A. W. Nugroho, “Investigation of the Production and Mechanical Properties of Porous Beta Titanium Alloy Compacts Prepared by Powder Metallurgy Processes for Biomedical Applications” no. April, 2013.

[35] N. Mitsuo, “Mechanical properties of biomedical titanium alloys” Mater. Sci. Eng. A, vol. 243, no. 1–2, pp. 231–236, 1998.

[36] W. S. W. Harun, M. S. I. N. Kamariah, N. Muhamad, S. A. C. Ghani, F. Ahmad, and Z. Mohamed, “A review of powder additive manufacturing processes for metallic biomaterials” Powder Technol., vol. 327, pp. 128–151, 2018.

[37] A. T. Sidambe, “Biocompatibility of advanced manufactured titanium implants-A review” Materials (Basel)., vol. 7, no. 12, pp. 8168–8188, 2014.

[38] A. M. Khorasani, M. Goldberg, E. H. Doeven, and G. Littlefair,

References:

"Titanium in biomedical applications-properties and fabrication: A review" Journal of Biomaterials and Tissue Engineering. 2015.

[39] Y. Yang, "Surface treated cp-titanium for biomedical applications : a combined corrosion , tribocorrosion and biological approach" p. 205, 2015.

[40] M. A. Hussein, A. S. Mohammed, and N. Al-Aqeeli, "Wear characteristics of metallic biomaterials: A review" Materials (Basel)., vol. 8, no. 5, pp. 2749–2768, 2015.

[41] A. Radtke et al., "Bioactivity studies on titania coatings and the estimation of their usefulness in the modification of implant surfaces" Nanomaterials, vol. 7, no. 4, 2017.

[42] F. J. O'Brien, "Biomaterials & scaffolds for tissue engineering" Mater. Today, vol. 14, no. 3, pp. 88–95, 2011.

[43] Buddy D. Ratner, and Allan S. Hoffman " Biomaterials Science" 1996.

[44] Y. Kirmanidou et al., "New Ti-Alloys and Surface Modifications to Improve the Mechanical Properties and the Biological Response to Orthopedic and Dental Implants: A Review" Biomed Res. Int., vol. 2016.

[45] S. Abdi, "Investigation of new Ti-based metallic glasses with improved mechanical properties and corrosion resistance for implant applications" (1980).

[46] T. M. Sridhar, "Nanobioceramic coatings for biomedical applications" Mater. Technol., vol. 25, no. 3–4, pp. 184–195, 2010.

[47] V. vijay, K.Arjun, and H. Kumar " Review of Various surface treatment techniques on titanium alloys and their protective effects against corrosion" vol. 23, no. 1-2, pp. 49-58, 2007.

References:

[48] G. A. dos Santos, "The Importance of Metallic Materials as Biomaterials" Adv. Tissue Eng. Regen. Med. Open Access, vol. 3, no. 1, pp. 300–302, 2017.

[49] S. Kaur, K. Ghadirinejad, and R. H. Oskouei, "An overview on the tribological performance of titanium alloys with surface modifications for biomedical applications" Lubricants, vol. 7, no. 8, 2019.

[50] S. Bahl, S. Suwas, and K. Chatterjee, "Comprehensive review on alloy design, processing, and performance of β Titanium alloys as biomedical materials" Int. Mater. Rev., vol. 66, no. 2, pp. 114–139, 2021.

[51] D. Campoccia, L. Montanaro, and C. R. Arciola, "A review of the biomaterials technologies for infection-resistant surfaces" Biomaterials, vol. 34, no. 34, pp. 8533–8554, 2013.

[52] H. Unal, U. Sen, and A. Mimaroglu, "Abrasive wear behaviour of polymeric materials" Mater. Des., vol. 26, no. 8, pp. 705–710, 2005.

[53] F. Findik, "Wear Properties of Ti-Based Biomaterials" Curr. Trends Biomed. Eng. Biosci., vol. 12, no. 3, pp. 10–12, 2018.

[54] A. P. Harsha and U. S. Tewari, "Two-body and three-body abrasive wear behaviour of polyaryletherketone composites" Polym. Test., vol. 22, no. 4, pp. 403–418, 2003.

[55] A. Vadiraj and M. Kamaraj, "Characterization of fretting fatigue damage of PVD TiN coated biomedical titanium alloys" Surf. Coatings Technol., vol. 200, no. 14–15, pp. 4538–4542, 2006.

[56] L. Thair, U. K. Mudali, N. Bhuvaneswaran, K. G. M. Nair, R. Asokamani, and B. Raj, "Nitrogen ion implantation and in vitro corrosion behavior of as-cast Ti-6Al-7Nb alloy" Corros. Sci., vol. 44,

no. 11, pp. 2439–2457, 2002.

[57] G. Wu, P. Li, H. Feng, X. Zhang, and P. K. Chu, “Engineering and functionalization of biomaterials via surface modification” J. Mater. Chem. B, vol. 3, no. 10, pp. 2024–2042, 2015.

[58] M. kawano, Y. Takeda, K.Ogasawara "Pathological Analysis of Metal Allergy to Metallic Materials " pp. 305-321, 2015.

[59] X. B. Chen, A. Nouri, P. D. Hodgson, and C. E. Wen, “Surface modification of TiZr alloy for biomedical application” Adv. Mater. Res., vol. 15–17, pp. 89–94, 2007.

[60] M.Losertova "Advanced Materials" textbook, 2014.

[61] L. Mohan and C. Anandan, “Wear and corrosion behavior of oxygen implanted biomedical titanium alloy Ti-13Nb-13Zr” Appl. Surf. Sci., vol. 282, pp. 281–290, 2013.

[62] S. Shaikh, S. Kedia, D. Singh, M. Subramanian, and S. Sinha, “Surface texturing of Ti6Al4V alloy using femtosecond laser for superior antibacterial performance” J. Laser Appl., vol. 31, no. 2, p. 022011, 2019.

[63] Y. X. Leng, J. Y. Chen, P. Yang, H. Sun, and N. Huang, “Structure and properties of passivating titanium oxide films fabricated by DC plasma oxidation” Surf. Coatings Technol., vol. 166, no. 2–3, pp. 176–182, 2003.

[64] D. Gospodinov, N. Ferdinandov, and S. Dimitrov, “Classification, properties and application of titanium and its alloys” Proc. Univ. Ruse, vol. 55, no. 2, pp. 27–32, 2016.

[65] C. Cui, B. M. Hu, L. Zhao, and S. Liu, “Titanium alloy production technology, market prospects and industry development” Mater. Des.,

vol. 32, no. 3, pp. 1684–1691, 2011.

[66] E. D. Stoica, F. Fedorov, M. Nicolae, M. Uhlemann, A. Gebert, and L. Schultz, "Ti6Al7Nb surface modification by anodization in electrolytes containing HF" UPB Sci. Bull. Ser. B Chem. Mater. Sci., vol. 74, no. 2, pp. 277–288, 2012.

[67] M. Basiaga, Z. Paszenda, W. Walke, P. Karasiński, and J. Marciniak, "Impact of surface modification of Ti-6Al-7Nb alloy on electrochemical properties in the environment of artificial blood plasma" Solid State Phenom., vol. 227, pp. 491–494, 2015.

[68] X. Shen et al., "Altering the wetting properties of orthopaedic titanium alloy (Ti–6Al–7Nb) using laser shock peening" J. Alloys Compd., vol. 801, pp. 327–342, 2019.

[69] A. Radtke, M. Ehlert, T. Jędrzejewski, and M. Bartmański, "The Morphology, Structure, Mechanical Properties and Biocompatibility of Nanotubular Titania Coatings before and after Autoclaving Process" J. Clin. Med., vol. 8, no. 2, p. 272, 2019.

[70] C. N. Elias, J. H. C. Lima, R. Valiev, and M. A. Meyers, "Biomedical applications of titanium and its alloys Biological Materials Science 46-49" Biol. Mater. Sci., no. March, pp. 1–4, 2008.

[71] B. Moretti et al., "Peripheral neuropathy after hip replacement failure: Is vanadium the culprit" Lancet, vol. 379, no. 9826, p. 1676, 2012.

[72] S. Holmberg "Functionalizing C-MEMS: From Surface Modification to Structural Modification" 2018,

[73] S. V Dorozhkin, "Dental Applications of Calcium Orthophosphates ($CaPO_4$)" J. Dent. Res., vol. 1, no. 1, pp. 024–054, 2019.

[74] M. Almasri, "Introductory Chapter : Dental Implantology, The

Challenging Scenarios between Training, Resources, and Patients' Demands" Dent. Implantol. Biomater., 2016.

[75] E. Chikarakara et al., "In vitro fibroblast and pre-osteoblastic cellular responses on laser surface modified Ti-6Al-4V" Biomed. Mater., vol. 10, no. 1, 2015.

[76] A. Kurup, P. Dhatrak, and N. Khasnis, "Surface modification techniques of titanium and titanium alloys for biomedical dental applications: A review" Mater. Today Proc., vol. 39, no. xxxx, pp. 84–90, 2020.

[77] R. Bosco, J. V. Van Den Beucken, S. Leeuwenburgh, and J. Jansen, "Surface engineering for bone implants: A trend from passive to active surfaces" Coatings, vol. 2, no. 3, pp. 95–119, 2012.

[78] M. Kulkarni, A. Mazare, P. Schmuki, and A. Iglič, "Biomaterial surface modification of titanium and titanium alloys for medical applications" Nanomedicine, 2014.

[79] L. C. Zhang and L. Y. Chen, "A Review on Biomedical Titanium Alloys: Recent Progress and Prospect" Adv. Eng. Mater., vol. 21, no. 4, pp. 1–29, 2019.

[80] Liu, Xuanyong, Chu, Paul K., and Ding, Chuanxian "Surface modification of titanium, titanium alloys, and related materials for biomedical applications" Materials Science and Engineering R: Reports, vol.47, no. 3-4, pp. 49-121, 2004.

[81] S. V. Dorozhkin, "Calcium orthophosphate deposits: Preparation, properties and biomedical applications" Mater. Sci. Eng. C, vol. 55, pp. 272–326, 2015.

[82] M. T. Mohammed, Z. A. Khan, and A. N. Siddiquee, "Surface

Modifications of Titanium Materials for developing Corrosion Behavior in Human Body Environment: A Review" Procedia Mater. Sci., vol. 6, no. Icmpc, pp. 1610–1618, 2014.

[83] S. V. Dorozhkin, "Bioceramics of calcium orthophosphates" Biomaterials, vol. 31, no. 7, pp. 1465–1485, 2010.

[84] D. Ferro, S. M. Barinov, J. V. Rau, R. Teghil, and A. Latini, "Calcium phosphate and fluorinated calcium phosphate coatings on titanium deposited by Nd:YAG laser at a high fluence" Biomaterials, vol. 26, no. 7, pp. 805–812, 2005.

[85] S. V. Dorozhkin, "Multiphasic calcium orthophosphate (CaPO4) bioceramics and their biomedical applications" Ceram. Int., vol. 42, no. 6, pp. 6529–6554, 2016.

[86] Y. Sasikumar, K. Indira, and N. Rajendran "Surface Modification Methods for Titanium and Its Alloys and Their Corrosion Behavior in Biological Environment: A Review" Journal of Bio- and Tribo-Corrosion, vol.5, no.2, 2019.

[87] L. Mohan, D. Durgalakshmi, M. Geetha, T. S. N. Sankara Narayanan, and R. Asokamani, "Electrophoretic deposition of nanocomposite (HAp + TiO 2) on titanium alloy for biomedical applications" Ceram. Int., vol. 38, no. 4, pp. 3435–3443, 2012.

[88] L. T. De Jonge, S. C. G. Leeuwenburgh, J. G. C. Wolke, and J. A. Jansen, "Organic-inorganic surface modifications for titanium implant surfaces" Pharm. Res., vol. 25, no. 10, pp. 2357–2369, 2008.

[89] E. S. Thian, J. Huang, and M. Aizawa, "Nanobioceramics for Healthcare Applications",2017.

[90] A. Afzal, "Implantable zirconia bioceramics for bone repair and

replacement: A chronological review" Mater. Express, vol. 4, no. 1, pp. 1–12, 2014.

[91] R. Morrell, "Ceramic Matrix Materials", no. May 2015. Elsevier Ltd., 2016.

[92] W. liu, S. liu, and L. wang "Surface Modification of Biomedical Titanium Alloy: Micromorphology, Microstructure Evolution and Biomedical Applications" Coatings, vol.9, no. 4, pp. 249, 2019.

[93] A.Dehghanghadikolaei, and B.fotovvati "Coating techniques for functional enhancement of metal implants for bone replacement: A review" Materials, vol.12, no.11, 2019.

[94] R. O. Hussein, and D. O. Northwood, "Production of anti-corrosion coatings on light alloys (Al, Mg, Ti) by plasma-electrolytic oxidation (PEO)", (2014) Dr. Thesis, Developments in Corrosion Protection.

[95] A. Gao, R. Hang, L. Bai, B. Tang, and P. K. Chu, "Electrochemical surface engineering of titanium-based alloys for biomedical application" Electrochimica Acta. 2018.

[96] Y. Wang, H. Yu, C. Chen, and Z. Zhao, "Review of the biocompatibility of micro-arc oxidation coated titanium alloys" Mater. Des., vol. 85, pp. 640–652, 2015, doi: 10.1016/j. matdes.2015.07.086.

[97] R. E. White, "Applications of Electrochemistry and Nanotechnology in Biology and Medicine I" no. 52.

[98] H. Lord, W. Zhan, and J.Pawiszyn "Fundamentals and applications of needle trap devices" Comprehensive Sampling and Sample Preparation, vol.2, pp. 677-697, 2012.

[99] A. Nowakowski "Quantitative active dynamic thermal ir-imaging and thermal tomography in medical diagnostics" handbook, 2006.

References:

[100] A. Krząkała, A. Kazek-Kęsik, and W. Simka, “Application of plasma electrolytic oxidation to bioactive surface formation on titanium and its alloys” RSC Adv., vol. 3, no. 43, pp. 19725–19743, 2013.

[101] D.Yuting, L.Zhiyang, and M. Guofeng "The research progress on micro-arc oxidation of aluminum alloy" IOP Conference Series: Materials Science and Engineering, vol.729, 2020.

[102] M. Qadir, Y. Li, K. Munir, and C. Wen, “Calcium Phosphate-Based Composite Coating by Micro-Arc Oxidation (MAO) for Biomedical Application: A Review” Crit. Rev. Solid State Mater. Sci., vol. 43, no. 5, pp. 392–416, 2018.

[103] L. Xia, J. Han, J. P. Domblesky, Z. Yang, and W. Li, “Investigation of the Scanning Microarc Oxidation Process” Adv. Mater. Sci. Eng., vol. 2017, 2017.

[104] O. Riyad, and O. Derek "Production of Anti-Corrosion Coatings on Light Alloys (Al, Mg, Ti) by Plasma-Electrolytic Oxidation (PEO)" Developments in Corrosion Protection, 2014.

[105] X. Z. Lin, M. H. Zhu, J. F. Zheng, J. Luo, and J. L. Mo, “Fretting wear of micro-arc oxidation coating prepared on Ti6Al4V alloy” Trans. Nonferrous Met. Soc. China (English Ed., vol. 20, no. 4, pp. 537–546, 2010.

[106] Z. Q. Yao et al., “Synthesis and properties of hydroxyapatite-containing porous titania coating on ultrafine-grained titanium by micro-arc oxidation,” Acta Biomater., vol. 6, no. 7, pp. 2816–2825, 2010.

[107] X. Han et al., “In vitro Biological Effects of Ti2448 Alloy Modified by Micro-arc Oxidation and Alkali Heatment” J. Mater. Sci. Technol.,

vol. 27, no. 4, pp. 317–324, 2011.

[108] S. Cheng, D. Wei, and Y. Zhou, “The effect of oxidation time on the micro-arc titanium dioxide surface coating containing Si,Ca and Na” Procedia Eng., vol. 27, no. 2011, pp. 713–717, 2012.

[109] L. T. Duarte, S. R. Biaggio, R. C. Rocha-Filho, and N. Bocchi, “Surface characterization of oxides grown on the Ti-13Nb-13Zr alloy and their corrosion protection” Corros. Sci., vol. 72, pp. 35–40, 2013.

[110] L. C. Campanelli, L. T. Duarte, P. S. C. P. da Silva, and C. Bolfarini, “Fatigue behavior of modified surface of Ti-6Al-7Nb and CP-Ti by micro-arc oxidation” Mater. Des., vol. 64, pp. 393–399, 2014.

[111] A. R. Ribeiro et al., “Micro-arc oxidation as a tool to develop multifunctional calcium-rich surfaces for dental implant applications” Mater. Sci. Eng. C, vol. 54, pp. 196–206, 2015.

[112] W. Ping, W. Ting, P. Hao, and G. X. Yang, “Effect of NaAlO2 concentrations on the properties of micro-arc oxidation coatings on pure titanium” Mater. Lett., vol. 170, pp. 171–174, 2016.

[113] L. Xu et al., “Micro-Arc oxidation enhances the blood compatibility of ultrafine-grained pure titanium” Materials (Basel)., vol. 10, no. 12, pp. 1–18, 2017.

[114] C. Wang et al., “The influence of alloy elements in Ti–6Al–4V and Ti–35Nb–2Ta–3Zr on the structure, morphology and properties of MAO coatings” Vacuum, vol. 157, no. July, pp. 229–236, 2018.

[115] A. Sobolev, A. Kossenko, and K. Borodianskiy, “Study of the effect of current pulse frequency on Ti-6Al-4V alloy coating formation by micro arc oxidation” Materials (Basel)., vol. 12, no. 23, 2019.

[116] A. Zakaria, H. Shukor, M. Todoh, and K. Jusoff, “Bio-functional

coating on Ti6Al4V surface produced by using plasma electrolytic oxidation" Metals (Basel)., vol. 10, no. 9, pp. 1–16, 2020.

[117] T. Alloy, "coatings Effects of Micro-Arc Oxidation Process Parameters on Characteristics of Calcium-Phosphate Containing" coating , vol.10, pp. 745, 2020.

[118] X. Nie, A. Leyland, and A. Matthews, "Deposition of layered bioceramic hydroxyapatite/TiO2 coatings on titanium alloys using a hybrid technique of micro-arc oxidation and electrophoresis" Surf. Coatings Technol., vol. 125, no. 1–3, pp. 407–414, 2000.

[119] B.Ng, I.Annergren, and A.Soutar "Characterisation of a duplex TiO2/CaP coating on Ti6Al4V for hard tissue replacement" Biomaterials, vol.26, no. 10, pp.1087-1095, 2005.

[120] Y. Li, I. S. Lee, F. Z. Cui, and S. H. Choi, "The biocompatibility of nanostructured calcium phosphate coated on micro-arc oxidized titanium" Biomaterials, vol. 29, no. 13, pp. 2025–2032, 2008.

[121] H. Cimenoglu, M. Gunyuz, G. T. Kose, M. Baydogan, F. Uğurlu, and C. Sener, "Micro-arc oxidation of Ti6Al4V and Ti6Al7Nb alloys for biomedical applications" Mater. Charact., vol. 62, no. 3, pp. 304–311, 2011.

[122] S. Yu, Z. T. Yu, G. Wang, J. Y. Han, X. Q. Ma, and M. S. Dargusch, "Preparation and osteoinduction of active micro-arc oxidation films on Ti-3Zr-2Sn-3Mo-25Nb alloy" Trans. Nonferrous Met. Soc. China (English Ed., vol. 21, no. 3, pp. 573–580, 2011.

[123] M. H. Hong, D. H. Lee, K. M. Kim, and Y. K. Lee, "Study on bioactivity and bonding strength between Ti alloy substrate and TiO2 film by micro-arc oxidation" Thin Solid Films, vol. 519, no. 20, pp.

7065–7070, 2011.

[124] I. J. Hwang and H. C. Choe, “Hydroxyapatite coatings containing Zn and Si on Ti-6Al-4Valloy by plasma electrolytic oxidation” Appl. Surf. Sci., vol. 432, pp. 337–346, 2018.

[125] H. P. Teng, H. Y. Lin, Y. H. Huang, and F. H. Lu, “Formation of strontium-substituted hydroxyapatite coatings on bulk Ti and TiN-coated substrates by plasma electrolytic oxidation” Surf. Coatings Technol., vol. 350, pp. 1112–1119, 2018.

[126] W. Yang, D. Xu, Q. Q. Guo, T. Chen, and J. Chen, “Influence of electrolyte composition on microstructure and properties of coatings formed on pure Ti substrate by micro arc oxidation” Surf. Coatings Technol., vol. 349, no. June, pp. 522–528, 2018.

[127] D. R. N. Correa et al., “Growth mechanisms of Ca- and P-rich MAO films in Ti-15Zr-xMo alloys for osseointegrative implants” Surf. Coatings Technol., vol. 344, pp. 373–382, 2018.

[128] C. Garcia-Cabezón et al., “Application of plasma electrolytic oxidation coating on powder metallurgy Ti-6Al-4V for dental implants” Metals (Basel)., vol. 10, no. 9, pp. 1–15, 2020.

[129] Iijimaa, D.T. Yoneyamab, H. Doib, H. Hamanakab, and N. Kurosakia " Wear properties of Ti and Ti–6Al–7Nb castings for dental prostheses " a Department of Oral Diagnosis and General Dentistry, Graduate School, Tokyo Medical and Dental University, vol. 45, no.1-5, pp.113-8549, 2003.

[130] S. Steel, “The Influence of Surface Wettability and Topography on the Bioactivity of TiO_2 / Epoxy Coatings on AISI” 2019.

References:

[131] M. Qadir, Y. Li, K. Munir, and C. Wen ,"Calcium Phosphate-Based Composite Coating by Micro-Arc Oxidation (MAO) for Biomedical Application: A Review" , vol. 43, no.5, pp.392–416, 2018.

[132] Y. Li, W. Wang, J. Duan, and M. Qi, "A super-hydrophilic coating with a macro/micro/nano triple hierarchical structure on titanium by two-step micro-arc oxidation treatment for biomedical applications" Surf. Coatings Technol., vol. 311, pp. 1–9, 2017, doi: 10.1016/j. surfcoat. 2016.12.065.

[133] Tavsanoglu and Tolga. "Deposition and Characterization of Single and Multilayered Boron Carbide and Boron Carbonitride Thin Films by Different Sputtering Configurations" PhD Diss. University Technique d'Istanbul, 2009.

[134] K. Praveenkumar, and V. R. Kabadi "Realistic Approach to Pin –on-Disc Wear Testing Measurement" International Journal of Advanced Production and Industrial Engineering, vol.610,pp.47-53, 2017.

[135] B. Mellor "Surface coatings for protection against wear"

[136] Hahn RG. "Volume kinetics of infusion fluids. Anesthesiology " vol.113, pp. 470–81, 2010.

[137] Giacomelli F. C., C. Giacomelli and A. Spinelli "Behavior of a Co-Cr-Mo Biomaterial in Simulated Body Fluid Solutions Studied by Electrochemical and Surface Analysis Techniques" J. Braz. Chem. Soc., vol. 15, No. 4, PP. 541-547, 2004.

[138] Shalabi, M. M.,Wolke, J. G. and Jansen, and V. M "Evaluation of bone response to titanium-coated polymethacrylate resin (PMMA)implants by X-ray tomography" J. Mater sic. Mater Med, vol.18,pp.2033-2039, 2007.

References:

[139] M. Farrokhi-Rad and T. Shahrabi, "Effect of triethanolamine on the electrophoretic deposition of hydroxyapatite nanoparticles in isopropanol" Ceramics International, vol. 39, no. 6, 2013, pp. 7007-7013.

[140] A. Santos-Coquillat, R. Gonzalez Tenorio, M. Mohedano, E. Martinez-Campos, R. Arrabal, and E. Matykina, “Tailoring of antibacterial and osteogenic properties of Ti6Al4V by plasma electrolytic oxidation” Appl. Surf. Sci., vol. 454, pp. 157–172, 2018.

[141] V. S. De Viteri et al., “Structure, tribocorrosion and biocide characterization of Ca, P and I containing TiO 2 coatings developed by plasma electrolytic oxidation” Appl. Surf. Sci., vol. 367, pp. 1–10, 2016.

[142] L. Xu et al., “Effect of oxidation time on cytocompatibility of ultrafine-grained pure Ti in micro-arc oxidation treatment” Surf. Coatings Technol., vol. 342, pp. 12–22, 2018.

[143] D. Quintero et al., “Anodic films obtained on Ti6Al4V in aluminate solutions by spark anodizing: Effect of OH^- and $WO4^{-2}$ additions on the tribological properties” Surf. Coatings Technol., vol. 310, pp. 180–189, 2017.

[144] M. Shamsuzzoha, and E.Development "TMS2014 Annual Meeting Supplemental Proceedings" The Minerals, Metals & Materials Society, vol.1, pp.1057-1062, 2014.

[145] X. Shen, P. Shukla, S. Nath, and J. Lawrence, “Improvement in mechanical properties of titanium alloy (Ti-6Al-7Nb) subject to multiple laser shock peening” Surf. Coatings Technol., vol. 327, pp. 101–109, 2017.

References:

[146] M. Fellah, M. Labaiz, O. Assala, L. Dekhil, and A. Iost, “Tribological behavior of biomaterials for total hip prosthesis” Trends Biomater. Artif. Organs, vol. 29, no. 1, pp. 22–30, 2015.

[147] W.Lei, K.Mittal, and Z.Yu "Adhesion measurement of coatings on biodevices/implants: A critical review" Reviews of Adhesion and Adhesives, vol. 4, no. 4, pp. 367-396, 2016.

[148] M. B. Sedelnikova et al., “Modification of titanium surface via Ag-, Sr- and Si-containing micro-arc calcium phosphate coating” Bioact. Mater., vol. 4, no. July, pp. 224–235, 2019.

[149] O. Oleshko et al., “Biocompatibility and antibacterial properties of zno-incorporated anodic oxide coatings on TiZrNb alloy” Nanomaterials, vol. 10, no. 12, pp. 1–15, 2020.

[150] A. Cunha, “Multiscale femtosecond laser surface texturing of titanium and titanium alloys for dental and orthopaedic implants To cite this version : HAL Id : tel-01215468 DOCTEUR DE L ’ UNIVERSITÉ DE BORDEAUX ET DE L ’ INSTITUTO SUPERIOR TÉCNICO DE L ’ UNIVERSITÉ DE” 2015.

[151] A. C. Alves et al., “Effect of bio-functional MAO layers on the electrochemical behaviour of highly porous Ti” Surf. Coatings Technol., vol. 386, no. October 2019, p. 125487, 2020.

[152] W.Yang, D.Xu, and Q.Guo "Influence of electrolyte composition on microstructure and properties of coatings formed on pure Ti substrate by micro arc oxidation" Surface and Coatings Technology, vol. 349, pp.522-528, 2018.

[153] M. B. Sedelnikova et al., “Functionalization of pure titanium MAO coatings by surface modifications for biomedical applications” Surf.

Coatings Technol., vol. 394, no. March, p. 125812, 2020.

[154] A. Khandan, N. Ozada, D. Ogbemudia, and S. Saber-Samandari " Novel technology for bone cancer tumor by using hyperthermia treatment via bioceramic mechanism" UFGNSM , vol.12,pp. 13 , 2017.

[155] L. Lara Rodriguez and P. A. Sundaram, “Corrosion behavior of plasma electrolytically oxidized gamma titanium aluminide alloy in simulated body fluid” Mater. Chem. Phys., vol. 181, no. September, pp. 67–77, 2016.

[156] M. Metikoš-Huković, A. Kwokal, and J. Piljac, “The influence of niobium and vanadium on passivity of titanium-based implants in physiological solution” Biomaterials, vol. 24, no. 21, pp. 3765–3775, 2003.

[157] H. Khalaf, Z.Abdulhamied, and A. Dawod "Effect of surface modification of Si wafers on solar cell efficiency ZnO/P-Si thin films prepared by plasma sputtering" IOP Conference Series: Materials Science and Engineering, vol. 571, no. 1, 2019.

Appendix

Appendix

XRD Analysis:

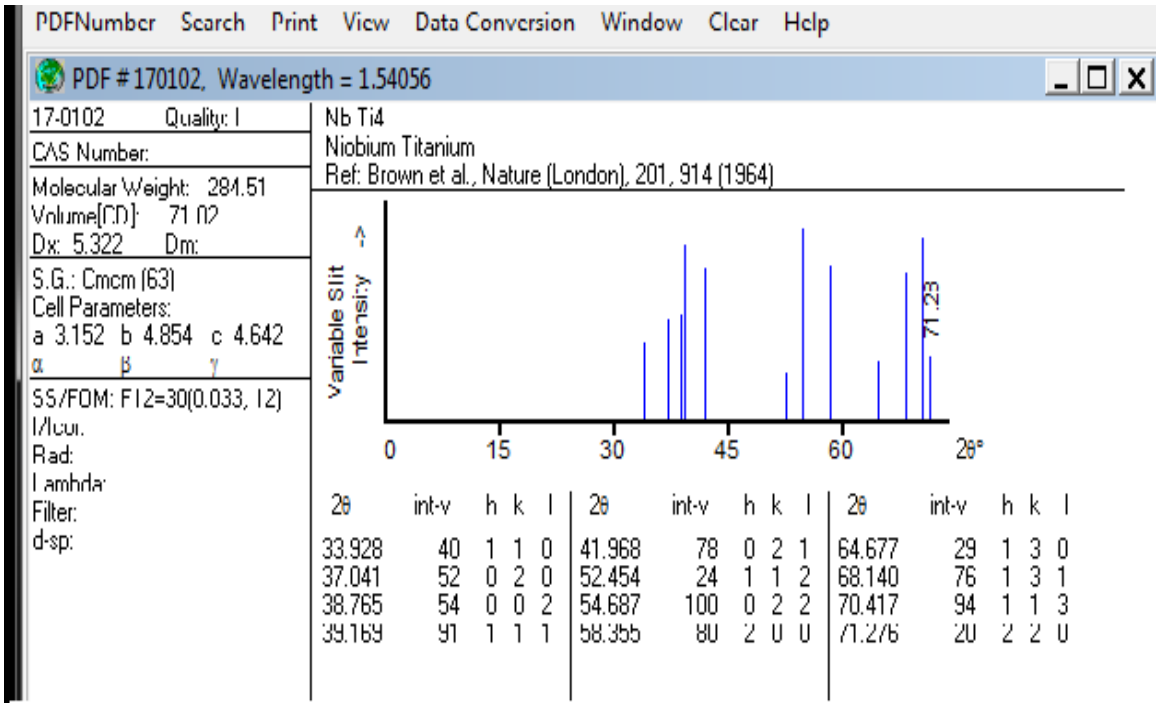

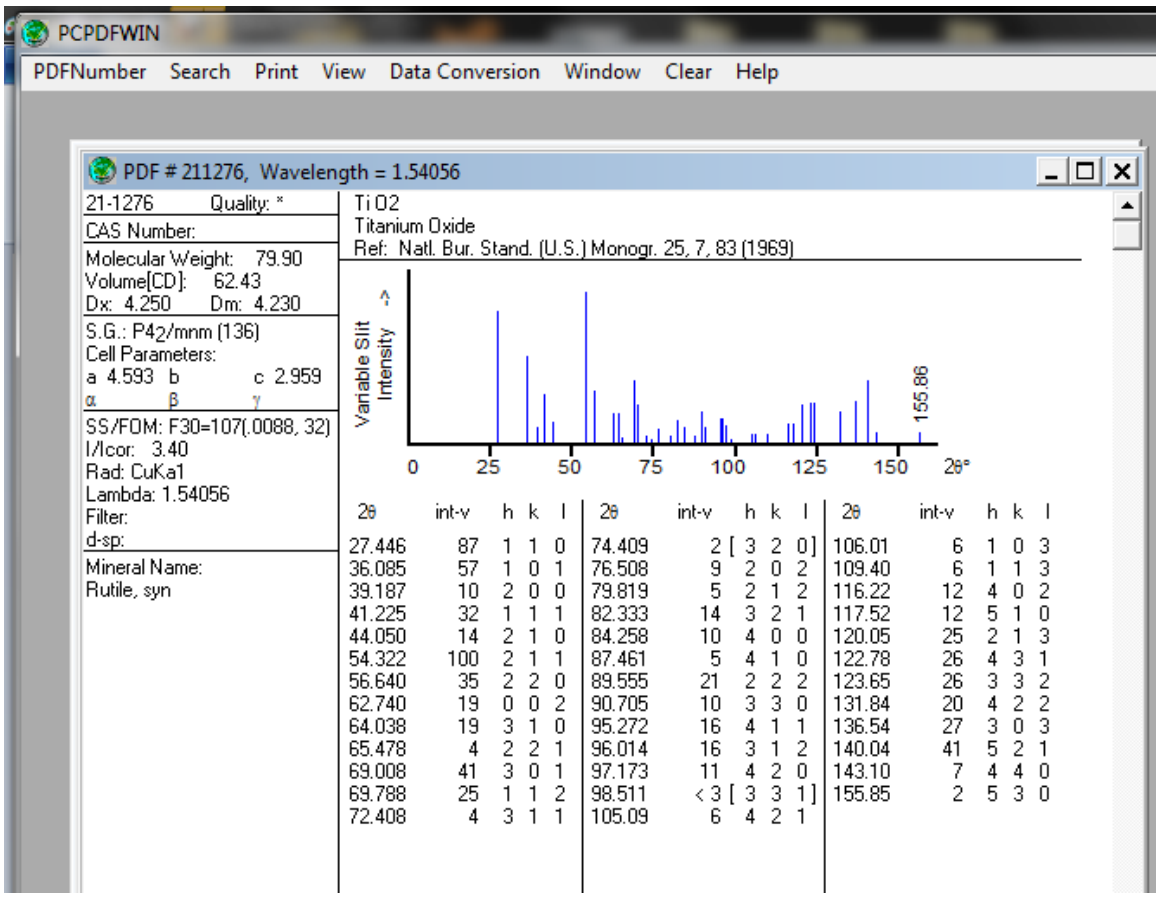

Appendix

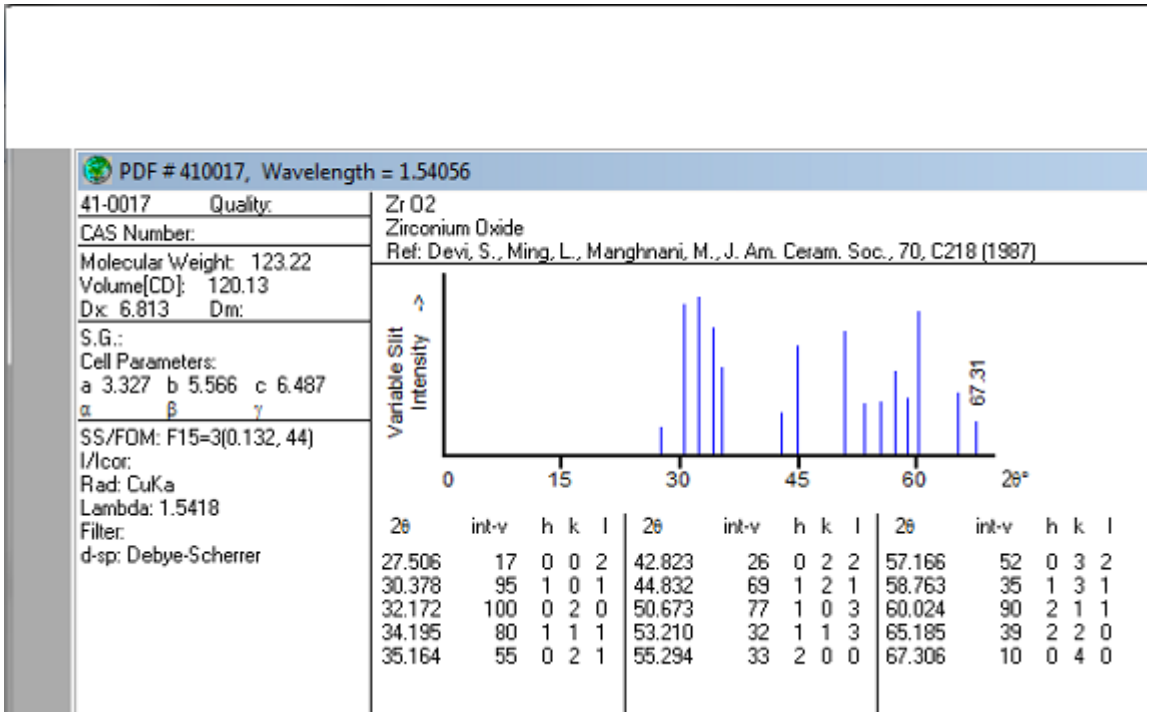

PDF # 410017, Wavelength = 1.54056

41-0017 Quality:
CAS Number:
Molecular Weight: 123.22
Volume[CD]: 120.13
Dx: 6.813 Dm:
S.G.:
Cell Parameters:
a 3.327 b 5.566 c 6.487
α β γ
SS/FOM: F15=3(0.132, 44)
I/Icor:
Rad: CuKa
Lambda: 1.5418
Filter:
d-sp: Debye-Scherrer

Zr O2
Zirconium Oxide
Ref: Devi, S., Ming, L., Manghnani, M., J. Am. Ceram. Soc., 70, C218 (1987)

2θ	int-v	h	k	l	2θ	int-v	h	k	l	2θ	int-v	h	k	l
27.506	17	0	0	2	42.823	26	0	2	2	57.166	52	0	3	2
30.378	95	1	0	1	44.832	69	1	2	1	58.763	35	1	3	1
32.172	100	0	2	0	50.673	77	1	0	3	60.024	90	2	1	1
34.195	80	1	1	1	53.210	32	1	1	3	65.185	39	2	2	0
35.164	55	0	2	1	55.294	33	2	0	0	67.306	10	0	4	0

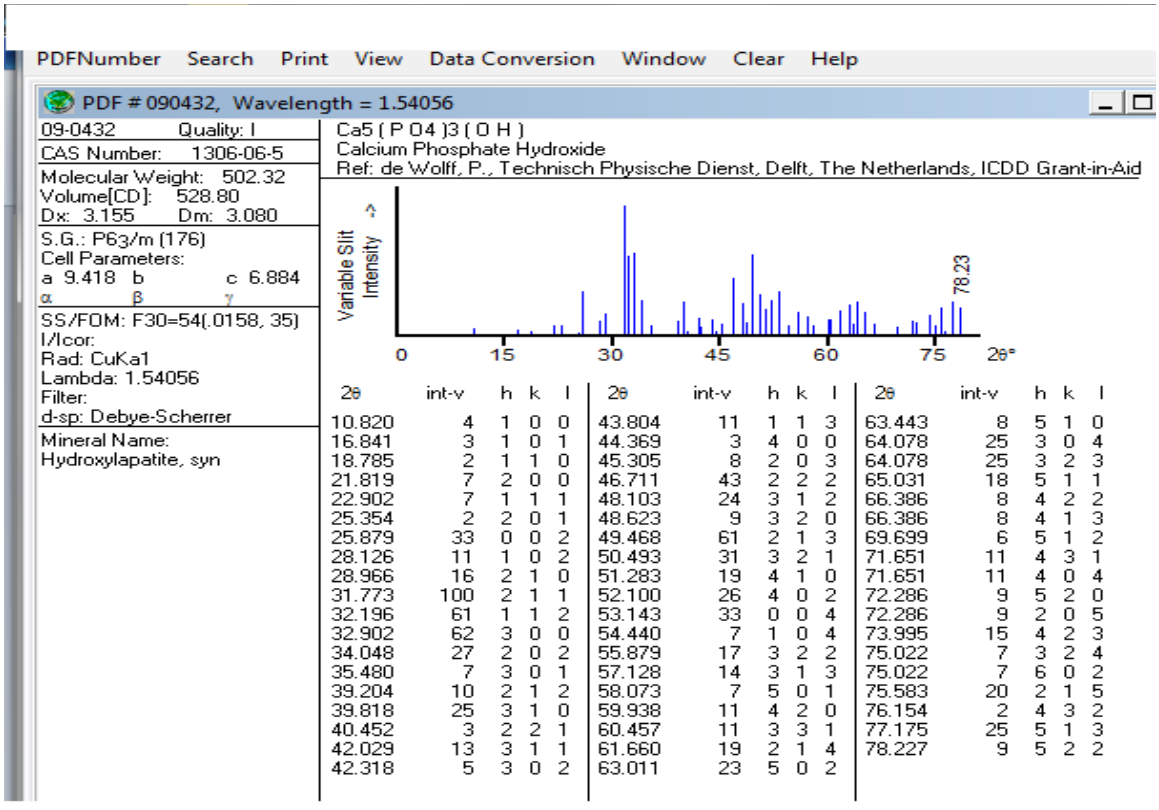

PDFNumber Search Print View Data Conversion Window Clear Help

PDF # 090432, Wavelength = 1.54056

09-0432 Quality: I
CAS Number: 1306-06-5
Molecular Weight: 502.32
Volume[CD]: 528.80
Dx: 3.155 Dm: 3.080
S.G.: P63/m (176)
Cell Parameters:
a 9.418 b c 6.884
α β γ
SS/FOM: F30=54(.0158, 35)
I/Icor:
Rad: CuKa1
Lambda: 1.54056
Filter:
d-sp: Debye-Scherrer
Mineral Name:
Hydroxylapatite, syn

Ca5 (P O4)3 (O H)
Calcium Phosphate Hydroxide
Ref: de Wolff, P., Technisch Physische Dienst, Delft, The Netherlands, ICDD Grant-in-Aid

2θ	int-v	h	k	l	2θ	int-v	h	k	l	2θ	int-v	h	k	l
10.820	4	1	0	0	43.804	11	1	1	3	63.443	8	5	1	0
16.841	3	1	0	1	44.369	3	4	0	0	64.078	25	3	0	4
18.785	2	1	1	0	45.305	8	2	0	3	64.078	25	3	2	3
21.819	7	2	0	0	46.711	43	2	2	2	65.031	18	5	1	1
22.902	7	1	1	1	48.103	24	3	1	2	66.386	8	4	2	2
25.354	2	2	0	1	48.623	9	3	2	0	66.386	8	4	1	3
25.879	33	0	0	2	49.468	61	2	1	3	69.699	6	5	1	2
28.126	11	1	0	2	50.493	31	3	2	1	71.651	11	4	3	1
28.966	16	2	1	0	51.283	19	4	1	0	71.651	11	4	0	4
31.773	100	2	1	1	52.100	26	4	0	2	72.286	9	5	2	0
32.196	61	1	1	2	53.143	33	0	0	4	72.286	9	2	0	5
32.902	62	3	0	0	54.440	7	1	0	4	73.995	15	4	2	3
34.048	27	2	0	2	55.879	17	3	2	2	75.022	7	3	2	4
35.480	7	3	0	1	57.128	14	3	1	3	75.022	7	6	0	2
39.204	10	2	1	2	58.073	7	5	0	1	75.583	20	2	1	5
39.818	25	3	1	0	59.938	11	4	2	0	76.154	2	4	3	2
40.452	3	2	2	1	60.457	11	3	3	1	77.175	25	5	1	3
42.029	13	3	1	1	61.660	19	2	1	4	78.227	9	5	2	2
42.318	5	3	0	2	63.011	23	5	0	2					

Appendix

AFM test:

Avg. Diameter:85.47 nm	**<=10% Diameter:55.00 nm**
<=50% Diameter:80.00 nm	**<=90% Diameter:120.00 nm**

Diameter (nm)<	Volume(%)	Cumulation(%)	Diameter (nm)<	Volume(%)	Cumulation(%)	Diameter (nm)<	Volume(%)	Cumulation(%)
35.00	0.41	0.41	70.00	9.09	33.06	105.00	6.20	78.10
40.00	0.41	0.83	75.00	4.96	38.02	110.00	2.07	80.17
45.00	1.24	2.07	80.00	7.02	45.04	115.00	4.55	84.71
50.00	2.48	4.55	85.00	8.68	53.72	120.00	3.72	88.43
55.00	4.13	8.68	90.00	6.20	59.92	125.00	3.31	91.74
60.00	6.61	15.29	95.00	5.79	65.70	130.00	2.89	94.63
65.00	8.68	23.97	100.00	6.20	71.90	135.00	5.37	100.00

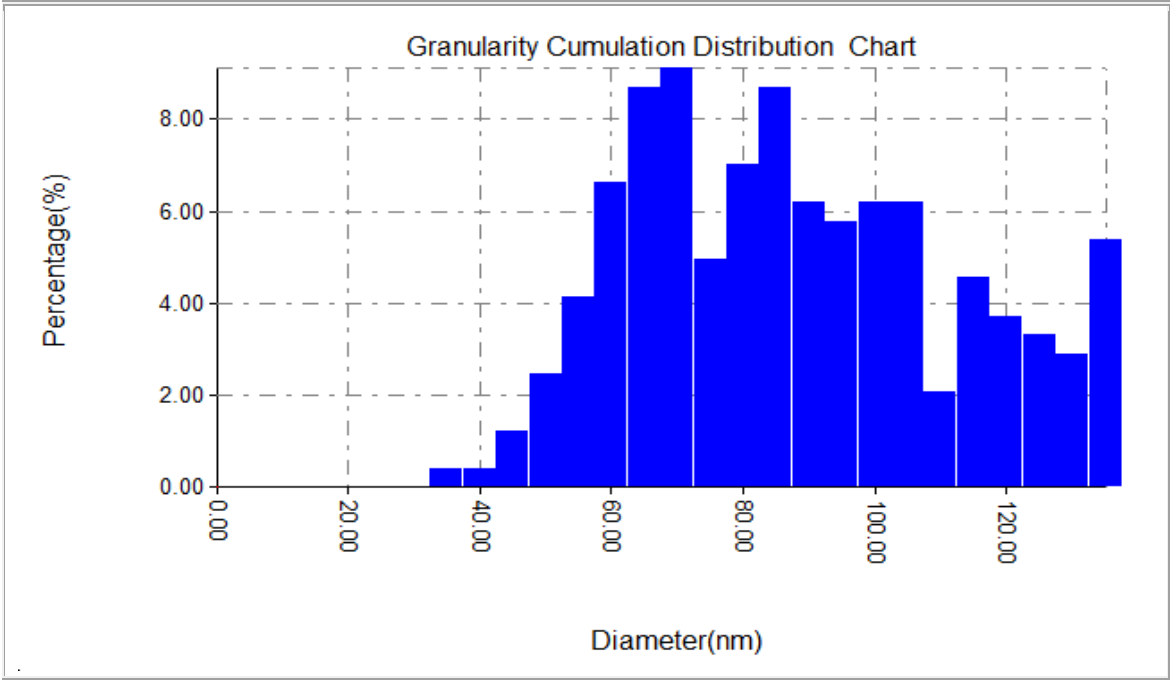

Avg. Diameter:95.54 nm	**<=10% Diameter:75.00 nm**
<=50% Diameter:90.00 nm	**<=90% Diameter:120.00 nm**

Diameter (nm)<	Volume(%)	Cumulation(%)	Diameter (nm)<	Volume(%)	Cumulation(%)	Diameter (nm)<	Volume(%)	Cumulation(%)
75.00	4.32	4.32	100.00	9.35	64.75	125.00	5.04	93.53
80.00	15.83	20.14	105.00	8.63	73.38	130.00	4.32	97.84
85.00	12.95	33.09	110.00	4.32	77.70	135.00	2.16	100.00
90.00	13.67	46.76	115.00	7.91	85.61			
95.00	8.63	55.40	120.00	2.88	88.49			

Appendix

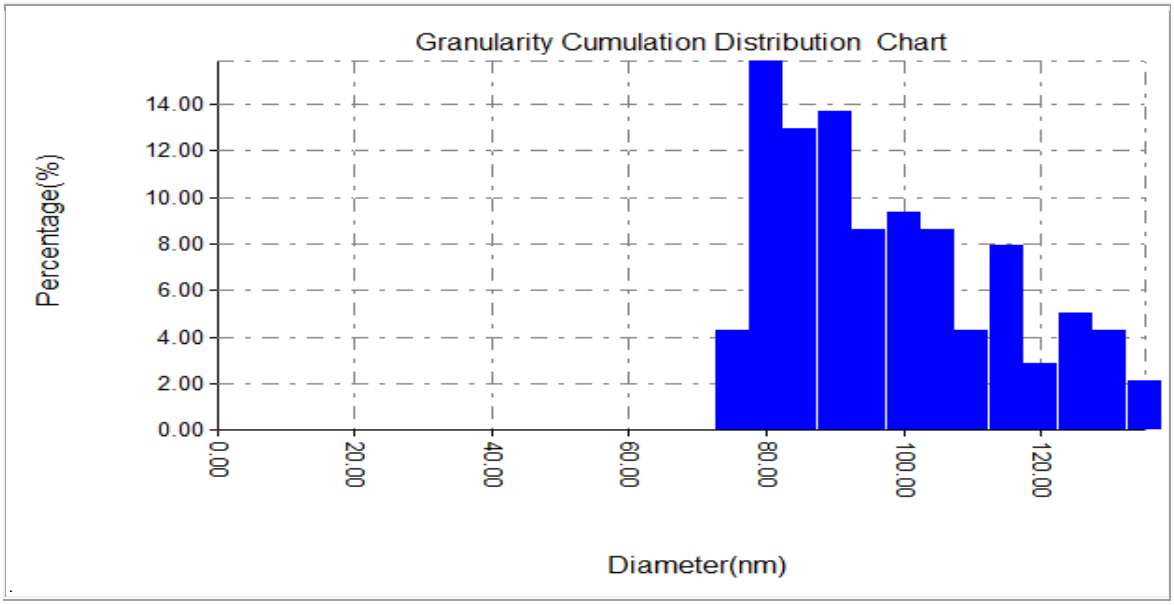

Avg. Diameter:74.15 nm	**<=10% Diameter:40.00 nm**
<=50% Diameter:70.00 nm	**<=90% Diameter:110.00 nm**

Diameter (nm)<	Volume(%)	Cumulation(%)	Diameter (nm)<	Volume(%)	Cumulation(%)	Diameter (nm)<	Volume(%)	Cumulation(%)
40.00	4.38	4.38	80.00	6.33	63.75	120.00	2.92	95.86
45.00	6.33	10.71	85.00	6.08	69.83	125.00	1.46	97.32
50.00	6.08	16.79	90.00	4.87	74.70	130.00	0.97	98.30
55.00	9.00	25.79	95.00	4.38	79.08	135.00	0.49	98.78
60.00	6.57	32.36	100.00	4.87	83.94	140.00	0.49	99.27
65.00	8.52	40.88	105.00	1.95	85.89	145.00	0.24	99.51
70.00	8.76	49.64	110.00	3.41	89.29	150.00	0.24	99.76
75.00	7.79	57.42	115.00	3.65	92.94	160.00	0.24	100.00

Appendix

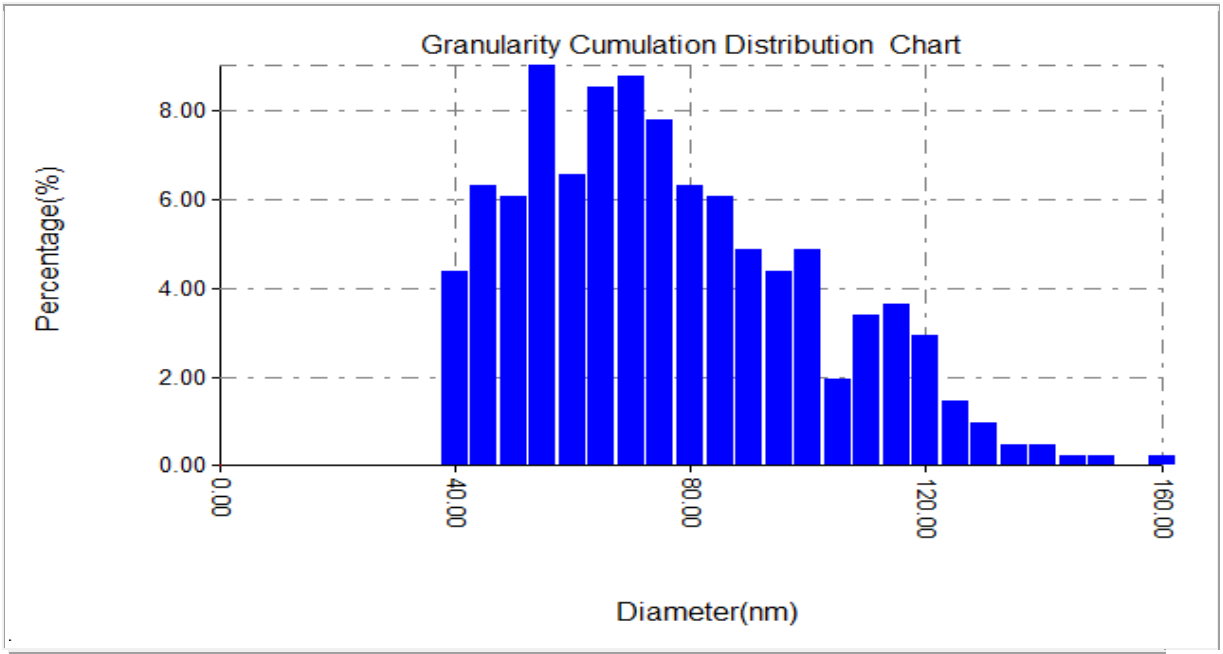

Avg. Diameter:62.75 nm	**<=10% Diameter:40.00 nm**
<=50% Diameter:60.00 nm	**<=90% Diameter:80.00 nm**

Diameter (nm)<	Volume(%)	Cumulation(%)	Diameter (nm)<	Volume(%)	Cumulation(%)	Diameter (nm)<	Volume(%)	Cumulation(%)
25.00	0.22	0.22	55.00	11.61	32.59	80.00	8.26	85.49
35.00	0.89	1.12	60.00	13.62	46.21	85.00	7.37	92.86
40.00	4.02	5.13	65.00	12.28	58.48	90.00	3.35	96.21
45.00	6.03	11.16	70.00	10.04	68.53	95.00	2.68	98.88
50.00	9.82	20.98	75.00	8.71	77.23	100.00	1.12	100.00

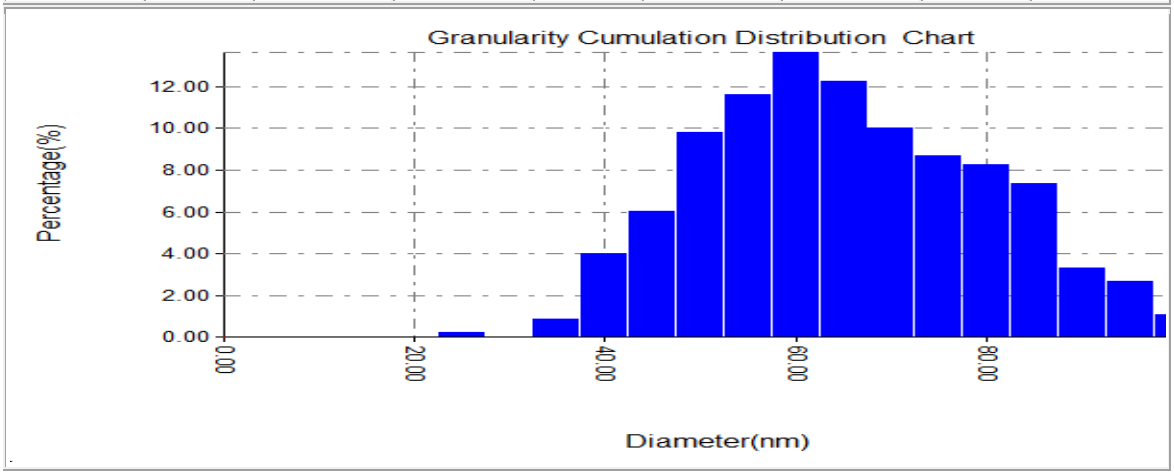

Avg. Diameter:82.84 nm	**<=10% Diameter:35.00 nm**

Appendix

<=50% Diameter:80.00 nm	<=90% Diameter:130.00 nm

Diameter (nm)<	Volume(%)	Cumulation(%)	Diameter (nm)<	Volume(%)	Cumulation(%)	Diameter (nm)<	Volume(%)	Cumulation(%)
15.00	1.28	1.28	70.00	5.45	34.29	125.00	3.21	87.82
20.00	0.64	1.92	75.00	6.41	40.71	130.00	1.92	89.74
25.00	2.88	4.81	80.00	4.49	45.19	135.00	2.56	92.31
30.00	2.24	7.05	85.00	7.69	52.88	140.00	1.28	93.59
35.00	1.92	8.97	90.00	8.97	61.86	145.00	1.60	95.19
40.00	2.24	11.22	95.00	7.05	68.91	150.00	1.28	96.47
45.00	1.92	13.14	100.00	4.81	73.72	155.00	1.92	98.40
50.00	4.17	17.31	105.00	4.17	77.88	165.00	0.96	99.36
55.00	2.56	19.87	110.00	2.88	80.77	170.00	0.32	99.68
60.00	5.13	25.00	115.00	1.60	82.37	175.00	0.32	100.00
65.00	3.85	28.85	120.00	2.24	84.62			

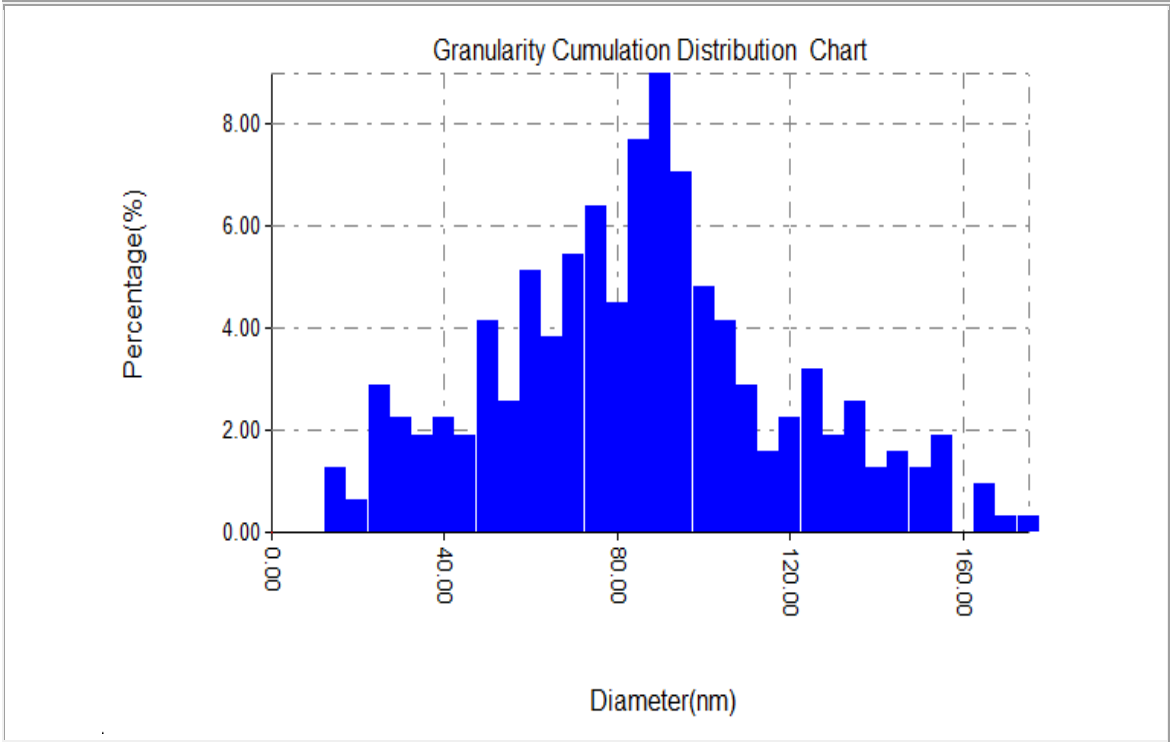

Appendix

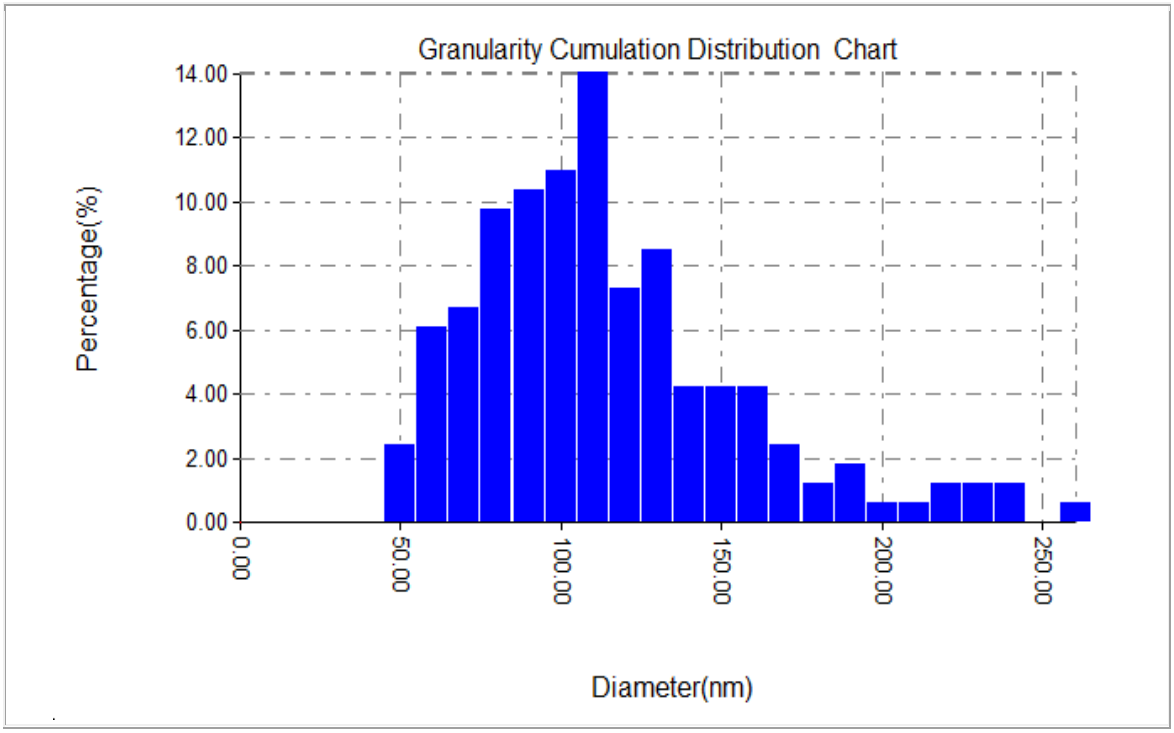

Avg. Diameter:88.29 nm	**<=10% Diameter:60.00 nm**
<=50% Diameter:85.00 nm	**<=90% Diameter:110.00 nm**

Diameter (nm)<	Volume(%)	Cumulation(%)	Diameter (nm)<	Volume(%)	Cumulation(%)	Diameter (nm)<	Volume(%)	Cumulation(%)
30.00	0.65	0.65	70.00	9.03	22.58	105.00	5.81	74.84
40.00	0.65	1.29	75.00	4.52	27.10	110.00	9.03	83.87
45.00	1.29	2.58	80.00	4.52	31.61	115.00	7.74	91.61
50.00	1.94	4.52	85.00	7.10	38.71	120.00	7.10	98.71
55.00	1.94	6.45	90.00	11.61	50.32	125.00	1.29	100.00
60.00	0.65	7.10	95.00	9.68	60.00			
65.00	6.45	13.55	100.00	9.03	69.03			

Appendix

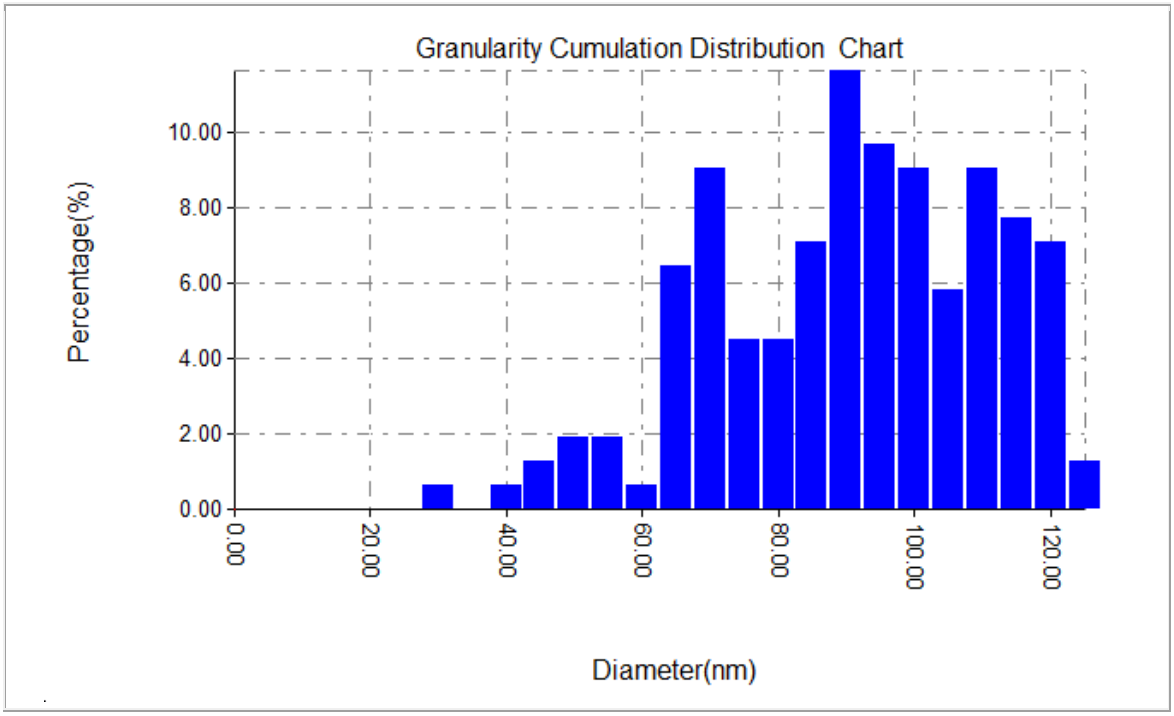

Avg. Diameter:71.86 nm	**<=10% Diameter:35.00 nm**
<=50% Diameter:70.00 nm	**<=90% Diameter:105.00 nm**

Diameter (nm)<	Volume(%)	Cumulation(%)	Diameter (nm)<	Volume(%)	Cumulation(%)	Diameter (nm)<	Volume(%)	Cumulation(%)
10.00	0.68	0.68	65.00	6.59	43.18	120.00	2.50	95.68
15.00	0.45	1.14	70.00	6.59	49.77	125.00	1.36	97.05
20.00	1.36	2.50	75.00	5.23	55.00	130.00	0.68	97.73
25.00	0.91	3.41	80.00	7.05	62.05	135.00	0.91	98.64
30.00	2.27	5.68	85.00	6.82	68.86	140.00	0.23	98.86
35.00	2.27	7.95	90.00	6.14	75.00	145.00	0.23	99.09
40.00	3.86	11.82	95.00	3.64	78.64	150.00	0.45	99.55
45.00	5.91	17.73	100.00	3.86	82.50	155.00	0.23	99.77
50.00	5.00	22.73	105.00	5.00	87.50	160.00	0.23	100.00
55.00	6.36	29.09	110.00	3.64	91.14			
60.00	7.50	36.59	115.00	2.05	93.18			

Appendix

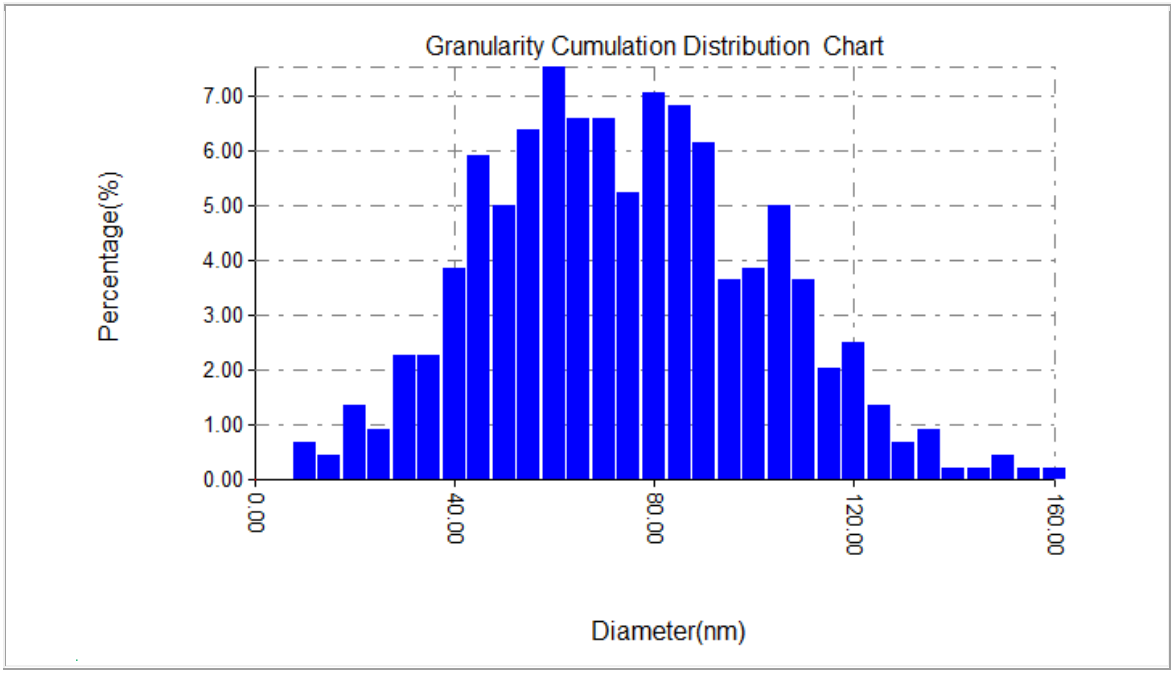

Avg. Diameter:68.11 nm	**<=10% Diameter:50.00 nm**
<=50% Diameter:70.00 nm	**<=90% Diameter:80.00 nm**

Diameter (nm)<	Volume(%)	Cumulation(%)	Diameter (nm)<	Volume(%)	Cumulation(%)	Diameter (nm)<	Volume(%)	Cumulation(%)
35.00	1.85	1.85	55.00	9.88	17.90	75.00	19.14	64.20
40.00	1.23	3.09	60.00	9.26	27.16	80.00	17.90	82.10
45.00	1.23	4.32	65.00	9.88	37.04	85.00	17.90	100.00
50.00	3.70	8.02	70.00	8.02	45.06			

Avg. Diameter:103.63 nm	**<=10% Diameter:70.00 nm**
<=50% Diameter:90.00 nm	**<=90% Diameter:140.00 nm**

Diameter (nm)<	Volume(%)	Cumulation(%)	Diameter (nm)<	Volume(%)	Cumulation(%)	Diameter (nm)<	Volume(%)	Cumulation(%)
70.00	4.37	4.37	120.00	13.59	78.64	170.00	2.91	98.06
80.00	17.48	21.84	130.00	6.80	85.44	180.00	0.49	98.54
90.00	12.62	34.47	140.00	3.88	89.32	200.00	0.49	99.03
100.00	17.48	51.94	150.00	3.40	92.72	210.00	0.97	100.00
110.00	13.11	65.05	160.00	2.43	95.15			

Appendix

Avg. Diameter:96.53 nm	**<=10% Diameter:0 nm**
<=50% Diameter:85.00 nm	**<=90% Diameter:130.00 nm**

Diameter (nm)<	Volume(%)	Cumulation(%)	Diameter (nm)<	Volume(%)	Cumulation(%)	Diameter (nm)<	Volume(%)	Cumulation(%)
70.00	12.25	12.25	110.00	6.37	73.53	150.00	1.96	95.59
75.00	9.80	22.06	115.00	3.92	77.45	155.00	0.98	96.57
80.00	9.80	31.86	120.00	8.82	86.27	160.00	1.47	98.04
85.00	9.80	41.67	125.00	0.98	87.25	165.00	0.49	98.53
90.00	9.31	50.98	130.00	1.47	88.73	170.00	0.98	99.51
95.00	5.39	56.37	135.00	2.45	91.18	220.00	0.49	100.00
100.00	5.88	62.25	140.00	1.47	92.65			
105.00	4.90	67.16	145.00	0.98	93.63			

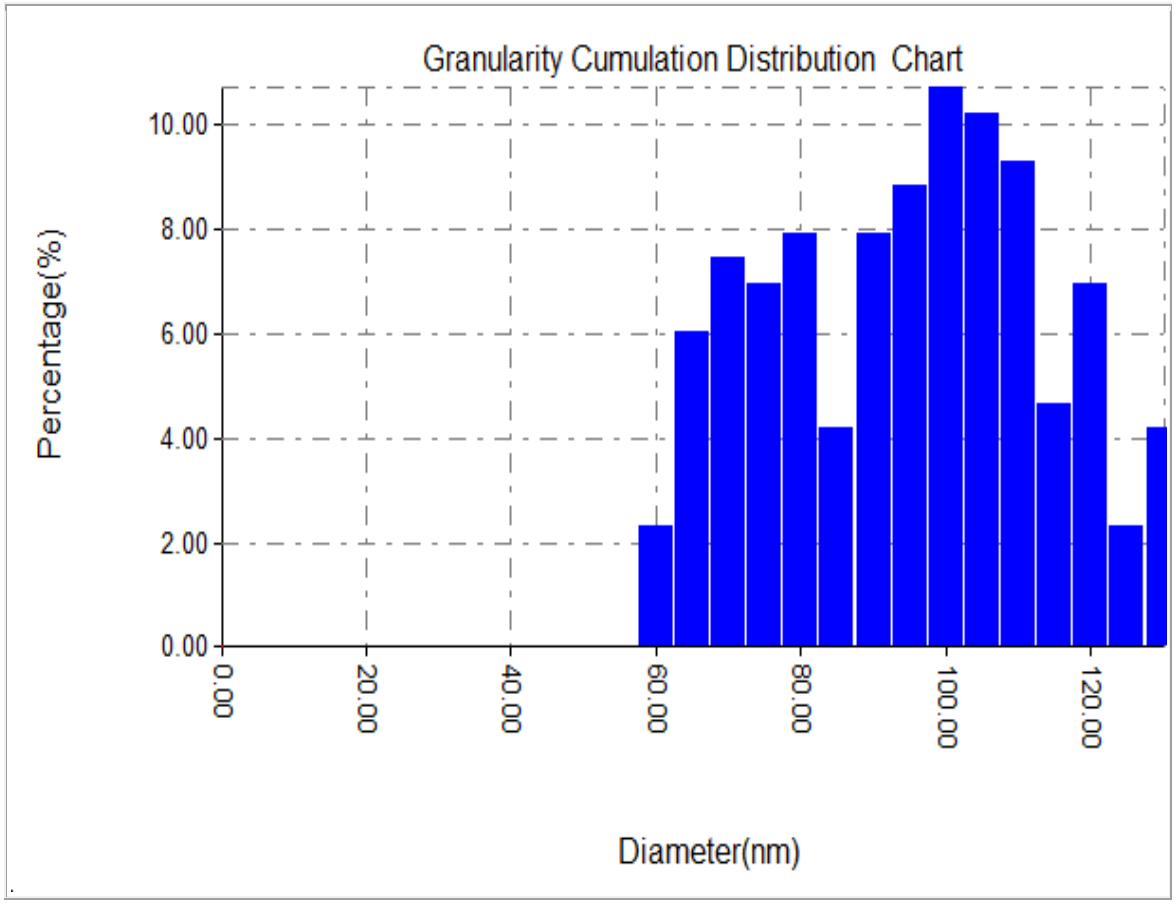

Appendix

Avg. Diameter:113.26 nm	**<=10% Diameter:50.00 nm**
<=50% Diameter:110.00 nm	**<=90% Diameter:170.00 nm**

Diameter (nm)<	Volume(%)	Cumulation(%)	Diameter (nm)<	Volume(%)	Cumulation(%)	Diameter (nm)<	Volume(%)	Cumulation(%)
40.00	0.63	0.63	110.00	12.66	50.00	180.00	1.90	91.14
50.00	3.80	4.43	120.00	13.92	63.92	190.00	1.90	93.04
60.00	6.33	10.76	130.00	8.86	72.78	200.00	2.53	95.57
70.00	5.70	16.46	140.00	6.96	79.75	210.00	1.27	96.84
80.00	6.33	22.78	150.00	1.90	81.65	220.00	0.63	97.47
90.00	5.06	27.85	160.00	5.06	86.71	230.00	1.90	99.37
100.00	9.49	37.34	170.00	2.53	89.24	240.00	0.63	100.00

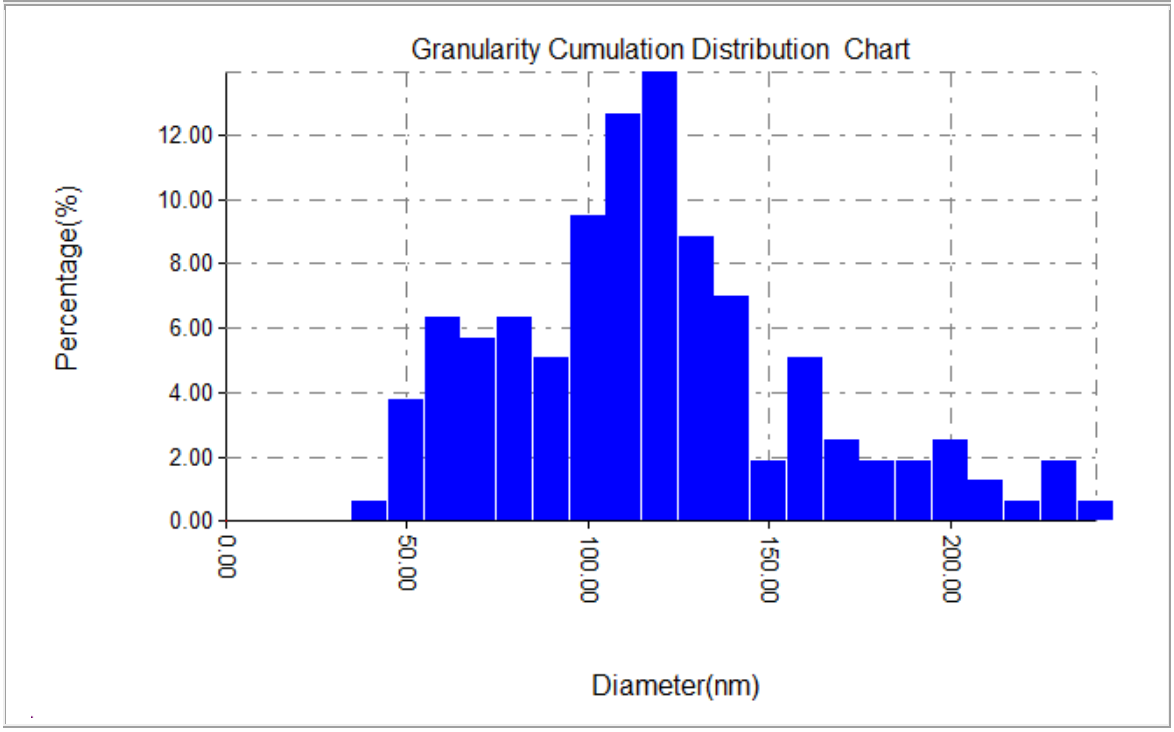

Avg. Diameter:97.27 nm	**<=10% Diameter:65.00 nm**
<=50% Diameter:95.00 nm	**<=90% Diameter:130.00 nm**

Diameter (nm)<	Volume(%)	Cumulation(%)	Diameter (nm)<	Volume(%)	Cumulation(%)	Diameter (nm)<	Volume(%)	Cumulation(%)
35.00	1.63	1.63	85.00	7.32	30.89	115.00	8.94	75.61
60.00	2.44	4.07	90.00	9.76	40.65	120.00	4.07	79.67
65.00	4.07	8.13	95.00	5.69	46.34	125.00	4.88	84.55
70.00	5.69	13.82	100.00	8.94	55.28	130.00	4.88	89.43

Appendix

75.00	3.25	17.07	105.00	6.50	61.79	135.00	6.50	95.93
80.00	6.50	23.58	110.00	4.88	66.67	140.00	4.07	100.00

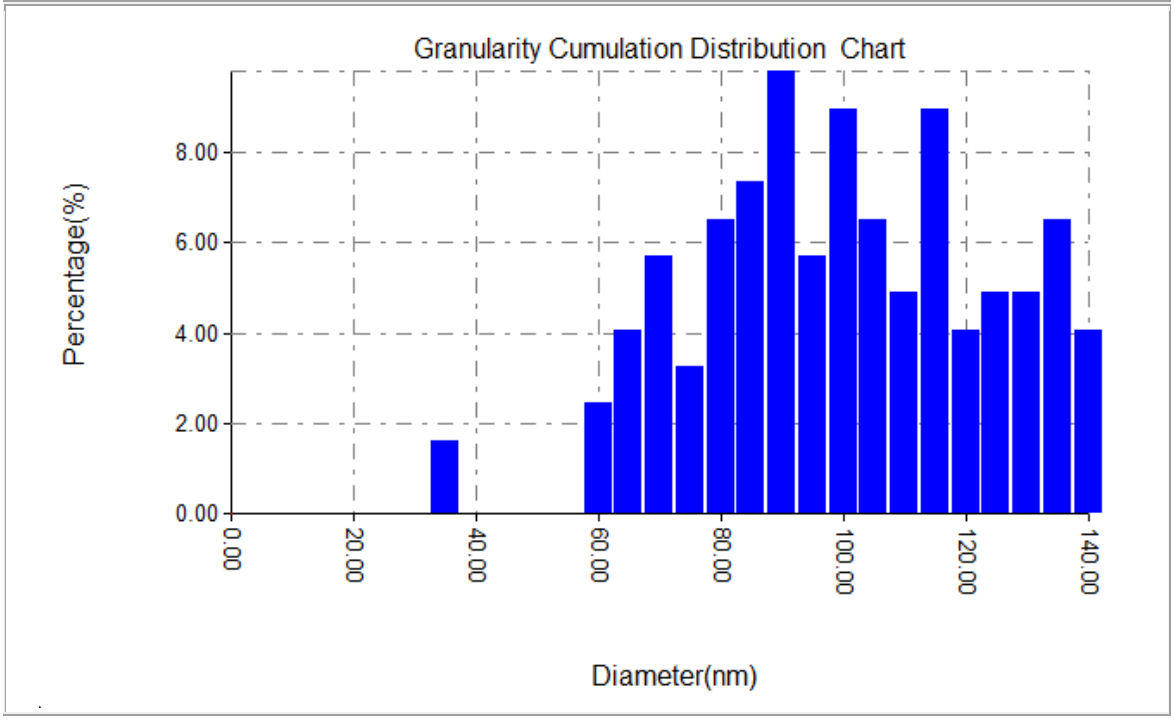

Avg. Diameter:76.49 nm

<=10% Diameter:45.00 nm

<=50% Diameter:75.00 nm

<=90% Diameter:105.00 nm

Diameter (nm)<	Volume(%)	Cumulation(%)	Diameter (nm)<	Volume(%)	Cumulation(%)	Diameter (nm)<	Volume(%)	Cumulation(%)
20.00	0.24	0.24	65.00	6.31	32.04	110.00	2.43	90.78
25.00	1.46	1.70	70.00	7.77	39.81	115.00	3.16	93.93
30.00	0.73	2.43	75.00	9.47	49.27	120.00	2.43	96.36
35.00	2.43	4.85	80.00	7.28	56.55	125.00	0.97	97.33
40.00	1.70	6.55	85.00	7.77	64.32	130.00	1.46	98.79
45.00	2.91	9.47	90.00	6.80	71.12	135.00	0.73	99.51
50.00	4.37	13.83	95.00	6.55	77.67	140.00	0.24	99.76
55.00	5.10	18.93	100.00	5.83	83.50	145.00	0.24	100.00
60.00	6.80	25.73	105.00	4.85	88.35			

Appendix

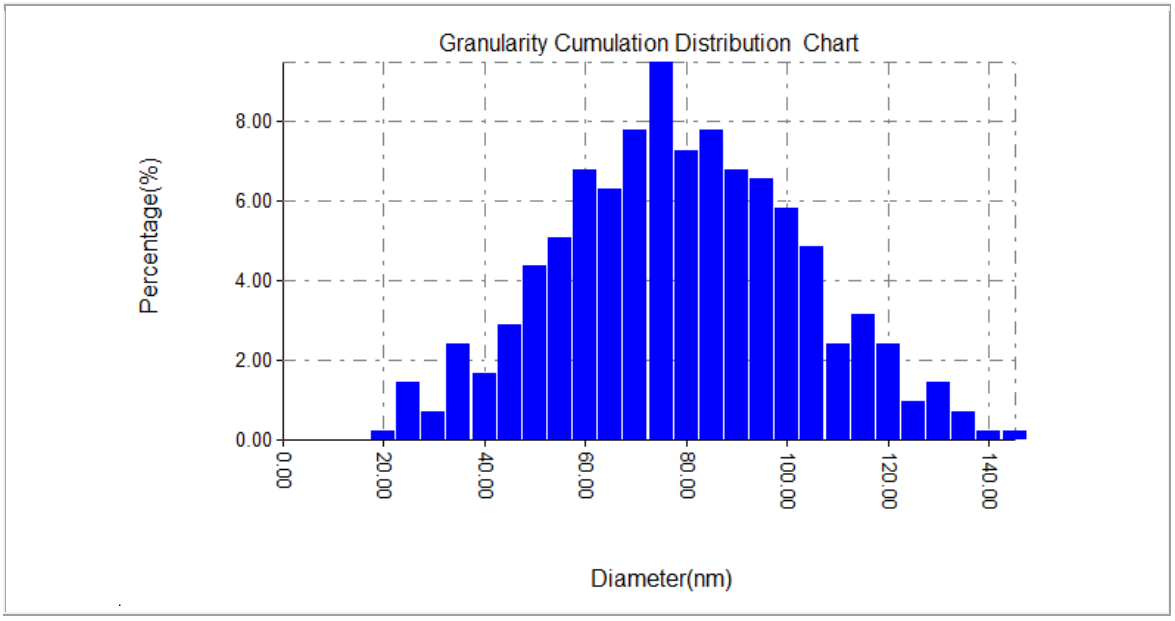

Wear test :

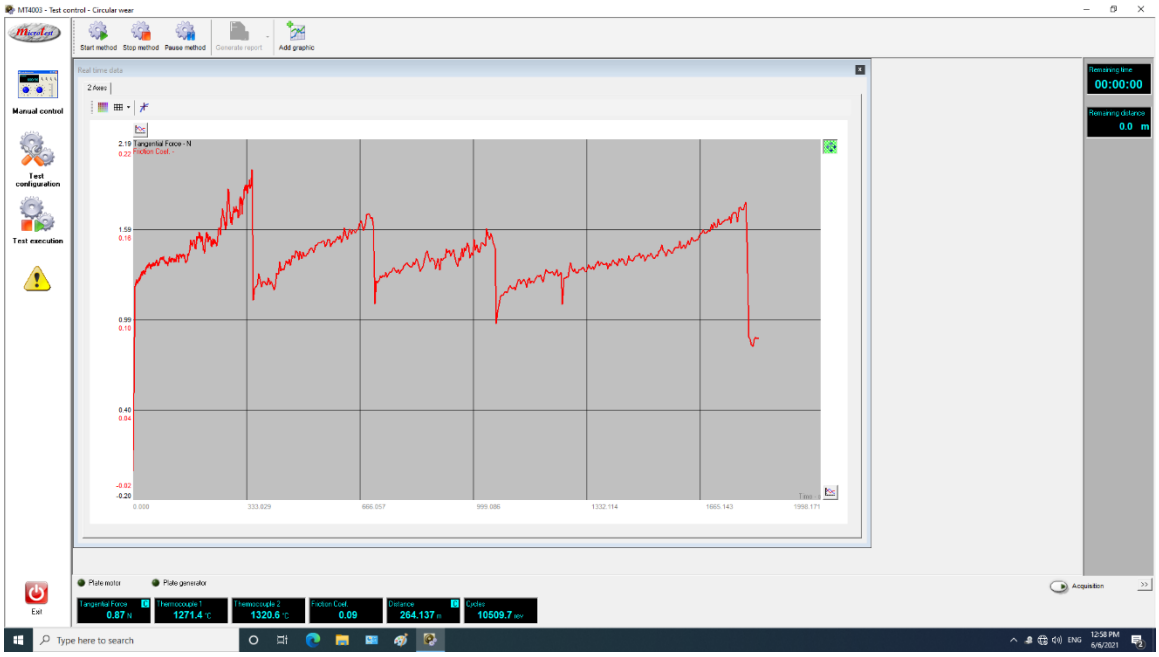

Appendix

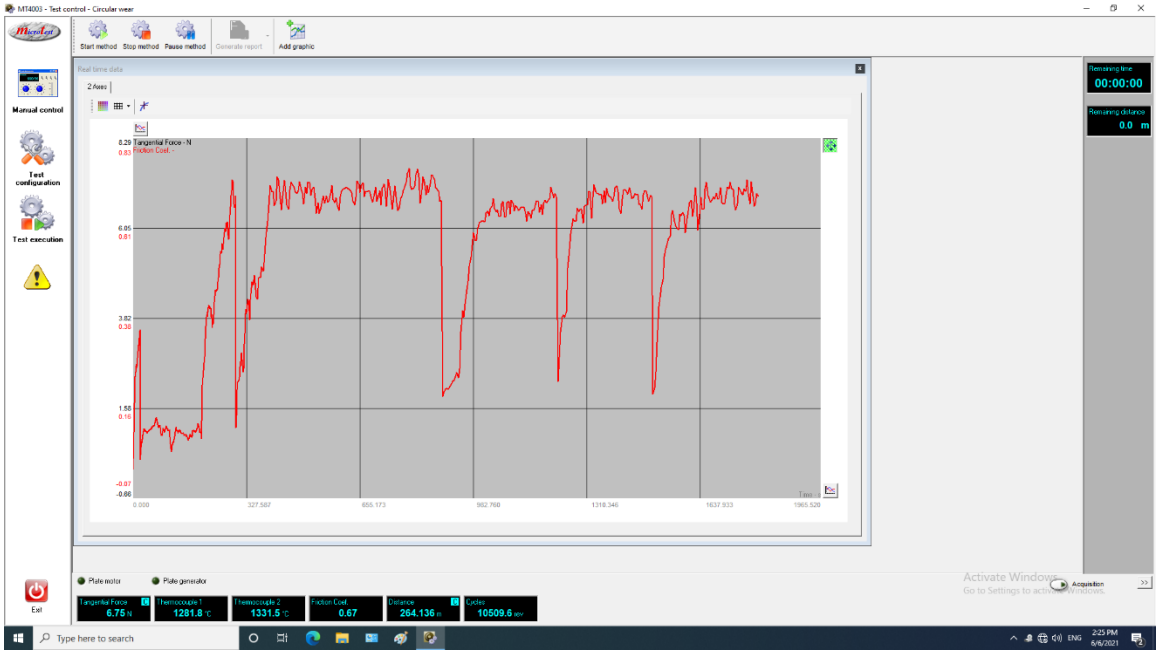
MT4003 - Test control - Circular wear
Start method
Stop method
Pause method
Generate report
Add graphic
Manual control
Test configuration
Test execution
Exit
Real time data
2 Axes
Tangential Force - N
Friction Coef. -
Remaining time
00:00:00
Remaining distance
0.0 m
Plate motor
Plate generator
Tangential Force 6.75 N
Thermocouple 1 1281.8 °C
Thermocouple 2 1331.5 °C
Friction Coef. 0.67
Distance 264.136 m
Cycles 10509.6
Acquisition
Activate Windows
Type here to search
ENG
2:25 PM
5/6/2021

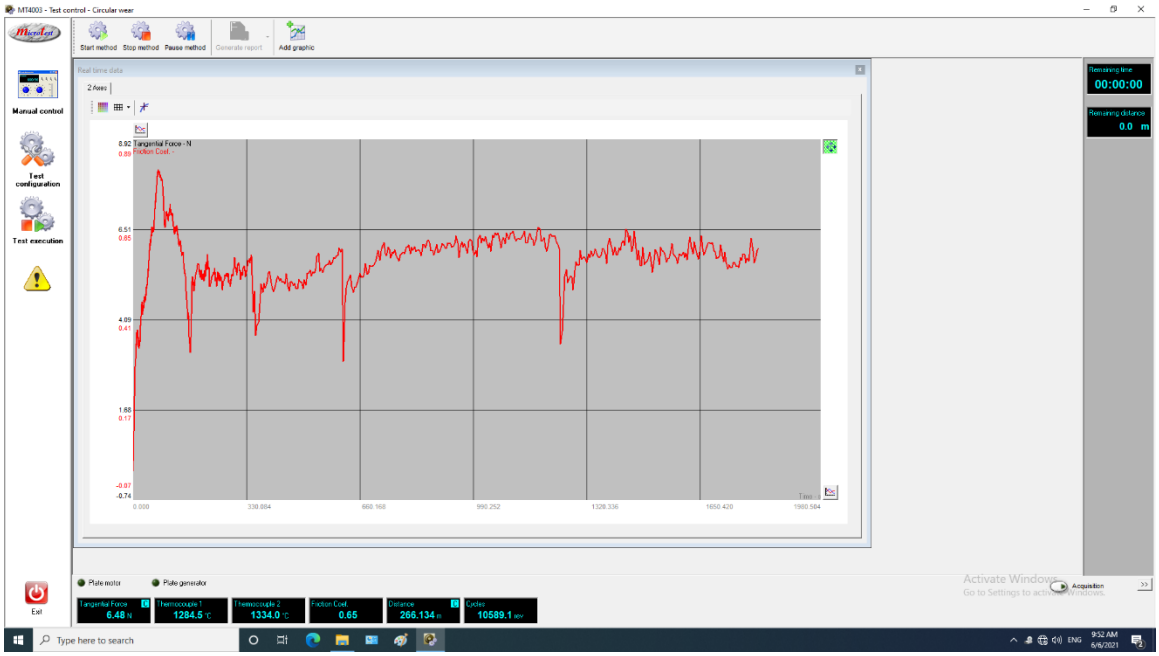
MT4003 - Test control - Circular wear
Start method
Stop method
Pause method
Generate report
Add graphic
Manual control
Test configuration
Test execution
Exit
Real time data
2 Axes
Tangential Force - N
Friction Coef. -
Remaining time
00:00:00
Remaining distance
0.0 m
Plate motor
Plate generator
Tangential Force 6.48 N
Thermocouple 1 1284.5 °C
Thermocouple 2 1334.0 °C
Friction Coef. 0.65
Distance 266.134 m
Cycles 10589.1
Acquisition
Activate Windows
Type here to search
ENG
9:52 AM
5/6/2021

Appendix

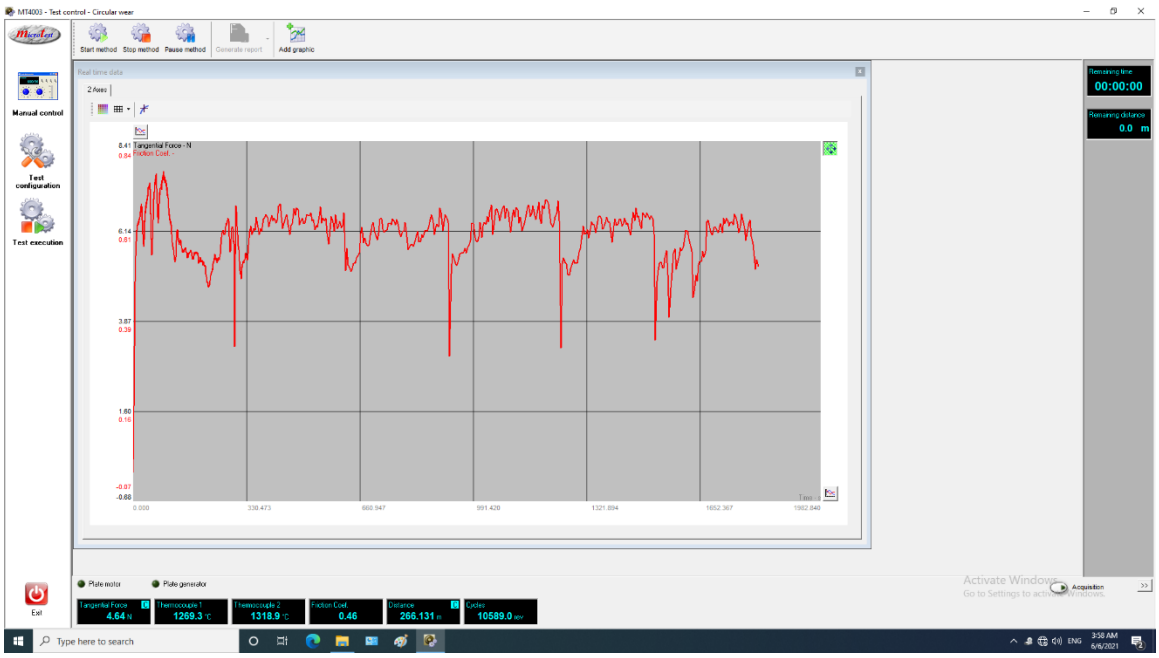
MT4003 - Test control - Circular wear
Start method
Stop method
Pause method
Generate report
Add graphic
Manual control
Test configuration
Test execution
Exit
Real time data
2 Axes
Tangential Force - N
Friction Coef. -
Remaining time
00:00:00
Remaining distance
0.0 m
Plate motor
Plate generator
Tangential Force 4.64 N
Thermocouple 1 1269.3 °C
Thermocouple 2 1318.9 °C
Friction Coef. 0.46
Distance 266.131 m
Cycles 10589.0
Acquisition
Activate Windows
Type here to search
ENG
3:58 AM
5/6/2021

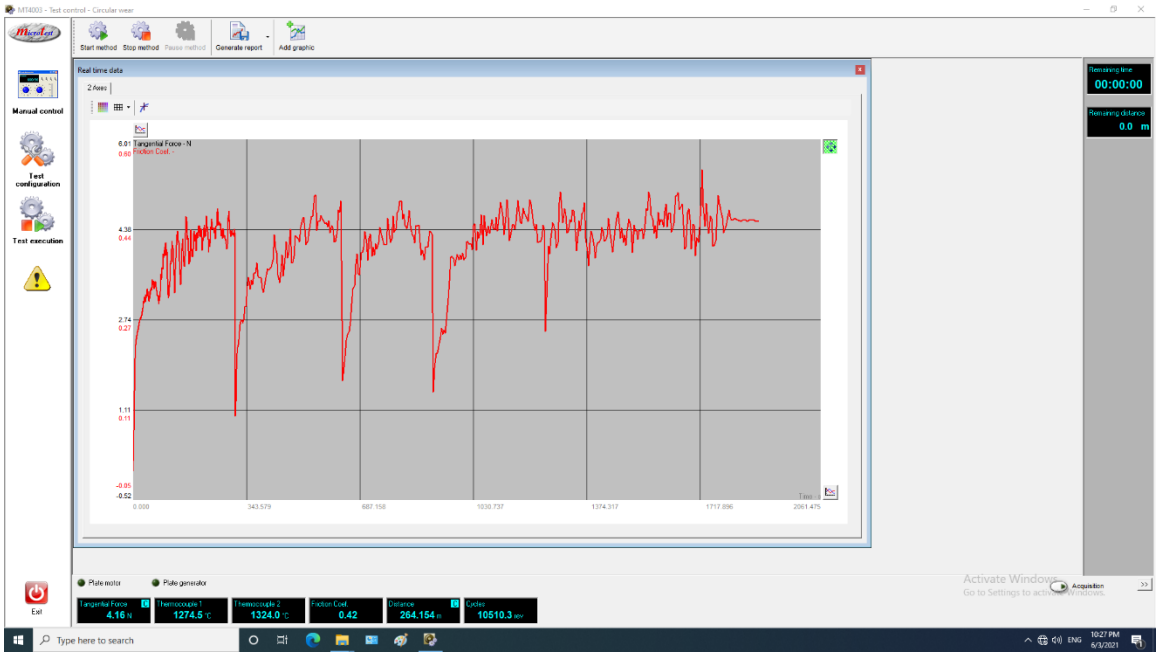
MT4003 - Test control - Circular wear
Start method
Stop method
Pause method
Generate report
Add graphic
Manual control
Test configuration
Test execution
Exit
Real time data
2 Axes
Tangential Force - N
Friction Coef. -
Remaining time
00:00:00
Remaining distance
0.0 m
Plate motor
Plate generator
Tangential Force 4.16 N
Thermocouple 1 1274.5 °C
Thermocouple 2 1324.0 °C
Friction Coef. 0.42
Distance 264.154 m
Cycles 10510.3
Acquisition
Activate Windows
Type here to search
ENG
10:27 PM
5/3/2021

Appendix

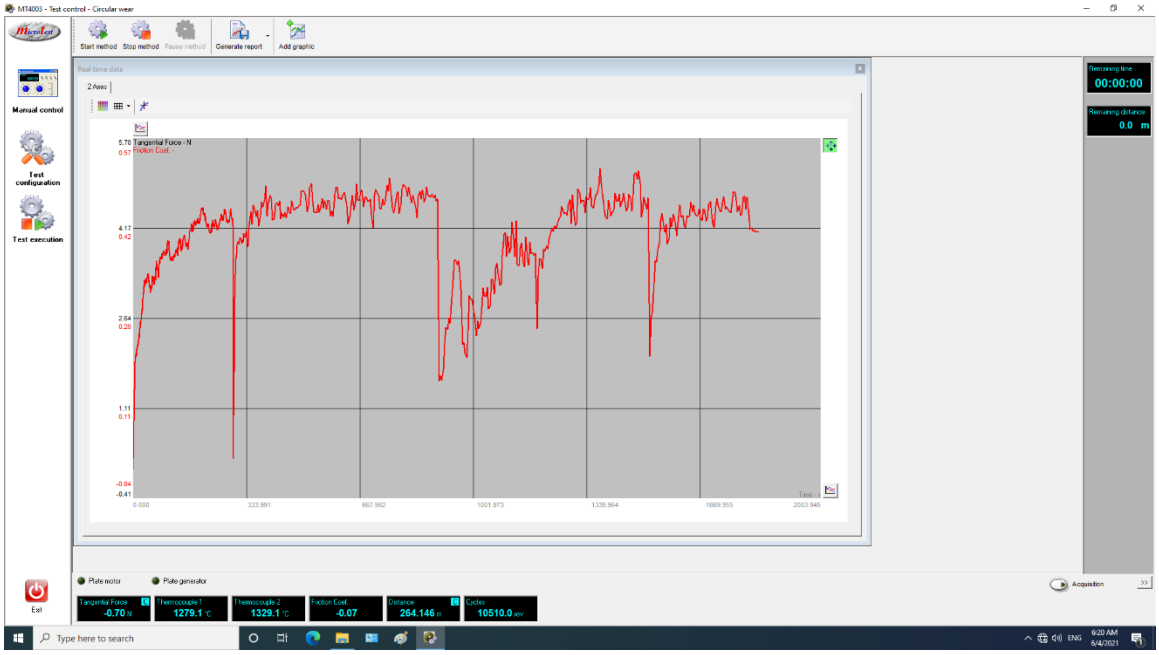
MT4003 - Test control - Circular wear
Start method
Stop method
Pause method
Generate report
Add graphic
Manual control
Test configuration
Test execution
Exit
Real time data
2 Axes
Tangential Force - N
Friction Coef. -
Remaining time
00:00:00
Remaining distance
0.0 m
Plate motor
Plate generator
Acquisition
Tangential Force
-0.70 N
Thermocouple 1
1279.1 °C
Thermocouple 2
1329.1 °C
Friction Coef.
-0.07
Distance
264.146 m
Cycles
10510.0 ev
Type here to search
ENG
9:20 AM
5/4/2021

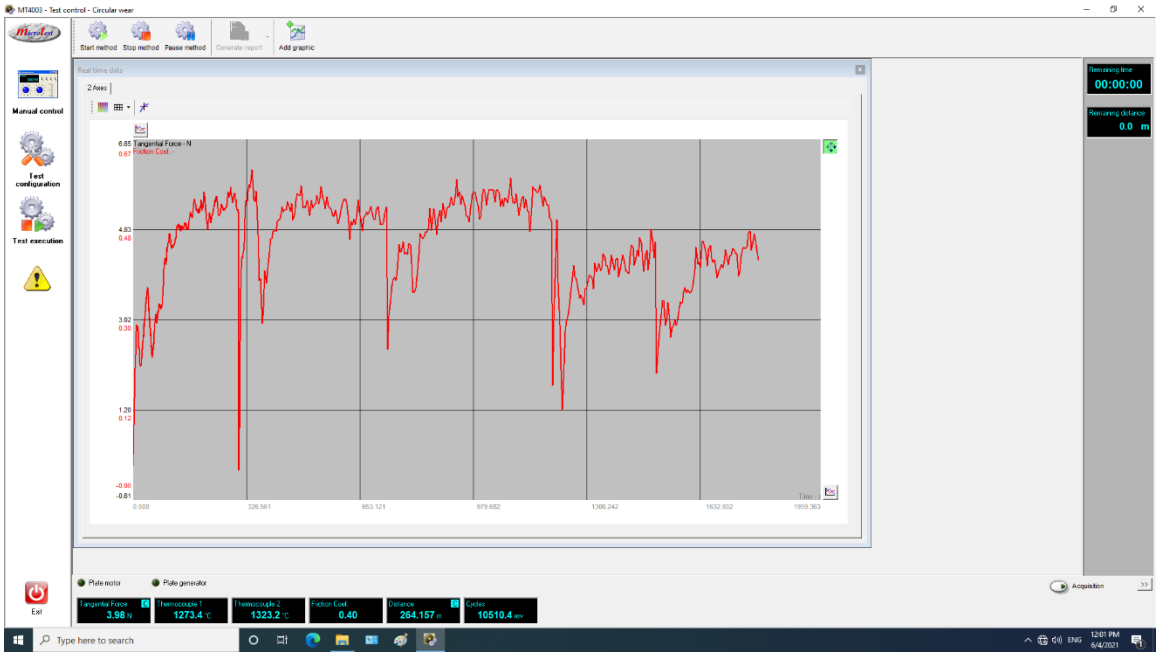
MT4003 - Test control - Circular wear
Start method
Stop method
Pause method
Generate report
Add graphic
Manual control
Test configuration
Test execution
Exit
Real time data
2 Axes
Tangential Force - N
Friction Coef. -
Remaining time
00:00:00
Remaining distance
0.0 m
Plate motor
Plate generator
Acquisition
Tangential Force
3.98 N
Thermocouple 1
1273.4 °C
Thermocouple 2
1323.2 °C
Friction Coef.
0.40
Distance
264.157 m
Cycles
10510.4 ev
Type here to search
ENG
12:01 PM
5/4/2021

Appendix

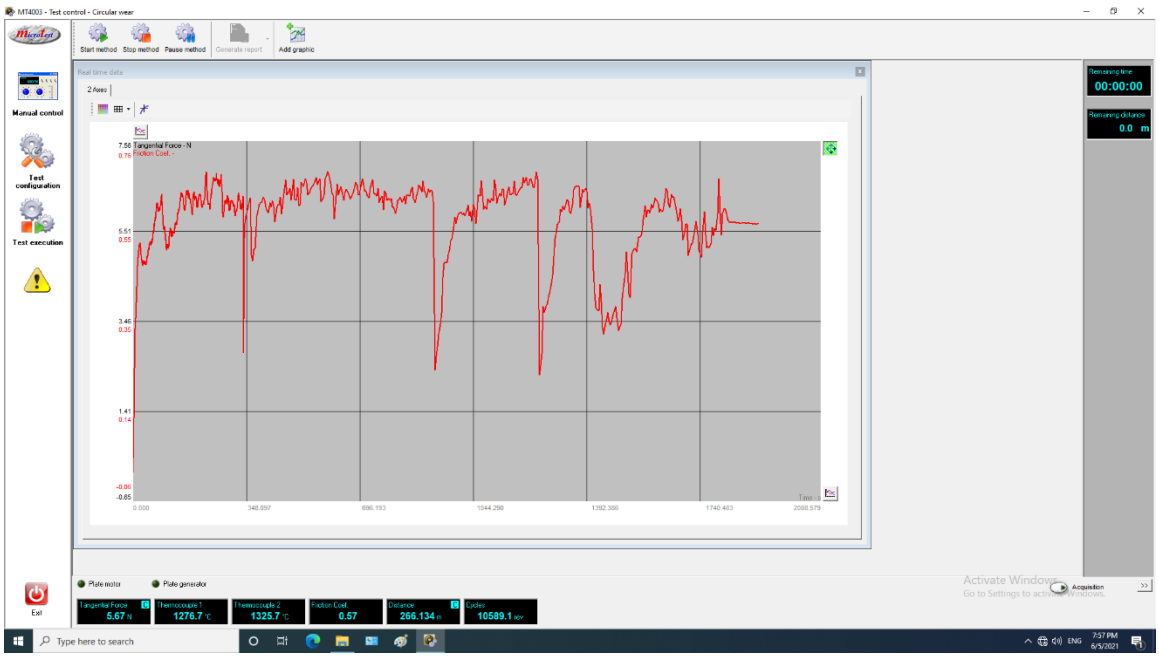

Potentiodynamic Polarization Test:

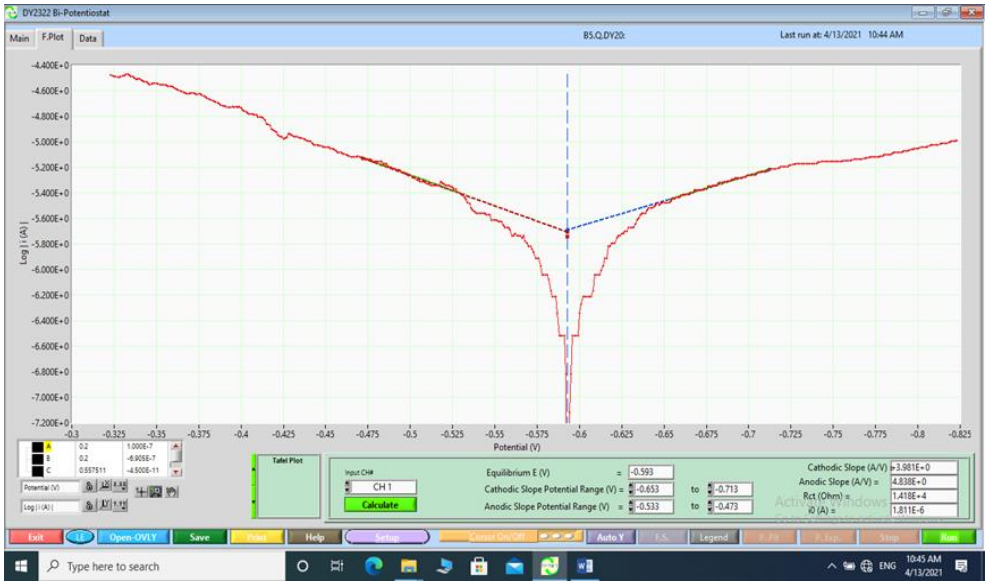

Appendix

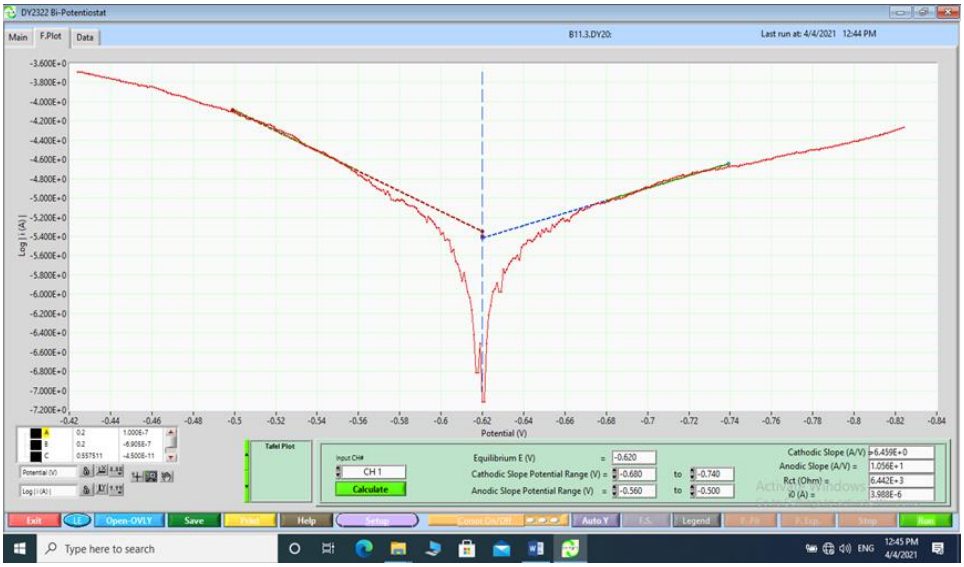
DY2322 Bi-Potentiostat
Main
F.Plot
Data
B11.3.DY20:
Last run at: 4/4/2021 12:44 PM
Log | i (A) |
Potential (V)
Tafel Plot
Input Ch#
CH 1
Calculate
Equilibrium E (V) = -0.620
Cathodic Slope Potential Range (V) = -0.680 to -0.740
Anodic Slope Potential Range (V) = -0.560 to -0.500
Cathodic Slope (A/V) = -6.459E+0
Anodic Slope (A/V) = 1.056E+1
Rct (Ohm) = 6.442E+3
i0 (A) = 3.988E-6
Exit
Open-OVLY
Save
Print
Help
Setup
Auto Y
F.S.
Legend
Stop
Run
Type here to search
ENG
12:45 PM
4/4/2021

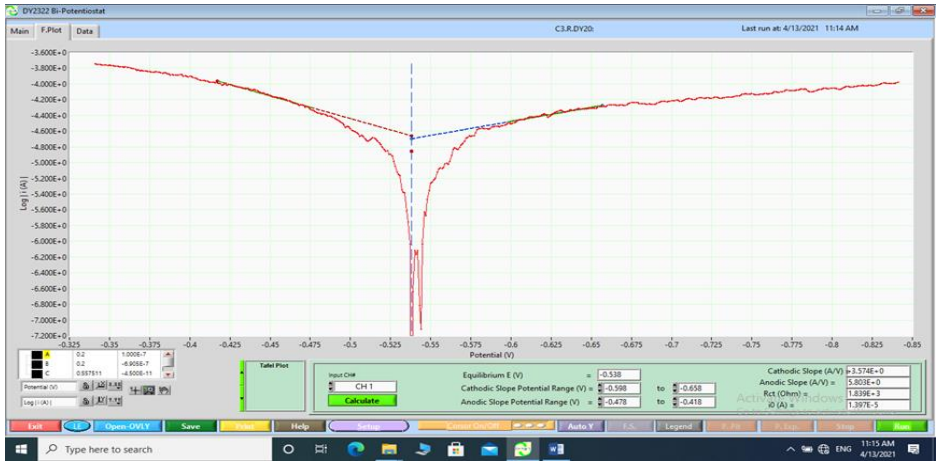
DY2322 Bi-Potentiostat
Main
F.Plot
Data
C3.R.DY20:
Last run at: 4/13/2021 11:14 AM
Log | i (A) |
Potential (V)
Tafel Plot
Input Ch#
CH 1
Calculate
Equilibrium E (V) = -0.538
Cathodic Slope Potential Range (V) = -0.598 to -0.658
Anodic Slope Potential Range (V) = -0.478 to -0.418
Cathodic Slope (A/V) = -3.574E+0
Anodic Slope (A/V) = 5.803E+0
Rct (Ohm) = 1.839E+3
i0 (A) = 1.397E-5
Exit
Open-OVLY
Save
Print
Help
Setup
Auto Y
F.S.
Legend
Stop
Run
Type here to search
ENG
11:15 AM
4/13/2021

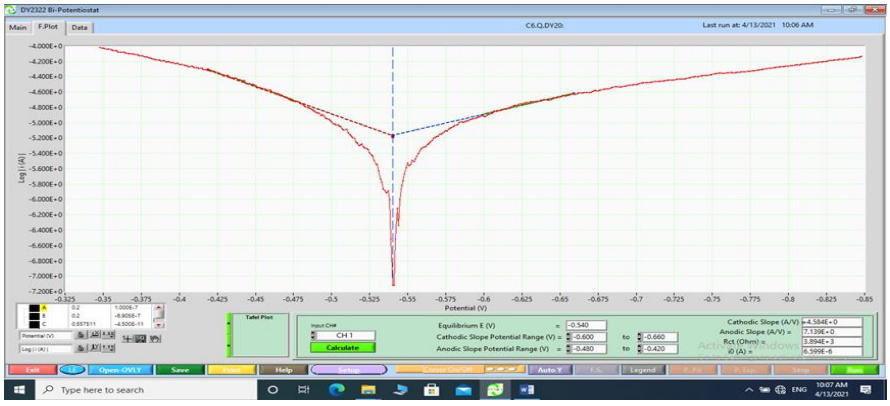
DY2322 Bi-Potentiostat
Main
F.Plot
Data
C6.Q.DY20:
Last run at: 4/13/2021 10:06 AM
Log | i (A) |
Potential (V)
Tafel Plot
Input Ch#
CH 1
Calculate
Equilibrium E (V) = -0.540
Cathodic Slope Potential Range (V) = -0.600 to -0.660
Anodic Slope Potential Range (V) = -0.480 to -0.420
Cathodic Slope (A/V) = -4.584E+0
Anodic Slope (A/V) = 7.139E+0
Rct (Ohm) = 3.894E+3
i0 (A) = 6.599E-6
Exit
Open-OVLY
Save
Print
Help
Setup
Auto Y
F.S.
Legend
Stop
Run
Type here to search
ENG
10:07 AM
4/13/2021

Appendix

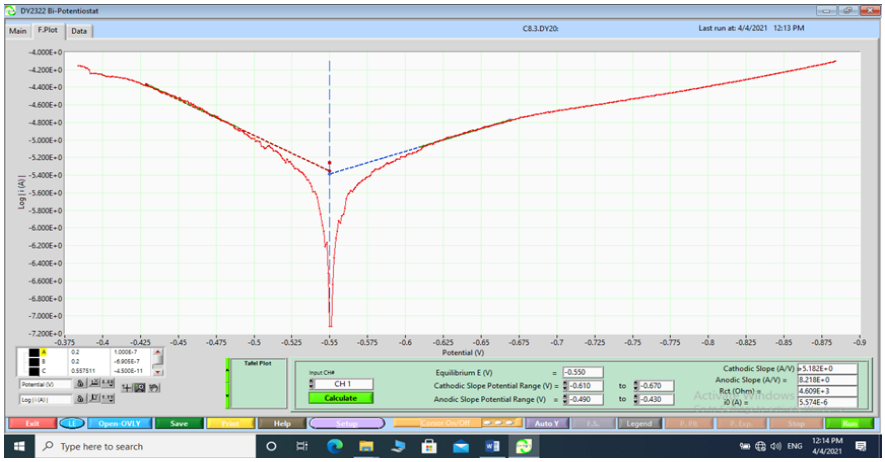
DY2322 Bi-Potentiostat
Main
F.Plot
Data
C8.3.DY20:
Last run at: 4/4/2021 12:13 PM
Log | i (A) |
Potential (V)
Tafel Plot
Input CH#
CH 1
Calculate
Equilibrium E (V) = -0.550
Cathodic Slope Potential Range (V) = -0.610 to -0.670
Anodic Slope Potential Range (V) = -0.490 to -0.430
Cathodic Slope (A/V) = 5.182E+0
Anodic Slope (A/V) = 8.218E+0
Rct (Ohm) = 4.609E+3
i0 (A) = 5.574E-6
Exit
Open-OVLY
Save
Print
Help
Setup
Cursor On/Off
Auto Y
F.S.
Legend
P. Fit
P. Exp.
Stop
Run
Type here to search
ENG
12:14 PM
4/4/2021

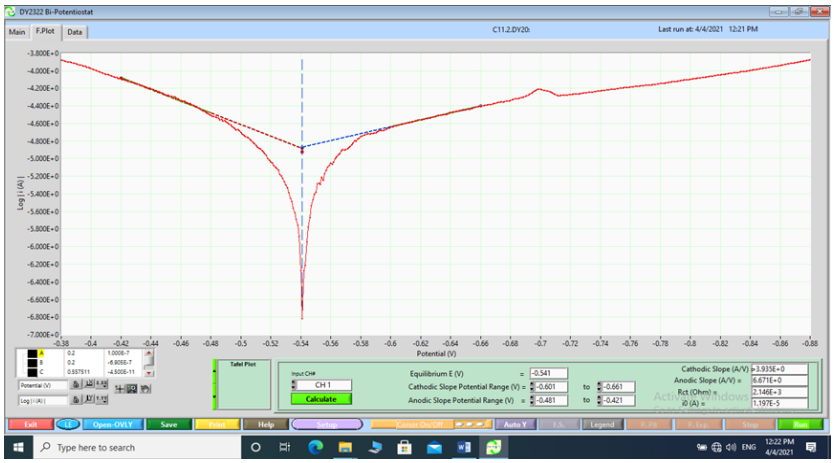
DY2322 Bi-Potentiostat
Main
F.Plot
Data
C11.2.DY20:
Last run at: 4/4/2021 12:21 PM
Log | i (A) |
Potential (V)
Tafel Plot
Input CH#
CH 1
Calculate
Equilibrium E (V) = -0.541
Cathodic Slope Potential Range (V) = -0.601 to -0.661
Anodic Slope Potential Range (V) = -0.481 to -0.421
Cathodic Slope (A/V) = 3.935E+0
Anodic Slope (A/V) = 6.671E+0
Rct (Ohm) = 2.146E+3
i0 (A) = 1.197E-5
Exit
Open-OVLY
Save
Print
Help
Setup
Cursor On/Off
Auto Y
F.S.
Legend
P. Fit
P. Exp.
Stop
Run
Type here to search
ENG
12:22 PM
4/4/2021


DY2322 Bi-Potentiostat
Main
F.Plot
Data
D9.8.DY20:
Last run at: 5/6/2021 10:08 AM
Log | i (A) |
Potential (V)
Tafel Plot
Input CH#
CH 1
Calculate
Equilibrium E (V) = -0.559
Cathodic Slope Potential Range (V) = -0.619 to -0.679
Anodic Slope Potential Range (V) = -0.499 to -0.439
Cathodic Slope (A/V) = 2.094E+0
Anodic Slope (A/V) = 7.414E+0
Rct (Ohm) = 6.690E+2
i0 (A) = 3.840E-5
Exit
Open-OVLY
Save
Print
Help
Setup
Cursor On/Off
Auto Y
F.S.
Legend
P. Fit
P. Exp.
Stop
Run
Type here to search
ENG
10:09 AM
5/6/2021

Appendix

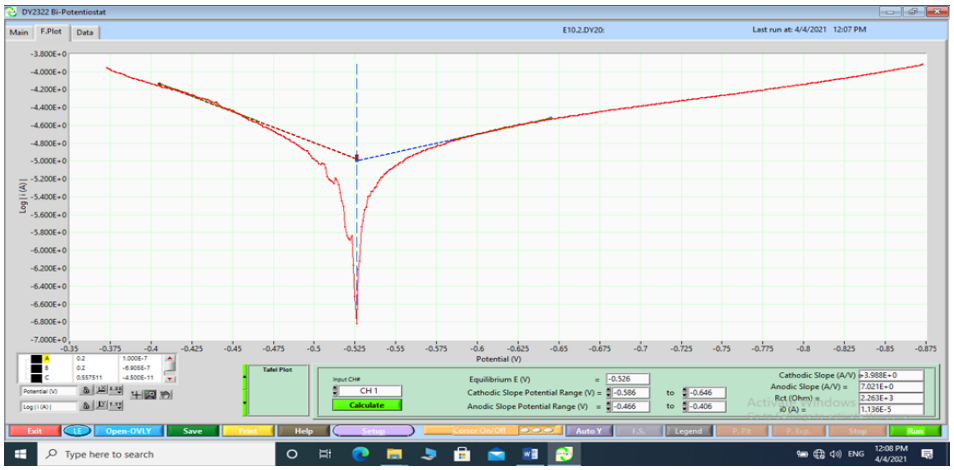
DY2322 Bi-Potentiostat
Main
F.Plot
Data
E10.2.DY20:
Last run at: 4/4/2021 12:07 PM
Potential (V)
Log | i (A) |
Tafel Plot
Input CH#
CH 1
Calculate
Equilibrium E (V) = -0.526
Cathodic Slope Potential Range (V) = -0.586 to -0.646
Anodic Slope Potential Range (V) = -0.466 to -0.406
Cathodic Slope (A/V) = -3.988E+0
Anodic Slope (A/V) = 7.021E+0
Rct (Ohm) = 2.263E+3
i0 (A) = 1.136E-5
Exit
Open-OVLY
Save
Print
Help
Auto Y
Legend
Run
Type here to search
ENG
12:08 PM
4/4/2021

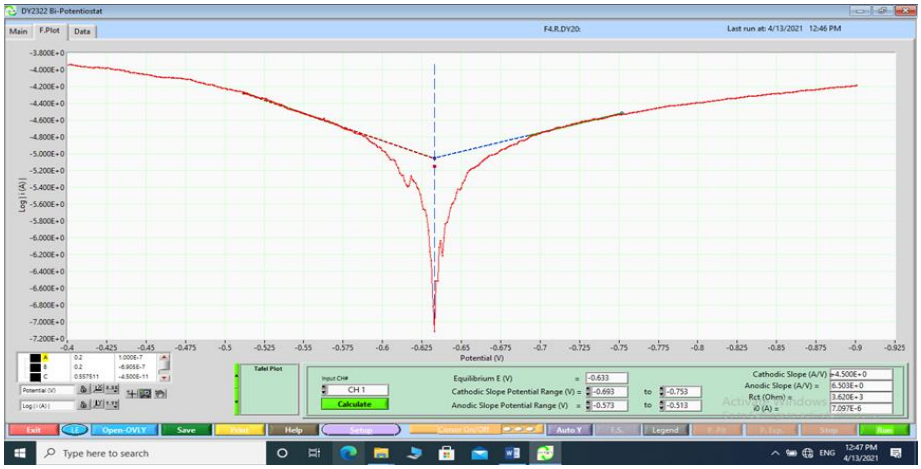
DY2322 Bi-Potentiostat
Main
F.Plot
Data
F4.R.DY20:
Last run at: 4/13/2021 12:46 PM
Potential (V)
Log | i (A) |
Tafel Plot
Input CH#
CH 1
Calculate
Equilibrium E (V) = -0.633
Cathodic Slope Potential Range (V) = -0.693 to -0.753
Anodic Slope Potential Range (V) = -0.573 to -0.513
Cathodic Slope (A/V) = -4.500E+0
Anodic Slope (A/V) = 6.503E+0
Rct (Ohm) = 3.620E+3
i0 (A) = 7.097E-6
Exit
Open-OVLY
Save
Print
Help
Auto Y
Legend
Run
Type here to search
ENG
12:47 PM
4/13/2021

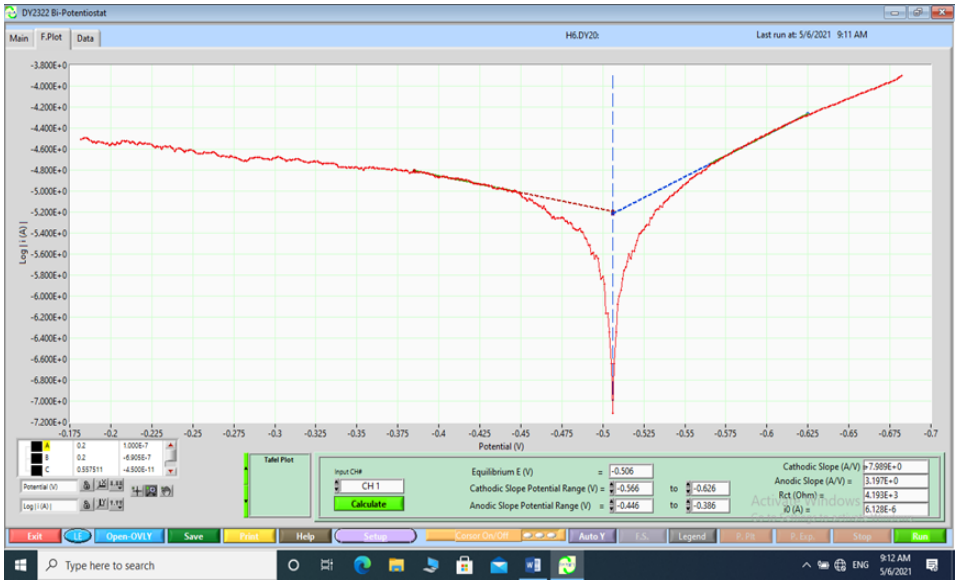
DY2322 Bi-Potentiostat
Main
F.Plot
Data
H6.DY20:
Last run at: 5/6/2021 9:11 AM
Potential (V)
Log | i (A) |
Tafel Plot
Input CH#
CH 1
Calculate
Equilibrium E (V) = -0.506
Cathodic Slope Potential Range (V) = -0.566 to -0.626
Anodic Slope Potential Range (V) = -0.446 to -0.386
Cathodic Slope (A/V) = -7.989E+0
Anodic Slope (A/V) = 3.197E+0
Rct (Ohm) = 4.193E+3
i0 (A) = 6.128E-6
Exit
Open-OVLY
Save
Print
Help
Auto Y
Legend
Run
Type here to search
ENG
9:12 AM
5/6/2021

Appendix

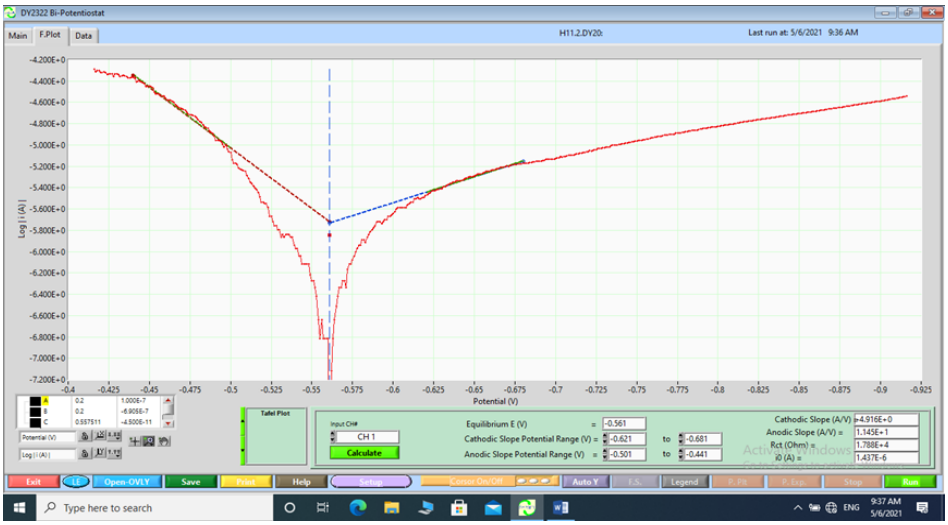
DY2322 Bi-Potentiostat
Main
F.Plot
Data
H11.2.DY20:
Last run at: 5/6/2021 9:36 AM
Log | i (A) |
Potential (V)
Tafel Plot
Input CH#
CH 1
Calculate
Equilibrium E (V) = -0.561
Cathodic Slope Potential Range (V) = -0.621 to -0.681
Anodic Slope Potential Range (V) = -0.501 to -0.441
Cathodic Slope (A/V) = 4.916E+0
Anodic Slope (A/V) = 1.145E+1
Rct (Ohm) = 1.788E+4
i0 (A) = 1.437E-6
Exit
Open-OVLY
Save
Print
Help
Setup
Cursor On/Off
Auto Y
F.S.
Legend
P. Pk
P. Exp.
Stop
Run
Type here to search
ENG
9:37 AM
5/6/2021

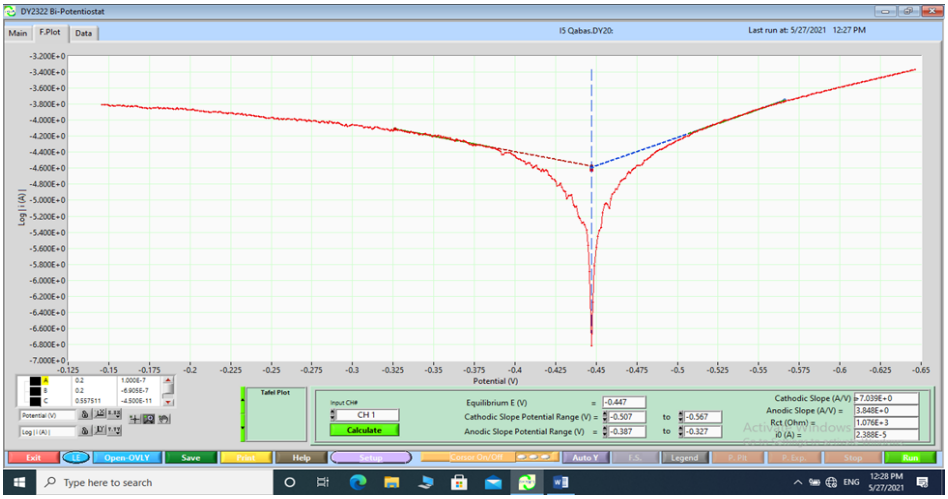
DY2322 Bi-Potentiostat
Main
F.Plot
Data
I5 Qabas.DY20:
Last run at: 5/27/2021 12:27 PM
Log | i (A) |
Potential (V)
Tafel Plot
Input CH#
CH 1
Calculate
Equilibrium E (V) = -0.447
Cathodic Slope Potential Range (V) = -0.507 to -0.567
Anodic Slope Potential Range (V) = -0.387 to -0.327
Cathodic Slope (A/V) = 7.039E+0
Anodic Slope (A/V) = 3.848E+0
Rct (Ohm) = 1.076E+3
i0 (A) = 2.388E-5
Exit
Open-OVLY
Save
Print
Help
Setup
Cursor On/Off
Auto Y
F.S.
Legend
P. Pk
P. Exp.
Stop
Run
Type here to search
ENG
12:28 PM
5/27/2021


DY2322 Bi-Potentiostat
Main
F.Plot
Data
I4 Qabas.DY20:
Last run at: 5/27/2021 12:22 PM
Log | i (A) |
Potential (V)
Tafel Plot
Input CH#
CH 1
Calculate
Equilibrium E (V) = -0.449
Cathodic Slope Potential Range (V) = -0.509 to -0.569
Anodic Slope Potential Range (V) = -0.389 to -0.329
Cathodic Slope (A/V) = 7.683E+0
Anodic Slope (A/V) = 2.712E+0
Rct (Ohm) = 1.174E+3
i0 (A) = 2.188E-5
Exit
Open-OVLY
Save
Print
Help
Setup
Cursor On/Off
Auto Y
F.S.
Legend
P. Pk
P. Exp.
Stop
Run
Type here to search
ENG
12:23 PM
5/27/2021

Appendix

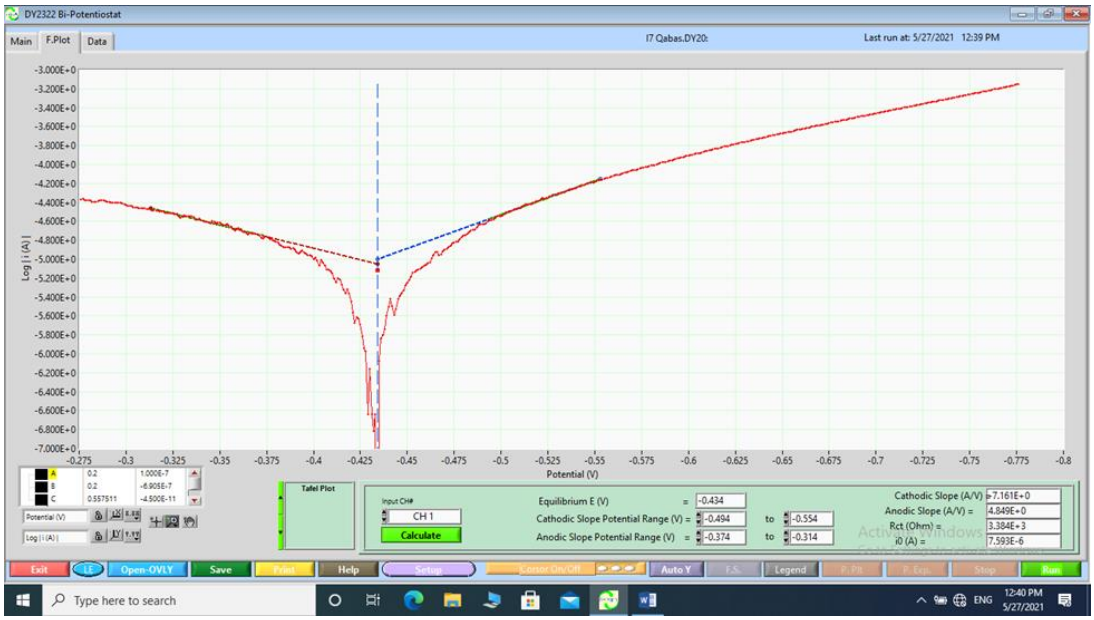

Cycle Polarization Test :

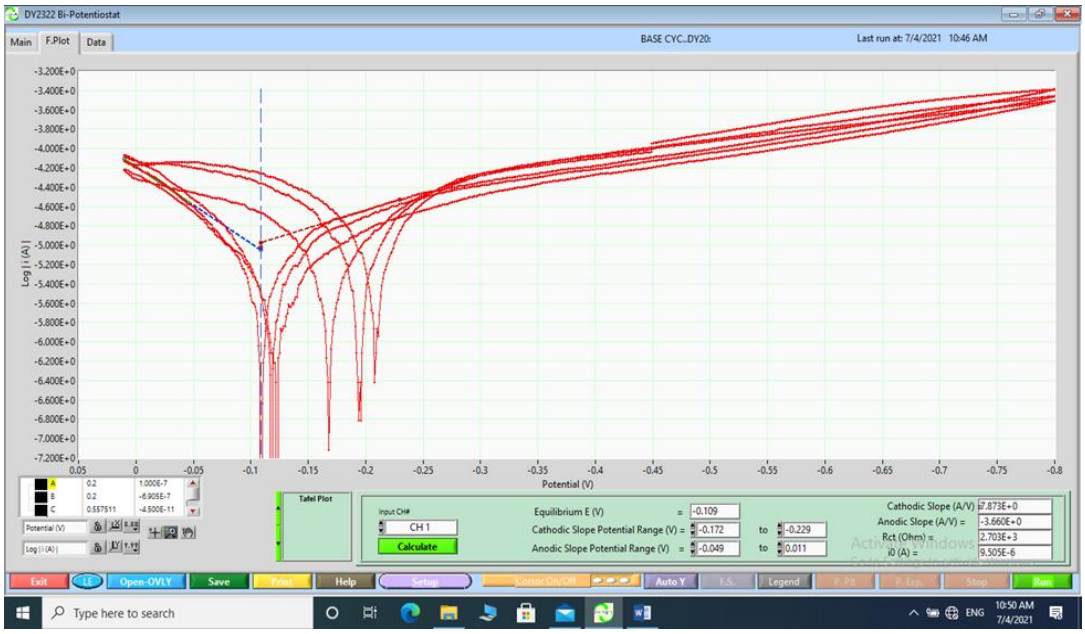

Appendix

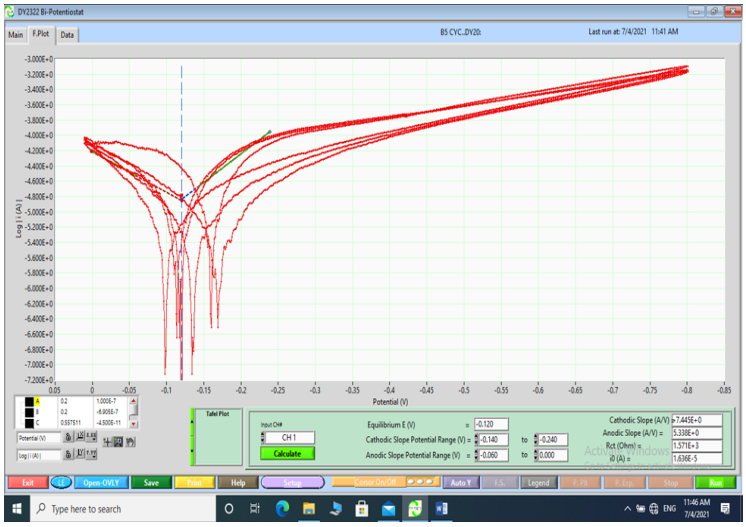
DY2322 Bi-Potentiostat
Main
F.Plot
Data
B5 CYC..DY20:
Last run at: 7/4/2021 11:41 AM
Log | i (A) |
Potential (V)
Tafel Plot
Input CH#
CH 1
Calculate
Equilibrium E (V)
Cathodic Slope Potential Range (V)
Anodic Slope Potential Range (V)
Cathodic Slope (A/V)
Anodic Slope (A/V)
Rct (Ohm)
i0 (A)
Exit
Open-OVLY
Save
Print
Help
Setup
Auto Y
Legend
Run
Type here to search
ENG
11:46 AM
7/4/2021

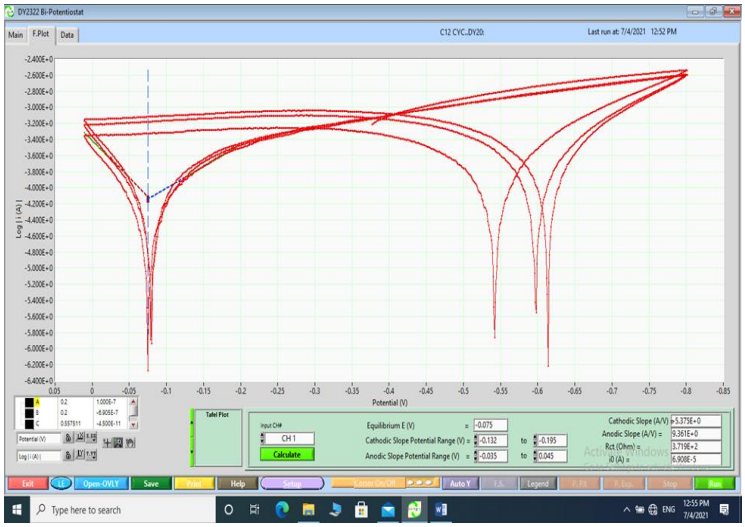
DY2322 Bi-Potentiostat
Main
F.Plot
Data
C12 CYC..DY20:
Last run at: 7/4/2021 12:52 PM
Log | i (A) |
Potential (V)
Tafel Plot
Input CH#
CH 1
Calculate
Equilibrium E (V)
Cathodic Slope Potential Range (V)
Anodic Slope Potential Range (V)
Cathodic Slope (A/V)
Anodic Slope (A/V)
Rct (Ohm)
i0 (A)
Exit
Open-OVLY
Save
Print
Help
Setup
Auto Y
Legend
Run
Type here to search
ENG
12:55 PM
7/4/2021

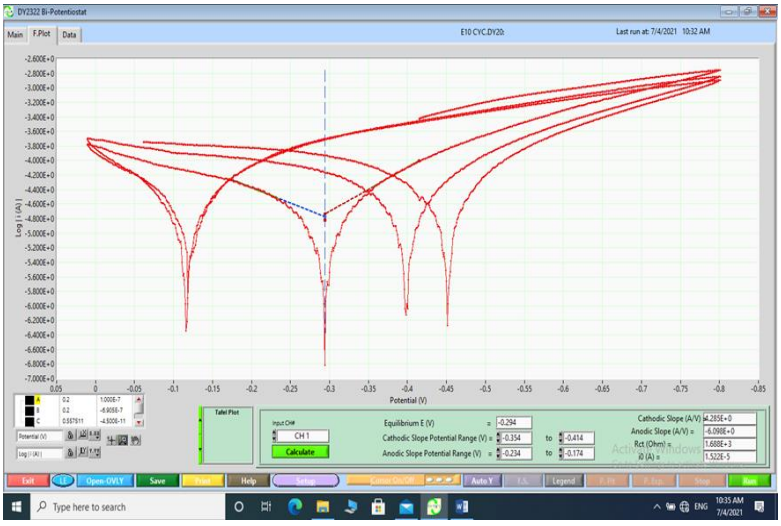
DY2322 Bi-Potentiostat
Main
F.Plot
Data
E10 CYC.DY20:
Last run at: 7/4/2021 10:32 AM
Log | i (A) |
Potential (V)
Tafel Plot
Input CH#
CH 1
Calculate
Equilibrium E (V)
Cathodic Slope Potential Range (V)
Anodic Slope Potential Range (V)
Cathodic Slope (A/V)
Anodic Slope (A/V)
Rct (Ohm)
i0 (A)
Exit
Open-OVLY
Save
Print
Help
Setup
Auto Y
Legend
Run
Type here to search
ENG
10:35 AM
7/4/2021

Appendix

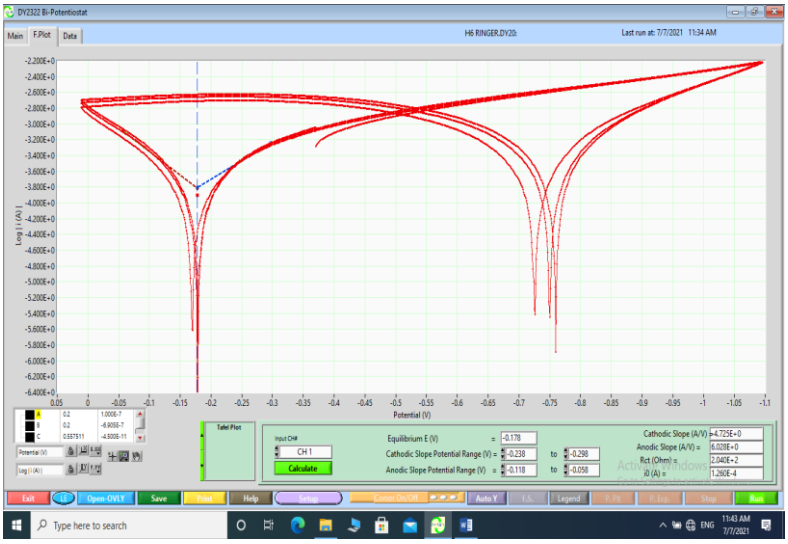
DY2322 Bi-Potentiostat
Main
F-Plot
Data
H6 RINGER.DY20:
Last run at: 7/7/2021 11:34 AM
Log | i (A) |
Potential (V)
Tafel Plot
Input CH#
CH 1
Calculate
Equilibrium E (V) = -0.178
Cathodic Slope Potential Range (V) = -0.238 to -0.298
Anodic Slope Potential Range (V) = -0.118 to -0.058
Cathodic Slope (A/V) = -4.725E+0
Anodic Slope (A/V) = 6.028E+0
Rct (Ohm) = 2.040E+2
i0 (A) = 1.260E-4
Exit
Open-OVLY
Save
Print
Help
Auto Y
Legend
Run
Type here to search
ENG
11:43 AM
7/7/2021

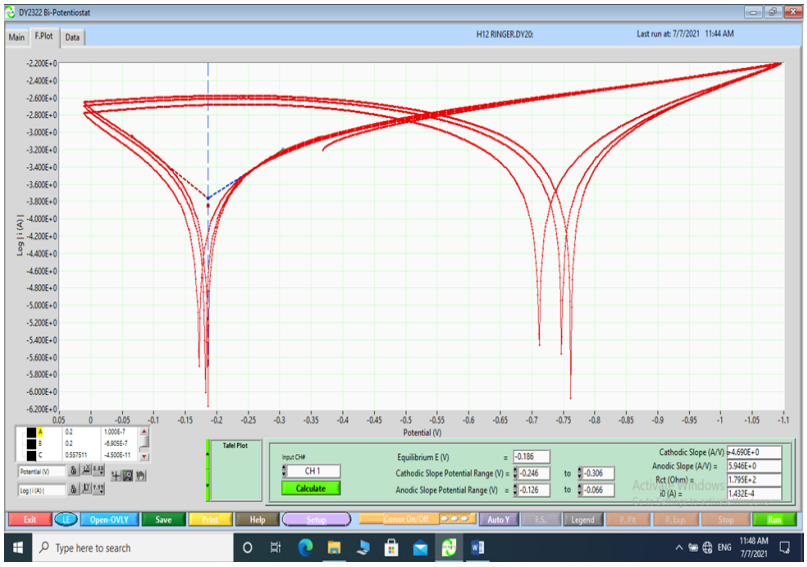
DY2322 Bi-Potentiostat
Main
F-Plot
Data
H12 RINGER.DY20:
Last run at: 7/7/2021 11:44 AM
Log | i (A) |
Potential (V)
Tafel Plot
Input CH#
CH 1
Calculate
Equilibrium E (V) = -0.186
Cathodic Slope Potential Range (V) = -0.246 to -0.306
Anodic Slope Potential Range (V) = -0.126 to -0.066
Cathodic Slope (A/V) = -4.690E+0
Anodic Slope (A/V) = 5.946E+0
Rct (Ohm) = 1.795E+2
i0 (A) = 1.432E-4
Exit
Open-OVLY
Save
Print
Help
Auto Y
Legend
Run
Type here to search
ENG
11:48 AM
7/7/2021

الخلاصة :

تهدف هذه الدراسة إلى استخدام سبيكة تيتانيوم Ti-6Al-7Nb في التطبيقات الطبية. هذه السبيكة لها تطبيقات واسعة على رغم من أن التيتانيوم وسبائكه ذات مقاومة البلى ضعيفة وصلادة قليلة لذا فأن طريقة الأكسدة الميكروية وهي طريقة غير تقليدية (كيمائية / كهروكيميائية) لترسيب طبقات السيراميكية سميكة في محلول مائي يحتوي على عناصر معدلة من خلال تطبيق جهد الانهيار . وبصورة عامه تم أجراء العديد من المحاولات لدراسة تأثيرات المضافات الكيميائية وأنماط التيار في تحسين الطلاء السيراميكي .

تم استخدام أضافات نانوية مثل الهيروكسي ابايت واكسيد الزركونيوم في عملية الترسيب وبعد عدة تجارب تم اعتماد أربع مجاميع من المحاليل الألكترولتيه. وتمت العملية بتراكيز مختلفة من الاضافات الطبيعية والنانوية في ظروف الفولتية المختلفة (300, 350, and 400)V والتيار (1-5)A وبأزمان ترسيب (7, 15, 30, and 60)min بواسطة منظومه طلاء محلية الصنع. عدة فحوصات جرت لجميع النماذج مثل فحوصات البنية المجهرية (FE-SEM) لمعرفه تضاريس السطحية وسمك طبقة الطلاء وفحص حيود بالأشعة السينية (XRD) والتحليل الطيفي (EDX) وأختبار (AFM) لرؤية البنية المورفولوجيا وطوبوغرافية للطلاءات والخشونة وأختبار الصلادة والبلى وزاوية التبلل (Wetting angle) وكذلك أختبار التأكل باستعمال الاستقطاب والدوري وأختبار تحرر أيونات وتصرف البكتريا المعروفه بال *E.coli* لدراسة طبقة الطلاء .

نتائج الاختبارات أوضحت : أمكانية ترسيب طلاءات السيراميكية على سطح سبيكة (Ti-6Al-7Nb) باستخدام الاضافات وظروف مختلفة فولتية وزمن ترسيب. تم حصول على طبقة سيراميكة من أوكسيد التيتانيوم (TiO_2) الذي يتكون على سطح خلال عملية الطلاء مسامية ومتجانسة في مجموعه A وذات صلادة عالية (311.5HV) عند عينة (350V & 30min)ومقاومة البلى حيث أدت الى فقدان بالوزن ونقصان معدل البلى (9.46×10^{-6}) وتأكل ممتازة تصل الى معدل التأكل (0.1114mpy) ومقدار تحرر أيونات أقل من سبيكة الاساس افضل مقارنه بالسبيكة غير مطلية ومع زيادة في الفولتية وزمن الترسيب أدت الى زيادة سمك الطبقة الى (56µm) وزيادة في المسامية والخشونة وزيادة قابلية الترطيب .

الطبقة مركبة سيراميكة من هيدروكسي ابايت (HA) وأكسيد التيتانيوم (TiO_2) في مجموعة B, طبقة من أوكسيد الزركونيوم (ZrO_2) وأكسيد التيتانيوم (TiO_2) في مجموعة C و الطبقة السيراميكه من هيدروكسي أبايت (HA) وأوكسيد الزركونيوم (ZrO_2) وأكسيد التيتانيوم (TiO_2) في مجموعة D حيث لوحظ مع زيادة في فولتية وزمن ترسيب يزداد سمك طبقة ويزيد من تركيز HA وZrO2 وتقل المسامية مقارنه بالمجموعة (أ) وبالتالي أفضل نتائج تم حصول عليها من حيث صلادة (368.1HV عند 300V و 30min) , (466.7HV عند 300V و 30min) و (584.9HV عند 300V و 15min) . مقاومة البلا تساوي (4.33×10^{-7} عند 300V و 30min) , (1.06×10-7 عند 300V و 30min) و (9.84×10-8 عند 300V و 15min) .

تحسين مقاومة التاكل لمحلولين بواسطة استقطاب والدوري تساوي (87.4% و 87.83 محلول رنكر واللعاب الصناعي على التوالي) , (94% و 88.13% في محلولين) و (88% و 91.12% في محلولين) و كذلك زيادة قابلية الترطيب بواسطة نقصان زاوية التلامس عند 300V و 30min .

كمية تحلل الايونات تقل مقارنتا بالسبيكة الاساس للمحلولين تساوي (0.0183PPm في محلول رنكر) و (0.0191 ppm في اللعاب الصناعي) لطلاء TiO_2 و (0.0074PPm في محلول رنكر) و (0.0077ppm في اللعاب الصناعي) لطلاء HA/TiO_2 و طلاء ZrO_2/TiO_2 تصل (0.0066ppm في محلول رنكر) و (0.0048ppm في اللعاب) وفي الطلاء النانوي المركب $HA/ZrO_2/TiO_2$ (0.0017ppm و 0.0011ppm) لكلا المحلولين .

طلاء ZrO_2/TiO_2 و $HA/ZrO_2/TiO_2$ تكون مضادة جدا للبكتريا وتمنع نمو البكتريا .

جمهوريه العراقية
وزارة التعليم العالي والبحث العلمي
جامعة بابل
كلية هندسة المواد
قسم هندسة المعادن

التحسين السطحي لسبيكة Ti-6Al-7Nb الحياتية باستخدام طلاءات حياتية سيراميكية بطريقة الاكسدة المايكروية (MAO)

اطروحة

مقدمة إلى قسم هندسة المعادن في كلية هندسة المواد/ جامعة بابل كجزء من متطلبات نيل درجة الدكتوراه فلسفة في هندسة المواد/ معادن

من قبل

قبس خالد ناجي صالح

بكالوريوس هندسة مواد (2013)
ماجستير هندسة مواد (2016)

بإشراف

أ.د. جاسم محمد سلمان المرشدي
أ.د. نوال محمد داود

2022م 1443هـ